



**HAL**  
open science

# Contribution to the design and fabrication of a Stirling cycle thermal micromachine with stirling cycle

Alpha Dassimou Diallo

► **To cite this version:**

Alpha Dassimou Diallo. Contribution to the design and fabrication of a Stirling cycle thermal micromachine with stirling cycle. Electric power. Université Bourgogne Franche-Comté, 2019. English. NNT : 2019UBFCD035 . tel-02500736

**HAL Id: tel-02500736**

**<https://theses.hal.science/tel-02500736v1>**

Submitted on 6 Mar 2020

**HAL** is a multi-disciplinary open access archive for the deposit and dissemination of scientific research documents, whether they are published or not. The documents may come from teaching and research institutions in France or abroad, or from public or private research centers.

L'archive ouverte pluridisciplinaire **HAL**, est destinée au dépôt et à la diffusion de documents scientifiques de niveau recherche, publiés ou non, émanant des établissements d'enseignement et de recherche français ou étrangers, des laboratoires publics ou privés.

**THESE DE DOCTORAT DE L'ETABLISSEMENT UNIVERSITE BOURGOGNE FRANCHE-COMTE  
PREPAREE A L'INSTITUT DE RECHERCHE FEMTO-ST**

Ecole doctorale n°37

Ecole Doctorale SPIM

Doctorat de Sciences pour l'ingénieur

Par

**M. Alpha Dassimou DIALLO**

**CONTRIBUTION A LA CONCEPTION ET A LA REALISATION D'UNE MICROMACHINE THERMIQUE A CYCLE  
DE STIRLING**

Thèse présentée et soutenue à Besançon, le 11 Octobre 2019.

Composition du Jury:

M. Skandar BASROUR	Professeur, Univ. Grenoble	Président
Mme Lavinia GROSU	MCF HDR, Univ. Paris Nanterre	Rapporteur
M. Tarik BOUROUINA	Professeur, Univ. Paris-Est	Rapporteur
Fabien FORMOSA	Professeur, Univ. Savoie Mont Blanc	Examinateur
Michel DE LABACHELERIE	DR CNRS, FEMTO-ST	Directeur de thèse
François LANZETTA	Professeur, Univ. FC, FEMTO-ST	Codirecteur de thèse
Magali BARTHES	MCF, Univ. FC, FEMTO-ST	Co-encadrante de thèse
Sylvie BEGOT	MCF HDR, Univ. FC, FEMTO-ST	Co-encadrante de thèse

# SPIM

## Thèse de Doctorat

UFC

école doctorale sciences pour l'ingénieur et microtechniques  
UNIVERSITÉ DE FRANCHE-COMTÉ

**DOCTORAL THESIS OF THE UNIVERSITY OF BOURGOGNE FRANCHE-COMTE**

**PREPARED AT THE FEMTO-ST RESEARCH INSTITUTE**

Title

**CONTRIBUTION TO THE DESIGN AND CONSTRUCTION OF A THERMAL  
MICROMACHINE WITH STIRLING CYCLE**

Author

**M. Alpha Dassimou DIALLO**

**Composition of the Jury:**

M. Skandar BASROUR	Professeur, Univ. Grenoble	Président
Mme Lavinia GROSU	MCF HDR, Univ. Paris Nanterre	Rapporteur
M. Tarik BOUROUINA	Professeur Univ. Paris-Est	Rapporteur
Fabien FORMOSA	Professeur, Univ. Savoie Mont Blanc	Examinateur
Michel DE LABACHELERIE	DR CNRS, FEMTO-ST	Directeur de thèse
François LANZETTA	Professeur, Univ. FC, FEMTO-ST	Codirecteur de thèse
Magali BARTHES	MCF, Univ. FC, FEMTO-ST	Co-encadrante de thèse
Sylvie BEGOT	MCF HDR, Univ. FC, FEMTO-ST	Co-encadrante de thèse

---

*À Dieu, qui a enjoint à l'Homme de la bonté envers ses père et mère : sa mère l'a péniblement porté et en a péniblement accouché ; et sa gestation et sevrage durent trente mois.*

*À mes parents, Amadou Kindy et Fatimatou Diallo, comme ils m'ont élevé tout petit alors que je n'étais rien. Toute ma fortune restera également le fruit de vos efforts. Dieu seul sait combien je vous aime.*

*À ma tante Diamilatou Bah, la femme courageuse qui a participé à mon éducation, puis, malheureusement, s'en est allée au ciel trop tôt. Comme j'aurai aimé que tu puisses goûter à ma réussite.*

*À ma femme Hassatou Diallo, si tendre épouse, plein de courage, d'ambition et de patience. Et reconnaissante envers ses parents. Que ton père, qui ma fait confiance, trouve ici toute ma gratitude.*

*À ma fille Mariam, princesse de mon cœur et la joie de mes yeux, cette réussite t'appartient. Ta venue au monde pendant la thèse a rechargé les batteries de ma détermination.*

---

## **REMERCIEMENTS**

*Toutes ma reconnaissance et mes remerciements vont d'abord à Celui qui,  
Gratuitement, m'a créé, m'a mis dans une voie de paix et fait battre mon cœur continuellement.  
« O Seigneur! Inspire-moi pour que je rende grâce au bienfait dont Tu m'as comblé ainsi qu'à mes père et mère,  
et pour que je fasse une bonne œuvre que Tu agrées. Et fais que ma postérité soit de moralité saine.  
Je me repens à Toi et je suis du nombre des Soumis ». (Coran : 46 :15)*

Cette thèse a été réalisée au sein du département **MN2S** (Micro Nano Sciences et Systèmes) de l'Institut **FEMTO-ST**. Je tiens à exprimer toutes ma gratitude à la région **Bourgogne Franche Comté** et l'**EUR EIPHI** (Ex Labex ACTION) pour le financement de ce travail. Je remercie Mr. Laurent **Larger** directeur de l'Institut, Mr. Wilfrid **Boireau** directeur du département **MN2S** ainsi que Mr. Christophe **Gorecki** directeur de l'équipe **MOEMS** et également Mme Thérèse **Leblois** directrice de l'école doctorale **SPIM** pour m'avoir accordé un bon accueil au sein de ce grand laboratoire de recherche pour réaliser mes travaux de thèse.

J'aimerais témoigner toute ma reconnaissance à Mme Lavinia **Grosu** et Mr. Tarik **Bourouina** pour l'intérêt qu'ils ont manifesté pour ma thèse en acceptant d'en être les rapporteurs. Je remercie également Mr. Skandar **Basrou** et Mr. Fabien **Formosa** d'avoir accepté d'en être les examinateurs. Merci pour vos questions et remarques constructives.

J'exprime ma profonde reconnaissance à Mr. Michel De **Labachelerie** d'avoir accepté de me confier cette thèse et d'en être le directeur. J'ai eu beaucoup de plaisir à travailler avec lui. Merci pour sa patience, sa grande contribution scientifique, son aide et ses conseils qui ont été d'une grande utilité pour réaliser et finir ce travail en temps voulu. Qu'il trouve ici l'expression de ma sincère reconnaissance.

J'adresse mes sincères remerciements à Mr. François **Lanzetta**, co-directeur de thèse et Mme Sylvie **Bégot** co-encadrante, pour leurs aides, conseils et leurs bonnes humeurs inébranlables. Cette thèse a pu être menée à bien grâce à leurs constantes contributions.

*Eh! ouais!* comment pourrais-je oublier Mme **Magali Barthès** co-encadrante de la thèse, qui m'a aidé dès mes premiers jours à m'adapter à la ville de Besançon. Je la remercie pour toutes ses suggestions de manips, la rigueur scientifique qu'elle a su m'inculquer avec pédagogie, ses conseils et remarques constructives et sa bonne humeur inaltérable qui m'ont permis de surmonter les difficultés rencontrées et faisant renaitre, à chaque fois, dans les moments de doute, ma motivation et ma détermination tout au long de cette thèse. Ton humilité et ta magnanimité m'ont permis de me remettre en question afin de remodeler mes qualités humaines.

Je ne remercierai jamais assez Mr. Ravinder **Chutani** pour son aide notamment les techniques de microfabrication méticuleux qu'il a su me transmettre et de m'avoir donné les premières formations en salle blanche. Merci également à Olivier **Gaiffe** et Nicolas **Passilly** pour leurs contributions scientifiques et leurs conseils.

Je voudrais aussi souligner les importantes contributions de Mr. Xavier **Gabrien** et Mr Vincent **Placet** du département de mécanique Appliqué (**DMA**), ainsi que Mr. Muamer **Kadic**, Mr. Jean-Marc **Cote**, Mr. Franck **Lardet-Vieudrin**, Mr. Emmanuel **Dordor**, Mr. Ludovic **Gautier** du Département **MN2S** et Mr. Eric **Andrey** du département Temps Fréquence (**TF**), Mr Franck **Cholet**, Mr. Sébastien **Euphrasie**, Mr. Jean-françois **Manceau**, Mr. Frédéric **Cherieux** pour avoir toujours eu la porte de leurs bureaux ouvertes pour moi et pour tous leurs conseils et idées précieuses sans lesquels je ne serais jamais arrivé au bout de ce travail, surtout en ce qui concerne la réalisation des bancs de caractérisations et bien d'autres choses.

Une thèse sur la microfabrication d'une micromachine comme celle-là contient une partie technologique MEMS très importante, c'est pourquoi je voudrais particulièrement remercier tout le personnel de la salle blanche **MIMENTO**, et mention spéciale à Laurent **Robert**, Sylwester **Barguiel** et Florent **Bassignot** pour toutes leurs aides, formations et conseils, sans lesquels, je n'aurais jamais réussi à accomplir la réalisation de cette micromachine complexe.

Mes pensées vont aussi aux bons moments partagés avec mes collègues de bureau (José **Carrión Pérez**, Stéphane **Perrin**, Vincent **Maurice**, Quentin **Tanguy**) les remercier pour l'ambiance amicale et les discussions sympathiques que nous avons pu avoir. Et également, tous les doctorants que j'ai connus au laboratoire pour les

---

remercier pour l'ambiance amicale, les discussions sympathiques et l'entraide. Mes pensées vont également à Mr. Etienne **Coffy** et Mr. Souleymane **Diallo**, vos conseils et vos aides ont été précieux.

Je remercie aussi Patricia **Gorecki**, Sophie **Marguier** pour leurs aides et les discussions sympathiques que nous avons pu avoir. Mention spéciale à Mme Sandrine **Chatrenet**, Mme Sandrine **Pyon**, Mme Valérie **Fauvez** et Mme Ayoko **Afanou** pour leurs aides et soutient dans les tâches administratives pendant cette thèse.

Je tiens à remercier Mme Aude **Bolopion** qui a bien voulu me recruter en tant qu'ingénieur après la fin des trois années de mon contrat de thèse et qui m'a accordé du temps pour préparer la soutenance de cette thèse. Qu'elle trouve ici toute ma reconnaissance pour sa confiance.

Toute ma reconnaissant à tous ceux qui ont contribué à établir un environnement de travail plaisant et encourageant et ont bien voulu partager leur savoir avec humilité. Enfin, toutes mes excuses aux personnes que j'aurai oublié dans mes remerciements.

---

## TABLE OF CONTENTS

<b>TABLE OF CONTENTS</b> .....	<b>6</b>
<b>LIST OF SYMBOLS AND ACRONYMS</b> .....	<b>10</b>
<b>RÉSUMÉ</b> .....	<b>11</b>
<b>ABSTRACT</b> .....	<b>12</b>
<b>INTRODUCTION</b> .....	<b>13</b>
<b>CHAPTER 1 : CONTEXT AND LITERATURE REVIEW</b> .....	<b>14</b>
1.1. Context of the thesis.....	15
1.1.1. Project history and context .....	15
1.1.2. Objectives of this thesis.....	17
1.2. Vibrational Energy Harvesting and transducers .....	18
1.3. Stirling motors .....	19
1.3.1. Principle and thermodynamic cycle .....	19
1.3.2. Stirling motor architectures.....	21
1.3.3. Modeling the operation of Stirling motors.....	24
1.4. Small scale devices with internal combustion.....	27
1.5. Small scale devices (motors and harvesters) without internal combustion .....	34
1.5.1. Non-Stirling type: micro-devices and heat harvesting .....	35
1.5.2. Stirling motors and their miniaturization approach .....	38
1.6. Conclusion .....	44
<b>CHAPTER 2 : STIRLING ENGINE DESIGN CHALLENGES</b> .....	<b>46</b>
2.1. Mechanical and design challenge.....	46
2.1.1. Pistons versus membranes .....	46
2.1.2. Mechanical connection challenge .....	47
2.1.3. Ratio between mechanical powers output and micromachine Stirling sizes.....	47
2.1.4. Swept volume: design of the membrane .....	48
2.1.5. Confinement of the membrane.....	49
2.1.6. Membrane: mechanical properties and influence on motor performances.....	53
2.1.7. Membranes final design and chosen materials.....	57
2.1.8. Minimizing dead volumes in Expansion and compression chambers .....	60
2.2. The micro-motor architecture importance .....	61
2.2.1. 1-D Architecture .....	61
2.2.2. 2D architecture .....	61
2.2.3. 3D architecture .....	62
2.3. Thermal Challenges .....	63
2.3.1. Conduction.....	64
2.3.2. Convection.....	64

2.3.3.	Radiation.....	65
2.3.4.	The heat transfer coefficient of a stack.....	65
2.3.5.	Thermal study of the 2D and 3D configurations.....	66
2.4.	Microfluidic Challenge.....	72
2.4.1.	Characteristic length: the hydraulic diameter.....	73
2.4.2.	The different gas flow regimes.....	73
2.4.3.	Alternating flows and associated dimensionless number.....	74
2.4.4.	Friction coefficient and pressure drop.....	80
2.5.	The chosen design of the micro Stirling motor.....	84
2.5.1.	The MISTIC design.....	84
2.5.2.	Dead space: the influence of the regenerator design.....	86
2.5.3.	Summary.....	88
2.6.	Conclusion.....	89
<b>CHAPTER 3 : MICRO-ENGINE MANUFACTURING .....</b>		<b>90</b>
3.1.	Cleanroom methods introduction.....	91
3.1.1.	Lithography technique.....	91
3.1.2.	Thin film deposition techniques onto silicon and glass.....	91
3.1.3.	Physico-chemical etching with inhibitor or DRIE.....	92
3.2.	Microfabrication.....	92
3.2.1.	Compression and Expansion Chambers.....	93
3.2.2.	Membranes.....	94
3.2.3.	Microfabrication of the glass thermal insulation part.....	97
3.2.4.	Assembly of the different parts of the micro machine.....	101
3.2.5.	Different versions of fabricated micromachines.....	106
3.3.	Study of room temperature thermocompression.....	107
3.4.	Conclusion.....	116
<b>CHAPTER 4 : MEMBRANES CHARACTERIZATIONS AND RESULTS.....</b>		<b>117</b>
4.1.	The RTV-silicone.....	118
4.2.	Characterization of RTV-Silicone layer mechanical properties.....	119
4.2.1.	Stress and Strain.....	119
4.3.	Stress-Strain relationship: Young modulus.....	120
4.4.	Hysteresis.....	121
4.5.	Characterization of RTV-silicone material by tensile tests: influence of thickness.....	122
4.5.1.	Tensile tests setup.....	122
4.5.2.	Tensile test results and discussions.....	124
4.6.	Characterizations of single membranes: static pressure measurement.....	126
4.6.1.	Uniformly loaded circular membrane.....	127
4.6.2.	Center-loaded circular membrane.....	131
4.7.	Characterizations of Membrane: dynamic tests.....	135
4.7.1.	Materials and methods.....	135



4.7.2.	Results and discussion .....	137
4.8.	Influence of thermal treatment on membranes properties.....	139
4.8.1.	Thermal bench.....	140
4.8.2.	Mass Bench.....	141
4.8.3.	Study methodology.....	141
4.8.4.	Results: effect of the temperature on the membranes .....	141
4.9.	Conclusion .....	146
<b>CHAPTER 5 : CHARACTERIZATIONS OF THE STIRLING MICRO-MACHINE .....</b>		<b>147</b>
5.1.	Stirling micro-machine instrumentation difficulties.....	147
5.2.	Static displacement of hybrid membranes in corresponding chambers.....	148
5.3.	Schmidt simulation for the MISTIC micro-machine.....	150
5.4.	Hybrid Membranes Pistons: liquid and solid connections .....	153
5.5.	Temperature measurements: Platinum resistance thermometer calibration.....	156
5.6.	Motor mode.....	157
5.6.1.	Test bench for the motor mode .....	158
5.6.2.	Experimental results for the motor mode.....	160
5.7.	Cooling Mode.....	161
5.7.1.	Test bench for the cooling mode.....	161
5.7.2.	Experimental results for the cooling mode .....	162
5.7.3.	Possible explanations for the problems encountered with the fabricated 3-phases micro-machine and perspectives for a simpler test architecture.....	167
5.7.4.	Conclusion .....	169
<b>CONCLUSION .....</b>		<b>170</b>
1.1.	Comparisons of various energy harvesters .....	171
1.2.	Comparison of energy harvester architecture .....	171
1.3.	Piezoelectric transducers: state-of-the-art devices and materials.....	173
1.3.1.	PZT thin films .....	174
1.3.2.	AlN thin films .....	174
1.4.	Electromagnetic transducers.....	175
<b>APPENDIX B: STIRLING MOTOR.....</b>		<b>176</b>
1.1.	Carnot efficiency.....	176
1.2.	Advantages and disadvantages of Stirling motors .....	177
1.2.1.	- Advantages .....	177
1.2.2.	Disadvantages.....	178
1.3.	Schmidt model.....	178
1.3.1.	Zero order analysis .....	178
1.3.2.	First order analysis or Ideal Isothermal Analysis .....	179
1.3.3.	Second order analysis or Ideal Adiabatic Analysis.....	185
<b>APPENDIX C : MICROFLUIDICS .....</b>		<b>188</b>
1.1.	For permanent flows .....	188

---

1.1.1.	Effect of low Reynolds number in Microsystems .....	188
1.1.2.	hydrodynamic resistance notion .....	188
1.1.3.	hydrodynamic capacity notion .....	189
1.1.4.	The bottleneck effects .....	190
1.1.5.	Fluid-structure interaction.....	192
1.2.	Permanent Vs Alternate flows.....	194
1.2.1.	Permanent Flow.....	194
1.2.2.	Alternate flow at $\Delta T = 0^{\circ}C$ .....	194
1.2.3.	Alternate flow at $\Delta T = 40^{\circ}C$ .....	195
1.3.	Oscillating flow pressure drop coefficient.....	196
<b>APPENDIX D: MEMS MANUFACTURING TECHNIQUES.....</b>		<b>199</b>
1.1.	Use of MEMS technologies: environment, materials used and limitations .....	199
1.2.	The clean room environment .....	199
1.4.	MEMS scales .....	199
1.5.	Basic material in clean room .....	199
1.5.1.	Hard technologies.....	200
1.5.2.	Soft technologies .....	201
1.6.	Photolithography method .....	202
1.7.	Thin film Deposition techniques onto silicon and glass .....	203
1.8.	Etching techniques of silicon and glass .....	204
1.9.	Bonding techniques .....	206
<b>BIBLIOGRAPHY.....</b>		<b>209</b>

## LIST OF SYMBOLS AND ACRONYMS

Symbol	Definitions	units
Cp	Specific heat	[J.kg <sup>-1</sup> .K <sup>-1</sup> ]
D <sub>h</sub>	Hydraulic diameter	[m]
Ec	Eckert number	[-]
k <sub>B</sub>	Boltzmann constant (=1.38064852 10 <sup>-23</sup> )	[J.K <sup>-1</sup> ]
L	Length	[m]
Lc	Characteristic length	[m]
M	Molecular weight	[g.mol <sup>-1</sup> ]
Ma	Mach number	[-]
P	Pressure or Power	[Pa]  [W]
Pr	Prandtl number	[-]
R	Ideal gas constant (=8.314462)	[J.K <sup>-1</sup> .mol <sup>-1</sup> ]
r	Specific gas constant Or radius	[J.K <sup>-1</sup> .kg <sup>-1</sup> ]  [m]
Re	Reynolds number	[-]
Re <sub>ω</sub>	Kinetic Reynolds number	[-]
r <sub>h</sub>	Hydraulic radius	[m]
T	Temperature	[K]
t	Time	[s]
U (or u)	Velocity	[m.s <sup>-1</sup> ]
V	Volume	[m <sup>3</sup> ]
Va	Valensi number	[-]
Wo	Wormesley number	[-]
x	distance	[m]
Ra	Rayleigh number	[-]
e	Thickness	[m]
S	Surface	[m <sup>2</sup> ]
h	height	[m]
d	diameter	[m]

Greek letter	Definitions	units
α	Thermal diffusivity	[m <sup>2</sup> .s <sup>-1</sup> ]
Γ	Wet perimeter	[m]
ε	Emissivity Or porosity	[-]  [-]
η	Dynamic viscosity	[Pa.s]
λ	Thermal conductivity	[W.m <sup>-1</sup> .K <sup>-1</sup> ]
λ <sub>M</sub>	Mean free path	[m]
ν	Kinematic viscosity	[m <sup>2</sup> .s <sup>-1</sup> ]
ρ	Density	[kg.m <sup>-3</sup> ]
φ	Heat flux	[W.m <sup>-2</sup> ]
ω	Angular frequency	[rad.s <sup>-1</sup> ]

## RÉSUMÉ

**Titre : Contribution à la conception et à la réalisation d'une micro-machine thermique à cycle de Stirling**

**Mots clés :** micromachine, stirling, membranes hybrides, salle blanche, MEMS

En France, on estime que plus de 27 TWh de chaleur à une température comprise entre 100 et 200°C sont perdus chaque année. La récupération de cette chaleur perdue est donc un enjeu important pour réduire la consommation globale d'énergie. La récupération de la chaleur peut se faire à l'aide de machines de Stirling, qui sont des machines thermodynamiques réversibles convertissant la chaleur en mouvement mécanique - lequel pourrait ensuite être converti en électricité - à partir de deux sources de température suffisamment différentes. La récupération de la chaleur produite par les systèmes électroniques pourrait être faite avec une machine de Stirling miniaturisée capable de produire de l'électricité à partir de n'importe quelle source de chaleur. Une telle micro-machine peut aussi fonctionner en mode "réfrigérateur" (transport de la chaleur d'une source chaude vers une source froide grâce à un travail mécanique) et pourrait être utilisée pour refroidir des composants électroniques. Le rendement énergétique des machines Stirling peut atteindre 38% (avec une source chaude à 200°C) et leur entretien est réputé être minimal. Cependant, aucune machine Stirling n'a encore été démontrée avec un volume inférieur à un centimètre cube. En 2015, une architecture de micromachine Stirling triphasée pouvant être miniaturisée grâce aux technologies MEMS a été proposée et testée avec succès en macro-volume (avec une taille d'une vingtaine de centimètres). Le présent travail de thèse a été consacré à la miniaturisation de ce nouveau concept de micromachine Stirling pour la récupération de chaleur entre 50 et 200°C, en utilisant les technologies MEMS. Cette approche permettrait la production simultanée de grandes quantités de micro-machines et donc la création éventuelle de réseaux de micromachines à faible coût par watt d'électricité produite.

Les micromachines sont constituées d'un empilement de tranches de silicium et de verre. Leurs défis de conception ont été étudiés en détail et leur puissance mécanique de sortie attendue a été estimée. Les procédés de fabrication nécessaires ont été développés et la caractérisation de chaque élément a été effectuée avant l'assemblage. Elles comportent notamment des membranes hybrides de 5 mm de diamètre et de 200 microns d'épaisseur qui jouent le rôle des pistons en micro-volumes et sont des éléments clés de la micro-machine. Ces membranes sont constituées de pièces en silicium (spirales et disques) noyées dans une membrane souple en élastomère de silicone dont les propriétés mécaniques ont donc été étudiées en détail. Des simulations numériques du comportement mécanique et dynamique de ces membranes hybrides ont été présentées. L'accord entre les simulations numériques et les caractérisations a été considéré comme très satisfaisant. Ces membranes se sont révélées très robustes et le déplacement de leur centre peut atteindre 1 à 2 mm sans dommage. Leurs fréquences de résonance vont de 850 Hz à 2800 Hz et il a été montré qu'elles peuvent fonctionner à 200°C sans vieillissement. De plus, l'optimisation d'un procédé d'assemblage par thermocompression d'or (Au) a permis d'obtenir des contraintes de rupture en traction d'environ 20 à 30 MPa, parmi les meilleures rapportées dans la littérature. Des prototypes de micromachines triphasées de 20x20x8mm ont été assemblés, mais leur fonctionnement en mode moteur n'a pas pu être observé, même pour une différence de température de 100 °C. Cependant, en insérant des aimants pour provoquer le déplacement des membranes par excitation électromagnétique, il a été possible d'observer un effet de refroidissement encourageant. Grâce aux travaux réalisés, les principaux éléments de base sont maintenant disponibles et devraient permettre des optimisations ultérieures dans des conditions beaucoup plus favorables.

---

## **ABSTRACT**

**Titre: Contribution to the design and construction of a Stirling cycle thermal micromachine.**

**Mots clés:** micromachine, stirling, hybrid membranes, clean room, MEMS

In France, it is estimated that more than 27 TWh of heat at a temperature between 100 and 200°C is lost each year. The recovery of this lost heat is therefore an important issue in reducing overall energy consumption. Heat recovery can be done using Stirling machines, which are reversible thermodynamic machines that convert heat into mechanical motion, which could then be converted into electricity from two sufficiently different temperature sources. The recovery of the heat produced by electronic systems could be done with a miniaturized Stirling machine capable of producing electricity from any heat source. Such a micro-machine can also operate in "refrigerator" mode (transporting heat from a hot source to a cold source through mechanical work) and could be used to cool electronic components. The energy efficiency of Stirling machines can reach 38% (with a hot source at 200°C) and their maintenance is considered minimal. However, no Stirling machine has yet been demonstrated with a volume of less than one cubic centimeter. In 2015, a three-phase Stirling micromachine architecture that can be miniaturized using MEMS technologies has been proposed and successfully tested in macro-volume (with a size of about twenty centimeters). The present thesis work was devoted to the miniaturization of this new Stirling micromachine concept for heat recovery between 50 and 200°C, using MEMS technologies. This approach would allow the simultaneous fabrication of large quantities of micro-machines and thus the possible creation of micromachine networks at low cost per watt of electricity produced.

The studied micromachines are made up of a stack of silicon and glass wafers. Their design challenges have been studied in detail and their expected mechanical output power has been estimated. The necessary manufacturing processes were developed and the characterization of each element was carried out prior to assembly. In particular, they include hybrid membranes 5 mm in diameter and 200 microns thick that act as micro-volume pistons and are key elements of the machine. These membranes are made up of silicon parts (spirals and discs) embedded in a flexible silicone elastomer membrane whose mechanical properties have therefore been studied in detail. Numerical simulations of the mechanical and dynamic behavior of these hybrid membranes were presented. The agreement between the numerical simulations and the characterizations was considered to be very satisfactory. These membranes proved to be very robust and the displacement of their center can reach 1 to 2 mm without damage. Their resonance frequencies range from 850 Hz to 2800 Hz and it was shown that they can operate at 200°C without aging. In addition, the optimization of a gold thermocompression assembly process has resulted in tensile breaking stresses of about 20-30 MPa, among the best reported in the literature. Prototype of 20x20x8mm three-phase micromachines were assembled, but their operation in motor mode could not be observed, even for a temperature difference of 100°C. However, when magnets were inserted to induce the displacement of the membranes by electromagnetic excitation, it was possible to observe an encouraging cooling effect. As a result of the work carried out, the main basic elements are now available and should allow further optimization under much more favorable conditions.

---

## INTRODUCTION

In the context of the development of connected sensors that will be used in the billions to accurately track pollution, reduce energy consumption, optimize machines operations or manage the home, it will be necessary to have energy recovery systems in the vicinity of the sensors to avoid managing thousands of connections to the electricity grid (i. e. microgeneration of energy). These energy recovery systems can of course convert solar energy when possible, but also recover energy from mechanical vibrations (when the collectors are installed on transport systems for example) or use any other energy source available near the sensor (e. g. glucose batteries to power collectors located in the human body). Among these various possibilities, thermal energy recovery is an option that may be of interest in a number of cases (waste heat recovery in electrical systems, automotive exhaust pipes, etc.). The purpose of this thesis is to study thermal energy recovery solution using Stirling machines capable of converting heat that has been lost until now into electricity.

Stirling machines are thermodynamic machines with external heat supply, which allows them to operate with a wide variety of heat sources (waste heat recovery, solar heat or renewable energy). In addition, their energy efficiency can be excellent and their maintenance minimal, which is why they are used in high-end applications such as space technologies for example. In "motor" mode, these machines produce a mechanical movement from two sources of sufficiently different temperatures. In "refrigerator" mode, they allow heat to be transported, from a mechanical work, between a cold source and a hot source and, thus, to cool the cold source.

The main obstacle to the use of these machines in the micro-energy generation sector is the difficulty of their miniaturization. Indeed, most of the attempts to make Stirling micro-machines have ended in failure without being able to identify their exact causes. In 2015, the subject was relaunched following a proposal for a Stirling micromachine architecture which could be miniaturized using MEMS technologies and which was first successfully tested in macro-volume (with a size of around twenty centimeters). The miniaturization of this architecture was the subject of the ANR "MISTIC (Micro-STirling Clusters)" project, and in this context the FEMTO-ST institute was responsible, on the one hand, for the optimization of micromachine regenerators and, on the other hand, for studying the technological aspects of micromachine production using MEMS-type technologies.

The thesis work presented in this manuscript is oriented towards this last objective, consisting in studying the various functional elements of the micromachine as well as their integration, in order to be able to carry out a first test of the complete microsystem.

This document is organized into 5 chapters:

- the first chapter aims to present the state of the art on thermal micromachines and in particular Stirling type ones
- the second chapter presents the challenges raised by the miniaturization of the machine and the choices made for its design
- the third chapter deals with the microfabrication issues raised by the constraints of micromachine production and the solutions that have been provided to them
- the fourth chapter focuses on a key element of the micromachine: the membranes that compress and circulate the gas inside the micromachine
- the last chapter presents the tests carried out on the assembled micromachines

## CHAPTER 1 : CONTEXT AND LITERATURE REVIEW

Numerous facts, such as the current energy crisis, its impact on the economy, the increase in the price of a barrel of oil, the decline in hydrocarbon and nuclear fuel reserves and the need to reduce air pollution put the energy issue at the forefront of global emergency. From an economic point of view, a reliable source of energy is essential for the industrial progress that underpins the economic development of any country [1]. Concerning environmental pollution, existing batteries to date have their own environmental issues, and their production and disposal present an environmental hazard. In 2001, Tanaka [2] showed that only 17% of primary and less than 5% of rechargeable batteries were respectively correctly recycled. At the same time, the energy needs of the industry (ENI) continue to increase and represent more than 1/3 of the total energy consumed (TEC) in the industrialized countries. For example, in 2014 the ENI in France was 19.2% (Energy balance), 70% in China [3] and 33% in the USA [4]. The problem that must be emphasized is that 20 to 50% of this consumption is dissipated by conduction, convection and radiation from hot equipment or in the form of hot smoke, as this is the case in the USA [5]. In France, for example, it is estimated that more than 27 TWh of heat whose temperature is between 100 and 200°C is lost each year [5]. In the United Kingdom, it is estimated that 14 TWh / year is recoverable, which represents 4% of its annual energy consumption [5]. Moreover, in an internal combustion motor, it is estimated that 75% of the thermal energy generated during combustion is lost through the motor equipment [6]. Thus, the recovery of heat energy lost in different fields (*cf.* Figure 1-1) such as power plants, industries, electric or thermal motors, electronic components and so on, is an invaluable way to reduce the energy crisis. Other energy sources such as vibrations, water flow and airflow could be harvested [7]. Nowadays, the harvesting and conversion of these energies present in the environment plays a prominent role in the fight for both the reduction of hydrocarbon consumption and the autonomous and continuous energy supply of MEMS (Micro-electromechanical systems) devices (such as mobile phone devices, remote devices etc.) to achieve a long operating time. Therefore, self-powered systems that harvest their operating energy from the environment hold great promise to power future portable and wearable electronics. Some conversion techniques of energies available in the environment and soil (like hydrocarbons) are summarized in the Table 1-1 and they depend on the type of energy.

Type of natural energy present in the environment	Vibrations	Oils	Wind	Heat
Conventional means of conversion	Electromechanical Systems (EMS)	Thermal motors with internal combustion	Wind Turbines	Thermal Motors with External Heat input (TEEH) & thermoelectric materials (TEM)
Essentials components involved in harvesting	Mass, spring	Cylinder, pistons	Blades (helix)	Cylinder, pistons (for TEEH)
Essentials components involved in electrical conversion	Coil & magnet or piezoelectric material	Coil & magnet	Coil & magnet	Coil & magnet or a piezoelectric material (for TEEH)

Table 1-1 : The energies present in the environment and their traditional techniques of exploitation.

These different machines or techniques used to recover these energies require a material or a combination of materials to convert them into electric energy. In fact, usually, energies from the environment are first converted into mechanical energy, and then into electrical one. To do so, conventional machines can rely on, for instance, electromagnetic systems (a combination of magnet and electric coil). Electric energy is particular, in the sense that it is not a primary energy, *i.e.* it requires another energy to produce it. In addition, it is, in turn, used directly to produce light or heat and can be converted into mechanical energy by powering an electric motor or can also be used to produce some chemical reactions.

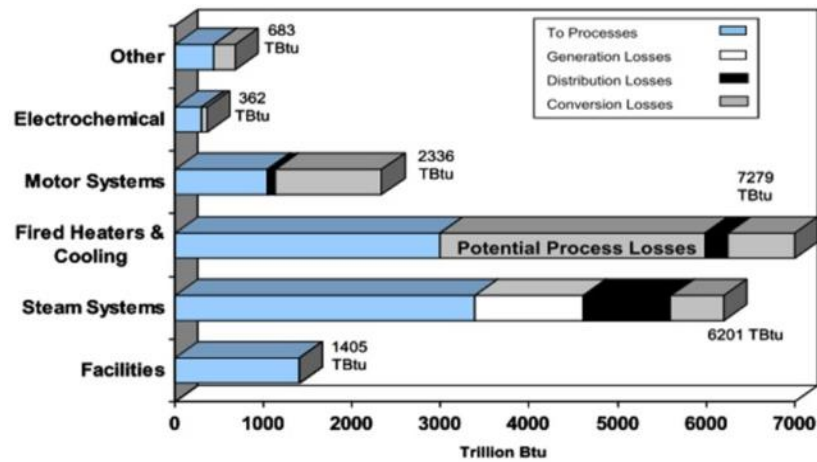


Figure 1-1 : Estimation of energy losses for major energy use areas in manufacturing according to the U.S. Department of Energy (Industrial Technology Programs estimated by Energetics Incorporated) [8].

This lost thermal energy is divided into three categories, defined as follows [4]:

- low temperatures when below 230 °C.
- average temperatures when between 230 and 650°C.
- high temperatures when above 650 °C.

One way of harvesting this energy (lost otherwise) is the use of Stirling motors. For instance, cogeneration systems are commercialized, consisting of a conventional boiler that provides heat to homes and a Stirling motor coupled to it that recovers heat losses to convert it into electricity [9]. A working prototype of a portable micro motor, such as a miniature Stirling motor, capable to generate electric energy from any natural source of heat in the environment (or industrial heat losses) could interest various industries such as automotive, aeronautics, microelectronics and telecommunications ones.

The aim of this PhD was to design a prototype of a miniature Stirling motor that could be used for heat energy harvesting. First, the general context of this work will be presented. In the case of miniaturized machines, three main transduction mechanisms are used to obtain electric energy: piezoelectric, electromagnetic and electrostatic ones. Some harvesters based on mechanical vibration will be shortly presented in the section 1.2. a more detailed presentation will be given in appendix A. Then a focus on the Stirling motor will be proposed, followed by a literature review of some power generation and energy harvesting device at small scales.

## 1.1. Context of the thesis

### 1.1.1. Project history and context

This PhD thesis, started in 2015, was part of the MISTIC (Micro STirling Clusters for low temperature heat recovery) ANR (National Agency of Research) project, which started in January 2013, (duration: 42 months)<sup>1</sup>. The project's partners were the SYMME institute (University of Savoie; project promoter), the FEMTO-ST Institute (University of Bourgogne Franche-Comté) and the UMI-LN2 institute (Universeurity of Sherbrooke). The project aimed to do a proof of concept of a Stirling micro-motor fabricated with MEMS technology's batch fabrication for the recovery of waste heat at low temperatures in industrial thermal processes, with a specific architecture, based on a meso-scale (tens of centimeters) motor develop at SYMME institute (*cf.* Figure 1-2).

The use of MEMS technologies (collective structuring and assembling) was chosen, since it will allow the implementation of clusters of this type of machines (as illustrated on the left in Figure 1-3) to reduce the cost per electric Watt generated.

A preliminary work was to build the meso-scale machine to validate the feasibility. Therefore, in 2013, the first 6 months of the project were devoted to the modelling and identification of manufacturing strategies. This work led

<sup>1</sup> This project is part of the ANR program named Systèmes Energétiques et Décarbonés (SEED)



to the production of an instrumented centimeter-scale Stirling motor (C-SE) at the SYMME laboratory, as shown in Figure 1-2. This motor architecture was inspired from a symmetric three-phase free-piston Stirling motor system developed by Der Minassians and Sanders (*cf.* Figure 1-4 [10]).

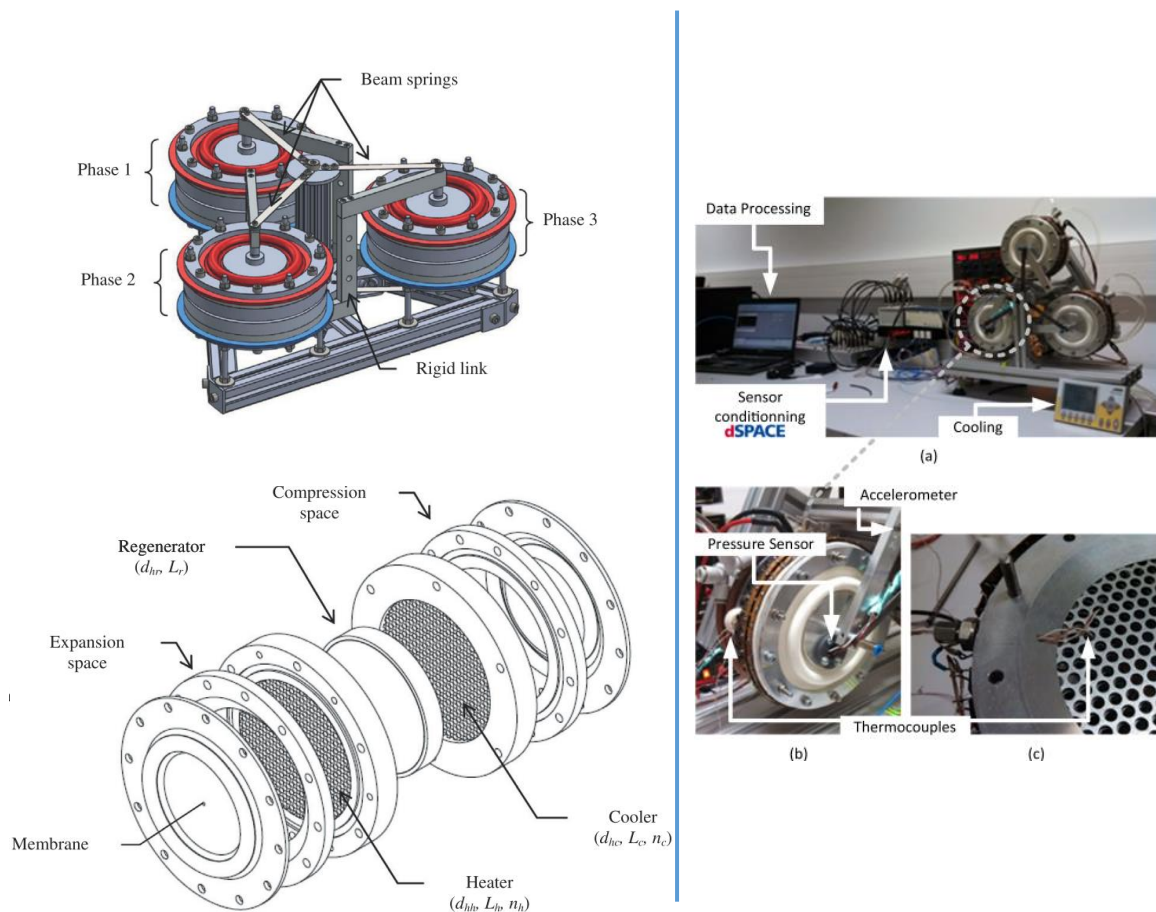


Figure 1-2 : On the left : the meso-scale Stirling motor design [11] and below the description of one module. On the right: a) Global view of the experimental setup and (b and c) close up of the motor instrumentation [5].

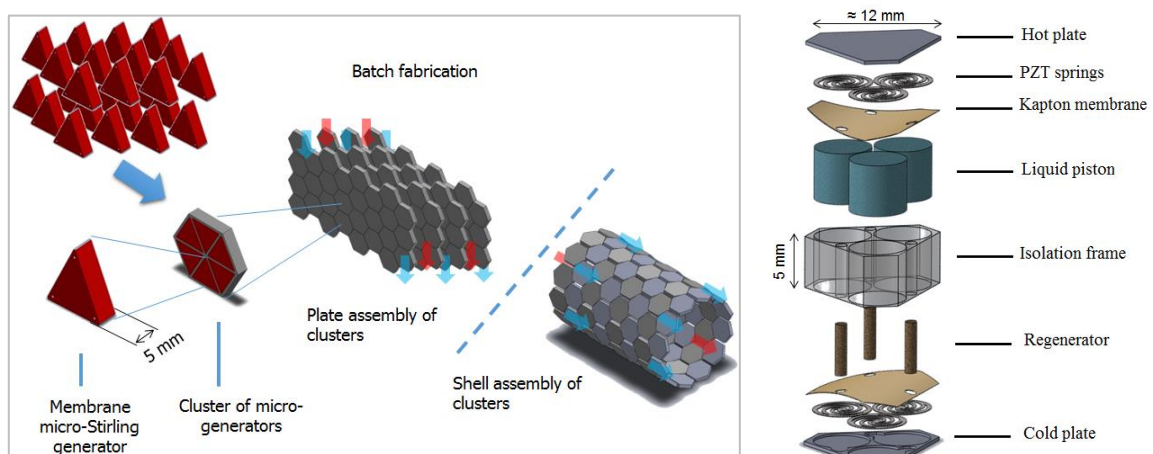


Figure 1-3 : Concept and general design of the MISTIC project. On the left are clusters schema and on the right the schematic view of the Stirling micromotor.[Images From ANR project MISTIC]

This architecture has many advantages, such as technological simplicity and reliability (such as a multiphase double acting membranes avoiding friction losses). In the C-SE, the connection between membranes was ensured by mechanical links and experimental measurements were to be used to validate those made with the micro machine after its microfabrication. Therefore, at first, a new design for the C-SE instrumentation became mandatory and

had to be built. The global initial design of the micro-Stirling motor for the MISTIC project, with its constitutive parts, is given in the right part of the Figure 1-3.

At the beginning of this PhD thesis in november 2015, the main scientific outputs were that, at the University of Savoie, a design tool based on an equivalent electrical network analogy has been proposed and validated in relation to the experimental results of the meso-scale Stirling motor [11].

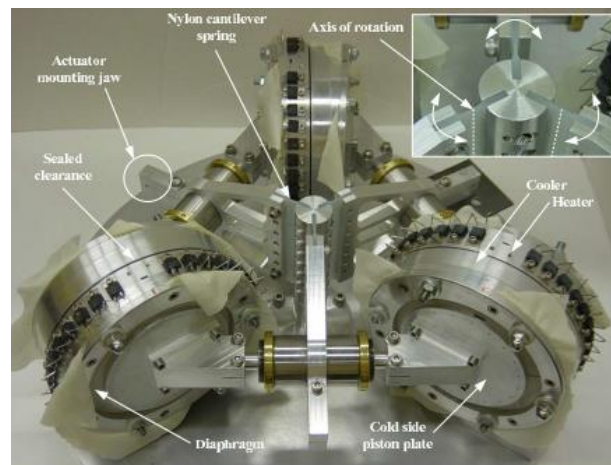


Figure 1-4 : Fabricated three-phase Stirling motor system of Der Minassians and Sanders [10].

Regarding the Stirling micro-motor, square membranes containing a liquid, with the aim of reducing their natural oscillation frequencies, have been designed, manufactured and dynamically characterized at the FEMTO-ST Institute [12]. A MEMS-based micro-regenerator to boost the Stirling micro-motor efficiency was also being designed and manufactured [13] at FEMTO-ST Institute.

### 1.1.2. Objectives of this thesis

The main objectives of this PhD were the design optimization, the microfabrication in the MIMENTO clean room facility and the characterization of the Stirling micromotor (based on the design given in Figure 1-3). Therefore, this work implies scientific and technological challenges linked to an motor size reduction.

Our contribution focused on all parts of the micro machine such as:

- a) The design part:
  - Improvement and optimization of the initial design of the membranes (shape, size, arrangement, resonance frequency):
    - Creation of a numerical model under COMSOL for the prediction of the stresses and the natural frequency of the membranes.
    - Design of test specimens to characterize the mechanical properties of the elastic material of the membranes.
  - Introduction of the location of thermal regenerators (under development in the FEMTO-ST ENERGY department)
  - Design of the micro chambers for compression and expansion of the membranes as well as their connecting channels.
  - Designing the new ducts for the liquid filling (for the intermembrane connection) and assembly steps of the motor to avoid several technological problems related to the contamination of the equipments (availables in FEMTO-ST clean room) encountered with a former geometry.
  - Identification of an efficient assembly technique and design of test samples
- b) The manufacturing part:
  - Fabrication of membranes for necessary complementary tests
  - Optimization of the membrane manufacturing process (repeatability, reproducibility) in a clean room.
  - Manufacture of compression and relaxation chambers
  - Integration and assembly, by the appropriate bonding methods, of all the constituent parts of the micro-machine (membranes, chambers, channels) to obtain the full micro motor.

c) The characterization part:

- Installation of thermal characterization benches (temperature resistance of membranes, *etc.*), dynamic (resonance frequency) and static (flexion or elasticity of membranes).
- Mechanical tests of membranes's material properties with dedicated machines.

The conversion part (mechanical motion into an electrical energy) was not the aim of this work. Thus we'll only shortly begin by presenting the means to harvest and convert mechanical energy. Then we'll focus on the Stirling motor principle followed by a literature review on works on miniature motor and/or harvesters.

## 1.2. Vibrational Energy Harvesting and transducers

Vibration sources are an attractive option for the development of adequate power sources for low power supplying or for the autonomy of remote sensors and portable electronics. The typical vibration frequencies are between 20 to 100 Hz [14], [15] and acceleration values greater than  $9.807 \text{ ms}^{-2}$  are very rare in environment and industrial applications. The estimated harvestable power is in the micro to milliWatt range [16]. Energy transducers are materials, or combinations of materials, that convert energy into another form of energy (usually electrical). The main transducers to obtain electrical energy from vibrations are piezoelectric, electromagnetic and electrostatic. Piezoelectric materials are active materials that generate charges when mechanically stressed. Electromagnetic systems employ electromagnetic induction resulting from the relative movement between a permanent magnet (magnetic flux) and an electrical conductor as a coil. Electrostatic converters use the vibration-induced relative movement between charged plates (electrically isolated) against the electrostatic force to generate energy. Because of their low-cost manufacturing process, piezoelectric transducers, have often been proposed to implement easily exploitable energy harvester systems. But, solutions combining both electromagnetic and piezoelectric transducers were also explored to improve the energy density and the conversion efficiency [17]. Other solutions such as electrets or magnetostrictive materials have also been proposed for this purpose [18]. More details on the state of the art concerning all the converters above are presented in Appendix A.

Vibration-powered generators are generally constituted with inertial spring and mass systems (*cf.* Figure 1-5) employing the three main transduction mechanisms (piezoelectric, electromagnetic and electrostatic) to obtain electric energy from vibrations. A term commonly used to describe the adequacy between the harvester and its electric transducer is the coupling coefficient ( $k_c$ ), which connects the total input energy ( $U_{in}$ ) with the output energy of the transducer ( $U_{st}$ ) as follows:

$$K_c = \sqrt{\frac{U_{st}}{U_{in}}} \quad \text{Eq. 1-1}$$

From a practical point of view, the energy harvesters must deliver the minimum output mechanical power required by power converters (*i.e.* transducers) to operate with acceptable efficiency.

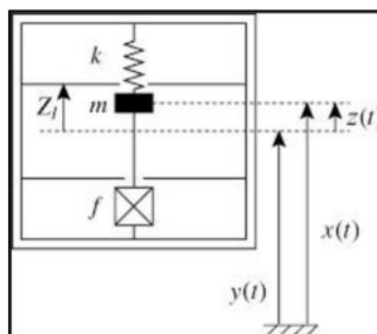


Figure 1-5 : Generic principle of vibration energy harvesting [7].

Thanks to the improved technology of MEMS, potentially integrable vibratory energy sensors exist with low power applications such as Wireless Sensor Network (WSN) nodes [16], [17], [19], [20]. Several energy harvesters in the literature used to have low output power and voltages, are large and bulky. But, fortunately, their efficiency is now turned to not peak only in a very narrow frequency range, thus making them suitable to scavenge energy from actual ambient vibrations. Research activities are currently oriented towards the improvement of the power

efficiency and the output power of the vibration energy harvester, to decrease the size of the transducers, the operating frequency to match the low frequency ambient vibrations. Moreover, knowing that ambient vibrations rarely occur at exact frequencies, their bandwidth widening is necessary to maximize the energy collection [21].

The vibrational energy harvesting mechanisms and architectural development in the recent years have been discussed. There have been many improvements on the designs (*e.g.* more compact, flexible, and wearable...). However, the main challenges, such as the wide bandwidth of ambient vibrations, make the vibrational energy harvesting systems with significant performances complicated to achieve. Development of MEMS system with low resonance frequencies are a real challenge.

### 1.3. Stirling motors

Motors that can use heat energy (released from burning an energy-rich fuel like coal, gasoline, etc.) to make a gas expand, push a piston, drive a vehicle or factory machines wheel, are examples of heat motors. Heat (or thermal) motors can be classified into two types:

- **Internal combustion motors** (for example, Otto car motors): these motors burn the fuel and produce the mechanical power in exactly the same place inside the motor. In a car Internal combustion motor, it all happens in the rigid metal cylinders.
- **External combustion motors** (such as steam motors): In these types of motors, the place where the fuel is burned is completely separated from the place where the mechanical power is generated.

The Stirling motor belongs to the category of external combustion motors while remaining unique because it heats, cools and recycles the same gas (environmental friendly gas like air) to produce a useful mechanical power [22].

#### 1.3.1. Principle and thermodynamic cycle

In 1824, Carnot developed a theoretical thermodynamic cycle whose efficiency is maximum [23]: a motor cycle, which is only valid theoretically and which consists of four successive transformations (reversible isothermal compression at a cold temperature ( $T_k$ ), reversible adiabatic compression, reversible isothermal relaxation at a hot temperature ( $T_h$ ) and reversible adiabatic relaxation). The output of this cycle is the ratio between the useful output work ( $W$ ) and the input thermal energy ( $Q$ ):

$$\eta_c = -\frac{W}{Q_h} = 1 - \frac{T_k}{T_h} \quad \text{Eq. 1-2}$$

For instance, with  $T_h = 500$  K (230 °C) and  $T_k = 293$  K (20°C), we have a maximum yield of 41.7%. It should be noted that with these temperature levels, under no circumstances will it be possible to exceed this yield.

The yield of Carnot, which constitutes the ideal case, makes it possible to compare the different systems of conversion of thermal energy to a theoretical maximum, and this even when the levels of the temperatures between these machines are different. It therefore serves as a reference for existing thermal machine technologies. Consequently, the efficiency ( $\eta_r$ ) of any thermal machine is the ratio between the yield of the considered motor ( $\eta$ ) and the yield of the Carnot cycle calculated at the same temperatures:

$$\eta_r = \frac{\eta}{\eta_c} \quad \text{Eq. 1-3}$$

In the early 19<sup>th</sup> century (1816) during the Britain industrial revolution [24], Reverend Robert Stirling (Scottish pastor) invented the Stirling type motor (*i.e.* external combustion motor (*cf.* Figure 1-6)) when he was only 26 years old. The original patent number of 1816 was 4081 and was entitled "*Improvements for Diminishing the Consumption of Fuel, and in particular an Motor capable of being Applied to the Moving (of) Machinery on a Principle Entirely New*" [25].

This motor was invented well before the diesel motor (1893), the gasoline motor (1860) and the electric motor (1869), and it was, at that time, with the steam motor, almost the only possibility to convert heat into mechanical energy. Since steam motors are rather reserved for the great powers, the motor (2 Horse Power  $\approx$  1.5 kW) that he developed had a very important commercial success until the beginning of the 20<sup>th</sup> century in the field of low-power

motors [26]. Figure 1-6 presents the Stirling motor (a) and its working principle (b). The classical Stirling motor will be composed of two chambers (a hot and a cold one) usually separated by a heat regenerator component (to improve the motor yield).

If we consider the theoretical case of a perfect regenerator (*i.e.* a heat transfer without heat loss), the efficiency of the Stirling machine becomes equal to the yield of Carnot. Therefore, the invention of the regenerator by Robert Stirling has significantly improved the performance of its motor

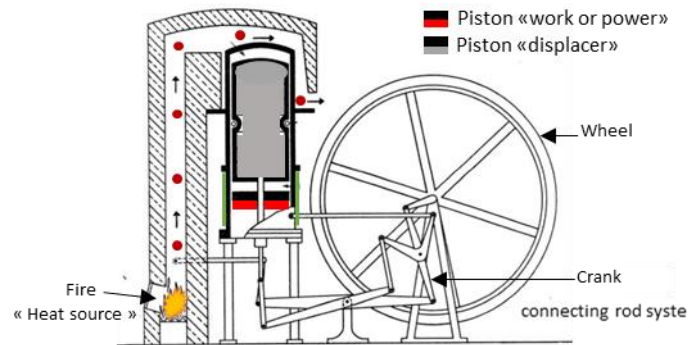


Figure 1-6: The first Stirling motor, as specified in the 1817-1840 patents [25]. Coloration and annotation is added.

In general, any Stirling motor contains at least two pistons (which do not necessarily have the same geometry) called according to their location (or their role) "displacer"-piston and "work-" or "power"-piston:

- **The "displacer" piston** is a piston (sometimes with a little space between the edge of the piston and the cylinder wall depending on motor configuration) whose job is to move the gas between the heat source and the heat sink.
- **The "working" piston** or power piston (closely adapted to the cylinder wall), transforms the expansion of the gas into useful mechanical work that drives everything the motor feeds.

In conventional Stirling motors (Figure 1-6), pistons are usually connected to a heavy flywheel that allows the machine to operate smoothly. In operation, the two pistons move constantly, but they are out of phase. Generally, the displacer piston is in advance of  $90^\circ$  (*i.e.* a quarter cycle) in front of the working piston and they are powered back by the same flywheel. Being linked, the two pistons ensure that heat energy is repeatedly being moved from the heat source to the heat sink and converted into useful mechanical work. A Stirling motor converts thus heat energy into mechanical energy by repeating a series of operations, known as its thermodynamic cycle (*cf.* Figure 1-7 Figure 1-6c). The gas inside is alternately expanded and compressed, and in between, moving from a hot side (expansion side) to a cold side (compression side) and so on. The work piston (in red color Figure 1-6 b) is pushed by the pressure from the expansion of the gas to drive the flywheel, then it compresses back the gas so the cycle can repeat. The (gray) displacer piston displaces the gas from the hot side of the motor to the cold side (on the right) and so on. The theoretical thermodynamic cycle of the Stirling motor (*cf.* Figure 1-7 a), and c) for associated cycle) can be divided into four steps:

- **1-2 Isochoric transfert through the regenerator:** the gas (shown by the red circles in Figure 1-6) is heated without volume variation at the hot end of the cylinder
- **2-3 Isothermal expansion :** the heated gas has its pressure which increases until it expands. As the gas expands, it pushes the working piston, which, in turn, drives the flywheel. It is in this part of the cycle that the motor converts thermal energy into mechanical energy. In the ideal cycle, the expansion is assumed isothermal.
- **3-4 Isochoric transfert through the regenerator :** The displacer piston thanks to the inertia of the flywheel brings the hot gas towards the cooled part. Before arriving in the cold part, the gas passes through the regenerator, it gives up some of its heat on the way at constant volume.
- **4-1 Isothermal compression :** During this phase, the gas (shown by the green circles) is at the cooled cylinder. The piston compresses the gas while its heat is removed by the heat sink. Thanks to the flywheel's inertia, the displacer piston brings the cold gas back to the hot part of the machine. Before reaching this

part, the gas (at constant volume) heats as it passes through the regenerator, the latter gives up part of its stored heat from the previous phase of the cycle.

In theory, it is considered that the expansion and compression phases are isothermal and that the thermal phases (*i.e.* heating and cooling) are isochoric. In fact, the four steps are not physically separated but merge into each other. Although the motor goes through a cycle, it is not a symmetrical process: heat energy is constantly removed from the hot source and released at the heat sink and the real Clapeyron diagram is modified as shown in Figure 1-7 b).

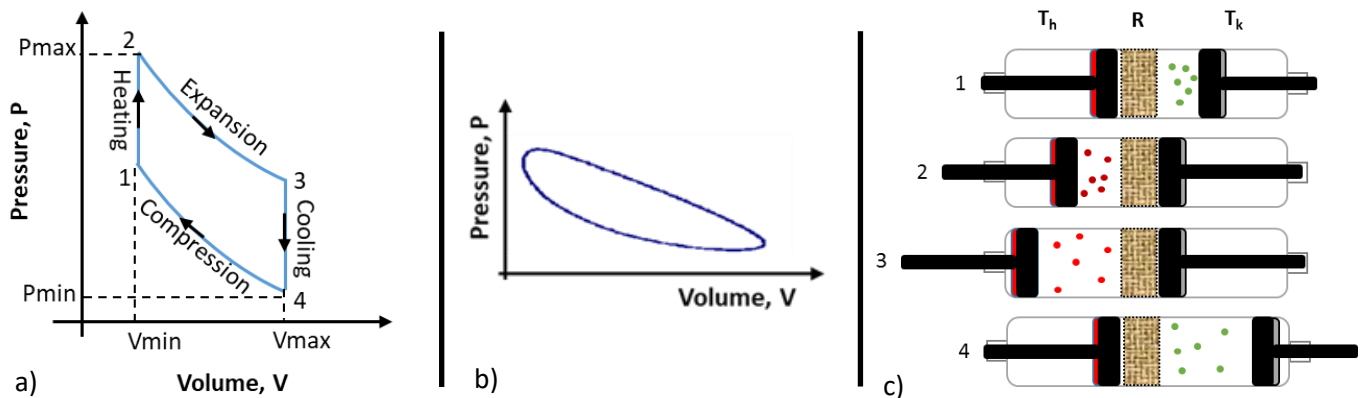


Figure 1-7: Clapeyron diagram Pressure-Volume diagram of a) an ideal Stirling motor cycle. b) a real cycle of a Stirling motor. c) Simplified working principle of a Stirling motor, the subscripts “h” and “k” will respectively stand for “hot” and “cold” and the letter “R” on the figure is for the regenerator, “c” and “e” will represent respectively the compression and the expansion.

That happens because the hot gas when it expands does a certain amount of work on the work piston, but the piston does not do the same work when compressing the cooled gas and returning it to the start point [27], [28]. Those differences between real and ideal cycles are mainly due to the following facts:

- The heat exchangers and the regenerator are not perfect.
- Dead spaces exist (volumes not swept by the pistons) in the actual motor.
- The synchronization of the pistons is not discontinuous: it is often approached by a continuous sinusoidal movement
- The gas flow dissipations and frictional drag generate pressure drop.
- The viscous dissipations in the different components of the machine primarily in the regenerator cause mechanical power loss.
- Mechanical losses such as vibrations are present
- Seal leakage through the rings results in a loss of gas pressure.
- Gas spring effects generate hysteresis losses.
- Heat conduction happens through the walls and from the hot side to the cold side of the machine.

When you apply mechanical energy into a Stirling motor and run it backward, the motor will effectively remove heat from the heat sink part of the motor and will expel it towards the part that should be heated. That turns a Stirling motor into a very efficient cooling device (“cryocooler”) [29]. Due to the high efficiency achieved by Stirling macro machines for cooling, Stirling micro chillers are a potentially interesting alternative for small devices cooling. This cooling mode will be studied in chapter 5.

### 1.3.2. Stirling motor architectures

#### 1.3.2.a. Mechanical connection of pistons

There are several Stirling motor architectures, the most classic being able to be considered as the types Alpha ( $\alpha$ ), Beta ( $\beta$ ) and Gamma ( $\gamma$ ), and distinguished as follows [30]:

- **Alpha** motors (*cf.* Figure 1-8) have two separate cylinders in each of which is a piston. Variations in hot (expansion space) and cold (compression space) volumes are created separately by separate piston

movements. Their main advantage is the possibility to assemble several Alpha motors to give rise to compact configurations (multicylinders motor) that provide more power.

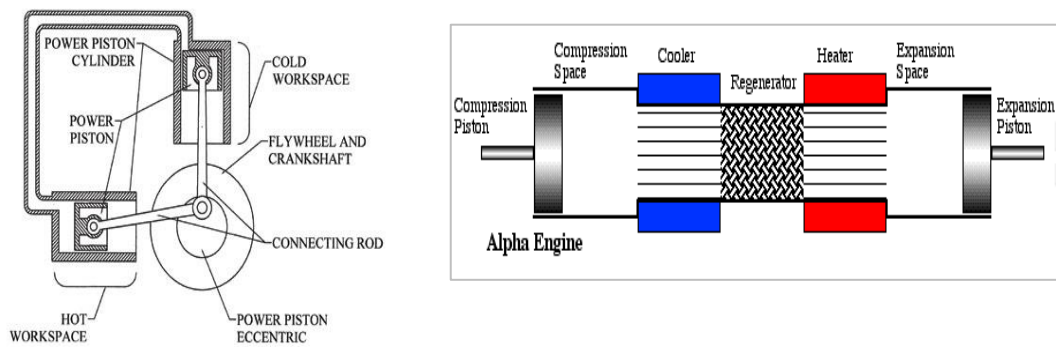


Figure 1-8: Alpha type Stirling machine configuration (left) and its simplified view (right).  
(<https://www.ohio.edu/mechanical/stirling>)

- **Beta** type motors (*cf.* Figure 1-9) designate a single-cylinder arrangement. The displacer piston, and the working piston, move together linked by a crank shaft mechanism. Variable hot and cold volumes are created by the combined action of the two pistons.

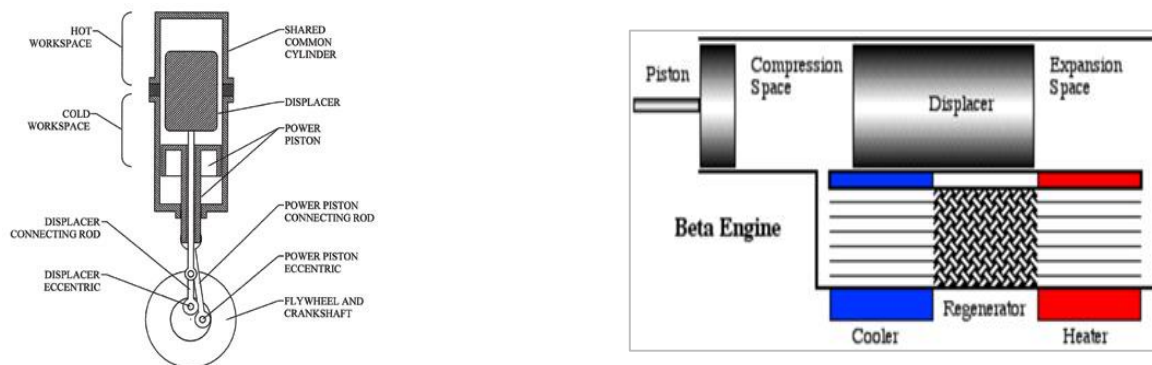


Figure 1-9: Beta type Stirling machine configuration (left) and its simplified view (right).  
(<https://www.ohio.edu/mechanical/stirling>)

- **Gamma** type motors (*cf.* Figure 1-10) have two cylinders like the Alpha type but variable hot and cold volumes are created as for the Beta type. The Gamma type has more dead space, which reduces its specific power.

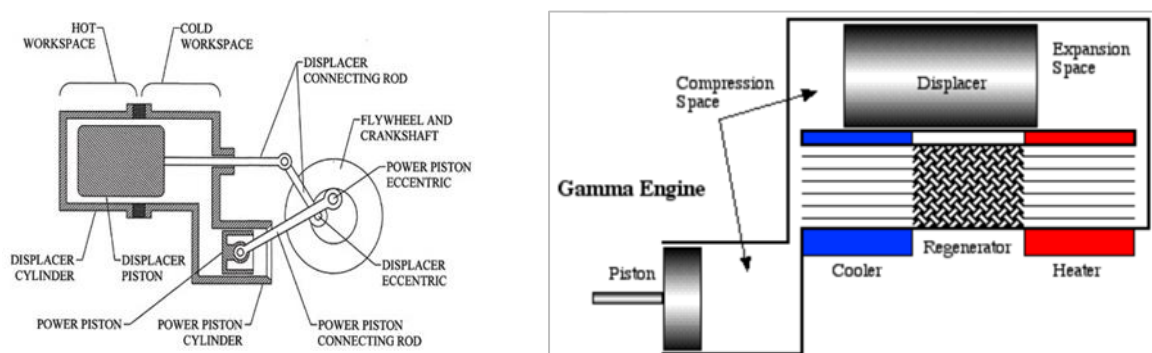


Figure 1-10: Gamma type Stirling machine configuration (left) and its simplified view (right).  
(<https://www.ohio.edu/mechanical/stirling>)

There are several types of drive systems that ensure the appropriate movements of the working gas to achieve the Stirling cycle [31], [32], [33]. The Stirling motor can operate from a linked kinematic chain or free pistons type version.

### 1.3.2.b. *Linked kinematic chain*

The standard links use conventional mechanical elements such as cranks, connecting rods, flywheels. Standard Kinetic drive mechanisms are crank-slider drive, rhombic drive, swach-plate drive, Ross-Yoke drive (diagrams can be found in [31]).

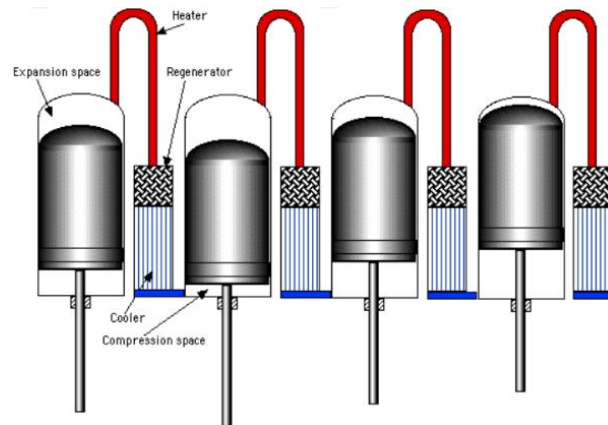


Figure 1-11: Compact multiple cylinder configuration of Alpha Stirling Motors. (<https://www.ohio.edu/mechanical/stirling/>)

There are other categories of Stirling machines. The multiphase architectures (multicylinder) where a piston have a double action ; plays the role of power piston and displacer for two Alpha Stirling motors connected. This system consists of several Stirling motors assembled in series. Figure 1-11 is a diagram illustrating the concept. One of the essential aspects of these motors is to have imposed kinematics, namely that the piston stroke and the phase shift are fixed by specific mechanical elements [5].

### 1.3.2.c. *Free-piston Stirling motor*

In a free-piston Stirling motor, reciprocating pistons are coupled to springs and move entirely in response to spring forces (gas, membrane or mechanical spring) acting upon them. Invented by Beale [34] in 1969, a Free-piston Stirling motor is a dynamic resonant system. The operating frequency is determined by the stiffness provided by the springs and the mass of the moving elements. Although this system seems mechanically simple, free-piston Stirling motor is the most difficult and complicated to put into practice [31].

The main characteristics of free-piston Stirling motors are :

- It is a resonant system operating at a constant frequency.
- A self-starting capability. When it is heated up, the system changes into an unstable equilibrium state and starts to oscillate automatically at a natural frequency without any requirement for external excitation.
- The displacements of moving pistons change accordingly with the mass. If more loads are added, the displacements decrease.
- Pistons move linearly inside the cylinders.
- The requirement for lubrication is ensured by the working gas rather than oil. Oil-free operation of the motor eliminates the problem of regenerator contamination.
- Motor cylinders are hermetically sealed thereby eliminating entirely the problems of dynamic seals of kinetic Stirling motors.
- Motor operation is quieter and more stable compared to kinetic Stirling motors.

If the piston in a free-piston Stirling motor is replaced by a diaphragm, the mechanical friction and wear are eliminated. This type of special free-piston Stirling motor is called the diaphragm Stirling motor, invented by Cooke–Yarborough in the 1960s [35] as a power generator with a substantially higher efficiency than thermoelectric systems at the time [35], [36]. To date, the disadvantage of diaphragm Stirling motor is the low power density because of the much smaller swept volumes of diaphragms compared to those of pistons.

To model a Stirling machine, there are numerical models that we will briefly introduce in the next section. However, for more information and details (on the calculations for example) we invite the reader to consult the appendice A.



### 1.3.3. Modeling the operation of Stirling motors

There are generally four theoretical approaches to modeling Stirling motors. These different theoretical analyzes are classified according to a concern of increasing accuracy with respect to the actual operation of the machine. The first model, which is the simplest because approximate, is the zero-order analysis. The second model is the first order one and is based on the isothermal analysis developed by G. Schmidt [37]. The second order, which is a little complex, includes the calculation of the various losses assumed to be decoupled (*i.e.* separately calculable from each other). Last, the most complex is the third-order analysis or "coupled analysis". In this work, only the zero, first and second order method are detailed below. More informations on the more complex approach can be found in [28] and more details on the simple approaches listed above are presented in appendices.

There are other 1st order modelling methods in the literature that consider Stirling engine losses. These methods are based on the theoretical cycle but they allow obtaining results closer to reality than the Schmidt model. One example is the TDF (Thermodynamics in Finite Physical Dimensions) method [38] in which thermal and mechanical losses are individualized, thus making it possible to quantify them during actual engine operation. There is also the so-called direct method [39] allowing, through adjustment coefficients, to take into account the different losses of the Stirling engine during operation.

#### 1.3.3.a. Zero order analysis

Based on experimentally obtained results, the zero-order analysis developed by William Beale during the 1970s [33], makes it possible to determine corrective coefficients for the theoretical formulas. According to Beale [34], when considering a Stirling machine running in the motor cycle, its mechanical power  $W_m$  could be expressed by the relation (Eq. 1-4).

$$W_m = C_t \cdot P_{cycle} \cdot f \cdot V_{swc} \cdot f(T) \quad \text{Eq. 1-4}$$

With  $C_t$  a constant depending on the system,  $P_{cycle}$  the pressure over a cycle,  $f$  the frequency,  $V_{swc}$  the swept volume in the compression chamber and  $f(T)$  a function of the temperature.

Around 1980, Walker ([40]) based on several practical tests on Stirling machines, proposed the following formulation of Beale's initial formula:

$$W_m = 0.15 P_{cycle} \cdot f \cdot V_{swc} \quad \text{Eq. 1-5}$$

In general, the Beale formula is used in optimizing the choice of the temperature regime. Its formula has been widely used by Senft (1982) [41], West (1986) [42] and Organ (1992) [43]. These scientists validated it by including the effects of the temperature ratio. According to West [42], Beale's formula should be modified as follow:

$$W_m = 0.25 P_{cycle} \cdot f \cdot V_{swc} \frac{T_h - T_c}{T_h + T_c} \quad \text{Eq. 1-6}$$

For Stirling machines operating in a cooling cycle (cryogenic), Walker in 1983 [32] (based on the Beale formula) establishes an expression to approximate the cooling capacity of a Stirling machine based on the analysis of experimental results :

$$Q_c = 10^{-6} P_{cycle} \cdot f \cdot V_{swc} T_c \quad \text{Eq. 1-7}$$

Results such as thermal efficiency and power, obtained from these formulas, are estimates that can only give an order of magnitude in pre-studies for a Stirling machine design. In fact, this Beale analysis is about an ideal Stirling machine, the results are not realistic because there are very important differences between the ideal Stirling cycle and the actual operation of a Stirling machine.

#### 1.3.3.b. First order analysis or Ideal Isothermal Analysis

The first order analysis (or isothermal), proposed by Gustave Schmidt in 1871 [37], makes it possible to estimate the mechanical power of an motor as well as its performance. It is often the basis of pre-studies of the Stirling motor. In Schmidt's model there are assumptions:

- The movement of the pistons is sinusoidal and their oscillation frequency is constant.
- The evolution of compression and expansion phases are isothermal.

- The gas is ideal so the ideal gas state equation is applicable.
- The regenerator is perfect (infinite heat capacity).
- The mass of injected gas is constant and its instantaneous pressure is uniform (no leakage) so that the conservation of the mass applies.
- The thermal equilibrium conditions are then assumed to be established. There is no mass accumulation inside a chamber.

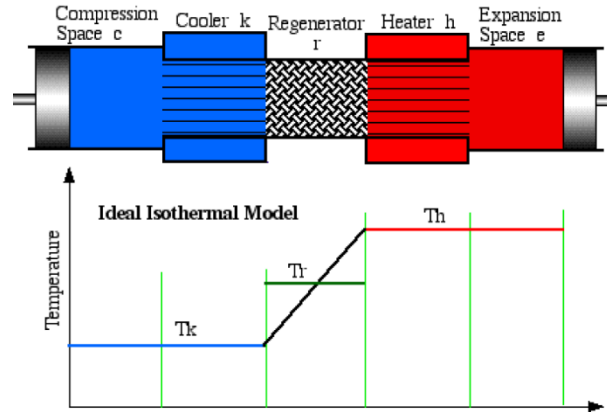


Figure 1-12 : Schematic view of the zones and cells of the isothermal model [28] extracted from <https://www.ohio.edu/mechanical/stirling/>

$\beta = \arctan \left( \frac{\frac{V_{swe}}{T_h} \sin \alpha}{\frac{V_{swc}}{T_k} + \frac{V_{swe}}{T_h} \cos \alpha} \right)$ $c = \frac{1}{2} \sqrt{\left(\frac{V_{swe}}{T_h}\right)^2 + 2\frac{V_{swc}}{T_k} \frac{V_{swe}}{T_h} \cos \alpha + \left(\frac{V_{swc}}{T_k}\right)^2}$ $s = \frac{V_{clc}}{T_k} + \frac{V_{swc}}{2T_k} + \frac{V_k}{T_k} + V_r \frac{\ln\left(\frac{T_h}{T_k}\right)}{(T_h - T_k)} + \frac{V_h}{T_h} + \frac{V_{cle}}{T_h} + \frac{V_{swe}}{2T_h} \quad \text{and } b = \frac{c}{s}$	
Schmidt number	$S_c = \pi \left[ \frac{V_{swc}}{V_{sw}} \sin \beta + \frac{V_{swe}}{V_{sw}} \sin(\beta - \alpha) \right] \frac{(\sqrt{1-b^2} - 1)}{b}$
Mean pressure (with $r = R/M$ )	$P_{mean} = \frac{m r}{s \sqrt{1-b^2}}$
Work in the compression and expansion chambers	$W = S_c P_{mean} V_{sw}$
Power	$\dot{W} = W f$
Heat transferred over a complete cycle on the expansion chamber (equal to the work done in the expansion chamber)	$Q_e = \pi V_{swe} P_{mean} \sin(\beta - \alpha) \frac{(\sqrt{1-b^2} - 1)}{b}$
Efficiency	$\eta = \frac{W}{Q_e}$

Table 1-2: Parameters and expressions for isothermal analysis

Based on the first order analysis, the Table 1-2 presents the main equations describing the performances of a Stirling motor (more details concerning the equations determination are given in appendix B). The letters c, k, r, h and e respectively designating the compression chamber, the cold exchanger, the regenerator, the hot exchanger and the expansion chamber (*cf.* Figure 1-12 and Figure 1-8). The known data are the volumes of the cold space  $V_k$ , of the regenerator  $V_r$ , of the hot space  $V_h$  and the temperatures of cold space  $T_k$  and hot space  $T_h$ . The swept volume in the compression and expansion chambers are respectively denoted  $V_{swc}$  and  $V_{swe}$ .  $\alpha$  is the phase shift between the piston and the displacer. This angle represents the phase advance of the expansion space volume variations with respect to the compression space volume variations.  $R$  and  $M$  are respectively the ideal gas constant and the molecular weight.

### 1.3.3.c. Second order analysis or Ideal Adiabatic Analysis

This analysis allows to determine the effects of the adiabatic operation of the compression and expansion spaces on the motor performance and to examine the detailed behaviour of the relevant variables across the cycle (temperature ratio, phase angle, swept volume ratio, ratio of dead space). This model (*cf.* Figure 1-13 for a schematic view of the parameters) is more realistic for estimating the mechanical power of an motor as well as its performance from its geometry.

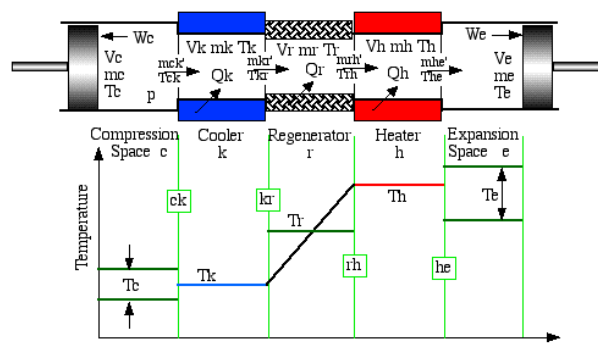


Figure 1-13: Schematic view of the zones and cells of the adiabatic model [28], extracted from <https://www.ohio.edu/mechanical/stirling/>

The advantages of this analysis are that the amount of heat transferred to the regenerator is estimated and the method may include heat transfer and friction flow analysis of the heat exchangers. The disadvantage is that this analysis leads to nonlinear differential equations that can only be solved numerically. A detailed presentation of this model, that was not used in this PhD (due to the number of unknown variables), is given in the appendix B.

To conclude on this part, Stirling motor can be used, for instance, as motorization motor; as cooler or heat pump, as heat harvester *etc.* In this present work, it is this last application we will focus on. Classical Stirling motors are usually macro-size or (more rarely) meso-size. Nowadays, many devices in the millimeter scale range are being fabricated using MEMS batch-manufacturing techniques with low unit cost characteristics [44], [45] and rapid prototyping, with basic materials such as silicon and glass that are like those used in the integrated circuit/microchip industry. Although initially the micro-devices fabricated using MEMS were sensors and actuators, recently more complex mechanical devices such as micro-coolers, pumps and motors are being developed. Indeed, a miniaturized device, even with a moderate conversion efficiency (of heat or hydrocarbon fuels into electric energy), would indeed increase the lifetime and reduce the weight of an electronic or mechanical system often powered by heavy batteries [46]. Moreover, the numerous advantages related to the miniaturization of electromechanical systems such as their use in isolated locations that are difficult to access (for example in space or in the deep sea) have increased the need to produce microgenerators of power (milliwatts to watts) which are not bulky, have low weight and long lifetime. Since thin films batteries are still in development and are not sufficient ( $\sim 1 \text{ kJ} / \text{g}$ ) to sustain small device's power requirements during long periods [47], producing miniaturized power-generation devices opens exciting new opportunities, especially in the field of everyday-devices size reducing and sophistication. Improvements in this area can make possible new applications and/or capabilities.

On the next sections, we will present a literature review on heat generation and harvesting methods at small scales: first for miniature motor with internal combustion/heat source, then for miniature motor with external combustion/heat source. Knowing that we are trying to manufacture a micro machine to convert thermal energy

into electrical one, even if it has the particularity of being able to exploit any heat source to work as its heat source is external, there is a certain similarity with the "micro" motors exploiting heat from micro-scale combustion (*i.e.* in micro chambers) to produce electrical energy. Therefore, we will also talk about this micro combustion field and technology advantages and limits in order to avoid some technological issues related to motor's miniaturization

#### 1.4. Small scale devices with internal combustion

The race towards miniaturization of electromechanical devices or phones, that can lead to smaller, more compact, more powerful, more portable, low power consumption, less bulky, high resolution and reliable has led to the need for high microscale power generators (milli-watts to watts) [48], [49]. The high efficiencies obtained in macro-scale combustion motors encourage the development of their miniaturization with the expectation that competitive devices can be developed. This tandem has led to the development of the field of microscale combustion. Progress in this field has evolved considerably with more than 15 years of research and development [50]. It could be interesting to take stock of achievements in this area.

The innovative idea behind this field is to utilize the high-specific energy density of liquid hydrocarbon fuels (typically 45 MJ/kg of energy per unit mass) in combustion driven micro-devices to generate high power at small scale [51], since top batteries (such as Lithium/thionyl chloride, 0.6 MJ/kg for an Alkaline battery) as well as rechargeable new ones, had not yet demonstrated a specific energy greater than 1.2 MJ/kg [46].

Therefore, a MEMS-based combustion microdevice, even with a mere 3-4% system efficiency of hydrocarbon fuels energy conversion, would compete with top batteries in term of energy density (*cf.* Figure 1-14a).

Furthermore, there are some specific applications for which mechanical power, or simply heat, are desired (such as for instance with Stirling motor) and for which a combustion-based microdevice will have the additional advantage of providing this power directly. The overall weight of typical portable consumer electronics consists largely of their battery weight. These devices also suffer from short operation cycles between charges or battery replacement. A typical example of this problem is depicted in Figure 1-14b) on which a hearing aid (a MEMS sensing /communication network device) of a 63mm<sup>3</sup> is powered by one of the smallest batteries [46]. Therefore, the size and the weight of these available batteries limit the miniaturization of mechanical devices such as robots, airplanes *etc.* [52].

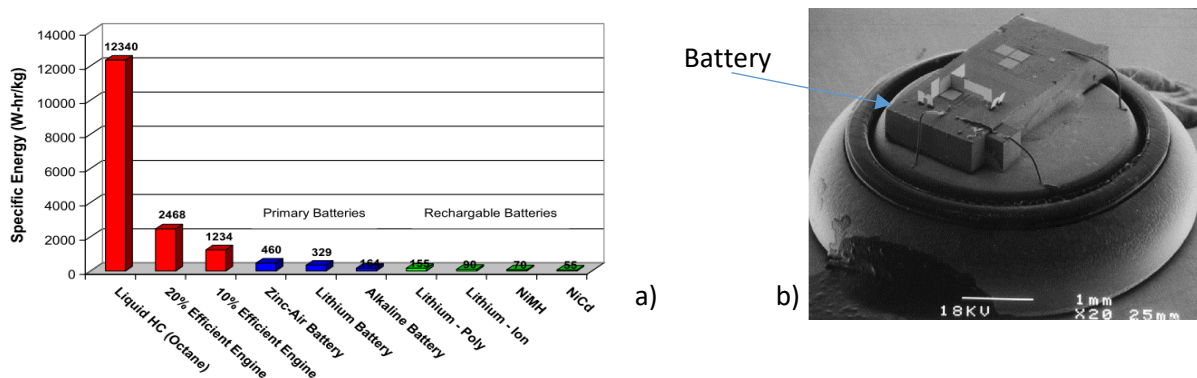


Figure 1-14 : a) Specific energy for iso-octane and several primary and secondary battery technologies [46]. b) Autonomous bidirectional communication mote with MEMS optics chip containing a corner-cube retroreflector on the large die, a CMOS application-specific integrated circuit (ASIC) for control on the 300 x 360 micron die, and a hearing aid battery for power.

The micro-power generation field is still, in most of the cases, in the feasibility stage because of no proper understanding of thermal and chemical management of microcombustion. Even if only a few projects on micro-power generation have been funded [46], [53], [54], several meso-scale and micro-scale combustors have been developed and they appear to operate with acceptable combustion efficiencies [46], [55], [56]. Some of these combustors have already been applied to energize thermoelectric systems to produce electrical power although with low overall efficiency. Several turbines/motors have been developed, some of them currently producing positive power with low efficiency [48], [57], [58]. Some micro-rockets using solid or liquid fuels have also been successfully built since they manage to produce a thrust [46].

In next sections, some of the technological issues related to meso and micro-scale combustion, the operation of thermochemical devices for power generation and some of the systems currently being developed will be presented and described. However, first let us clarify the definitions of micro, meso and macro in this field.

#### 1.4.1.a. *Scaling parameters*

Different micro-devices such as motors [59], [60], [61], propellants [62], [63]- [64] and reactors [65], [66] have been developed in recent years. However, the definition of “micro-scale combustion” is confusing because of the arbitrary choices of reference length scales. Sometimes “mesoscale combustion” is confused with micro scale combustion in the literature.

The definition of “micro-scale” combustion from previous studies is generally based on three different length scales listed in Table 1-3:

- The first is **the physical size of the combustion chamber**, which was the length scale widely used to define the combustion scale (micro and meso). Thereby, if the combustor length is below 1 mm, the micro-combustion is considered. Otherwise, the combustion is called mesoscale combustion if the combustor length is greater but in the 1 cm order. This definition of scale of combustion is widely used in the development of micro-motors [59].
- The second definition is based on a **reference length scale of the flame** with respect to the quenching diameter [67]. In this definition, the combustion is micro-scale if the diameter of the quench is larger than the size of the combustion chamber. This definition is favored by researchers for fundamental studies of micro-combustion. It is difficult with this method to quantitatively define the limits of micro and meso combustion since the quenching diameter depends on several factors such as the composition of the mixture and properties of the wall (temperature and surface reactivity).
- The third definition consists of using **the relative length scale of the entire device** compared to that of conventional macro devices. For example, a micro-combustion chamber for a micro-satellite only indicates that the combustion chamber is used for a micro-satellite [62]. The latter approximately 10-100 kg is considered "micro" compared to a conventional commercial satellite that exceeds 1000 kg. Thus, this definition is used by researchers in the field of micro-propulsion for specific applications.

Definition based on	Combustion regime	Length scale	Examples	Applications
Physical length	Mesoscale	1-10 mm	Rotary motor (UCB)	MEMS power
	Microscale	1-1000 $\mu\text{m}$	Micro-reactor (UIUC)	Thruster
Flame quenching diameter	Mesoscale	$\sim$ Quenching diameter (equilibrium)	Swiss-roll combustor (USC)	Power generation
	Microscale	Quenching diameter $\sim$ Mean-free path (non-equilibrium)	Fuel Cells Nano-particle reactors	Energy conversion
Device scale	Microscale	Smaller than conventional motor size	Micro-thrusters (PSU) Micro-gas turbine (MIT)	Micro-satellites Micro-air planes

Table 1-3 : Definition of micro-scale and mesoscale combustion using different length scales [50].

The purpose of this state of the art is not so much to give the details of the tests and the concepts of small-scale internal combustion energy generation systems, but rather to present an overview of their development, focusing on the miniaturization approaches and techniques adopted by these specialists, the equivalences of mechanical parts between small and large motors, the physical phenomena that they have been able to observe on a small scale, the manufacturing difficulties. Thus, this knowledge gained in small-scale combustion can be applied to our work to avoid certain pitfalls or other new systems involving small-scale transport and chemical reactions to improve energy conversion efficiency. For the present study, we will use the physical length (such as the height of the chambers) to define the scale.

#### 1.4.1.b. *Current technologies in micro and meso-combustors*

Several micro or meso-combustors are currently being developed, using either piezoelectric or thermoelectric materials as electrical transducer material with the main advantage of no moving or rotating parts. However, the problem generally lies in the low efficiency of the complete system.

### i Micro-combustors with thermoelectric transducers

Some small scale combustion device combined with thermoelectric power-generation ones have been developed using the Swiss roll approach [55], [56], [68] (*cf.* Figure 1-15). The project goal of the University of Southern California was to batch fabricate a highly miniaturized, integrated static power generator to power down MEMS scales devices [55], [68], [69]. The 3-D Swiss roll reactor that was built is shown in Figure 1-15 : it consisted of two connected sections, one in which the heat is transferred to the incoming chemical reactants, and another one that eliminates unconverted heat to the cold surroundings. According to them, this 3D design highly reduces heat losses and appears to be suited for MEMS scale devices. But, complications appeared during the implementation of the thermoelectric unit [70] and both the heat lost and the amount of input fuel to feed the combustor were considerable [71].

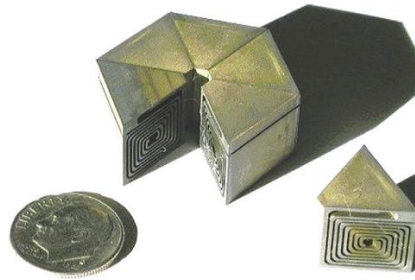


Figure 1-15 : 3-D "Swiss-roll " type combustor at University of Southern California (USC) [46].

In 2001, Zhang *et al.* [72] (University of Michigan) developed a thermoelectric power generator based on catalytic combustion in a micro-machined combustion chamber. The small device (*cf.* Figure 1-16) had a  $2 \times 8 \times 0.5 \text{ mm}^3$  chamber covered by a dielectric diaphragm that integrates polysilicon Platinum thermopiles. The device produced a power of  $1 \mu\text{W}$ / thermocouple when hydrogen/air mixtures was used.

Holladay *et al.* [59] developed a micro-scale power device which combined a combustion driven fuel reformer and a fuel cell in 2001. The electric power was generated by the fuel cell which use the hydrogen stripped from a hydrocarbon fuel tank to the reformer. A reactor volume of around  $0.5 \text{ mm}^3$  was assembled and fabricated. Methanol or butane were used in preliminary testing of the fuel reformer, which was able to provide up to 100mW of hydrogen at an efficiency of 4.8%.

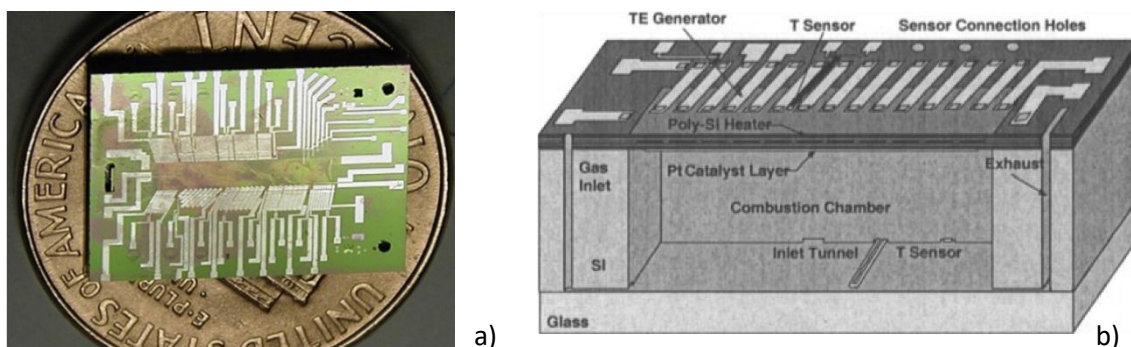


Figure 1-16 : a) Integrated catalytic combustor/ thermoelectric micro-power generator developed at the University of Michigan [46]. b) Illustration of the combustion TE power generator [72] .

In 2002, Vican *et al.* [56] (at Princeton University) presented a prototype of a MEMS scale device of chemical energy conversion and electric power-generation consisting of a recirculating catalytic 2-D Swiss roll reactor of  $12.5 \times 12.5 \times 5.0 \text{ mm}$  in size. The device was made of alumina ceramic and platinum as catalyst and a thermopile unit. The reactor operated with hydrogen over a wide range of fuel-air mixtures and chemical energy inputs from 2 to 12 W at  $300^\circ\text{C}$  of operation temperature. The resulting electric power of this 2D-structure was sufficient to power a 100 mW light bulb. However, the problem with this microdevice was the high heat lost [73] and the amount of input required fuel.

Yoshida *et al.* [74] at Tohoku University fabricated a micro-thermoelectric (TE) generator that relied on catalytic combustion. The device consisted of a fuel ejector, a combustor and a thermoelectric component. The platinum-based catalytic combustor had a size of  $10 \times 20 \times 0.3 \text{ mm}^3$  with a BiTe thermoelectric element. The device generated 138 mW at a total efficiency of 3% using a forced hydrogen and air mixture. However, the ejector pumping mechanism integration was initially unsuccessful for system operation.

Kyritsi *et al.* [75], at Yale University, developed a meso-scale catalytic combustor (about  $16 \cdot 10^3 \text{ mm}^3$ ) with a reported combustion efficiency of the order of 97% [46]. A liquid fuel was electro-sprayed into the combustor chamber and the reported catalytic temperature was in the range of 650-1000°C. As this combustor was to be coupled with direct energy conversion modules, its coupling to a Stirling motor demonstrated, in 2007, an impressive overall efficiency about 20% [76].

### ii Miniature gas turbines/motors

Epstein *et al.* in 1997 [48], and Mehra *et al.* in 2000 [60] participated on the MIT Gas Turbine Laboratory "Micromotor project" (1994-2011). The project goal was to develop silicon radial inflow gas turbine. Their device, constructed from six silicon substrates, is a MEMS-based gas turbine motor potentially capable of producing 10–20 W of electrical power while consuming 10g of jet fuel per hour [48]. Figure 1-17 shows details of the microdevice : an optical picture of a section (a) and schematic views (b, c and d) of the micro-gas turbine comprising the main non-rotating functional components of the motor, the compressor (12 mm in diameter and 3 mm thick) and the turbine (4 mm in diameter;  $1,2 \cdot 10^6 \text{ rev/min}$  at 1100°C) [46]. The whole device (radial compressor/turbine unit, a  $0.195 \text{ cm}^3$  combustion chamber and electrical generator incorporated in the compressor) measured  $2.1 \text{ cm} \times 2.1 \text{ cm} \times 0.37 \text{ cm}^3$ . Despite, the fact that the development of the different components was well advanced (turbine, compressor and combustor) in 2000, the device did not produce a positive power yet [46]. The major problems keeping the efficiency of the turbine low appeared related to the difficulty in achieving good fabrication tolerances, together with good heat transfer from the combustion chamber to the compressor/intake air.

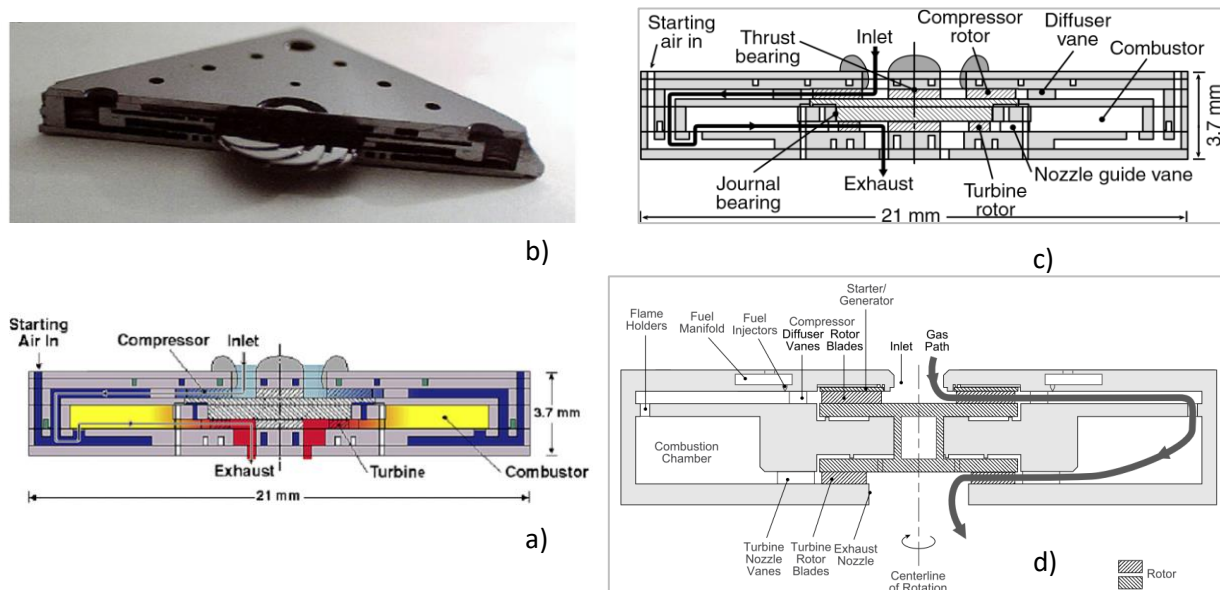


Figure 1-17 : a) A schematic of the silicon radial inflow gas turbine [48]. b) Schematic view of H<sub>2</sub> demo gas turbine chip [46]. c) H<sub>2</sub> demo motor design with conduction-cooled turbine constructed from six silicon wafers. d) Micro-gas turbine generator cross-section [48].

Yang *et al.* [77] in 2000, at Honeywell, proposed a free piston-based thermal micro-motor called "knock" operating with Homogeneous Charge Compression Ignition (HCCI) of hydrocarbon fuels. HCCI was used to minimize the flame quenching effect. In micro-combustors, significant amount of heat is transferred through the walls because they have a large surface area to volume ratio, which leads sometimes to flame quenching [59]. The device package volume was  $103 \text{ mm}^3$  and the expected output electric power was 10W. The motor must operate at kilohertz frequencies, regarding allowable ignition delay times to achieve reliable auto ignition of the fuel and to develop these power densities. Although compression ignition could have been achieved in a 3 mm diameter piston / cylinder section operating over several cycles, the inefficiency of the motor appeared to be related to sealing problems.

Fu *et al.* [57] (University of Berkeley, Combustion Laboratory) presented in 2001 a silicon-based MEMS rotary internal combustion motor potentially capable of delivering milliwatts using liquid hydrocarbon-fuel. “Micro-rotary” motors (Wankel-type) with rotor diameters of 2.3 mm and 1 mm were fabricated to examine various micro fabrication techniques [50], [57]. A larger rotor diameter of 12.5 mm was fabricated from hardened stainless steel by electro-discharge machining (illustrated in Figure 1-18 a) to investigate combustion efficiency, motor operation behavior and design issues. This larger “mini-rotary” motor was expected to develop up to 50 W power [46]. Preliminary testing of the mini-motor with H<sub>2</sub>-air mixtures combustion produced a net power output of about 3 W at 10000 rpm, the goal being the production of 30 W at 40000 rpm [57]. However, the highest performing of this motor produced 33 W of power with an efficiency of 3.9% using a methanol/nitromethane mixture [46]. The microfabrication and assembling of a 2.4 mm MEMS-based micro-motor with 1mm rotor diameter based on a solid SiC rotor and SiC coated Si housing was ongoing (Figure 1-18). The project aimed to produce 10 to 100 mW of mechanical power with a motor chamber size of less than 1 mm<sup>3</sup> [59], with 0.08 mm<sup>3</sup> of rotor swept volume [57]. Unfortunately, problems remain on many levels, including the manufacturing process, materials, sealing, fuel dispensing valves, friction phenomena, fuel vaporization, ignition, combustion, thermal management, and thermal insulation.

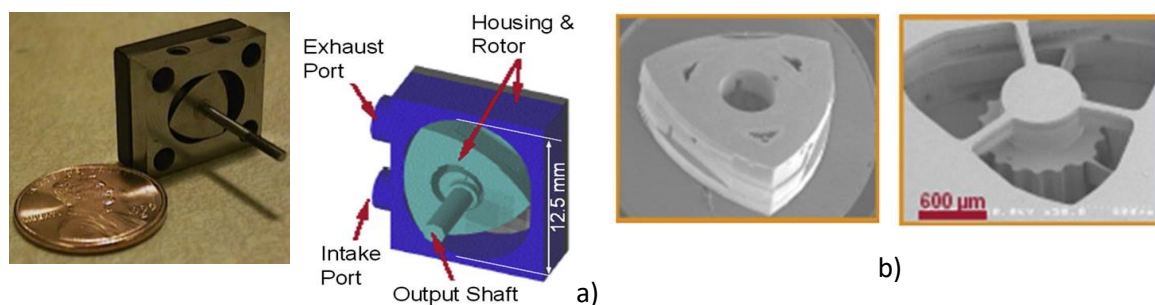


Figure 1-18 : a) EDM technologies steel fabricated mini-rotary motor with a 10 mm rotor [46], [59]. b) micro-rotary motor [50].

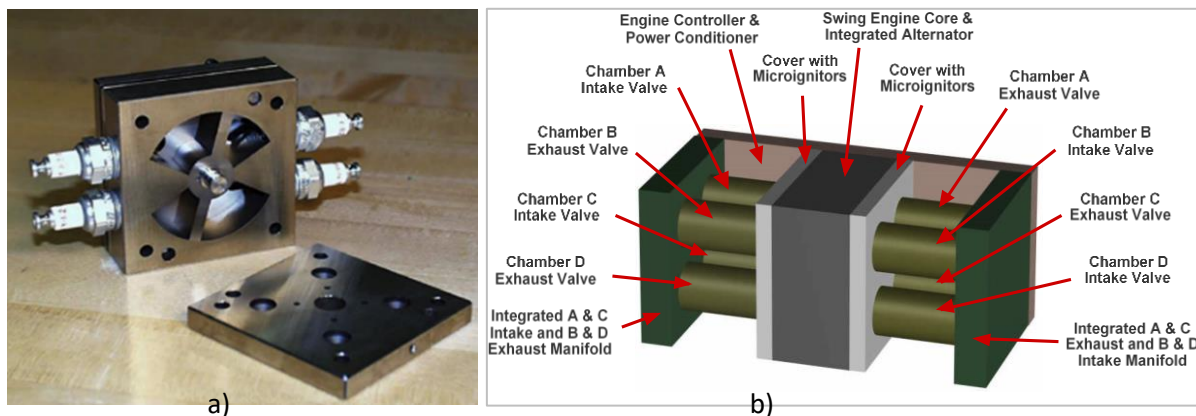


Figure 1-19 : a) Meso-scale Internal Combustion Swing Motor (MICSE). b) Assembly concept for all non-fuel components of the 20W MICSE chemical-to-electrical energy conversion system indicating major system components [78].

The palm-scale Micro Internal Combustion Swing Motor (MICSE), shown in Figure 1-19, is a rotationally oscillating free-piston motor based on four distinct combustion chambers from a single housing separated by a rotating arm. It was developed in 2002 by Dahm *et al.* [78] at the University of Michigan. The motor operation principle is a four-stroke Otto cycle, and the arm oscillations make mechanical torque coupling inefficient, but relatively simple for direct electrical power generation. The design goals of this motor were the production of 20 W of electrical power from liquid hydrocarbon fuel with 54 g of projected system mass and 17cm<sup>3</sup> of volume.

Annen *et al.* [61] (Aerodyne Research Inc.) in 2003, presented another quasi-free-piston approach. The device is a combination of a linearly oscillating piston based two-stroke motor, a double-helix spring and linear electric alternator. This device formed an electric power generation system capable of producing 10 W. The basic unit, shown in Figure 1-20, had a 15 mm diameter and 45 mm length [46]. They performed two tests, named A and B. By



supposing the scavenging efficiency to be 50% for these tests, they estimated that the efficiency of power conversion was 4.7% for Test A and 7.5% for Test B [61].

At the Korea Institute of Science and Technology (KIST), Lee *et al.* [79] worked on an alternative design for electrical extraction from this free-piston design. In this new design, a three-layer sandwich of photosensitive glass (Foturan) was used to reduce thermal losses (when compared to silicon).

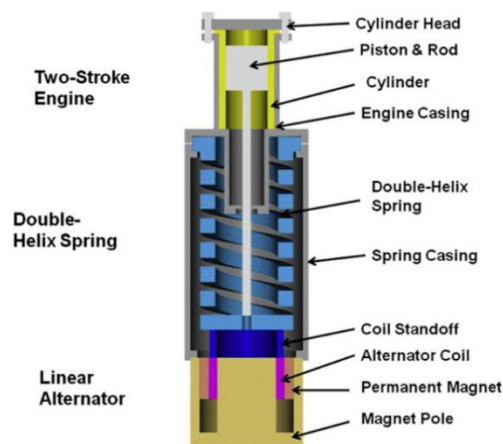


Figure 1-20 : Linearly Oscillating Miniature Internal Combustion Motor (MICE) [46].

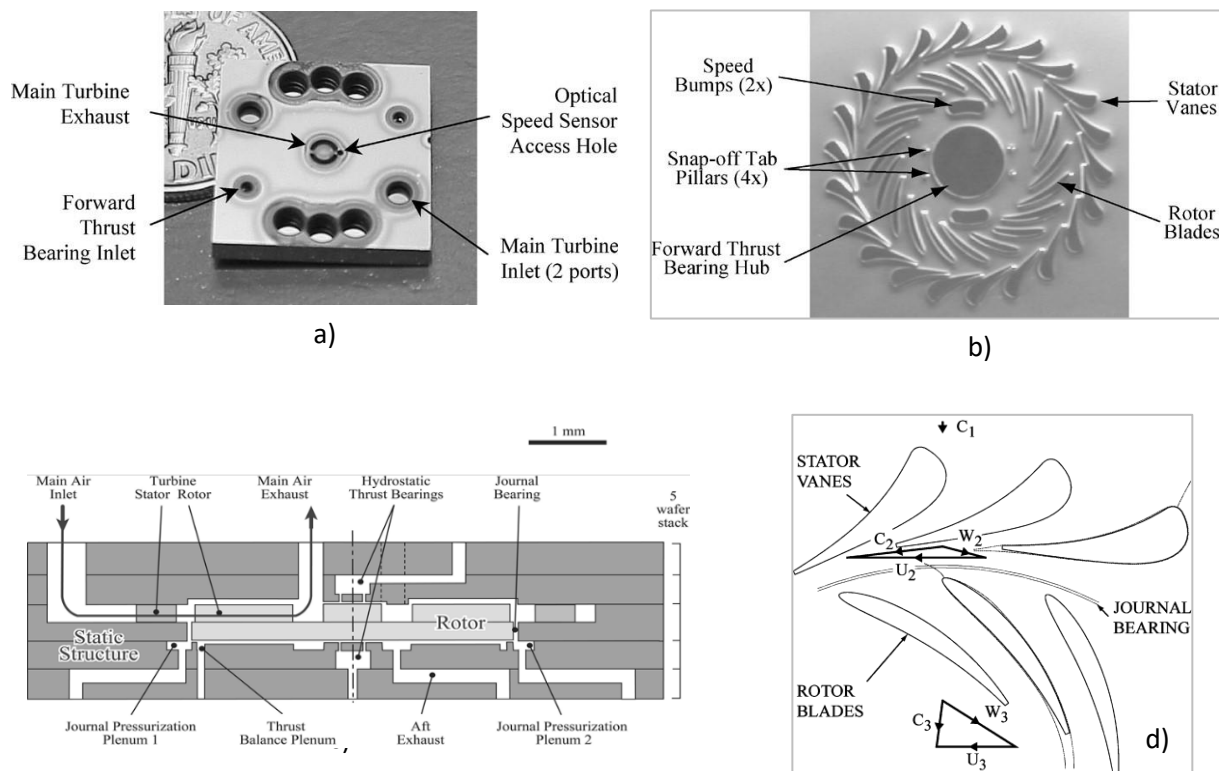


Figure 1-21 : a) Microturbine-driven bearing rig die, consisting of a diced five-wafer bonded stack (15 mm x 15 mm), which encloses a free silicon rotor. b) Optical photograph of the 4.2-mm diameter microturbine showing the stator and rotor blades (150  $\mu\text{m}$  tall) c) Schematic view of a cross section of the microturbine-driven bearing rig. d) Velocity triangles through the microturbine (computed with MISES at a design rotation rate of 250000 rad/s). Dashed lines around a stator vane and rotor blade outline the boundary layers [80].

In 2005, Fr chet te *et al.* [80] at University of Sherbrooke proposed an air turbine supported on gas-lubricated bearings operating at  $1.10^6$  rev/min with about 5 W of mechanical power levels. The microturbine (micromachined in a single-crystal silicon) converts the fluid energy to mechanical energy consequently generating torque on the rotor. The rotor consists of a planar disk with radial turbine blades etched on its front side. The combination of this torque and the rotor's angular rotation rate constitute the overall power transferred to the rotor.

The microturbine is constituted of a rotor of 4.2 mm-diameter encapsulated in a stack of five aligned silicon substrates (15 mm x 15 mm), through-etched and fusion-bonded. The device operates as follow, the pressurized

air enters near the outer edge of the device, flows radially inward (through the turbine), and then axially exhausts near the device center. The microturbine device and its components are presented in Figure 1-21.

Peirs *et al.* [81] at Belgium institute for research and education, proposed a turbo-shaft set-up for measuring compressor and turbine maps for an ultra-miniature gas turbine (impeller diameter of 20 mm) generator of 1 kW. The entire setup, the schema and the assembled components are shown respectively in Figure 1-22 a), b) and c). They tested their device for speeds up to 75 000 rpm and it produced a relative pressure up to 35 mbar. The installation works well, but imbalance issues have limited the test speed [81].

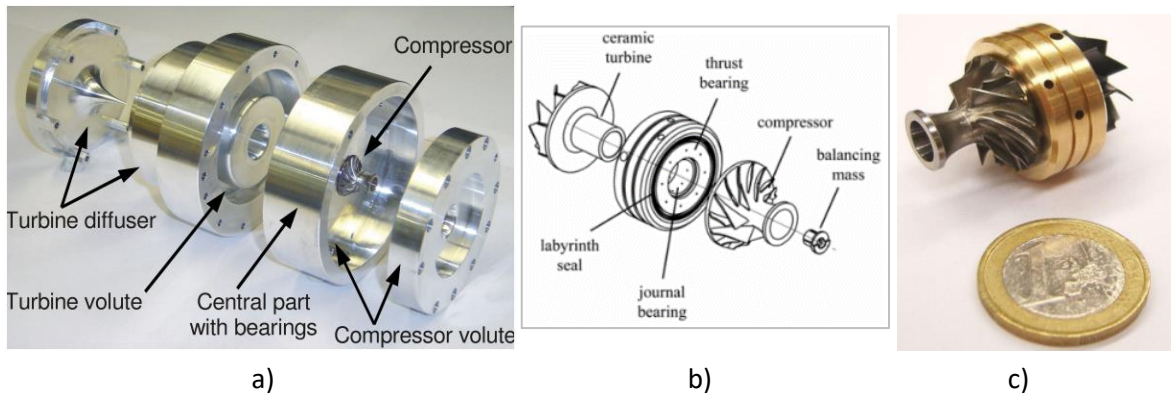


Figure 1-22 : a) Turbo-shaft setup. b) Schematic view of the compressor and turbine. c) Compressor (left), turbine (right) and air bearing insert (Rotor diameter: 20 mm- Size compared to 1 euro coin) [81].

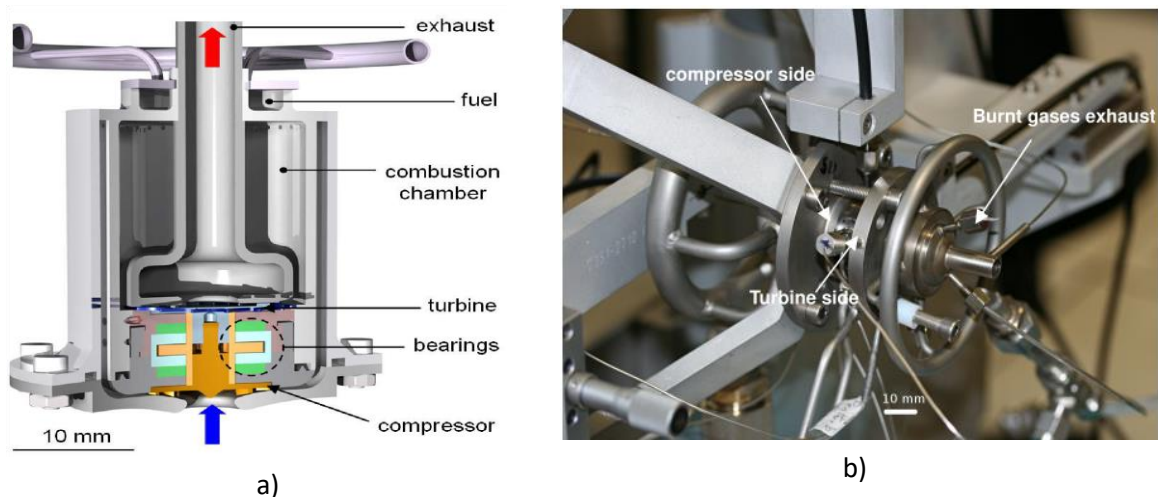


Figure 1-23 : a) Architecture of the micro gas turbine motor [82]. b) Prototype on the test bench.

In 2013, Dessornes *et al.* [82] at ONERA worked on a research project called DecaWatt. The objective of the project was to realize a prototype of a micro gas turbine motor, based on Brayton-Joule cycle, capable of generating about 50 to 100 Watts of electrical power. A sketch of the device architecture is illustrated in Figure 1-23a) and Figure 1-23 b) shows a picture of the actual prototype installed in their test lab. According to them, with realistic assumptions, an overall efficiency of about 5% to 10% (for a gas temperature of 1600°K) could be achieved which is about 200 W / kg while considering the mass of the motor of the micro-gas turbine, its electronics, fuel and packaging. The major micro turbine components chamber (combustion, micro compressor, and microgenerator) were designed and tested separately after a performance analysis step. Without considering the dimensions of the outer packaging, the electronics or the fuel tank, the micro gas turbine, alone, has a diameter of 22 mm and a height of 32 mm. The complete setup was under fabrication until 2011. However, the small size (around 12 cm<sup>3</sup> of total volume) of the complete micro turbine causes many issues such as the rotating parts efficiency, the necessity of gas bearings because of the very high rotation speed, the heat management or the combustion in very small combustors [82]. The flows at very low Reynolds number in channels have limited the mixing between the air and the fuel. The short residence times of the mixture becomes of the order of the chemical reaction times and increased heat losses, which was already increased due to larger viscous forces [48].

Fernandez-Pello [59], Chigier *et al.* [83] and walther *et al.* [46] produced three reviews on small-scale energy production using combustion. In these reviews, the authors presented a detailed summary of the opportunities, technological advances, design challenges, and operational issues faced by specialists in the manufacture and implementation of internal combustion micro-power generators. In their analysis, challenges such as frictions, liquid fuel injection, fluid-wall interaction, air-fuel mixture, thermal quenching, catalytic combustion, and microfabrication are commonly encountered in small-scale devices. The main factor causing the low efficiency of micro combustors is often due to the thermoelectric component and not to the combustion process itself. In turbines/motors developed (or being developed) in the literature, the problem appears to be linked to fabrication and thermal management which both limit the tolerances in moving parts (leakage, low compression ratio) reducing the efficiency of individual components such as compressor and combustion chamber. Moreover, there are some additional issues that must be taken into account, such as environmental and thermophysical ones.

There is an expectation of non negligible unburned hydrocarbons (such as CO and other products of incomplete combustion) due to the smaller combustion efficiencies, which would require post-combustion treatment. Regarding the use of hydrogen, many devices concepts claiming only water emissions are in development. However, CO<sub>2</sub> is emitted since those devices are usually coupled with an on-board reformer (usually from a source of methanol) [84]. Moreover, the energy required for the water gas shift reformation process should be considered. A major hindrance of the silicon-based MEMS combustors implementation is their oxidation upon exposure to high-temperature and humidity affecting device performance.

The small size of the micro devices and of their components induces particular behavior in the physics involved in the device operation (fluid mechanics, heat transfer and combustion). The Reynolds<sup>2</sup> and Peclet<sup>3</sup> dimensionless numbers both decrease when the characteristic length of the device is reduced. As a result, the viscous effects and diffusive transport of mass and heat become more and more important. The basic requirement for micro-combustion to occur is that the time available for combustion called physical time (or residence time) must be larger than the combustion time (*i.e.* the time required for the chemical reaction to occur). Regarding combustion, the fuel residence time decreases as the length of the combustion chamber decreases, knowing that it must be longer than the chemical time for complete combustion to occur. The fluid flow is primarily laminar for MEMS-scale micro-devices with very small characteristic lengths (small Reynolds and Peclet numbers consequently). Another consequence is that the diffusive and viscous terms can become dominant while the convective and floating effects become negligible. This implies that in micro-devices it will be difficult to keep fluid flow velocities, mass concentration and temperature differences, at the same magnitude than in classic “meso” or “macro” motors. In the next section, we will focus on miniaturized devices with external sources of energy (no internal combustion).

### 1.5. Small scale devices (motors and harvesters) without internal combustion

The harvesting of energy is a very broad field that encompasses the exploitation of the natural energies of the environment, but also the recovery of lost or dissipated energies because of the inefficiency of energy conversion systems (motors, metallurgical foundry, Joule effect *etc.*) as well as the heat lost in the heating systems (heating plate and electric oven...) *etc.* This field provides a route to create complete autonomous and self-powered electronic devices like free wireless environmental sensors and actuators.

This is particularly relevant when one is interested in the labor costs to install complex wired systems and sensors deployed in inhospitable or hard to reach areas as well as the time and cost that is necessary to replace and maintain their batteries. Therefore, energy harvesting is a subject that continues to receive both industrial and academic interest. The energy recovery devices that will come out of this area of research will have the ability to deliver

<sup>2</sup> Reynolds number : defined as the ratio of inertial forces to viscous forces within a fluid.  $Re = \frac{U.L}{\nu}$  with U the velocity [m/s], Lc the characteristic length [m] and  $\nu$  the kinematic viscosity [m<sup>2</sup>/s].

<sup>3</sup> Peclet number: defined as the ratio of the rate of advection (of a physical quantity) by the flow to the rate of diffusion (of the same quantity) driven by an appropriate gradient. In heat transfer, it is the product of the Reynolds and the Prandtl number (ratio of momentum diffusivity to thermal diffusivity,  $Pr = \frac{C_p \cdot \nu}{\lambda \cdot \rho}$  with Cp the specific heat [J/(K.kg)],  $\lambda$  the thermal conductivity [W/(m.K)] and  $\rho$  the density [kg/m<sup>3</sup>])

sustainable energy to a wireless system network (safety-monitoring devices, structure-embedded micro-sensors and medical implants) through energy recovery from their immediate environment.

However, being small in size, an energy recovery microsystems typically provide very small amounts of electrical power ( $\mu\text{W}$  to  $\text{mW}$ ). Nevertheless, this power could be enough to run small daily life device (*i.e.* wireless sensors and actuators). In many situations, this lost heat could be captured and converted into useful electric energy. The advantages of using MEMS technology is that it would allow the fabrication of small, easily integrable micro device to harvest this lost thermal energy. In the next sections, we will thus present some micro-devices among which some are, or could be, used to harvest heat energy.

### 1.5.1. Non-Stirling type: micro-devices and heat harvesting

Lost heat is everywhere around us. Whatever the initial form of each energy process (kinetic, chemical or electrical), it eventually turns into heat, which eventually degrades at room temperature. Every year, billions of dollars' worth of energy is thrown away in the form of waste heat from industries, cars, and household appliance *etc.* For example, only 25% of the energy generated from a car's internal combustion motor produces motion, and through the alternator, generates electricity to power electronic accessories. The remaining 75% of the energy from the combustion are lost through heat [6].

The waste heat sources include cooking plates, motor exhaust, cooling, the leading edge of an aircraft wing, electronic devices, building air conditioning, solar radiation and even human body.

In heat harvesting technology, **Thermoelectric Generators** (TEG) are the state of the art, to directly convert heat into electricity. However, TEGs still suffer from low conversion efficiency and high costs, since they are made up with rare earth materials (e.g. bismuth telluride) and they also suffer from low thermal insulating properties [6]. To date, the typical conversion efficiency of a TEG device is in the range of 10 to 20 microwatts per square centimeter ( $\mu\text{W}/\text{cm}^2$ ). Therefore, any improvement on the conversion efficiency would result in significant module size reduction and cost savings. Recently, BMW company announced the use of 24 TEGs modules on a car exhaust pipe that generated 600 watts of electrical power on highway driving conditions, which represents 30% of car's electrical energy requirement [6]. In addition, the human body generates an estimated average heat power of  $5.3 \text{ mW} / \text{cm}^2$ . Generating electricity efficiently by harvesting this heat would enable autonomous wireless health monitoring technology. The implementation of this idea has already been attempted by the use of a TE generator attached to the human body to power portable wireless detection system. Apparently, two factors made the portable wireless detection system unusable, namely the limited conversion efficiency of TE device combined with the low temperature gradient between the human body and its immediate environment [6].

In 2003, Whalen *et al.* [47] at Washington State University proposed a dynamic micro heat motor called  $\text{P}^3$  based on expansion and compression by membranes of a two-phase working fluid (*cf.* Figure 1-24) [85]. The  $\text{P}^3$  micro heat motor, which heat source is external is fabricated with standard micro-fabrication techniques. The  $\text{P}^3$  denomination refers to the three-part strategy that the micromotor use to produces electrical power. The expander membrane had a  $3 \mu\text{m}$  PZT layer sandwiched between Pt electrodes. For the first time they demonstrated the electrical power production by a dynamic micro heat motor (with a novel thermodynamic cycle) converting heat into mechanical power then electrical power using thin-film piezoelectric membrane. The device consists of two thin membranes encapsulating a cavity filled with a saturated, two-phase working fluid. The top membrane being a thin-film piezoelectric generator as illustrated in Figure 1-24 b). The power produced by the  $\text{P}^3$  micro heat motor is determined by dissipating, across a load resistance (a decade resistance box is used), the electrical output power from the piezoelectric membrane. A peak power of  $0.8 \mu\text{W}$  was obtained at a load resistance of  $14 \text{ k}\Omega$  using the resistance box for the piezoelectric membrane impedance matching [47].

In 2009, Cho *et al.* [86], from Washington State University, proposed the integration of the  $\text{P}^3$  micro heat motor (which heat input is external) with a Swiss roll type combustor for power production (a type of swiss roll was previously presented (*cf.* Figure 1-15). The images of the combustor and the micromotor are shown in Figure 1-25 a) and c) and the diagram of the assembly is shown in Figure 1-25 b). The combustor burns the hydrocarbon fuels to provide the heat transfer required to power the  $\text{P}^3$  micro motor.  $60\text{--}80^\circ\text{C}$  of operating temperatures were enough to run the micromotor with a reaction temperature of  $150\text{--}230^\circ\text{C}$  required by the Swiss roll combustor.

The maximum mechanical power of the motor is  $220 \mu\text{W}$  at a cycle speed of 8 Hz. The motor generated a peak to peak voltage of 400 mV at 2 Hz.

In 2005, Landis *et al.* [87] in their patent, proposed a heat motor made from MEMS technologies and comprising an electrostatic-interaction based converter in a generator capacitor. An oscillating gas alternately activates and deactivates the transfer of thermal energy from a heat source to the motor medium. The operating principle of the motor is described in Figure 1-26. The objective was to manufacture a low cost, reliable and maintenance free small-scale heat motor based on a gas enclosed in a chamber for electrical production.

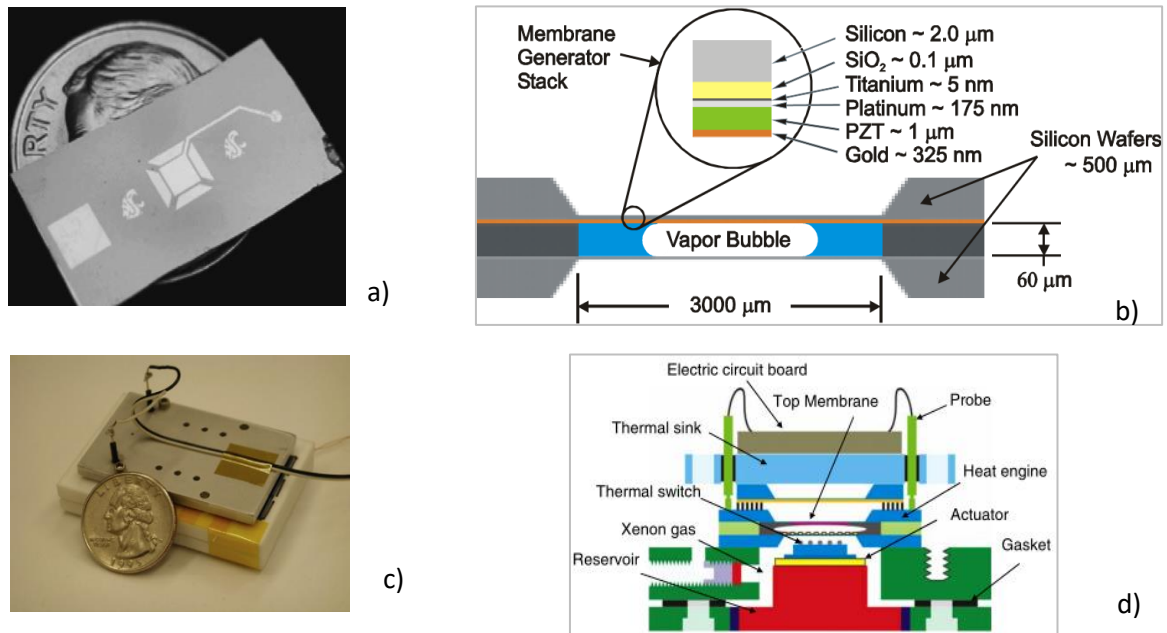


Figure 1-24 : a) Photograph of a completed P<sup>3</sup> piezoelectric membrane generator. b) Cross-section of the prototype micro heat motor and composition of the piezoelectric membrane generator. c) Photograph of P<sup>3</sup> micro-motor integrated with the thermal switch set-up. d) Schematic of an integrated micro motor and thermal switch set-up. Whalen *et al.* [47] [88], [85].

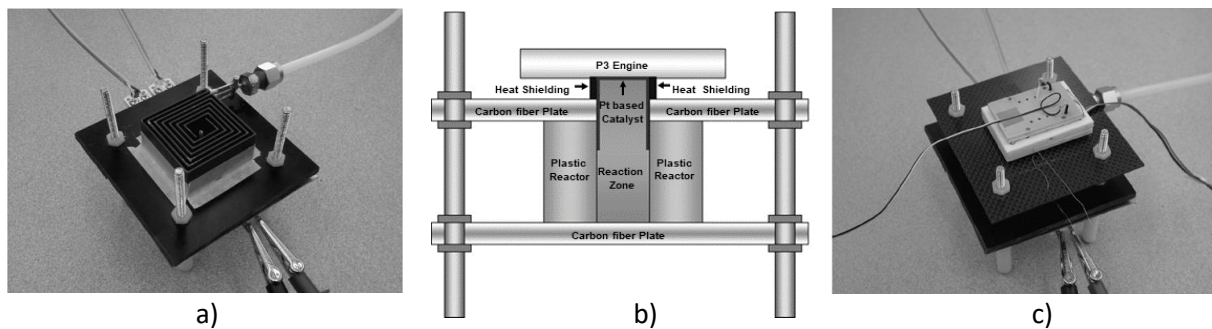


Figure 1-25: a) CNC-milled Vespel™ Swiss roll combustor in experimental stand; top plate removed for clarity, b) schematic of experimental configuration. c) micro-motor mated with Swiss roll combustor in experimental stand [86].

In 2010, Huesgen *et al.* [89] at university of Freiburg proposed a micro heat motor fabricated in silicon micro technology (*cf.* Figure 1-27). The device working principle is based on a cavity filled with a liquid–gas phase-change that performs a self-controlled reciprocating motion between a heat source and a heat sink. The respective upward and downward driving forces upon expansion and contraction of the working fluid in the cavity are generated by a bistable buckling membrane. The motor performance prediction at a temperature difference of 37 K is an operating frequency of 0.72 Hz and a mechanical output power of  $1.29 \mu\text{W}$ . As test case to verify this model, they fabricated a functional demonstrator. Experimental results showed an operation frequency of 0.71 Hz at a temperature difference of 37 K.

In 2015, Arnaud *et al.* [90] proposed the use of a thermal motor based on bi-metallic bistable membranes to convert heat into mechanical energy as illustrated in Figure 1-28 a) and b). These bimetallic strips (*cf.* Figure 1-28 c) use their thermo-mechanical properties to convert heat into mechanical energy. According to them, these bimetallic strips are simple and therefore their miniaturization is possible with MEMS fabrication techniques. In their study,

they evaluated the ability of these bimetallic strips to convert heat regardless of their size, as well as the theoretical thermomechanical yields that can be obtained with these harvesters.

In 2018, Zhan et al. [6] in their patent proposed a MEMS-based bi-stable cantilever heat harvester located between a hot temperature surface and a cold temperature surface. This kind of harvester (*cf.* Figure 1-29) is different from conventional thermoelectric techniques that use a direct heat-to-electricity conversion mechanism. The harvester is made up of three materials of different thermal conductivity coefficients and a mechanical-to electrical energy converter like a piezoelectric device or an eletret. Heat is first converted into mechanical strain energy by inducing vibration in the bi-stable MEMS cantilever, which is then converted to electricity via an integrated electro-mechanical converter. The temperature difference makes a tension bar enabling the bi-stable MEMS cantilever to vibrate between its two stable positions, with significant tip displacement.

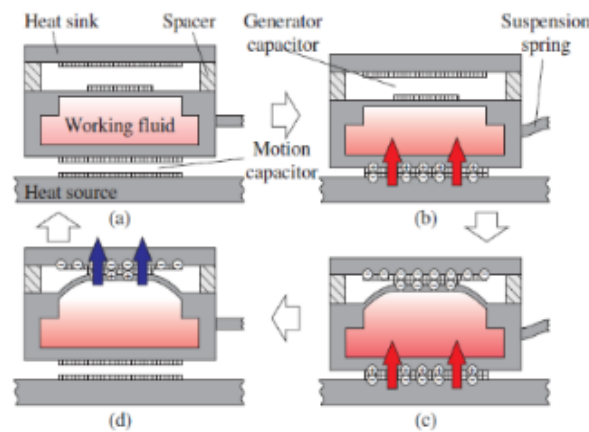


Figure 1-26 : Explanation of the operating principle of the Landis motor (US Patent 1995) [87].

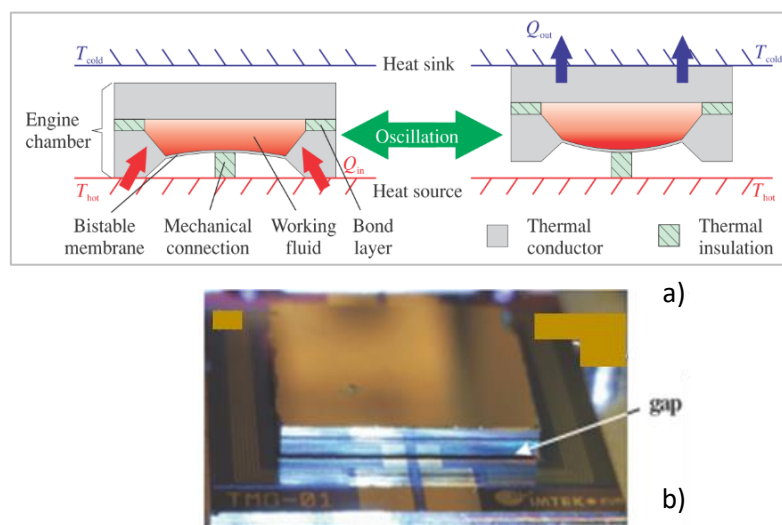


Figure 1-27 : a) Schematic cross-sectional view of the micro heat motor in 'down-state' and in 'up-state' [89]. b) Optical micrograph of the micro heat motor.

The tension bar is in series with a thermally expandable bar, which realizes a self-adjusting mechanism to guarantee a thermally induced vibration between the bi-stable MEMS cantilever's two stable positions. Unfortunately, performance data is not provided in the patent.

In 2018, Salamon et al. [8] have proposed an oscillating thermoelectric device made from silicon. This small device (diameter of 2 cm, thickness less than 2mm), designed with three silicon layers, converts heat into electricity by applying phenomena of liquid-gas phase change and piezoelectricity. The device consists of evaporation chambers and condensation, a channel connecting these two chambers and to ensure energy conversion, a layer of PZT is mounted on the top of the structure.

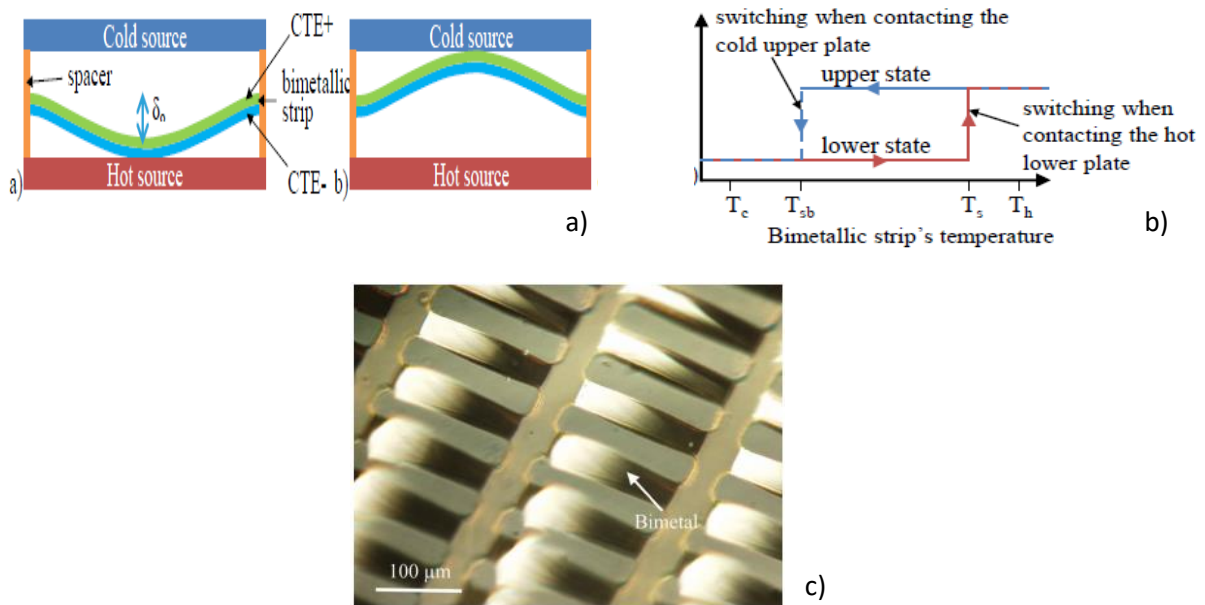


Figure 1-28 : a) Scheme representing the bistable harvester operation. b) bistable operating cycle. c) Micro-bimetals in Ti–Au fabricated [90].

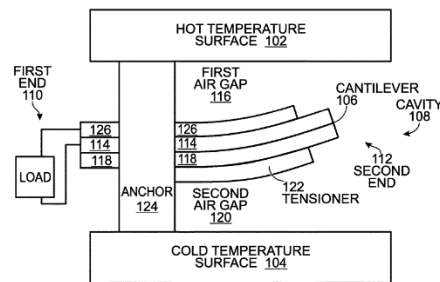


Figure 1-29 : Schematic view of the Bi-stable MEMS cantilever heat harvester [6].

To conclude, there exists numerous type of harvesters, mainly based on conversion of heat or mechanical energy into electricity. Usually, the harvesters based on thermal exchanges required a heat source that is often a combustion motor. The devices previously presented excluded the devices based on miniature Stirling motor. Those last ones are focused on in the next section.

### 1.5.2. Stirling motors and their miniaturization approach

Because Stirling motor don't internally involve burning fuel, their biggest advantage is that they can run from all kinds of different sources, and thus be much cleaner and environmental friendly. Moreover, they are quieter than internal combustion motors, because they do not have the complex system of opening and closing valves. The Stirling cycle has also great potential because it has a performance superior to the efficiency obtained from the Rankine or Joule cycle, its configuration coming close to the ideal cycle of Carnot. Currently, electrical efficiencies of macro and meso Stirling motors are around 35% to 40% when the motor itself is optimized [22].

To our knowledge, in the literature, there are no concrete (or operating) achievements concerning a MEMS-based Stirling type micromotor, whatever the intended application. Besides the Stirling micromachine, as regards the recovery of thermal energy by micro-machines, the number of practical achievements in the literature remains very low. We have done a study on the existing achievements of these motor. The word motor refers to a thermomechanical or thermo-electro-mechanical system if an electric converter is integrated. Before presenting the literature review concerning miniature Stirling motor, we will begin by shortly presenting some literature concerning the regenerator in MEMS technologies.

### 1.5.2.a. The regenerator in MEMS technologies

The regenerator plays a crucial role in the Stirling cycle, in particular by absorbing and alternately releasing heat from and to the working fluid, making it possible to recycle the heat released during the isochoric cooling. At meso and macro scales, the regenerator is often a porous medium through which the working fluid flows between the hot source and cold sink. Consequently, the good concept will be one that will not be subject to thermal efficiency problems including heat losses by thermal conduction in the axis of the solid matrix and inefficiency of the heat transfer between the latter and the working fluid. Two of the recommended solutions are to put thermal barriers in the microstructure or to create rapid physical disturbances in the volume of the substrate.

Nevertheless, when considering microscopic scales, research on regenerators are quite rare. Nevertheless, Moran's work suggested a design consisting of a stack of staggered composite patterns as a regenerative element [91] (*cf.* Figure 1-30 a). Ibrahim [92], also, proposed a segmented involute-foil as a regenerative element (*cf.* Figure 1-30 b). Vanapalli [93], meanwhile, suggested micro pillars etched by DRIE in a microchannel. The micropillars with microchannel were constituting the regenerator.

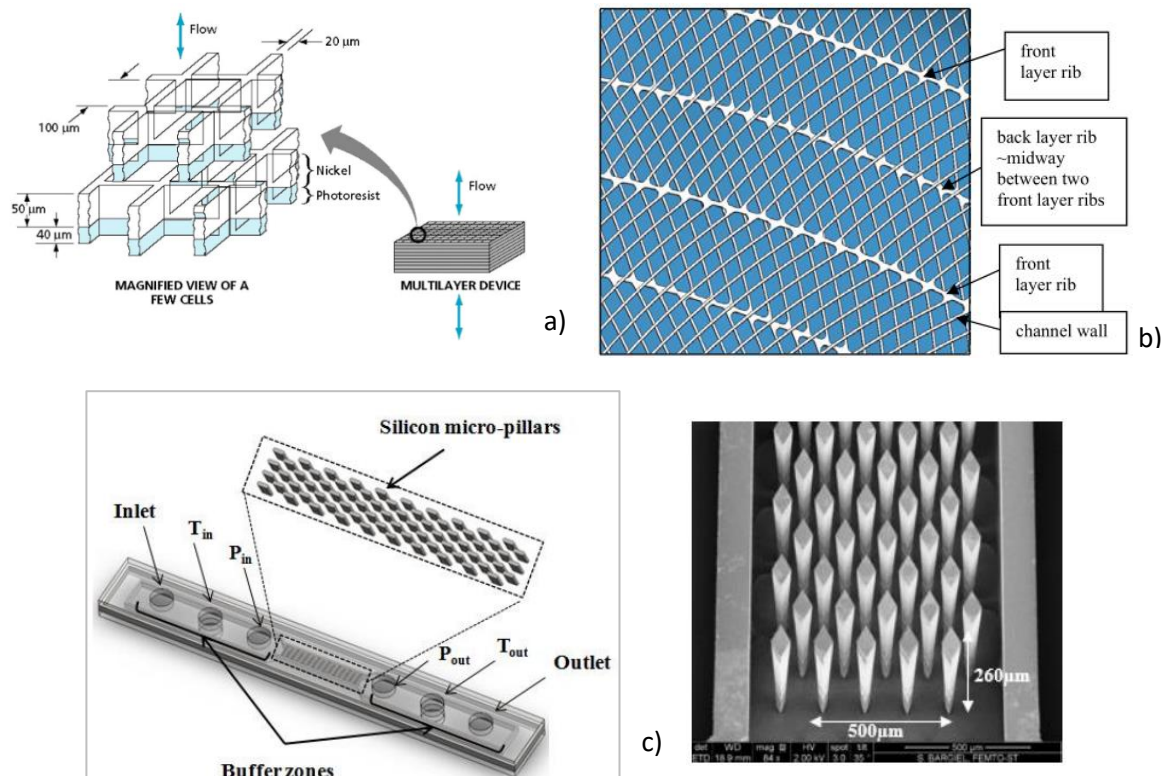


Figure 1-30: a) Sketch of balanced design of Moran [94]. b) Frontal view of two layers of microfabricated-segmented-involute foil. The other layers are repeats of these two types of layers [92]. Microdevice assembly and SEM of the etched microstructure with housing walls [13]

Recently, based on the previous studies, Dellali *et al.* [13] suggested a particular microregenerator geometry consisting of an integrated silicon microchannel with staggered micropillars etched by DRIE and encapsulated between two glass slices (*cf.* Figure 1-30 c). The porosity of the system ranges from 0.8 to 0.9. Among the three gases (air, helium and hydrogen) that they have simulated by Computational Fluid Dynamics, the results obtained show that helium has the highest pressure drop because it is the most viscous gas. This loss with helium (the fastest gas to heat) is more than twice that recorded with hydrogen. They had raise the need to find a compromise between heat transfer related to the thermal power and viscosity-related pressure drop when choosing the fluid and the regenerator design to obtain a viable microdevice. Their results have also shown that the transfer of heat energy from the heated walls to the working gas is mainly through thermal diffusion rather than advection even if forced convection is taken into account. Their discovery is interesting because the time that the heat exchanges between the gas flow and the heated microstructures occur was supposed to be very short (about  $10^{-3}$  seconds). However concerning the pressure drop, the existing correlations were not appropriate, so they could not, therefore, evaluate the coefficient of pressure drop along the microchannel. This silicon-based micro regenerator is planed to to be integrated into the micro-Stirling manufactured during this present PhD [95].



### 1.5.2.b. Micro-Stirling machine for heat harvesting

In 1989, Nakajima *et al.* [36] were among the first to attempt to build a small Stirling motor that can fit on the palm of a hand with a size less than cubic centimeters for applications such as a micro-actuator and a micro-heat pump (*cf.* Figure 1-31) . They began by applying dimensional analysis and computer simulation to, first, examine how design parameters vary when motor size is reduced. Based on this analysis and simulation, they designed a small Stirling motor about 2cm wide and 3cm high (external dimensions) weighing about 10g and swept volume about 0.05cm<sup>3</sup>. This small centimetric Stirling motor was able to produce about 10mW of mechanical power at 10Hz with 100K of temperature difference between hot and cold walls (*cf.* Figure 1-31). They also showed the problems related to the miniaturization of the motor up to a few cubic millimeters. Figure 1-31 show a photograph of their centimetric Stirling motor.

Concerning the problems linked to miniaturization, Peterson [96] in his study in 1998 of scaling analysis of regenerative heat motors concluded that, in order to maintain a thermal efficiency above 50% of the Carnot efficiency, the lowest size of a regenerative heat motor should not exceed 1 mm approximately.

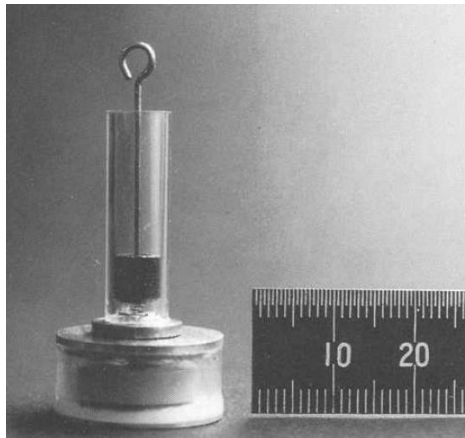


Figure 1-31 : Image of the micro-Stirling motor [36].

Reference	Notes	Working gas	Pressure (MPa)	Frequency (Hz)	Temperature (°C)	Output power (W)	Efficiency (%)
Nakajima et al. [36]	"Snap-action spring-type displacer, annual gap regenerator, swept volume of 0.11 cm <sup>3</sup>	Air	0.1	10	$\Delta T=100$	0.02	N/A
	Magnet-embed type displacer, annual gap regenerator, swept volume of 0.05 cm <sup>3</sup>	Air	0.1	10	$\Delta T=100$	0.01	N/A

Table 1-4: Data on Nakajima small Stirling motors. [36]

In 2010, Formosa [97] at university of Savoie proposed a new design of membrane-based Stirling type micromotor. To test the potential performance of this micro-Stirling, he assumed that a micromotor with 100mm<sup>3</sup> membrane stroke volume at 680 Hz, could theoretically produces 1.5W of mechanical power corresponding to 0.18 W/cc. This is equivalent to an efficiency of 48% of that of Carnot or an overall efficiency of 12%. Figure 1-32 show the axisymmetrical architecture of this micro-Stirling design. He showed that many performance losses would result from thermal transfert through the structure static parts and through the expansion diaphragm central part. The other losses were attributed to the working-fluid flow viscous friction throughout microchannels ducts and the regenerator. His results pointed out that the heat conduction losses through the structure was the most significant source of performance dissipation, which was simulated to reach 1.3 W for his design.

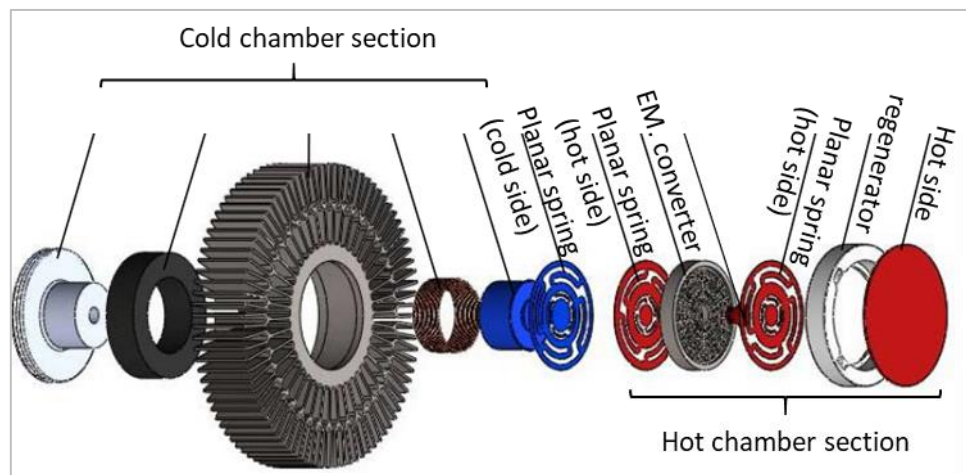


Figure 1-32 : MicroStirling generator architecture design [97].

Steiner and Archibald [98] in 2014 developed a diaphragm Stirling motor in which the diaphragm was connected to the drive shaft through a folded spring tube with a large stiffness as shown in Figure 1-33. In their motor two flexure structures with tuned resonant frequency acted as the displacer. The diaphragm displacement was within 1 mm which was one or two orders smaller than those of pistons in traditional Stirling motors. But, the main feature of the motor was the lack of high tolerance sliding seals which enabled it to have a low cost and long life. There are also several studies using silicone as the diaphragm material [10], [11]. According to them, the system can only withstand ambient filling pressure, and had very limited power outputs. The above studies indicate also that high frequency and high pressure are critical approaches for improving the power outputs of diaphragm Stirling motors for practical uses.

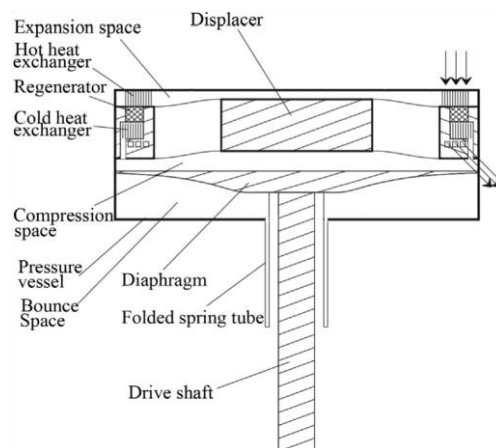


Figure 1-33: Diaphragm Stirling motor built by Steiner and Archibald [98].

### 1.5.2.c. Micro-Stirling machine for cooling

In a micro scale Stirling cooler, heat is released from the hot chamber during the compression phase and absorbed from the cold chamber during the expansion phase.

The craze for the miniaturization of Stirling coolers for application in the cooling of electronics for example, have been restrained to scale by the use of traditional components (eg pistons, crank-rod and pressurized chamber) [99], [100]. Efforts to build a micro-scale Stirling cooler prototype, through a series of cryocooler patents [94], [101], have solved the problems of friction losses and gas leaks by replacing conventional pistons and the associated links by electrostatic diaphragms.

In 1995, Bowman *et al.* [101] in their patent proposed a planar Stirling microcooler constituted by silicon plates carrying membranes and a bonded intermediate regenerator. This thermomechanical Stirling cycle transducer, as it was called, was manufactured using semiconductor planar processing techniques and was driven by a controlled circuit designed to operate at about 1kHz.

The regenerator is located between two plates located at the ends and constituting the zones of compression and expansion of the micro-cooler. The state of the art at that time for Stirling cycle machines considered an upper limit of operating frequency of the order of 50 Hz. Thus, a machine up to 120 Hz was considered the highest frequency never built. The goal of the invention was to construct a Stirling type cryocooler whose size and weight are sufficiently small with a specific acceptable capacity and which is also compatible with equipment using electronic circuits. The cryocooler had to be able to suck the electronic devices heat at a sufficiently high speed to keep them at cryogenic temperatures.

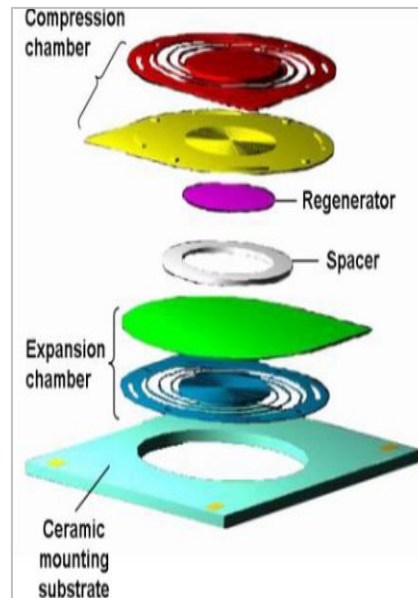


Figure 1-34: Micro-Stirling cooler design and assembly step [94].

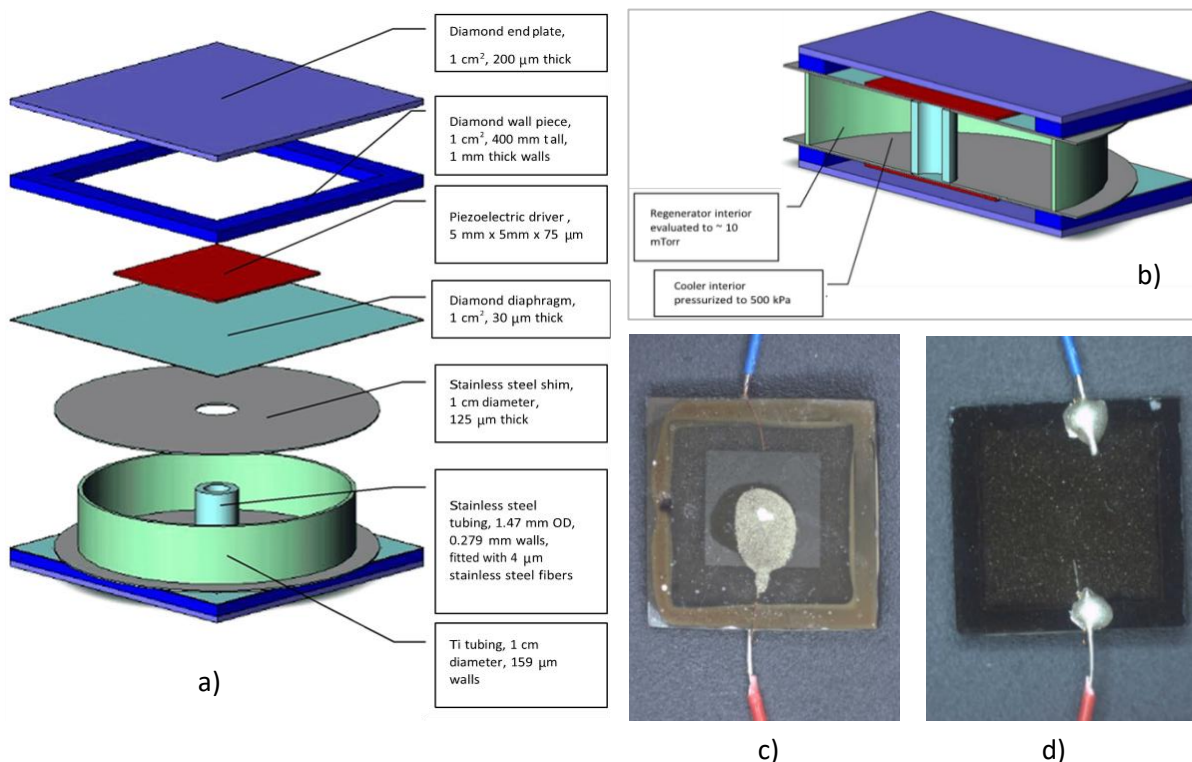


Figure 1-35 : a) Side view and b) Blow-apart views of the final design of the diamond-based MEMS Stirling cryocooler c) The diaphragm side view shows the internal components and d) the backside view shows the external lead attachment [102].

Moran ([91], [94]), in his concept of micro Stirling cooler, (*cf.* Figure 1-34) used silicon membranes of 1 to 2 cm in diameter powered by vertical electrostatic comb controls to move the working gas through a double regenerator layer (metal / polymer). High heat losses from the hot side to the cold side remain difficult to minimize.

Patterson et al. [102] in 2007, proposed an alpha miniature Stirling cooler, 1 cm x 1 cm x 3 mm in size, with CVD-deposited diamond films as illustrated in Figure 1-35 a) and b). The diamond layers are deposited on the heat exchange plates and the compressor and expansion membranes (*cf.* Figure 1-35 c) and d)) to increase their heat capacity ( $>900 \text{ Wm}^{-1} \text{ K}^{-1}$ ). Internally fixed crystal piezoelectric transducers power these membranes. The device also has a reduced dead space and a regenerator with low thermal conductivity. The objective of this micro-refrigerator made with MEMS technologies was to provide a solution to the growing need for a high-performance miniature chiller.

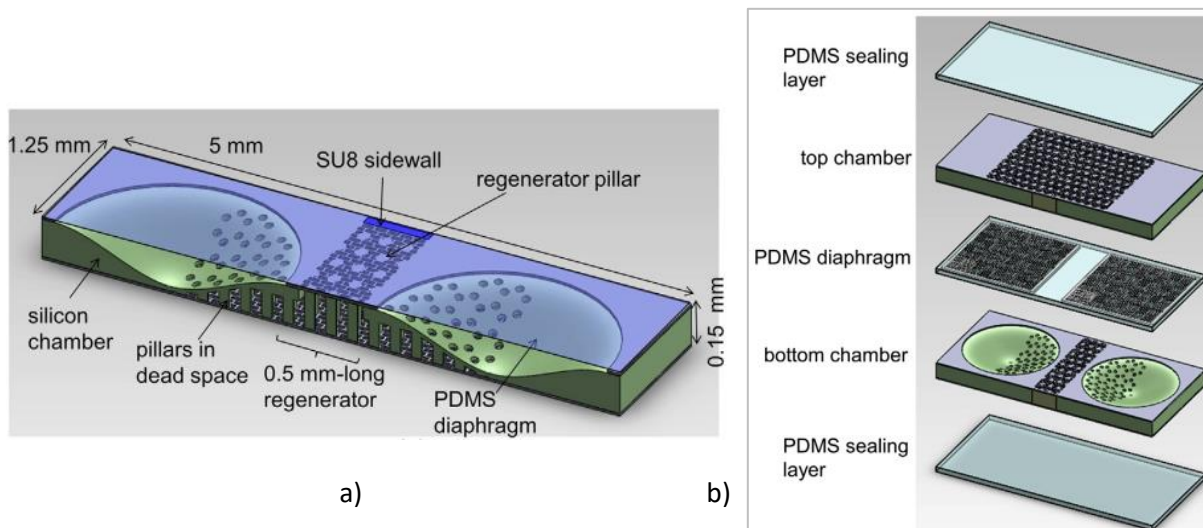


Figure 1-36 : a) Solid-model cross-section view of the Stirling microcooler system. b) The micro cooler in exploded view ( $5 \times 2.5 \times 150 \mu\text{m}$ ): The assembled structure has five parts: the diaphragm layer in the middle, the top and bottom chamber substrates, and two sealing PDMS layers [103].

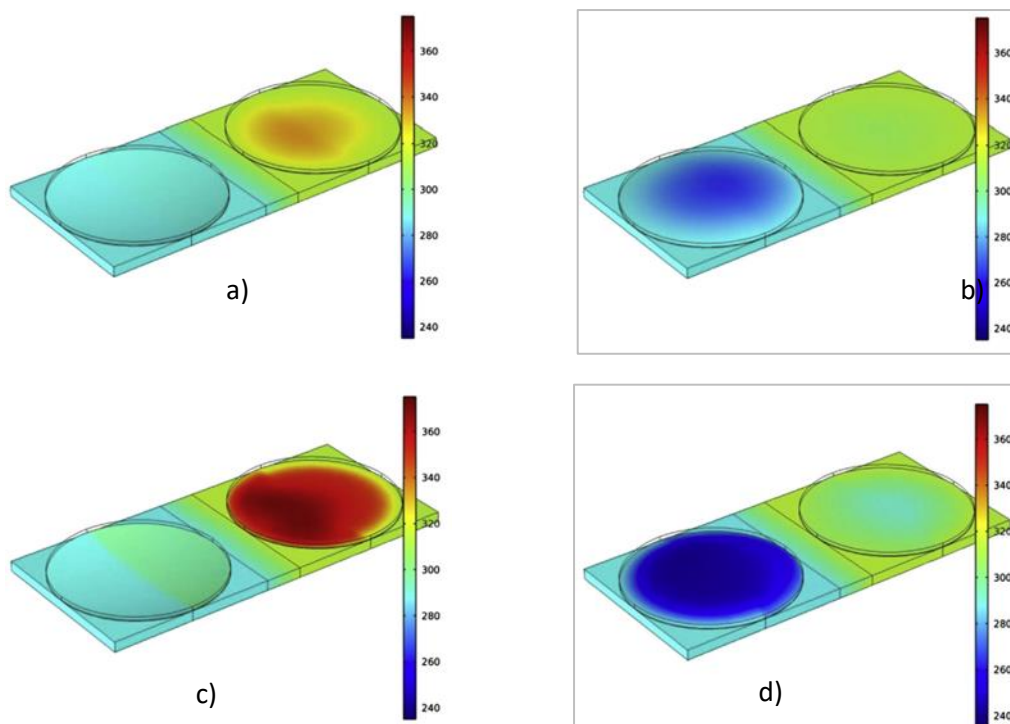


Figure 1-37 : Temperature contours for the full Stirling cooler system simulation at: a) One quarter of the cycle at an operating frequency of 100 Hz. b) Three quarters of the cycle at an operating frequency of 100 Hz. c) One quarter of the cycle at an operating frequency of 800 Hz. d) Three quarters of the cycle at an operating frequency of 800 Hz [104].

Both membranes oscillate at several kilohertz with an approximate phase shift of 90 degrees. The displacement amplitude of the chilling membrane is 4 microns and the working gas is charged at a pressure of 500 kPa to improve the efficiency of the device. Their experimental results showed that a membrane strokes larger than 5mm and higher frequencies larger than 10 kHz lead to rapid failure of the diaphragms. Although the microStirling performance modeling showed that it could deliver 68 mW of power with a temperature difference of 20 K between the two hot and cold plates of the device, experimental tests on many of their prototypes manufactured showed no reproducible cooling effect. The reason for the inefficiency of operation seems to come from the parasitic heat losses related to the miniaturization according to a further modeling.

In 2013, Guo et al. [103] reported the design of a new micro-scale Stirling cooling system, which includes two diaphragms and a regenerator that separates the hot and cold chambers. The micro Stirling cooler design in silicon have a length of 5 mm, a width of 2.5 mm and a thickness of 0.15 mm. Figure 1-36 a) shown a cross section view of the Stirling micro cooler design and Figure 1-36 b) illustrates the different parts of the micro-cooler. The compression and expansion chambers are distanced with a low thermal conductivity 0.5 mm-long passage (the regenerator) to minimize conduction heat losses across the regenerator. The regenerator is constituted by an array of vertical silicon pillars intended for transferring heat to and from the working gas during the cycle. The device is designed to operate with a working fluid such as air at 2 bar and the fluid flow is driven by electrostatically-actuated PDMS diaphragms.

Silicon pillars are also put in spaces between the two chambers and the regenerator (*i.e.*, the dead space) for improving the convective heat transfer between the gas and the silicon around the chambers. But, these pillars (in the dead space) are part of one continuous piece of silicon, as illustrated in the cross-section view. When diaphragms are (manually) sinusoidally actuated, they oscillate with 90° out of phase when the heat is extracted to the cold chamber and released from the hot chamber. The concept was modeled and numerically simulated and some results are presented in Figure 1-37. With their numerical simulation results, the authors found a cooling capacity of 4.2 W/cm<sup>2</sup> (COP<sub>4</sub>= 2.93) when the operating frequency of the system was set at 600 Hz and the temperatures of the heat source and heat sink were respectively 313.15 K and 288.15 K [104].

## 1.6. Conclusion

The trend towards energy-generators miniaturization is motivated by the need to reduce current small- devices weight (consisting largely of battery weight), increase their operational lifetime, and reduce the cost of daily life MEMS devices [49], [105] or compete with the price of high energy density small batteries. Unfortunately, challenges in the development of power-generation systems at small scales are still considerable. Many demonstrations that have emerged in recent years bear witness to the significant progress that were made in the field of power generation at small scale (electrical and mechanical), pushing this new frontier of technological development. However, the field is still, basically, in a feasibility phase because of the many technological challenges to be solved as mentioned previously [46].

The preferred approach to date is the miniaturization by downsizing (scaled-down) of large-scale classics combustion motors currently in use. However, on a small scale, there are many problems associated with fluid flow in micro-channels, heat losses and mass transport, good performance prediction and micro devices fabrication and characterization. Potential solutions reside in an effort of basic and applied research and development of manufacturing. Research needs to include, on the one hand, the study of fluid flow in low Reynolds number channels, fluid-structure interaction and thermodynamic modeling, investigation diagnoses, material selection. On the other hand, the manufacture of high precision structures and high aspect ratio (for adequate sealing for high compression ratios) and complex geometries, assembly, testing and characterization are required. Materials capable of withstanding the high temperature, harsh chemical environment, stress and wear due to combustion events and moving parts need to be developed. A repeatable and simple assembly technique must be developed for the mass production of devices as well as advanced functional testing and characterization techniques to optimize their performance. Note that, some might think that these problems could be avoided if the miniaturization approaches were based on new designs of small systems rather than the scale reduction of macro systems.

---

<sup>4</sup> COP= coefficient of performance, defined as the ratio of useful heating (or cooling) supplied by the system over the work required

Since we are going to miniaturize a motor in our work, it naturally seems necessary to study the state of the art in the miniaturization of internal combustion motors to understand the difficulties field's specialist faced during the miniaturization of moving parts and the solutions they could use or proposed to circumvent them. Moreover, since the Stirling machines have external heat input for their operation, one could well imagine using an external miniature combustion chamber as micro-Stirling motor's heat source, knowing that the hydrocarbons have a very high energy density that can lead to an extremely high temperature gradient. Micro-scale combustion seems to be possible with an understanding of the appropriate thermal and chemical management.

Moreover, some micro motors have been developed (albeit with very low yields or not operating) or are under development. However, more detailed modeling efforts are needed to design and improve existing designs to avoid friction losses, sealing issues, manufacturing and assembling challenges [83]. As to whether these mechanical problems can be solved, opinions differ. What is certain is that leaks, friction (caused by mechanical moving parts), wear and lack of thermal insulation result in a significant reduction in mechanical, thermal and combustion efficiencies. If these efficiency reductions are dominant, the small scale device may be unacceptable.

The particular interest on Stirling motor is justified by its high theoretical efficiency. For example, in the ideal case, the maximum efficiency is 38 % for a heat source at 200 °C and a cold source at 20 °C. Even if a few research groups have explored some aspects of the miniaturization of Stirling motors or combustion motor, many questions remain open, such as: what are the optimal configurations for a miniaturized Stirling motor? What are the sizes and materials of optimal components for these configurations? How do the limitations imposed by the current state-of-the-art in microfabrication technologies (clean room equipment's) affect the design of micro-Stirling motors?

The goal of this present thesis is to explore some of these questions. "Micro-Stirling motor" in this study means a miniature Stirling motor with a size smaller than a cubic centimeter. The type of Stirling motor chosen to be miniaturized in this work is a multiphase free piston double acting. It is constituted by three alpha-type motors arranged in a double-acting configuration by interconnecting several Alpha units in a series to form a loop and the next chapter is devoted to its design and the challenges related to the miniaturization.

**The main results of chapter 1 :**

A complete review of the literature about thermal micromachines and Stirling motors has been done, showing many attempts and few working machines.

## CHAPTER 2 : STIRLING ENGINE DESIGN CHALLENGES

As presented in chapter 1, the MISTIC project aimed at the miniaturisation of a macro motor composed of three alpha type Stirling motor linked to each other. The CAD scheme for the design of this double action multiphase Stirling micro-engine, proposed during the MISTIC project, is presented in Figure 2-1. The spirals (for instance, piezo material) were aimed to convert mechanical motion into electric energy or *vice versa*. The term "double action multiphase" basically means that several units Stirling micro motors are mechanically associated with each other by their chambers, knowing that the last module is connected to the first to form a looped system [5]. As a result, the energy of the gas expansion stage of a module provides the energy required for the next module compression step. The phase shift difference between the membranes is imposed by the number of associated modules [5], [106]. In the presence of three micro motor modules, the phase difference between the membranes is 120°C.

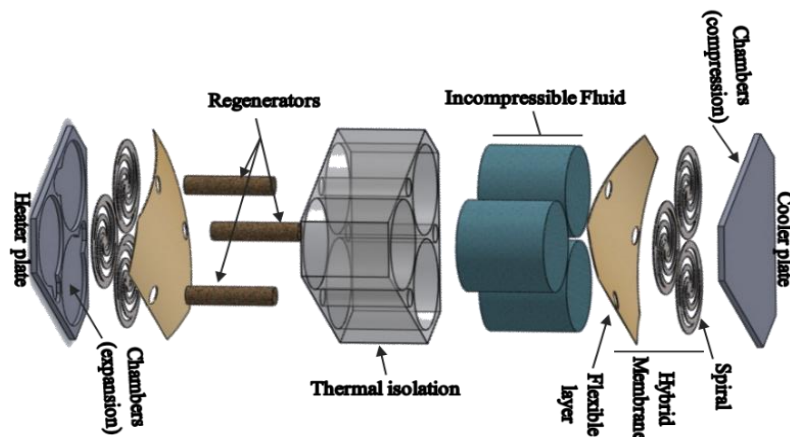


Figure 2-1: Schematic view of the MISTIC free piston multi-cylinder double acting microStirling motor [107].

The physical equilibrium or the balance of power between some physical phenomena changes when one miniaturizes mechanical systems with moving parts, such as for example motors. In practice, before miniaturizing, it is necessary to first determine the new physical equilibrium that may appear in microsystems to know if it is not disadvantageous to miniaturize. With respect to the reduction of the machine's dimensions, it is especially necessary to check:

- The behaviour of the thermal gradient or pressure to know if it will be maintained at small scale and to what extent.
- The impact of friction losses (fluidic and mechanical type) in small ducts and changes of direction or section (major and minor losses).
- Convective heat transfer between fluid and medium, the ratio of volumes, etc.

These factors affect the performance or the risk of non-operation of the reduced machine. This first analysis also makes it possible to know, during miniaturization, whether the size of an element of the macroscopic motor should be simply reduced or whether a complete design of a new element is necessary to accomplish the same final function for the micro-motor.

In this chapter, a mechanical, geometric, fluidic and thermal analysis of the risks related to the size reduction of the Stirling motor was carried out to evaluate the influence of various physical phenomena likely to change with the reduction of the scale. This chapter ends with the presentation of the final architecture of the machine. This latter corresponds to the compromise between thermal, fluidic, mechanical and technological pre-requisites.

### 2.1. Mechanical and design challenge

#### 2.1.1. Pistons versus membranes

In our study case, we tried to miniaturize an alpha type motor. At macroscopic scales, the setting in motion of the fluid in a Stirling motor is ensured by pistons. In MEMS technology, a miniaturized Stirling motor could basically consisted in two pistons in two cylinders connected by a regenerator canal (*cf.* Figure 2-2).

However, the problem with miniaturizing pistons is that it will increase the impact of leakage and friction losses between the cylinder-piston space at small scale. Moreover, wear is present in this friction zone located at the interface between the piston and the walls of the cylinders in classic macro motors. In fact, this zone must provide two antagonistic functions, namely keeping both a seal for the gas under pressure and at the same time limiting mechanical friction. Knowing that obviously to ensure a sufficient seal, it is necessary to tighten the piston in the cylinder while in order to limit the friction it is necessary to limit the contact. When miniaturizing, these friction losses can become proportionally predominant and be a critical point for the proper operation of the motor: one of the main challenges is thus to replace the piston with another element (to ensure sealing while minimizing friction losses). A solution recommended by **Der Minassian** to remedy this dilemma is the use of flexible membranes instead of conventional pistons [10]. These membranes allow both to completely eliminate these mechanical friction, and can at the same time provide a good seal when they are made of a suitable material.

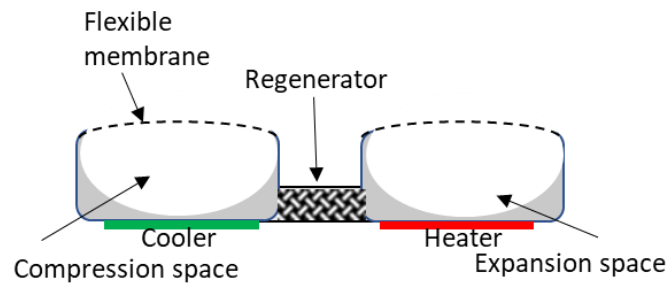


Figure 2-2: Basic model of an alpha Stirling machine in MEMS technologies

### 2.1.2. Mechanical connection challenge

Furthermore, the mechanical connection system conventionally used in macroscopic Stirling motors (such as crank-flywheel mechanism) is inefficient for MEMS motors because the power output of the flywheel is greatly reduced (due to friction losses) as the size is reduced too. Nakajima *et al.* [36], through computer simulations, has reported that the flywheel mechanism had a miniaturization limit of 9 mm before it became ineffective. Moreover, Peterson in 1998 [96], presented a detailed scaling analysis of regenerative heat motors and came to the conclusion that the lower size limit of a regenerative heat motor was approximately 1 mm. Note that, this size limit was set to keep a thermal efficiency above 50 % of the Carnot efficiency. The use of a flying wheel or an alternative energy reservoir is inevitable for a motor, because for every thermodynamic cycle a motor requires energy for the compression of the working gas. The analysis of the macroscopic Stirling motor shows that the phase angle of the displacer must be maintained theoretically at 90° in advance of the power piston. It would then be necessary to find a phase shift system in MEMS technology equivalent to the crank and flywheel system in conventional Stirling machines.

Taking into account the previous recommendations, for our MEMS Stirling motor, we chose a system of membranes fixed on the edges of their chambers: only their central part moves which limits the friction against the wall. The present section is dedicated to the mechanical challenges related to the replacement of the piston by a membrane.

### 2.1.3. Ratio between mechanical powers output and micromachine Stirling sizes

The Schmidt model (*cf.* details given in Annexe A) allows, for a simplified system and under assumption, to estimate the mechanical power that the Stirling motor could provide. At first, in order to fix the ideas on the size of our system and to verify the good agreement with the literature, we carried out an isothermal analysis. For this study, we set the hot temperature at 473K (maximal aimed temperature in the MISTIC project), and the cold temperature at 293K. Air properties were taken at the mean temperature, 383K (*cf.* Table 2-1). For this example, we used a similar geometry as the one given in the Figure 2-2, with a classical phase shift of 90°. The chambers are cylinders with a height set here at 600  $\mu\text{m}$ . The canal containing the regenerator was set constant at a volume of 4.6  $\text{mm}^3$ . Moreover, we assumed here the ratio between the swept volume and the chamber volume equal to 0.7.

T K	$\rho$ $\text{kg.m}^{-3}$	$\eta$ Pa.s	$C_p$ $\text{J.kg}^{-1}.\text{K}^{-1}$	$\lambda$ $\text{W.m}^{-1}.\text{K}^{-1}$	M $\text{g.mol}^{-1}$
383	0.922	2.215 10 <sup>-5</sup>	1013	0.0325	28.965338

Table 2-1 : Air properties at 383K [108].



To emphasize the influence of the motor size on the power, we only changed the chamber diameter, varying from 10 to 0.02 mm in diameter. *NB: Note that any change in the motor length would have a similar influence on the power since the volumes would change, we took here one example and choose to vary only one parameter to allow comparison.* Table 2-2 shows, for a frequency set at 1kHz and for different chambers radius (i.e. for different machine sizes), the chamber volume  $V_c$ , the dead space of the chamber  $V_d$ , and the resulting mechanical power.

The estimation of the machine power according to its size by the Schmidt isothermal analysis shows the size limit from which the mechanical power supplied by the micromachine would no longer be significant (cf. Figure 2-3 on the left), they are consistent with the recommendations found in the literature [36], [96]. Note that, since thermal losses in the case of a micromotor (and even in the case of a micro-cooler) were not considered in the present calculations, they are underestimated. Moreover, in the alternating flows that take place in the Stirling motor, at high frequency (as it could be the case with the use of membranes for the displacement of the gas), the fluid will heat up and there will be losses by compression-expansion of the gas. It could even lead to slow the fluid flow until it stops (because unable to follow the imposed movement). For all those reasons, in addition to the motor size and the dead space, the thermal and fluidic criterions must also be taken into account.

Chamber radius (mm)	5	4	3	2	1	0.5	0.25	0,1	0.01
Chamber volume $V_c$ ( $m^3$ )	4.71 $10^{-08}$	3.02 $10^{-08}$	1.70 $10^{-08}$	7.54 $10^{-09}$	1.88 $10^{-09}$	4.71 $10^{-10}$	1.18 $10^{-10}$	1.88 $10^{-11}$	1.88 $10^{-13}$
Chamber dead space $V_d$ ( $m^3$ )	1.41 $10^{-8}$	9.05 $10^{-9}$	5.09 $10^{-9}$	2.26 $10^{-9}$	5.65 $10^{-10}$	1.41 $10^{-10}$	3.53 $10^{-11}$	5.65 $10^{-12}$	5.65 $10^{-14}$
Powers (mW)	980	592	297	101	11	8.35 $10^{-1}$	5.50 $10^{-2}$	1.43 $10^{-3}$	1.43 $.10^{-7}$

Table 2-2: Schmidt model: examples of Power variation for different size of the Stirling motor

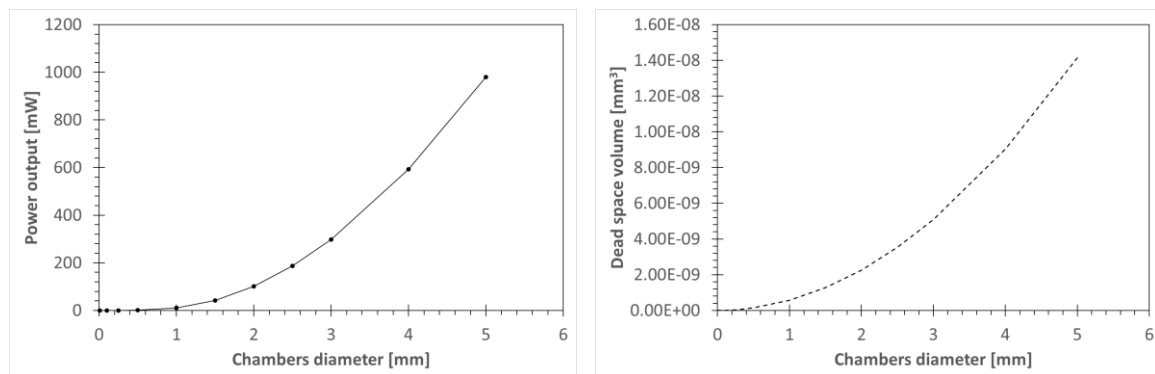


Figure 2-3: Example of the power output of a Stirling motor (determined with the Schmidt model) versus the chamber radius variation (i.e. the motor size variation) on the left, and of, on the right, the dead space evolution versus the chambers diameter.

From the Figure 2-3 (left), it is obvious that the larger the motor is, the better its power. Unfortunately, increasing the size of the micromotor could raise another issue: the increase of the dead spaces. For a given geometry (for instance, cylindrical chambers with membranes), the dead spaces will increase rapidly when increasing the size of the machine (cf. Figure 2-3 on the right). Thus, what the machine is gaining in power with the size increases will be lost due to dead spaces. Therefore, dead spaces are a major difficulty in MEMS micromachines and it is very difficult to reduce them without drastically reducing the power of the resulting micromachine. Our device should fulfil the previous recommendations and so the chosen size was a few mm. We'll see later on that, the size had also to fulfill technological requirements. The next section concerns the geometry that the membranes (used instead of pistons) should have to minimize dead spaces, taking into account the technological stresses related to the clean room possibilities and the MISTIC project requirements.

#### 2.1.4. Swept volume: design of the membrane

An important parameter that has influence on the efficiency of the motor is the swept volume. The conventional pistons are generally cylindrical solid blocks which slide inside a hollow cylinder. In addition, in the case of a piston, since it is usually made of a rigid body (hardly deformable) like grey cast iron, cast steel and aluminium alloy, the shape and volume swept during a movement are easily predetermined [65]. Moreover, the piston is not fixed at

the ends (or surroundings) of the cylinder, which allows it to make large linear displacements. It also has a substantial mass to reduce its thermal expansion and operating frequency.

As previously mentioned, the use of a piston in a micro-motor is not relevant. The solution is to use, instead of piston, a flexible membrane. The latter is, in the literature, often made of a resilient polymer of 2D cylindrical shape (which means that its thickness is negligible compared to its length or its diameter). As the membrane is sealed by its ends, it does not leave much room for a large displacement. Thus, the membrane and its environment must be designed so that the swept volume is important, and surpout more than the dead space of his chamber (we consider in this section only the volume of the chamber and not the regenerator-related dead space, which will be studied later on *section 2.4.*)

### 2.1.5. Confinement of the membrane

The use of membranes instead of pistons makes it possible not only to avoid friction losses, but also to reach high frequencies, to obtain a good sealing and to reduce thermal losses since their material are generally poor thermal conductor polymers (in comparison with metals used for solid pistons). In addition, if a membrane is free (*i.e.* not confined in a small cavity) it can easily be combined with an actuation system with a variety of mechanical actuators, such as a piezoelectric layer, an electromagnetic or electrostatic system *etc.*

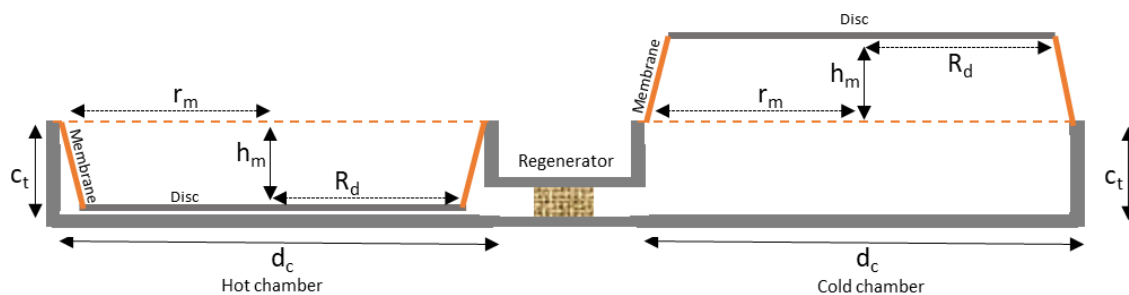


Figure 2-4: Simplified diagram of a Stirling micromachine in 2D configuration.

Unfortunately, this is not the case for a miniature motor because its membranes are confined into chambers of a few hundred micrometres high (*cf.* Figure 2-4). As a result, the integration of an electromagnetic system becomes complicated because of the small volume of the chamber and the space reduction generated by the presence of a permanent magnet inside. Furthermore, the number of coil turns necessary to obtain sufficient force to drive the membrane (or, conversely, to convert the periodic mechanical movements into electricity) and the rigidity of the diaphragm are all limiting parameters.

Taking into account these issues, several solutions were envisaged, among which that of incorporating a piezoelectric module on the membrane or incorporating a magnet under the membrane (not in contact with the hot or cold chambers).

#### 2.1.5.a. Membrane and chamber design importance

One of the problems inherent in Stirling motors is the presence of dead spaces (unswept internal volumes). For macroscopic motors, those dead spaces are almost negligible (*cf.* Figure 2-5). The small spaces named  $V_{clc}$  and  $V_{cle}$  which represent these dead spaces on the pistons side are deliberately left as a safety spaces to prevent the pistons from banging on the bottom of the cylinders. Thus, inside the cylinders containing the pistons, there are almost no dead spaces, or, in any case, they are very negligible compared to the volumes swept by the pistons.

The design objectives we have set ourselves are to create simple heat exchangers (*i.e.* compression and expansion chambers), resistant to a maximum temperature of 200°C, identical for both sides (hot and cold) and achievable in a clean room at low cost. The choice made for the MISTIC macro motor [107] was to make it up of 25 stainless steel grids tightly mounted in an aluminium ring. Knowing that the main role of the chambers is to contain and heat the gas (by transferring heat from the hot source), then cool the gas by removing its heat to the cold source.

On the one hand, the heat exchange is more important with larger exchange surface and also with an insulating material between the hot and cold chambers. On the other hand, an increase of this surface would cause more viscous dissipation related to the flow of the working gas. Proportionally, more dead spaces (when using membranes) and limitations due to possible swept volume (thickness of the canals and the chambers) will rise up.

The characteristic parameters of the membrane and chamber assembly are therefore their diameter, their thickness and the length of the connecting channel between the chambers.

When using a membrane instead of a piston, one of the drawbacks is the reduction of the ratio of the swept volume compared to the dead spaces. These last ones must be minimized to ensure optimal performance. In order for the membrane to sweep a large volume in the chamber, its bending shape must therefore correspond best to that of the chamber in which it moves (as in the case of pistons).

To minimize the dead spaces, a specific design taking into account the possible problems of heat exchange and microfluidic was considered. Indeed, the dead spaces become significant when the chamber shape does not conform to that of the moving membrane. But also, when the volume swept into the chambers becomes comparable to that in the micro-pipes of the regenerator and chambers' connectors (channels).

**There are two chambers geometries that are possible.** The first one is to give the chamber a spherical cap shape, knowing that a symmetrical circular membrane moved by a gas that expands naturally take such a shape. Nevertheless, whereas in MEMS technology a cylindrical chamber shape is easily achieved by DRIE in a silicon substrate, etching a spherical shapes (in either silicon or glass substrate) is more complicated and requires the use of wet etching.

The second possibility is then to keep a simple shaped chamber (cylinder type, easily achievable with the current technology available in FEMTO-ST clean room) and modify the membrane design to reach a proper displacement shape so that it fit as closely as possible the contours of the chamber. Nevertheless, the elaboration of the membrane in clean room using non-classical materials is a little more complex since the elastomeric materials are often considered as pollutants in clean room environment [108].

In our case, since the material needed to create a spherical cap-shaped chamber was not easily available, we choose this last solution: a simple cylindrical shaped chamber with both the structure and the design of the membrane modified.

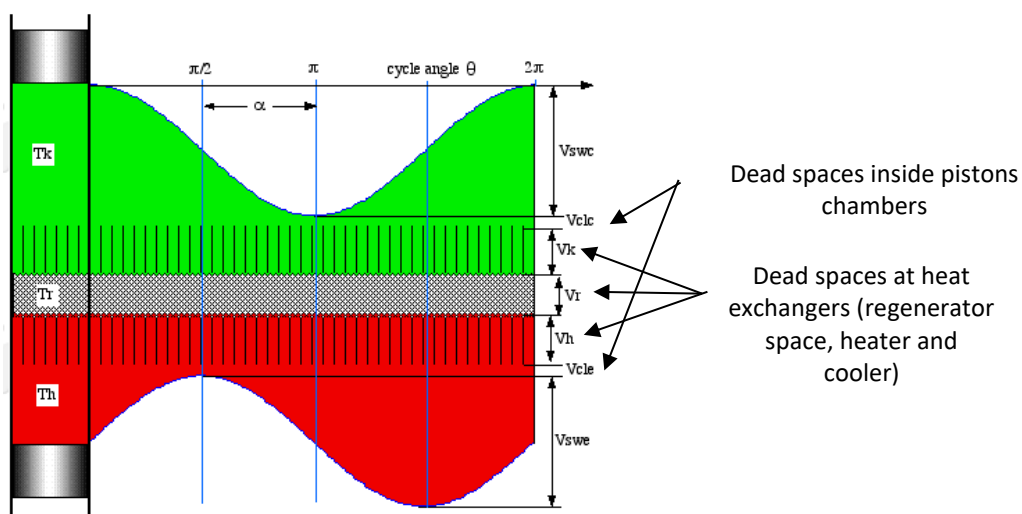


Figure 2-5: Dead spaces in a classic Alpha Stirling machine symbolized by  $V_{clc}$ ,  $V_{cle}$ ,  $V_h$ ,  $V_k$  and  $V_r$  (Extracted from <https://www.ohio.edu/mechanical/stirling/> and [28]).

Let us consider a classical membrane clamped at its end to a cylindrical chamber. We will determine here the swept volume and then compare it with a membrane with a different design. The displacement of the membrane will be assumed to be caused by the pressure of a gas. Two cases will be presented: the membrane with in shape of a spherical cap and the membrane with a solid central disk in its center.

### *i The spherical cap*

In this case, represented on the Figure 2-6, the membrane is modelled as a sphere of a radius  $R_s$  that is connected to the silicon circular hole of diameter  $r_m$  and depth  $h_m$ . The sphere radius is the given by:

$$R_s = \frac{h_m^2 + r_m^2}{2h_m}$$

Assuming that the height chamber  $c_t$  equal to the swept height  $h_m$ , the volume of the cylindrical chamber is given by  $V_c$ :

$$V_c = \frac{\pi}{4} d_c^2 h_m$$

Thus, the maximum swept volume  $V_{sw}$  of the membrane would be given by :

$$V_{sw} = \frac{\pi}{3} h_m^2 (3R_s - h_m) \tag{Eq. 2-1}$$

And the ratio between swept volume and the volume of the chamber  $\chi$  is given by :

$$\chi = \frac{4}{3} \frac{h_m(3R_s - h_m)}{d_c^2} \tag{Eq. 2-2}$$

NB: with .

In the particular case when  $R_s = 2c_t = 2h_m$ , the ratio  $\chi$  is then equal to  $\chi = \frac{20}{3} \left(\frac{c_t}{d_c}\right)^2 = \frac{20}{3} \left(\frac{h_m}{d_c}\right)^2 = \frac{5}{9}$  and the dead space is equal to  $V_d = \frac{4}{3} \pi h_m^3 = \frac{4}{9} V_c$ .

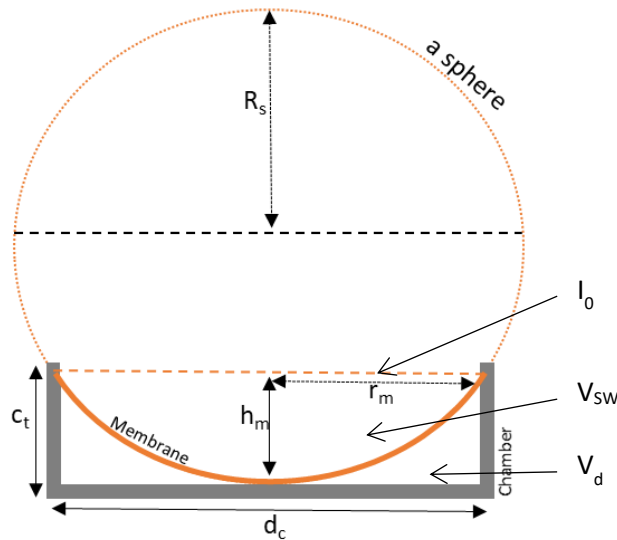


Figure 2-6: Spherical cap shape flexible membrane clamped at its ends and moving in a cylindrical chamber. With  $R_s$  the radius of the sphere;  $d_c$  the diameter of the cylindrical chamber;  $C_t$  the height the chamber;  $l_0$  the initial position of the membrane,  $V_{sw}$  the swept volume,  $h_m$  the swept height and  $V_d$  the dead space.

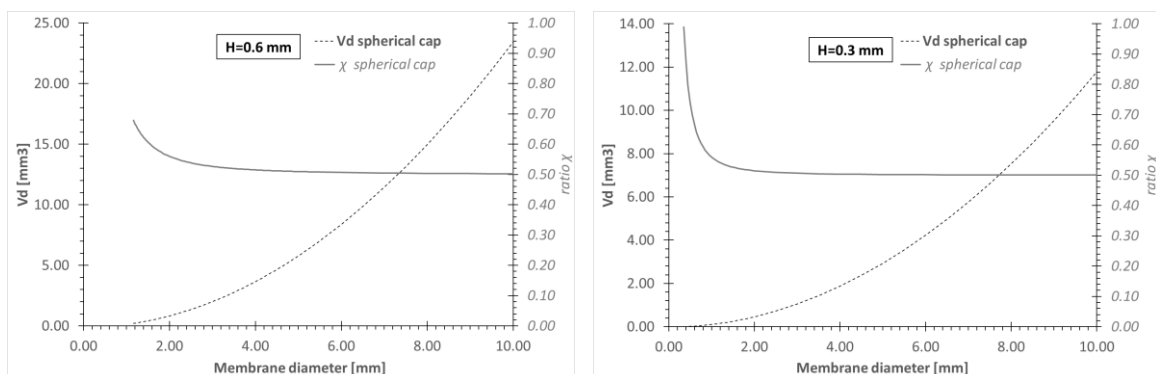


Figure 2-7 : Dead space and ratio  $\chi$  (between swept and chamber volumes) versus membrane diameter for a cylindrical chamber (chamber diameter=membrane's one) with, on the left a chamber height of 600 $\mu$ m and, on the right, a chamber height of 300 $\mu$ m.

In clean room, since the silicon substrates can reach a thickness of one millimeter (classical thickness = 500 $\mu$ m) and diameter of more than 100 mm, a cylindrical chamber thickness of 0.6 mm (or 0.3 on a 500 $\mu$ m Silicon wafer) and 5 mm of diameter is possible. Indeed, at the time this PhD begins with clean room available equipment, the chamber had to be etched in Silicon and to have a cylindrical shape.

Since clean room classical Silicon wafer have a thickness of 500 $\mu\text{m}$ , the maximum height of the chamber with these wafers was set at 300 $\mu\text{m}$  (to keep at least 200 $\mu\text{m}$  of Silicon). With thicker wafer, a height of 600 $\mu\text{m}$  was considered.

As explained in section 2.1.3, dead spaces are a major difficulty in MEMS micro machines. As an example, we will consider cylindrical chambers, with a height set either at 600  $\mu\text{m}$  or at 300  $\mu\text{m}$ , and a chamber's diameter that is equal to the membrane's diameter.

With a spherical cap membranes, the Figure 2-7 shows that the dead spaces increase rapidly while the ratio  $\chi$  (between the swept volume and the chamber volume) decreases rapidly when increasing the size of the chambers, and thus of the motor. This type of membrane could be suitable for our device since the geometric parameters can be tuned easily (for example, it could be suitable for a chamber with a large diameter and a small high).

### ii The membrane with a solid central disk

In this case we consider a flexible membrane with a solid disc (silicon type for example) located in its center ( cf. Figure 2-8 ) to impose a displacement in the form of a truncated cone that better fits the shape of the cylindrical chamber and thus enable the dead space to decrease. Moreover, to keep a solid disk on the membrane will increase its weight and thus decrease the resonance frequency, which could be interesting to adjust the resonance frequency to the imposed one in some MEMS systems. With the same assumption than before ensuring good tightness and minimize dead spaces, *i.e.* membrane radius  $r_m$  equal to the chamber radius  $d_c/2$  and chamber height  $c_t$  equal to the swept height  $h_m$ , the maximum swept volume  $V_{sw}$  of the membrane would be given by :

$$V_{sw} = \frac{\pi}{3} h_m (R_d^2 + r_m^2 + R_d \cdot r_m) = \frac{\pi}{3} h_m r_m^2 \left( \frac{R_d^2}{r_m^2} + 1 + \frac{R_d}{r_m} \right) = \frac{V_c}{3} \left( \frac{R_d^2}{r_m^2} + 1 + \frac{R_d}{r_m} \right) \quad \text{Eq. 2-3}$$

With  $V_c$  the volume of the cylindrical chamber :  $V_c = \pi r_m^2 h_m$

And the ratio  $\chi$  is given by :

$$\chi = \frac{1}{3} \left( \frac{R_d^2}{r_m^2} + 1 + \frac{R_d}{r_m} \right) \quad \text{Eq. 2-4}$$

The expression  $V_{sw}$  as a function of  $V_c$  shows that theoretically the swept volume depends on the volume of the chamber and the ratio of the radius of the central disk of the membrane and that of the chamber. The two extreme cases (spherical and truncated cone) are compared, for a chamber diameter of 5 mm and three different central disks, in the Table 2-3. Thus, with a chamber of 5mm in diameter, and a central disc radius of 2 mm, the swept volume is then given by:

$$V_{sw} \approx 0.8 V_c$$

dc [mm]	Rd [mm]	$\chi$ half sphere	$\chi$ truncated cone
5	0.5	$\approx 0.67$	$\approx 0.41$
	1		$\approx 0.52$
	2		$\approx 0.81$

Table 2-3: Comparison of ratio  $\chi$  obtained in the half-sphere case and in the truncated cone case for a cylindrical chamber of 6 mm in diameter.

The volume swept with a truncated cone becomes really interesting for central disks of radius superior or equals to 2mm. But, other parameters that will have a major influence on the motor performance and must be taken into account in our design are the membrane stiffness and resonance frequency.

**We now consider the same cases as before** : a cylindrical chambers, with a height set either at 600  $\mu\text{m}$  or at 300  $\mu\text{m}$ . Two central disks diameter are tested : 1mm and 2mm. The Figure 2-9 shows that the dead spaces increase rapidly while the ratio  $\chi$  (between the swept volume and the chamber volume) decreases rapidly when increasing the diameter of the chambers, and thus the size of the motor.

For both chambers heights (300 and 600  $\mu\text{m}$ ), the most efficient membrane diameter (to obtain low dead spaces) would be around 2 mm in diameter. Nevertheless, for larger membrane diameters, the central disk of 2 mm is more suitable.

Taking into account the resonance frequency that should be as low as possible (*i.e.* with a sufficient membrane's weight) and the harvesting method planed during the MISTIC project [107], the best compromise was to set the

membrane's diameter at 5 mm. With such a membrane diameter, the best central disk diameter has to be 2 mm instead of 1 mm: it indeed enables to obtain lower resonance frequency while the ratio  $\chi$  (between swept and chamber volumes) is higher than with a 1 mm disk.

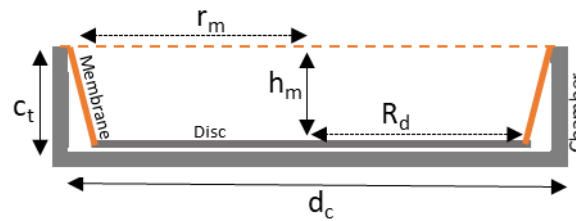


Figure 2-8: A flexible membrane clamped at its ends with a central disc moving in the form of a truncated cone in a cylindrical chamber. With  $d_c$  the diameter of the cylindrical chamber;  $C_t$  the height the chamber;  $h_m$  the swept height;  $r_m$  the membrane radius and  $R_d$  the central disk radius.

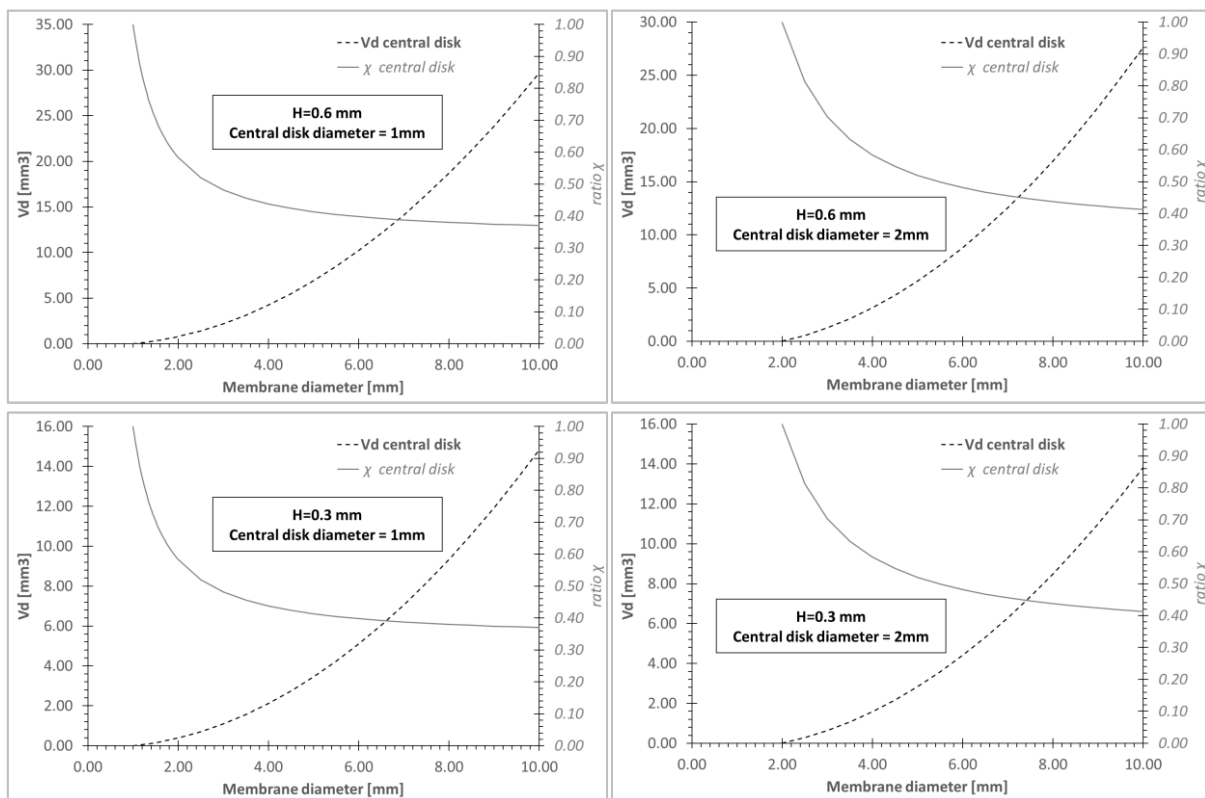


Figure 2-9: Dead space and ratio  $\chi$  (between swept and chamber volumes) versus membrane diameter for a cylindrical chamber (chamber diameter=membrane's one; chamber height=600 $\mu$ m for the two figures on the top; chamber height=300 $\mu$ m for the two figures on the bottom) with, on the left a central disk of 1mm in diameter and, on the right, a central disk of 2mm in diameter.

## 2.1.6. Membrane: mechanical properties and influence on motor performances

### 2.1.6.a. Operating frequency and mechanical power of a Stirling motor

As previously mentioned, with macro Stirling motors, the piston has the advantage of sweeping almost all the volume of the cylinder that it occupies because it has a shape identical to the chamber (generally cylindrical). On the other hand, a membrane leaves important dead spaces unless it is possible to design a chamber shape that will follow the shape of the moving membrane, as is the case with pistons. But one main disadvantages with the piston is that it cannot operate at high frequency (beyond a hundred Hertz) for mechanical reasons, noise or security. Knowing that the mechanical power is strongly related to the frequency, the membranes, because of their high vibration frequency, could counterbalance the losses due to the reduction of the size of the machine. These losses are related to small swept volumes caused by the choice of membrane instead of a piston in the chambers. For an motor with geometric parameters from Table 2-7 and for a hot and a cold temperature of respectively 473K and

293K, the mechanical power was calculated using the Schmidt model. Moreover, we used here the membrane with a central disk of 2mm in diameter (cf. section 2.1.5.a. ii).

In this part, the subscripts c, k, r, h and e respectively designate the compression chamber, the cold exchanger, the regenerator, the hot exchanger and the expansion chamber. T is the temperature, m the total mass of the gas inside the motor ( $m=m_c+m_k+m_r+m_h+m_e$ ), r the specific gas constant (equal to the molar gas constant for ideal gas divided by the molar mass of the gas) and  $\alpha$  the phase shift between the piston the displacer (phase advance of the expansion space volume variations with respect to the compression space volume variations). With V the volume,  $V_{clc}$  and  $V_{cle}$  respectively the dead spaces of compression and expansion chamber;  $V_{swc}$  and  $V_{swe}$ , respectively the swept volumes in the compression and expansion chamber, the mechanical work (W) is then given by :

$$W = \frac{\pi V_{swc}}{c} m r \frac{(\sqrt{1-b^2}-1)}{\sqrt{1-b^2}} [\sin \beta + \sin(\beta - \alpha)] \quad \text{Eq. 2-5}$$

With the parameters c,  $\beta$  and b given by:

$$c = \frac{1}{2} \sqrt{\left(\frac{V_{swe}}{T_h}\right)^2 + 2 \frac{V_{swc}}{T_k} \frac{V_{swe}}{T_h} \cdot \cos \alpha + \left(\frac{V_{swc}}{T_k}\right)^2}$$

$$\beta = \arctan\left(\frac{\frac{V_{swe}}{T_h} \sin \alpha}{\frac{V_{swc}}{T_k} + \frac{V_{swe}}{T_h} \cdot \cos \alpha}\right)$$

$$b = \frac{c}{s} \quad \text{with} \quad s = \frac{V_{clc}}{T_k} + \frac{V_{swc}}{2T_k} + \frac{V_k}{T_k} + V_r \frac{\ln\left(\frac{T_h}{T_k}\right)}{T_h - T_k} + \frac{V_h}{T_h} + \frac{V_{cle}}{T_h} + \frac{V_{swe}}{2T_h}$$

To determine the mechanical power (P), the work (W) is multiplied by the operating frequency (f) of the micro-motor

$$P = W \cdot f \quad \text{Eq. 2-6}$$

We can see from these results (cf. Figure 2-10) that when the frequency increases, for instance, from 50 Hz to 1000 Hz, we have a factor of 20 on the power. These results show the interest of reaching higher frequency, with respect to thermal and fluidic possible operating frequencies : the power gained should be higher with a membrane (since it can reach higher frequency values) than with as a classical piston. As a consequence, the resonance frequencies, and thus the membrane parameters (stiffnes, weight...), must be taken into account in the membrane design.

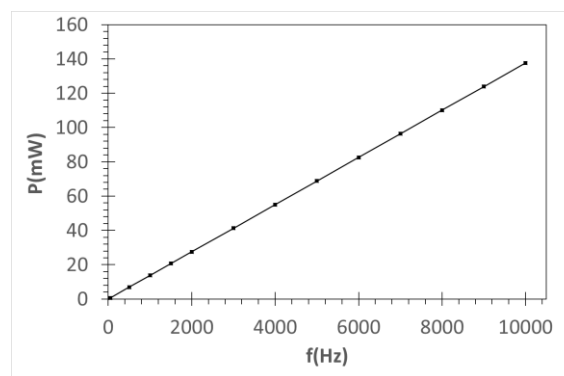


Figure 2-10: Power of the Stirling micromachine as a function of the frequency

### 2.1.6.b. Stiffness and final design

**Membranes have two main functions.** The first role is to guarantee the gas tightness of the chambers and the second is to ensure the compression of the gas and recovery of its thermal relaxing energy in the chambers. When a periodic excitation force (denoted  $f_e$ ) is applied to the upper surface of a flexible membrane closing a chamber (cf. Figure 2-11), the latter periodically deforms, pumping the fluid inside the chamber. Its vibration can be described through the variation of its vertical deflection W in space and as a function of time. This deflection is reasonably small in comparison with the shortest characteristic length of the membrane regarding micropumps.

The thin plate curvature theory is then applicable, and the deflection can be described by the following equation [109]:

$$f_e - P = \frac{Eh^3}{12(1-\mu^2)} \nabla^4 W + h\rho_m \frac{\partial^2 W}{\partial t^2} \quad \text{Eq. 2-7}$$

With  $W$  the deflection,  $E$  the membrane's elastic modulus,  $\rho_m$  the membrane's density,  $h$  the membrane's thickness,  $\mu$  the membrane's Poisson ration,  $t$  the time variable,  $P$  the dynamic pressure exerted by the fluid on the membrane's surface and  $\nabla^4$  the Laplacian operator in 2D, i.e.  $(\frac{\partial^2}{\partial x^2} + \frac{\partial^2}{\partial y^2})^2$ .

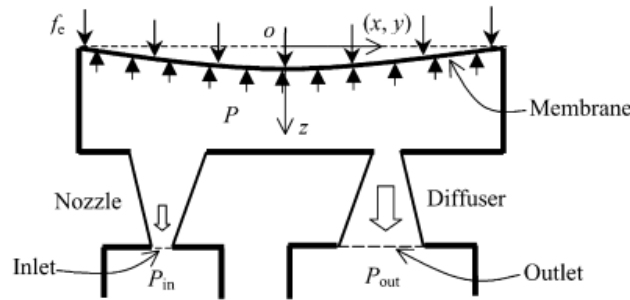


Figure 2-11: Schema of the cross-section of a membrane micropumps with fluid inlet and outlet nozzles [109].

The design objectives are to realize a flexible membrane, so that the stiffness of the mechanical part is controlled by the gas springs (the gas in expansion and in compression) and not by the membrane. Indeed, the behaviour of the gas is better known theoretically than that of the membrane. Its dimensioning should be made so that it can withstand large deformations while keeping enough mechanical strength and negligible hysteresis. Indeed, it will be necessary to minimize the mechanical damping (difficult to calculate from a theoretical point of view) which is intrinsic to the material of the membrane because it is also a source of dissipation of energy. When designing a membrane for a Stirling motor, the elastic restoring force that is necessary to ensure their periodic operation is thus an important parameter. This force must be taken into account in determining the appropriate actuation system. This can be achieved by a numerical simulation. However, the mechanical properties of the polymeric materials are not all available and often change depending on their polymerization conditions [110]. Thus, without exact determination of the properties of each membrane material, the error made (during the numerical simulation) can lead to a bad design. The determination of the mechanical properties of our membrane will be presented in chapter 4.

For the micromachine to be effective, the membranes must provide a large swept volume with a low dead space. Indeed, the amount of volume swept depends on the deflection height of the membrane and the shape that it adopts during a deformation (*cf.* Figure 2-11). The membrane being confined in a restricted space constituted by its chamber, is constrained in displacement, if it is not well configured such away that its deformation shape matches that of the chamber. Another parameter that is relevant is the operating frequency, and thus the resonance frequency of the membrane should be adjusted to the closest to the operating frequency : stiffness and weight have also their importance. Thus, to meet these requirements, two versions of the membranes were studied : a first one with a central disk in its centre, and a second one with a spring to increase the stiffness. They are made of two constituents: silicon (for the central disk or the spiral) and a polymer. In both cases, the central portion consists of a silicon disk (in order to stiffen the elastomeric layer and thus limit the mechanical deformations): the displaced volume of gas can be approximated as being the volume swept by this central part.

**The first type of membrane**, presented in section 2.1.5.a. ii, consisted in a single central disk located in the center of the membrane (*cf.* Figure 2-12 a). Its advantage lies in the fact that its flexibility will depend only on the layer of material between the disc in the center and the embedding with the support of the membrane. Moreover, it enables to obtain a uniform stress distribution [waters2001] in the radial direction of the membrane when loaded. There is also other advantages such as its simplicity of manufacture and a large deflection potential with less internal stress.

**The second design**, presented on Figure 2-12 b, is based on a design from F. Formosa from the MISTIC project and presented in the work of Chutani *et al.* [12]. It consisted in a planar spring made of two spirals interwoven with a central disk embedded in a polymer. It allows a good deflection with larger stiffness than the first type of



membrane. Since the membrane must perform important deflections, to be able to minimize the internal stresses is crucial. For uniform stress distribution along the planar spring, its width varies proportionally with spiral angle. The Figure 2-12 c) shows the variation in the width of the turns of the spiral which increases from the center towards the edges. The space between the turns also varies for better deformability.

As a conclusion, the role of each part of the membrane is summarized in Table 2-4. Table 2-4 presents also the role of the logarithmic spirals geometry defining the planar springs. The spiral springs allow to obtain a flexural shape like a piston, a controlled spring restoring force and as its coil (or turns) width increases from the centre towards the edges, it allows to control the distribution of stresses during an oscillation. The central disk is used to control the inertia and the membrane swept volume (trunked conic-shaped volume) during an oscillation. The polymer layer is for elasticity and air tightening the membrane, and to increase the yield strength of the spiral, for a more robust and flexible membrane.

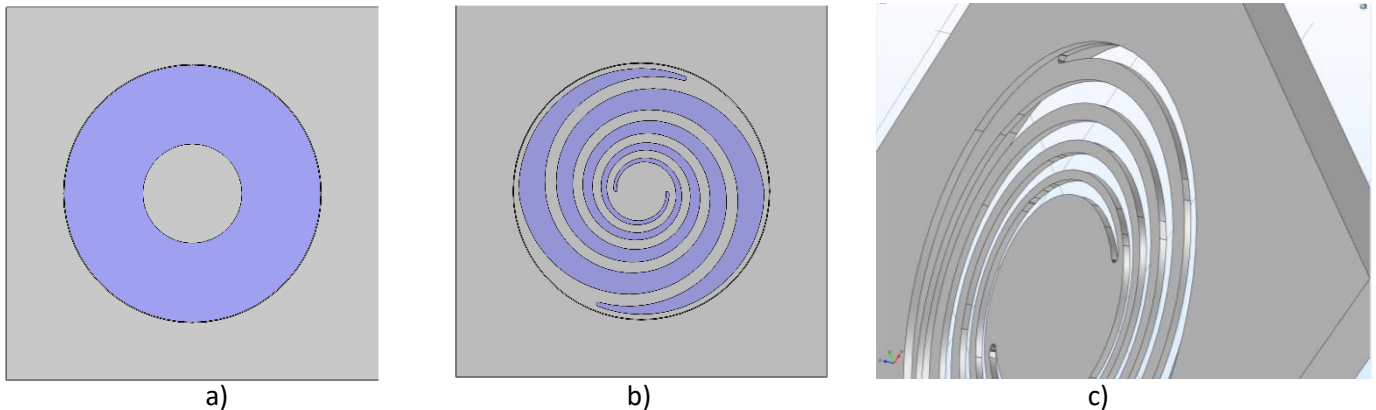


Figure 2-12 : the two membranes design a) with a central disk in the centre of the polymer (in blue) b) with a solid spiral spring architecture and polymer (in blue) in between the turns of the spiral. c) Variations in the width of the turns for a spiral membrane (variation of spacing between turns)

Components	Controls/goals
Spiral spring	Stiffness, Flexural shape (piston shape), Uniform stress distribution (width vs angle, stresses), Spring restoring force
Central disc	Inertia and Swept volume control for overall efficiency
Polymer layer	Good sealing, Robustness for the spiral, Elasticity increase

Table 2-4: The role of each part of the hybrid membranes HM.

### 2.1.6.c. Mechanical connections between membranes

**The main technological difficulty** related to the integration of membranes in miniature motors is mainly the mechanical link between them. Recall that the mechanical connection (or drive system) ensures the proper movements of the working gas to complete the Stirling cycle (especially the compression part). Classic macro-Stirling motors are often classified, according to the mode of connection between the pistons, as follows: kinetic, thermoacoustic, free piston and liquid piston types. In kinetic Stirling motors, the mechanical pistons, such as those shown in Figure 2-13 a), are driven by, for example, the simple crank-shaft with connecting pistons rods ( Figure 2-13 b). In this simple configuration, the drive system (crankshaft and rods) is designed in such a way that the piston at the hot end should always move in advance in comparison of that at the cold end.

**If we use a crankshaft with rods** connecting the membrane in a miniature machine (alpha configuration for example), friction losses would be huge, since there are at least four places where there will be frictions caused by the rotation of the mechanical connection: between the crankshaft and its point of attachment, with the rods and between these rods and the two pistons. We can already see the technological difficulty of making and integrating these ball joints using MEMS technologies and the risk that the rods pierce the membranes when the pressure increases in the micro-machine if they are not mechanically very resistant. Therefore, it is necessary for our micro-motor to rethink the mechanical phase shift system by imagining another type of "mechanical" connection between the membranes.

The design parameters to be taken into account are the mass of the rigid part and the stiffness of the membrane springs. In order to avoid a risk of piercing the membrane during assembly and to facilitate manufacture, two solutions were considered and will be presented more precisely in the following chapters: the first one is to use an incompressible liquid which will fill the space between the two membranes (in a glass block). The second one is to bond a fine solid “piston” to the center of the two membranes (*cf.* chapter 5).

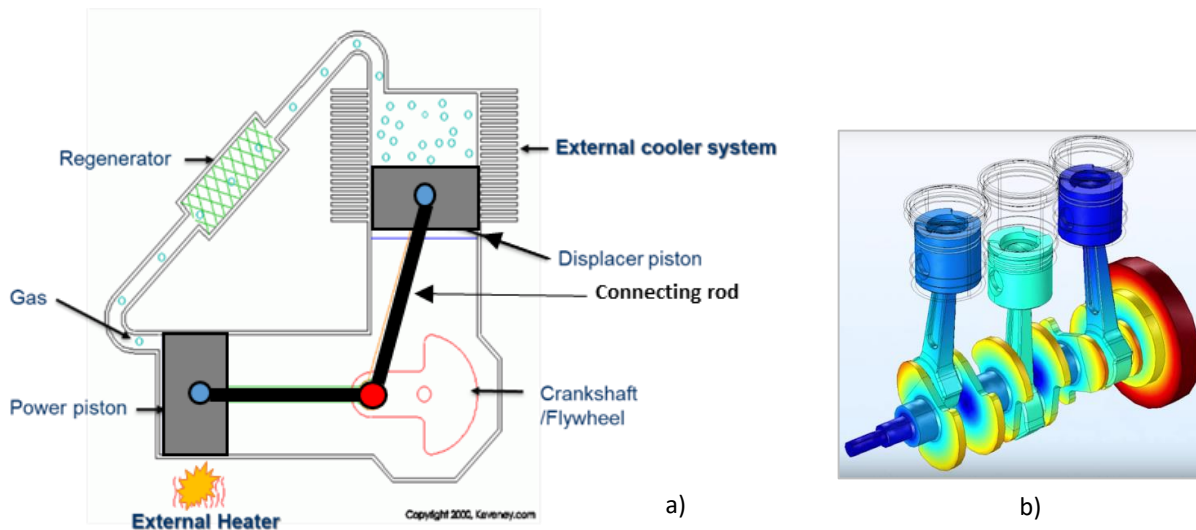


Figure 2-13: a) Classic macro-Stirling motor model with crankshaft and connecting rods highlighting the friction zones (1, 2 and 3). b) crank-shaft and connecting rods highlighting the harmonically displacements. (extracted from <https://www.youtube.com/watch?v=qNc03bW18JE>)

### 2.1.7. Membranes final design and chosen materials.

As a conclusion of this section 2.1. , when miniaturizing the Stirling motor, the design of the membranes, the chamber and the regenerator is a compromise between clean room possibilities, material used, minimizing dead space and allowing high operating frequencies. When manufacturing the membranes of a thermal micro-motor containing a working fluid, the choice of materials must consider the temperature resistance, the elasticity, the mechanical strength in bending, the porosity and the integration of the latter on a substrate.

**To fulfil at best those criteria**, while being compatible with cleanroom manufacturing, we choose to create our membrane as a hybridization of two materials: a polymer and Silicon. Concerning the polymer, it must support operating temperature of 473K. Nevertheless, during clean room process, to bond the element, temperatures at a minimum of 573K can be reached. The polymer must be either very elastic, to obtain a very flexible membrane (it must therefore be an elastomer) but can also withstand temperatures of about 573K. RTV-silicone (Room temperature Vulcanizing Silicone) was found to be a suitable material after a survey among potential candidates with high thermo-mechanical properties. The properties of this material can be found in chapter 4.

**To obtain membranes with good stiffness** while enabling to reach good swept volumes, two kind of structure were manufactured (*cf.* Figure 2-14):

- The first one, which was discussed in a previous paragraph (2.1.5.a. ii), consisted in a RTV silicone membrane with a Silicon central disk. To find the best compromise between membrane elasticity (possible value of  $h_m$  to obtain) and swept volume, we choose to use central disk of 2mm in diameter (central disk of 1 mm were also tested).
- The second one, which is based on the design of Chutani *et al.* [12] consisted in a silicon spiral with a central disk embedded in RTV silicone.

Both those designs will be further explained in the next chapter. Different thickness of silicon/RTV, leading to different resonance frequency and stiffness, were used based on numerical simulation results that will be presented in the chapter 4.

To allow a great flexibility and to ensure a good mechanical strength, the chosen thickness for hybrid membranes was set at 200 $\mu$ m. Note that membranes of smaller thicknesses had been previously made and presented problems

of mechanical strength. The ratio RTV thickness/silicon thickness can be adjusted to obtain a specific resonance frequency (cf. chapter 4 for the complete study).

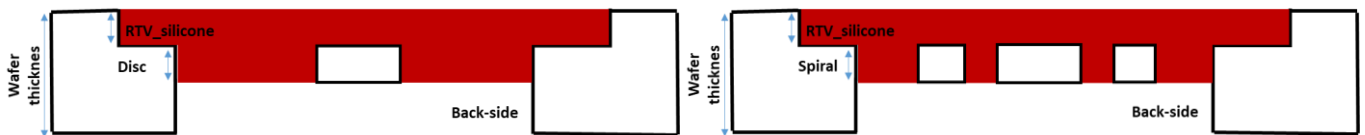


Figure 2-14 : The two designs of the membrane. On the left, the membrane composed of RTV silicone (red) with a Silicon (white) central disk in its centre. On the right, a silicon spiral (white) embedded in the RTV silicone (red), based on the work of [109]

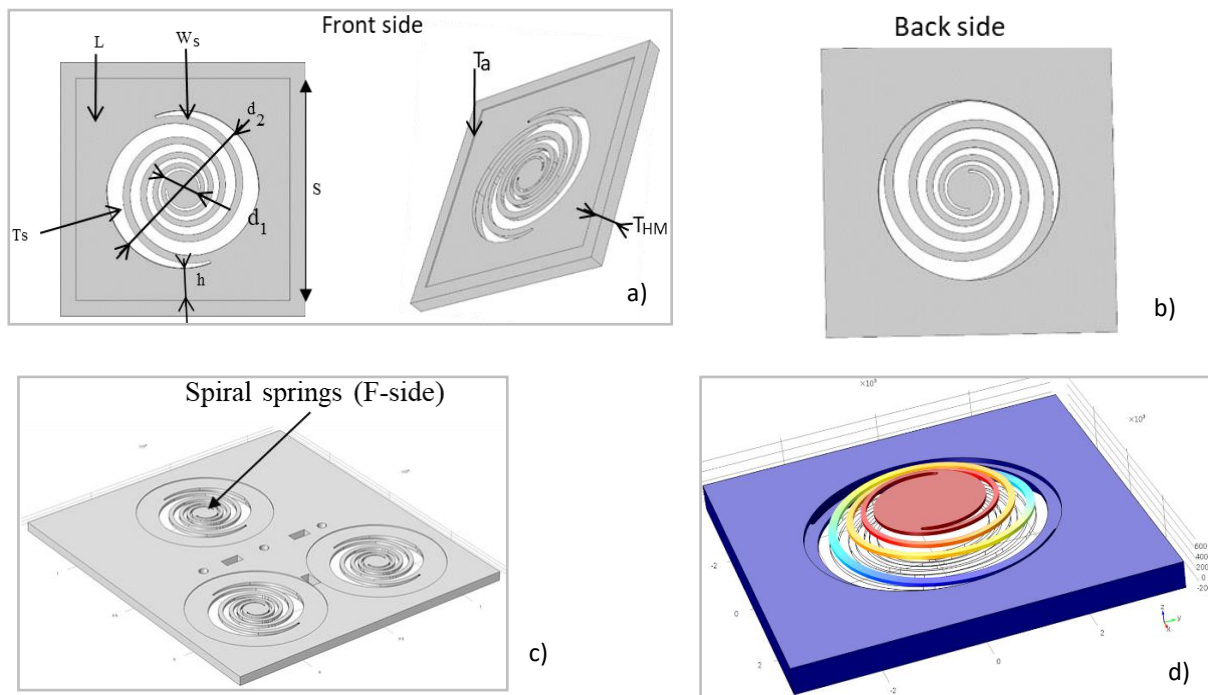


Figure 2-15: Membrane rigid part design: a) Silicon spiral spring architecture and geometrical parameters ( $L$  is the location of the RTV-silicone layer deposited by a squeegee,  $W_s$  is the width of the turns of the upper part of the spiral). b) back-side of the membrane. c) the 3 membranes necessary for the micromachine. d) simulation of deflection shape

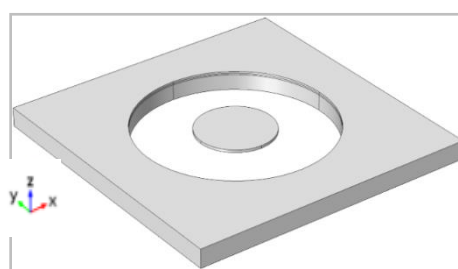


Figure 2-16: Second type of membrane rigid part

### 2.1.7.a. Hermetic and high temperatures resistant membranes

To correctly seal the different parts of the micromotor, heating at high temperature up to  $300^{\circ}\text{C}$  is required. Moreover, the planar spring alone is not hermetic, which is not adequate to the intended application.

A polymer layer is then added (cf. Figure 2-17 a) and b) for spiral membranes and Figure 2-18 a) for central disc membranes). This layer of polymer must be very elastic to obtain a very flexible membrane (cf. Figure 2-18 a and Figure 2-18 b). It must therefore be an elastomer. However, the problem is that in the clean room the annealing and bonding steps during microfabrication require the use of temperatures of  $120^{\circ}\text{C}$  and  $300^{\circ}\text{C}$ , respectively. Therefore, this layer of elastomer must be chosen so that it can withstand these high temperatures.

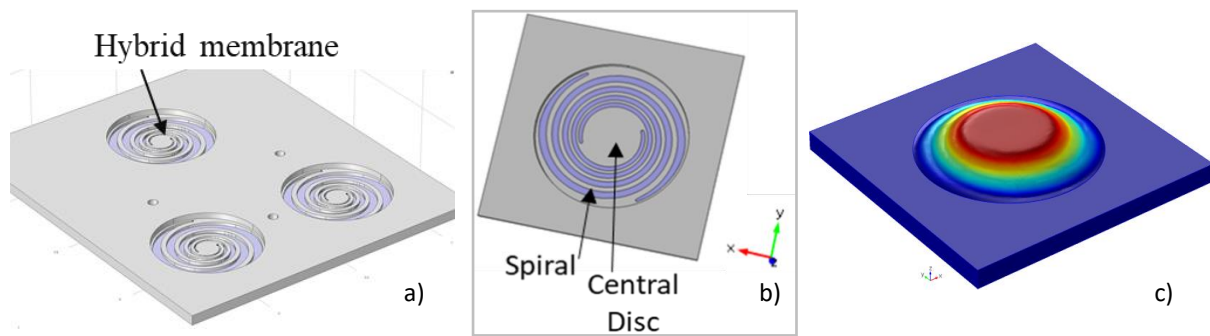


Figure 2-17: Second part of membranes. a) A chip of 3 Spiral membranes. b) A zoom of one spiral membrane. c) deformation shape of an hybrid membrane with spiral.

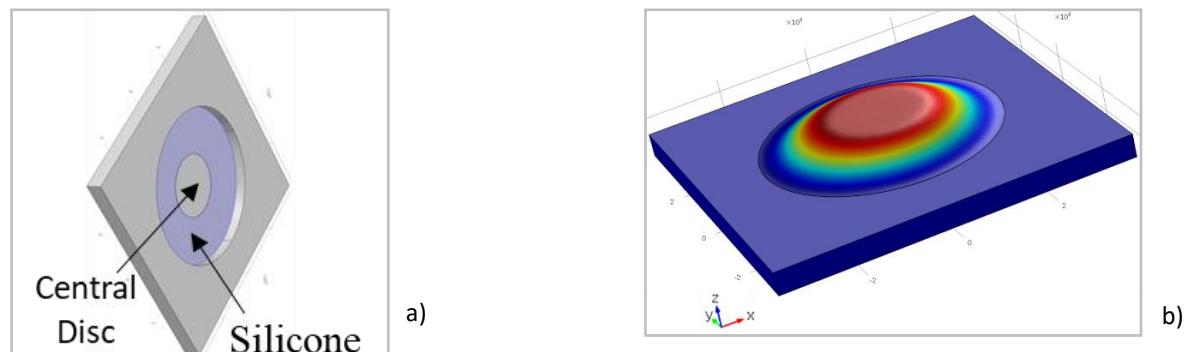


Figure 2-18: a) Hybrid membrane with only a disc at the center. b) Deformation shape

### 2.1.7.b. Membranes mechanical links

Our objective being to obtain a Stirling motor with free piston double action multiphase, it was necessary to design the mechanical connection which must connect the membrane of the cold side to that of the hot side of the following phase. This connection was to be held in place between the suspended membranes which would provide a restoring force.

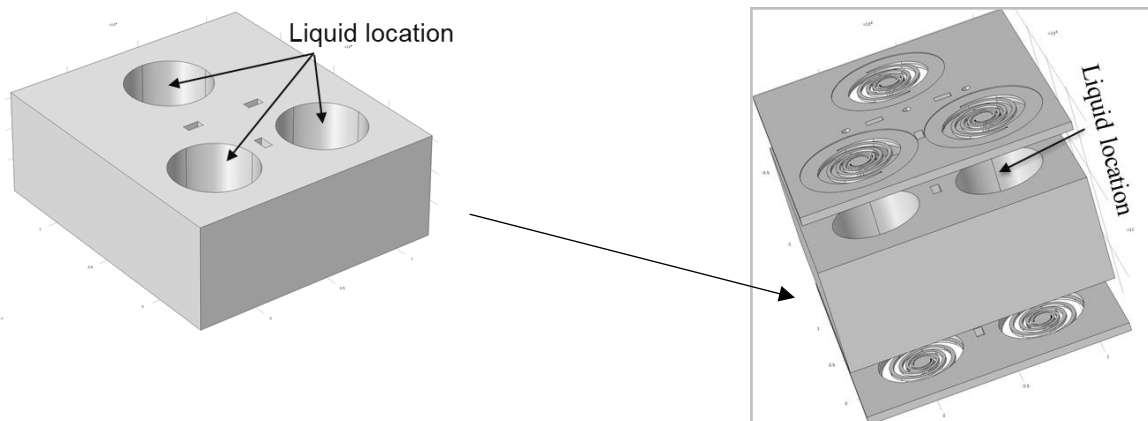


Figure 2-19: Bloc for hybrid membranes mechanical connection

This mechanical connection between the membranes must be rigid or non-compressible in order to transmit the stresses without loss (*cf.* Figure 2-19 a). The design parameters to be taken into account are the mass of the rigid part and the stiffness of the membrane springs. In order to avoid a risk of piercing the membrane during assembly and to facilitate manufacture, an incompressible liquid filling the space between two membranes in a glass block has been chosen as a mechanical link for the first version of the prototype (*cf.* Figure 2-19 b).

### 1.1.1.a. Electromagnetic transducer of membranes oscillations

As the movement that will be produced by the membranes of the micromotor is linear and not rotating, the initial idea was to integrate customized piezoelectric spiral. But this choice proved unrealizable and unsuitable with the technology of squeegee deposit because the spiral is not, therefore, firmly embedded in the support. We were

therefore interested in an electromechanical conversion and kept the spiral in silicon to control the movement of the membrane. This linear electromagnetic generator could be on the one hand, a small permanent magnet glued to the surface of the central disk located on the lower face of the membrane (the face that is not in contact with the chambers) and on the other hand a planar coil deposited on the outer face of the two plates containing the compression and expansion chambers. This magnet must have a diameter less than or equal to that of the central disk of the membrane to avoid congestion effects. The oscillations of the membrane will make the permanent magnet to oscillate which will, in turn, induce a displacement of electrons in the coil, creating, thus, an exploitable electric current. In addition, this electromagnetic system would help to control the deflection of the membranes acting like actuators.

### 2.1.8. Minimizing dead volumes in Expansion and compression chambers

To minimize the dead volumes, a specific design taking into account the possible problems of heat exchange and microfluidic was considered.

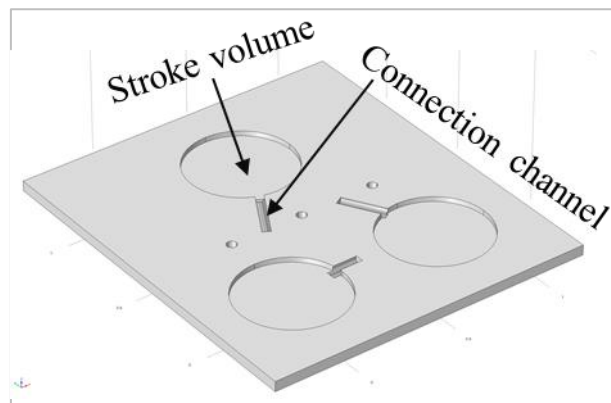


Figure 2-20: 3D CAD view of 3 chambers configuration of the Stirling Micromachine

The important design parameters to consider are the exchange surface, the shape, the dimensions and the type of materials.

To meet these criteria, the choice was to constitute a silicon hollow cylinder 5mm in diameter, 300 $\mu$ m thick with an outlet channel 1mm wide. This chamber is connected to this horizontal channel, then a vertical channel to connect the upper chambers (cold side) to the lower one (hot side). They are etched in a 4-inch silicon wafer of 500 $\mu$ m thick polished on both sides. The three-chamber CAD view is shown in Figure 2-20. The chambers are made by dry etching of a cylinder shape cavity having the same diameter as the membrane. The outlet channel of the chamber is cone-shaped in order to obtain a "soft" transition zone more favorable to the flow of gas.

The advantages of such a choice are the simplicity of microfabrication and the low pressure loss due to the absence of right-angled sections, but rather rounded contours. It also helps to facilitate integration with the rest. The hot source and the cooling source are external as the faces of the silicon wafers are polished with a very good flatness (TTV <3). Any flat surface, hot or cold can therefore represent a thermal source when the micromachine is placed there.

For the micromachine to work, a difference in temperature must be installed between the two sides (hot and cold) of the micromachine. In other words, an element that can prevent heat from moving quickly to the cold side is necessary, which involves choosing a thermal insulation material, but which must be machinable in a clean room. The best option that we had in the clean room was to use a glass block for the insulation part.

#### 2.1.8.a. Adequate bonding techniques for components assembling steps.

As the micromachine is therefore composed of several components to assemble, the choice of suitable bonding techniques achievable in a clean room is required. The goal is to obtain a good hermeticity with a good mechanical connection of bonding. However, depending on the material the adequate techniques are not always compatible for a multi-wafer assembly exceeding two wafers. In other words, for an assembly of two wafers, they work properly and give a good quality of bonding. But from three wafers, the second bond can have a "de-bonding" effect on the first. This is the case of anodic bonding. However, this technique gives good quality of hermeticity between glass and silicon wafers. Therefore, anodic Bonding and Thermocompression bonding were chosen as bonding

techniques. The membranes are assembled to the chambers by thermocompressive bonding allowing to fix the membranes to the chambers and to make sure of the tightness, and then this is assembled with the rest of the micromotor in full with successive anodic bonding steps.

## 2.2. The micro-motor architecture importance

In order to categorize the different approaches of the Stirling motor miniaturization, they are organized according to the spatial arrangement of the created entities (membranes, regenerator, compression and expansion chambers) on the substrate. For instance, if these entities are created by thin films deposited technique on the surface of the substrate, the system will be here called the 1-D architecture. When the arrangement of components is in the substrate plane created by etching, the structure is referred as the 2-D architecture. And when more than 2 substrates are used and the arrangement of the entities (by etching and assembling) is in the perpendicular plane of substrates, the resulting architecture is called the 3D one. Efforts will be made to address the major advantages and disadvantages of each configurations, as well as to address the sizes and resolution of features that can be generated. Note that here the mechanical link, which enable the phase shift, is not considered: these first studies aimed at the determination of the most suitable geometry from a thermal, then later on, from a fluidic point of view.

### 2.2.1. 1-D Architecture

**1-D features** are mostly constituted by thin films with only the thickness as a critical parameter. Their conformity relates to how uniform the film thickness is across the wafer. Note that, the majorities of these thin films can be deposited from the gas phase by chemical vapour deposition (CVD), the liquid phase by spin-coating and/or spray-coating techniques or plating, and from the solid phase by evaporation / sputtering processes. Concerning CVD technique, precisely temperature-controlled ovens with gases such as silane ( $\text{SiH}_4$ ), phosphine ( $\text{PH}_3$ ) and ammonia ( $\text{NH}_3$ ) flowing around the substrate lead to surface deposition of materials such as phosphosilicate glass (PSG) or Silicon Nitride ( $\text{Si}_3\text{N}_4$ ) and polySilicon (poly). During the deposition process, the gas-phase and surface kinetics control the rate at which the desired film material is deposited on to the substrate. Thin glass films like phosphosilicate glass (PSG), low temperature oxide (LTO) and thermal oxide (silicon dioxide) are often used as electrical, thermal insulation and structural layers. Note that the maximal thin film layer thickness is typically less than  $10\ \mu\text{m}$  and the speed of films deposition by CVD vary widely, from tens of  $\text{\AA}/\text{min}$  for LPCVD to tens of  $\text{nm}/\text{min}$  for APCVD [46]. However, in view of the deposition rate and the complexity of the techniques, it would be difficult, slow and not advantageous to use this means to develop cavities such as compression chambers, expansion and the regenerator channel.

Initially, photoresist materials were primarily used in conjunction with lithography step to pattern the substrate, but recently they were used also as a structural material. Polymers materials, such as silicones (PDMS for example) and epoxies, can also be deposited on substrates in this manner as well to create entities. The problem is that these polymers and elastomers are thermal insulators. So they cannot be used to constitute compression and relaxation chambers, nevertheless, they can constitute membranes.

To conclude, since, that would require depositing thick layers (beyond  $300\ \mu\text{m}$  to be significant ) of metallic materials to realize the chambers of compression and expansion as well as the heat exchangers (regenerator, heater and cooler), it would be difficult and very expensive to manufacture any thermomechanical micro-machine using a 1D architecture. Not to mention that it will also be necessary to deposit and structure flexible membranes and ensure a tight closure to keep the working fluid and also ensure their connection (*i.e.* the required phase shift). Thus, this architecture was not further studied.

### 2.2.2. 2D architecture

The second architecture is the 2D one. It consists in a planar structure on a substrate that is obtained by structuring the substrate to create the desired characteristic.

A simple 2D architecture of alpha-type Stirling machine could consist of two horizontal chambers (compression and detente) connected by a horizontal channel, the whole motor being etched into a substrate (*cf.* Figure 2-21). The channel could be closed by a second substrate (glass or silicon) by a sealed bonding and this substrate could wear these membranes to facilitate their prototyping. The regenerator could be etched in this channel during

microfabrication. One could also imagine another solution that would be to fabricate a large thin film of membrane of the size of the substrate that could be directly used to close the system (chambers and channel) thus avoiding the use of the second substrate. This film will represent both the membranes and the closure system. Nevertheless, one can already consider the problems of tightness related to the bonding of thin polymer films on a solid substrate.

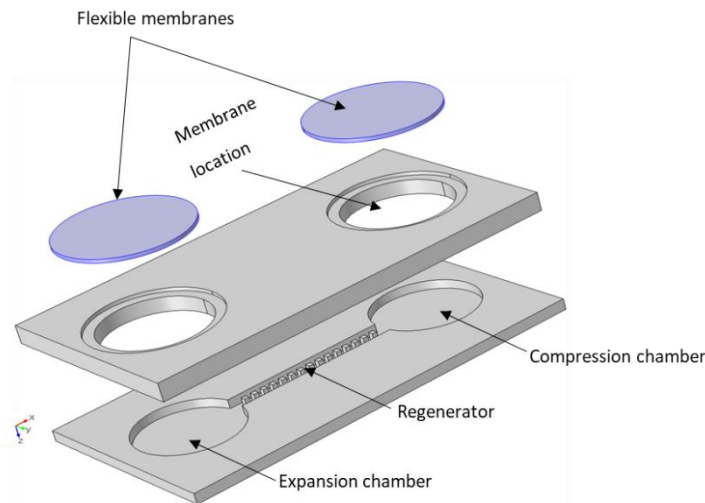


Figure 2-21: A schematic view of a possible 2D architecture of a MEMS Stirling motor.

However, while two-dimensional architectures are very important for electronics applications, they are less important in thermomechanical systems that require large volumes of working fluids, as is the case with the Stirling machine, since the whole system is made on the plane of a single substrate. A Stirling micro machine in 2D operating as a frigorific machine could be advantageous since in this case the membranes are moved electrically by means of electromagnetic actuation systems, electrostatic or piezoelectric for example, in a controlled manner to ensure the proper phase shift (which depends on number of membranes used) [103]. Knowing also that in the Stirling machine one needs to isolate the hot part from the cold part, it could be very complicated to achieve an insulation in 2D. Thermal losses by conduction, after a certain period of operation of the micro machine, will occur between the hot and the cold part. A numerical thermal study of the 2D configuration was carried out and will be presented in the section 2.3.5.a. .

### 2.2.3. 3D architecture

An achievable 3D structure Stirling micro-machine (Alpha type) would be to vertically arrange the two opposing chambers in the plane perpendicular to the substrate connected by a channel as illustrated in Figure 2-22. To be clean room compatible, and taking into account the substrate possibilities (material and thickness), the use of glass instead of silicon enable both the increase of the middle chambers volume and the thermal insulation between the hot and cold chambers. The system could be thus etched in a 6.5 mm thick glass substrate (available borofloat glass thickness in cleanroom). Etching of thick glass in a clean room is very slow (compared to silicon) and the structuring of thick glass can be performed by ultrasonic machining or by laser techniques. Nevertheless, the use of such a thickness of glass is a challenge since compatibility problems related to the high thickness could be encountered with the equipment available in clean room (bonding process). As for the 2D configuration, it could be possible to close both faces of the motor using two large thin membrane films directly on the glass wafer and, to ensure a good thermal exchange, to deposit a thin metal film in place of both silicon substrates. Alternatively, to simplify the etching/structuring of the thick glass (from two steps to an etching step), the chambers could be directly structured in the wafers of silicon and both cold and hot chambers could be closed by two gas-tight elastomeric membranes fixed on the silicon substrates. Thus, only the channel through the glass wafer, carrying the regenerator, would be etched in the thick glass.

Another advantage to use Silicon to design the hot and cold part is its high thermal conductivity. The thickness of the chambers will depend on the elasticity of the membrane material and its dimensions. Sealing problems related to the welding of these polymer films (since they are to put on both sides of the glass) must be taken care of.

The advantage of this 3D architecture is that we gain in thermal insulation (*cf.* section 2.3.5.b. for a thermal study of this 3D machine), in rigidity of the device and also, with the two hot and cold chambers being on the opposite sides of the wafer, this allows a simpler and more efficient heating and cooling as well as an easier access for

measurements and actuating system (for an motor operating as a cooling machine, the phase shift can be easily chosen). One of the main difficulty is to integrate a mechanism ensuring the phase shift between the membranes.

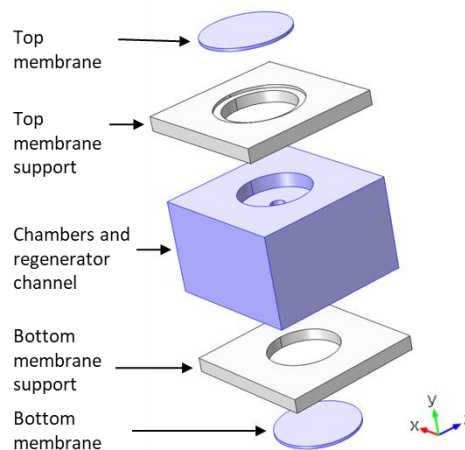


Figure 2-22: A schematic view of a possible 3D architecture of a MEMS Stirling motor.

As it will be presented in the section 2.5. , in order to design a machine whose structure in 3D is similar to the specifications of the ANR project, the full motor must be composed of 3 machines connected to each other. The final machine will therefore be based on the 3D concept presented here but with an additional problem related to the leasing of machines between them. Concerning the mechanism ensuring the mechanical link between membranes, two configurations will be tested: one with a solid piston, the other one with an incompressible liquid.

The next section is devoted to the thermal study of the 2D and 3D configuration that was taken into account to choose one configuration over the other one.

### 2.3. Thermal Challenges

The thermal challenges mainly concern the maintenance of the temperature gradient between the hot and cold sources of the micro-machine, the heat exchange between the working fluid and chambers and the integration of an effective and adequate regenerator. Pfriem [111] has shown for the macroscopic thermal motor, in the case of an alternating flow, the existence of a  $45^\circ$  phase difference between the heat flux at the wall and the temperature difference between the gas and the internal wall. Subsequently, he has shown that, for low operating frequencies, the heat flux exchanged at the wall and the temperature gradient between gas and wall remains almost in phase. However, in the case of membrane micro machines the frequency is necessary high, so the contact surfaces between the working gas and the chamber walls must be maximized. The integration of a regenerator therefore greatly influences the performance of Stirling machines ( [43]). Technologically the fabrication of a regenerator in MEMS technology (during the micro motor fabrication), is rather complicated because the structure of the regenerator should be etched inside the thick glass wafer (for the 3D configuration) in the vertical direction. During this PhD, current DRIE etching equipment were not capable of etching this kind of structure in a thick glass wafer. Therefore, the regenerator had to be first designed and fabricated, and then integrated later on. The design and characterization of the regenerator that will be located in the miniature motor was the subject of another PhD thesis ( [95]) and will be therefore only shortly presented later on. In this chapter, the location for the regenerator will remain empty (*i.e.* empty channel).

When two elements of different temperatures are in contact, a natural heat exchange is established from the hot body to the cold one. Three heat exchange mechanism exist: conduction (mainly in solids), convection (in fluids) and radiation.

**Convection and radiation** will depend on surface properties (emissivity, temperature...) and/or fluid properties (viscosity, thermal properties...) whereas conduction will depends on properties of the material, such as its thermal conductivity  $\lambda$ , its density  $\rho$  and its specific heat at constant pressure  $C_p$ . These are physical quantities, which depend on the temperature  $T$ , but since they vary very little in the temperature ranges considered (20-200°C), we will suppose them constant. Thermal conductivity  $\lambda$  ( $W \cdot m^{-1} \cdot K^{-1}$ ) is the amount of heat passing through  $1m^2$  of material, one meter thick and for a difference of 1 degree of temperature. It characterizes the ability of the material



to transfer the heat so, the lower the conductivity of the material, the more insulating the material is. Therefore, the choice of a material with an adequate  $\lambda$  is important. Moreover, the thermal diffusivity  $\alpha$  (defined as  $\alpha = \frac{\lambda}{\rho \cdot Cp}$ ) and which represents the thermal inertia of the material, must also be taken into account in the material choice.

One way to represent heat flux contribution is by using equivalent electrical model, with thermal resistance to represent the steady state heat transfer, and thermal capacitance to take into account the transient heat flux.

Let us first introduce some thermodynamic notions necessary for the understanding and the foundation of our thermal micro-machine model. Then, we will use an electrical analogy as much as possible to show the challenges related to heat transfer on MEMS-based micro-motors under certain conditions.

### 2.3.1. Conduction

Consider a homogeneous material (*i.e.* having the same composition everywhere), isotropic (*i.e.* having the same properties in all directions) and without internal heat source (*i.e.* no Joule effect, no chemical reaction in the medium...). The heat passing by conduction through a thickness “ $e$ ” of a given material of thermal conductivity “ $\lambda$ ” and surface “ $S$ ” during one second is called heat flux density “ $\varphi$ ” ( $W \cdot m^{-2}$ ). In its one-dimensional form, under steady state conditions and for a propagation throughout a constant surface, the conductive heat flux density calculated from Fourier’s law is expressed as follows [108], [112], [113]:

$$\varphi = \lambda \frac{\Delta T}{e} \quad \text{Eq. 2-8}$$

With “ $\Delta T$ ”, the temperature difference between the hot and the cold faces of the material. For a given  $\Delta T$ , to decrease the heat flux, one can choose a material with a low  $\lambda$  and with a great thickness.

For the micro-machine, it is rather the latter that is problematic because in clean room the thickness of the substrate materials is limited to few millimeters for the glass, and about 1mm for silicon. Moreover, those material are quite, to very, conductive (about  $1.2 \text{ W} \cdot \text{m}^{-1} \cdot \text{K}^{-1}$  for the borofloat glass @363K [113]), and  $150 \text{ W} \cdot \text{m}^{-1} \cdot \text{K}^{-1}$  for the silicon @300K [114].

In one-dimension, for a heat flux propagation throughout a constant surface and in steady state, the conduction resistance “ $R_{th}$ ” (expressed in  $K \cdot W^{-1}$ ) is deduced from the equation of the heat flux (by an electrical analogy) [112], [113]:

$$R_{th} = \frac{e}{\lambda \cdot S} \quad \text{Eq. 2-9}$$

Since the thickness of the material “ $e$ ” is directly proportional to the thermal resistance and inversely proportional to the thermal conductivity “ $\lambda$ ” and the cross-sectional area “ $S$ ” (perpendicular to the path of heat flux), the miniaturization effects and the use of clean room compatible materials are both enhancers of heat transfer. In other words, the significance of the phenomena of thermal inertia are radically reduces by miniaturization.

### 2.3.2. Convection

The convection mode concerns fluids (gas or liquid). When a cold fluid meets a hot element, the latter transfers some of its heat to the fluid. The difference in temperature induces a difference in density and therefore fluid displacements. The heat flux density exchanged by convection,  $\phi_{conv}$ , between a surface (at a temperature  $T_2$ ) and a fluid (at a temperature  $T_1$ ) in which the surface is given by Newton's law [112], [113]:

$$\phi_{conv} = h_c(T_1 - T_2) \quad \text{Eq. 2-10}$$

$h_c$  is the convection heat transfer coefficient and  $S$  the contact surface between the medium and the animated convective fluid. The thermal resistance ( $K \cdot W^{-1}$ ) associated with the convective heat transfer is [112], [113]:

$$R_{conv} = \frac{1}{h_c \cdot S} \quad \text{Eq. 2-11}$$

For miniaturized systems, the convection phenomenon accelerates the return to thermal equilibrium after a heating step of a microdevice. One main problem is that the convection heat transfer are determined using correlation based on experimental results. Whereas, at macro scales, those correlations exist and are well

documented, at micro-scales, there are still few works. Usually, those correlations are expressed as function of the Rayleigh number, defined as:

$$Ra = \frac{\rho \cdot g \cdot L \cdot c^3 \cdot \beta \cdot \Delta T}{\eta \cdot \alpha} \quad \text{Eq. 2-12}$$

With  $\rho$  the density ( $\text{kg} \cdot \text{m}^{-3}$ );  $g$  the acceleration due to gravity;  $\beta$  the thermal expansion coefficient ( $\text{K}^{-1}$ );  $\Delta T$  the temperature difference between the wall and the fluid;  $\eta$  the viscosity of the fluid ( $\text{Pa} \cdot \text{s}$ ) and  $\alpha$  the thermal diffusivity ( $\text{m}^2 \cdot \text{s}^{-1}$ ).

### 2.3.3. Radiation

Thermal radiation is the mechanism of heat transfer between distant bodies at different temperatures, separated by vacuum or (partially or fully) transparent media (*i.e.* which do not completely absorb radiation). The heat emitted by thermal radiation depends on the emissivity of the material " $\varepsilon$ ". Let us consider the model of the black body (*i.e.* absorbing all the radiations it receives), which is the ideal body releasing the maximum energy by thermal radiation at a given temperature  $T$ . The power emitted by thermal radiation by a black body, when it is at equilibrium at temperature  $T$ , is given by the Stefan-Boltzmann law [115], [113]:

$$P_{\text{radiated}} = \sigma S T^4$$

Where  $\sigma = 5.67 \cdot 10^{-8} (\text{W} \cdot \text{m}^{-2} \cdot \text{K}^{-4})$  is the Boltzmann constant and  $S$  the radiating surface area.

For a surface that is not a black body, the power must take into account the emissivity of the surface  $\varepsilon$ , and the expression of the radiated power becomes:

$$P_{\text{radiated}} = \varepsilon \sigma S T^4$$

The net radiative heat transfer density, given here in  $\text{W} \cdot \text{m}^{-2}$ , from one surface to another one (*i.e.* the difference between the radiation leaving the first surface and the radiation from the second surface) is then given by:

$$\Phi_{\text{rad}} = f(\varepsilon_1, \varepsilon_2, F_{1 \rightarrow 2}) \cdot \sigma (T_1^4 - T_2^4) = h_r (T_1 - T_2) \quad \text{Eq. 2-13}$$

With  $\varepsilon_1, \varepsilon_2$  the emissivity of respectively surfaces 1 and 2;  $F_{1 \rightarrow 2}$  the view factor (proportion of the radiation which leaves surface 1 and strikes surface 2);  $f(\varepsilon_1, \varepsilon_2, F_{1 \rightarrow 2})$  a function of  $\varepsilon_1, \varepsilon_2$  and  $F_{1 \rightarrow 2}$  (this function depending on conditions and geometry) and  $h_r$  the radiation coefficient (function of temperatures, view factor and emissivity). For temperatures difference below 100K, the above expression of the net radiative heat transfer can be simplified.

The radiation thermal resistance " $R_{\text{rad}}$ " ( $\text{K} \cdot \text{W}^{-1}$ ) is defined as:

$$R_{\text{rad}} = \frac{1}{h_r S} \quad \text{Eq. 2-14}$$

For the specific case of a small object (at  $T_1$  exchanging on its surface  $S_1$ ) contained in a big room, with a view factor of 1 and making the assumption that the air is a fully transparent medium, the net radiative heat flux density between the small object at  $T_1$  and the environment at  $T_2$  can be simplified as follow:

$$\Phi_{\text{rad}} \approx \varepsilon_1 \cdot \sigma \cdot (T_1^4 - T_2^4) \quad \text{Eq. 2-15}$$

In that specific case, the radiative resistance is given by:

$$R_{\text{rad}} = \frac{1}{h_r S} \approx \frac{1}{\varepsilon_1 \cdot \sigma \cdot S_1 \cdot (T_1^2 + T_2^2) \cdot (T_1 + T_2)} \quad \text{Eq. 2-16}$$

For miniaturized systems, taking into account the phenomena of thermal radiation depends on the heating temperature, and for operating conditions of about 200 °C, this phenomenon cannot be fully neglected.

### 2.3.4. The heat transfer coefficient of a stack

Usually, microfabrication can require the use of several different wafers, bonded together. They then form a global medium, composed of different media. A homogeneous medium is a medium whose interfaces are continuous without thermal bridges and without a layer of another material within it. The surface resistance characterizes the part of the heat exchange that takes place on the surface of the medium by convection and radiation. It depends

on the direction of heat propagation and the orientation of the medium. The properties of the thermal resistances (expressed in K/W) are the same than the electrical ones: when resistances are in series, the equivalent (global) resistance will be the sum of each resistance; and when resistances are in parallel, the equivalent resistance will be the inverse of the inverses sum.

For instance, for exchanges on an internal face of a device (respectively external face), the equivalent surface resistance (taking into account both convection and radiation, those two resistances being in parallel) is noted  $R_{s-in}$  (respectively  $R_{s-ex}$ ). The total thermal resistance " $R_{th_w}$ " of a homogeneous medium characterizes both its resistance to conductive heat transfer " $R$ " and its resistance to surface heat exchanges by convection and radiation " $R_{s-in}$ " and " $R_{s-ex}$ ". Those three resistances being in series, the total thermal resistance is therefore calculated by adding the thermal resistances to the conduction of the various constituents of the medium and the corresponding surface resistances [112], [113].

$$R_{th_w} = \sum R + R_{s-in} + R_{s-ex}$$

The thermal transmission coefficient, noted " $U_c$ " ( $W \cdot m^{-2} K^{-1}$ ) characterizes the amount of heat escaping through a stack of homogeneous materials of  $1m^2$  for one degree of temperature difference. It is calculated by doing the inverse of the total resistance of this medium. It is used to characterize heat leakage through a component or device composed of one material or several materials [112], [113].

$$U_c = \frac{1}{R_{th_w,S}} \quad \text{Eq. 2-17}$$

The higher this coefficient is, the more heat leaks and the less the device is thermally efficient. In the case where the stack contains integrated thermal bridges, the heat transfer coefficient is calculated by adding the thermal transmittance coefficient of the homogeneous components ( $U_c$ ) with the thermal leakage due to the integrated thermal bridges (punctual points  $X_j$  or linear  $\psi_i$ ) relative to the area of the components. For computing convenience, a reference surface called "reproducible component surface" noted A is often used [112].

$$U_w = U_c + \frac{\sum_i \psi_i L_i + \sum_j X_j}{A}$$

With:

$\psi_i$  : Linear coefficient of the structural thermal bridge i, in  $W \cdot m^{-1} \cdot K^{-1}$ .

$L_i$  : Integrated thermal bridge length i, in m.

$X_j$  : Point coefficient of integrated thermal bridge j, in  $W \cdot K^{-1}$ .

A : Total surface of the medium, in  $m^2$ .

In microsystems, these thermal points can be constituted by the deposition of thin metal layers, whether for electrical connection (necessary to electrically connect the two faces of the micro device) or to achieve a fusion weld metal. These thin metal layers that are often based on copper or noble materials are very good thermal conductor. For ensuring a good thermal insulation of the device, those thin metal layers must be as few as possible.

The next section is devoted to the electrical analogy and a numerical thermal study of the two possible configurations (2D and 3D) of the Stirling micro-machine (presented in the section 2.2.2 and 2.2.3).

### 2.3.5. Thermal study of the 2D and 3D configurations.

In miniaturized systems, the purpose of thermal insulation is to curb this exchange phenomenon by conduction since it is impossible to fully prevent it. Considering the materials classically used in clean room (glass, silicon and sometimes PDMS<sup>5</sup>), from a technological point of view, in the case of a plane micro-machine of the 2D type, a stack of two materials that are silicon and polymer can be considered (*cf.* Figure 2-23). For the 3D micro-machine, a combination of the three materials (Silicon, PDMS and glass) is considered (*cf.* Figure 2-27). In this part, the membrane we used are just PDMS ones *i.e.* spherical cap shapes (no central disk in the middle, nor spiral). We will now study the thermal behavior of the two types of micro-machine architectures (*i.e.* 2D and 3D).

<sup>5</sup> PDMS : Polydimethylsiloxane

### 2.3.5.a. 2D configuration

The 2D configuration, previously presented on section 2.2.2, is here studied.

All the geometric parameter for the 2D study are given in the Table 2-5. They were chosen by taking into account materials available thickness, clean room process possibilities, and a compromise between thermal (conductivity of materials compatible with clean room process, good thermal resistances related to the choice of the geometry...) and fluidic (hydraulic diameter above 100 $\mu\text{m}$ , Ar values around 1... *cf.* section 2.4. for the fluidic study). For instance, concerning the clean room requirements, the height of the chambers were set at 600 $\mu\text{m}$  : the initial idea was to use 2 silicon wafers (thickness = 500 $\mu\text{m}$ ) bonded together. When etching, to avoid to obtain very fragile motors, we decided to leave, at least, 200 $\mu\text{m}$  of Silicon. Therefore, the chambers (as well as the air canal) were 600 $\mu\text{m}$  in high. The Chambers diameters, corresponding to the membranes diameter, were set at 5mm (*cf.* section 2.1. ).

From a thermal point of view, since the micro-machine's heat source is external, to account for the rapid homogenization of the temperature through the 2D structure by thermal conduction, let us consider the thermal model of micro motor shown in Figure 2-23a). In this model, let us consider that the right chamber is heated from below ( $T_H$ ) while the other chamber is cooled ( $T_c$ ). Natural convection and radiation will occur on the downward and upward facing surfaces, and on the vertical surfaces. Conduction will occur in the silicon, and inside the PDMS. In the air canal, depending on its dimensions, convection and/or conduction will be considered (radiation will be neglected).

Concerning the equivalent global resistance, we choose to simplify the study and, since the aim of this part is the study of the heat transfer in the canal direction, we decided to focus only on the heat flux from the hot part to the cold part, *i.e.* to focus on the green area on Figure 2-23 a. Moreover, the ambient temperature is assumed to be at the same temperature than the cold one, and the air inside the canal is supposed to be motionless. With these hypotheses, the equivalent electrical analogy obtained is given on the b) part of the same figure.  $R_{EXT}$  represents the resistance due to both convection and radiation on the external surfaces of the motor;  $R_{PDMS}$  stands for the resistance of the chosen polymer, *i.e.* PDMS;  $R_{Si}$  is the resistance of the silicon;  $R_c$  is the equivalent resistance of the horizontal canal (filled with a gas) and  $C_{St}$  is the capacitance (energy storage). For the green area, the global equivalent resistance  $R$  (in K/W) will be:

$$R = \frac{1}{\frac{1}{R_{EXT}} + \frac{1}{R_{PDMS}} + \frac{1}{R_C} + \frac{1}{R_{Si}}}$$

$L_{tot}$ [mm]	$L_c$ [mm]	$l_{tot}$ [mm]	$l_c$ [mm]	$D_M$ [mm]	$e_{tot}$ [mm]	$e_{PDMS}$ [ $\mu\text{m}$ ]	$e_c$ [ $\mu\text{m}$ ]
20	7	10	1	5	1	200	600

Table 2-5 : Parameters and the chosen values in the 2D model

Materials	Monocrystalline silicon	Glass (Borofloat 33)	PDMS	Air
$\lambda(\text{W}\cdot\text{m}^{-1}\cdot\text{K}^{-1})$	150	1.2	0.2	0.03

Table 2-6: Materials thermal conductivity used in the model

For averaged values of thermal conductivities (*cf.* Table 2-6), we estimated the different resistances and determined the equivalent thermal resistance corresponding to the electrical analogy of 2D model (Figure 2-23 b). Based on ideal gas assumption for the free convection, the transfer coefficient "h" taking into account both natural convection at low Rayleigh numbers [116] and radiation was determined using correlations and solid's emissivity : depending on the surfaces orientation, a transfer coefficient with the surrounding between 12 and 47  $\text{W}\cdot\text{m}^{-2}\cdot\text{K}^{-1}$  was calculated. The smallest resistance is the silicon one which has an order of magnitude of 0 ( $R_{Si} = 5.07 \cdot 10^0 \text{ K}\cdot\text{W}^{-1}$ ) whereas the other resistances have an order of magnitude of at least 2. The equivalent resistance of PDMS, canal and exchanges with the ambient is around  $3.41 \cdot 10^3 \text{ K}\cdot\text{W}^{-1}$  (with the assumption of conduction inside the air canal; when assuming natural convection inside the canal, this value will decrease up to  $3.11 \cdot 10^2 \text{ K}\cdot\text{W}^{-1}$ ). The equivalent thermal resistance of the green area is then found to be equal to  $5.00 \text{ K}\cdot\text{W}^{-1}$  : it is then almost equal to the Silicon one. The associated heat transfer coefficient of the green area is thus about  $2.00 \cdot 10^4 \text{ W}\cdot\text{m}^{-2}\cdot\text{K}^{-1}$  ( $0.20 \text{ W}\cdot\text{K}^{-1}$ ). From the resistance values, it can be deduced that in the 2D configuration, the heat will be quickly transmitted through

the silicon to the cold part (unheated). It will thus be difficult to maintain an important temperature gradient between the hot and the cold part when the cold part is only ensured by natural convection.

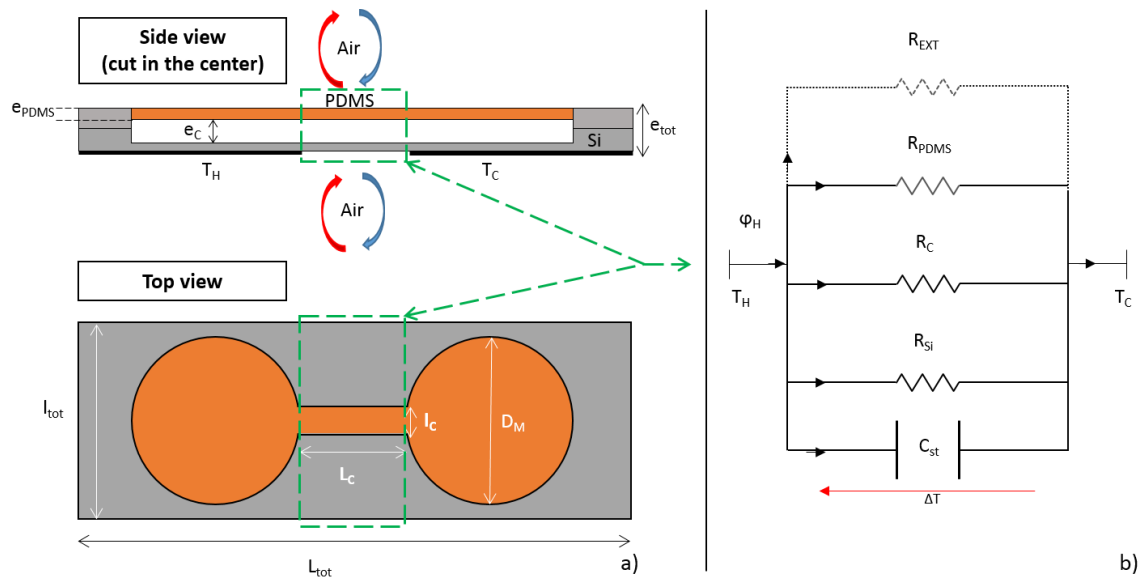


Figure 2-23: a) 2D configuration and b) electrical analogy corresponding to the green area.  $T_H$  and  $T_C$  are respectively the hot and the cold temperature. Colour code: in grey, the silicon; in orange the PDMS; in white, the gas (air).

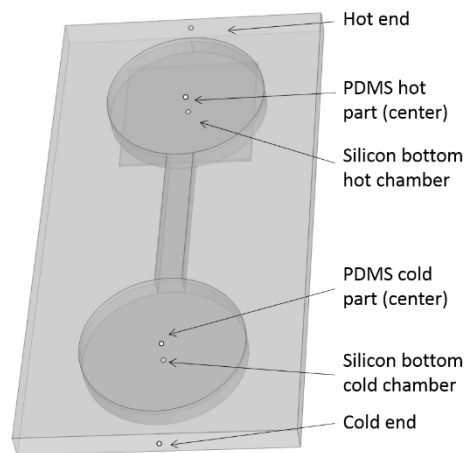


Figure 2-24: View of the 2D geometry and details of the points used in Figure 2-25.

To get an idea of the time at which the silicon substrate of the 2D model becomes quasi static in temperature (*i.e.* the steady state is reached and the temperatures are maintained constant), we carried out a time-dependant thermal simulation on COMSOL-Multi-physics. The Figure 2-24 gives the COMSOL geometry and on this figure, the location of the different points of interest is given. The simulation was a 3D time dependant one using the heat transfer module, with an imposed hot wall temperature.

A temperature of 393K was imposed on the plate located below the so-called “hot chamber”, the rest of the substrate being subjected to both radiative and natural convection of air at 273K with a global heat transfer coefficient at low Rayleigh [116], [117] of  $h = 12 \text{ W}\cdot\text{m}^{-2}\cdot\text{K}^{-1}$  on the bottom surfaces; on the top surface  $h = 20 \text{ W}\cdot\text{m}^{-2}\cdot\text{K}^{-1}$  for Silicon and  $h = 22 \text{ W}\cdot\text{m}^{-2}\cdot\text{K}^{-1}$  on PDMS. Finally,  $h = 47 \text{ W}\cdot\text{m}^{-2}\cdot\text{K}^{-1}$  on the vertical surfaces.

The results of the simulation, given on Figure 2-25, show that it took about five seconds to obtain homogenized temperatures on the silicon substrate. After about 15 seconds, the steady state was reached for all the materials. When considering the temperature difference between the hot and cold ends (*cf.* Figure 2-26) it was found to decrease and stabilize at almost 4.1 K. These results confirm that, with such geometry and materials, the expected

thermal gradient between the hot and cold part will be very small. If assuming a hot part temperature of 473 K (corresponding to the maximal targeted temperature in the MISTIC project), and keeping the surrounding at 293 K, the stabilized temperature difference is then equal to 7.5 K.

Thus, the 2D configuration could be suitable if an additional insulating material was added between the two chambers in order to limit heat transfer by thermal conduction between them. Due to clean room process and materials/equipment available at the beginning of this PhD work, such a design was not the most suitable (the introduction of an insulation between the hot and cold part being quite difficult) so, as a conclusion, the 2D configuration was, at first, dismissed.

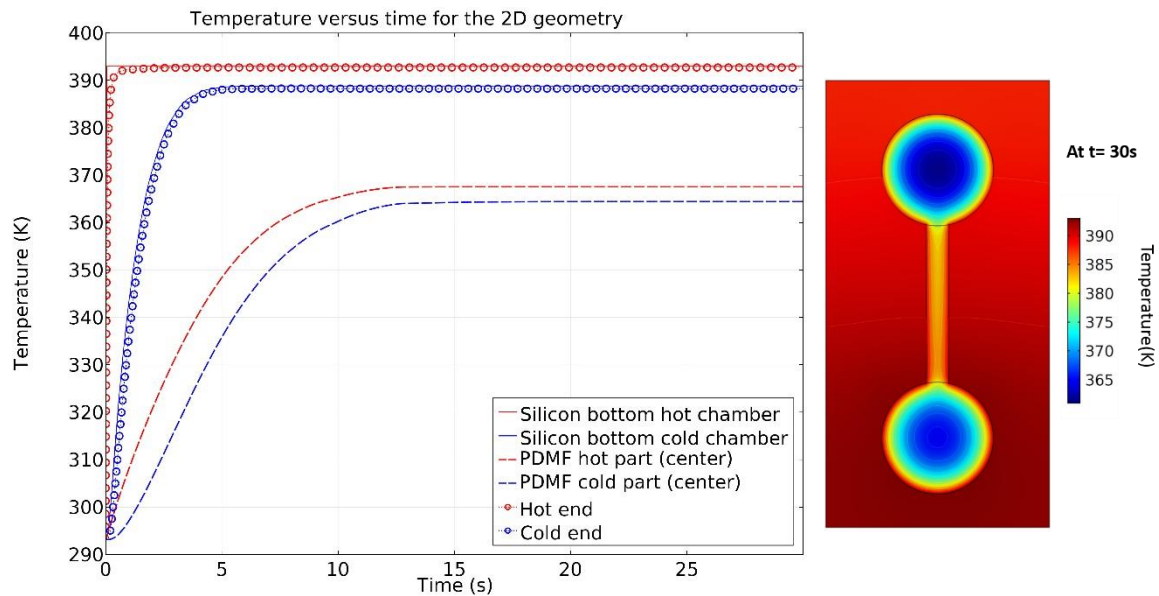


Figure 2-25: Results of 2D time-dependant thermal simulation with Comsol multiphysics. Surrounding temperature set at 293K and heating surface set at 393K.

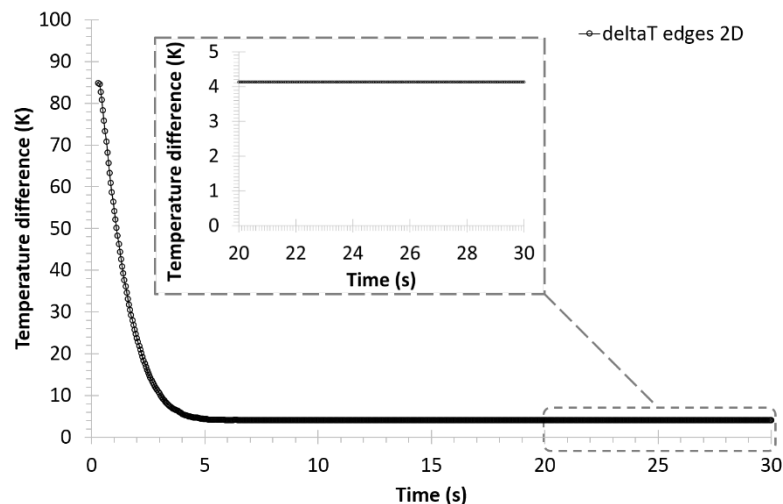


Figure 2-26: Temperature difference between the hot and cold ends for the 2D geometry. Surrounding temperature set at 293K and heating surface set at 393 K.

### 2.3.5.b. 3D configuration

In this model, the 3D configuration corresponds to the one previously presented on Figure 2-22. It is composed of 4 materials: Silicon, borofloat 33, PDMS and air. A schematic 2D side view is given on Figure 2-27a. The Figure 2-28 shows the 3D view of the geometry with the details of the points used later on in the simulation. The geometric parameter for the 3D motor are given in the Table 2-7. They were chosen to obtain the same chambers volumes than in the 2D configuration (chambers height = 600  $\mu\text{m}$ , membrane diameter = 5 mm). They were also chosen by

taking into account materials available thickness (borofloat, silicon) and the best compromise between thermal (thermal resistances) and fluidic requirements (such as Hydraulic diameter above 100 μm, Ar values around 1, cf. section 2.4. for the fluidic study).

For the 3D geometry, the associated equivalent electrical analogy is given on the b) part of the Figure 2-27. As for the 2D geometry, we made some assumptions: the ambient temperature (air and surrounding) is assumed to be at the same temperature than the cold one, the air inside the vertical canal is supposed to be motionless. The exchange with the surrounding is assumed to be with a wall temperature equal to the hot As for the 2D geometry,  $R_{EXT}$  represents the resistance due to both convection and radiation on the external vertical surfaces of the motor;  $R_{PDMS}$  stands for the resistance of the chosen polymer, *i.e.* PDMS;  $R_{Si}$  is the resistance of the silicon;  $R_{G1}$  and  $R_{G2}$  are the glass resistances for the two different glass thicknesses, respectively  $e_G$  and  $L_c$ .  $R_{AIR1}$  and  $R_{AIR2}$  are the air resistances for the chamber and the vertical canal for the two different air thicknesses, respectively  $e_G-L_c$  and  $L_c$ . Last,  $C_{St}$  is the capacitance (energy storage) of the whole device. For the 3D motor, the global equivalent resistance  $R$  (in K/W) will be:

$$R = \frac{1}{\frac{1}{R_{EXT}} + \frac{1}{2 \cdot R_{Si} + R_{G1}} + \frac{1}{2 \cdot R_{PDMS} + 2 \cdot R_{AIR1} + \frac{R_{AIR2} \cdot R_{G2}}{R_{AIR2} + R_{G2}}}}$$

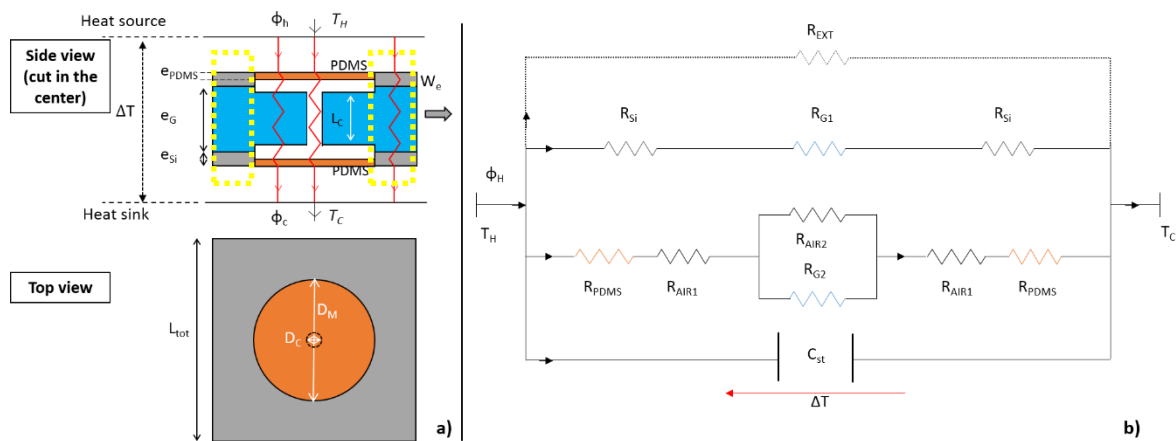


Figure 2-27: a) 3D configuration: schematic view and b) its electrical analogy.  $T_H$  and  $T_C$  are respectively the hot and the cold temperature. Colour code: grey for silicon; blue for glass (borofloat 33); orange for PDMS and white for the gas (air).

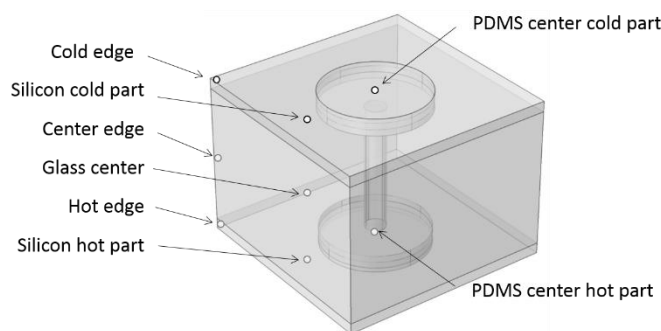


Figure 2-28 : View of the 3D geometry and details of the points used in Figure 2-29

$L_{tot}$ [mm]	$L_c$ [mm]	$D_M$ [mm]	$D_c$ [mm]	$e_{Si}$ [mm]	$e_{PDMS}$	$e_G$ [mm]
10	5.9	5	1	0.5	0.2	6.5

Table 2-7 : Parameters and the chosen values in the 3D model

With geometric parameters from Table 2-7 and for averaged values of thermal conductivities (cf. Table 2-6), we estimated the different resistances and determined the equivalent thermal resistance corresponding to the electrical analogy of 3D model (Figure 2-27 b). As for the 2D geometry, based on ideal gas assumption for the free

convection, the transfer coefficients taking into account both natural convection at low Rayleigh numbers [116] [117] and radiation were determined using correlations and solid's emissivity. The transfer coefficients with the surrounding were found to be between 20 and 25  $\text{W}\cdot\text{m}^{-2}\cdot\text{K}^{-1}$ .

The smallest resistance is again the Silicon one, with a value for the whole silicon part of  $8.3 \cdot 10^{-2} \text{K}/\text{W}$ . On the whole configuration, the smallest equivalent resistance is the one in the solid part without air (Silicon/glass/Silicon, represented with the yellow dots on the Figure 2-27) which has an order of magnitude of 1 ( $R_{\text{Si/G1/Si}} = 6.75 \cdot 10^1 \text{K}\cdot\text{W}^{-1}$ ) whereas the other equivalent resistance (corresponding to the part outside the yellow dots, and assuming air conduction) have an order of magnitude of 3 ( $1.42 \cdot 10^3 \text{K}/\text{W}$ ). NB: with the assumption of natural convection inside the canal, this value remains larger than  $R_{\text{Si/G1/Si}}$  but will slightly decrease up to  $1.28 \cdot 10^3 \text{K}\cdot\text{W}^{-1}$ .

Taking into account the surrounding, the full 3D geometry has an equivalent thermal resistance equal to  $4.5 \cdot 10^1 \text{K}\cdot\text{W}^{-1}$ . The associated heat transfer coefficient is thus  $2.22 \cdot 10^2 \text{W}\cdot\text{m}^{-2}\cdot\text{K}^{-1}$  ( $0,022 \text{W}\cdot\text{K}^{-1}$ ). This value is only very little modify when considering air convection inside the canal and the chamber ( $2.23 \cdot 10^2 \text{W}\cdot\text{m}^{-2}\cdot\text{K}^{-1}$ ).

When comparing those values to the ones for the 2D configuration, it can be deduced that the 3D geometry will be more suitable than the 2D one to maintain a larger temperature gradient between the hot and the cold part (when the cold part is only ensured by natural convection), since the difference between the global thermal resistances of the 2D and 3D configurations is about a factor 10.

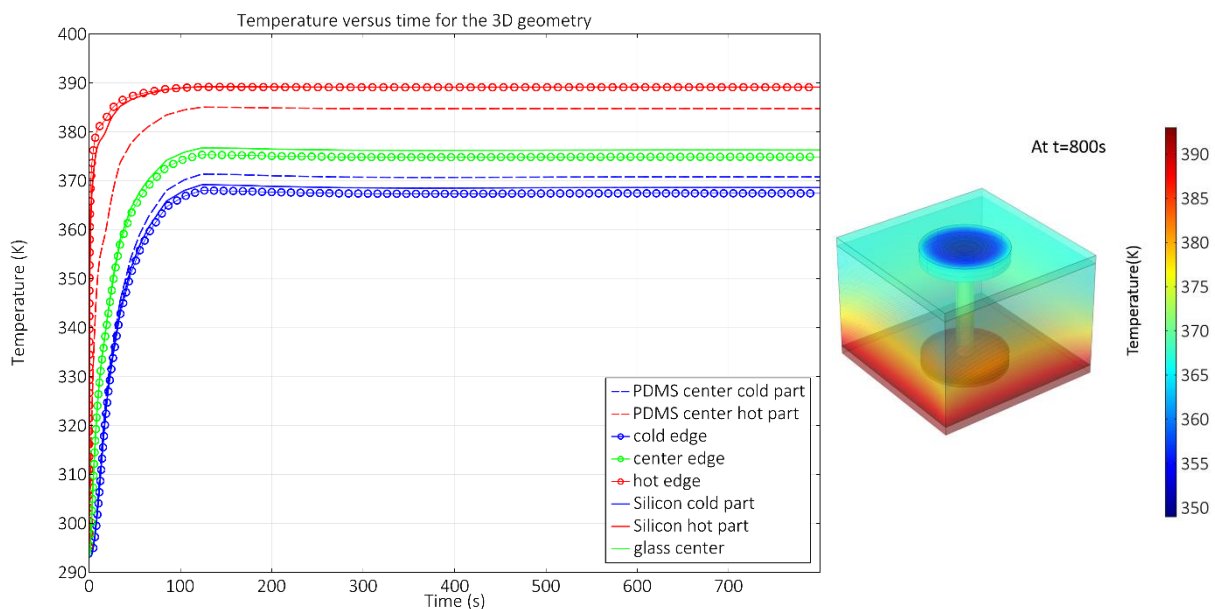


Figure 2-29: Results of 3D time-dependant thermal simulation with Comsol-multiphysic

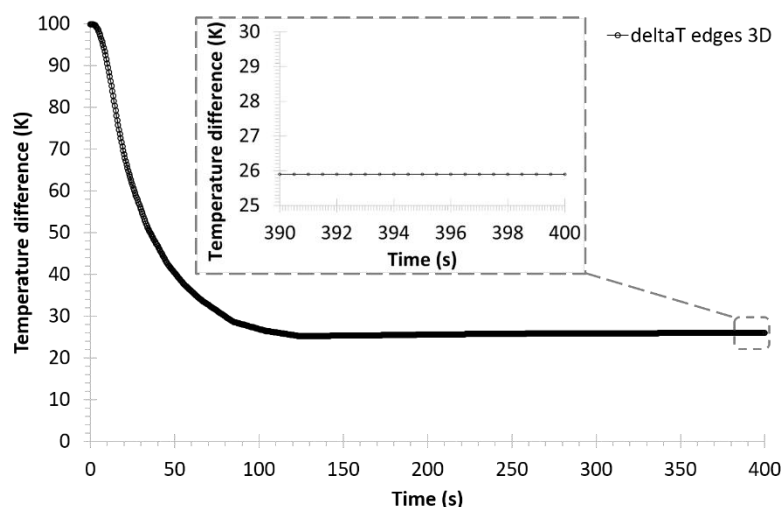


Figure 2-30: Temperature difference between the hot and cold edges for the 3D geometry.



We carried out a time-dependant thermal simulation on COMSOL-Multi-physics. The Figure 2-28 gives the COMSOL geometry and the location of the different points of interest that are used for the results in the Figure 2-29 . The wall temperature at the bottom of the geometry was set at 393K and the rest of the substrate was subjected to both radiation and natural convection with air. All the surrounding was set at 293K with a global heat transfer coefficient “h” taking into account both radiation and convection (based on [116] and [118]) for convection, and on materials emissivity for radiation) of  $h = 24 \text{ W.m}^{-2}.\text{K}^{-1}$  on the vertical silicon surfaces;  $h = 25 \text{ W.m}^{-2}.\text{K}^{-1}$  for the vertical glass surfaces; and  $h = 22 \text{ W.m}^{-2}.\text{K}^{-1}$  on the PDMS horizontal surface and  $h = 20 \text{ W.m}^{-2}.\text{K}^{-1}$  on the silicon horizontal surfaces.

The results of the simulation, given on Figure 2-29 and Figure 2-30, show that the steady state is obtained after more than 200 s, which is much more longer than with the 2D geometry but which was expected due to the differences in thickness, surfaces and materials.

Indeed, the temperature of the expansion chamber which is in direct contact with the hot wall immediately increases and reaches of the temperature of the source, since silicon substrate is very thin and is a very good thermal conductor. The glass substrate, assembled in series with the rest of the stack, serves here as a “breaking element” for thermal conduction (*i.e.* limiting progression of heat flow from the hot source), which could not have been achieved only with silicon substrate since its high thermal conductivity. The PDMF membranes, being assembled in parallel, do not really allow slowing the heat transfer. Even with “large” thickness of the material (few millimetres here for the glass substrate), the heat flux cannot be effectively curbed. The quite long time required to reach the steady state can be explained by the effect of heat exchange with the surrounding plus the glass substrate, which is sandwiched between two silicon wafers and acts as an electrical capacitor that charges in a very low characteristic time ( $\tau$ ). According to Tabeling [108], the characteristic time “ $\tau$ ” can be estimated by the following equation for a solid material:

$$\tau \sim \frac{\rho C_p}{\lambda} Lc^2 \quad \text{Eq. 2-18}$$

With “ $\rho$ ” the density, “ $C_p$ ” the specific heat at constant pressure, “ $\lambda$ ” the thermal conductivity and “ $Lc$ ” the thickness of the object. Without taking account exchanges with the surrounding, for the borofloat 33 ( $C_p=0.83 \text{ kJ.kg}^{-1}.\text{K}^{-1}$ ;  $\rho=2.23 \cdot 10^3 \text{ kg.m}^{-3}$ ) with a thickness of 6.5 mm, this time is equal to about  $\tau=65\text{s}$ . The influence of surroundings is rather important on the time needed to reach the steady state.

When considering the temperature difference between the hot and cold ends (Figure 2-30), it was found to decrease and stabilize at 25.8K. This result confirm that, with such geometry and materials, the expected thermal gradient between the hot and cold part will larger than with the 2D geometry. If assuming a hot part temperature of 473K (corresponding to the maximal targeted temperature in the MISTIC project), and keeping the surrounding at 293K, the stabilized temperature difference increases up to 46.5 K. To increase further the thermal gradient, either the thickness of the glass substrate should be increased, remaining within the allowable limits of the dimensions of the machines in clean room; or other material/structured materials should be used, still while remaining in the clean room authorized materials.

To conclude on the thermal part, comparing 2D and 3D possible architecture (in adequacy with the possibilities of the clean room) we chose the 3D architecture. This choice was due to two principal reasons. First, both analytical and thermal numerical simulations for a 3D architecture seemed to provide more encouraging results than the 2D one. Moreover, since this work was part of the MISTIC (Micro Stirling Clusters for low temperature heat recovery) ANR project, in which the aim was to miniaturize an existing macro device with its specific architecture composed of three motors working with a phase shift, the only corresponding architecture was the 3D one. This whole architecture will be more precisely presented in the last section of this chapter. In the next sections, the 2D architecture will be a little be studied (to justify the choice of geometric parameters used in the thermal study) but later on, only the 3D architecture will be focus on.

## 2.4. Microfluidic Challenge

The microfluidic challenges mainly concerns the limitation of the pressure loss. One major difficulty when considering the Stirling motor is the fact that the flows are alternate ones. If the literature begins to be quite well documented at macro-scales, it is not the case anymore when reaching millimetric and micrometric scales. This section will be an attempt to address and limit, as well as possible, problems related to miniaturization and the resulting shift in balance of forces.

### 2.4.1. Characteristic length: the hydraulic diameter

In fluid mechanics, the characteristic length is often the so-called hydraulic diameter “ $D_h$ ”. This last one is mainly used to characterize the constituent channels of heat exchangers or regenerators crossed by the flow [119] and is defined as:

$$D_h = \frac{4S_p}{\Gamma} = 4r_h \quad \text{Eq. 2-19}$$

with “ $S_p$ ” the free passage section of the fluid, “ $\Gamma$ ” the wet perimeter of the channel and  $r_h$  the hydraulic radius.

When considering the flow in the regenerator, which is a porous medium, the hydraulic diameter expression is modified and expressed as a function of the diameter of mesh diameter “ $D_w$ ” (e.g. for metal grids, widely used, the diameter of the wire), of the porosity “ $\varepsilon$ ” and of the form factor “ $\psi$ ” [120]:

$$D_h = \frac{4}{\psi} \frac{\varepsilon}{1 - \varepsilon} D_w$$

The porosity “ $\varepsilon$ ” is the ratio between the volume occupied by the pores (voids) and the total volume of the porous medium (solid and voids included). The work of Shin [121] suggested that the tortuosity should be taken into account to “correct” the hydraulic diameter by multiplying it with the ratio  $\sqrt{\frac{L}{L_e}}$  with  $L$  the length and  $L_e$  the real path length.

### 2.4.2. The different gas flow regimes

In a microfluidic system, the size of the fluid particle is not always negligible compared to the size of microchannel branches, thus the classical Navier-Stokes equation cannot always be used. The dimensionless number that is classically used to determine which physical approach (gas dynamic regime) and equations can be used is the Knudsen number [122]. This number is equal to the ratio of the mean free path  $\lambda$  of the gas to the characteristic size “ $L_c$ ” of the system [108]:

$$Kn = \frac{\lambda_M}{L_c} \quad \text{Eq. 2-20}$$

In kinetic theory, for an ideal gas and assuming hard-sphere gas having the same viscosity as the gas, the mean free path  $\lambda_M$  of a particle can be determined and expressed using macroscopic parameters:

$$\lambda_M = \frac{k_B \cdot T}{\sqrt{2} \cdot \pi \cdot d^2 \cdot P} \approx \frac{\eta}{\rho} \cdot \sqrt{\frac{\pi \cdot M}{2 \cdot R \cdot T}} \quad \text{Eq. 2-21}$$

With “ $k_B$ ” the Boltzmann constant, “ $T$ ” the temperature (K), “ $d$ ” the particle diameter,  $P$  the pressure (Pa), “ $\rho$ ” the gas density ( $\text{kg} \cdot \text{m}^{-3}$ ),  $\eta$  the dynamic viscosity (Pa.s),  $M$  the molecular mass and  $R$  the ideal gas constant.

When the flow is governed by small numbers of Knudsen, “ordinary” hydrodynamic equations are usable. For higher Knudsen numbers, a free molecular flow can be obtained. The different regimes that can be observed on the Knudsen number are [108]:

- When  $Kn < 0.01$ , the fluid is considered as a continuous medium and described with macroscopic variables: the Navier-Stokes equation can be applied to describe the flow.
- For  $0.01 < Kn < 0.3$ , the flow is in the “slip” regime. The Navier-Stokes equations are applicable (the gas is treated as a continuum), but the gas “slides” on the surfaces: there are discontinuities in velocity (and temperature) at solid boundaries. Velocities of the molecular layers on the surface are different from those of these latter molecular layers. Therefore, in this type of regime, only the boundary conditions are to be modified.
- For  $0.3 < Kn < 10$ , we are in the presence of the so-called “intermediate” regime characterized by the effects of the rarefaction of the volume starting to appear. In this type of regime, the Navier-Stokes equations must be modified: a microscopic approach is usually required and from a statistical study of the trajectories of molecules, macroscopic variables can be obtained.

- Finally, for  $Kn > 10$ , the regime that is set up is called the highly "rarefied gas" (or free molecular) one. In this regime, the gas is no longer described by the Navier-Stokes equations but rather by the Boltzmann equations.

P (kg.m <sup>-3</sup> )	$\eta$ (Pa.s)	Cp (J.kg <sup>-1</sup> .K <sup>-1</sup> )	$\Lambda$ (W.m <sup>-1</sup> .K <sup>-1</sup> )	M (g.mol <sup>-1</sup> )
1.177	1.85 10 <sup>-5</sup>	1006	0.0262	28.965338

Table 2-8 : Air properties at 300K

It is important to note that, depending on the authors, those thresholds may be different. For instance, for Kandlikar *et al.* [123] the continuum flow is for  $Kn < 10^{-3}$ ; The slip flow is for  $10^{-3} < Kn < 10^{-1}$ , the transition flow for  $10^{-1} < Kn < 10$  and the free molecular flow for  $Kn > 10$ .

To remain in the classical Navier-Stokes physics ( $Kn < 0.01$  [108] or  $Kn < 0.001$  (Kandlikar, Garimella, Li, Colin, & King, 2006), we had to determine the smallest characteristic length we could use. For our motor, the fluid flow (air) will take place in canals, meaning that the characteristic length will be the hydraulic diameter  $D_h$  (*cf.* section 2.4.3.a. ). We determined that the air mean free path at 300K was equals to 67 nm (air properties at 300K given in Table 2-8). Thus, for a  $Kn < 0.01$ , the canals for air flow that we will design must be with a hydraulic diameter larger than  $7\mu\text{m}$ , and for  $Kn < 0.001$  the hydraulic diameter must be larger than  $67\mu\text{m}$ . To ensure a continuum flow, we thus decided to design canals with hydraulic diameter of at least  $100\mu\text{m}$ .

### 2.4.3. Alternating flows and associated dimensionless number

The gas flow in the Stirling motor is an alternating (or oscillating) one, that is to say a periodic alternating non-stationary flow with an averaged flow velocity equals to zero [124]. The velocity of an alternating flow will vary between a maximum and a null value, this last one being reached at each half-period. This implies that the coefficient of friction should vary between a specific value for the highest velocity, and which is function of the flow regime (laminar or turbulent) and the properties (geometry, roughness, temperature...), and go through two infinite theoretical values (at null velocity). The friction coefficient cannot thus be determined based on steady flow conditions [119]. For example, Zhao and Cheng [125], in their studies on transient flows, showed that the pressure drop coefficients could be 2 to 6 times those of permanent unidirectional flows. For an established oscillating flow of a viscous fluid in a tube, at macroscopic scale, the annular velocity profile can be very different from the one of the permanent flow. Whereas for a permanent laminar flow the transverse velocity gradient is maximum at the centre, for an oscillating flow, the transverse velocity gradient is maximum near the wall [126], *cf.* Figure 2-31. This velocity profile depends on parameters such as the frequency, the viscosity and the hydraulic diameter [127].

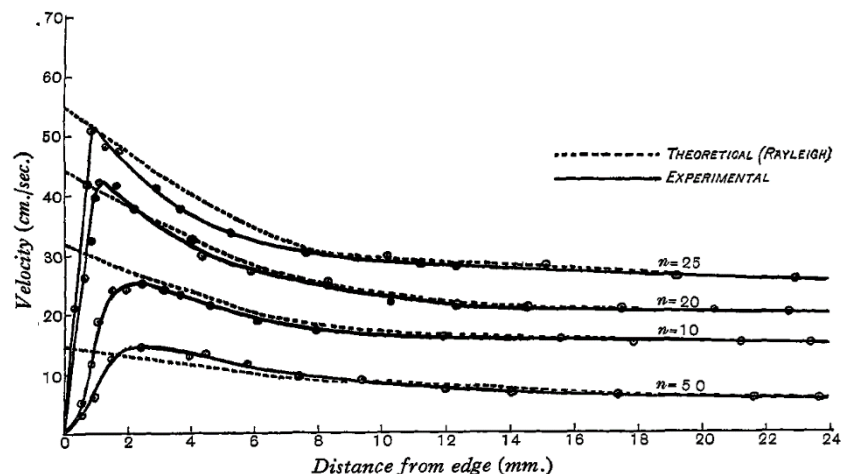


Figure 2-31 : Velocity profiles inside a round section pipe of circular section (6.2 cm in diameter) with two flats formed at the sides, at an operating frequency "n" from 5 to 25 Hz and for a piston length of stroke of 0.95cm. Extracted from [126]

If there exists works at macroscopic scales, the literature is rather poor regarding alternating gas flows in micro-channels: the design of small scales alternating fluid exchangers (such as the ones for Stirling motors) remains an area not yet very well known. The different researchers who studied the alternating flow, from the point of view of microfluidics or thermal transfers, did it generally for liquids and as a function of specific parameters or dimensionless numbers. This makes the comparison difficult and therefore not easily transposable to other conditions (geometries, clean room materials). To determine the thermofluidic characteristics such as pressure

drop and heat transfer coefficients, some authors made some correlations but, for the most part, they were based on simplified assumptions such as a flow in only one direction and supposed to be almost permanent (knowing although this one is transitory), while the physics is not transposable [119].

Therefore, for the design and optimization of the Stirling thermal micro-machines (operating with a gas with alternating flow) a better knowledge of these types of flows is necessary.

### **2.4.3.a. Parameters and dimensionless numbers used for the study of oscillating flows**

Dimensionless numbers and different parameters are used by researchers to characterize alternate flow in a variety of geometries of systems [128]. The choice of these parameters is very important since it allows the interpretation and the physical understanding of the flow, but also the comparison of different results between them. Characteristic dimensionless numbers for alternate flows are the Reynolds number “Re”, the frequency Reynolds number “ $Re_\omega$ ”, the relative amplitude of the arbitrary displacement of the fluid “Ar” [129]. Other classical dimensionless numbers, such as Prandtl or Mach number, are also relevant in the study of alternate flows and will be thus presented.

#### **i Reynolds number**

For unidirectional flows, the Reynolds number Re represents the ratio between the inertial force and the viscosity force. It characterizes the transition from a laminar flow to a turbulent one. When widths of canals in microsystems are on the order of tens of micrometres, typical fluid velocities do not exceed a centimetre per second and; it follows that, in general, Reynolds numbers in these microfluidic systems do not exceed  $10^{-1}$  [108].

For a flow through a duct, it is obtained by the following expression [119]:

$$Re = \frac{U.L_c}{\nu} = \frac{U.D_h}{\nu} \quad \text{Eq. 2-22}$$

With “U” the fluid velocity,  $L_c$  the characteristic length, here equal to the hydraulic diameter “ $D_h$ ” (since we considered a duct), and “ $\nu$ ” the kinematic viscosity of the fluid.

To determine the Reynold number for an alternate flow, since the velocity of the fluid “U” is variable and periodic, it is possible to use a maximum value of the velocity amplitude [120], [130], [125]: in this case, the Reynolds calculated with previous equation is usually called “ $Re_{max}$ ”. It is also possible to use an average time value of the velocity over a half-period ( [131], [132], [133], [134]). With axial parietal temperature gradient, some authors will use a mean average velocity between the hot and cold sides of the regenerator [135].

Another specific Reynolds number, the kinetic Reynolds number “ $Re_\omega$ ” is widely used with oscillating flows:

$$Re_\omega = \frac{\omega.D_h^2}{\nu} \quad \text{Eq. 2-23}$$

Where  $\omega$  is the angular velocity. Note that we can also find the Valensi number “Va”, which is defined either as  $Re_\omega$  or as  $\frac{Re_\omega}{4}$  depending on the authors. For this work, we will refer at Valensi number with this formula:

$$Va = \frac{\omega.D_h^2}{4\nu} \quad \text{Eq. 2-24}$$

#### **ii Womersley number**

Alternate flows, and more precisely the non-stationarity of the flow, can also be characterized by the dimensionless number of Womersley [136], [137] defined by:

$$W_0 = \sqrt{\frac{\omega L_c^2}{\nu}} = \sqrt{\frac{\omega D_h^2}{4\nu}} = \sqrt{\frac{Re_\omega}{4}} = \sqrt{Va}$$

$L_c$  is a characteristic length that can represent a radius  $r$  of a channel [138], a hydraulic radius  $r_h$  [139] or any characteristic dimension:

$$Re_\omega = 4.W_0^2$$

This parameter can highlight the so-called "annular" phenomenon: a maximum velocity of the fluid near the wall rather than at the center of the channel. This phenomenon was experimentally emphasized by Richardson and Tyler [126] who showed that, in a circular tube, the velocity profile of the fluid remains parabolic for Womersley numbers less than unity, *i.e.* the behavior in that case is the same than for unidirectional permanent laminar flows. However, for higher Womersley numbers, the velocity near the wall is maximum and flattens at the center of the tube [140], [141], [142]. Zhao and Cheng, in a numerical study of the alternating flows of a cylindrical channel, have found that for relatively high Reynolds numbers, the annular effect also exists in the temperatures profile near the inlet and the outlet [143].

### iii Displacement Relative amplitude

The maximum displacement amplitude of the fluid  $X_{max}$  is given by the formula of Simon and Seume [128] in the case of a generated flow, which is alternating, incompressible and sinusoidal:

$$X_{max} = \frac{u_{max}}{\omega} \quad \text{Eq. 2-25}$$

The relative amplitude of fluid displacement (dimensionless displacement) is then defined by [128]:

$$A_r = \frac{2X_{max}}{L} = \frac{2u_{max}}{\omega L} = \frac{D_h Re_{max}}{2L Va} = \frac{2D_h Re_{max}}{L Re_\omega} \quad \text{Eq. 2-26}$$

Where L is the tube length (heat exchanger length).

$A_r$  is a very useful parameter for the design of heat exchangers since it is characteristic of the passage time of the particles of the fluid in the channels:

- If  $Ar \ll 1$ : the length is too high, some fluid particles remain trapped in the channels, so they do not participate to the heat transfer;
- If  $Ar = 1$ : this is the ideal case since all the fluid run through the whole length of the tube.
- If  $Ar \gg 1$ : the tube length is too short. There is a portion of the initial volume of fluid that passes entirely through the heat exchanger.

Note that according to Zhao and Cheng [125], [143] and Leong and Jin [130], the definition of the maximum displacement (denoted here  $x_{max}$  to avoid confusion with  $X_{max}$ ) for an incompressible sinusoidal alternating flow is different from the previous one and is given by:

$$x_{max} = \frac{2u_{max}}{\omega} = 2X_{max} \quad \text{Eq. 2-27}$$

Hence, another definition of the dimensionless displacement, this time called  $A_{Dh}$ , is given [125]:

$$A_{Dh} = 2 \frac{Re_{max}}{Re_\omega} = \frac{x_{max}}{D_h} \quad \text{Eq. 2-28}$$

In an alternating fluidic regime,  $A_{Dh}$  makes it possible to characterize the relative displacement of the fluid in the thermal machines having regenerators. On the one hand, it characterizes the effects of the displacement amplitude of the fluid and on the other hand the effects of the frequency of fluid alternations ( $Re_\omega$ ).

The link between  $A_r$  and  $A_{Dh}$  is thus:

$$A_r = \frac{D_h}{L} A_{Dh}$$

### iv Mach number

The Mach number makes it possible to characterize the compressibility of the working fluid. In unidirectional flow, the compressibility of the fluid is generally characterized by a Mach number greater than 0.3 [144]. With the assumption of an ideal gas, the Mach number can be expressed as follows [119]:

$$Ma = U \sqrt{\frac{M}{\gamma_{is} RT}}$$

with  $U$  the flow velocity,  $M$  the molar mass,  $T$  the Temperature,  $\gamma_{is}$  the isentropic expansion factor (adiabatic index) and  $R$  the ideal gas constant.

In alternate flows, even for low Mach numbers, experimental work by Kornhauser [145] has shown that the effect of compressibility may not be negligible. According to them, the pressure variation of the working fluid during the compression and expansion phases causes a variation in temperature and consequently a variation in the density of the fluid. To study the compressibility effect of gas, Kornhauser thus introduced a “heat transfer Mach number” defined as the “ratio of the speed of propagation of a temperature wave to that of a pressure wave” ([145], p. 97-98):

$$M_{\omega} = \sqrt{\frac{\alpha\omega}{\gamma_{is}rT}} = \sqrt{\frac{\alpha\omega M}{\gamma_{is}RT}}$$

With  $\alpha$  the thermal diffusivity ( $\alpha = \frac{\lambda}{\rho c_p}$ ),  $\omega$  the angular frequency,  $r$  the specific gas constant.

The compressibility of the alternating flow is, in general, related either to the effect of increasing the pressure during the change of section of the working fluid from the heat exchanger, or to the acoustic effects caused by the pressure waves propagation.

### **v Eckert number and Prandtl number**

The number of Eckert is used only for very high fluid velocity, or above the speed of sound. It relates the kinetic energy to the enthalpy of a fluid [146], comparing the importance of advective transport and of the heat dissipation potential:

$$E_c = \frac{U_{max}^2}{C_p(T_{ch} - T_{fr})}$$

This number accounts for the viscous dissipation during the flow. Viscous dissipation can no longer be neglected when the Eckert number is greater than or equal to 1. Therefore, this dissipation can significantly influence the heat transfer [147].

Another dimensionless number is the Prandtl number that assesses momentum transport and thermal transport capacity of a fluid [146]:

$$Pr = \frac{c_p \eta}{\lambda}$$

### **2.4.3.b. Oscillating laminar flow transition to turbulence**

In a permanent unidirectional flow, the determination of the pressure drop coefficient (or heat exchange coefficient) requires knowledge of the flow regime (laminar or turbulent) to choose the corresponding correlation. In this part, we will focus only on internal flows. As for classical permanent flows, there is a transition phase (cf. Figure 2-32) between laminar and turbulent regime for internal oscillating flows which depends on various parameters, such as the fluid displacement amplitude and the frequency of alternation of direction of flow [148]. In a completely laminar flow during the whole cycle, there is no disturbance in the shape of the velocity curve, whereas in a disrupted laminar flow, small amplitude perturbations occur at the beginning of the acceleration ([149], [150], [151], [152]). The general shape of the velocity curve remains consistent with the theoretical laminar profiles. In an alternating flow, the appearance of turbulence is also different from that of unidirectional quasi-stationary flow ([143], [149], [153]). This turbulence appears only at the beginning of deceleration, whereas in phase of acceleration the flow regime is quasi-laminar ([150], [154]).

If some authors carried out studies to quantify, for alternate flow, the transition between laminar and turbulent flow (such as for instance the experimental study of Akhavan *et al.* [155]), there is still no universally accepted model for predicting this transition.

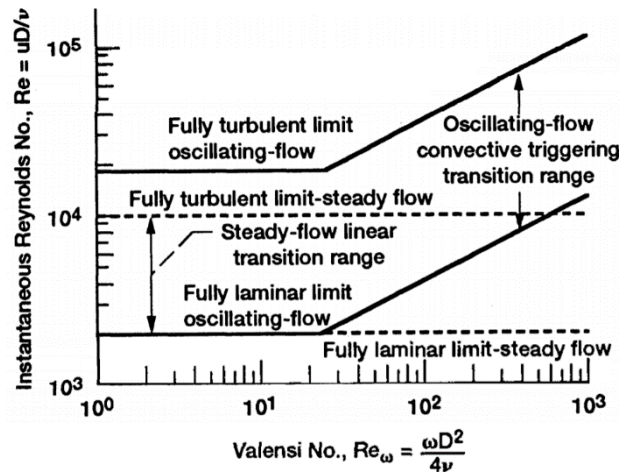


Figure 2-32 : Comparison of steady-flow and oscillating-flow transition criteria, from [148].

According to a numerical study carried out for an incompressible alternating flow by Zhao and Cheng [143], with  $A_{D_h}$  and  $x_{max}$  being respectively the dimensionless displacement and the maximum displacement amplitude of the fluid, for  $8.05 < A_{D_h} < 121.1$  and  $23 < Re_\omega < 540$ , the critical parameter of the laminar / turbulent transition is defined by:

$$\beta_c = (A_{D_h} \sqrt{Re_\omega}) = \left( x_{max} \sqrt{\frac{\omega}{\nu}} \right) = 761$$

According to Bouvier [142] and Bouvier *et al.* [156], some works (based on semi-empirical correlations) enable to determine the Reynolds  $Re_{trans}$  at which the transition from laminar flow to turbulent one (for an internal flow) occurs. Some of them are given in the Table 2-9.

Reference	Equation	Domain and condition
Sergeev (1966) [157]	$Re_{trans} = 700(Va)^{1/2} = 700 \left( \frac{Re_\omega}{4} \right)^{1/2}$	$64 \leq Re_\omega \leq 6400$ $14.5 < L/D < 263$
Park and Baird (1970) [158]	$Re_{trans} = 188(Va)^{2/3} = 188 \left( \frac{Re_\omega}{4} \right)^{2/3}$	$140 \leq Re_\omega \leq 4000$
Grassmann and Tuma (1979) [159]	$Re_{trans} = 49,7(Re_\omega)^{3/4}$ $Re_{trans} = 15300$	$160 \leq Re_\omega \leq 2070$ $Re_\omega > 2070$
Ohmi <i>et al.</i> (1982) [153]	$Re_{trans} = 2450$ $Re_{trans} = 882(Va)^{1/2} = 882 \left( \frac{Re_\omega}{4} \right)^{1/2}$	$\sqrt{\frac{Re_\omega}{4}} < 1$ $18.4 \leq Re_\omega \leq 546$ $\sqrt{\frac{Re_\omega}{4}} > 7$

Table 2-9: Some laminar / turbulent transition equations from the literature. L: length of the tube; D: diameter of the tube; Va: Valensi number.

One of the requirements to obtain an efficient Stirling motor is that the Ar number is around 1 (*cf.* previous section). To determine the geometric parameters given in the thermal study, we used the Ar number. For the 2D geometry,

the length and width of the canal was chosen to obtain a  $Ar$  value around 1 and also to both enable to put later on a regenerator inside the canal, and to obtain as much as possible motors on a same wafer. Thus, we obtained  $Ar$  values of 0.5 for the spherical cap membrane and 1.9 for the 2 mm central disk membrane with a canal's width of 1mm and a length of 7 mm. NB: We didn't used the required length to obtain a fully developed regime since these equations were only related to unidirectional flows.

Frequency [Hz]	1	10	100	1000	10000
$Re_{\omega}$	0.22	2.25	22	225	2249
<b>Re with a spherical cap membrane</b>	0.49	4.86	49	486	4864
<b>Re With 2mm in diameter central disk in the centre of the membrane</b>	1.95	19.49	195	1949	<u>19488</u>
<b>Value of <math>Re_{trans}</math></b>					
Sergeev [157]	---	---	---	---	---
Park and Baird [158]	---	---	---	2759	12805
Grassmann and Tuma [159]	---	---	---	2886	15300
Ohmi <i>et al.</i> [153]	2450	2450	---	6613	20912
<b>Value of <math>\beta</math> (Zhao and Cheng [125] [143]) (<math>\beta_c=761</math>)</b>					
spherical cap membrane	2	6	21	65	205
2mm in diameter central disk in the centre of the membrane	8	26	82	260	<u>822</u>

Table 2-10 : Kinetic Reynolds and transition Reynolds values for the 2D configuration and for 5 frequencies. --- corresponds to a not applicable correlation/condition.

Frequency [Hz]	1	10	100	1000	10000
$Re_{\omega}$	0.4	4	40	400	3997
<b>Re with a spherical cap membrane</b>	2	25	248	2477	<u>24774</u>
<b>Re with 2mm in diameter central disk in the centre of the membrane</b>	10	99	992	<u>9925</u>	<u>99250</u>
<b>Value of <math>Re_{trans}</math></b>					
<i>Sergeev [157] Condition L/D not verified</i>	---	---	---	6998	22129
Park and Baird [158]	---	---	---	4049	18792
Grassmann and Tuma [159]	---	---	---	4443	15300
Ohmi <i>et al.</i> [153]	2450	2450	2788	8817	27882
<b>Value of <math>\beta</math> (Zhao and Cheng [125] [143]) (<math>\beta_c=761</math>)</b>					
spherical cap membrane	8	25	78	248	<u>784</u>
2mm in diameter central disk in the centre of the membrane	31	99	314	<u>993</u>	<u>3140</u>

Table 2-11 : Kinetic Reynolds and transition Reynolds values for the 3D configuration and for 5 frequencies. --- corresponds to a not applicable correlation/condition. Italic values do not verify the condition  $L/D$  corresponding to the range of Sergeev study.



For the 3D geometry, only several glass thickness were available. In a first step, we assumed we will use the thicker borofloat wafer (6.5 mm) to obtain better thermal resistance, and 500  $\mu\text{m}$  thick silicon wafers. Thus, the canal length was equal to 5.9 mm. The canal diameter had to be large enough to enable to place a regenerator inside it ([95]). Thus, the diameter was set at 1mm. With these values, we had Ar values of 2 and 8 for spherical shape membrane and membrane with a 2 mm central disk respectively.

Based on the literature, we calculated, for 5 frequencies, the transition Reynolds. For the 2D geometry, we used parameters given in Table 2-5. The classical Reynolds number is calculated with an average velocity on the section (using total swept volume displaced on half a period that passes through the section of the canal). Air properties were taken from Table 2-8. The results are given in the Table 2-10. From those results, it is quite obvious that, for identical conditions, there is a great discrepancy between values of  $Re_{\text{trans}}$ .

With a spherical cap membrane, the flow should remain laminar for all the tested frequencies. For the membranes with a 2 mm central disk in its centre, for operating conditions up to 1 kHz, the flow should stay laminar. Whereas, for frequency of 10 kHz, the flow should be either in the transition or turbulent. Thus, to remain laminar, a frequency below 10 kHz should be used. More precisely, according to Park and Bair [158] equation (which is the one that gives lower transition Reynolds number) the frequency should not exceed 2.5 kHz.

Same calculations are carried out with the 3D geometry, using parameters from Table 2-7. Results are given in the Table 2-11 . With a spherical cap membrane, the flow should remain laminar for Reynolds numbers up to 1 kHz, and be turbulent for a frequency of 10 kHz.

For the membranes with a 2 mm central disk in its centre, for operating conditions up to 100 Hz, the flow should stay laminar. Whereas, for frequency of 1 kHz, the flow should be turbulent. Since there is a great discrepancy between theoretical values, to remain laminar, the frequency should remain below 700Hz according to Omni *et al.* [153], below 580Hz according to Zhao and Cheng [143], and below 200 Hz according to Park and Baird [158] and Grassmann and Tuma [159].

With the chosen geometric parameters, and at frequency of, at maximum, hundreds of Hertz, the flow in the 2D and 3D motor should remain laminar. Since this PhD was part of the MISTIC project, with a 3D design, and since, we found that the 3D design was thermally more suitable, from now, we will only talk about the 3D geometry. The next section will shortly present another parameter that is of great importance: friction losses.

#### 2.4.4. Friction coefficient and pressure drop

One challenge in miniature structure is the pressure drop due to friction. When miniaturizing a system, the predominance of pressure losses can quickly become a real problem. If friction coefficient and pressure drop are well documented at large scales and for unidirectional flows, the literature is rather poor when it comes to miniature systems with oscillatory flows.

The similarity criterion associated with the viscosity forces is the coefficient of friction  $C_f$ . In the permanent internal flows, it is constructed with a reference speed which is the fluid flow speed  $U$  and the mean parietal stress  $\tau_p$  [119]:

$$C_f = \frac{\tau_p}{\frac{\rho U^2}{2}}$$

$C_f$  is related to the coefficient of linear pressure loss  $C_f'$ . This other coefficient of pressure loss, called Fanning coefficient, represents the ratio between the frictional stress at the wall and the kinetic energy of the fluid by the following relation:

$$C_f = \frac{C_f'}{4}$$

For a unidirectional and laminar flow in a pipe, the nature or the surface roughness of the internal walls of the microchannel have no influence on the coefficient of pressure drop  $C_f'$ . This coefficient is then determined by the following equation:

$$C_f' = \frac{64}{Re}$$

In the same conditions (unidirectional flow in a pipe) but in the turbulent regime (*i.e.*  $Re > 4000$ ), the coefficient of pressure drop  $C'_f$  depends on the surface roughness and is expressed for instance by the classical Colebrook formula:

$$\frac{1}{\sqrt{C'_f}} = -2 \log_{10} \left( \frac{2.51}{Re \sqrt{C'_f}} + \frac{k}{3.7 D_h} \right)$$

With  $k$  the roughness of the internal surface of the pipe. When considering microchannel, the flow regime is usually the laminar one.

The linear pressure drop on a length  $L$  for a permanent flow is expressed by:

$$\frac{\Delta P}{L} = C'_f \frac{\rho U^2}{2} \frac{1}{D_h}$$

This relation is not valid in alternate flow because the quantities such as the pressure, the speed, the flow, the temperature of the fluid are subject to phase differences in the temporal evolutions, which is not the case for the permanent flows

Another factor that will have influence on the pressure loss is the fluid compressibility. Due to the compressibility of the gases, their volume, density and viscosity vary very significantly as a function of the pressure and the operating temperature. Therefore, unlike liquids (considered almost incompressible) the pressure drop due to the flow of a gaseous fluid is accompanied by an expansion that results in an increase in flow (*i.e.* the speed), a decrease in the density and an increase in the dynamic viscosity [160]:

$$K_e = \frac{2}{1 + \sqrt{1 - \frac{2\Delta p_l}{P_e}}}$$

With  $\Delta p_l$  = linear pressure loss calculated as if the fluid was incompressible (singular losses not included);  $P_e$  = Absolute pressure at the point at the inlet of the piping, or at the point of origin of the section considered.

Nevertheless, when considering alternate flows, the friction coefficient is rather different. No universal law exists since the studies are often carried out with porous media (*cf.* Annexe B section regenerators), which can be found in the regenerator parts of the Stirling motors. For alternate flows, since, the flow's velocity passes through a zero value at each half-period. This speed increases, between these two null values, reaches a maximum and decreases ([142], [161]). Therefore, the coefficient of friction goes through two theoretical values when the velocities become zero (infinite) and a particular value at maximum velocity that depend on the regenerator geometry and the nature of the flow (laminar or turbulent). As a result, this coefficient of friction cannot be characterized by previous equations established with steady flow conditions.

Experimental studies on the pressure drop coefficient (or Darcy coefficient) in alternating flows are not numerous. The determination of the coefficient of pressure loss requires, in the first place, relying on the resolution of the equation of momentum of a one-dimensional unsteady flow. According to Smith [162], under the assumption of an ideal gas and for a Newtonian fluid, in an empty, the equation of mass conservation and of momentum can be expressed as follows:

$$\frac{\partial \rho}{\partial t} + \frac{\partial}{\partial x}(\rho u) = 0$$

$$\rho \left( \frac{\partial u}{\partial t} + u \frac{\partial u}{\partial x} \right) = - \frac{\partial P}{\partial x} + \frac{4}{3} \frac{\partial}{\partial x} \left( \eta \frac{\partial u}{\partial x} \right)$$

With the fluid density  $\rho$ , the pressure  $P$  and the velocity  $u$  functions of  $x$  (distance) and  $t$  (time) and  $\eta$  the dynamic viscosity.

In the regenerator, in a channel of circular section with the assumption of a one-dimensional flow of an ideal gas, neglecting the gas and matrix heat conduction along the matrix and assuming no temperature difference across the regenerator, the momentum equation is as follows [135]

$$\rho \left( \frac{\partial u}{\partial t} + u \frac{\partial u}{\partial x} + u \frac{\partial u}{\partial r} \right) \approx -\frac{\partial P}{\partial x} - C_f(t) \frac{\rho u^2}{2D_h}$$

With  $r$  the radial coordinate.

The instantaneous oscillatory flow friction factor is then [135]:

$$C_{f_{INST}} = \frac{-\frac{\partial P}{\partial x} - \rho \frac{\partial u}{\partial t} - \rho u \frac{\partial u}{\partial x} - \rho u \frac{\partial u}{\partial r}}{\frac{\rho u^2}{2D_h}}$$

By integrating the preceding equation over the entire length of the regenerator  $L$ , it then comes:

$$C_f(t) = \frac{\Delta P}{\rho \frac{L}{2D_h} u(t)^2} - \frac{2D_h}{u(t)^2} \frac{\partial u}{\partial t} - \frac{2D_h}{L} \frac{\Delta u}{u(t)} - \frac{2D_h}{u(t)} \frac{\partial u}{\partial r} \approx \frac{\Delta P}{\rho \frac{L}{2D_h} u(t)^2} - \frac{2D_h}{u(t)^2} \frac{\partial u}{\partial t}$$

where the two right-hand terms of the equation represent respectively the similar pressure loss coefficient of the permanent unidirectional flow and the term of inertia [135]. The inertia term of the equation can be negligible at low oscillation frequencies. Therefore, the equation would become [135]:

$$C_f(t) = \frac{\Delta P}{\rho \frac{L}{2D_h} u(t)^2}$$

Some works can be found on pressure drop inside porous media (regenerator). Since the study of the regenerator was the subject of another PhD work [95] that was part of the MISTIC project, no further details on the regenerator and pressure drop inside it will be given here. Some complementary correlations and experimental results can be found in Appendix C for studies carried out in regenerator, with porous media.

One of the main objectives of this PhD was also to minimize, as well as possible, the pressure loss in the canals of the miniature device. At first, some technological, thermal and fluidic considerations enable to get an idea of the geometry of the motors. Here, we will only focus on the 3D geometry. In miniature devices, since the piston/membranes have generally a short stroke (below 1mm), the workspaces should be thinner and the height are limited by the wafer standard thickness (500  $\mu\text{m}$  for standard silicon wafers). The regenerator empty space is located in the canal which links the membranes working spaces. In the first simplified 3D version of the micro motor, the regenerator micro channel went through the glass component. In the MISTIC project, the three 3D motors are linked altogether, thus the hot chamber of the first motor must be linked to the cold chamber of the second motor, and so on (Figure 2-1). The channel of the regenerator being hollowed out in the glass substrate is, therefore, arranged vertically with respect to the plane of the substrate, whereas the channel connecting the chambers to the regenerator part are horizontal. Due to clean room limitation at the time of this PhD work, the angle between the horizontal and vertical channels was a 90° right angle. When considering pressure loss, this kind of angle is the worst-case scenario: a smoother curvature of the channels would decrease the pressure drop. Given that channels configuration, local gas flow phenomena will be problematic in this region and gas transition effects should be mitigate. Since the working gas is displaced in and out of the working spaces, the later should be designed to reduce pressure losses (also known as pumping losses) at the inlet/outlet of the chamber. This process requires a thorough knowledge of the characteristics of the flow, which is not easy to reach through analytical pathways, because of the small-scale geometry and non-traditional oscillating gas flow (classical works concerning pressure loss in small channels concern permanent flows [163]).

During MISTIC project, in an experimental approach, the characterization of the pressure losses in the spaces containing the working gas was investigated in a stable unidirectional flow by Hachey *et al.* [106] in order to find the best configurations. The critical starting parameters of a membrane Stirling micro-machine are generally determined by a numerical model characteristic of free-piston Stirling motors [11]. Since, if the frequency increases, the gas displacement distance can be affected (the gas can then only be expanded and compressed without real displacement in the length direction of the microchannels), the determination of the frequency of the operation, pressure losses, etc. is very important. Based on an equivalent electrical network model of a double acting free piston Stirling motor [11], the operating frequency of such a structure can be determined : Hachey *et al.* [106] thus expected that, with mm<sup>3</sup> displacement (given that frequency scales inversely to length) working operation in a

miniature motor was expected to reach at least 2000 Hz . In addition, given that most microchannels were a few hundred micrometres in diameter, this implied high flow speeds that can reach for some of them, a Mach number equals to 0.2 [106]. They found that pressure losses were at a minimum when the diameter of the regenerator matches the diameter of the channel in which it is located, and when the ratio between the hydraulic diameter in the inlet/outlet region with the diameter of the chamber (=membrane diameter) was almost equal to one.

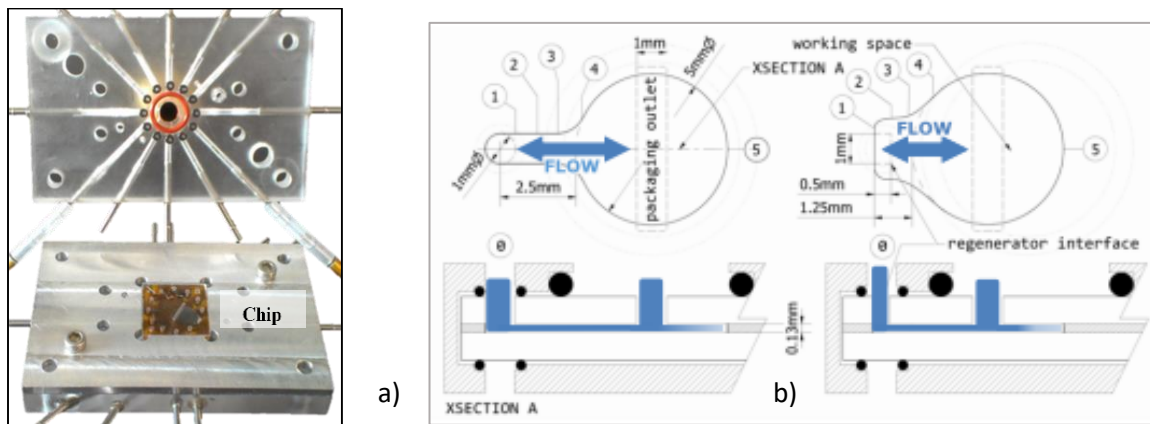


Figure 2-33: a) Packaging used in experiments with an exposed chip. b) a drawing showing the ability of the packaging to accept the original (left) and revised (right) versions of the workspace. From [106]

Their experimental device (*cf.* Figure 2-33) was a 15x15 mm glass-Kapton-glass stack in a Plexiglas / aluminum package, and the pressure taps of the chips were accessible through conventional fittings and tubes. For an incrementing unidirectional flow rate (inlet), in a range of 100 to 1500 cm<sup>3</sup>/min, they measured the static pressure at different points along the working gas path (1 to 5 in Figure 2-33) and determine the pressure loss in these specific areas. The pressure tap 0 (not shown in the figure) was located in an intake manifold.

For a flow direction of the gas from the regenerator to the chamber, the results show that the pressure drops occurred mainly in the zone 0-1 corresponding to the 90° wedge between the regenerator and the horizontal channel leading to the chamber. They found that the change from the original to the revised version (*cf.* Figure 2-33 - b) enable to reduce 84% of the pressure drop at  $Re = 700$ , but they assumed this result was due from increasing the hydraulic diameter at tap 1 from 200 to 260  $\mu\text{m}$ . The final geometry of the 2nd version of the workspace has been preserved for a more favourable and symmetrical pressure loss in a stationary flow [106].

Since, in our case, the 90° angle cannot be avoided, to limit the pressure drop, the junction between the horizontal canal and the chamber has to be smooth. To avoid too important dead spaces, we did not increase the hydraulic diameter or the horizontal canal, which would imply to increase also the vertical canal diameter. On the contrary, we decreased the hydraulic diameter due to both clean room consideration and targeted  $Ar$  values. One way to decrease the  $Ar$  value would be to change the chamber height (the other parameters being difficult to change). With a new chamber height of 300 $\mu\text{m}$ , the  $Ar$  value would decrease by a factor two and we would have  $Ar=1$  for the spherical cap membrane;  $Ar=4$  for the 2mm central disk membrane.

Moreover, to fullfill clean room process, this 300 $\mu\text{m}$  were the most suitable in our case: with classical silicon 500 $\mu\text{m}$  high, when etching chambers of 300 $\mu\text{m}$  high, the process will leave a thickness of 200 $\mu\text{m}$  of Silicon which is necessary to ensure the mechanical resistance of the chambers. Thus, since the important design parameters to consider are the exchange surface, the shape, the dimensions and the type of materials, to meet these criteria, the choice was to constitute a silicon hollow cylinder of 5mm in diameter, 300 $\mu\text{m}$  thick with an outlet channel of 1mm wide. Chambers are etched in a 4-inch silicon wafer of 500 $\mu\text{m}$  thick polished on both sides. A CAD view of the 3 chambers is shown in Figure 2-38. The outlet channel of the chamber is cone-shaped in order to obtain a "soft" transition zone more favourable to the gas flow (to avoid as much as possible the pressure losses). The advantages of such a choice on a wafer are the simplicity of microfabrication and the low-pressure loss due to the absence of right-angled sections, but rather rounded contours. It also helps to facilitate integration with the rest. The hot source and the cooling source are external as the faces of the silicon wafers are polished with a very good flatness ( $TTV < 3$ ). Any flat surface, hot or cold can therefore represent a thermal source when the micro-machine is placed there.

For the 3D motor, the previous conclusions concerning flow regime (*cf.* section 2.4.3.b. ) remain the same when the chamber is only 300 $\mu\text{m}$  in height (instead of 600 $\mu\text{m}$ ) : for both membranes' type, for operating frequencies under 500 Hz, the flow should remain laminar (lower value obtained from equations in Table 2-9). Concerning the surface roughness, it was dependant on the clean room process and on the material. Moreover, for the actuated version of the motor, the intended working frequencies are lower than 100Hz, meaning the flow will be laminar: knowing that for unidirectional flow, the coefficient of pressure loss is independent of the roughness, one can suppose that it will be the case also for an alternate flow. The next section will present the final 3D architecture, based on MISTIC requirements, and technological, thermal and fluidic consideration previously presented.

## 2.5. The chosen design of the micro Stirling motor.

### 2.5.1. The MISTIC design

The model of this first Stirling micromachine prototype with free-acting double action hybrid membranes is the micrometric version of the first multi-phase Stirling macro-motor prototype (*cf.* Figure 2-34a)) developed by Fenies through its thesis work [5] as part of the MISTIC project in 2016. The macro motor developed by Fenies at the University of Savoie, is a free-piston motor based on flexible membranes that are mechanically interconnected by rigid metallic bars. These membranes oscillate thanks to the gas springs that constitute the heated and cooled air in the compression and expansion chambers. Note also that, in this motor, each module, alone, represents a Stirling motor whose gas is sealed inside and that the connection between the three modules is through the mechanical connection bars (*cf.* Figure 2-34 b). From numerical simulations of the yield and losses, performed at the SYMME laboratory, it was this motor configuration that seemed to have the most benefit.

The MISTIC project aimed at the miniaturisation of this macro motor. The CAD schema of the whole initial design is recall on the Figure 2-1. This initial design was modified to be adapted to the clean room technology and requirement: this design, presented in Figure 2-35 a), is the one that was developed during this PhD work. The phase difference between the membranes is imposed by the number of associated modules. Figure 2-35 -b) illustrates a three-phase Stirling motor with free-double-acting diaphragms (connected membranes). To ensure the mechanical link between the membranes, at first, an incompressible liquid (*cf.* Figure 2-35 -b) was used. We will see later on that this option represented a simple solution, but raised issues due to the liquid filling (pollution of surfaces, clean room compatibility). Thus, another mechanical link was also tested (*cf.* next chapter) and consisted in a small cylinder bonded between the top and bottom membranes in a large chamber filled with a gas.

To summarize, the Stirling micro-machine is composed of two opposite flat faces, consisting of one side of a flexible membrane in a cold chamber and the other side of another flexible membrane in a hot chamber, with three micro channels for connecting the hot chamber of the first motor to the cold chamber of the second motor, and so on (*cf.* Figure 2-37). These three microchannel necessarily consist of a first horizontal microchannel, followed by a second vertical microchannel, then a third horizontal microchannel, the vertical microchannel containing the regenerator. The first horizontal microchannel connects the hot chamber to the regenerator, the latter being connected to the third horizontal microchannel leading into the cold chamber. For the motor configuration, the external flat face of these chambers will be in contact with a thermal source (hot or cold) and the other face will be occupied by the membrane which compresses and / or displaces the working gas.

The Stirling micro-machine system indeed exploits the inertia of suspended membranes to act on the working gas. Thus, the cyclic pressure applied between the membranes causes a phasing of the latter at a well-defined phase angle. In motor mode, the membranes produce a work due to the expansion of the working gas but also compresses and displaces the latter during the thermodynamic cycle.

The simplest (and most compact) size and shape of the upper wall of the chamber is obtained when its shape and perimeter correspond to the perimeter of the moving membrane, since this upper wall (*i.e.* the exchanger) and the membrane share the same workspace. For energy conversion, the diameter of the membrane can be chosen between 5 and 10 mm, with a thickness between 50 to 250 microns, to limit its resonance frequency to kHz. As previously presented, taking into account, the previous remarks and calculations in section 2.1. , we fixed the chamber (and membranes) diameter at a value of 5 mm.

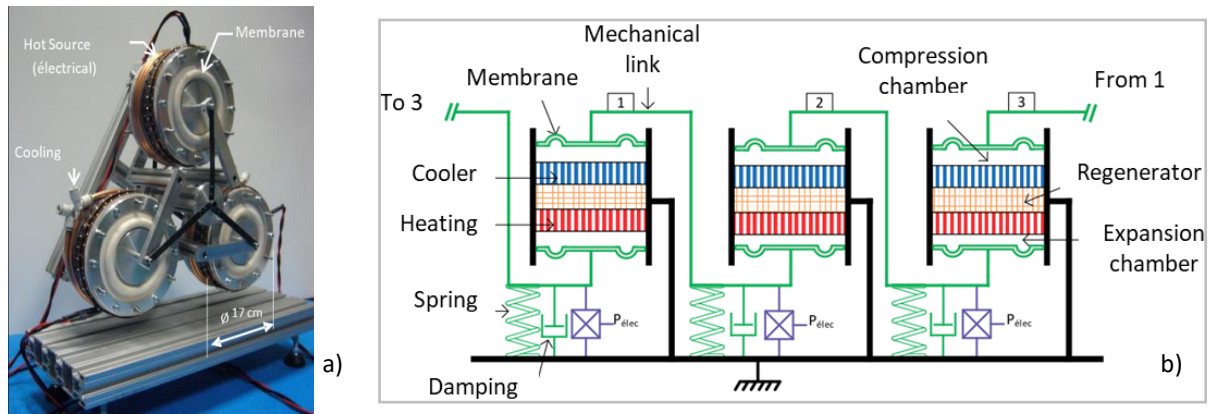


Figure 2-34: a) Picture and b) Diagram of the three-phase Stirling motor with double action free pistons demonstrated at SYMME Laboratory [5].

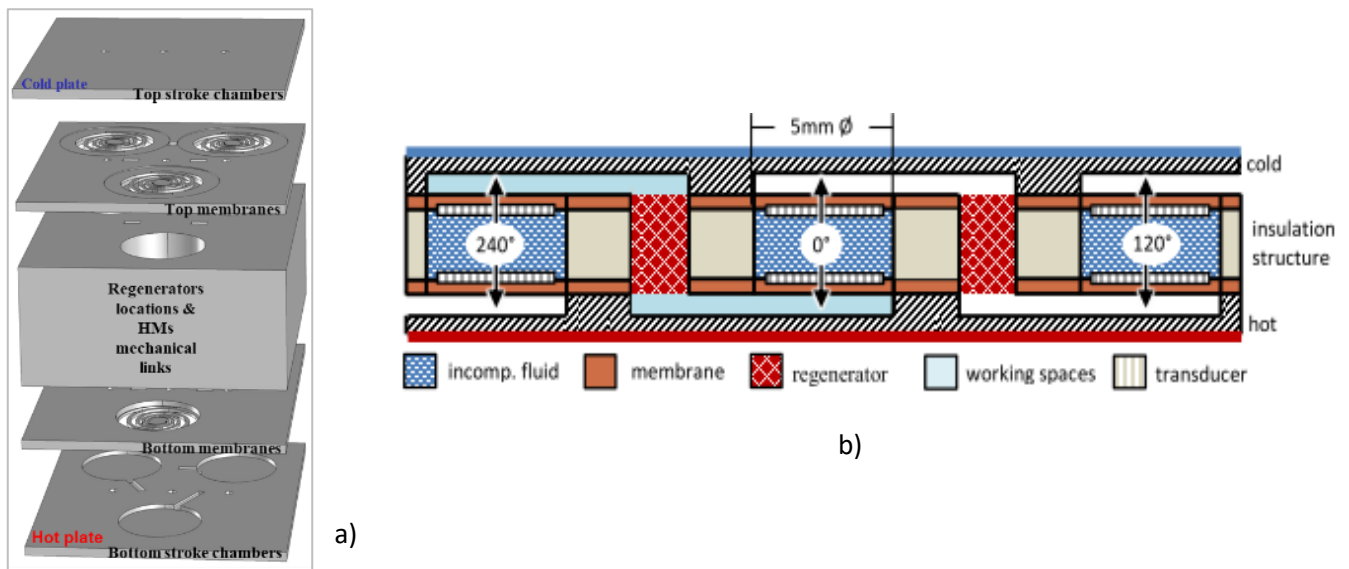


Figure 2-35: a) 3D schema of the micro-machine designed at FEMTO-ST institute. b) Depiction of a cross-section plane passing through the micro machine's three modules, from [106].

**The regenerator.** The main function of the regenerator is the storage and return of the heat to the gas as it flows, in the first place from the hot exchanger to the cold exchanger, and secondly in the other direction. Recall only that the constraints are to obtain a regenerator with a high thermal capacity, a good radial thermal conductivity, a large exchange surface, a low dead volume, as well as a high porosity, in order to limit the pressure losses. In the MISTIC project, the regenerator has been the object of a thesis [13] that will lead to a prototype to be implemented in our micromachine. It is therefore, as far as we are concerned, to correctly predict its location (*cf.* Figure 2-36 a) knowing its dimensions (*cf.* Figure 2-36 b). This will allow, more generally, to replace it easily to test different materials or architectures of regenerators. We have already presented the architecture and materials chosen that will compose this micro-generator in the previous chapter.

In our work, since the location of the regenerator also has a role in thermal insulation between the hot and cold side, requiring low thermal conductivity in the longitudinal direction, we chose to use a 6.5mm-thick block of borofloat glass. In this block are drilled the locations of the regenerators. These locations are made of rectangular cavity 1mm in length for 0.5mm width. The glass has a low thermal conductivity compared to silicon. The rectangular cartridges of regenerators can, therefore, be inserted into these cavities.

To achieve the objectives listed above, we will, in the next sections, begin by describing the constraints that we had to face in the choice of each constituent element of the micro-machine.

In the next section, we will focus on the influence of the MISTIC configuration on dead spaces. Then in the last section, the final micro-motor geometry, summarizing all the results and remarks from the previous sections, will be presented.

To achieve the objectives listed above, we will in the next sections begin by describing the constraints that we had to face in the choice of each constituent element of the micro-machine.

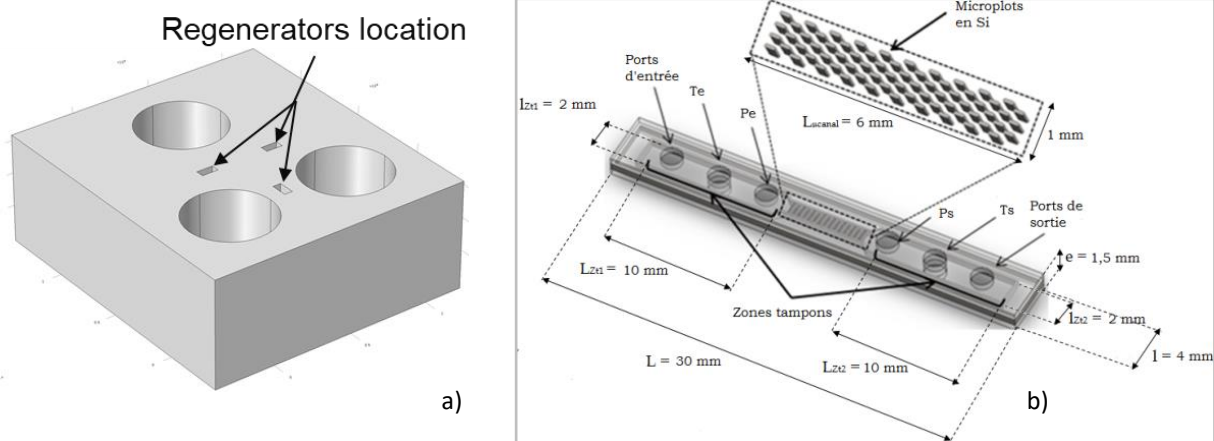


Figure 2-36: a) Three holes for the location of the tree regenerators cartridges. b) 3D sketch of the MISTIC regenerator microdevice [95].

### 2.5.2. Dead space: the influence of the regenerator design

Let us now consider the dead space due to the addition of the regenerator channel. The aim of the regenerator is to store and dispose of thermal energy, thus, due to thermal insulation stresses between the two chambers, the regenerator cannot be too close from the chambers, increasing the length of the channels and thus the dead space volume.

This configuration is best suited when one needs to associate several chambers to form for example a double acting Stirling motor. As previously explained, it would be difficult to make a Stirling micro-machine for the conversion of heat (*i.e.* produce a mechanical work), using only two membranes (or two chambers). The problem lies in the creation of the phase shift between the membranes. Recall that, if the objective of the micro-machine is primarily oriented towards the production of cold, then in this case, the design is easier because the phase shift is imposed by the operating mode of the membranes. However, if the machine operates in motor mode, a good solution is the concept of double acting free piston motors with at least three machines. In this case, there will be a need to physically connect the membranes to each other, but since the regenerator channel must necessarily be shifted, it would be necessary to create two horizontal channels to connect the latter to the two chambers (top and bottom).

**To fulfill the MISTIC architecture**, the hot chamber of the first motor must be linked to the cold chamber of the second motor and so on. Thus, the simplified 3D geometry presented previously must be changed by adding horizontal channels to link cold and hot chambers from different motors. This channel design is restrained by clean room process possibilities. Whereas the vertical channel can be etched or drilled as a cylinder (since it crosses right through the wafer), in the horizontal plane, the channel cannot be a cylinder and must have a vertical rectangular section (*cf.* chapter 3 for the clean room process). Two different configurations are given on the Figure 2-37: the one corresponding to the simplified 3D geometry (a) and the final one corresponding to the MISTIC requirement (b). On this figure,  $r_m$  is the membrane radius;  $C_c$  is the chamber height;  $R_d$  is the central disk radius;  $h_m$  is the maximum swept height;  $d_c$  is the chamber diameter,  $C_r$  is the vertical channel diameter;  $L_{can}$  is the length of the vertical channel;  $L_{rh}$  is the length of the horizontal channel and  $H_{rh}$  is the height of the horizontal channel. The width of the horizontal channel, not visible on the 2D figure, is denoted  $l_{rh}$ .

To simplify this part, we will consider that the regenerator channel (the vertical one) is empty (*i.e.* no metal layer or matrix).

The total swept volume  $V_{sw}$ , assuming the membrane height able to reach the chamber height (*i.e.*  $C_t = h_m$ ) for both configurations and with a membrane with a central disk in its centre (*cf.* eq. 2-6), is given by :

$$V_{sw} = \frac{2}{3} V_c \left( \frac{R_d^2}{r_m^2} + 1 + \frac{R_d}{r_m} \right)$$

With  $V_c$  the volume of cylindrical chamber ( $V_c = \pi r_m^2 h_m$ )

For the MISTIC configuration, the total motor volume  $V_t$  is then:

$$V_t = V_{can} + 2V_{rh} + 2V_c = \pi \left(\frac{C_r}{2}\right)^2 L_{can} + 2L_{rh}l_{rh}H_{rh} + 2 \cdot \pi r_m^2 h_m$$

With  $V_{can}$  the volume of the vertical channel;  $V_{rh}$  the volume of one horizontal channel and  $V_c$  the volume of one chamber.

The dead space related to one chamber can be determined from  $V_c$  and eq. 2-6. The dead space related to the channels is the channels volume, *i.e.*  $V_{can} + 2V_{rh} = \pi \left(\frac{C_r}{2}\right)^2 L_{can} + 2L_{rh}l_{rh}H_{rh}$ .

The ratio  $\chi$  between the swept volume and the total volume can then be calculated:

$$\chi = \frac{V_{sw}}{V_t} = \frac{\frac{2}{3} V_c \left(\frac{R_d^2}{r_m^2} + 1 + \frac{R_d}{r_m}\right)}{\pi \left(\frac{C_r}{2}\right)^2 L_{can} + 2L_{rh}l_{rh}H_{rh} + 2 \cdot \pi r_m^2 h_m}$$

And the ratio  $\chi_d$  between the total dead space  $V_d$  and the total volume  $V_t$  is given by:

$$\chi_d = \frac{V_d}{V_t} = \frac{V_c \left(1 - \frac{1}{3} \left(\frac{R_d^2}{r_m^2} + 1 + \frac{R_d}{r_m}\right)\right) + V_{can} + 2V_{rh}}{\pi \left(\frac{C_r}{2}\right)^2 L_{can} + 2L_{rh}l_{rh}H_{rh} + 2 \cdot \pi r_m^2 h_m}$$

The adjunction of 2 horizontal canals decrease the ratio  $\chi$  from 36 to 33% and in both cases, the dead spaces are very significant: they are bigger than the swept volumes when an empty canal for a regenerator is considered. Note that with a regenerator inside the canal, the dead space due to the canal would decrease and the ratio would be improved.

Since we know that the 3D architecture is more advantageous, the regenerator channel can then be developed in another substrate of different material. This material would then be chosen from among the most thermally insulating available in a clean room. Another dilemma arises, knowing that in this channel one would like the heat of the working gas to be absorbed during its passage, then to restore on its return, this would require a material that has the best possible thermal diffusivity.

Figure 2-37	$C_t=h_m$ [mm]	$C_r$ [mm]	$L_{can}$ [mm]	$r_m$ [mm]	$R_d$ [mm]	$L_{rh}$ [mm]	$l_{rh}$ [mm]	$H_{rh}$ [mm]	$\chi$	$\chi_d$
Case a)	0.3	1	6.5	2.5	1	0	0	0	36%	46%
Case b)						3	1	0.3	33%	52%

Table 2-12 : Parameters and values of the 3D models from Figure 2-37.

Therefore, in other words, the channel must thermally isolate the two chambers, but the regenerator has to recover the heat of the gas which is not feasible with a thermal insulating material, hence the dilemma. As thermal insulation is more problematic, the channel material should be a thermal insulator. To overcome this difficulty, the regenerator is made from a matrix of silicon micro pillars on glass substrate [95]. The difficulty with this method is that the insertion is done manually in a channel of less than one millimetre in diameter. If the shape of the regenerator does not match the channel shape (*i.e.* cylindrical) it may block part of the channel or not be symmetrical. Knowing that the regenerator substrate has a certain thickness, when it is then introduced into the channel, problems related to the circulation of the working gas may occur.



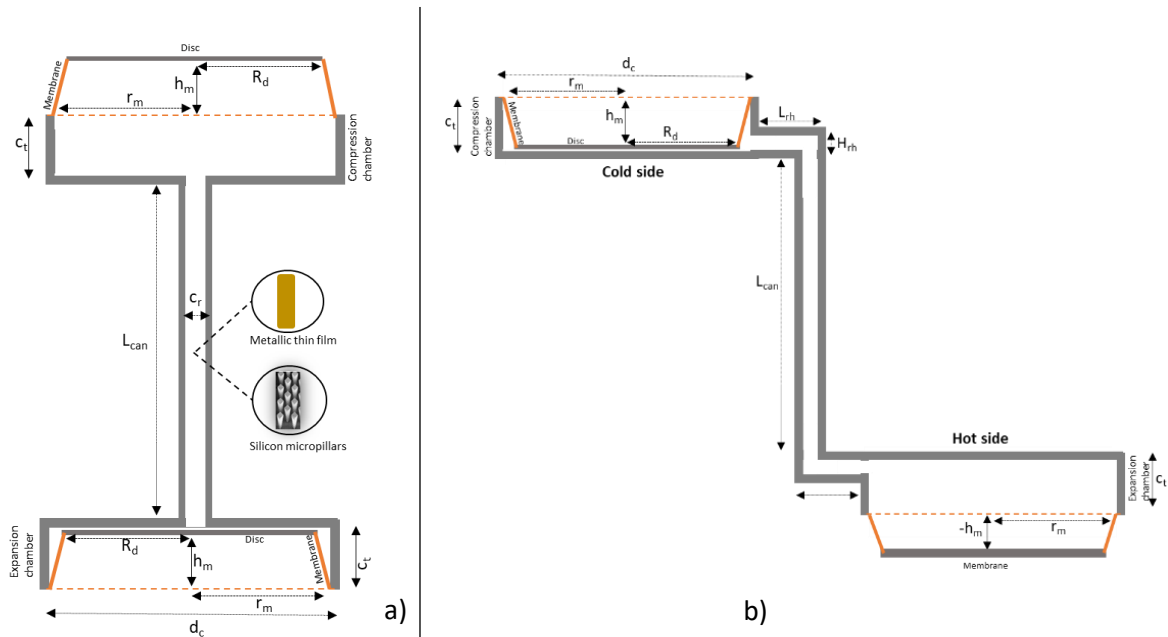


Figure 2-37: A complete 3D MEMS motor (alpha configurations) with two flexible membranes clamped at their ends with a central disc moving in the form of a truncated cone in two cylindrical chambers connected by a) one vertical channel or b) a vertical and two horizontal channels (MISTIC). With  $r_m$  the membrane radius;  $C_t$  the chamber height;  $R_d$  the central disk radius;  $h_m$ , the maximum swept height;  $d_c$  the chamber diameter,  $C_r$  the vertical channel diameter;  $L_{can}$ , the length of the vertical channel;  $L_{rh}$  the length of the horizontal channel and  $H_{rh}$  the height of the horizontal channel.

### 2.5.3. Summary

During the design of this micro-machine, we recall that the parameters that influenced our choices are the following:

- Compatibility with technology available in clean room
- Simplicity of implementation for the motor, operating temperature between 20 and 200°C with good thermal insulation between the hot and cold zones
- Hermetic membranes oscillating at the lowest possible frequencies but with a large and controlled swept volume
- A connection between these membranes, allowing a reduction of the potential sources of losses or failures
- Ensure a gas flow from the chamber of a module to the other adjacent module chamber,
- Use a so-called dual-action multiphase free piston motor architecture for the synchronization between the moving elements in order to avoid a new source of energy dissipation by friction.
- A small number of moving parts, reliable and low-cost microfabrication.

Each horizontal side of our micromachine has 3 membranes (*cf.* Figure 2-35). The Figure 2-38 summarize all the parts and constitution of the complete motor. On this figure, a 3D CAD view of the chambers and membranes alone and assembled with the rest is presented. This motor consisted of five different parts: four silicon plates (membranes and chambers) and a thick glass plate (thickness consistent with clean room process, and thick enough to ensure a thermal insulation). This last one carries cavities for the mechanical connection of the membranes by means of an incompressible liquid or by means of solid cylinder bonded to the membranes central part. The canals for the regenerators (to boost the conversion efficiency) are also located in the thick glass wafer. On two silicon wafers, compression and expansion chambers are etched, the other two carrying the membranes.

The compactness of this arrangement not only saves space on a wafer and simplify microfabrication, but also maintain symmetry for proper operation of the micro-motor. The full clean room process will be presented in the chapter 3.

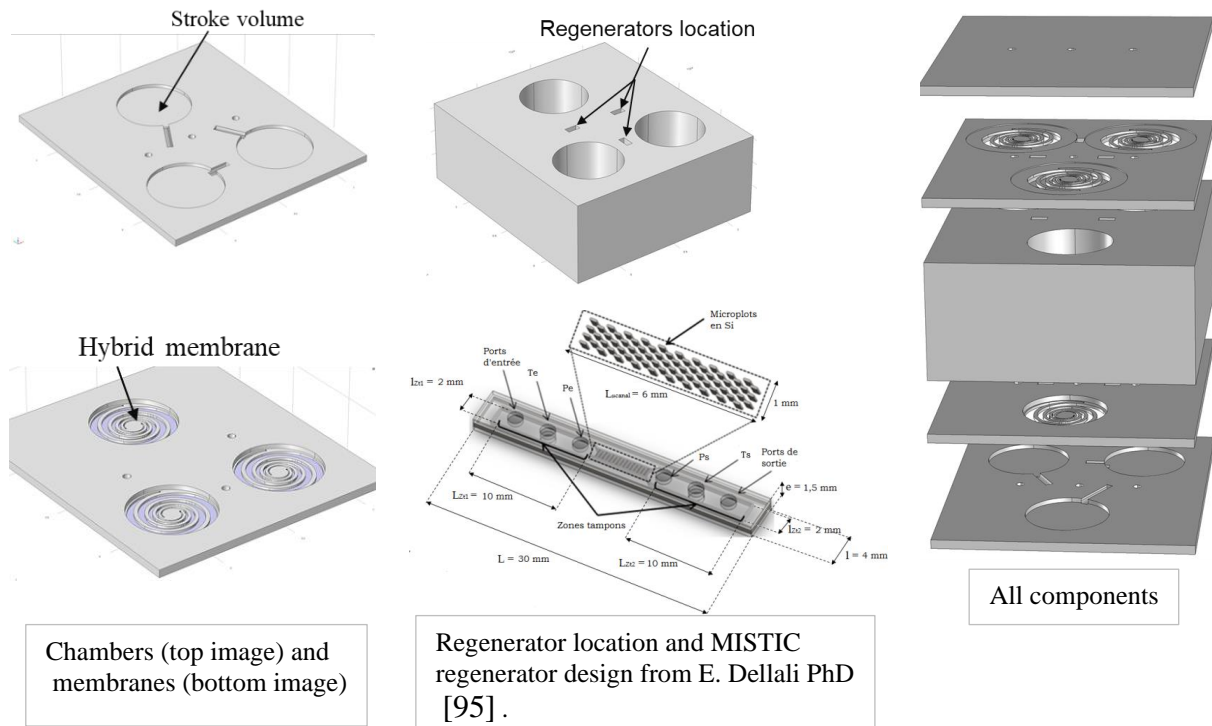


Figure 2-38: 3D CAD view of the constitutive elements of the micro motor.

## 2.6. Conclusion

A basic Schmidt model of the Stirling motor was described and applied to estimate the order of magnitude of the machine power and efficiency.

Several challenges with respect to miniaturization of Stirling motors have been described such as: the usage of membranes instead of pistons, the thermal design to maintain a temperature difference that is large enough between the hot and cold source or the critical influence of dead volumes.

## CHAPTER 3 : MICRO-ENGINE MANUFACTURING

This chapter concerns the microfabrication of the Microscale-Stirling Motor (MSE) for the recovery of low temperature thermal energy ranging from 20 to 200°C. The architecture of the prototype that was built is inspired by the work of FENIES [5] (cf. Figure 2-34 a)) during the MISTIC project. The constitutive geometric elements were adapted to the MEMS technology. Each of the machine elements (exchangers, chambers, membranes, mechanical connection) are redesigned as part of what is achievable using cleanroom technology constrained by the materials and equipment available. In order to limit the cost and ensure reproducibility, a proper and simple configuration has been developed. In the same way, air at ambient pressure is chosen as the working gas. This MSE consisted of a stack of silicon, glass and hybrid membranes (HMs) based on a silicone elastomer embedding a planar silicon spring and a mechanical link. The material chosen for the membrane is RTV-silicone, which withstands the envisaged temperature level (200°C). The membranes were made in a clean room by a succession of photolithography steps followed by etching and then scraping the RTV-silicone paste. The idea of liquid as mechanical link between hybrid membranes is based on the work of Chutani et al. [12]. In the following we will detail each step of components fabrication till the final assembly of the micromachine.

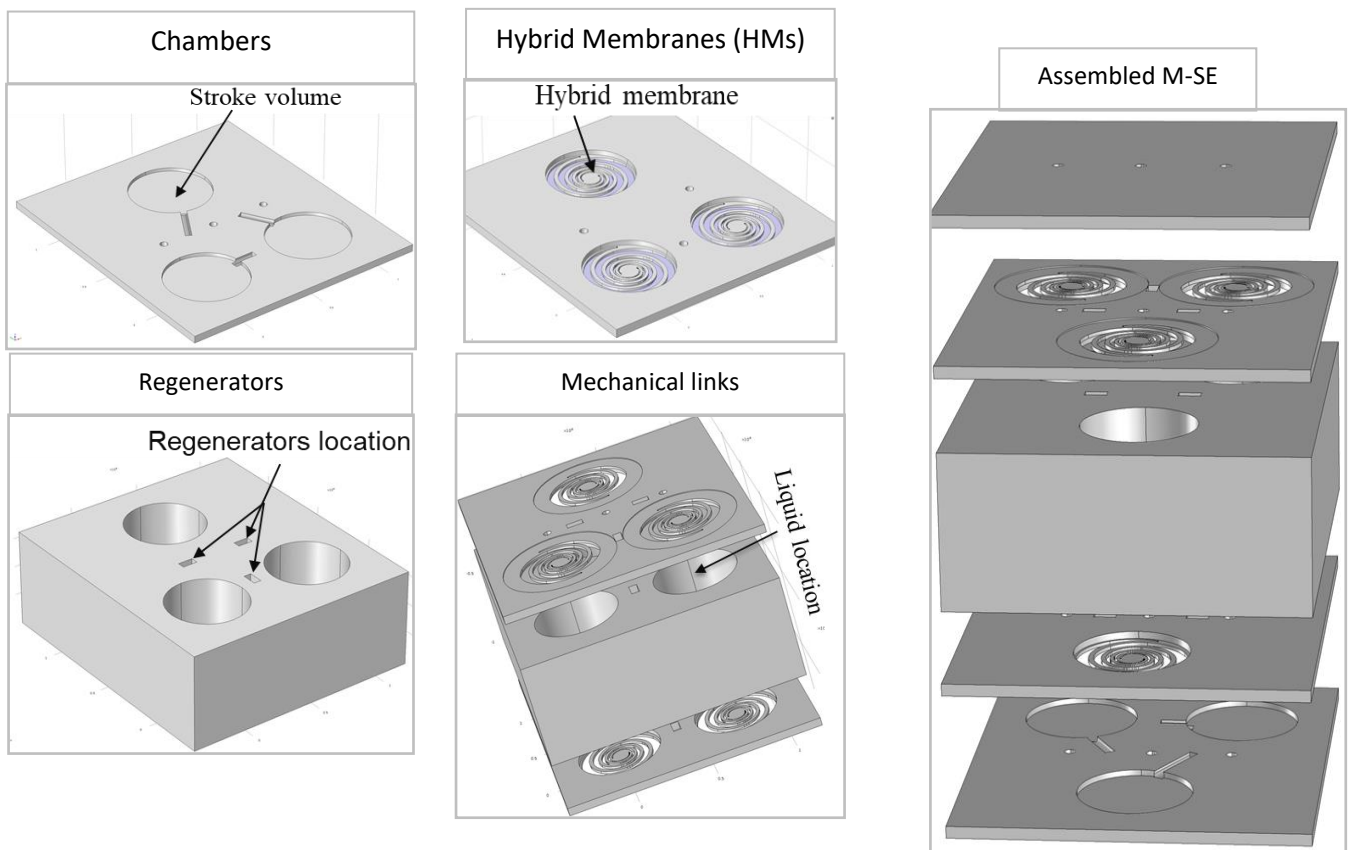


Figure 3-1: 3D CAD view of chambers and membranes alone and assembled to complete the micromachine

To finalize the development of the prototype, the different subsets (four silicon plates and a thick glass plate) of the machine are assembled using four successive bondings steps. To assemble the silicon wafers, we used thermocompression and to assemble these wafers with the glass wafer we used the technique of anodic bonding. To illustrate this description, the assembly is shown in Figure 3-1, where a 3D CAD view of the chambers and membranes alone and assembled with the rest is detailed. We will now briefly present the clean room methods used during the manufacture of this Stirling micromachine before moving on to the manufacture of each component.

### 3.1. Cleanroom methods introduction

At FEMTO-ST Institute, we have a clean room called "MIMENTO" dedicated to the manufacture of microsystems (<https://www.femto-st.fr/fr/plateforme-mimento>). The two types of possible MEMS geometries (2D and 3D) for the miniaturization of an alpha type Stirling machine have been discussed in chapter 2. The purpose of this these is to realize a 3D micro-Stirling motor with a size smaller than a cubic centimeter by the use of standard microfabrication tools.

Before detailing the microfabrication of the micromachine, MEMS manufacturing techniques will be briefly summarized in order to give the reader a good idea of this technology. Traditional surface and bulk micromachining, material removal (etching) and material addition (deposition) techniques are presented in detail in Appendix D.

Silicon is the most commonly used structuring material because of its well-known properties and well-developed manufacturing tools. The fabrication of a MEMS prototype in a clean room occurs by first patterning a substrate (a silicon wafer for example) by lithography and then depositing or removing material from it. Often, many of these steps are repeated to create 'features' on the substrate. Sometimes it is then necessary to assemble several substrates to produce the final product or for encapsulation to protect a device against the aggression of the environment (to increase its lifetime). Note that in clean rooms, equipment cannot structure all materials. In general, only silicon and glass are used as basic materials to be structured. Much more comprehensive coverage of materials can be found in Madou [44] or Kovacs [164] or in [108].

#### 3.1.1. Lithography technique

Lithography technique is the transfer of a master pattern or design feature to the working substrate. There are several types of lithography classified according to the combination of material and energy used to transfer the pattern on the substrate. The choice of the type of lithography to use depends on the resolution or the size of the smallest desired pattern. There are two major types of lithography, electronic lithography using an electron beam as structuring energy and photolithography based on light beam (generally UV between 300 and 400 nm) [108]. In our work, we used this last technique, which resolution is between 0.13  $\mu\text{m}$  linewidth to 5 $\mu\text{m}$ . In conventional photolithography, the working substrate is initially coated with a light sensitive chemical material called photoresist. The photoresist layer is then patterned by exposure to UV light through a pattern mask. A mask is a master image of the desired pattern made on a quartz plate by chromium deposit forming the patterns with sub-micron precision. Masks are often made using electron beams lithography technique, which will not be described here.

The photoresist is deposited on the substrate using a spin-coater rotating at a speed between 1000 and 10000 rev / min. Indeed, it is a drop which is deposited in the center of the substrate then the substrate is rotated. The thickness of photoresist obtained is uniform to about ten nanometers. After spreading, the resist typically still contains 15% of solvent [108], which must be evacuated to avoid cracks once the film has completely polymerized. The film is slightly heated (around 100 °C for a few minutes) to evaporate the rest of the solvent before the next step, which is insolation. During this insolation step, the light flux initiates physicochemical reactions involving a modification (weakening or strengthening of the chemical bonds) of the resist solubility in certain liquid solvents called developers. For a so-called positive resist, it will cause a rupture or weakening of the covalent internal bonds by causing a rearrangement of the latter in a soluble form in a specific solution. Then a development process allows for the removal of UV exposed areas of the substrate generating the desired pattern on the substrate in the case of positive resist. Subsequent surface or bulk micromachining (etching or depositing) then will defines a feature directly on the surface or in the volume of the substrate. Depending on the complexity of the desired feature, this lithography and micromachining process is repeated until the desired structure is fabricated. Feature resolution on the substrate depends on the wavelength of light used during the exposure.

#### 3.1.2. Thin film deposition techniques onto silicon and glass

There is a variety of deposition techniques that make it possible to deposit metals. But in our case, we have used the physical vapor deposition by sputtering. In this technique, the substrate is put into contact with a gas containing species, certain species in the gas adsorb on the substrate, forming a layer that constitutes the deposit. Regarding sputtering, the materials to be deposited is placed on the cathode and the substrate is placed on the anode. The system is then placed in a cold plasma. The cathode is then subjected to a high energy particle flux (of the order of 0.3 to 2 keV) which produces an ejection of material deposited on the substrate due to the electric polarization.

Good adhesion between the layer and the substrate is achieved because the energetic ions collect at the target and penetrate one or two of the first molecular layers of the substrate.

### 3.1.3. Physico-chemical etching with inhibitor or DRIE

A simple physicochemical dry etching (RIE), which is the most common in the field of microfabrication, the physical and chemical etchings actions are combined. It is carried out by removal of material by bombarding the surface of the sample with active ions and by chemical reaction of reactive species in the plasma. The etching rates are of the order of  $0.1 \mu\text{m}\cdot\text{min}^{-1}$  [108].

For the DRIE the difference with simple physicochemical etching is the use of a protective layer along the sides of the etched cavities while the bottom is attacked chemically and physically by the reactive species and plasma ions. This type of engraving makes it possible to produce geometries with a high aspect ratio. We then speak of deep reactive ion etching DRIE or ionic etching with inhibitor and makes it possible to obtain very deep engravings of more than  $500 \mu\text{m}$  with aspect ratios exceeding 100:1. In an RIE process, an inhibitory film is formed with plasmas produced from  $\text{CCl}_4$  and  $\text{CF}_2(2\text{Cl}_2)$  compounds. This phenomenon, coupled with plasma energy sources called Ion Plasma Coupling (ICP), gives rise to very deep etchings that can cross the thickness of the standard 1mm silicon wafer with a fast speed of the order of  $10 \mu\text{m} / \text{min}$  [108]. It is also called a BOSCH process that alternates a silicon etching phase ( $\text{SF}_6$  Sulfur Hexafluoride) and a deposition phase (or passivation) producing a layer very close to Teflon due to the decomposition of  $\text{C}_4\text{F}_8$ . Passivation of the etched sidewalls enables preserving the etching anisotropy.

In what follows, we will explain the steps of microfabrication by detailing the flowchart and briefly, how are done the design of photolithography masks and their manufacture in a clean room.

## 3.2. Microfabrication

The fabrication process of the micromachines (chambers, hybrid membranes, glass spacer, assemblies) is carried out in a batch process which is one of the biggest advantage of MEMS technologies. Nevertheless, before proceeding to microfabrication in a clean room, the preliminary work includes the elaboration of the patterns (*i.e.* the geometry of the design) via the k-Layout software which can then be reproduced on a special support. This free software for designing and editing files in .DXF format is intended for microfabrication of MEMS devices and integrated circuits. After this drawing step, the patterns are printed using chromium on a glass support. This support thus comprises areas that are opaque or transparent to UV rays and is therefore, called a mask. In the clean room, if we work with a 4" wafer, we use a 5" mask.

When all masks required for microfabrication of the micromachine are ready, a series of different operations are carried out for successful microfabrication, namely:

- Cleaning of the substrate, a coating of photoresist, and a photolithography step for transferring the patterns on the substrate.
- Deep dry etching by DRIE to structure in depth the silicon substrate. The advantage with DRIE is that it allows anisotropic etching with vertical and relatively smooth sidewalls. Indeed, the roughness of the surfaces during etching is generated by the scalping effect [165] for a ratio between height and width of the trench ( $R.A < 30$ ).
- Deposit of thin metallic layers (Al and Au) for structuring the surface of the substrate. These layers are also used as a DRIE etching stop layer for subsequent protection against chemical or thermocompressive bonding intermediate layers.
- Silicon-silicon and glass-silicon bonding steps.
- Ultrasonic drilling is used to make the openings in the thick glass block. This technique is not a batch processing technique but was used here because we do not already have a fabrication equipment able to realize high vertical sidewalls in glass.
- Anodic bonding to assemble the silicon wafers with this pierced glass spacer.

The choice of the material for the interconnected spiral planar spring depends on two factors:

- Thermal properties allowing resistance to temperature variations induced by hot and cold sources and heat exchange with the working fluid. Suitable mechanical properties, especially resistance to alternating pressure cycles required for the machine operation without fatigue.
- Manufacturing processes available in a clean room.

The material chosen to produce the planar spring and chambers is silicon, a material with high thermal conductivity, low density and large stiffness, that can be used over long periods of time without showing signs of fatigue, deformation or breakage. It is also the most used material for MEMS technology.

### 3.2.1. Compression and Expansion Chambers

#### 3.2.1.a. Mask

The drawing of the chambers realized on k-layout for the elaboration of the photolithography masks is represented on the Figure 3-2 a), b) and c). The resulting microfabricated masks, which were used in the microfabrication of the compression and expansion chambers, are shown in Figure 3-2 d).

#### 3.2.1.b. Flowchart

The fabrication flowchart for the compression and expansion chambers is given below:

- **Steps 1-3:** photolithography of the chamber and regenerator channel cross-section
- **Step 4:** fabrication of chambers by DRIE (définition of horizontal channel on the left and beginning of etching of the regenerator channel on the right)
- **Step 5:** photolithography of the regenerator channel from the backside
- **Step 6:** etching of the vertical channel by DRIE from backside

#### 3.2.1.c. Microfabrication results

After successive steps of photolithography and DRIE etching, the obtained wafer is shown on Figure 3-3 a). A zoom on three chambers is presented in Figure 3-3 b) and a zoom on a chamber is given in Figure 3-3 d).

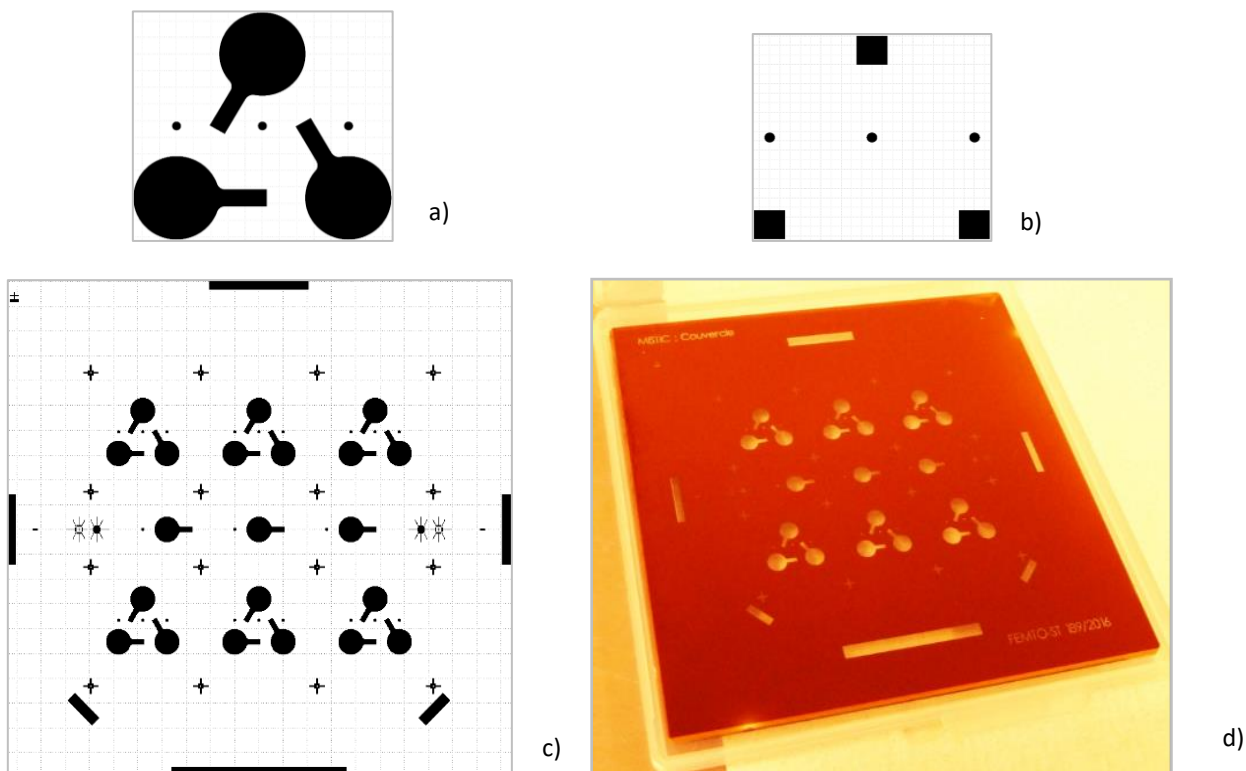


Figure 3-2: Zoom on the design of the three chambers necessary for a micromachine. b) The complete design of the mask for the chambers. c) The design for drilling the external filling holes of the micromachine. d) The physical mask of chambers manufactured in a clean room.

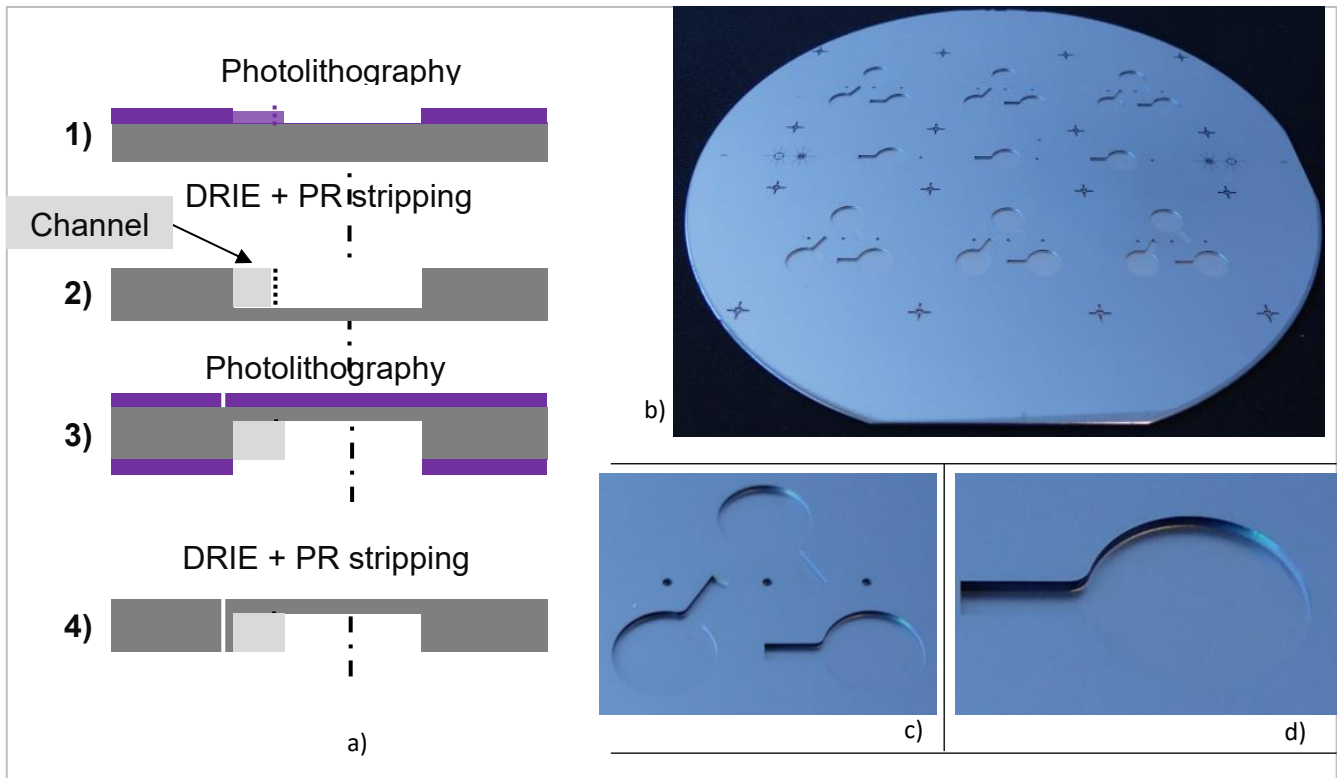


Figure 3-3: a) Chambers process flow, b) silicon substrates carrying compression and expansion chambers. c) Zoom on the three chamber of the micromachine. d) zoom on one chamber and its horizontal channel.

### 3.2.2. Membranes

#### 3.2.2.a. Masks

For the microfabrication of the membranes, we manufactured four physical masks. Figure 3-4 shows the detailed design geometry of the micro-machine concerning the organization of the membranes, the arrangement of the 3 liquid filling holes and the location of the 3 cavities of the regenerators. The membranes have a part (constituted by the outer ring of circles 6 mm in diameter in the figure) allowing it to be encased on the silicon support. This part, consisting of 1mm in width, allows to maintain it after the step of hanging the membrane by DRIE etching of the lower part of the wafer.

The compactness of this arrangement not only saves space on a wafer and simplify microfabrication, but also maintain symmetry for proper operation of the micromachine. The four drawings used for realization of all four masks used for microfabrication of hybrid membranes in a clean room are shown in Figure 3-5. The parts colored black in the drawing will be transparent parts on the physical masks manufactured. Therefore, on the wafers coated with the positive resists, it is these parts, which will be dissolved in the developer and which will be etched by DRIE.

The first mask defines the location of the first membrane layer which is 6 mm in diameter. The second mask defines the planar springs and the disks corresponding to the second layer of the membranes. The third mask protects the virgin surface of the wafer against the polymer layer during its application to keep it clean for the next steps. This mask therefore enables, through the photoresist, to deposit the polymer layer only in the membrane cavities without contaminating the rest of the wafer surface. The fourth mask defines membrane suspensions at the back of the wafers. The diameter of the disks on this mask is 5mm. Therefore, it is this part which constitutes the moving part of the membranes after microfabrication. It is thus possible to manufacture 21 membranes on a silicon wafer thanks to mass fabrication made possible by cleanroom technology.

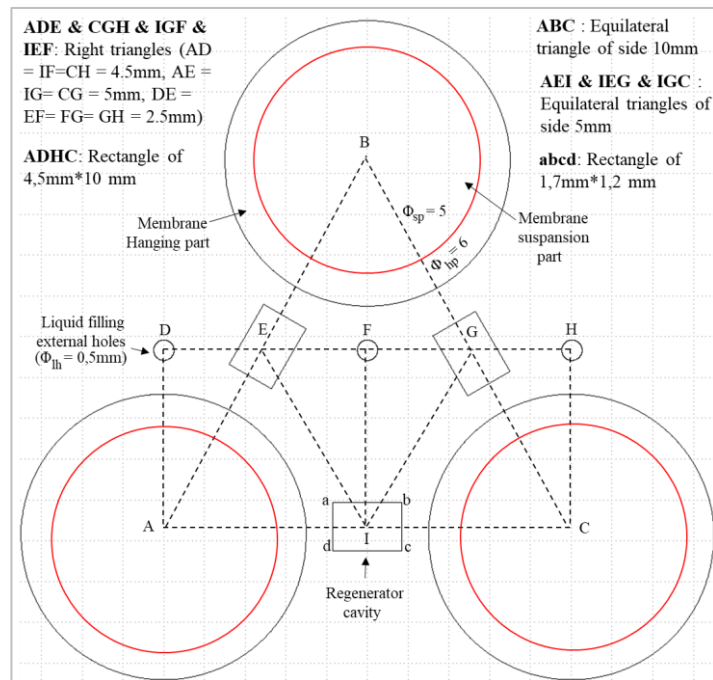


Figure 3-5 : The design of the three membranes of the micromachine with the layout of each element.

After describing the usefulness of each mask, we present below the microfabrication process for the membranes (cf. Figure 3-8).

**3.2.2.b. Flowchart**

The fabrication flowchart (design of the 3 masks for membrane microfabrication) for the compression and expansion chambers is given below (Figure 3-8, Figure 3-7 and Figure 3-8):

Mask n°.	Design	Fabricated masks
1st		

Figure 3-6 :The photolithographic mask number 1.



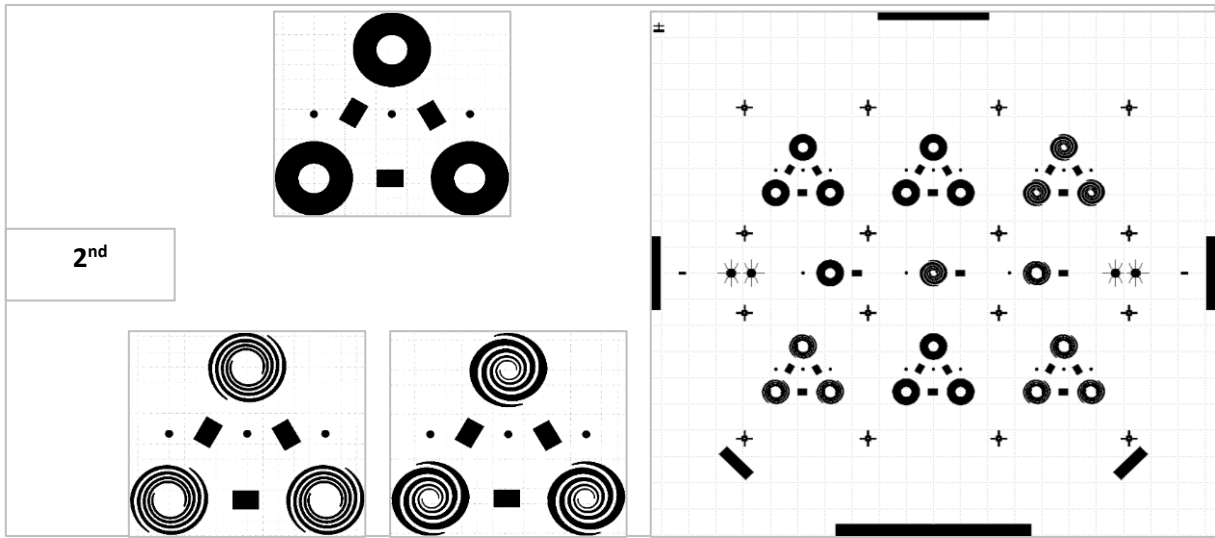


Figure 3-7: The photolithographic mask number 2

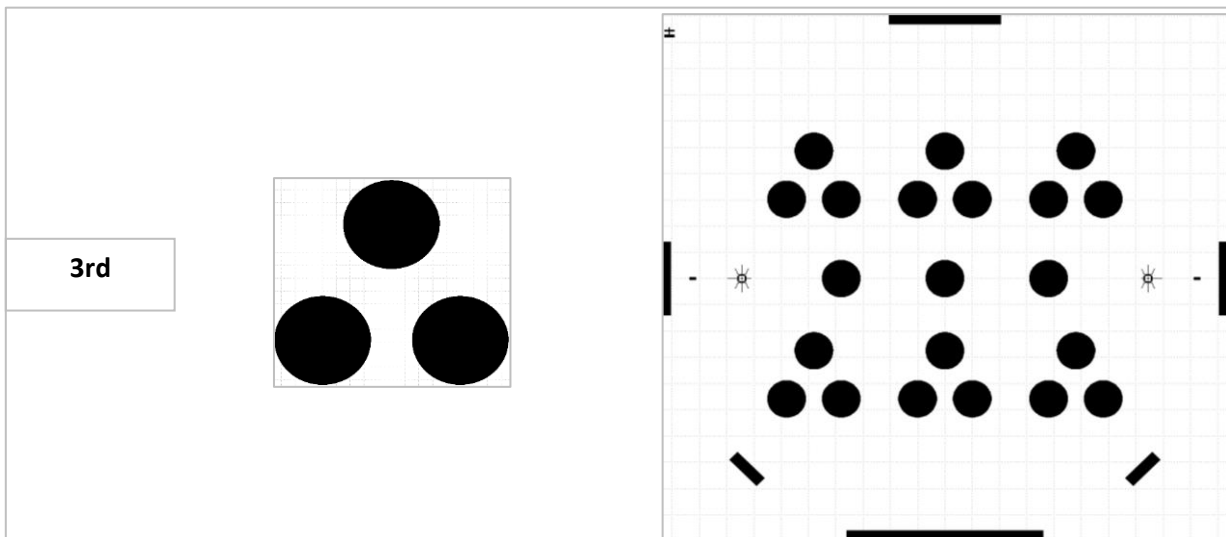


Figure 3-8 : The photolithographic mask number 3

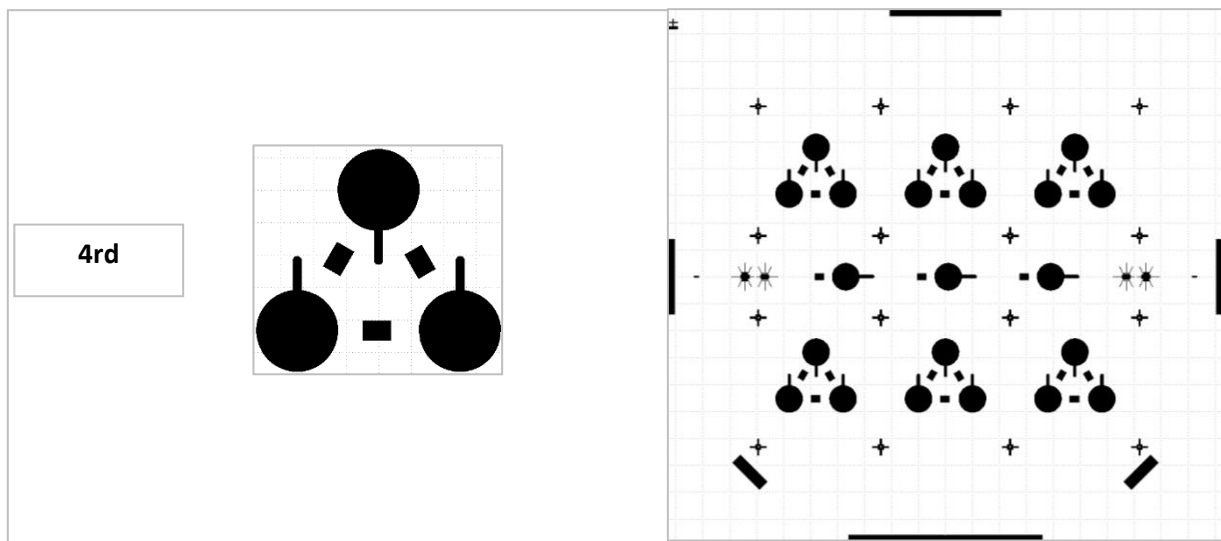


Figure 3-9 : The photolithographic mask number 4 for suspension.

- Step 1 - 2: Photolithography of the membrane  $\varnothing 6\text{mm}$  cavity by Photoresist spin-coating (Mask 1). DRIE etching of the membrane  $\varnothing 6\text{mm}$  cavity
- Step 3: Photolithography of the spiral (and disc) structure by Photoresist spray-coating (Mask 2)
- Step 4: DRIE etching of the spiral (and disc) structure and 100nm Al deposition
- Step 5: Photoresist deposition by spray-coating to protect the wafer from silicone (Mask 3). Structuring of the silicone rubber: it has been found that the RTV-silicone paste is too viscous to be deposited by spin-coating. A « squeegee-coating » has thus been used to make the silicone rubber membrane.
- Step 6 - 7: Photolithography and suspensions by backside DRIE (Mask 4)

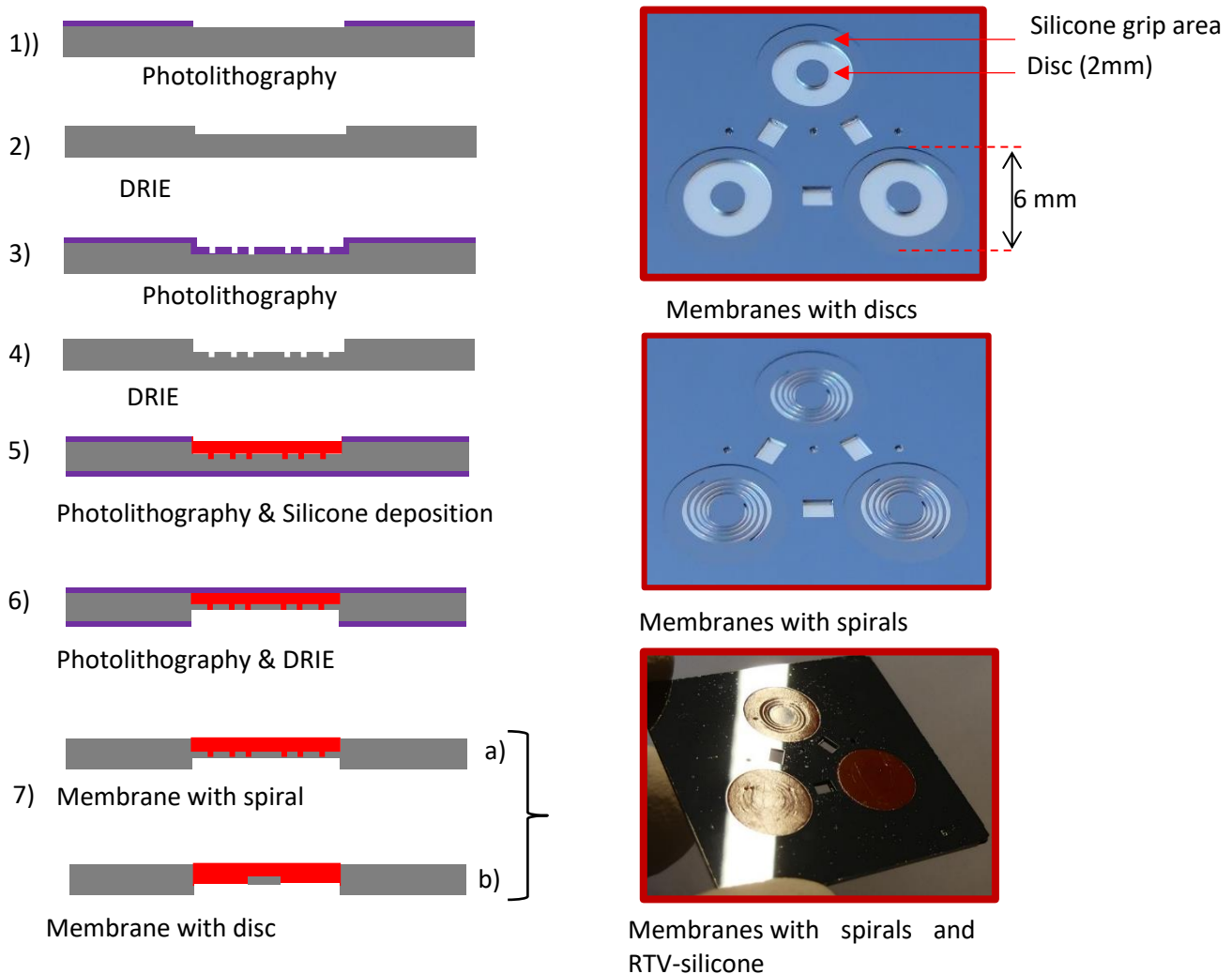


Figure 3-10: HMs Microfabrication micro-fabrication process flow: a) Hybrid membrane with spiral and central disc process, b) Hybrid membrane with only central disc. Optical picture of hybrid membranes before RTV-silicone squeegee-coating:

### 3.2.3. Microfabrication of the glass thermal insulation part

The part of the micromachine containing the incompressible liquid and the cartridges of the regenerators is a thick block (6.5 mm) made of glass to maintain a temperature gradient between the upper and lower chambers of the micromachine. In order to structure the holes for the liquid and for the "regenerative" microchips, a first approach that can be adopted is wet chemical etching with BHF-buffered hydrofluoric acid by applying two chromium/gold films of thickness equal to 20nm and 200nm to protect the non-etched parts of the wafer. But this type of etching being isotropic, the openings we will obtain will exceed the desired diameter  $\phi = 5 \text{ mm}$ , because of the under-etching at the walls [13]. However, we have chosen to explore the ultrasonic etching technique, which has been slow because of the thickness of the substrate, but much more precise about the shape of the structure [6].

Ultrasonic machining is a microfabrication technique particularly well suited to fragile materials such as glass. This type of machining method differs from other existing methods in that the machining is performed without direct contact between the tool and the workpiece. Indeed, ultrasonic machining is a method of reproducing form by abrasion, particularly suitable for machining hard, fragile and brittle materials (glasses, ceramics, quartz, precious stone, semiconductor ...).

### 3.2.3.a. Principle of Ultrasonic machining

Ultrasonic machining is based on the mechanical vibration (ultrasonic frequency) etching of the end of a machining tool called sonotrode and via a liquid containing abrasive particles projected between the tool and the workpiece (*cf.* Figure 3-11 a). These particles in turn act on the latter to tear out small pieces and gradually peel. The etching relies on three physical phenomena to remove the material from an object: shear, erosion and abrasion. Shearing and abrasion are achieved by a mechanical action due to the projection and pounding of abrasive grains against the surface of the workpiece. Cavitation erosion is due to pressure variations within the liquid, caused by vibrations in the sonotrode. A chemical action due to the carrier fluid is possible depending on the materials to be machined but this action is not used in our case.

The machine that does the ultrasonic machining consists of an electrical part (a high-frequency current generator), an acoustic assembly (transducer, amplifier and sonotrode), a frame comprising a table that receives the assembly workpiece holder; a column supporting the machining head and a device for supplying and circulating an abrasive material (*cf.* Figure 3-11 b). The vibration amplitude of the acoustic assembly tool (amplified generally by the tool holder) is between 0.002 and 0.15 mm and the power to be supplied by the transducer is of the order of 1 kW.

The transducer is cooled by a circulation of compressed air. The nominal power of the generator available on the market reaches 10 kW. The machining tool often called "sonotrode" by analogy with an electrode vibrates at a frequency of about 20 kHz which corresponds to the field of ultrasound. This frequency is obtained by transforming an electric current into a mechanical vibration transmitted to the sonotrode, thus vibrating at the same frequency of the electrical signal. The transformation of the electrical signal into mechanical vibration is provided by piezoelectric ceramic converters compressed between two metal parts (to obtain a sufficient vibration amplitude: a few microns to a few tens of micrometers) operating in reverse piezoelectric mode. As a result, under the action of an electric field, a proportional mechanical stress is produced whose sign depends on the direction of the field. It follows a mechanical deformation. Thus, under the action of an alternating electric field, a mechanical vibration is then created.

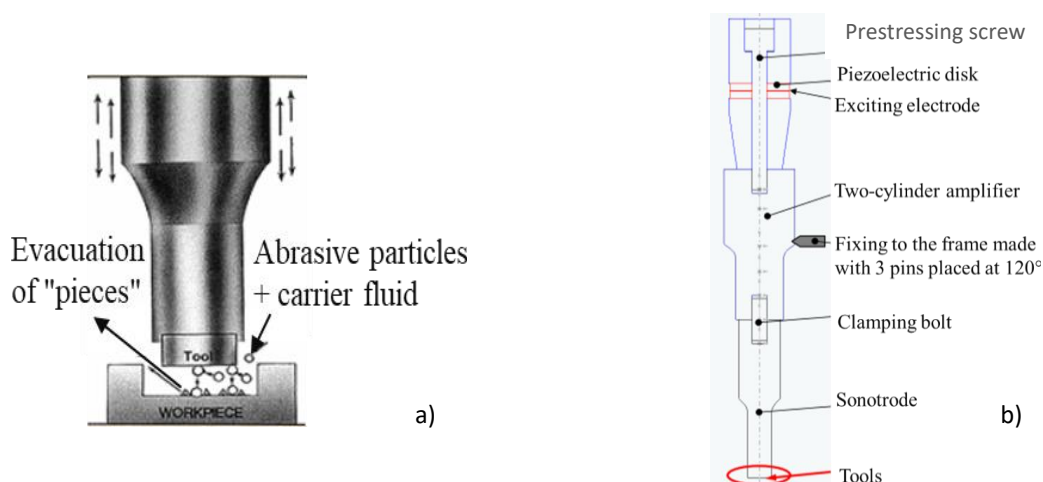


Figure 3-11: a) Principle of the ultrasonic machining b) Description of the ultrasonic machine.

The sonotrode is a solid tool (cylinder shape or more complex) to bring the acoustic energy into the work area (*cf.* Figure 3-11 d). It has the negative shape of the part to be made and is fixed to the amplifier by screwing with studs. This attachment is considered as a weak point of the device as they do not allow to position precisely, which then requires adjustment operations on the machine. The displacement of the tool head is obtained by a micro-displacement table. The sonotrodes are made of steel or titanium, and the working surface reaches 400 mm<sup>2</sup>. The abrasives used are boron carbide, alumina, diamond or silicon carbide in aqueous suspension. The diameter of the grains is chosen between 0.005 and 0.8 mm. The surface condition obtained is finer as the grains are small, but the working speed varies inversely [166]. Abrasive particles are the real cutting tools. Their nature and the size of their

grains must be adapted to the material to be machined (hardness) and to the quality of the desired surfaces. Thus, preferably, a material of greater hardness or at least equal to that of the workpiece is chosen to neglect fragmentations and to maintain a constant "gap". Indeed, only the wear of the sonotrode will be responsible for dimensional changes during machining.

ABRASIVE	Hardness	Cutting power
Natural Diamond	6500/7000	1
Synthetic diamond	- id -	0.7
Boron carbide	2800	0.5 - 0.6
Silicon carbide	2500	0.25 - 0.45
Alumina	2000 to 2100	0.14 - 0.16

Table 3-1: Details on the abrasives commonly used for micromachining by ultrasound

The details on the abrasives commonly used are presented in Table 3-1. These abrasives are diamond, boron carbide or silicon carbide, which are very hard materials. The concentration of abrasive is optimal when it is 30% by volume in the carrier liquid. The grain size of the abrasive influences the speed of vibration and especially the surface condition of the workpiece. The optimal grain diameters (commonly) used to make a good hole are shown in Table 3-2.

Thus, ultrasonic drilling method consists on projecting very strong abrasive particles on the workpiece and using a sonotrode, vibrating at an ultrasonic frequency, to etch a substrate. These particles are brought into the working area by a carrier fluid (eg water). Peeled's pieces evacuation and abrasive grain renewal are ensured thanks to a constant liquid flow. However, the work of removing the material as well as the wear depend on many parameters such as the vibration (frequency and amplitude), the static pressure, the grains of abrasive (size, nature, concentration within the carrier liquid), the depth of penetration, the carrier fluid (nature, circulation conditions), the machining tool (nature of the material, shape and dimensions) and the workpiece (nature of the material, shape to be produced).

For the draft	For finishing	For refinement
50 to 120 $\mu\text{m}$	20 à 40 $\mu\text{m}$	< 12 $\mu\text{m}$

Table 3-2: The optimal grain diameters commonly used to make optimal holes

All these factors make the performance of this type of machining difficult to analyze. However, we can characterize them by three criteria: the quantity of material removed, the relative wear of the sonotrode, the surface state of the flanks and the bottom of drilling (if not opening).

### 3.2.3.b. Machining of the glass block

Before machining the glass block, it is necessary to print the patterns to be etched (*cf.* Figure 3-12a). To do this, we first designed and then realized a mask (*cf.* Figure 3-12 b)) then we proceeded to a cleaning of the glass block respecting the levels described in the Figure 3-13. After drying the wafer with a nitrogen pistol, we performed on both sides, a deposition of thin layer (300nm) of aluminum by sputtering, then a negative resist coating since we wanted to protect the part not intended for machining by a layer of metal (preferably aluminum).

We then made a photolithography step to proceed to the etching of the patterns at the level of the aluminum layer through the resist that protects the rest of the wafer against the aluminum etching solution for structuring. The Al layer was etched using a chemical etching solution without shaking for 4 minutes. The wafers were then placed in an EDI bath. The patterned photoresist layer was then removed by placing the wafers in an acetone bath. The wafers were then rinsed in an ethanol bath and finally dried with nitrogen. Leaving alignment crosses in the center of each pattern is very important as it facilitates alignment during ultrasound etching. Indeed, to perform the machining, the centering of the sonotrode requires crosses of alignment in the center of each structure to be etched. Thus, using a micro-displacement table  $x, y, z$  (150,150,100 $\mu\text{m}$ ) precise to  $\pm 5\mu\text{m}$ , the center of the structures is positioned successively in the center of each sonotrode before the start of the machining of the structure concerned [167].

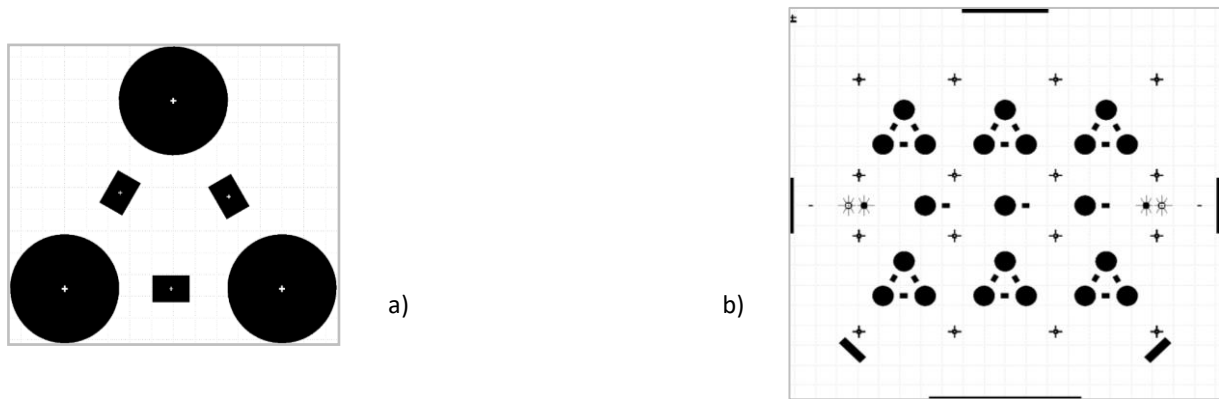


Figure 3-12: Pattern drawing of the mask used to etch thick glass. a) A zoom on the three elements necessary for the micromachine and b) all the patterns by wafer.

For example, the dimensions and the final shape of the holes in our large cylindrical cavities (which are 6mm in diameter and 6.5mm in height) depend on how the gap and wear of the sonotrode are controlled during machining. Nevertheless, we obtained correct machining to 3 or 4 $\mu\text{m}$  thanks to a good understanding of the action of abrasives. Since the depth to be etched is high, it was necessary to provide several sonotrodes to maintain such precision over the entire height. The last, larger diameter working only for the removal of a very weak thickness of material, possibly with a grain of smaller diameter to improve the surface condition ( $<20\mu\text{m}$ ). In this case, the final surface finish obtained will reveal cavities whose depth will be less than one-tenth of the grain diameter, that is to say 2  $\mu\text{m}$ . The machining of the cavities of the regenerator cartridges is more restrictive because the problem in this case lies in the realization of the corresponding rectangular sonotrodes. Indeed, since these sonotrodes are reduced in size (1.7mm \* 1.2mm), their wear intensifies as the machining progresses thus causing the modification of their rectangular shape for a circular shape. Thus, to correct the shape, it is necessary to manufacture several sonotrodes to make several passages during the etching.

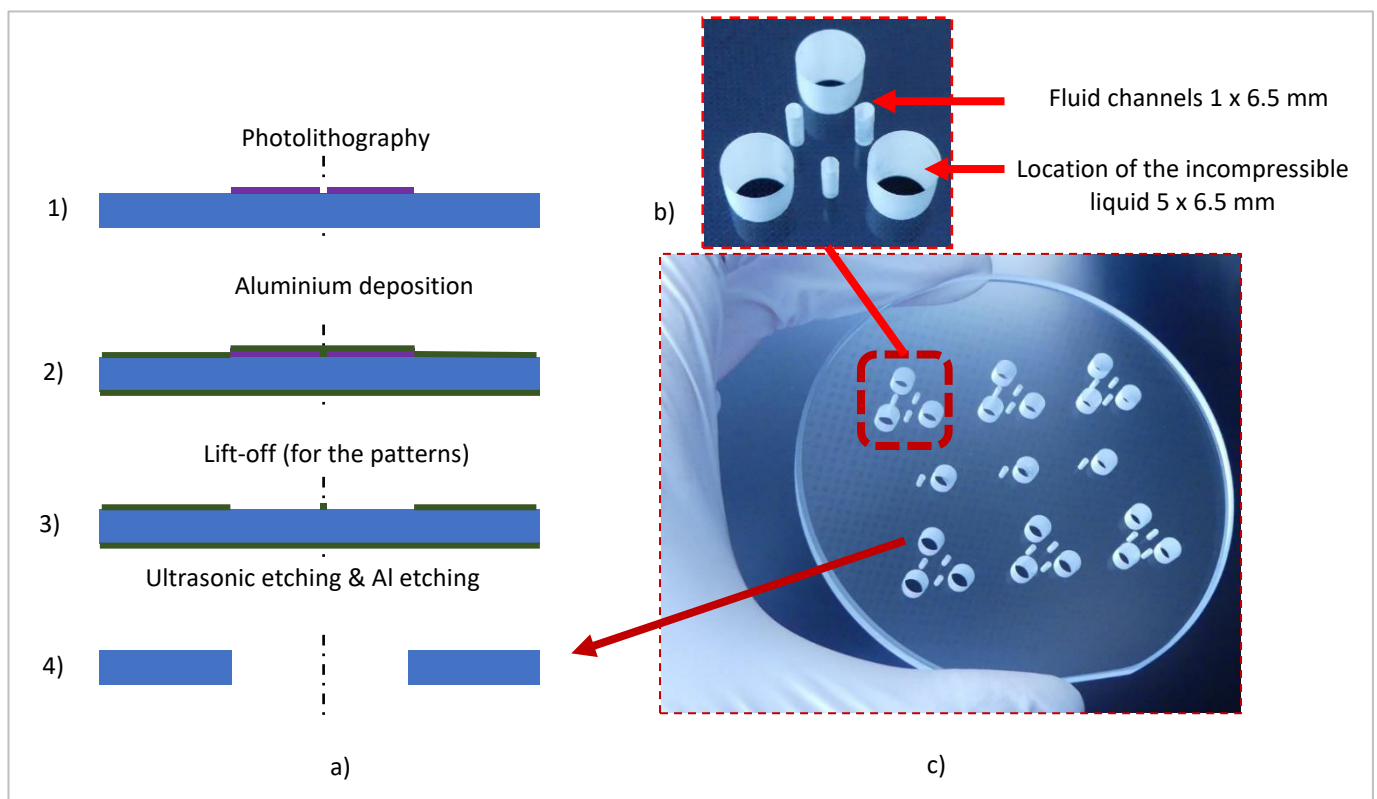


Figure 3-13: a) Flow chart used to make patterns on thick glass. b) Zoom on the three cavities of a micromachine. c) View of the whole thick wafer completely etched by ultrasounds.

### 3.2.4. Assembly of the different parts of the micro machine

#### 3.2.4.a. Overview of the assembly procedure

After manufacturing the required components (chambers, membranes, regenerator), we started by assembling the upper chambers with the upper membranes and the lower chambers with the lower membranes. These Si-Si assemblies will be performed by Au-Au thermocompression bonding for the reasons that are presented below.

Then, one of these two stacks (Si-Si top), is assembled first, with one of the faces of the thick block of glass. Finally, the second stack (Si-Si bottom) is assembled with the second face of the glass block. Anodic bonding at the lowest possible temperature, to avoid destroying the polymer membrane, will perform these Si-Glass assemblies.

The Figure 3-14 shows the five wafers to be assembled and the bonding technologies used.

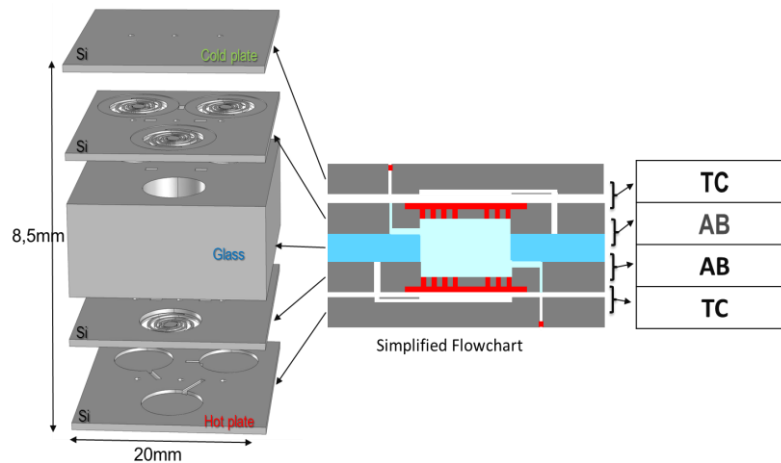


Figure 3-14: Summary of the assembly techniques used to realize the complete micro machine. TC: Thermocompression bonding, AB: Anodic Bonding.

#### 3.2.4.b. Bonding requirements for the micro machine

The choice of the bonding techniques was done by reviewing the expected bond characteristics and the process stresses.

**REQUIRED BOND STRENGTH.** The micromachine power will increase with the working gas pressure, therefore the bonding strength should be large enough to sustain an inner pressure well above atmospheric pressure. If we seek a possible operation under a pressure difference of  $P_{\max} = 10 \text{ atm}$  (about 1 MPa) with the geometry of our machine, the inner pressure would tend to separate the wafers by exerting a force:

$$F_{\max} = P_{\max} \times S_{\text{chamber}}$$

where  $S_{\text{chamber}}$  is the area on which the inner pressure is applied.

The bond prevents the wafers from separating up to the breaking tensile stress. For  $P = P_{\max}$  the bond is subjected to a stress  $\sigma_{\max}$  that balances the pressure force  $F_{\max}$ :

$$\sigma_{\max} = P_{\max} \times (S_{\text{chamber}} / S_{\text{bond}})$$

Assuming that the top wafer is bonded on the whole contact surface, we have:

$$S_{\text{machine}} = S_{\text{chamber}} + S_{\text{bond}}$$

Therefore, the stress experienced by the bond is:

$$\sigma_{\max} = P_{\max} / [(S_{\text{machine}} / S_{\text{chamber}}) - 1]$$

For a 20x20 mm machine and 3 chambers of diameter 5 mm, we find that  $\sigma_{\max} = 173 \text{ kPa}$ , which shows that: **to use the machine with an inner pressure of 10 atmospheres, the bond breaking stress should be well above 200 kPa.** It should be noted that the requirement on the Glass-Si bonding strength is lower because the inner gas pressure is not applied directly to this bond.

**HERMETICITY.** For a high inner pressure, the inner gas will leak through the bond, therefore the inner pressure will gradually decrease thus limiting the machine lifetime. For this reason, it is necessary to make bonds that are as hermetic as possible.

**BONDING TEMPERATURE.** Since an RTV-silicone membrane is used in the machine, it would be destroyed at a temperature exceeding 330°C, even during a short time. In addition, this membrane could also break if it is submitted to a too large pressure difference during the fabrication process.

In the present work, the focus is on hermeticity, large bond breaking stress (> 200 kPa) and low temperature bonding (< 330 °C).

### 3.2.4.c. Assembly of the silicon wafers (chambers and membranes)

The chamber and the membranes are manufactured on silicon wafers. Each bonding pair consisted of a p-type 4-inch Silicon wafer with an average thickness of 525 µm and a Si-Si bonding technology is required.

**CHOICE OF THE ASSEMBLY TECHNOLOGY.** There are several known bonding techniques to assemble wafers, such as metal alloy bonding, anodic bonding adhesive bonding, plasma activated bonding fusion bonding, glass frit bonding and thermocompression bonding [168], [169]. All these bonding methods are used extensively in the microelectronics industry and their advantages and drawbacks are listed in Table 3-3. Each bonding technique listed above has its limitations, therefore a bonding technique that minimizes the number of required layers, cost and complexity should be selected. Bonding steps has been challenging because almost all 3D devices require a unique fabrication approach.

The simplest silicon-silicon bonding technique is « Direct Bonding », which means that there is no intermediate layer between the wafers and that they bond spontaneously, however this kind of bonding method requires a very high bonding temperature. Anodic bonding can only be used for the bonding of silicon and glass. A good Au-Si eutectic bonding occurs at temperatures exceeding 380°C [35]. Adhesive bonding requires a resist layer such as SU-8 [170], [171], [172] and is never completely hermetic. Bonding after plasma activation does not allow achieving the bonding at specific locations [173], [174] and glass frit bonding requires - as its name suggests - to melt a glass powder at rather high temperature.

**Therefore the most interesting bonding method seems to be the thermocompression bonding technology** allowing bonding of two silicon wafers through two thin metal layers at the interface with good hermeticity and toughness [175].

Techniques	Advantages	Drawbacks
<i>Bonding without intermediate layer</i>	<i>Hermetic</i>	<i>Flat surface required</i>
Anodic	Strong bond	Hight-voltage, bond time, sodium glass
Direct	Strong bond	High-T, Very flat surface required
Low-T direct	Low-T	Very flat surface required
<i>Metallic interlayer</i>	Hermetic, non-flat surface ok	Specific metals required
Eutectic	Strong bond	Flat surface required
Thermocompression	Non-flat surface ok	High forces required
Solder	Sef-aligning	Bonding flow possible
<i>Insulating interlayer</i>	<i>No-flat surface ok</i>	<i>Varies</i>
Glass frit	Hermetic, common in MEMS	Large area, medium to high-T
Adhesive	Versatile	Non-hermetic

Table 3-3: Bonding methods extensively used in microelectronics industry [176].

The development of a **thermocompression bonding process is thus needed** to obtain (i) a hermetic bond, (ii) made at a safe temperature for the membrane and (iii) with a bonding strength that is large enough. **This process is thus of uttermost importance for the micro machine and therefore, a more detailed study of this process has been achieved and is reported in section 3.3.**

**ASSEMBLY PROCESS FLOW.** The recommended parameters for thermocompression bonding were found thanks to the study described in §2.5. that has been developed is described in the following flowchart and consists of 4 main steps:

1. The process starts by depositing a 20 nm Ti adhesion layer followed by a 180 nm Au layer onto the substrates using a Plassys MP500 sputtering machine
2. Then the wafers are aligned using an EVG620 aligner machine and the chamber of EVG501 is configured in thermocompression mode using a specific metal tool
3. The EVG620 chamber is then pumped out at a pressure equal to  $10^{-3}$  mbar
4. The wafers are then bonded at  $150^{\circ}\text{C}$  using a bonding force of 4000 N for 1 hour.

Details concerning the Au-Au thermocompression bonding experimental procedure are given in the « Microfabrication Appendix ».

**RESULTS ON THERMOCOMPRESSION BONDING OF CHAMBERS TO MEMBRANES.** A number of assemblies were performed using the thermocompression bonding process described above. Views of the assembled parts (upper and lower silicon parts composed of two assembled wafers) are shown on the Figure 3-15 below.

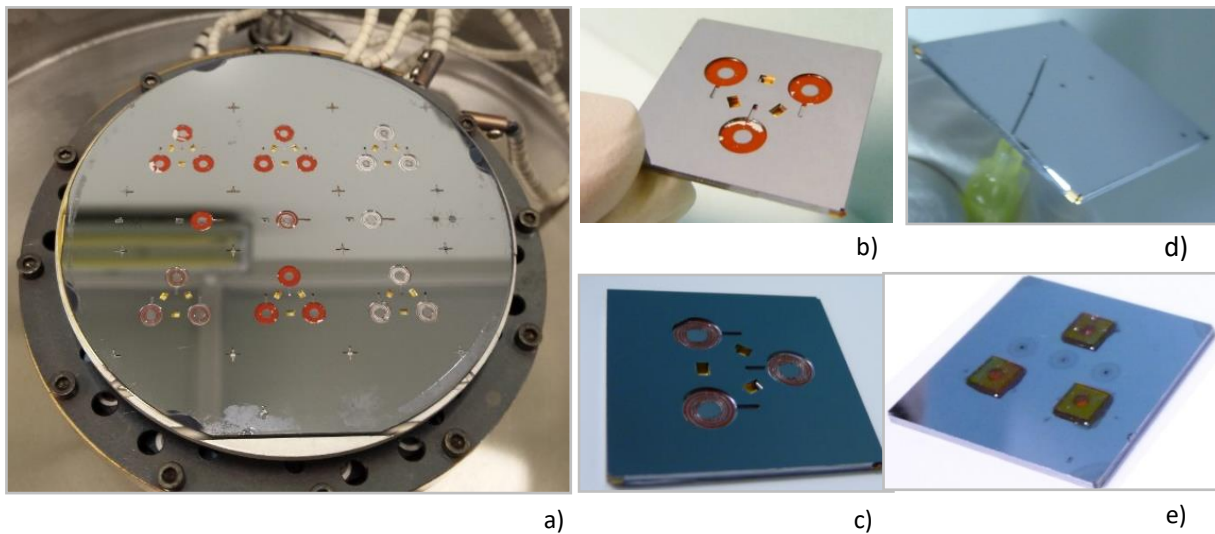


Figure 3-15: a) Result of the thermocompression between chambers and membranes: a) At the scale of the wafers, b) At the scale of a chip with membranes with central disks only, c) At the scale of a chip with spiral membranes, d) Backside of a chip, e) The front side of a chip with portholes for characterization

#### 3.2.4.d. Assembly by anodic bonding of the Si stacks and the glass spacer

**Anodic bonding** (or electrostatic bonding) is particularly used for the sealing of silicon wafers to borofloat glass BF33. Unlike thermocompression, anodic bonding requires, in addition to pressure and temperature, a high negative DC voltage that is applied to the top glass wafer by a thin metal electrode (cathode) installed with the quartz tool and a thick graphite plate, the silicon being connected to the anode electrode as can be seen on the following figure.

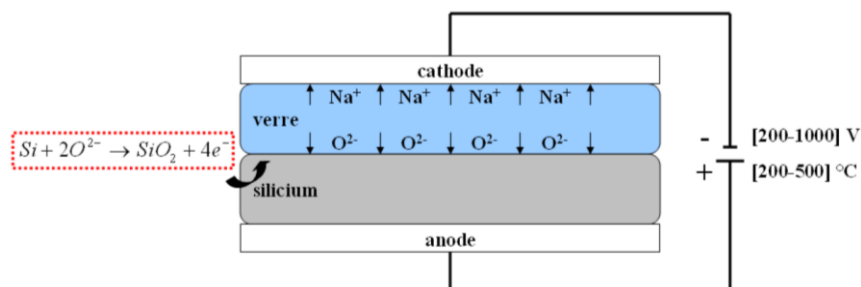


Figure 3-16: Principle of anodic bonding in the case of a glass and silicon substrate assembly.

Electrostatic forces hold the glass to silicon during the formation of an irreversible permanent bond under rather high temperature, generally greater than  $300^{\circ}\text{C}$  ([108], [177]).

Although anodic bonding is a classical MEMS process, in our case several challenges that require a full process validation should be mentioned:

- the **temperature** should be limited to  $330^{\circ}\text{C}$  in any case to avoid membrane destruction



- the glass **thickness** (6.5 mm) is much larger than for any previously reported bonding. Cleanroom bonding equipments (EVG501 or AML402P) are not designed for such a thick wafer
- then, the **number of wafers** to be assembled (5 wafers in total) is unusually large, causing difficulties of alignment and flatness of the structures.

**ASSEMBLY OF THE FIRST SILICON WAFER.** This process is illustrated in the Figure 3-17.

Figure 3-17 shows in (a) the thin wafer glass used to prevent the thick glass wafer (shown in b)) to be in direct contact with the electrode (since this surface will be bonded later) and (c) the 'Si-Si stack' (chamber-membranes) already bonded by thermocompression. Finally, the result of the first anodic bonding between an Si wafer and the glass spacer is shown in (d). After the first bonding at 300°C non-bonded areas visible at the interface still remained. Therefore, we closed the chamber to continue bonding, increased the upper plate temperature to 320°C (since we observed that the membranes deteriorate at 330°C), and removed the thin glass wafer protection (the glass block was in direct contact with the hot plate of the AML chamber). After this second bonding step no more unbonded areas could be seen.

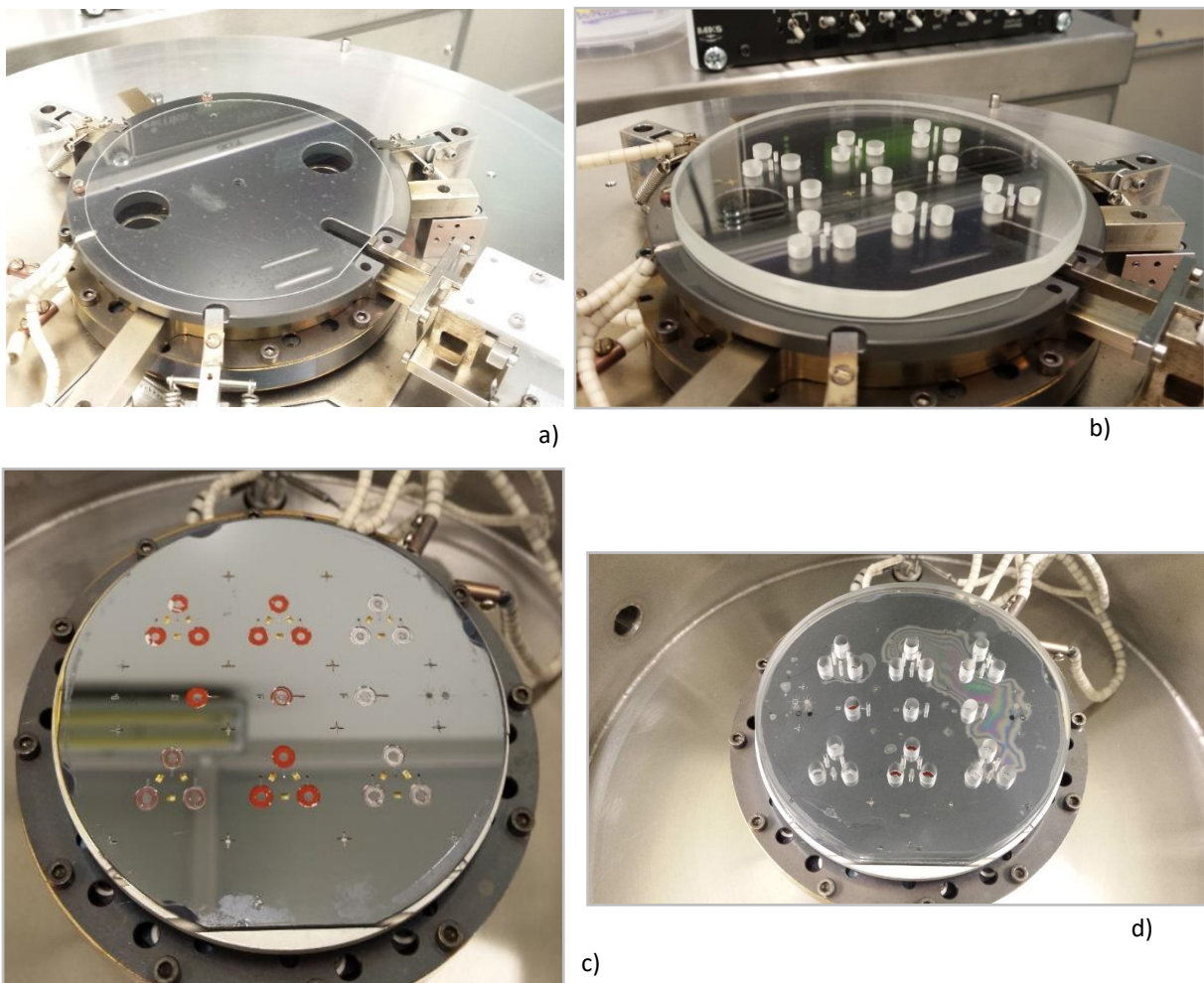


Figure 3-17: First anodic bonding [chamber-membrane] and thick wafer glass: a) wafer glass protection, b) fixing the wafer thick glass on the upper electrode, c) fixing the stack si-si (chamber-membranes), d) result of the first attempt at anodic bonding.

**ASSEMBLY OF THE SECOND SILICON WAFER.** After this first anodic bonding, a second anodic bonding is carried out (*cf.* Figure 3-18) to connect this new stack (lower chamber & membrane + glass block: total thickness of 7.5 mm) with the upper chamber & membrane (1mm thickness).

Here, the main difficulties are:

- that the thick stack containing the glass spacer is difficult to maintain on the upper electrode during the closure of the chamber,
- secondly, that this new anodic bonding may create a « debonding effect » of the first bond.

Indeed, the applied voltage can cause an inverted migration of the ions in the thick stack because the top silicon wafer carrying the chambers is connected to the positive electrode (*cf.* Figure 3-18). To avoid that, we created a short circuit by connecting the surface of the electrode with the glass block using small gold springs. Hence, a good bonding quality was obtained.

Figure 3-18 b) and c) shows the result of the last anodic bonding which completes the final assembly of the wafers necessary for the microfabrication of the clusters of Stirling micromachines.

In order to monitor the membrane movement with a laser sensor, a circular hole was etched through the external silicon wafer carrying the chambers and a thin glass window was bonded to close the chamber. This window was either made of a full glass wafer or a several smaller 1.5 mm diameter windows.

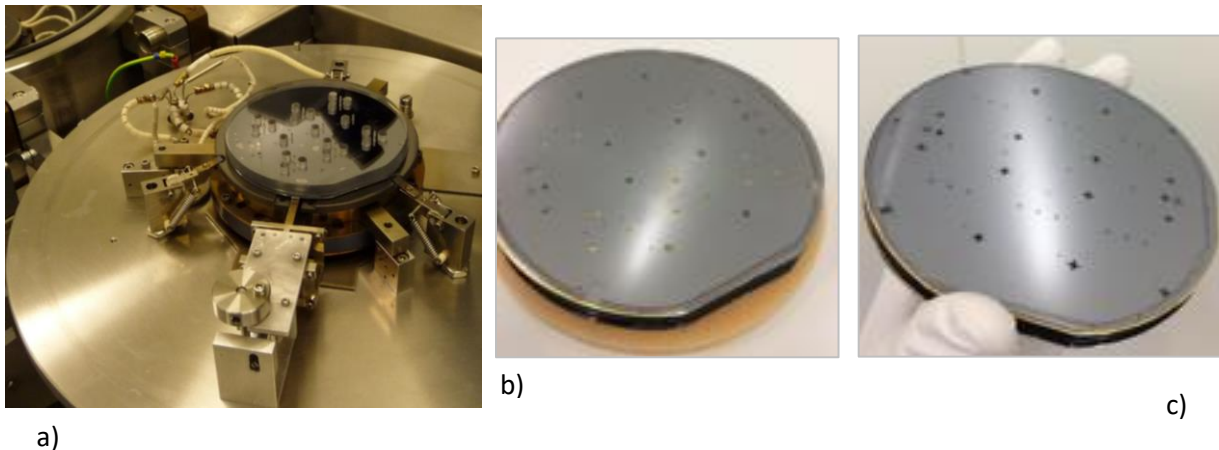


Figure 3-18 : Left: Preparation of the two stack (Si-Si-Glass and Si-Si) for the last anodic bonding (Front side view). Right: Result of final anodic bonding: Top chamber-membranes-thick wafer glass and Bottom chamber-membranes. b) Front side view, c) Backside view.

### 3.2.4.e. Procedure for liquid filling

The filling of the incompressible liquid providing the mechanical coupling between upper and lower membranes is performed after the final assembly of the micromachine.

**Design of liquid filling system.** The liquid filling step is a complex and critical step when carried out during microfabrication. Indeed, in a first case we first assembled only the two substrates carrying the membranes with the one carrying the cavities for the liquid, which is the thick glass block. Then fill the three cavities. The problem that happened is the liquid contaminated both sides of the stack during filling, preventing the possibility of correctly assembling this first stack with the rest (the two substrates carrying the chambers). In addition, after filling, as the bonding require heating at high temperatures ( $> 250^{\circ}\text{C}$ ) during the assembly process, the liquid may have boiled or exploded and thus may have contaminated the bonding equipment chamber inside the clean room. The best technique we have found to avoid this problem is to fill the liquid only after completely assembling the micromachine. For this, it was necessary to provide holes (through the substrate carrying the upper chambers) leading to channels (etched in the underside of the substrate carrying the upper membranes) giving access to the cavities provided for the liquid (in the glass block). The Figure 3-19 shows the external holes, which allow this final filling of the liquid after assembly of the micromachine.

The filling is carried out in batch process (*cf.* Figure 3-22) using a vacuum bell in which we put a crystallizer filled with an appropriate liquid (Vaseline type for instance). Then, after some aspirations to reduce the gas bubbles probably trapped in the liquid, the stack of wafers constituting the micromachines are plunged into the liquid. After closing the vacuum chamber, we pump out the air, allowing the liquid to enter the cavities from which the air has been extracted. The complete filling is completed after a few tens of minutes. Since liquid Vaseline is colorless, as transparent as the glass block, it is difficult to appreciate the level of filling. We proceed then to the sealing of the holes having served for the filling by using RTV-silicone.

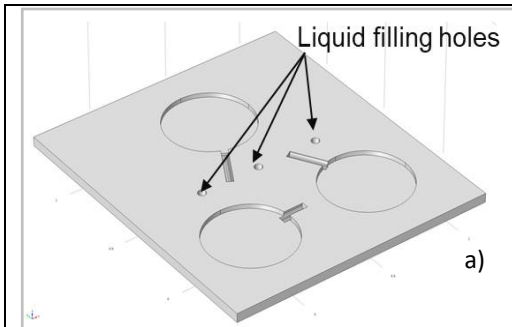


Figure 3-19 : External holes for liquid filling



Figure 3-20: vacuum chamber used for filling the liquid in the micromachine by sucking air from the chamber.

### 3.2.4.f. Dicing of the micromachines

The dicing is performed after filling the liquid at wafer scale. This operation consists in cutting the Si-Si / Glass / Si-Si stack of wafers in order to retrieve the micromachines individually and to characterize them one by one to look for possible defects. A DISCO DAD 321 precision saw is used to dice the stack (*cf.* Figure 3-22). The maximum cutting depth is 3.2 mm per face. The wafer stack, 8.5 mm thick, is fixed on an adhesive UV film and then is held by vacuum for cutting, using an annular blade cooled by water and rotating at 30000 rpm [167]. The blade diameter is 56 mm and its thickness is 200  $\mu\text{m}$ .

Since it is a thick stack of wafers, the cut is made in double or triple passes with a speed of 0.2 m/s. After cutting, the adhesive film is peeled off after UV insolation, liberating the micromachine chips. Photos of a Stirling micromachine obtained after cutting the stack are shown in the Figure 3-21. The kapton tape allows to temporarily close the filling holes after the liquid filling step. After the dicing step, the filling quality of a machine can be checked by observing the side of the glass spacer. If the filling is correct, the kapton tape is replaced by RTV-silicone at the filling holes of the liquid. Otherwise, the filling process should be continued.

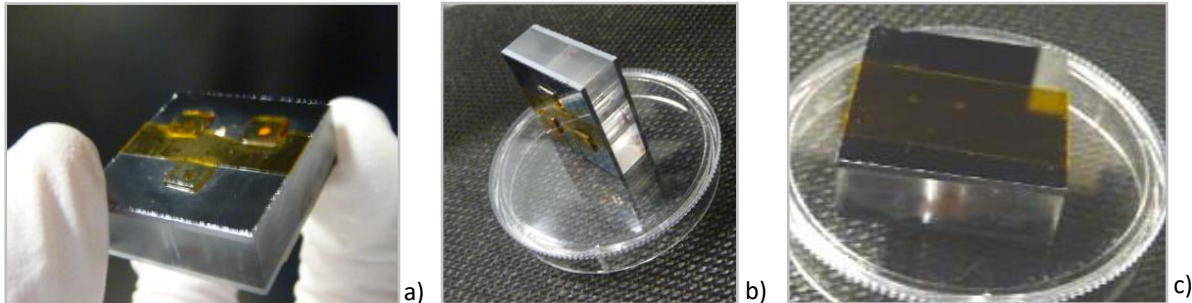


Figure 3-22 : A complete Stirling micromachine obtained after cutting the Stirling micromachine cluster stack: a) Front side with observation windows, b) Back side with kapton sealing film

## 3.2.5. Different versions of fabricated micromachines

### 3.2.5.a. Stirling Micromachines with liquid piston and magnets for operation in cooling mode

To be able to characterize the micromachines also in cooling mode, we have also assembled micromachines incorporating small permanent magnets glued on the membranes. These 3 mm diameter 1 mm thick  $\text{Nd}_2\text{Fe}_{14}\text{B}$  magnets were installed to allow membrane actuation through an external magnetic field. The magnet's additional mass is not negligible and to avoid unbalancing two of which are active, and one has been demagnetized. These magnets were glued on the lower surfaces of the three membranes inside the cavities containing the liquid piston. The remaining spaces were completed by the incompressible liquid. The membranes can thus be actuated with two external coils, placed in near the membranes with the active magnets.

### 3.2.5.b. Stirling Micromachines with a solid connection between membranes.

In addition, to avoid the difficulties related to the filling of the liquid and the risk of contamination of the equipment of the clean room, we have also assembled micromachines whose mechanical connection between membranes is provided by rigid bars, either in glass or in plastic. These machines were called « micromachines with solid

connections ». Glass connections were made by ultrasonic machining and plastic connections by 3D printing. The bars were attached to the central part of the membranes to connect them (cf. Figure 3-23) through the cavity in the glass block. At the other end of the bars, a permanent magnet was fixed, which was connected on the opposite side to the other membrane.

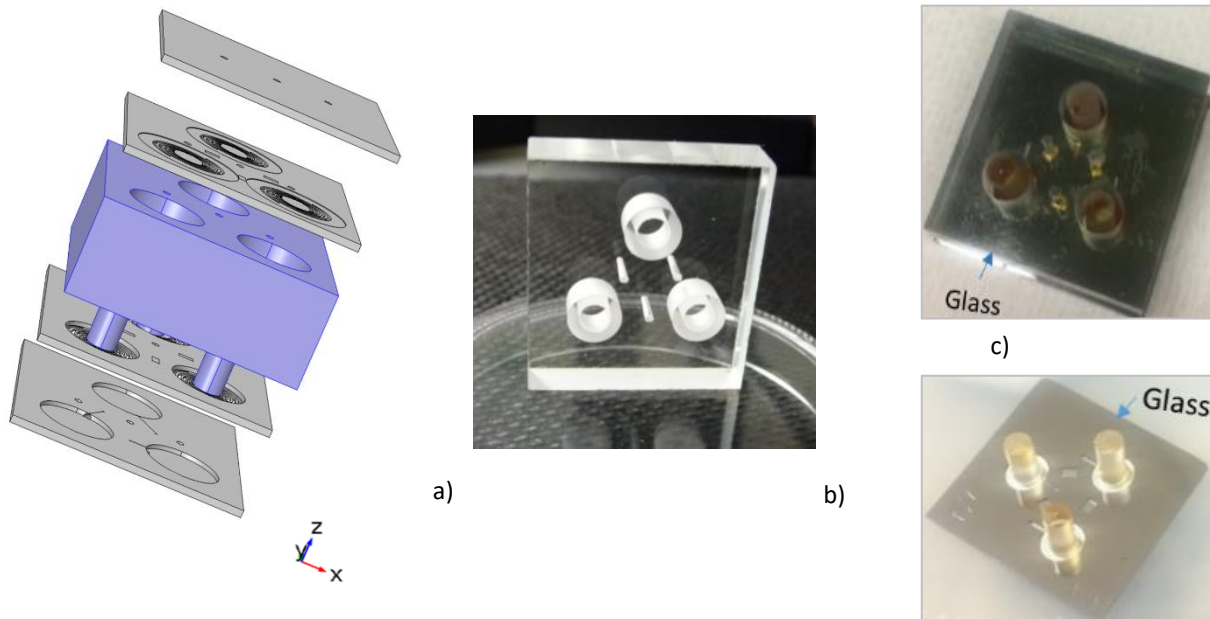


Figure 3-23: a) Solid piston first design. b) The central studs representing the solid glass piston etched in the thick block by ultrasonic machining

### 3.3. Study of room temperature thermocompression

#### 3.3.1.a. Introduction and objectives

Thermocompression bonding is a simple technique that requires the simultaneous application of temperature and pressure after bringing in contact the wafers to be bonded. The most successful thermocompression bonding procedures use copper or gold as intermediate bonding materials [178]. In our case we used gold as an intermediate layer, due to its resistance to corrosion, ductility, thermal conductivity, hermeticity as a bond metal and to the fact that it does not attract inorganic substances such as sludge particles. The Au-Au bond is achieved by means of interatomic attraction forces (at distances of some angstroms).

The elements influencing thermocompression bonding are the following:

**Bonding interface quality.** At the interface between the wafers, there may be ductile and mobile contaminants. They are protective barrier layers against the oxidation of gold: surface layers of oxygen, CO<sub>2</sub> or SO<sub>2</sub> [179]. Their mechanical and thermal characteristics can prevent a good contact at the interface since they resist up to a temperature of 350°C [180]. Oxides naturally present on the surface of the gold layer prevent the formation of solid bonds. They can be removed from the bond surface by the application of UV radiation.

There may also be at the interface, asperities and roughness. They have two effects on the bond: a positive effect and a negative effect. The positive effect is that it creates stress concentration points when brought into contact leading to a local plastic deformation allowing an instant bond to take place. The negative effect is a lack of hermeticity, which will require application of a greater force to flatten the interface during bonding. Finally, the flatness of the wafers (if they are a little curved) combined with a non-uniformity of their thicknesses (TTV) have a very negative effect on the bond and will require applying a very high pressure to flatten the substrates [178], [181], which is not possible when wafers contain fragile structures.

**Bonding pressure.** The pressure allows, among other things, to bring both surfaces (to be bonded) close enough to allow the interatomic attractive forces to take place [178]. It also enables deforming the interface (to overcome the asperities and curvatures of the wafers) and flattening because higher pressure induces interfacial shear stresses that scatter barrier films (contaminant). It also keeps the gold surfaces in intimate contact throughout the interatomic bond formation time, which corresponds to the duration of the bond. If the bonding is done at ambient

temperature, larger pressure may be required for the interatomic attraction to overcome surface roughness (Zhang, Ang, Chen, Wong, & Wei, 2007).

**Bonding temperature.** The effect of temperature is to initiate the rearrangement of atoms to initiate the formation of new Au-Au bonds made possible by a surface diffusion process between the Au layers in intimate contact. If more thermal energy is added, a lower bonding pressure is sufficient to achieve the same degree of bonding [178]. Indeed, the temperature increases the ductility of the gold layer and soften it, which facilitates the initiation of the bond [178]. When the deformations of the gold layer exceed 15%, its hardness coefficient decreases rapidly with increasing temperature. Indeed, such a deformation of the gold layer considerably weakens its thermal resistance [182]. In addition, a higher temperature decreases or breaks the films of organic contaminants, by tearing the barrier layer already deformed by the applied pressure, which allows obtaining a good hermeticity and a good bonding quality. However, reference [180] suggests that no strong bond can be obtained below a bonding temperature of 150 °C.

Therefore, it is concluded that substrates with low TTV, low roughness and low deformation are required since mechanical features of wafers (TTV, bow, warp) are important to achieve good bonding quality. A TTV <5 µm and Bow <40µm is advised for anodic bonding and a TTV <3 µm and Bow <20µm is advised for Au-Au bonding thermocompression. The thermocompression bonding quality increases with the application of high temperature during bonding (about 300°C). Otherwise, considerable pressure may be required to obtain thermocompression bonding at room temperature, which would likely damage the bonded parts if they were fragile.

In the literature, the authors often believe that to obtain a good quality of thermocompressive bonding, it is necessary to simultaneously apply a high pressure and a high temperature (> 350°C). Earlier attempts of thermocompression bonding required temperatures of about 400 °C, a peak pressure of 2.76 MPa and a bonding time of about 3 hours [183]. In the following reported bonding techniques, temperatures in the same range were used with changes in static pressure and bonding time. A successful bond was obtained at 300 °C by applying a pressure of 7 MPa, (corresponding to the gold-coated area), and a bonding time of 10 min [184]. Other successful approaches were described in [185], [186], [187], however, none of them shows a successful bonding at room temperature.

However, the micromachine membranes may be damaged by temperatures exceeding 300°C. Therefore, in order to fully and permanently preserve the mechanical properties of our membranes, it is necessary to find another low-temperature bonding technique that is as efficient and adapted as possible, or to do a thorough study of this thermocompression technique. We have chosen to perform a deep study on thermocompression at room temperature, since the bond quality also depends on the gold layer surface quality, the gold adhesion layer (Ti or Cr) [29], atmosphere prevailing in the bonding chamber (vacuum bonding or under specific atmosphere) and duration of the bond. The advantage of room temperature bonding is that we can achieve a reduction in bonding time (no loss of time for heating and cooling), an increase in wafer alignment accuracy, absence of thermal distortion and a larger flexibility in the selection of parts to be bonded.

Thermocompression remains one of the best bonding techniques to connect any type of solid material through a metal layer. Therefore, our ultimate goal is to find the optimal conditions to achieve an effective bonding at room temperature for the assembly of the micromachine without risk of damaging the membranes.

### **3.3.1.b. Study Methodology**

Starting with bonding parameters that have been found in the literature and in previous studies, we have tried to perform the thermocompression bonding at room temperature and then some parameters were optimized to obtain improved bonding reproducibility and better bond strengths. The previous results showed that:

- bonding of full wafers using thermocompression succeeded at room temperature
- bonding of gold patterns obtained by photolithography did not succeed (there was almost no adhesion between both patterned gold surfaces)
- In the case of our machine, we obviously need to pattern the gold adhesion surfaces. Therefore, we tried to investigate the following procedures :
- try to deposit the gold layer through a stencil mask to avoid patterning with a resist,
- enhance the adhesion by choosing the best gold adhesion layer between Cr and Ti,

- study the effect of substrate stripping before adhesion layer deposition and the effect of the morphology of the deposited gold layers [173].
- try again to bond surfaces patterned by lithography with a strong gold surface cleaning, to remove residual molecules coming from the photolithography process.

### 3.3.1.c. Bonding procedure

The study was based on the bonding of two 3-inch wafers, one of which is structured on the surface and the other has been gold-coated on the whole surface. The assembly of wafers is then cut into square chips, which will be glued on traction test pads designed specifically for a Bose type traction machine. The maximum pull force exerted by the machine before the wafers separate is recorded (breaking force) and this force is divided by the total bonded surface which gives the breaking stress (in N/mm<sup>2</sup> or MPa).

**Masks.** In order to avoid contaminating the gold surfaces by a lithography process we decided to structure the wafer gold patterns by using metal screen masks (*cf.* Figure 3-24) in the chamber of the Plassys MP500 sputtering machine. The metal layers are deposited through an aluminium screen and their pattern will thus reproduce the pattern of the screen holes. On the other wafer the deposition is made on the whole surface. In all cases, the wafers will be later divided in four 2 x 2 cm silicon chips.

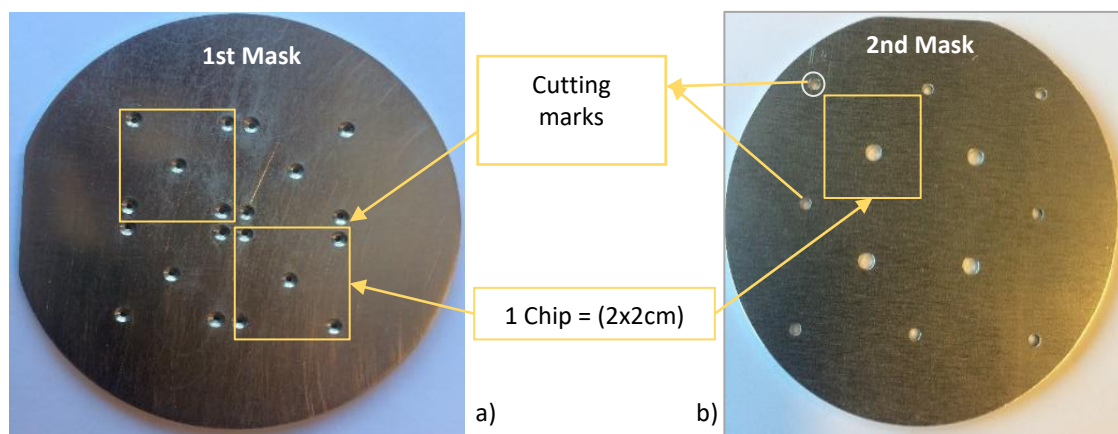


Figure 3-24: Screen masks used for the thermocompression study at room temperature: mask1 contains five Ø1 mm holes per chip (right) and mask2 one Ø3 mm hole per chip (right)

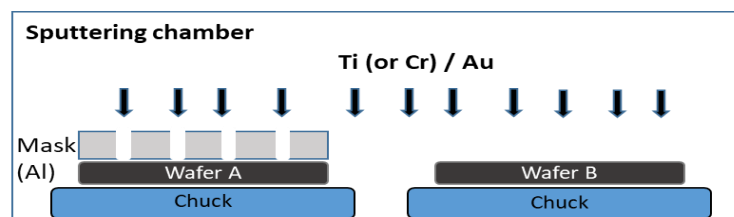


Figure 3-25: Schema showing silicon wafers, covered with screen mask inside the deposition machine.

Silicon wafers, covered with the screen masks, were introduced inside the deposition machine (*cf.* Figure 3-25). In some cases, a stripping procedure using an argon plasma was performed prior to metal deposition. Then a thin adhesion layer (Cr or Ti) was deposited, followed by a thicker layer of gold.

In the first screen (Mask1), five 1 mm diameter holes per chip were drilled, with 4 repetitions on the wafer (*cf.* Figure 3-24). These five holes are the areas where the gold will be deposited on the patterned wafer, with a total area of 3.93 mm<sup>2</sup> per chip. In the second screen (Mask2), we grouped these 5 holes in one 3 mm diameter hole (7.07 mm<sup>2</sup> per chip) centered on the chip.

**Bonding conditions.** Two series of tests have been carried out. In the preliminary tests, standard bonding parameters were used. In the confirmation tests, the bonding parameters were changed to try improving the results. For all cases, the adhesion layer and the gold layer are identical for the « bottom wafers » (with gold deposition on the whole surface) and the « top wafers » (containing several gold pads).

### 3.3.1.d. Preliminary tests.

The steps and the operating conditions for bonding are described below:

- Preparation of the wafers.** Piranha + Deionized water + Dry nitrogen
- Deposition of metal layers.** The alignment with the physical masks is done by aligning the flats of the wafers and the mask. Ti or Cr adhesion layers are deposited in the MP500 sputtering machine followed immediately by gold sputtering.
- Bonding (EVG machine).** The alignment also relies on the wafer flats. The bonding parameters are (1) the bonding force, (2) temperature, (3) time and (4) vacuum quality.
- Chips cutting.** Cutting lines are defined by making a local deposition of Al on one of the rear faces of the two wafers already bonded. Then at the cutting workshop, the stack is cut into four 2cmx2cm chips using a precision saw with a 100  $\mu\text{m}$  thick blade.

### 3.3.1.e. Confirmation tests

In order to improve the results obtained during preliminary test some parameters have been modified for the second series of tests:

- Deposited layers: Chrome (15nm) and Gold (180nm)
- Bonding conditions (EVG): F = 500N and Vacuum =  $10^{-3}$  mbar

The main bonding parameters are summarized in Table 3-4.

	Bonding force (N)	T (°C)	Bonding Time (min)	Vacuum (mbar)	Cr or Ti thickness (nm)	Au thickness (nm)	Total area bonded per Chip (mm <sup>2</sup> )
Preliminary tests	100	20	20	$10^{-2}$	15-25	100-180	Mask1: 3.93 mm <sup>2</sup>
Confirmation tests	500	20	20	$10^{-3}$	15-20-25	180	Mask2: 7.07 mm <sup>2</sup>

Table 3-4 : main bonding parameters used during the bonding tests

### 3.3.1.f. Characterization procedure

Among the variety of bond strength quantification methods available [188], tensile testing is the most relevant for this study. Indeed, separation of wafers in the micromachine due to high inner gas pressure will be produced by a tensile stress. Tensile testing is the second most reported method for the quantification of the wafer bond strength [188]. It is straightforward to use and the test procedure can be made operator independent.

A tensile strength measurements set-up, depicted in Figure 3-26, with equally sized specimen and stud was used. This also makes the glued area greater than the bond area, thus facilitating fracture to occur at the bond and not on the glue interface. The entire test set-up is firmly fixed to the tensile test machine, and the whole set-up was carefully aligned to avoid any parasitic shear stress. The tensile test machine was set-up to generate an axial force at a rate of 0.2 N/s and the bonded wafers were pulled apart. The force for which the bond breaks was recorded: this force divided by the total bonded area is reported as the tensile bond strength (in MPa).

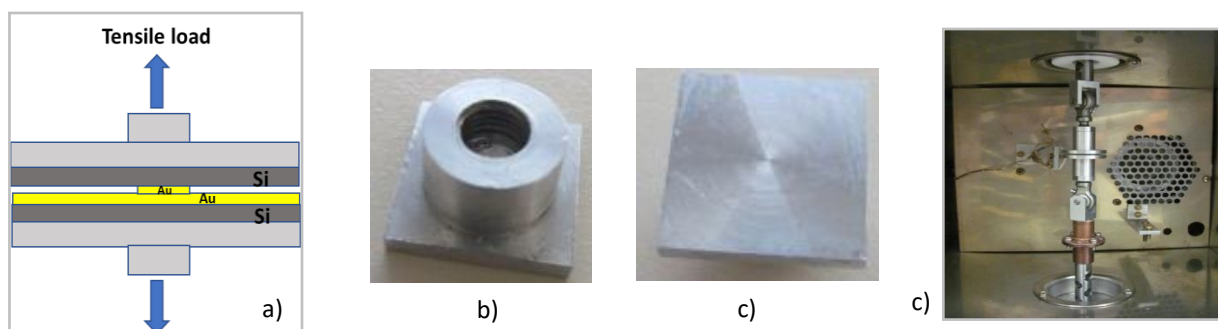


Figure 3-27: a) Schematic diagram of the Tensile Test, (b) & (c) pull studs used (c) ElectroForce® 3200 Instrument with fixed test set-up

The tensile test machine used was the commercially available ElectroForce<sup>®</sup> 3200 Instrument (cf. Figure 3-27). The preparation of Pull test metal holders is first carried out in the workshop by progressively polishing (papers grain of 600 then 1200) followed by rinse in demineralized water and then drying. The holders are cleaned with acetone and then dried. Then, the tested chips are glued with the two-component Polytec EP653-T glue prepared by mixing a part A (very viscous adhesive agent) and a part B (cross-linking agent) in a ratio of 100:35. We used 500 g of A and 175 g of B well-mixed. Finally, we deposited and spread a drop from the center of each metal support, stopping at 1mm from the edges, then we put in contact the two supports with a chip placed in the middle. To polymerize the glue, we placed the samples in an oven at 70°C for 2 hours, then we let them cool slowly in the cleanroom, before bringing them to do the Pull tests.

When spreading the glue, we stopped at 1mm from the edges of the metal holder, to avoid infiltration of the glue in the chip, which may increase the value of the separation force during Pull tests (even if negligible).

### 3.3.1.g. Results and interpretation of the performed tests

Five bond tests were performed with different bonding conditions. For each test, 4 samples bonded in the same conditions were characterized (when possible).

#### i General observations on Test#1: Si/CR is the weakest interface

For the Test #1, all samples underwent surface stripping of the substrate prior deposition of the adhesion layer. Chips 1.1 and 1.2 were measured, the two parts of chip 1.3 have separated at a very low pull force that could not be measured and chip 1.4 has broken during dicing. From the results of the first test, we observed that Au/Au adhesion is better than Cr/Si adhesion: on 15 bond points (Chips 1.1 to 1.3), 10 broke at the Cr/Si interface (cf. Figure 3-28, Figure 3-29 and Table 3-5).

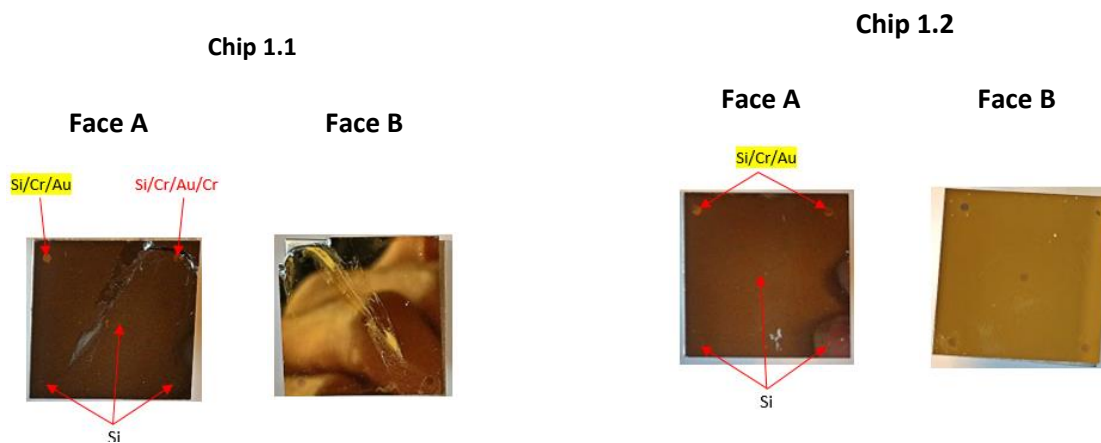


Figure 3-28: Results of pull test on Chips 1 and 2

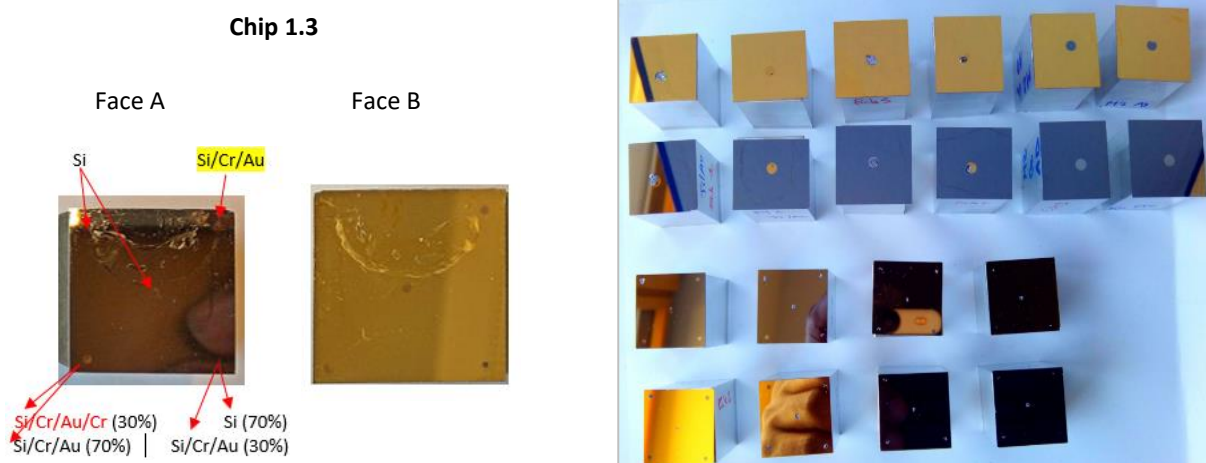


Figure 3-29: Failure interface after tensile test with two 3'' wafers  
(1-10  $\Omega$ .cm; <100>;  $380 \pm 25 \mu\text{m}$ ; NO; DF)



Then the bond strength was measured (Test#1) and the results are given for the 4 samples in the last column of the following table:

Test #	Mask nb.	Cr/Au thickness (nm)	Vacuum (mbar)	Bonding pressure	Si Stripping	Bond strengths of 4 samples (MPa)
1	1	Cr15 / Au100	$10^{-2}$	6.4 N/mm <sup>2</sup>	Yes	60 - 14 - 0 - NA (Avg. 24.7)

Table 3-5 : bond strength results of Test#1 for the 4 samples

**DISCUSSION OF FIRST TEST.** The results are very heterogeneous and infiltrations of glue between the two parts of chip1.1 were observed. Therefore, the large breaking stress (61 MPa) observed for chip1.1 may come from the adhesion of glue instead of Au/Au bonding (this result is thus not accurate). The breaking force for chip1.3 was close to zero and could not be measured. The only accurate measurement was made on chip1.2, which exhibits a bond strength of 14 MPa.

After this first test it was suspected that shadowing effects during Cr and Au depositions might limit the deposited metal thickness, especially for holes with small diameters. Therefore, it was decided to make a new mask (Mask2) for which the 5 contact points were grouped in a larger 3.9 mm<sup>2</sup> disc centered on the chip to minimize shadowing. In addition, thicker layers of gold were deposited to compensate for residual shadowing effects.

**SECOND TEST WITH MASK2.** The bonding with Mask2 was done with the same conditions as for Test1, except that the gold thickness was 180 nm and no silicon stripping was done.

**Observations.** For test2, pictures of the bonded surfaces taken after separation of the two parts of the chips are shown in Figure 3-30.

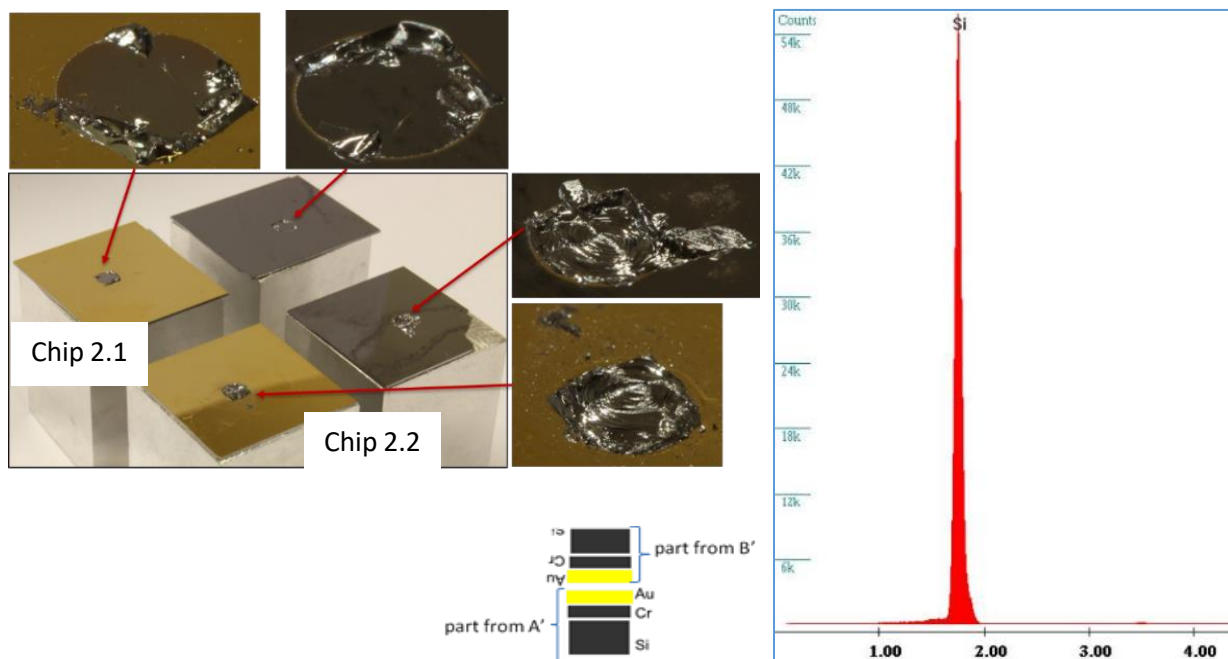


Figure 3-31 : For chips 2.1 and 2.2, Silicon has been torn from wafer A the one with a gold disk) and sticks to wafer B (the fully gold-coated one). Results obtained after the chip stripping tests made during the second study. Visual observation and EDS (Electron Discharge spectroscopy) of the bonded area

**For chip2.1,** we observe a 400  $\mu\text{m}$  deep hole larger than the gold disk in wafer A, and a kind of pad (partially made of silicon taken from wafer A) on wafer B. Therefore, we conclude that Au/Au adhesion was greater than Cr/Si which was greater than the bulk of silicon. Therefore, on A, we have only silicon left and on B, we have several layers which are made of Si/Cr/Au/Au/Cr (starting from the top of the chips).

SEM images accompanied by some EDS spectra (Electron Discharge spectroscopy) allowed observing more closely the interface where the breaks occurred. Since EDS is limited in depth to  $2\mu\text{m}$ , only silicon is observed in this case, because the silicon thickness torn from face A is much larger than  $2\mu\text{m}$ .

It can be said that for this chip the adhesion Au/Au has been greater than the adhesion Cr/Si which was itself greater than the cohesion of the silicon in the bulk.

**For the other chips**, it is observed that the breakage occurs at the Cr/Si interface of wafer B (the Cr layer is thus transferred to the wafer A) except on a part of the disk area where the Cr/Si interface is stronger and on this areas, silicon is torn from wafer B and transferred to wafer A. Therefore, there is generally a partial removal of silicon from wafer A (on 20% of the disc area for chip 2.2, 5% on chip 2.3 and 70% on chip 2.4).

**Observation of shadowing effects.** On chip 2.3, SEM observations of the chips after the pull tests show that there was a shadowing effect related to the physical hole of the masks used. In fact, the deposition goes well at the center but deteriorates towards the edges. The transition region is estimated to be  $20\mu\text{m}$  wide for the rather large hole of Mask2.

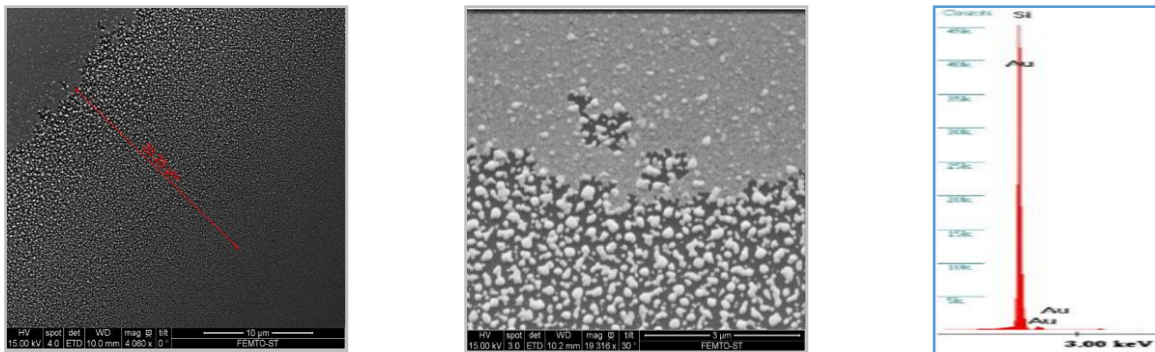


Figure 3-32: SEM image of the gold layer highlighting the peripheral part and EDS spectra showing a mixture of gold and silicon at the edge of the gold disk

**Pull-test results.** The bond strength results for test2 are given in the table below:

Test #	Mask nb.	Cr/Au thickness (nm)	Vacuum (mbar)	Bonding pressure	Si Stripping	Bond strengths of 4 samples (MPa)
2	2	Cr 15 / Au180	$10^{-2}$	$9.4\text{ N/mm}^2$	No	21 - 19 - 24 - 28 (Avg. <b>23</b> )

Table 3-6: The bond strength results for test2

The results were clearly much more reproducible than for test1 and the bonding strength is much better: all chips were bonded and bonding strengths ranged between 19 MPa and 28 MPa.

**CONFIRMATION TESTS.** Since several parameters have been modified between test1 and test2, it was necessary to perform a second series of tests to confirm the behavior of the bonding process. Three additional tests were done with results shown below :

Test #	Mask nb.	Cr/Au thickness (nm)	Vacuum (mbar)	Bonding pressure	Si Stripping	Bond strengths of 4 samples (MPa)
3	1	Cr25 / Au180	$10^{-2}$	$6.4\text{ N/mm}^2$	No	30 - 11 - 36 - 29 (avg. <b>26.5</b> )
4	2	Ti15 / Au180	$10^{-3}$	$9.4\text{ N/mm}^2$	No	19 - 29 - 43 - 19 (avg. <b>28</b> )
5	2	Cr25 / Au180	$10^{-3}$	$9.4\text{ N/mm}^2$	Yes	13 - 11 - NA - NA (avg. <b>12</b> )

Table 3-7: Three additional tests results

These results are discussed in the next sections.

### ii Effect of silicon wafer stripping prior to Cr/Au deposition

By comparing the pull-tests results of tests1 and 2, it can be inferred that stripping of the silicon wafer before bonding may degrade the results instead of improving them (as observed for full-wafer bonding).

Test3 was done with similar bonding conditions as test1 but without initial wafer stripping and also shows very good results. Therefore, it confirms that results are better without initial wafer stripping.

Another test with initial wafer stripping was done in test5 and again the results were much worse than for test2 (which confirms again that bad effect wafer stripping).

**INTERPRETATION.** This result is opposite to observations done on the bonding of two gold-coated full-wafers. However, we noticed that during the wafer stripping, the metal mask might also have been sputtered on the wafer: therefore, the silicon wafer may be contaminated by metal deposition before the first Chromium deposition (*cf.* Figure 3-33).

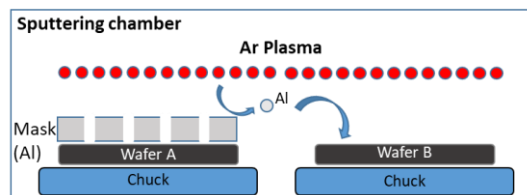


Figure 3-33: schema explaining the silicon wafer potential contamination by metal deposition from the screen mask before the first Chromium deposition.

**This contamination of the wafer may explain the bad results obtained when stripping the wafer through a metal stencil mask prior to Cr layer deposition, as well as the fact that the weakest interface is the Si/Cr interface.**

### iii Effect of adhesion layer material

Titanium is known as a good adhesion layer, therefore test4 was made with a titanium adhesion layer. First, we proceeded to stripping the Ti target for 2 min with a current of 1A under  $7 \times 10^{-3}$  mbar vacuum, then the deposition was performed during 20s with the same conditions of current and pressure. Chip bonding was carried out at room temperature with the same condition as for Cr adhesion layers. The observed bond strength is very high compared to the literature [175], [189], [190], [191], **and the average bond strength (28 MPa) is the best that has been obtained in this study.**

A comparison of **test4** to all other tests using chromium as an adhesion layer suggests that Ti may be even better than chromium. However, these results have to be confirmed on series of tests, but at least we can recommend using Titanium instead of Chromium to increase the probability of obtaining a strong thermocompression bond.

### iv Bonding of wafers patterned by photolithography

Bonding strength of gold disks structured by photolithography followed by Au and Cr etching	
Pre-processing before bonding	Resulting bonding strength
Without gold stripping	0
With 50W Ar plasma stripping of gold	0
With Piranha cleaning followed by 15 min Oxygen plasma cleaning and 150W Ar plasma stripping	0

Table 3-8: Results of the two tests done with gold surface structured by photolithography followed by Au wet etching

We have also tried to bond wafers whose gold layer are structured by photolithography followed by gold chemical etching solution and paid particular attention to cleaning of the gold surface before bonding to remove surface contamination of the gold layer from photoresist developer's solutions and chemical etching mixtures. After a reference test without cleaning, two tests were done with gold surface cleaning and the results are shown in Table 3-8.

For all tests, the bonding failed (the bond strength was almost zero). These results are quite amazing and are not fully explained to date.

However, it is important to notice that the gold surface was totally covered by the resist during the photolithography process, which will not be the case if we try to do the photolithography with a lift-off process (although the gold surface will see the resist developer in both cases).

Therefore, it is worth trying to structure the gold surface with a lift-off process to discriminate whether the problem comes from the resist or from the resist developer.

### 3.3.1.h. Conclusions and perspectives

- **Recommended bonding conditions.**

From the results of this study, we can recommend the following bonding process conditions for **room temperature Au-Au thermocompression bonding with stencil masks**:

Deposit on both wafers a 15 nm Ti adhesion layer (probably 25 nm may be better in case of small patterns) followed by 180 nm of gold sputtered in the same chamber without wafer stripping before Ti deposition

Do the bonding of freshly deposited gold patterns with an applied force of 10 N per mm<sup>2</sup> of gold coated area, under 10<sup>-2</sup> mbar vacuum or less

Under these conditions, **bond strengths in the range 20 - 30 MPa can be obtained.**

- **Comparison with the results obtained from the literature**

For most of the results obtained in recent papers, the bonding strengths are slightly higher than our results (more than 30 MPa), but bonding temperature is usually large and would not be applicable to fragile MEMS device such as those containing polymers. For instance, in [189] a bonding strength of 35 MPa was obtained using surface activated bonding, however the bonding temperature was 150°C, with an applied pressure of more than 100 MPa. In [175] an average bond strength of 33 MPa was obtained, at a bonding temperature of 420°C with a bonding pressure of 5.7 MPa. In [191], a bond strength in the range of 40-60 MPa was obtained, but for a bonding temperature of 380°C. We have thus demonstrated for the first time that Au thermocompression bonding was possible at room temperature with quite good bonding strengths.

In addition, none of the reported studies were performed with structured bonding pads: our results show that bonding is possible with bonding pads that were defined by using stencil masks.

- **Impact on the design of the Stirling Micromachine**

For the Stirling micromachine a required bonding strength of 200 kPa has been estimated in section 3.3.1.g. to prevent separation of the wafers, even under 10 bar inner gas pressure. Therefore, we conclude that **the bonding technology that was developed gives a bonding strength that is 100 times larger than the required one.**

- **Perspectives for thermocompression bonding**

**Applicability to other MEMS materials.** We have demonstrated that thermocompression bonding can be performed at room temperature with a high bond strength. This bonding has been done for Si-Si assemblies but may be also possible for various kind of substrates (glass, LiNbO<sub>3</sub>, sapphire, etc.). It can thus be used as a kind of « universal » assembly technology that does not require a large process temperature. It is expected to replace the anodic bonding step for the fabrication of Stirling micromachines.

**Bonding on gold pads structured by lithography.** Although bonding was not successful on gold pads obtained by photolithography, using a lift-off lithography process may avoid contacts between the gold pad and the photolithography resist. If the surface modification of the gold pad does not come from the developer, the bonding may be successful.

### 3.4. Conclusion

The main results of chapter 3 are the following:

- A **micromachine design** allowing batch microfabrication by assembling several wafers has been imagined and its fabrication has been fully validated
- An **RTV silicone-based membrane** able to sustain large deflections (~1 mm), tolerating temperatures up to 300°C and containing silicon springs that could be used later for energy harvesting, was fabricated and proved to be very robust
- **Anodic bonding of a multi wafer stack** has been achieved successfully
- The questions of **liquid filling** and micromachine sealing was solved
- Gold **thermocompression bonding** was demonstrated at room temperature on structured gold pads, with 20-30 MPa bond strengths that complies to the micromachine specifications and may further simplify the fabrication process.

## CHAPTER 4 : MEMBRANES CHARACTERIZATIONS AND RESULTS

In this chapter, we present the characterization of two types of membrane to be implemented in the Stirling micromachine. These membranes consist of an RTV-silicone layer associated with either a silicon planar spiral, or a silicon disk. The RTV-silicone is composed of Poly-dimethylsiloxane (PDMS) with an excess of silicon atoms. These membranes are to be used in a Stirling micro-machine continuously operating at 200°C (maximum temperature). Knowing that the temperature has an influence on the mechanical properties of PDMS-based membranes [192], an important issue is their behavior under high temperature operation.

Therefore, to properly design and be able to predict the natural oscillation frequency of these membranes, their mechanical and thermal properties should be identified. Indeed, the stability of their oscillation frequency is critical for the Stirling micro heat motor operation and optimization. Apart from the frequency stability of the membranes as a function of temperature, the microfluidic aspect (flow velocity of the working gas through the micro pipes, the time required for heat exchange) requires using membranes with low natural frequencies and large displacement amplitude.

Indeed, several membrane-based PowerMEMS devices require large swept volume to start and to be efficient [193], [12]. But, when a thin membrane is made with standard cleanroom materials (silicon for example), it cannot deliver such performance without breaking. One possibility is to add a complex system for amplitude amplification [194]. But this can lead to a high actuating force to deflect the membrane, which may increase the size of the final device. Consequently, elastomer materials, such as silicones, because of their unique properties (such as high elasticity, transparency, high temperature application, etc), are now widely preferred in the realization of membranes-based microsystems such as micropumps [195], fluidic systems [196], [197], [198], [199], [200], [201]), sensors and actuators ([202], [203], [204]). They are also used in microdevices packaging to protect components from environmental factors and mechanical shocks within a large temperature range (-50°C to +200°C) [205]. Their main advantages are [110]:

- Elasticity and soft nature (for low actuation load, reversible deformations),
- Rapid prototyping by molding/casting with high thickness homogeneity [206]
- Cost effectiveness [207], [208]
- Biocompatibility (biological assays),
- Optical transparency (for observations and characterizations such as biological/chemical analysis).

Regarding the characteristics of our RTV-silicone product the manufacturer (Permatex) does not provide much details on mechanical properties and aging. To our knowledge, there is still no bibliography on this RTV-Silicone in particular. Therefore, RTV-silicone material mechanical properties and their evolution with temperature are studied. Since the second part of membranes consists of either a planar silicon spring or only a central silicon disc, we have also studied the mechanical and thermal behavior of these two structures when embedded inside the RTV silicone layer.

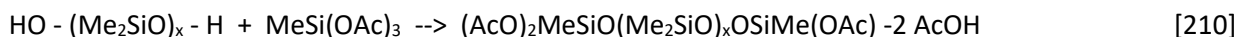
In this chapter we will present tensile tests that have been carried out on RTV silicone specimens to determine their elasticity. Then, after the membranes were manufactured, their natural vibration frequencies and mechanical properties (Young's modulus, residual stresses) were characterized by bending tests. A numerical simulation (finite element model) on the COMSOL software of the mechanical and dynamic behaviour of the membrane will also be presented. Finally, the experimental and simulation results are compared. Finally, we will conclude with a study of the effect of temperature on the behaviour of the membranes in the short and long term. The short periods are those necessary to achieve the anodic and thermocompressive bonds (at a temperature of 300°C) to assemble the Stirling micromachine in a clean room (*cf.* chapter 3). The long periods concern a membrane operating time at 200°C for more than a month represented by a study of the ageing of these membranes in an oven.

Before proceeding to the presentation of these studies on RTV-silicone and membranes, we present briefly the structure of RTV-silicone and review the mechanical behavior of solid materials in response to stress and introduce the terms often used in this field (stress, strain, yield point, elastic and plastic region, failure point, modulus of

elasticity, hysteresis etc.). This may help the reader to better understand the results of the studies that will be presented later in this chapter.

#### 4.1. The RTV-silicone

**Structure of the RTV-silicone.** The RTV-silicone material that we used is a viscous paste, consisting of organic macromolecules containing acetone molecules (-CHOOH, denoted Ac) on which silicon (Si) radicals are grafted. This product is formulated from a reactive polymer prepared from hydroxyl-terminated polydimethylsiloxane and a large excess of methyltriacetoxysilane [209]:

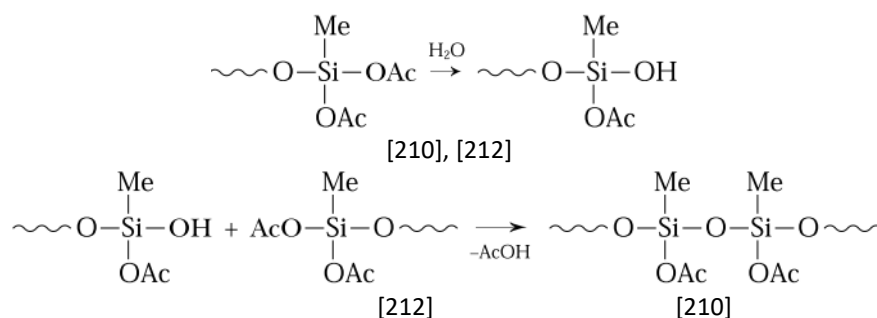


Since silicon is located just below carbon in the classification of the periodic table, similar compounds in which the silicon atom would replace the carbon atom have been mythologized. Indeed, most of these similar compounds do not exist or behave very differently because the Si - X bonds (in silicones) and the C - X bonds are very different. The length of the bond between a given element and silicon Si is shorter than the bond between carbon C and the same element. The electronegativity of the silicon Si atom (1.9) is lower than that of the carbon C atom (2.55). The Si - O bond is very strongly ionic and highly polarized, with a high bond energy (452 kJ/mol), while the Si - C bond has a slightly lower energy (around 318 kJ/mol), which is itself slightly lower than the C - C bond energy (347 kJ/mol), while the Si - Si bond is much weaker (193 kJ/mol). These values partly explain the stability of the silicones, the Si - O bond being in particular very resistant to homolytic cleavage [211].

The bonds between the atoms of a macromolecule are covalent. These covalent bonds (*e.g.* the C-H bond) are often asymmetrical, so they carry an electric dipole. These dipoles are at the origin of weak inter-macromolecular electrostatic interactions ensuring the cohesion of the polymer material. When the temperature rises, these weak bonds "melt" first. Their melting temperature is called the glass transition temperature ( $T_g$ ) of the polymer. Since the polymer comprises covalent bonds combined with weak bonds between non-metallic atoms, no electrons will be available in the conduction band. Therefore, this material is intrinsically an electrical and thermal insulator. The following section aims to briefly describe the polymerization of RTV-silicone.

**Polymerization of RTV-silicone.** These sealants are called RTV (Room Temperature Vulcanization) sealants, however, they require moisture as a second component. In general, common polymers have a behaviour characterized by a high apparent diversity. Rigid, brittle, ductile or rubbery (or elastic) polymers can be found under the same conditions of use. However, just by varying some of its characteristics, or simply its conditions of use, this diversity of physical states can be found for the same polymer. This does not mean that the behaviour of a polymer is uncontrollable. Indeed, it is precisely the parameters controlling its behaviour that are numerous. These behaviour transitions are indeed strongly linked to the structure of the polymer and vary significantly from one polymer to another.

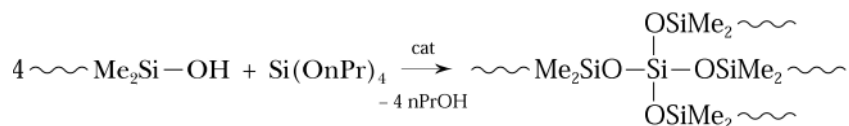
Concerning the crosslinking method, it does not require any mixing of products. Crosslinking begins when the product is removed from the cartridge and is exposed to moisture. A large excess of silane is used, so that the probability of two different chains reacting with the same silane molecule is low and all chains are blocked at the ends with 2 - OAc functions. The resulting product is still liquid and can thus be easily stored in sealed cartridges. Upon opening and contact with the moisture of the air, the acetoxy groups (-O-COOH) are hydrolyzed to give silanols, which allow further condensation to occur:



Thus, two chains have been linked and the reaction will continue further from the remaining acetoxy groups. This cross-linking requires that the moisture diffuse inside the product and the hardening will be from the outer surface

inwards. Acetic acid is released as a by-product of the cross-linking reaction. Instead of acetoxysilane, oxymosilane  $\text{RSi}(\text{ON} = \text{CR}'_2)_3$  or alkoxysilane  $\text{RSi}(\text{OR}')_3$  are sometimes used [209].

Condensation hardening is also used in two-part systems where cross-linking starts when the two components are mixed, for example a hydroxyl end-blocked polymer and an alkoxysilane such as tetra-*n*-propoxysilane [209].



In this case, no atmospheric humidity is required for polymerization. In general, an organotin salt is used as a catalyst; however, this limits the stability of the resulting elastomer for applications at high temperatures. Alcohol is released as a byproduct of the polymerization, resulting in slight shrinkage during polymerization. This prevents the manufacture of very precise objects (linear shrinkage of 0.5 to 1%) [211].

## 4.2. Characterization of RTV-Silicone layer mechanical properties

There are many techniques to characterize the mechanical properties of polymeric membrane [213]. For instance, the most used is the tensile tests [110], which require particular sample geometries ranging from the millimeter to the centimeter scale and a few microns thick. The Nanoindentation technique [214], on the other hand, requires a thin layer of the material over a rigid substrate. The near field characterization technique using an atomic force microscopy (AFM) is another alternative method of characterization [215]. In this last method a controlled force can be applied at a specific location on a sample (shaped as a cantilever single or double clamped) and the mechanical properties are deduced from the precise measurement of the deformation of the cantilever. However, this AFM technique still has limitations since the maximum measurement window is in the order of  $20 \mu\text{m} \times 20 \mu\text{m}$  and the sample stiffness should not exceed the force range capabilities of the AFM setup which is in the order of nN to  $\mu\text{N}$ . For internal stress measurements, there is also the technique of substrate curvature and for Young's modulus measurements, the acoustic wave technique [216]. Currently, the silicon MEMS technology has been widely used to prepare samples on silicon substrates, such as clamped structures [217], and membrane [218], allowing for the local measurement of these mechanical properties. For instance, the membrane load-deflection method enables to simultaneously determine the internal stress and Young's modulus, which are generally the most important properties for MEMS [219]. The main disadvantage of this technique is the difficulty of measuring the Poisson ratio, which is therefore, in most cases, chosen arbitrarily with respect to the nature of the tested material.

When a mechanical load is applied to a material, it develops an internal resistance (the magnitude of which depends on its rigidity) to the applied load. The strength of a material can be defined by its ability to resist these loads without deforming, tearing or breaking. The type of material, its microstructure, age, fluid content, temperature, speed and direction of loading are all factors that can alter the strength of a material.

### 4.2.1. Stress and Strain

Stress can be defined as a type of load (mechanical, thermal, etc.) that can be applied to a material. When the load is axial, we talk about axial stress. The axial stress of a material (generally denoted  $\sigma$ ) is therefore its internal resistance to an applied axial load. Figure 4-1 shows some loads that are of mechanical type: axial load (1, 2) for compression or tension and tangential (3, 4) for torsion or bending.

The axial stresses " $\sigma$ " measured in a tensile test is obtained by dividing the tensile load " $F$ " by the section " $S$ " of the test area:

$$\sigma = \frac{F}{S}$$

Under the effect of the applied tensile stress, the initial length " $L_0$ " of the test section increases to  $L(\sigma)$  and is generally described by the strain " $\epsilon$ ", which is commonly expressed in relative units or as a percentage change in material dimensions. The relative elongation  $\epsilon$  (percentage) is given by the following relationship:

$$\epsilon(\%) = \frac{\Delta L}{L_0} \cdot 100$$



where  $\Delta L = L - L_0$  is the elongation.

In our studies, we will use on one hand tensile tests (by stretching RTV-silicone specimens like in Figure 4-1 (2) and in the other hand flexural tests (by bending specimens like in Figure 4-1 (4)).

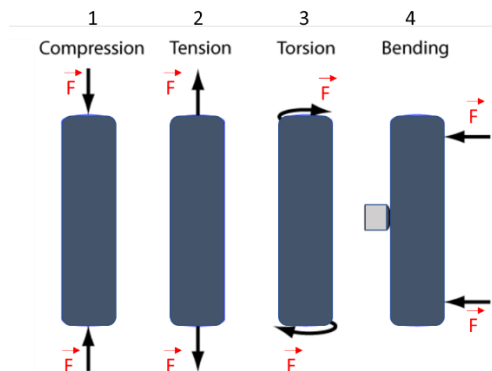


Figure 4-1: Different types of mechanical loads on a material: axial (1,2) and tangential (3,4).

### 4.3. Stress-Strain relationship: Young modulus

The relative strength of a solid material can be quantified by plotting its stress-strain relationship. The stiffness of the material is defined as the slope of its stress vs. strain curve. The inverse of the slope is the compliance of the material. Therefore, a material that deforms easily is said to be compliant. The Figure 4-2 (a) shows an example of a stress-strain curve for various materials.

The maximum amount of deformation that a solid material can withstand under a load and still return to its original shape after being unloaded is defined as the yield point; *cf.* Figure 4-2 (b). Therefore, the region of the stress vs. strain curve up to and including the yield point is called the elastic region (*cf.* Figure 4-2a). Usually, during an axial mechanical loading, many materials show a linear stress vs. strain response for low stresses. The stiffness of a material in this elastic region during axial loading is described by the Young's modulus which is also called the modulus of elasticity. When the material is loaded beyond this point, permanent damage occurs, and the material can no longer return to its original shape. Therefore, the region of the stress vs. strain curve beyond the yield point is called the plastic region or non-elastic region (*cf.* Figure 4-2a). If the material is loaded beyond plastic region, the material may break into two or more pieces (depending of its cristallinity) when the failure point (*cf.* Figure 4-2 a) is reached. Note that for a load just above the yield point, the permanent deformation may be microscopic and imperceptible.

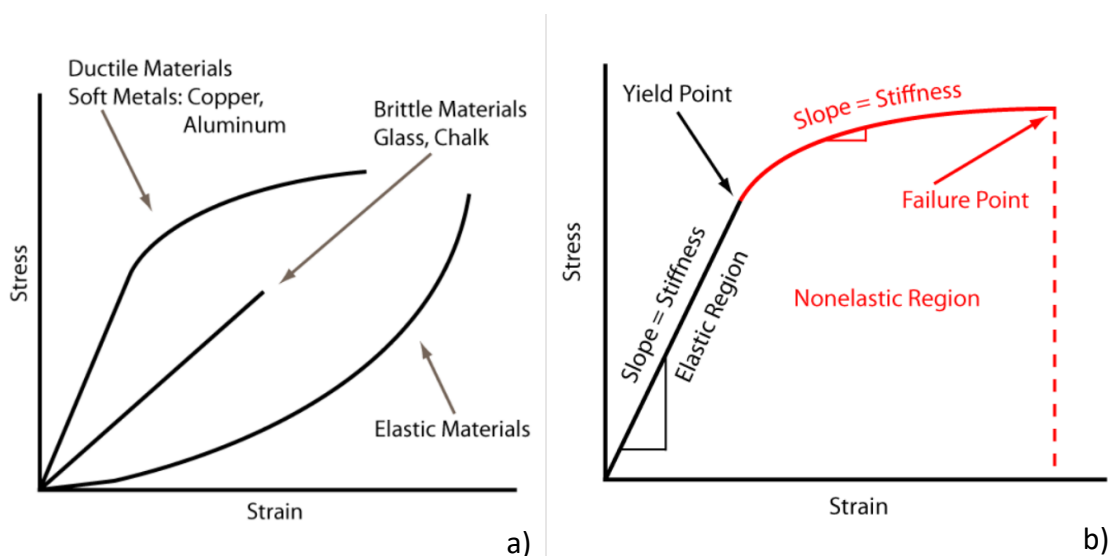


Figure 4-2 : a) Typical mechanical response for loading of a ductile ((b) zoom on this curve), brittle and elastic material [220]

The behavior of ductile materials is well represented by Figure 4-2 a. When a brittle material such as glass is subjected to loading, it will break with little deformation as the yield point and the failure point merge.

The stress vs. strain curve of elastic materials indicates that they are initially compliant and become progressively stiffer as the load is increased. Cross-linking of elastomer molecules, like silicones, is low enough to obtain an elastic behavior, but high enough to prevent the polymer chains from constantly moving relative to one another [221]. Being rubbery polymers, they can be stretched up to several times their initial length with a small stress while quickly recovering their original dimensions when the applied stress is released.

The Young modulus is essentially constant in the case of isotropic materials like copper or aluminum, however some materials (such as crystalline materials) do not exhibit a constant mechanical response when the loading direction is changed and are said to be mechanically anisotropic.

Some polymers, containing fibers within the material, can produce an anisotropic mechanical response. Therefore, the modulus of elasticity can vary versus loading direction: for a tensile test (*i.e.* load in the direction of the material fibers), one speaks of Young modulus in traction and in the case of a bending test, the Young modulus in flexion is measured.

The RTV-silicone elastomer, which constitutes the flexible part of our membrane, is a polymer in the rubbery state after cross-linking and is capable of very large viscoelastic deformations. It consists of a wide mesh network and, at room temperature, the weak links between polymer chains are melted (bridges between chains are formed under the effect of water vapor). When this polymer is stretched, the macromolecules are progressively aligned along the axis of the deformation. The modulus of elasticity of the cross-linked material is thus much higher when the load is applied along the the macromolecules axis than when it is applied along the short molecular bonds corresponding to flexural sollicitation (*cf.* Figure 4-3 a).

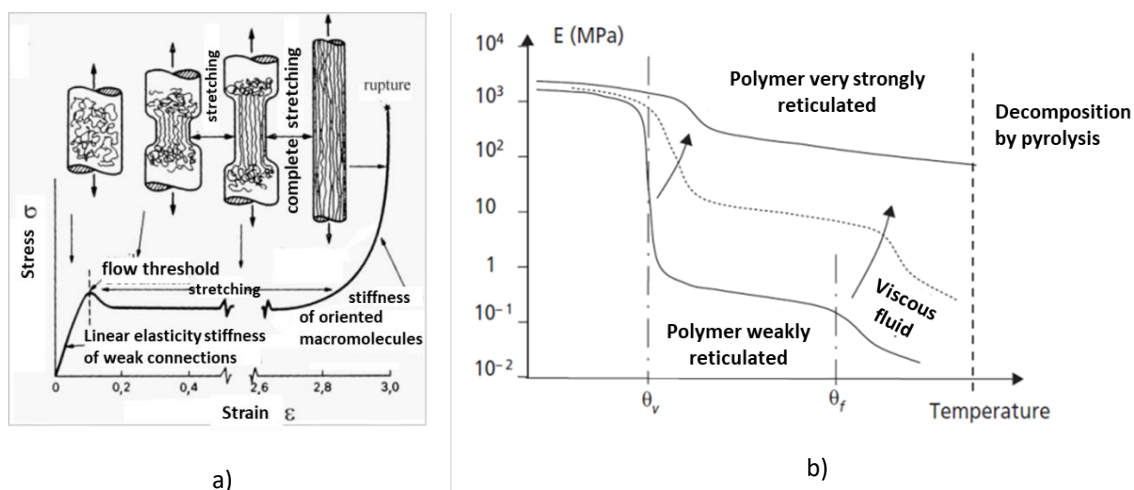


Figure 4-3: a) Schematic evolution of the Young's modulus  $E$  of a polymer as a function of temperature, for various levels of cross-linking. b) alignment of macromolecules by stretching [222], [220].

When the chains are cross-linked by transverse covalent bonds, the cross-links density determines the length of the free chain segments that can align: a high degree of cross-linking therefore permanently imposes a frozen amorphous structure. In the solid state, the structure of most polymers is amorphous because the entanglement of large size macromolecules makes their diffusion and crystalline order difficult.

#### 4.4. Hysteresis

When a pure spring is loaded (*cf.* Figure 4-4a), it will deform linearly depending on applied force and spring stiffness. When the load is removed, the spring releases all the elastic energy it has stored during the deformation process. Figure 4-4 b shows the stress vs. strain curves corresponding to the loading (black line) and unloading (blue line) phases of a viscoelastic material (an elastic material containing an amount of absorbed fluid). After deformation, the return to its original shape is delayed in time. It is slower to return to its initial position and the stress-strain curve of the discharge phase is different from the stress-strain curve of the charge phase: this is called a hysteresis effect. The area between the load and unload curves (in light blue) represents the amount of energy

absorbed by the material (converted primarily in heat). The area under the unload portion of the stress – strain curve (shown by the vertical red lines) represents the energy released by the material.

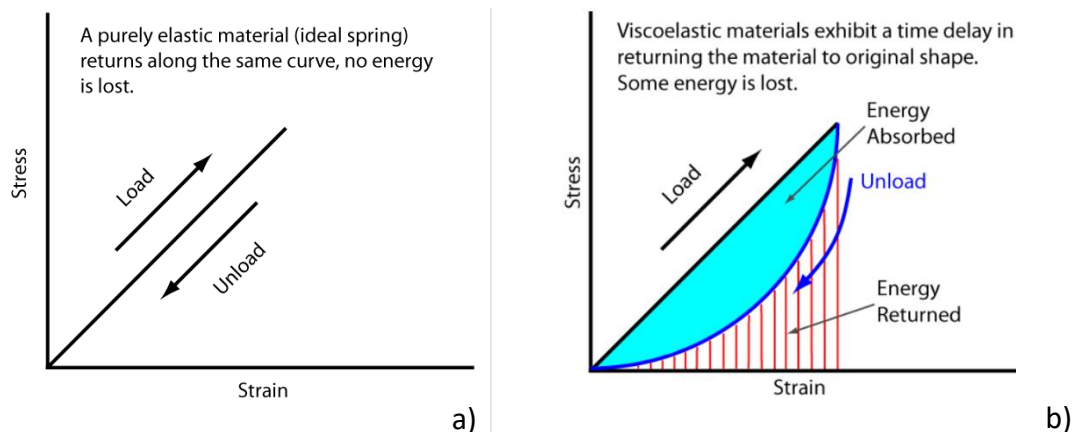


Figure 4-4: Stress - strain curves of a) an elastic material and b) a viscoelastic material : black line corresponding to the loading and blue line, unloading phases ( [222], [220]).

Since energy is absorbed by the viscous fluid in the material, this last one is called “viscoelastic”. It exhibits both viscous damping and an elastic response during deformation. Such materials are stiffer when loaded quickly than when loaded slowly.

#### 4.5. Characterization of RTV-silicone material by tensile tests: influence of thickness

In this section, RTV-silicone mechanical characterizations are presented. The mechanical properties of the thin layer of RTV-silicone are first investigated by tensile tests. For PDMS membranes, Liu *et al.* [110] demonstrated the dependence of mechanical strength and Young's modulus with the thickness of PDMS membranes, from thicknesses as low as 200  $\mu\text{m}$ . They observed that the chain reorganization during polymerization was dependent on the thickness of the molded PDMS: Young's modulus was therefore also dependent on the polymerization conditions. Since the resulting mechanical properties were dependent on this reorganization, they differed with thickness. Considering elastomeric silicone as a uniform material (like metallic ones [223], [224]) can therefore be misleading, since these materials depend on the reorganization of the monomer layers during polymerization [192]. For our type of RTV-silicone (RTV #81180, [225]), no size-dependent material properties have yet been reported in the literature. For the design of more efficient MEMS devices, through tensile testing, we therefore decided to check the dependence of the elastic properties with the thickness of the RTV silicone material.

##### 4.5.1. Tensile tests setup

**Preparation of the samples.** The single component RTV-silicone studied was purchased from Permatex<sup>Inc</sup>. This RTV-silicone material is a single component in the form of a very viscous paste. It has a good adhesion to metal and silicon substrates due to the presence of silane groups in the formulation [225]. When brought into contact with the moisture of the air, it polymerizes with very high elastic properties (tough and flexible rubber). Properties (from supplier) of uncured material and cured material after 7 days at 25°C and 50% relative humidity are shown in Table 4-1 and Table 4-2. The complete duration of polymerization (generally 24h [225]) depends on the thickness, temperature and humidity content of the surrounding air.

Properties	Typical Value
	Uncured material
Chemical Type	Acetoxy silicone rubber
Appearance	Red non-sag paste
Odor	Mild acetic
Extrusion rate @ 25°C, (g/min)	> 220
Flash Point °C	> 93

Table 4-1: Properties of uncured RTV-Silicone product from supplier PERMATHEX ( [225]).

Given the limited amount of published data in the literature and from this supplier, we analyzed the RTV-silicone material mechanical properties using tensile tests. For tensile tests, a casting method [226] was used to make shouldered bar shaped (or dog-bone shaped) test samples (denoted samples B) and rectangular ones (denoted samples A) with corresponding aluminum molds (*cf.* Figure 4-5). After curing, the bars were cut from moulds and the excess RTV silicone on the sides was removed with a scalpel. A total of four parts were produced. Prior to testing, the samples were degassed in a vacuum chamber to prevent the formation of microbubbles.

Mechanical properties	Typical Value
	Cured material
Hardness (Shore A)	> 20
Elongation, (%)	> 350
Tensile Strength (MPa)	> 1.5

Table 4-2: Properties of cured RTV-Silicone product from supplier PERMATEX ([225])

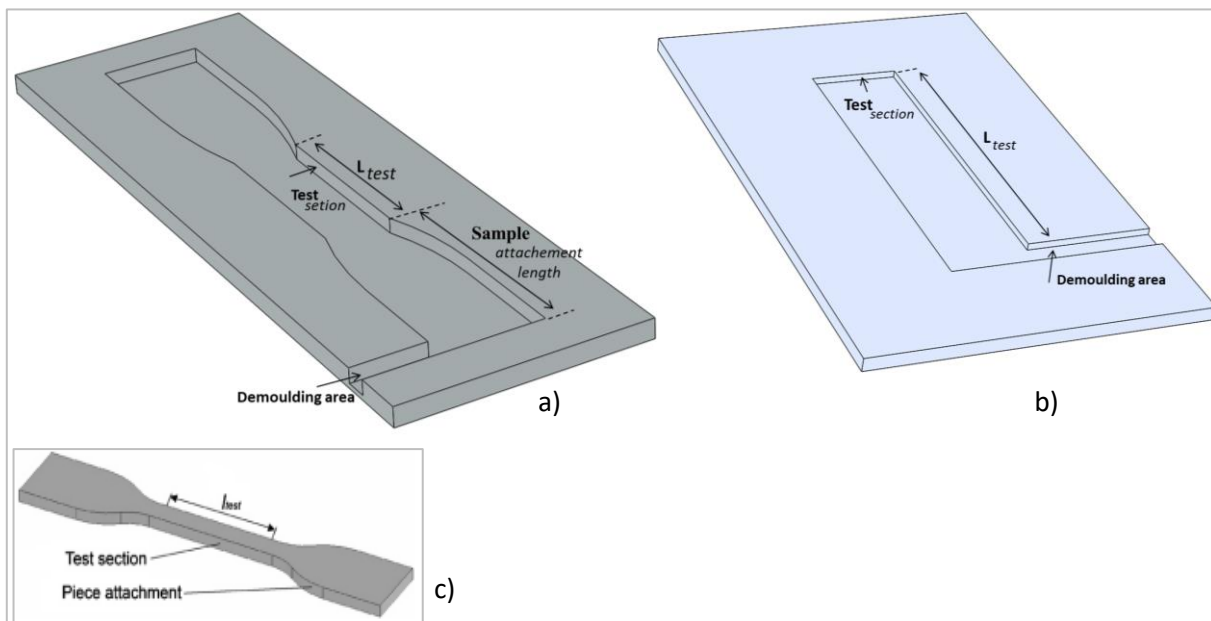


Figure 4-5: a) Mould for shouldered test bar, denoted sample B (thickness of 3 mm); b) Mould for rectangular samples, denoted B (thickness of 1mm); c) 3D Shouldered test bar (sample B) according to DIN53504 [110].

**Test and analysis procedure.** The mechanical properties of the RTV-silicone bars were measured by tensile tests at room temperature. The widest end sections of the shouldered bars are to be attached to the handles of the tensile device and the thinnest bar is the actual test section (*cf.* Figure 4-5). We focused on the dependence of the elastic modulus on thickness for samples of different thicknesses (two samples of 1 mm and two of 3 mm thicknesses). These moulded RTV-silicone specimens underwent the same curing conditions. Thus we tested two thin rectangular samples (*cf.* Figure 4-5 b) - denoted A - of  $24 \times 12.5 \times 1 \text{ mm}^3$  and two thick shouldered bar samples - denoted B - of  $35 \times 12.5 \times 3 \text{ mm}^3$  (*cf.* Figure 4-5 a). The specimens were mounted onto specially designed grippers, aligned and held firmly (*cf.* Figure 4-6 a) and b)). The test machines ran in position-controlled mode. Their grippers pulled the test bar on both ends at a constant strain rate while a force sensor measured the resulting force. This method was used to determine the elastic modulus for the characterized material (through the slope of the stress-strain curve) and also to determine the hysteresis (by load-unload steps).

The benches we used for tensile tests on A-samples was a Bose Electroforce machine with 350 N of maximum load capacity and a resolution of  $1 \mu\text{N}$ . Tensile tests on samples A were carried out with a maximum force of 22 N at 10 measures per second.

For samples B we used an MTS Criterion electromechanical machine with a capacity of 100 kN.

After sample installation, a 3 mm/s displacement speed was applied. The strain was measured either with a mechanical extensometer, or with a laser extensometer (EIRO5). This last one measured the distance between two reflective tapes stuck on the samples. These tapes delimited the test section on the specimens.

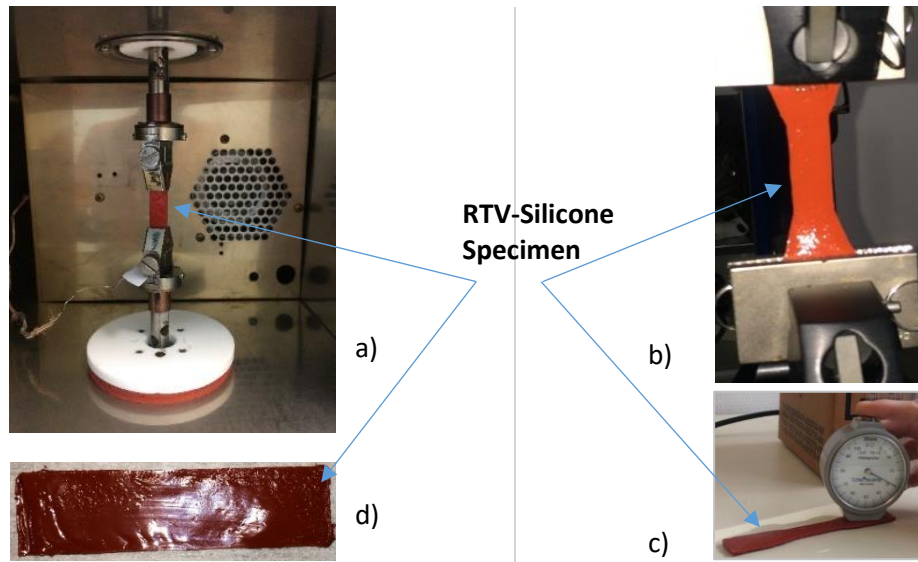


Figure 4-6 : a) Test setup for sample A (0.9mm); b) Test setup for sample B (3mm); c) Hardness test of sample B with a durometer. d) Picture of the rectangular sample.

#### 4.5.2. Tensile test results and discussions

**Stress vs. strain relations for large strains.** Since RTV-silicone elastomer are capable of developing large amounts of strain (much larger than 10%), according to references [110] and [221], the correct description of material elongation is obtained by using the true stress ( $\sigma' = \sigma (1 + \epsilon)$ ) and the true strain ( $\epsilon' = \ln(1+\epsilon)$ ), with the Young modulus  $E$  defined by the Hooke's law:  $\sigma' = E \cdot \epsilon'$ . For small values of  $\epsilon$ , the Hooke's law reduces to  $\sigma = E \cdot \epsilon$ .

**Corrected strain.** With a shouldered bar geometry, the strain in the wider end sections of the sample is much smaller than the strain  $\epsilon_{test}$  in the test region (thinner part of the specimen). However, the end sections contribute significantly to the total strain  $\epsilon_{total}$  that is automatically measured by the machine. Therefore, in order to calculate the deformation in the test area, it is necessary to correct the total strain value  $\epsilon_{total}$  measured by the machine by using a correction factor  $m$  (defined by  $\epsilon_{test} = m \epsilon_{total}$ ) [221]. This correction factor may not remain constant for large strains, indicating a nonlinear behavior of the material.

**Measured stress – strain curves.** The test machine gives the value of  $\epsilon = \epsilon_{total}$  versus applied force to the whole shouldered bar specimen. The stress  $\sigma$  inside the test section can be determined by dividing the force by the initial cross-section area of the test strip. Then  $\sigma$  versus  $\epsilon_{total}$  was first plotted in the “total strain curve”.

However,  $\epsilon_{test}$  was simultaneously measured through a direct laser measurement on the test section. Therefore, it was possible to plot directly  $\sigma$  versus  $\epsilon_{test}$  in the “test section strain curve” and determine the correction factor  $m$  for low strains.

Then, according to the work of Schneider *et al.* [221], we drawn the “corrected strain curve”, representing  $\sigma$  versus  $m \epsilon_{total}$  (determined from the machine measurements), in order to check the validity range of the correction factor  $m$  by comparison with the “test section strain curve”.

Finally, according to Liu *et al.* [110], the true stress  $\sigma'$ , which takes in account the reduction of this cross-section area under large elongations, is given by  $\sigma' = \sigma (1 + \epsilon)$ . It was plotted versus true strain  $\epsilon' = \ln(1 + \epsilon)$  in the “true strain curve”. This representation should eliminate nonlinearities coming from test cross-section variations and should therefore remain linear in a larger range of strains.

- **Results for the 3mm thick samples.**

Stresses and strains of the two 3 mm thick RTV-silicone test samples under tensile test are represented in Figure 4-7 and Figure 4-8. For clarity, corresponding measurement errors are given only for a few measuring points. Note that the extensometer used with sample 1 (Figure 4-7) was mechanical: its measuring range was limited and below the elongation-to-break. Sample 2 (Figure 4-8) was tested with a laser extensometer, whose measuring range exceeded the elongation-to-break. This difference in extensometer results in the fact that the elongation in the test area of sample 1 is limited to approximately 20%, whereas the test was carried out up to breakage.

On the other hand, it was possible to measure the elongation of the test area for sample 2 up to breakage. For the measurements corresponding to the test section, only the results of sample 2 will therefore be used. The analysis of the corresponding test section curve shows that the 3 mm thick test pieces have a breaking strength of 350 kPa and an elongation-to-break (measured in the test section) of 91%.

In both figures we observe that the model of a constant correction factor  $m$  becomes inaccurate for large strains. A close-up view of the linear part of the "trustrain" curves of samples 1 and 2 is shown in Figure 4-9 for a strain range up to 8%. This range corresponds to the measurement range we focus on in our work. It allows us to determine the associated Young's modulus (measured for low strains) which is found to be around 0.96 MPa (average value obtained on sample B2).

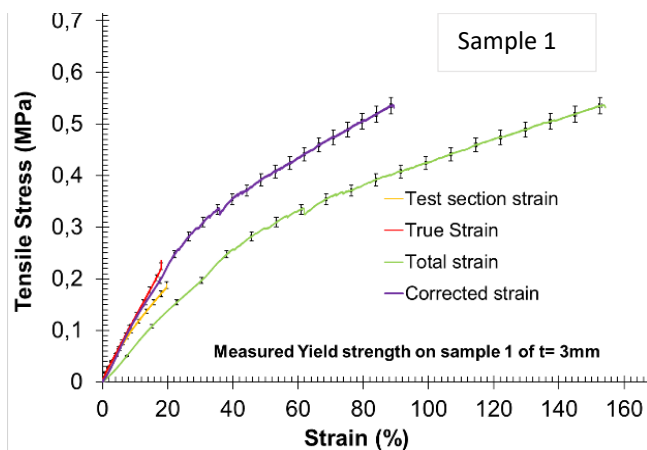


Figure 4-7: Stress-strain diagram for the first 3 mm thick RTV-silicone sample, B<sub>1</sub>, including true and corrected stress-strain curves. Mechanical extensometer.

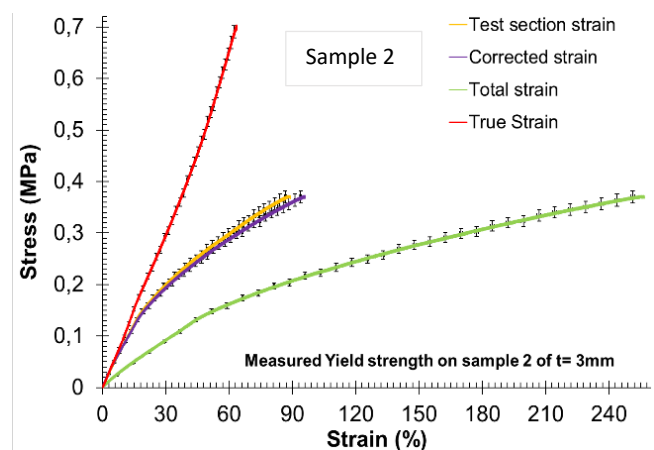


Figure 4-8: Stress-strain diagram for the second 3 mm thick RTV-silicone sample, B<sub>2</sub>, including true and corrected stress-strain curves. Laser extensometer.

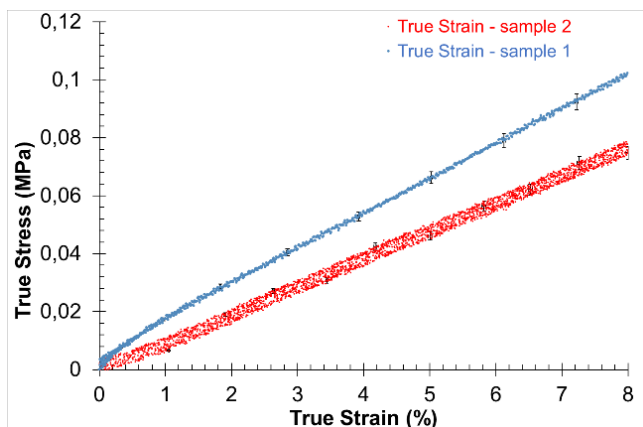


Figure 4-9: Close-up view of Figure 4-7 and Figure 4-8 showing only the true strain curve for B<sub>1</sub> and B<sub>2</sub> samples (3mm thick)

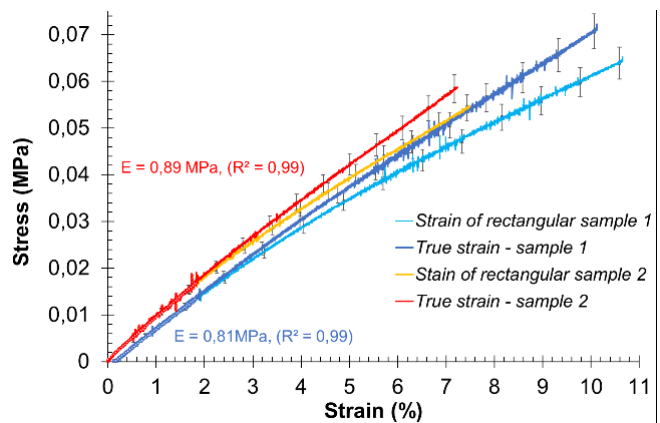


Figure 4-10: Stress-strain diagram for the two samples of 1mm thick RTV-silicone (samples A<sub>1</sub> and A<sub>2</sub>) including true stress-strain plots.

Unlike the behavior of solid materials such as mild steel for example, there is no "necking", which is linked to the decreases in cross-section, before rupture. On the contrary, it presents a uniform plastic deformation until rupture. It may be related to the fact that the silicone cross-linked fibers get cut as the traction continues beyond the elastic zone, leading to complete failure without the passage through a non-uniform plastic reduction of the sample cross-section.

- **Results for the 1mm thick samples.**

Figure 4-10 presents the stress-strain diagrams of two 1mm thick specimens, with measurement errors. For clarity, corresponding measurement errors are given only for a few measuring points. The true strain curves are linear and

these samples were found to have an average Young's modulus of about 0.85MPa, which is about 11% lower than with the thicker ones samples.

- **Comparison and discussion**

The thickness reduction seems to cause a decrease of the modulus of elasticity, which may indicate a different reorganization of the polymer chains during the crosslinking compared to thick samples. Stress and elongation at breakage (0.35 MPa, 91%), measured on the thick samples shows a weaker material than described in the manufacturer's reference data in (> 1.5 MPa, 350%).

RTV-thickness (mm)	3	1
Young modulus* (MPa)	0.96	0.85

Table4-3: Summary table of the Young's modulus and thicknesses of test samples subjected to tensile tests.

A comparison to the two most used silicones that are RTV 615 ( $E = 1.528$  MPa) and Sylgard 184 ( $E = 1.82$  MPa) [221], shows that this RTV-silicone (#81180) is about 50% more elastic. It is also more elastic compared to PDMS ( $E \approx 1.5$ MPa) which, for a thickness of  $350\mu\text{m}$ , presents a maximum deformation of 140% with an ultimate tensile strength of 25 MPa.

In addition, the Young's modulus of PDMS tends to increase as the thickness decreases. This trend is related to the often-used spin-coating technique, which influences the reorganization of the polymer chain during the spreading of the PDMS causing shear stress in the radial direction [110]. This phenomenon occurs during polymerisation: polymer chain coils reorder depends on the initial thickness deposited before polymerization, leading to a stronger cross-linked network. This may be due to the amorphous nature of this material and therefore to the shape of crosslinked networks of the polymer chains.

On Figure 4-10, the deviation of the Young's modulus for the same 1mm thick samples can be related to the viscoelastic properties of RTV-silicone, which occurs when the strain rate is slightly different during the tensile test. To get an idea of this viscoelasticity, we carried out a test of hysteresis (loading-unloading test with the same strain rate) on 3mm thick samples. The resulting stress strain curve is shown in Figure 4-11. Material loading correspond to "Rise" and material unloading to "Descent" on the Figure 4-11 legend.

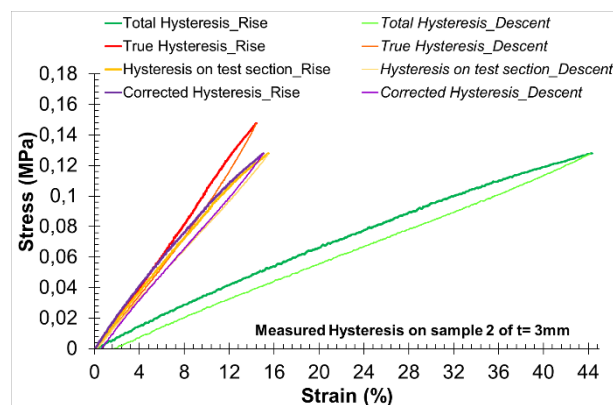


Figure 4-11: Hysteresis curve measured on the 3mm thick A1 sample. Traces of true and corrected stresses and deformations are also plotted.

As explained in section 4.4. , during viscoelastic deformation of the material, the latter absorbs energy, part of which is lost mainly in the form of heat which deflects the curve of the unloading phase, the area between both curves is related to the amount of energy absorbed by the material. An analysis of this curve shows that, there is a small hysteresis that manifests beyond 4% deformation.

#### 4.6. Characterizations of single membranes: static pressure measurement

After the mechanical characterization of the RTV-silicone material through tensile tests, we proceed to the mechanical characterization of the membranes through bending tests. Each sample that was tested contains 3 membrane (denoted M1 to M3 on the figures). Samples are denoted EchI to EchIV, according to the geometry. The mechanical behavior of membranes (constituted of either a planar silicon spring or a central silicon disc embedded in RTV-silicone, cf. Figure 4-24) are investigated by the load-deflection method [216], [227] to measure their Young's

modulus and residual stress. Two types of tests were carried out to confirm the experimental values of elastic properties: the first test consisted in applying uniformly loaded static air pressure and measuring the resulting membrane deflection. In the second test, we imposed a displacement at the center of the membrane and measured the resulting stiffness. Two cases are thus considered:

- circular membranes uniformly loaded
- circular membranes loaded at the center.

#### 4.6.1. Uniformly loaded circular membrane

**Setup presentation.** To study the deflection capacity of membranes and their hermeticity to gases, pressurized air was sent under the membrane and, thanks to a laser position sensor, the resulting displacements were measured. This method is also called the “swelling test”. The pneumatic air pressure was applied from a side aperture below the membrane. Then, by adjusting the input pressure, the membrane center deflection was measured by a laser position sensor (characteristics of the sensor in chapter 5, Figure 5-16). The experimental setup scheme for characterization is given in Figure 4-12.

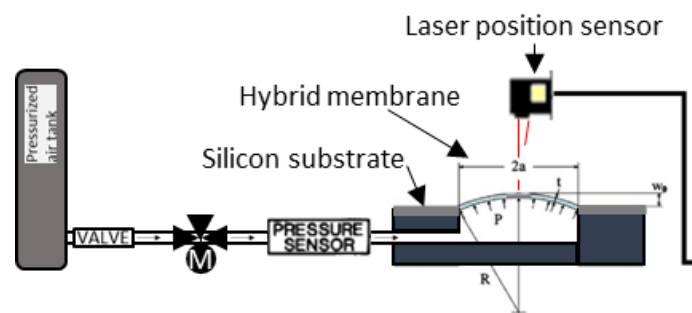


Figure 4-12: Experimental setup for Membrane static pressure characterization, with a schematic showing membrane geometry and loading conditions.

Figure 4-13 shows pictures of the laser sensor setup with membrane in operation during deflection tests. In a), a membrane with a spiral silicon and in b) of membrane without spiral but with only a central disc in silicon in its center.

Since membranes have a large diameter of 5 mm, the load-deflection test was chosen for characterization. Supposing the deflection of the membrane has a hemispherical shape, the analytical equation of the small deviation of the membrane is given by equation 4-1 (deflection of a membrane loaded by air pressure) ([218], [228], [229]):

$$P = \frac{2.67e}{r^4} \left( \frac{E}{1-\nu} \right) w_0^3 + \frac{4e}{r^2} \sigma_0 w_0 \quad \text{Eq. 4-1}$$

where “P” and “w<sub>0</sub>” are, respectively, the uniform pressure applied to the membrane and the resulting maximum deflection measured at its center. “e”, “r” and “σ<sub>0</sub>” are respectively its thickness, its radius and its residual (or internal) stress. “E” and “ν” are respectively the Young's modulus and the Poisson coefficient.

Since the above equation has the form  $P = a w_0^3 + b w_0$ , the internal stress and Young's modulus appear respectively in the linear term of  $w_0$  and in its cubic term. Therefore, these two quantities are independently determined on the deflection versus pressure curve by fitting the data to Eq. 4-1. The size and composition of the membrane used during this test are shown in Table 4-4.



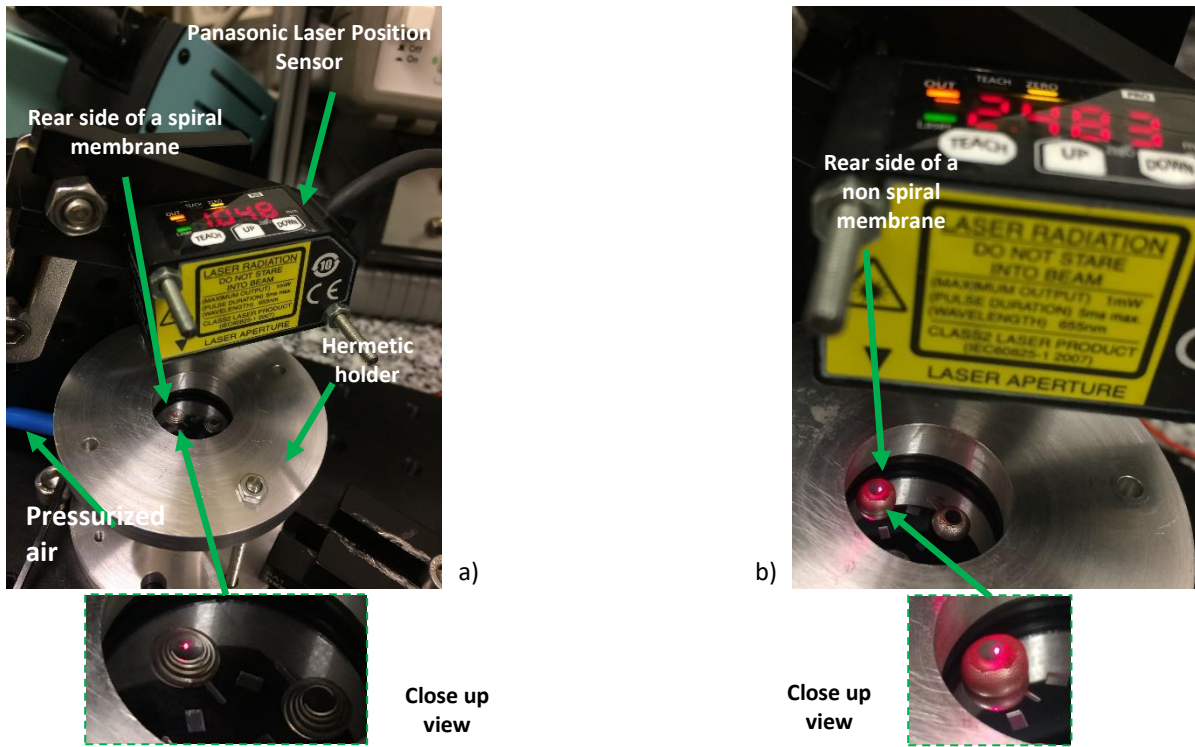


Figure 4-13: Deflection image of membrane a) with silicon spiral b) without spiral (with only a silicon central disc).

Samples names	RTV-silicone thickness (mm)	Silicon Spiral thickness (mm)	Silicon Disc thickness (mm)	Silicon Disc diameter (mm)	Membranes thickness ( $\mu\text{m}$ )	Thickness notation (RTV overlay $\mu\text{m}$ /silicon thickness $\mu\text{m}$ )
III-a	0.094	---	0.070	2	164	94/70
III-B	0.094	0.070	0.070	2	164	94/70
IV-a	0.100	---	0.100	2	200	100/100
IV-B	0.100	0.100	0.100	2	200	100/100

Table 4-4: Samples used for the measurement of membrane properties

**Results of the uniform loading test.** Three different groups of membranes of a 164 and 200  $\mu\text{m}$  thicknesses were tested (*cf.* details in Table 4-4). For each group of RTV-silicone membranes including silicon elements, two different geometries (with or without spiral) were tested. Moreover, the experiments were carried out after two different thermal treatments. We first performed this experiment on membranes at room temperature after fabrication. Then, to evaluate the influence of temperature on their elastic properties, these membranes were heated up to 300°C for 20 min and tested again at room temperature (details concerning the experimental setup and the method are given later on, in section 4.8. ). The experimental results for 94/70 membranes are shown in Figure 4-14.

Note that these membranes are composite membranes comprising silicon and polymer elements, therefore Eq. 4-1 will give Young's modulus and residual stress values for an homogeneous membrane that is « mechanically equivalent » to the real one.

**Silicon spirals have a clear effect on the membrane stiffness** as seen on Figure 4-14: spiral-free membranes are much more compliant than the others (as expected, the silicon spiral is causing an additional stiffness). For example, for a pressure of 0.02 MPa, a membrane deflection of 150  $\mu\text{m}$  is obtained with the silicon spiral whereas, for the same pressure and for membranes without spiral, a deflection up to 600  $\mu\text{m}$  can be reached. However, the displacement of the membrane with spiral is more linear than without a spiral.

**After being heated at 300°C**, the membranes become more elastic: for the same pressure of 0.02MPa, the deflection of the membranes with spiral is 2 times larger than without heating. For the same pressure and for the membranes without spiral, the deflection is 3.25 times larger with heating than without heating. The curves are also less linear after heating.

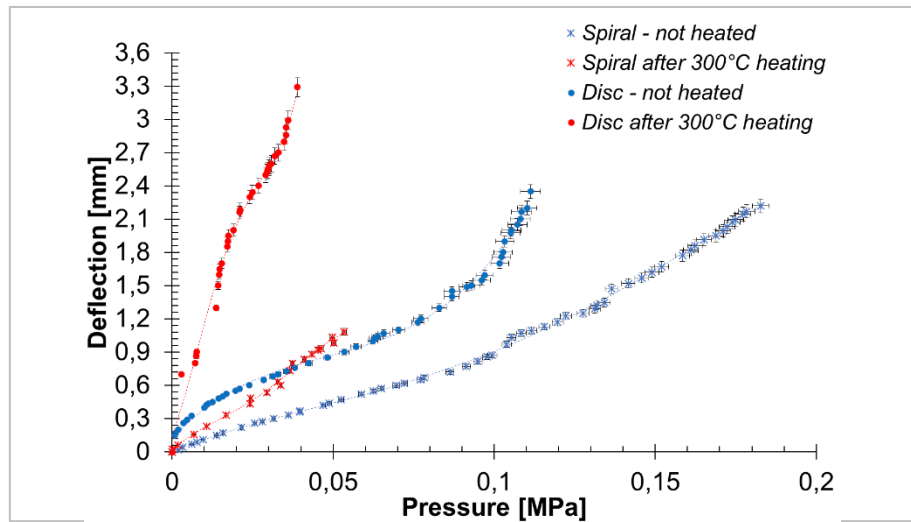


Figure 4-14 : Charge-deflection curves of two 164 $\mu$ m thick samples III-a-Disc and III\_B-Spiral before and after heating to 300°C. Red (resp. blue) lines show the behavior after (resp. before) heating.

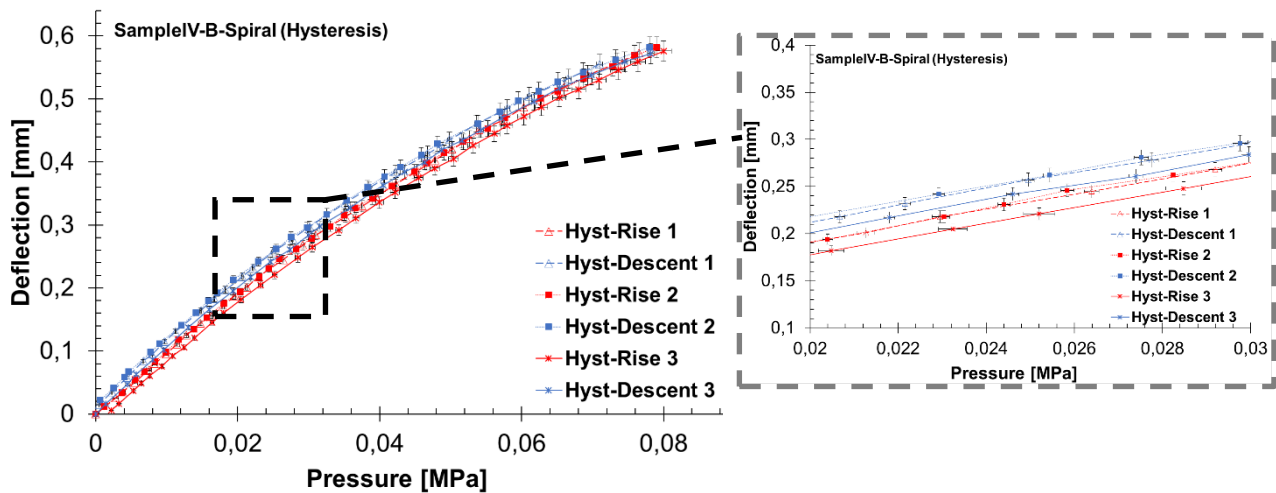


Figure 4-15 : On the left, hysteresis measured on the "IV-B-Spiral" sample comprising a 200 $\mu$ m thick membrane with spiral . On right side, a zoom on the linear region. Error bars are given in black.

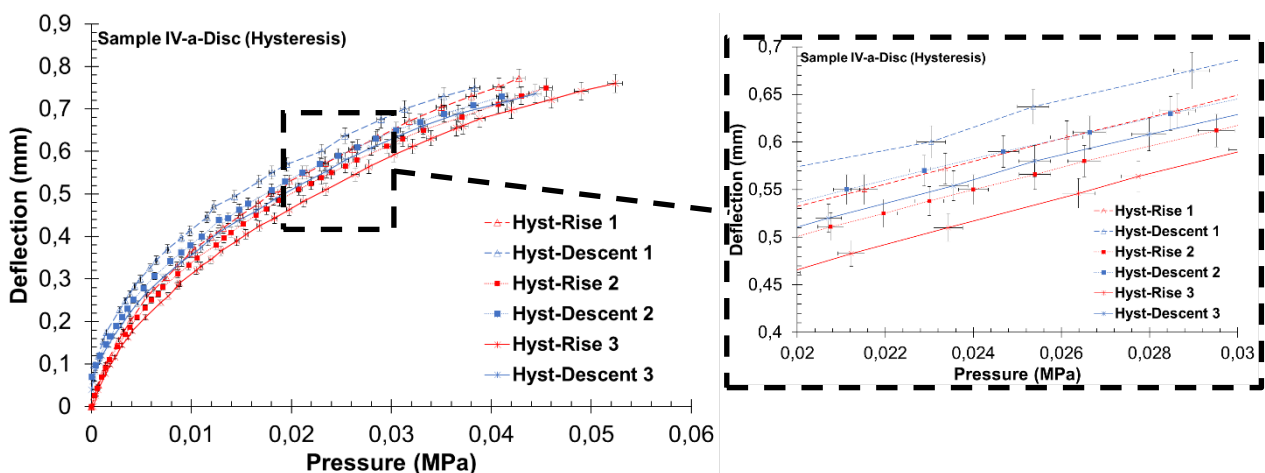


Figure 4-16: On the left, hysteresis measured on the "IV-a-Disc" sample with a 200 $\mu$ m thick membrane with a single disc at its center . On right side, a zoom on the linear region. Error bars are given in black.

**Hysteresis** was checked again for these thin membranes by performing 3 loading-unloading cycles. Results for membranes with spiral are given on the Figure 4-15. Same experiments were carried out for membranes with only a central disk (without spiral) and results are shown in Figure 4-16 . There is a small hysteresis in the membrane responses for membranes with spiral. For membranes without spiral, this hysteresis is larger. Nevertheless, for

deflection lower than 200 $\mu$ m, the membrane response was elastic, and can be reproducibly loaded and unloaded, without significant hysteresis.

**Fitting of the curves.** Figure 4-17 shows the pressure-deflection data obtained from a spiral-free membrane (having only a 2 mm disc in its center, Sample IV-a Disc) and another membrane having a spiral (and a central disc of 2mm). The dashed lines across the data dots represent the polynomial trend curves for calculating the Young's modulus and the residual stresses according to Eq. 4-1. It is found that the measured data for the membrane could be well characterized by this equation. Therefore, these data from the three loading and unloading cycles of each membrane were used to calculate the residual stresses and the Young modulus (assuming a Poisson ratio of  $\nu = 0.5$  [230]).

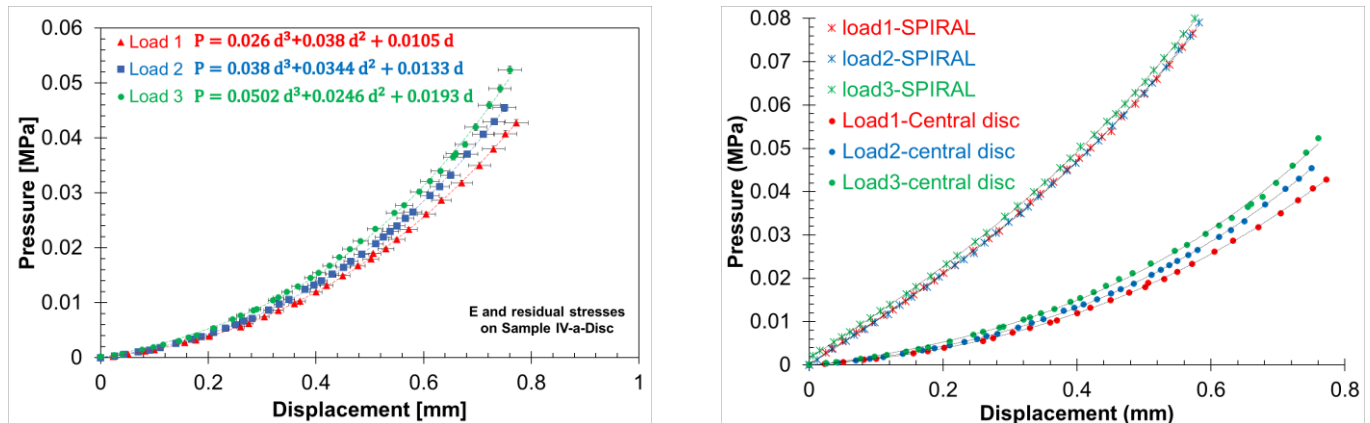


Figure 4-17: On the right, experimental load-deflection characteristics for samples with spirals (sample IV, 100/100, 2mm disc) and without spirals (sampl IV-a, 100/100, 2mm central disc) with fitting data curves from Eq. 4-1 represented in dotted lines. On the left, results obtained only with a central disc (sampl IV-a, 100/100, 2mm central disc).

**The calculated internal stresses and Young's modulus** for samples with and without spiral, before and after the heating step are summarized in Table 4-5 (100/100) and Table 4-6 (97/70). Residual stresses and Young modulus values of samples after being heated at 300°C are presented in brackets. It can be seen from these tables that, for the spiral-free central disk membranes, both the residual stresses (0.06-0.08 MPa) and the Young's modulus (0.46-0.73 MPa) are much smaller than those obtained for membranes with spiral (0.2-0.77 MPa of residual stresses and 1.34-1.35 MPa of Young's modulus).

The values of Young's modulus in bracket (0.42 and 1.2MPa for 97/70 membranes) show that temperature makes the membrane more flexible and may stabilize their modulus of elasticity after the heating step.

Samples (t=164 $\mu$ m)	Young modulus (MPa)	Internal stress (MPa)
III-a Disc (97/70)	0.46 [0.42]	0.06 – [0.14]
III-B Spiral&Disc (97/70)	1.34 [1.2]	0.2 – [0.4]

Table 4-5: Calculated Young 's modulus and residual stress values for 164  $\mu$ m RTV - silicone membrane from experiments using Eq. 4-1. Values without brackets are without heating, values inside brackets obtained after heating at 300°C .

Samples (t=200 $\mu$ m)	Young modulus (MPa)	Internal stress (MPa)
IV-a Disc (100/100)	0.73	0.08
IV-B Spiral&Disc (100/100)	1.35 [1.64]	0.77 [0.78]

Table 4-6: Calculated Young 's modulus and residual stress values for 200  $\mu$ m RTV - silicone membrane from experiments using Eq. 4-1. Values without brackets are without heating, values inside brackets obtained after heating at 300°C.

**Hermeticity.** Most of the data presented here come from experiments in which membrane were inflated with air. Although silicone materials are sometimes considered to be among the most gas-permeable [228], no change in

the pressure inside the fluidic chamber was observed during the duration of our experiments (1h30), which suggests that gas permeation through the membrane may be neglected during such times. This gas permeation should rather depend on the thickness of the deposited RTV-silicone layer.

In addition, Yang [231] proposed to use a vapor barrier layer between the working fluid and the silicone rubber membrane to remedy the permeability problem. However, if the material of this barrier is a rigid body, it may significantly reduce the flexibility of the composite membrane. He found that Parylene C (thermoplastic polymers) proved to be an effective barrier layer with a rather low Young's modulus [231], [232]. Thus, a flexible composite membrane could be made by depositing a thin layer of Parylene C. The common physical properties of Parylene C are listed in [232]. Besides, because of RTV-silicone low thermal conductivity, the heat loss to the outside of the structure is low, which reduces the operating power consumption in the case of a valve for example.

In the next section, we will present the results of the bending tests by pressing the center of the membrane with a pin.

#### 4.6.2. Center-loaded circular membrane

**Setup presentation.** A displacement was imposed on the silicon disc, which is located in the center of the membrane. The resulting stiffness was measured thanks to a 22N load sensor (*cf.* Figure 4-18). This weak force cell was chosen considering the Young's modulus found during the above tensile tests performed on the 1mm thick RTV-silicone test pieces. These tests have shown that this silicone material is very flexible, it does not require the application of great force to obtain a consequent displacement. The test machine used was the ElectroForce<sup>®</sup> 3200 Instrument in controlled displacement mode. The flexion test set-up was fixed to the test machine and the whole set-up was aligned to avoid possible parasitic shear stress. The flexion test mode was set-up to generate an axial displacement of 1 $\mu$ m and a scan time of 50ms.

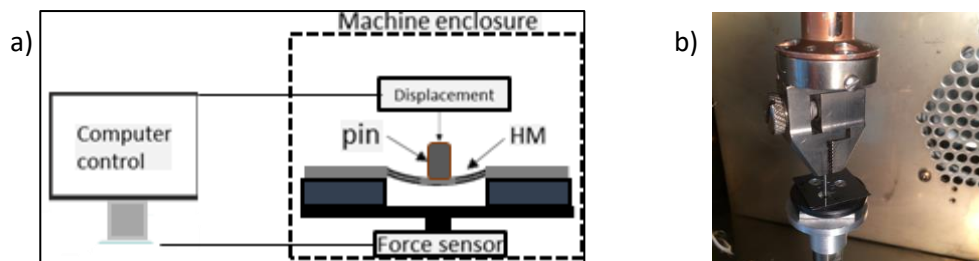


Figure 4-18: a) Block diagram of a computerized measurement system used for concentrically load deflection tests. B) Sample being tested with ElectroForce<sup>®</sup> 3200 Instrument with test set-up fixed.

Recall that all membranes have a silicon core disk of 1 or 2 mm in diameter embedded in a silicone layer. The disc being made of silicon, it stiffens the center of the membrane. In Table 4-8, the composition, the size and the thickness of the membranes used during this test are presented.

Samples names	RTV-silicone thickness( $\mu$ m)	Silicon Spiral thickness ( $\mu$ m)	Silicon disc diameter (mm)	Membranes total thickness ( $\mu$ m)
I-a	94	---	2	164
I-B	94	70	2	164
III-a	94	---	2	164
II-a	100	---	2	200
IV-C	100	100	2	200
IV-A	100	100	1	200

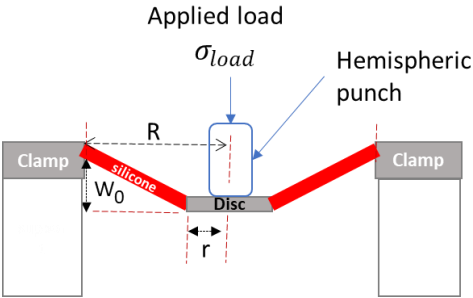
Table4-7: Constitution of the membrane used in the experiment.

It can be assumed that only the annular portion of the membrane, covered by RTV-silicone (and containing turns in the case of spiral membrane), is deformed when a pressure is applied to the membrane. The bending of an edge clamped circular membrane of thickness "e" and radius "R" containing a central rigid disc of radius r whose load is uniformly distributed along the rigid disc was already studied by Timoshenko in 1956 [233], and by Schomburg in 2015 [234]. The equation giving the central load as a function of membrane deflection (deflection of the center disc) is [234]:

$$\sigma_{load} = (b_p e^{\frac{E}{R^4}})w_0^3 + [(4\frac{e}{R^2})\sigma_0 + a_p \frac{e^3}{R^4} \frac{E}{(1-\nu^2)}]w_0 \quad \text{Eq. 4-2}$$

Where,  $\sigma_{load} = F_{applied}/S_{disc}$  is the applied stress on the stiff central disc,  $w_0$  the center membrane deflection,  $a_p$  and  $b_p$  are constants taking into account the presence of the central disc of the membrane :

$$a_p = \frac{16}{3} \frac{1}{(1 - \frac{r^4}{R^4} - 4 \frac{r^2}{R^2} \ln(\frac{R}{r}))}$$

$$b_p = \frac{7 - \nu}{3} \frac{(1 + \frac{r^2}{R^2} + \frac{r^4}{R^4}) + \frac{(3 - \nu)^2}{1 + \nu} \frac{r^2}{R^2}}{(1 - \nu)(1 - \frac{r^4}{R^4})(1 - \frac{r^2}{R^2})}$$


The constants are determined to satisfy the conditions of continuity above at the disc perimeter. It is again an equation of the form  $\sigma_{load} = A w_0^3 + B w_0$  therefore, the Young's modulus and the internal stresses of the membrane can be independently deduced from this equation by using the coefficients resulting from the experimental curve by third order polynomial fitting. For membranes with  $R = 2.5\text{mm}$  and  $r = 1\text{mm}$  (2mm central disk), we obtained  $a_p = 13.74$ ;  $b_p = 9.80$ .

**Results of the tests.** The concentrically loaded-deflection test measurements were carried out on four different samples, and repeated with three identical membrane for each of them (repeatability). The results are shown in Figure 4-19, Figure 4-20 and Figure 4-21.

Results obtained with membranes with and without spiral (samples I-a and I-B) of the same thickness ( $164\mu\text{m}$ ) and with a 2mm central disk are presented in Figure 4-19. It can be noted that, for each sample, the three membrane keep the same trend, which shows a good repeatability of microfabrication. The small variations can be explained by the flatness of the substrate (silicon wafer) which impacts on the uniformity of the thickness of the membrane during microfabrication, and also the inhomogeneity of the etching by DRIE (approximately  $5\text{-}10\mu\text{m}$ ) that could have contributed significantly. An analysis of this figure shows that the spiral-free membrane (samples I-a) have a displacement capacity approximately twice as high as that with spiral (sample I-B) for the same thickness, which confirms the results of the previous section. Indeed, samples with Silicon spirals move up to about 1mm before breaking because of the high rigidity and linearity of the silicon material [235]. By increasing the stress applied to the center of the membrane, the spiral is deformed until a maximum elongation, beyond which it would break since its embedding points at the membrane edge will be over stressed. For an applied pressure of 0.02 MPa, the deflection is almost identical for all membranes of the same kind (about 0.35 mm without spiral and about 0.2 mm with spiral). Beyond that, as the pressure increases, the spiral membranes have a greater deformation flexibility up to their breaking limit of 1mm. Spiral-free membrane can deform beyond this limit to reach displacements up to more than 2 mm.

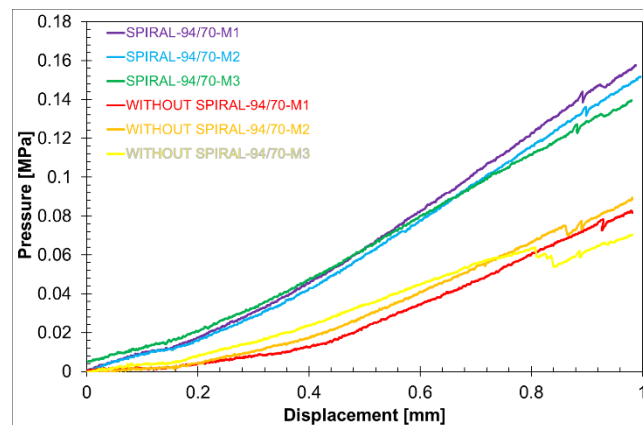


Figure 4-19: Measurements results on membranes with and without spiral (*i.e.* with only a central disc) of the same thickness (94/70). Central disk diameter : 2mm. 3 samples I-a (without spiral) and 3 samples I-B (with spiral).

Figure 4-20 concerns membranes with spirals (samples IV-C, IV-A) with different central disc diameters (1mm and 2mm). This figure allows a comparison between two samples types: IV-C (spiral and disc of 2 mm) and IV-A (spiral and disc of 1 mm) with the same thickness (200  $\mu\text{m}$ ) but different central disc diameters (1mm & 2mm). For each sample type, three identical membranes are tested. An analysis of this figure shows that there is not a great difference in stiffness between these membranes, even if the central disks diameter is doubled. The plots are almost equivalent up to a deflection of 0.65mm. The M2 membrane of sample IV-A (1mm central disk) deviates a bit, but this may be related to a defective spiral problem. The advantage of using a membrane with a 2mm central disc is mainly related to the swept volume and the ease of integration of actuators because it has a larger surface.

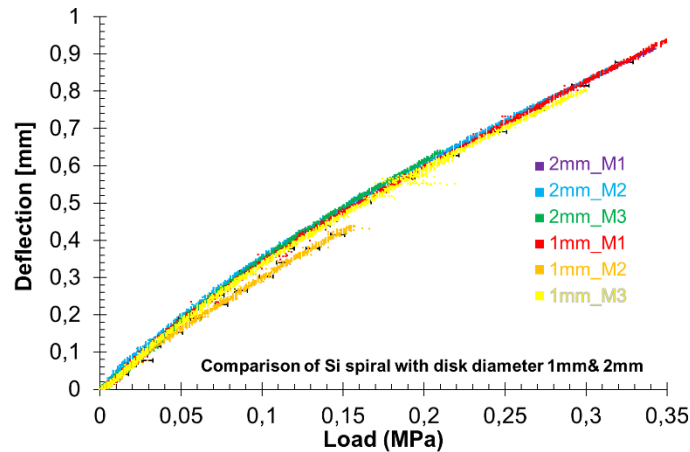


Figure 4-20: Results obtained on two samples with three membranes of the same thickness, (100/100 so 100 $\mu\text{m}$  thickness for both RTV and Si with a 100 $\mu\text{m}$  of RTV overlayer, *i.e.* 200 $\mu\text{m}$  of total thickness) having all identical spirals, but with different central disc diameters (1mm and 2mm)

Results for membranes with spirals (or without spiral) of different thickness are presented in Figure 4-21 (samples with spiral I-B and IV-C on the left; samples without spiral I-a, III-a and II-a on the right). This figure is a comparison of membrane with identical spirals and disc diameters but with different thickness of Silicon and RTV. In sample I-B, the thickness of membranes is 164  $\mu\text{m}$  (94 $\mu\text{m}$  RTV + 70 $\mu\text{m}$  Si) thick while the total thickness of sample IV-C is 200  $\mu\text{m}$  (100 $\mu\text{m}$  RTV + 100 $\mu\text{m}$  Si). We can see that all three membranes of a same sample fit perfectly together, which shows the very good reproducibility of manufacturing. The membrane stiffness is larger with a larger thickness, but up to a deflection of almost 400 $\mu\text{m}$ , the membranes have the same behaviour. For application in the micro-machine, the highest target displacement would be 300 $\mu\text{m}$ , so these membranes are perfectly suited for our application.

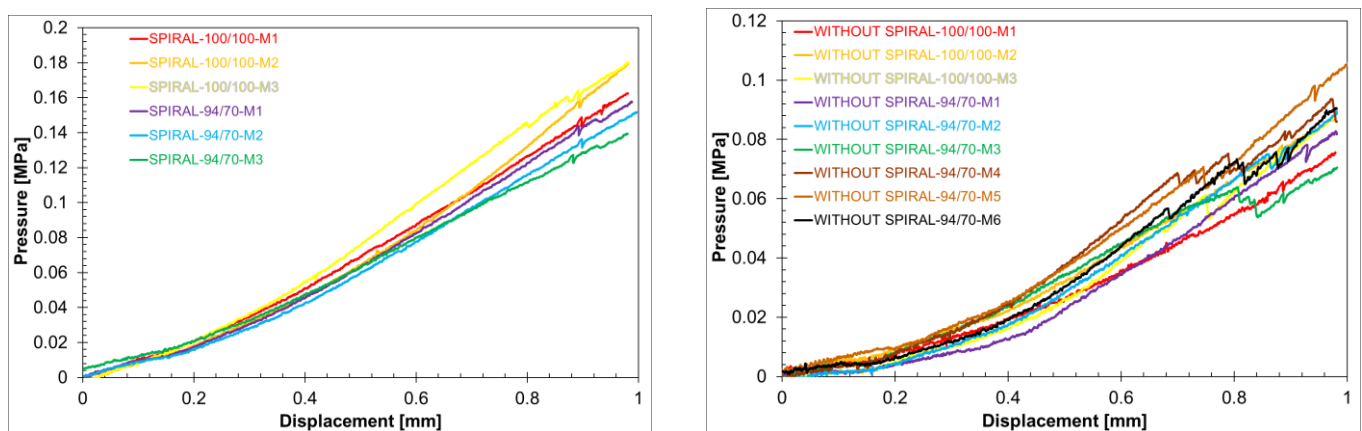


Figure 4-21: Result of deflection versus load of different thicknesses (164 $\mu\text{m}$  vs 200 $\mu\text{m}$ ) from identical spiral membranes (left) and for identical membranes with only a central disc (right).

**Effect of heating the membrane to 200 °C.** The behaviour of the I-a type sample after being heated at 200°C, and then naturally cooled at 23°C, is shown in Figure 4-22. Details concerning the experimental setup and the method used for the heating process are given later on, in section 4.8. Although the membranes behavior is different after heating at 200 °C, the difference is kept reasonable: the response fluctuates from its initial behavior for pressures between 0.05 and 0.3 MPa with a maximum deviation of about 20%. Therefore, heating the membrane at 200 °C has a little influence on its mechanical properties.

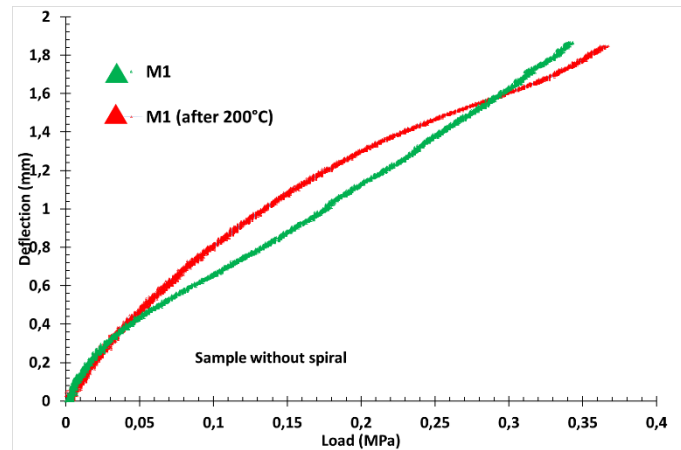


Figure 4-22: Comparison curves of the membrane M1 of the sample I-a Disc, before and after heating at 200°C.

**Young's modulus and residual stress.** To determine the Young's modulus and the residual stresses, we proceed to the fitting of the curve coming from the membrane M1 of the sample without spiral before heating à 200 °C. Thus, by identification with Eq. 4.2, we can determine:

- The Young's modulus  $E = 0.48 \text{ MPa}$
- The internal stress  $\sigma_0 = 8 \text{ MPa}$ .

The Table 4-8 summarizes the results of this section corresponding to the Young's modulus of all the different membranes tested above. This table shows an overview of the elasticity of the RTV-silicone alone and when combined with spiral and/or silicon disc.

Samples	Thickness (mm)	E (MPa)
A1	3	0.96
A2	1	0.85
Without Spiral	94/70	0.46
With spiral		1.34
Without Spiral	100/100	0.73
With spiral		1.35

Table 4-8: Summary table of the results of calculations on the Young's module

**The stiffness of membranes.** The calculation of the stiffnesses was made for the same membranes previously presented (without heating).

– **For the membranes without spiral**, the corresponding stiffness are given in the Table 4-9. It can be seen that for spiral-free membranes with a thickness of 94/70 the stiffness ( $\sim 0.08 \text{ N / mm}$ ) is lower than that of 100/100 ( $\sim 0.11 \text{ N / mm}$ ). Therefore, the membranes become stiffer as the thickness increases. To give an idea of mass, it would take about 8 g to obtain a deflection of 1mm with membranes of thickness 94/70 whereas it would take 11 g for those of 100/100.

– **For the membranes with a spiral** (hybrid spiral membranes), the results are summarized in Table 4-10. It is also observed here that the stiffness increases with the thickness of the membrane which is logical. For membrane with a thickness of 94/70 the stiffness is  $\sim 0.20 \text{ N / mm}$  while for membrane 100/100 the stiffness

is  $\sim 0.22$  N / mm. In other words, to obtain a displacement of the membrane of 1 mm, it takes about 20 g for those of 94/70 and 22 g for that of 100/100.

Types of membranes	Membrane reference	Average of k per membrane (N/mm)	Average k for each membrane geometry (N/mm)
RTV/Disc : 94/70 (without spiral)	I-a_M1	0.077	0.079
	I-a_M2	0.064	
	I-a_M3	0.093	
RTV/Disc : 100/100 (without spiral)	II-a_M1	0.096	0.11
	II-a_M2	0.14	
	II-a_M3	0.08	

Table 4-9: Comparison of stiffnesses for membranes without spirals

Types of membranes	Membrane reference	Average of k per membrane (N/mm)	Average of k for each membrane geometry (N/mm)
RTV/Spiral : 100/100 (with spiral)	IV-C_M1	0.2164	0.2159
	IV-C_M2	0.2169	
	IV-C_M3	0.2144	
RTV/Spiral : 94/70 (with spiral)	I-B_M1	0.2075	0.2046
	I-B_M2	0.2058	
	I-B_M3	0.2007	

Table 4-10: Comparison of stiffnesses for membrane with spirals

## 4.7. Characterizations of Membrane: dynamic tests

### 4.7.1. Materials and methods

Among the many techniques used in the dynamic characterization of MEMS devices, non-destructive optical measurement systems are the most used because they allow to determine different physical quantities such as resonant frequency, displacement, speed, etc. Depending on the direction of displacement of the moving parts of the microsystem in the measuring plane of the optical measuring equipment, three main technologies have been widely used in the literature for the characterization of microsystems:

- In the vertical (out of plane) direction:
  - The technique of Digital Holographic Microscopy [236] can be used for high-resolution 3D microstructure characterization.
  - The Laser Doppler Vibrometry (LDV) is the most used to measure fast movements.
- In the horizontal (in the plan) direction: Strobe Video Microscopy (SVM) is used to measure motion.

Techniques	Lateral resolution (typical)	Vertical resolution (typical)	Static shape	Dynamic response
Atomic Force Microscopy (AFM)	0.1 nm	0.1 nm	3D	No
Scanning Electron Microscope (SEM)	1 nm	---	2D	No <sup>1</sup>
Optical Microscopy (OM)	<1 $\mu$ m	<1 $\mu$ m	2D	No <sup>1</sup>
White Light Interferometer (WLI)	<1 $\mu$ m	<1 nm	3D	No <sup>2</sup>
Confocal Microscopy (CM)	<1 $\mu$ m	<0.01 $\mu$ m	3D	No
Digital Holographic Microscopy (DMEMBRANE)	<1 $\mu$ m	<1 nm	3D	Yes
Strobe Video Microscopy (SVM)	<0.01 $\mu$ m	<1 $\mu$ m	2D	Yes
Laser Doppler Vibrometry (LDV)	<1 $\mu$ m	<10 <sup>-6</sup> $\mu$ m <sup>3</sup>	No	Yes

Table 4-11: MEMS optical measurement equipments for MEMS device characterization [237]. <sup>1</sup>Dynamic response possible using video capture technique <sup>2</sup>Dynamic response possible using strobe technique <sup>3</sup>Resolution for dynamic response – not static



For more precision, optical measurement methods are summarized in the Table 4-11. They allow static and dynamic measurements. Static measurements allow the identification of physical parameters such as film dimensions, roughness, curvature or plane of a sample, etc. Dynamic measurements provide access to the real-time dynamic response of the microstructure with good resolution (less than 1  $\mu\text{m}$ ) such as vibration amplitude, resonant frequency and phase.

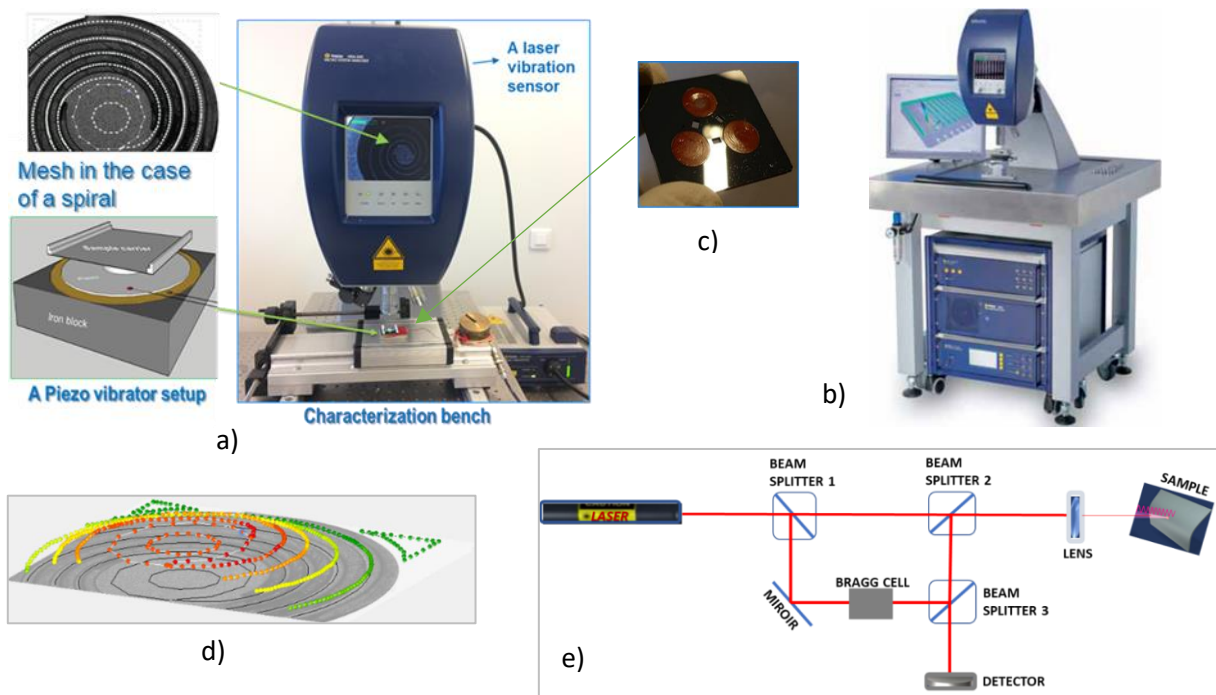


Figure 4-23: a) Membrane mounting setup on MSA-500 Micro Motion Analyzer equipment for frequency measurements. b) Picture of the equipment. c) A sample with three membranes on it. d) 3D motion obtained on the equipment control PC interface. e) Schematic optics of a modified Mach-Zehnder Interferometer.

In our case we used the Doppler laser vibrometer from Polytec (MSA-500 microsystem analyser) to study the dynamic behavior of membranes when submitted to harmonic excitation by a piezo vibrator setup (*cf.* Figure 4-23 a and b). This equipment uses the Doppler effect, in which the light scattered by a moving target contains information on the speed of the illuminated target along the laser axis. The optical frequency of the scattered beam is shifted by  $\Delta f$ , which is proportional to the target speed along the laser axis. The received light wave is mixed with the laser beam (using interferometric techniques) and recombines on a photodetector, which output current will contain the frequency shift  $\Delta f$  from which the target speed can be calculated.

The measuring accuracy of this equipment is from centimeters to picometers in displacement, from 0.02  $\mu\text{m/s}$  to 10 m/s in velocity amplitude and its dynamic measuring range is greater than 170 dB. These features allow measurements that are impossible with holographic or other techniques. The Polytec microscope uses three technologies:

- To measure of out-of-plane motion by laser Doppler vibrometry, the deviation shapes can be measured and displayed as 3D animations by automatically scanning the measurement beam.
- To provide a complete 3D motion measurement (*cf.* Figure 4-23 d), the Strobe video microscopy measures in-plane motion and thus extends the analysis to the in-plane direction.

To measure surface topography for a static shape, white light interferometry is added.

The basic principle of this vibrometer is based on a modified Mach-Zehnder interferometer [238] shown in Figure 4-23 e). This interferometer consists of a laser source, three beam splitters, a Bragg Cell, a mirror and a photodetector. A laser beam of frequency  $f_0$ , emitted by the source, is divided into two beams (using a first beam splitter), one serving as a reference and the other being frequency shifted by  $f_b$  (using the Bragg cell). This latter beam, of frequency  $f = f_0 + f_b$ , is directed towards the surface of the moving structure. The scattered beam and the reference beam are collected at the photodetector. The target velocity  $v(t)$  causes a frequency shift of the backscattered beam  $\Delta f(t)$ :

$$\Delta f(t) = \frac{2}{\lambda} v(t)$$

known as the Doppler frequency. The Doppler Frequency shift is used to measure the component of velocity  $v(t)$ , which lies along the axis of the laser beam. The velocity and displacement of the moving structure are measured from the frequency and phase of the detector output.

After membrane microfabrication, each sample with 3 membrane (denoted m1 to m3) was characterized at room temperature. These dynamic characterizations were performed for 15 samples denoted EchI to EchIV (according to the geometry-with and without spiral- and the RTV/Si thicknesses). In addition, numerical simulations on the finite element software “COMSOL-Multiphysics” giving mechanical and dynamic behavior of the membrane are presented.

### 4.7.2. Results and discussion

**Resonance frequency at room temperature.** There are two configurations of membranes: those with spirals and those without spirals having only disks at their centers. Figure 4-24 shows sketches of these two geometries. Since the silicon spiral is attached to the ends and embedded in the polymer, it will increase the overall stiffness of the membrane. For the spiral-free membrane, only its center is rigid because it consists of the silicon disc, the periphery of which is surrounded by the RTV polymer.

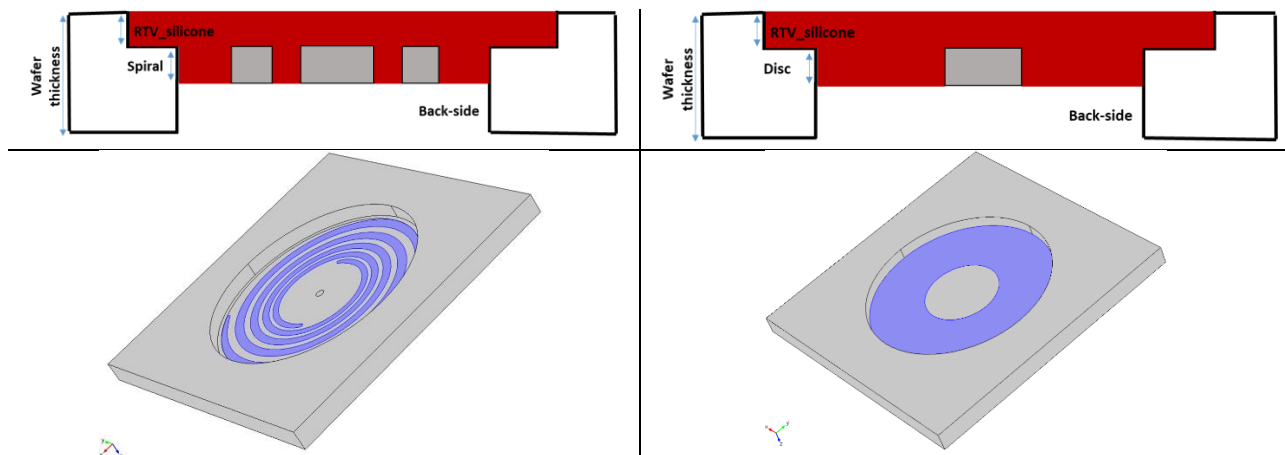


Figure 4-24 : Membrane configurations (spiral and disks shapes). The RTV-silicone layer is colored in blue on the 3D views.

For the membranes without spiral, for each type of geometry (dimensions), the dynamic characterizations were carried out for at least six different membranes, while for those with spiral, for each geometry, the measurements were carried out on at least nine membranes, each one being noted  $m_i$  (with  $i$  the number of the membrane  $i=1, 2 \dots$ ). At room temperature, the  $164\mu\text{m}$ -thick (94/70) membranes with spiral and 2mm diameter central disc presented an average resonance frequency around  $2168.0 \pm 95.5$  Hz, while those with 1mm central disc presented an average frequency of  $2083.5 \text{ Hz} \pm 70.9$  Hz. Membranes with only a central disc of 2mm (*i.e.* without spiral) presented an average resonance frequency around  $856.4 \text{ Hz} \pm 16.3$  Hz.

All frequency measurement results, including those for 200  $\mu\text{m}$  thick membranes, are presented in the with standard deviations (in italics). It can be seen that, for the same membrane thickness, the natural frequency is lower with the spiral-free membrane.

To numerically determine the eigen frequency, we carried out numerical simulation using COMSOL Multiphysics. The mesh was of normal type and contours of the membrane were fixed (*cf.* Figure 4-25). The properties of the RTV-silicone layer used during the simulations corresponded to those found in the bending tests on the non-spiral membranes described above. Since this type of membrane has only one silicon disc in its center, embedded in RTV-silicone layer, during the test the Young's modulus found corresponds well to that of the RTV-silicone layer, since the disc is considered undeformable. Numerical frequencies derived from these COMSOL simulations are also presented in Table 4-12. Comparison of the results (for measurements at ambient temperature) shows deviations between experimental and numerical results of 2.8% for a 94/70 membrane with a spiral and a 2 mm thick central

disc. This deviation increases significantly in the case of membranes without spiral (13-22%). Thus, in the case of spiral membranes, the simulations are therefore consistent with the experimental results.

Membrane	Configurations					
RTV thickness/ Silicon thickness	Central disc 2mm (without spiral)		Spiral+ Central disc of d= 2mm		Spiral+ Central disc of d= 1mm	
<b>Experimental Frequencies</b>						
	Eigen frequency (Hz)	Uncertainty (Hz)	Eigen frequency (Hz)	Uncertainty (Hz)	Eigen frequency (Hz)	Uncertainty (Hz)
94/70	856.4	± 16.3	2168.0	± 95.5	2083.5	± 70.9
100/100	850.2	± 16.3	2794,4	± 69.9	2778.2	± 50.2
<b>Numerical Frequencies</b>						
	Eigen frequency (Hz)	Deviation with experiments	Eigen frequency (Hz)	Deviation with experiments	Eigen frequency (Hz)	Deviation with experiments
94/70	666.6	22%	2230.8	2.8 %	1951.6	6.3 %
100/100	735.87	13%	2632.9	5.8 %	2507.2	9.7 %

Table 4-12: Average of Experimental Resonance Frequencies measured on Membrane. (Deviations mean deviations between numerical and experimental results)

**Natural frequencies**

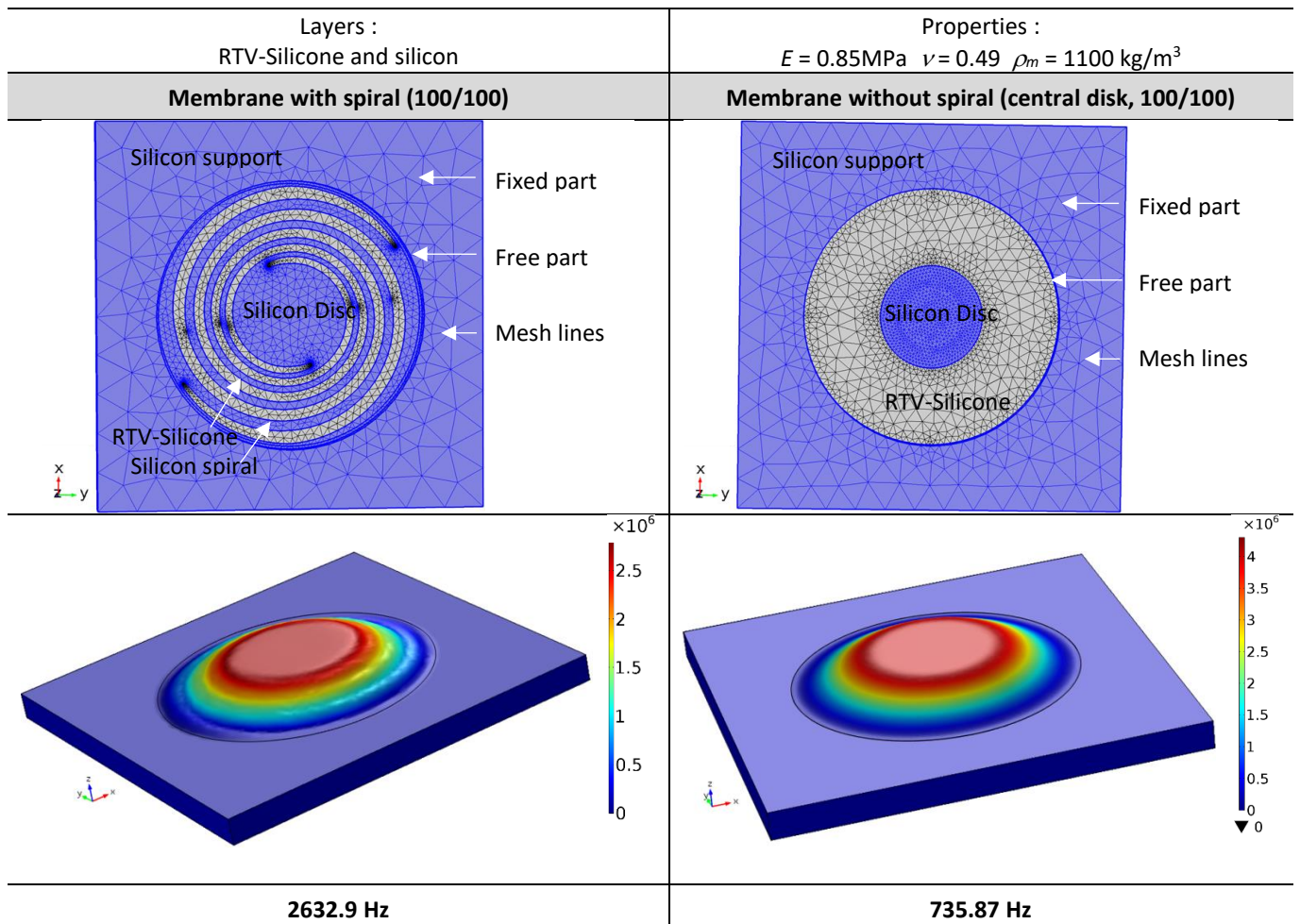


Figure 4-25: Result of the eigenfrequency simulation of the hybrid (100/100) membrane with spiral and 2mm disc

A mechanical-structural model with COMSOL Multiphysics of the membranes stresses was simulated, including the planar spring (cf. Figure 4-26 b) and the disc with RTV-silicone layer (cf. Figure 4-26 b) at room temperature. The objective of the simulation is to check the mechanical stresses corresponding to the maximum displacement of 300  $\mu\text{m}$ . The areas of high mechanical stress are highlighted in the Figure 4-26 for maximum displacement of the central disc and the spiral. The Von Mises stresses are equal to 2,7 MPa for the structure with a spiral, and to 308 MPa for structure without a spiral. Thus, the stresses remain within the yield strength of the silicon materials, which is 7GPa [235]. As expected, the areas of strong mechanical stresses were maximal at the salient points of the planar spiral spring. But, for the disc membrane, the stresses were localized in the zones of attachment of the RTV-silicone layer. We can conclude that the membrane, when used at this level of displacements, will remain within the elastic limit of the mechanical properties of the constituent materials.

While designing the spiral spring to aim at the desired stiffness value or frequency, this 3D FEM model can be used to study the effects of membrane thickness, and/or the effect of the RTV-silicone layer. The geometric parameters of the structure can be easily adjusted to provide inertial effects by increasing the thickness and / or width of the central disc. This last adjustment can allow an increase in the mass of the membrane. According to the simulation, we found that the layer trapped between the spiral turns increases drastically the resonant frequency of the membrane, which is consistent with experimental results (cf. Table 4-12).

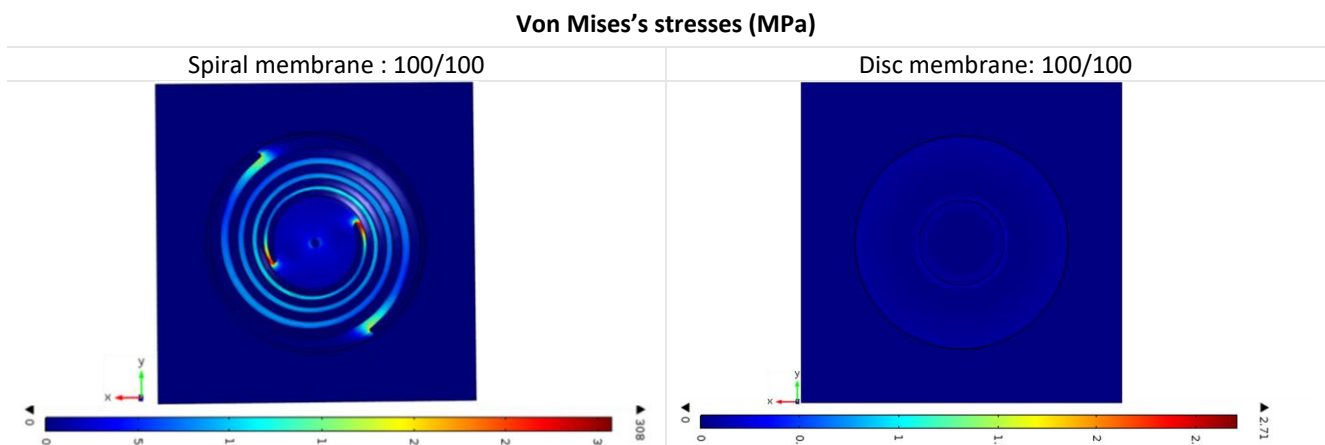


Figure 4-26: Result of the stress simulation of membrane: a) thickness (100/100) with spiral and 2mm disc, b) thickness (100/100) with 2mm disc without spiral

In conclusion, a comparison of the values of Table 4-8 with Table 4-12 shows that, for the same thickness of membrane, the spiral geometry is much more rigid and much more reproducible and repeatable than that with central discs only. In addition, the deflection shape is much better controlled with a spiral geometry based on static air pressure tests and the results of the simulations above. The stiffness results are consistent with those of air pressure tests and those in flexion.

#### 4.8. Influence of thermal treatment on membranes properties

The characterization of the membrane properties evolution with temperature is necessary as the application of the membrane implies continuous operation at a high temperature. Moreover, heating is normally used in the fabrication process including curing and bonding at high temperature (often more than 300°C) for wafers integration and/or packaging. Some studies in literature have shown that temperature has an impact on PDMS ( $E \approx 750 \text{ kPa}$ , which is also a stable rubber physically and chemically at room temperature). Indeed, Liu *et al.* [192] showed the influences of heating temperature on mechanical properties of PDMS (Young's modulus and ultimate tensile stress). They showed that the mechanical properties are independent of heating time for low temperatures, but higher heating (at about 200 °C) causes thermal decomposition of PDMS which reaches a peak at 310 °C, resulting in lower mechanical strength. Its shear modulus is independent of the applied frequency but linearly dependent on the temperature with a slope of 1.1kPa/°C. In addition, Schneider and Wallrabe [195] analyzed the dependence of the elastic modulus on the temperature, thinner concentration and thermal aging of two silicone products most commonly used in MEMS namely RTV615 (Bayer Silicones) and Sylgard184 (Dow Corning). The authors concluded that the isotropic and constant elastic modulus ( $E$ ) depends strongly on the hardening conditions. For instance, at high temperatures and long hardening time, in a range up to 40% strain, RTV 615 displays an elastic modulus  $E$  of 1.91 MPa and Sylgard 184 an elastic modulus of 2.60 MPa [195].

In the project, the assembly of the micro-machine requires clean room steps, including high temperature wafer bonding steps. We therefore had to verify the compatibility of the membranes with the heat treatment steps required in the clean room. We subjected them to various high operating temperatures.

#### 4.8.1. Thermal bench

To test the compatibility of membrane with high temperature clean room process like thermocompression or anodic bonding step up to 300°C, we used the EVG 501 bonding equipment (cf. Figure 4-28). Concerning their temperature stability during a short period at temperature up to 200°C, we made a heating system consisting of an aluminum block on which are inserted heating resistors (cf. Figure 4-27). Finally, for the temperature aging tests we used a furnace (in MIMENTO clean room) which can go up to 200°C and keep a stability over long time periods.

We will first shortly present the two heating setup, then we will present the procedure used with the aluminum test block as well as the one with the EVG equipment.

##### – First setup: Aluminum block heating system (for temperatures up to 200°C)

This bench is composed of a heating element, 2 types K-thermocouples, 4 heating resistors that can be used up to 700 °C (two of them with thermocouples), a PID thermal regulator and a multimeter. The details of these elements are given in the Appendix. At the level of the aluminum block we have reserved a location for the samples carrying the membrane and a lid is closed over to prevent convection and maintain a stable temperature for the membrane. The heating cartridges are controlled using the PID. The cooling is done through a mini fan next to which is a mini vacuum cleaner to avoid possible fumes related to the thermal paste we use to insert the cartridges.

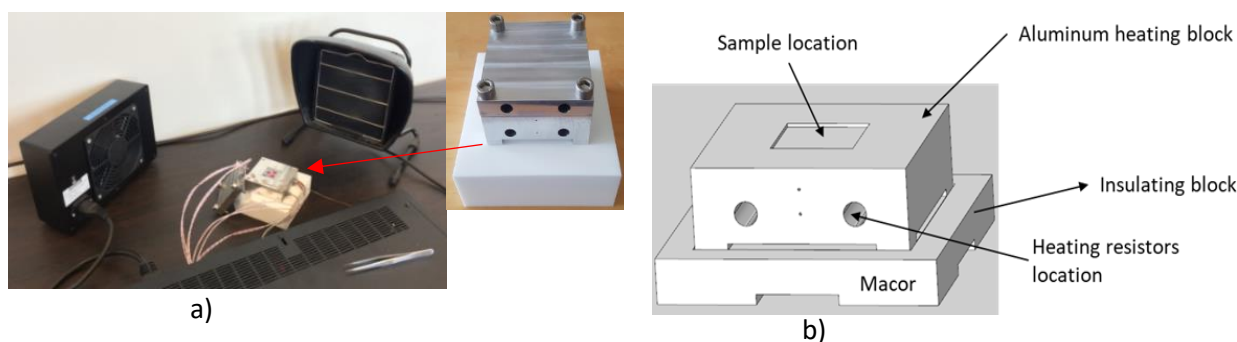


Figure 4-27 : Heating setup (100°C to 200°C for short time)

##### – Second setup: EVG 501 bonding equipment (for temperatures up above 330°C)

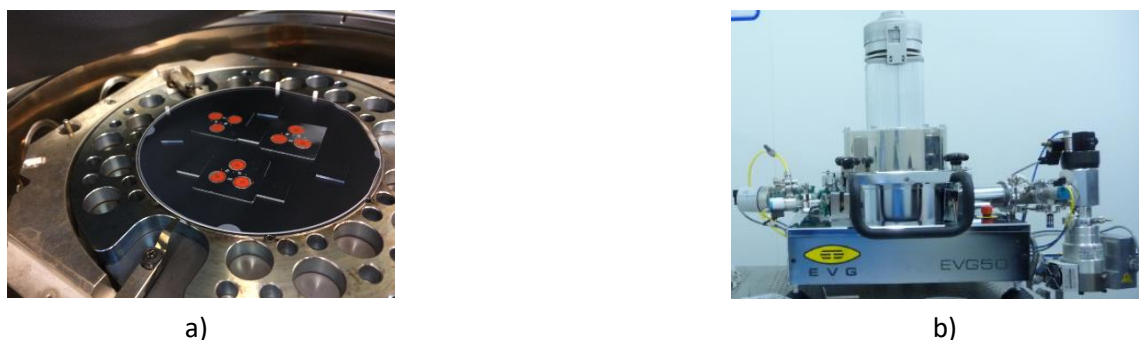


Figure 4-28: a) Membrane samples placed inside the chamber. b) Complete view of the welding machine type EVG501

**The heating protocol** used on the EVG501 welding machine is as follows: after the introduction of the samples and closure of the weld chamber, pumping at  $P = 5 \cdot 10^{-3}$  mbar is performed, followed by preheating in nitrogen  $N_2$ , with a ramp of 5 °C/min to 70 °C for 10 minutes. Then the nitrogen is pumped to heating at 100 °C (or 200 °C or 300 °C) in a vacuum of  $5 \cdot 10^{-3}$  mbar with 3 °C/min. At 100 °C (or 200 °C or 300 °C), the samples are left for 40 min. Then a cooling of 5 °C/min up to 70 °C is triggered. Finally, nitrogen  $N_2$  is purged and cooling continued until 50 °C before taking out the samples.

### 4.8.2. Mass Bench

The study of the mass variation of the samples was done by measuring their mass after their microfabrication, then for several days after their manufacture (to observe their stability), but also systematically before and after a heating step. The mass weighings were performed with an AND balance model 202.

Weighing capacity	Minimum weighing value	Repeatability (Standard deviation)	Linearity	Sensitivity drift (10 °C to 30 °C)	Weighing pan
42 g	0.01mg	0.02 mg	±0.03mg	±2 ppm/°C	Ø 85 mm
210 g	0.1 mg	0.1 mg	±0.2 mg		

Table 4-13: Characteristic of the scale that was used to test the variations of the membrane mass

### 4.8.3. Study methodology

**A first measurement at room temperature (RT)** of the frequencies and masses of the membranes was made before any heat treatment. The characterization carried out each time corresponds to the measurement of the resonance frequency and the measurement of the mass of the membranes. The samples characterized at room temperature were then subjected to given temperatures (100, 200 or 300°C) for given periods of time, consistent with those of an anodic bonding process. After removal from the oven, the mass of the samples and the resonance frequency of the membrane were measured at room temperature. The resonance frequencies were determined 15 minutes after leaving the oven, then after 24 hours of relaxation. All measurements after heat treatment were also performed at room temperature. In addition, some samples were also subjected to an ageing test at 200°C. Finally, a relaxation study was carried out by directly subjecting a sample of 3 membranes to a temperature of 300°C and then, after removal from the oven, to a measurement of the evolution of the resonance frequency of the membranes as a function of time.

We established the following **heating process**: first, samples I (denoted S-I) were heated at 100°C, samples II (denoted S-II) at 200°C and samples III (denoted S-III) at 300°C. Then, after their characterization, samples S-I were heated at 200°C. We characterized them and then, heated them at 300°C. Finally, once again, we characterized them. After their characterization, samples S-II were heated at 300°C. Finally, after their characterization and to test their temperature behavior over a long period, we subjected S-II and S-III to aging at 200°C for more than a month inside an oven.

### 4.8.4. Results: effect of the temperature on the membranes

Following the study methodology presented in the previous section, for each membrane, we calculated the difference between the resonance frequency found after being submitted to given operating conditions and the mean value of the initial frequencies of the studied samples before temperature treatment. The repeatability of the measurements we encountered for our samples on the Polytec MSA 500 equipment was between 50 and 200Hz.

Figure 4-29 shows the variation of the resonance frequency (1st mode or piston mode) as a function of the different heat treatments. The values on the y axis ( $\Delta f$ ) represent the difference between the average of the resonance frequencies of the membranes after heating and the average of their resonance frequency before sample heating. On the x-axis are noted the heating conditions and the relaxation time experienced by the membranes before the recovery of each measurement. The two types of structures of the membrane were tested (the structure with a spiral, and the other one with only the central disk, cf. Figure 4-24).

An analysis of Figure 4-29 shows that the average natural resonance frequency does not appear to be influenced by heat treatments up to 200 °C. From 200 °C, there is a small variation in the resonance natural frequency, which increases of the order of 60 Hz for the spiral membrane. This variation remains stable even after 24 hours of relaxation. Membranes without spiral (central disk) do not appear to be influenced by heating at 200 °C. But, at 300 °C, the frequency drops for both types of membrane structure. Indeed, for both membrane geometries, the frequency drops at 300 °C with a variation of the order of 100Hz compared to the natural resonance frequency before heating. The membranes with spiral stabilize after the fall at 300 °C probably because of the presence of the recessed spiral. For membranes without spiral, after 24 hours of relaxation, the frequency does not return to normal and seems to decrease to about 140 Hz of variation with respect to the initial frequency.

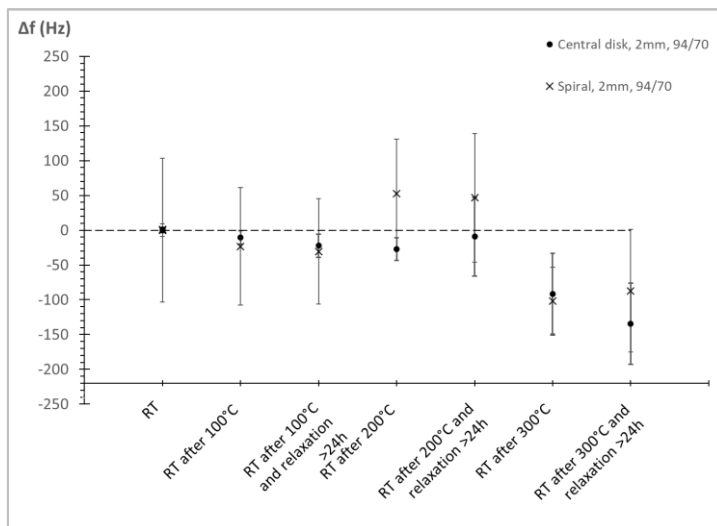


Figure 4-29: Average variation of the frequencies difference (between the average of the resonance frequencies of the membranes after heating and the average of their resonance frequency before heating) for different heating temperatures (100, 200 and 300°C) and without relaxation time or with more than 24h of relaxation time. Measurements for 94/70 membranes with spiral (denoted Spiral) or without spiral (denoted Central disk). 2mm central disk.

Consider, then, Figure 4-30, which represents the average variation of the frequency over a long relaxation period for a sample of 3 membranes without spiral (central disk). The dash line with error bars corresponds to the mean value of the three membranes (denoted III-a-m1, III-a-m2 and III-a-m3). The change of resonance frequency with temperature is clear after a 300°C heating. Indeed, this phenomenon is more pronounced on spiral-free membrane since they contain more RTV-silicone.

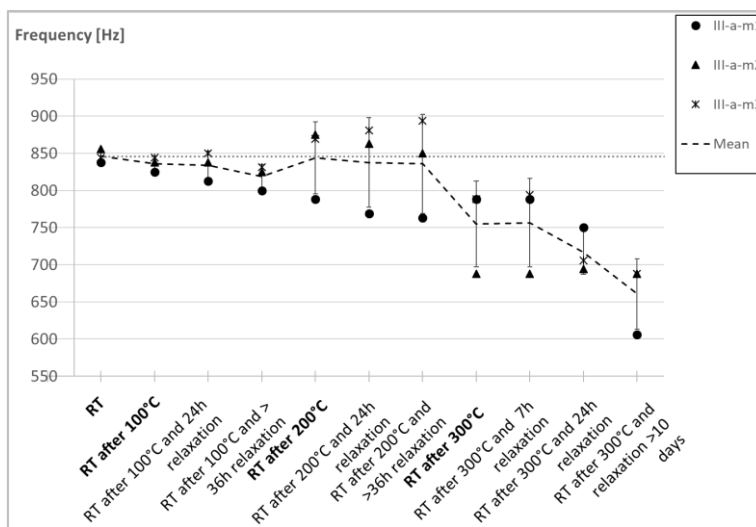


Figure 4-30: Average variation of the frequency over a long relaxation period of more than 10 days for a sample of three 94/70 membranes without spiral and with a 2mm central disk.

Figure 4-31 shows the mass variation of the samples (for both types of structure) before and after heat treatment. The mass appears to decrease slightly after heating (the lowest mass attained corresponds, at most, to a decrease of 0.4 mg, *i.e.* a "maximum" decrease of less than 1 per thousand). However, taking into account the weighing precisions, this trend is not clear and seems to appear from heating to 200 °C. At 300 °C, the mass of membranes decreases more markedly for membranes without spirals. This drop in mass is also observed on the membranes with spiral after heating at 300 °C. After relaxation, the average mass does not vary: there appears to be no significant adsorption (water vapor).

Figure 4-32 shows the change in membrane mass more clearly. The dotted line on this curve represents the change in mass before heating measured over several days. With this curve, we see the moment when the mass begins to vary, that is to say from 200 °C. On the other hand, at 300 °C, the variation is accentuated, the mass falls and this

phenomenon is especially observed on the membrane without spiral, which contains more RTV silicone. This mass drop may be due to a thermal shock causing degassing or a delusion of water vapor entrapped in the matrix of the polymer. After 24 hours of relaxation, for both types of membrane, the mass tends to increase, as if returning to normal.

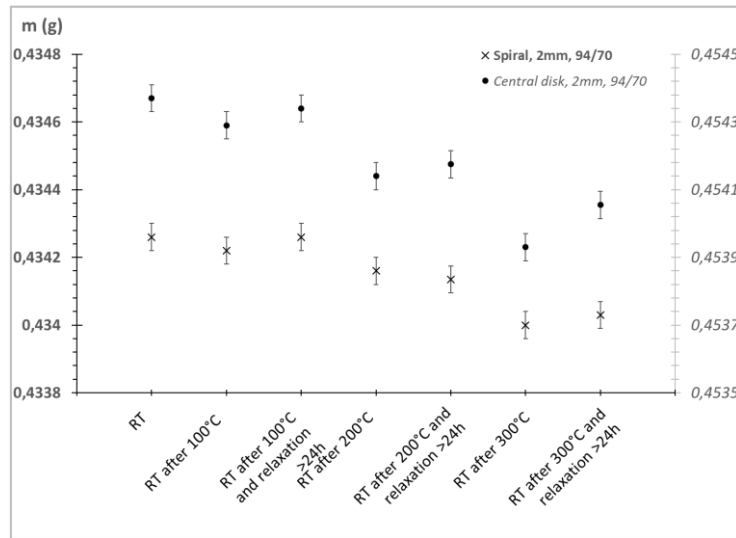


Figure 4-31: Variation of the mass of two samples (spiral & disc) after heating from 100 °C to 300 °C.

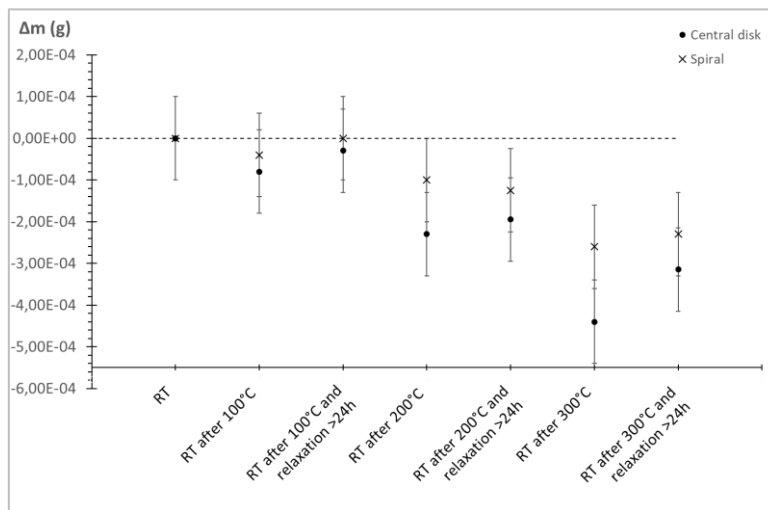


Figure 4-32: Controlled mass variation on two samples : with and without spiral. 94/70 membranes, with a 2mm central disk.

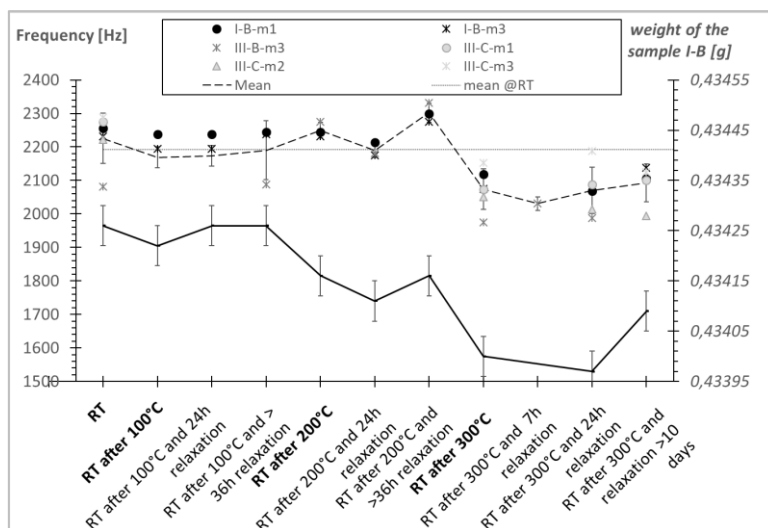


Figure 4-33: Variation in mass (right axis) and frequency (left axis) measured on three different samples (I-B, III-B and III-C). 94/70 membranes with spiral and with a 2mm central disk.



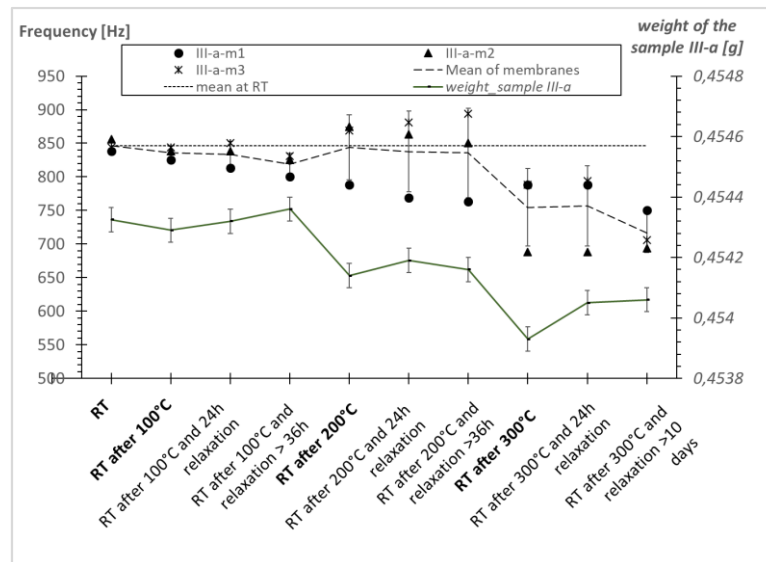


Figure 4-34: Variation in mass (right axis) and frequency (left axis) measured on a sample (III-a) of three 94/70 membranes without spiral and with a 2mm central disk.

Comparing with the variation of the resonant frequency (*cf.* Figure 4-33), there does not seem to be any effect / direct link between the mass variation and that of the resonance frequency: this can be related to the slight variations in mass (at most 1 ‰), insufficient to visibly influence the mechanical behavior of the membrane. There is rather a contradiction between the two curves because they go in the same direction, that is to say that the mass and the frequency decrease. While, physically, when the mass drops the frequency should increase according to

$$\text{the equation: } f = \frac{1}{2\pi} \sqrt{\frac{k}{m}}.$$

Indeed, this is explained by the fact that the stiffness of the RTV-silicone began to change at 300 °C, and that change must have been more significant than that of the mass. Consider the membrane without spiral (*cf.* Figure 4-34), since it is found that the frequency decreases under the effect of heat at 300 °C, the stiffness should also decrease. On the other hand, at 200 °C, the stiffness does not seem to vary (or varies insignificantly) since on the membrane with spiral, the mass decreases while the frequency increases: this is consistent with the formula above. This would mean that it is rather a slight decrease in mass than stiffness that is observed at 200 °C on these membranes. It can also be seen that after several days of relaxation following heating at 200 °C, the frequencies of the membrane for the two types of geometries remain stable (fluctuations after more than 36h of relaxation are largely included in the error bars). Therefore, it can be considered that after manufacture, to completely desorb the solvents present on the membrane, they could be heated to 200 °C.

In order to check whether the membranes are significantly impacted by heating to 300°C and whether they can partially recover their properties after relaxation, we heated membranes, without prior heat treatment, directly to 300°C. Then we measured their resonance frequencies from 15 minutes after they left the oven. These 15 min correspond to the time it takes to get out of the clean room to make the frequency measurements. To evaluate the changes over time, the resonance frequencies were measured over a total duration of about 500 minutes. The results are plotted in Figure 4-35 which represents the time variation of the frequency for 6 different membranes taken from 2 different samples (94/70 with spiral and 2mm central disk). This graphic delivers several pieces of information.

First, according to the curves, the resonance frequency is almost constant over time: no frequency decrease/increase over time is observed. The curves follow an affine straight equation, with very low and almost zero directing coefficients ( $10^{-4}$ - $10^{-3}$  range). This seems to indicate that on these structures, the relaxation can be reached very quickly, even before our first measurements which were carried out 15 min after the exit of the oven. These relaxation values are much than the ones that can be found in the literature (about 4h [239]).

Secondly, the membranes of the same batch and those of a different batch have -on average- very similar behaviours. Without taking into account measurement errors (which result in fluctuations of the order of 30 Hz around the central value in the worst case), there is a maximum difference, on average, of the order of 100 Hz

between the extreme values of the resonance frequencies. In the worst case, the variation is therefore less than 5%. This allows us to show the repeatability of our manufacturing process.

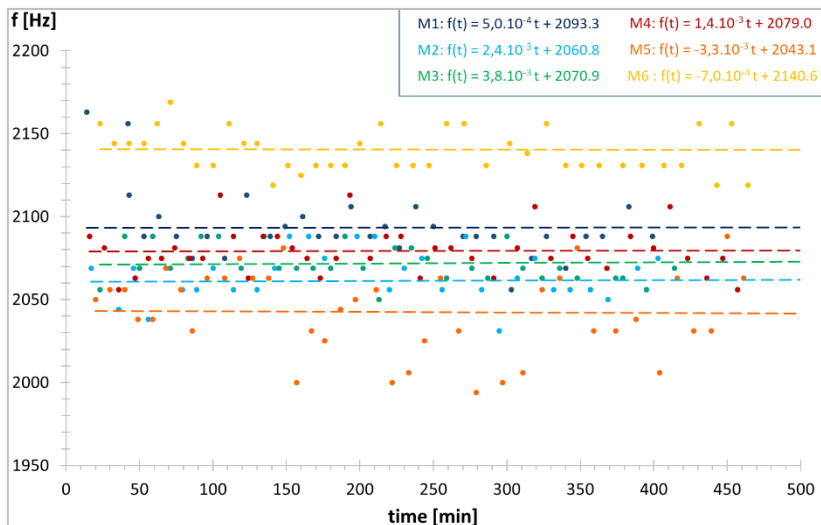


Figure 4-35: Variation of the resonance frequencies as a function of the relaxation time, after heating to 300°C, for 6 membranes (94/70, with spiral, 2 mm central disk) from 2 different samples.

The variations observed from 300°C could be related to the fact that it is an amorphous polymer of elastomer type. The latter have no apparent order (liquid-type structure), no precise melting temperature, but they have a softening phase. They are characterized by low shrinkage, impact resistance, dimensional strength and creep resistance.

Visual observation of the silicone RTV (*cf.* Figure 4-37) shows that it is red after structuring. This color becomes bright red after heating to 300°C. However, from 330°C onwards, there is a real degradation of the RTV-silicone, which becomes brittle. These membranes are therefore suitable for clean room processes up to a maximum temperature of 300°C.

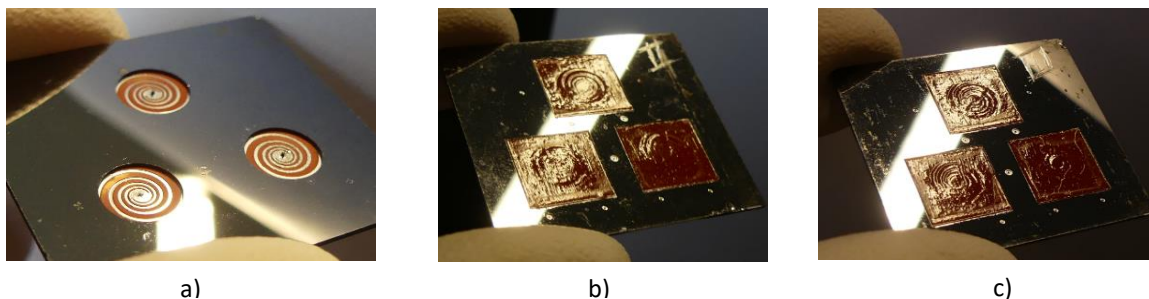


Figure 4-36: Samples pictures: a) before b) and c) after heating process at 20min/Step

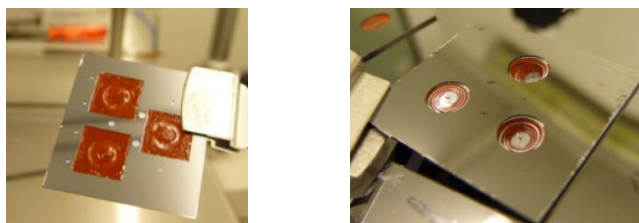


Figure 4-37: Pictures of deteriorated Membrane after being heated at 330 °C

To conclude, we carried out the characterizations of the membranes before (at room temperature) and after the heating process. The variation of the mass with the temperature follows a slight downward trend due to the degassing of the RTV silicone layer. The mechanical properties of the membranes seem to remain stable when heated to a temperature below 300°C. For heating to 300°C, we observed a decrease in resonance frequency, but no "physical" degradation of the membrane. Thus, the clean room process should not damage or significantly change the properties of the membranes, if the bonding temperature does not exceed 300°C. However, according to the manufacturer's data sheet, this RTV silicone is sold for use up to 343°C (350 F): our results do not comply with this specification. It may be necessary to specify a thickness above which the temperature can be raised to

343°C because with a thickness less than, or equal to, 200µm (that of our membranes), the maximum safe temperature has been found to be less than 330°C.

*Note: We focused in this work on the first mode of resonance. Nevertheless, we have noticed that apart from the 1st vibration mode which is the piston mode, the 6th mode is the following one which has an interesting amplitude because it is higher than the first one (results presented in [240]). But this mode corresponds to a vertical inclination of the central disc compared to the 1st mode which has the shape of a mobile cylinder. This means that the volume of fluid which can be displaced by this 6th mode is strongly reduced. However, it can be interesting for other applications where one is not looking for a swept volume, but rather a large displacement.*

## 4.9. Conclusion

Two types of membrane structures with RTV-silicone were studied: one with a silicon spiral spring and one with a central disc, all with different thicknesses and configurations. A stability study of the properties of the membrane subjected to thermal sollicitations, with aging tests for more than one week and study of relaxation after a stage of a short heating period at temperatures up to 300 °C, was carried out. Studies of dynamic stability of frequency and initial maximum displacement as well as a study of mass variation after heating were carried out. A significant increase in membranes displacement capacity was observed and a slight decrease in frequency related to an increase in the elasticity of RTV-silicone resulting from heating. Samples, each carrying three membranes, were successively heated from 100 °C to 300 °C with characterizations after each step. Then another sample was directly heated to 300 °C for a relaxation study over 8h. This relaxation study consisting of close frequency measurements on each sample membrane just after it leaves the oven at 300 °C.

We modelled, and experimentally demonstrated the stability of membrane resonance frequency (1st and 6th mode [240]), which are thus suitable for micromachines, especially thermal micromotors. The numerical simulation made it possible to highlight the zones of strong mechanical stresses and the expected piston-mode resonance frequency. Numerical results were in agreement with the experimental test results. Experimental results showed that high temperature processes, like anodic bonding, should therefore not change the mechanical properties of the membrane provided that the bonding temperature does not exceed 300°C. The micro fabricated membranes structures aimed at being implemented in the micromachine, so, in the next chapter, we implemented these fluidic membranes on the Stirling micromotor being assembled.

### The main results of chapter 4 are the following:

1. The **RTV silicone mechanical properties** have been evaluated since no precise measurements were found in the literature for small structures made of this material: a Young's modulus of about  $E = 1 \text{ MPa}$  was measured (which is less than  $E = 1.5 \text{ MPa}$  for PDMS), with a breaking strain of about 100%.
2. Two types of 5mm diameter RTV- silicone /silicon hybrid membranes were tested. The membranes with an embedded silicon spiral exhibited **deflections up to 1mm at center** without breaking and this deflection reached **up to 2 mm for membranes with only a central silicon disc**.
3. **The stiffness of the membrane is in the range of 0.2 N/mm** for those incorporating Si spirals, and of **0.1 N/mm for those incorporating discs only**.
4. **Resonance frequencies** are in the range of  $\sim 850 \text{ Hz}$  for membranes with a central disc and  $\sim 2100\text{-}2800 \text{ Hz}$  (depending on the membrane thickness) for membranes with spiral springs.
5. **The membrane does not seem to be significantly affected by heating at 200°C (even after aging for more than a month at this temperature), however a permanent drop of the resonance frequency is observed after heating at 300°C**. This shows that the membrane may be deteriorated during the assembly process by anodic bonding if the temperature reaches 300 °C on the membrane.

---

## CHAPTER 5 : CHARACTERIZATIONS OF THE STIRLING MICRO-MACHINE

This chapter concerns the characterization of assembled Stirling micro-machines in motor and cooling mode. The miniature machines presented in the previous chapters were assembled with different types of mechanical connections between the membranes (incompressible liquid or solid bonding rods).

First, we will explain the difficulties related to the instrumentation of the micro-machine. Then, we will present some results corresponding to static measurements for a membrane assembled with a chamber. After a brief reminder of the MISTIC configuration, estimation of its performance using the isothermal Schmidt model under Matlab has enabled to predict the expected machine output. The different types of assembled micro-machines are then presented: two types of mechanical connections were tested (incompressible liquid or solid connection) and the machines can operate either in motor mode (temperature controlled) or in cooling mode (mechanically controlled). To do so, some magnets were incorporated to allow the membranes displacement while minimizing as much as possible the space requirement that could interfere with the flow of the fluid. The characterization results associated with the various pistons (solid and liquid) used in micro-machines are presented. Finally, we will present the experimental setups for the two modes of the micro-machine, followed by the results and discussion.

### 5.1. Stirling micro-machine instrumentation difficulties

The prototype was instrumented to measure the main physical quantities involved experimentally: temperatures (hot and cold sides) and operation frequency. Before presenting the characterization of the micro-machine, we would like to underline the difficulties related to the instrumentation of the micro-machines fabricated in cleanroom.

The instrumentation of micro-machines for the acquisition of data such as temperature and pressure is a challenge. Mainly, because the height of the gas compression and expansion chambers and the regeneration channel are less than a millimeter (because in clean rooms the standard thicknesses of silicon substrates are 0.5 to 1 mm). To introduce a pressure sensor, it would have to be micrometric so that the sensor does not disturb the flow, the membrane deflection, or block the regenerator channel. In other words, a custom pressure sensor should be manufactured during the micro manufacturing of the micro-machine. The development of such a sensor can already be the subject of another thesis.

What is valid for the pressure sensor is also valid for the other sensors (temperature and fluid velocity). Regarding temperature measurement, currently the most commonly used sensors are thermocouples. Commercial ones have minimum diameters that are generally above 100 $\mu$ m. In the laboratory, and particularly at the Femto-st institute, it is possible to produce miniature thermocouples whose dimensions can be below one micrometer at the junction [241]. Nevertheless, the integration of such a sensor is technologically complicated: the smaller the sensors, the more fragile they are and their electrical connectors are usually larger than the available space. The case of the velocity sensor is even more complex, even if sensors combining speed and temperature measurements are being developed, particularly within our institute [242], [243] [244], [245].

Considering all these difficulties, one could think of an optical solution, such as laser sensors (temperature for example), but this requires transparent walls in the wavelength range of the light source. This is technologically difficult and would be a source of error on the measurements because the work spaces are hundreds of micrometers high, without the possibility of checking visually where the measurement is made exactly (since silicon is not transparent for visible light). Thus, the introduction of all these sensors, or even just one, is tricky and could affect the starting or proper operation of the machine.

In terms of measurements to be made on the micro-machine, we decided to focus on the external measurements of temperatures and membranes displacements. Temperature measurements will be made by an external temperature sensor (PT100 probe, thermocouple) and membrane displacement measurements will be made using optical sensors (laser or confocal sensors) through windows designed for. All the instrumentation used and the characterization setup will be presented later on in sections 5.5. , 5.6. and 0

In the previous chapter, we presented the study of the hybrid membrane (HM) alone (RTV + silicon). In the following sections, we will focus on the assembled hybrid membrane including chambers and/or mechanical connection between the membranes.

## 5.2. Static displacement of hybrid membranes in corresponding chambers

Static and dynamic results obtained with a membrane alone were previously presented in the chapter 4. The different types of membranes used in this study are recalled (as well as their dimensions) on the Figure 5-1. In this section, we focus on the change of behaviour when a membrane is assembled (bonded) with a chamber. The membranes (with a spiral or with only one central disc) are assembled with a 300 $\mu\text{m}$ -high silicon chamber. Figure 5-2 presents the 2D schematic view of these membranes, as well as their dimensions.

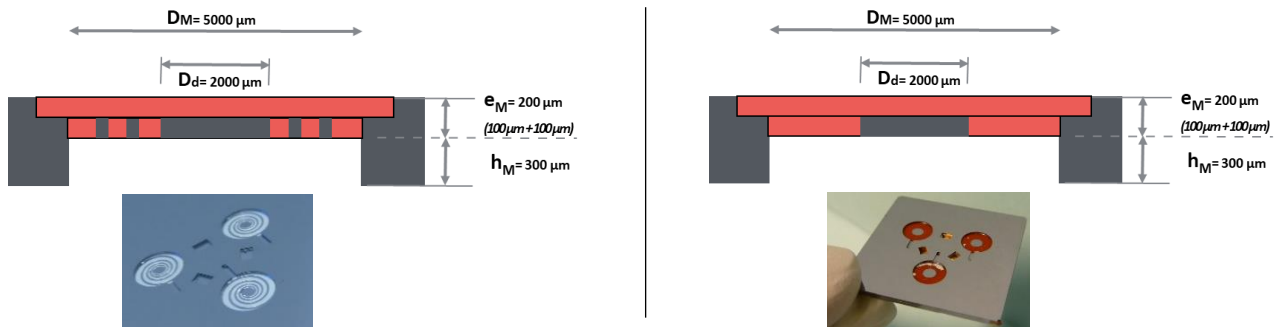


Figure 5-1 : The different types of membranes used in the present section. Both with a 100 $\mu\text{m}$  thick of silicon embedded in RTV-silicone and with above a 100 $\mu\text{m}$  thick RTV silicone over laye . Pictures are taken from below the membrane.

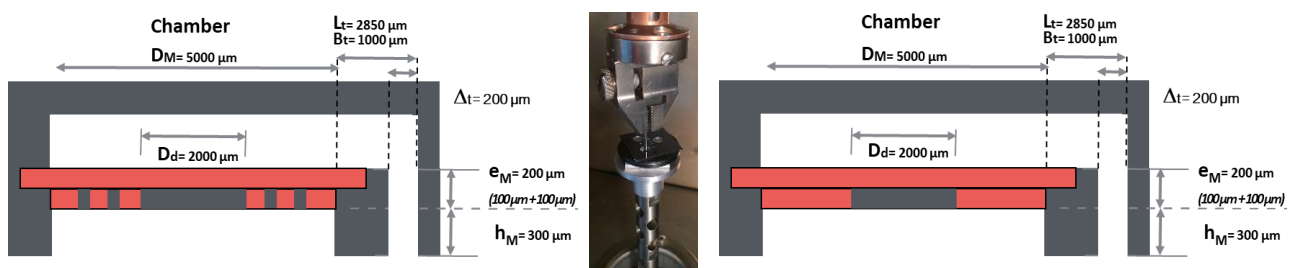


Figure 5-2: 2D schematic view of the assembled membrane with one chamber. On the left, the membrane with a spiral. On the right, the membrane with a central disc (no spiral). At the center, picture of the test setup.

– Setup presentation:

We carried out displacement tests with the same procedure than the one presented in the section 4.6.2. To determine the possible static displacement and the pressure required to achieve it, a force was applied (using a 1.7 mm diameter pin) on the central disc of the underside of the membrane. We are in the configuration of centrally charged circular membrane where a displacement is imposed at the membrane center silicon disc and the resulting stiffness is measured thanks to a 22N load sensor (*cf.* Figure 5-2, center image). The displacement speed of the pin is constant (10  $\mu\text{m}/\text{s}$ ) and the force applied to the pin is recorded. The membrane resistance is the result of the membrane stiffness and the pressure difference inside and outside the chamber. This pressure difference may depend on the speed of the pin: an excess pressure may appear inside the chamber at high speed since a finite time is needed to expel air from the chamber through the exhaust pipe. These tests can be used to determine the minimum pressure required to operate the micro-machine when it is fully assembled. The results obtained for both types of membranes are shown in Figure 5-3. The curves on the left are for membranes with a spiral containing a 2 mm central disc. The curves on the right are those of the membranes without spiral but with only a 2mm disc in the center.

– **For membranes with spiral** (Figure 5-3, on the left): the tests were performed for the 3 membranes (denoted membrane N°1, N°2 and N°3 on the figure) of each sample (there are 3 membranes on each chip studied). The

three curves represent, for each membrane, their displacement in their associated chamber. It can be seen that the three curves are relatively similar, which shows good reproducibility (or homogeneity) when microfabricated in clean rooms. The observed deviations may be related to measurement errors. Indeed, the deflection measurement is accurate to  $\pm 2\mu\text{m}$  and the pressure measurement is accurate to  $\pm 0.17\%$  (combination of errors due to force and surface measurements). It can be seen that, to deflect the membrane by  $300\mu\text{m}$ , *i.e.* for the membrane to touch the bottom of the chamber, a pressure of at least  $0.2\text{ MPa}$  (2 bars) is required. Note that for the membrane N°1, the pin slipped and damaged the membrane so the measurement could not be taken above  $0.07\text{ MPa}$ . This test validates the pressure resistance of the chamber and also the good quality of the wafer bonding.

– **For the membranes without spiral** (Figure 5-3, on the right): the tests were also performed for the 3 membranes (denoted membrane N°1, N°2 and N°3 on the figure) of each sample. A pressure of at least  $0.04\text{ MPa}$  (0.4 bar) is necessary to reach a deflection of  $300\mu\text{m}$ . This pressure is 5 times lower than the one required to obtain the same displacement with the membranes with spiral. Note that, since the range of applied pressure is five times smaller than the one for the spirals, there is less measurement points and the uncertainty of the measure is more visible. The membrane N°3 was damaged before the test (RTV-silicone damaged during manipulation), thus the result is not conclusive for this membrane. Concerning membranes N°1 and 2, they therefore seem to be more favourable to be used in a micro-machine because they required a force about 5 times less important than the one for the spirals : as expected, the necessary energy for the motion of the membrane should thus be less important with a central disk than with the spiral.

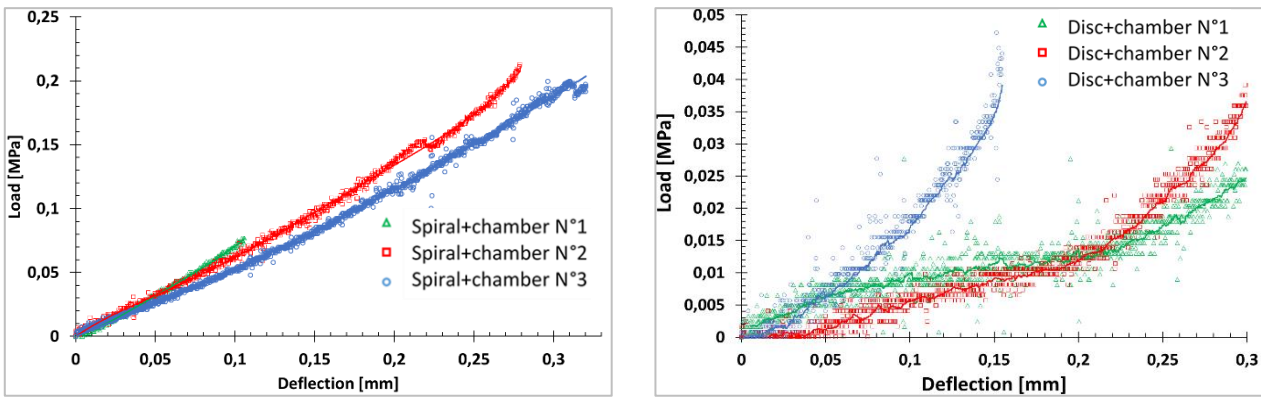


Figure 5-3 : Required pressure to deflect the membrane assembled with a chamber. On the left: for the membrane with a spiral ( $100\mu\text{m}$  of Silicon embedded in RTV, with an overlay of RTV of  $100\mu\text{m}$  thick). The central disk of the spiral has a diameter of  $2\text{mm}$ ). On the right, for a membrane with a silicon single central disk (no spiral). The central disk is  $2\text{mm}$  in diameter and  $100\mu\text{m}$  thick, embedded in RTV and with a RTV overlay of  $100\mu\text{m}$  thick.

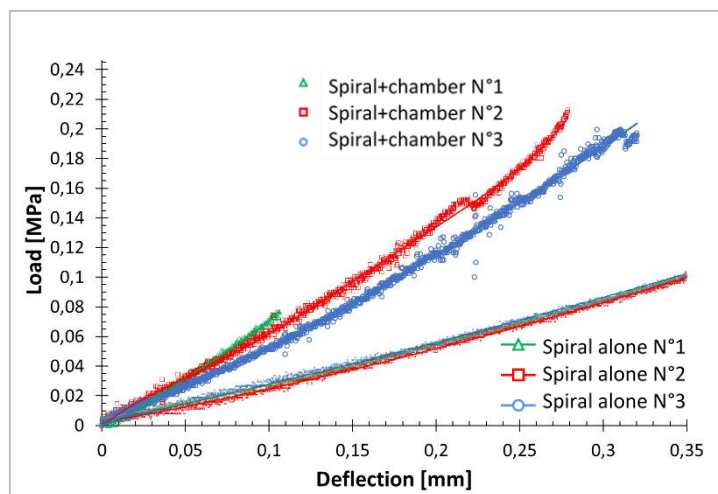


Figure 5-4: Comparison between the membranes alone (denoted “spiral alone”) and the membrane+chamber assembly (denoted “spiral+chamber”). The membranes are loaded in their center. All the membranes are with a spiral ( $100\mu\text{m}$  of Silicon embedded in RTV, with an over layer of RTV of  $100\mu\text{m}$ ).

In order to quantify the influence of the chamber on the force required to move the membrane, we compared the case of membranes alone (previously presented in chapter 4) and that of the membrane+chamber assembly. The results obtained for spiral membranes (100 $\mu\text{m}$ , 2mm central disc) are given in the Figure 5-4. We can see that the variation of the force as a function of displacement is different when the membrane is placed on a chamber with an outlet channel and when this membrane is alone. This variation is probably due to an overpressure in the chamber that occurs when the membrane compresses the gas contained in the chamber. The force  $F(t)$  that resists the displacement of the membrane consists of two terms:

$$F(t) \approx k \cdot z(t) + F_g(t) \approx k \cdot z(t) + \Delta P(t) \cdot \frac{V_c}{h}$$

where  $k$  is the stiffness of the membrane,  $z(t)$  its displacement as a function of time,  $F_g$  is the resistance of the gas,  $\Delta P$  the overpressure in the chamber as a function of time,  $V_c$  the chamber volume (supposed cylindrical here) and  $h$  its high.

We define  $\Delta F(t) \approx F(t) - k \cdot z(t)$  as the overpressure load extracted from the membrane-loading test, and thus, the overpressure in the chamber can be written as:

$$\Delta P(t) \approx \frac{h \cdot \Delta F(t)}{V_c}$$

The overpressure can thus be estimated in the chamber and is given on the Figure 5-5. This overpressure seems to remain at modest values, below 100 mbar (*i.e.* 10% of atmospheric pressure), which indicates that the outlet channel should not induced an excessive resistance to gas flow.

After these tests, we assembled the full engine. Different mechanical connections between the membranes were tested (*cf.* section 5.4. ): either with a liquid (incompressible) or with a solid rod connecting the two membranes. In the next section, we will present the different engines and look at the evolution of the resonance frequency when the membranes are connected.

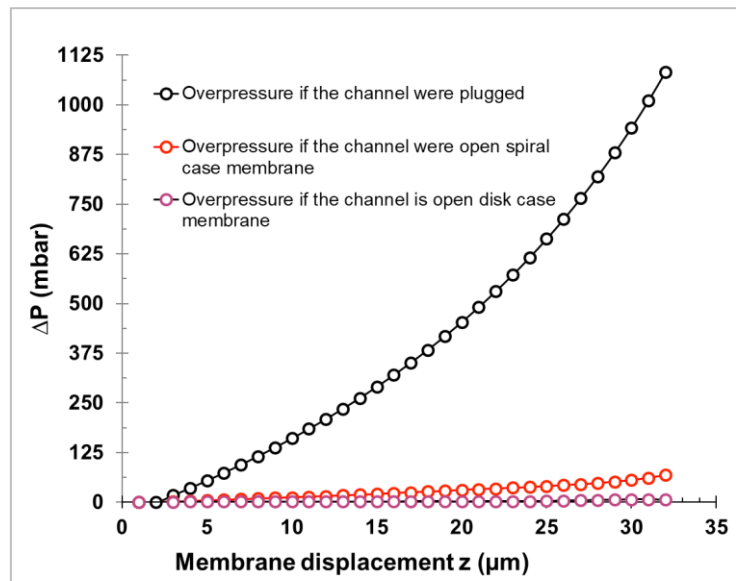


Figure 5-5: The force  $\Delta F$  (deduced from measurements presented in chapter 4) due to the overpressure in the chamber for two membranes with spirals and disk as a function of their displacement  $z$  ( $\mu\text{m}$ ).

### 5.3. Schmidt simulation for the MISTIC micro-machine

In what follows, we will first recall the configuration of the MISTIC micro-machine before presenting the numerical model based on the isothermal Schmidt's one. This model enables to predict the expected machine output.

– The MISTIC micro-machine:

The micro-machine operating with a liquid (as coupling element between the two membranes) is the prototype proposed in the MISTIC project. The structure of this micro-machine is such that, unlike conventional Stirling motors, the oscillations should begin without significant input of initial energy (as for the mesoscale motor at the

Symme Laboratory). The schema of this micro-machine is presented in Figure 5-6. This micro-machine is composed of six hybrid membranes connected two by two by an incompressible Vaseline liquid.

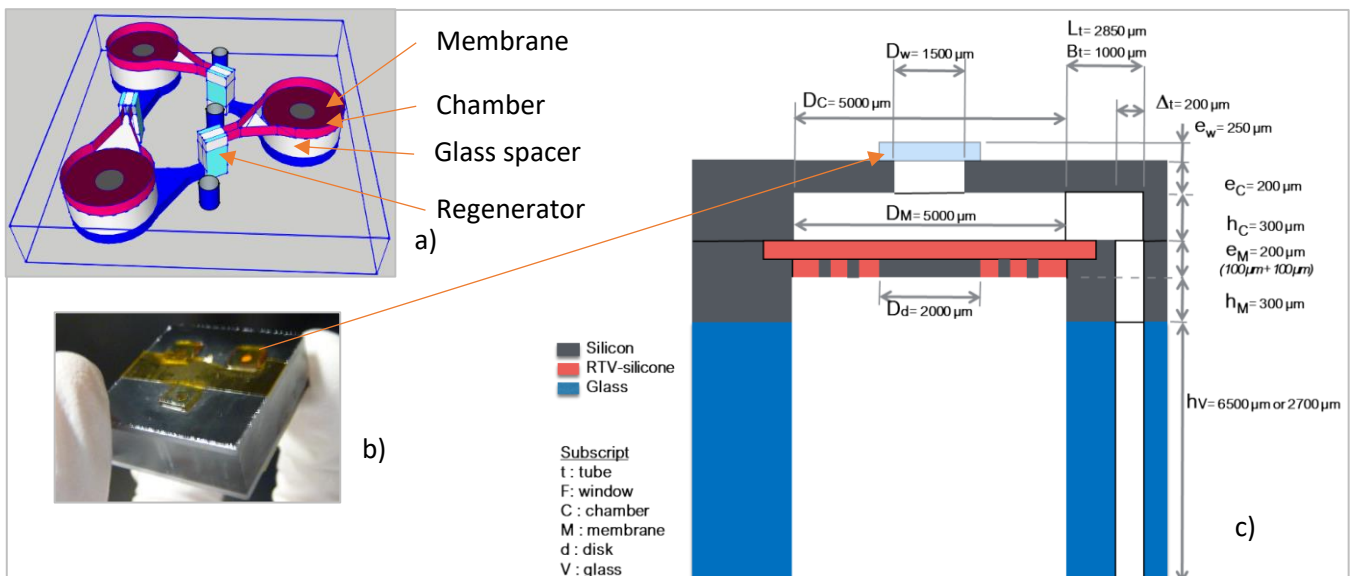


Figure 5-6 : a) Schema (realised on sketchup software) of the principle of the Stirling micro-machine proposed in the MISTIC project. b) Picture of a full engine. c) geometric dimensions of one module without the second membrane/chamber stack closing the module.

– The Schmidt analysis:

To theoretically estimate the performance of the MISTIC engine, we carried out a numerical calculation by adapting the isothermal model developed by Schmidt and presented in chapter 1. This simplified model (because it does not take losses into account) was chosen for several reasons and, in particular, because at these scales, estimating thermal and fluid losses requires precise knowledge of the phenomena and databases or correlations based on experience, which we do not have. We therefore decided to estimate the performances in an "ideal" case: the isothermal one. The input parameters are shown in Table 5-1. They include chamber sizes (compression and expansion), connection channels between compression and expansion chambers (six vertical channels and three vertical channels intended to contain the 3 regenerators) and diameters of the membranes and their central discs. On the other hand, the operating parameters (such as pressure, hot and cold side temperatures and angular phase shift) are also included in this table. The working fluid used here is air at ambient pressure, therefore the molar-weight-specific gas constant  $r = \frac{R}{M} = 287 \text{ Pa}\cdot\text{m}^3\cdot\text{kg}^{-1}\cdot\text{K}^{-1}$ .

Parameters	Name on Figure 5-6	Values
<b>Void volumes</b>		
Diameter of the regenerator [mm]	$B_t$	1
Height of the regenerator [mm]	$h_v + 2h_M + 2e_M$	7.5
Length of the horizontal channel [mm]	$L_t$	3
Width of the horizontal channel [mm]	--	1
Height of the horizontal channel [mm]	$h_C$	0.3
<b>Chambers</b>		
Height of the chamber [mm]	$h_L$	0.3
Radius of the chamber [mm]	$D_L/2$	2.5
Radius of hybrid membrane central disc [mm]	$D_d/2$	1
<b>The other operating parameters</b>		
Average pressure [Pa]		101325
Temperature of the cooler [K]		293
Temperature of the heater [K]		473
Phase shift alpha [°]		120 ( $2\pi/3\text{rad}$ )

Table 5-1: Parameters used in the Schmidt model for air at 300K and atmospheric pressure.



With an absolute pressure set at 1.013 bar and a hot temperature set at 200°C, the numerical results are shown in Table 5-2 for two operating frequencies: 1000Hz and 10 Hz. In these calculations, we used membranes whose swept volume will have the shape of a truncated cone (calculations detailing this have been presented in chapter 2). When the temperature difference between the hot and cold sides is sufficient (here set at 180°C), the motor must start and the membranes start to move. The output parameters for volumes are the total dead volumes, the swept volumes and the ratio between the swept volume and the dead volume of a chamber (for a deformation of the membrane in the form of a truncated cone). This result therefore gives an idea of the importance of the presence of the central disk. The operating temperature of the three regenerators is also an output parameter. The obtained compression and expansion energy, mechanical power and efficiency of the micro-machine are given in the Table 5-2. The mechanical power produced by the engine is the difference between the expansion power in the hot chamber and the compression power in the cold chamber, respectively calculated by integration on the PV diagram (cf. Figure 5-7). For an operating frequency of 1000 Hz, a mechanical Power output of 56 mW was found for this micro motor, and its efficiency was estimated to reach 38% of Carnot efficiency. It should be noted that the useful theoretical power of 56.7 mW is significant: the engine produces this low mechanical energy because it operates at no load. When the operating frequency decreases at 10 Hz, the efficiency remains the same whereas the power decreases up to 0.57 mW. Note that those results are obtained with an isothermal assumption, therefore they only give an estimation of the efficiency and power.

From the simulation results, the pressure was plot versus the volume (PV diagram, cf. Figure 5-7). The diagram's shape is quite different from the theoretical one (cf. chapter 1), which corresponds to an ideal cycle, with isothermal expansion and compression phases, and isochoric heating and cooling. As can be seen in this PV diagram figure, in a real cycle, the four steps are not physically separated but merge into each other. Although the engine goes through a cycle, it is not a symmetrical process: heat energy is constantly removed from the hot source and released at the heat sink and the real Clapeyron diagram looks like an ellipse. It is important to note that experimentally, there should be a slight discrepancy between the pressure of the hot and cold chambers, this being due to the compressibility and inertia effects of the gas. In addition, a difference in deflection amplitude resulting from viscous losses in the exchangers (chambers, regenerators and channels) is expected. Thus, it is important to keep in mind that the instantaneous pressures in the chambers should be slightly different.

Parameters	With an operating frequency of 1000 Hz	With an operating frequency of 10 Hz
<b>The volumes calculation results</b>		
Volume swept for the 3 expansion chambers [L]	9.2 10 <sup>-6</sup>	
Volume swept for the 3 compression chambers [L]	9.2 10 <sup>-6</sup>	
Total dead volume with a membrane moving with a truncated cone shape [L]	4.0 10 <sup>-5</sup>	
Ratio between the Swept volume in one chamber ( $V_{sw}$ ) and the volume of one chamber	0.52	
<b>The regenerator temperature</b>		
Temperature of the regenerator [K]	375.8	
<b>Energy, power and efficiency</b>		
Compression job [J]	-92 10 <sup>-6</sup>	
Expansion job [J]	149 10 <sup>-6</sup>	
Power supplied in Watt [mW]	56.7	0.57
Efficiency (% of Carnot efficiency)	38.05	

Table 5-2: The results of operating parameters (Calculation of volume swept and dead volume of chambers in the trunk case of a cone)

Since the structure of the micro-machine requires 3 pistons arranged in the shape of an equilateral triangle, and since one aim of the motor is energy harvesting (either conversion from vibrational energy into thermal one in cooling mode, or the contrary in the motor mode), the determination of the natural vibration frequencies of the micro-machines is important (to obtain a maximal swept volume). This will be the subject of the following section, in which different mechanical connections were tested (liquid, glass and plastic, with or without magnet...).

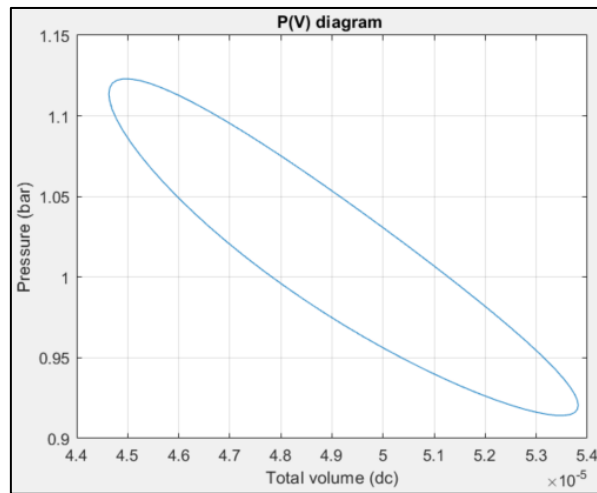


Figure 5-7 : The pressure versus volume (PV) diagram in the micro-machine

#### 5.4. Hybrid Membranes Pistons: liquid and solid connections

In addition to the MISTIC geometry using an incompressible liquid (Vaseline) for the mechanical coupling of the membranes, a geometry for which the membranes are connected with a solid rod (which we will call "solid piston") has been tested. The membranes were identical (same geometry, verified with a profilometer after manufacturing), their geometry was recalled on the Figure 5-1. In addition, in order to be able to operate the machines in motor or cooling mode, for the later, permanent magnets were included in some versions of the machine. Thus, four different types of micro-machines were assembled: with an incompressible liquid between the membranes (with or without magnets) and a solid connecting piston in air (with or without magnets):

– With incompressible liquid (*cf.* Figure 5-8):

- For the motor mode: the chamber between the two membranes is filled with Vaseline (MISTIC configuration) and no magnet was included.
- For cooling mode: the chamber between the two membranes is filled with Vaseline and one magnet under one of the upper membranes, another one on one of the lower membranes are included.

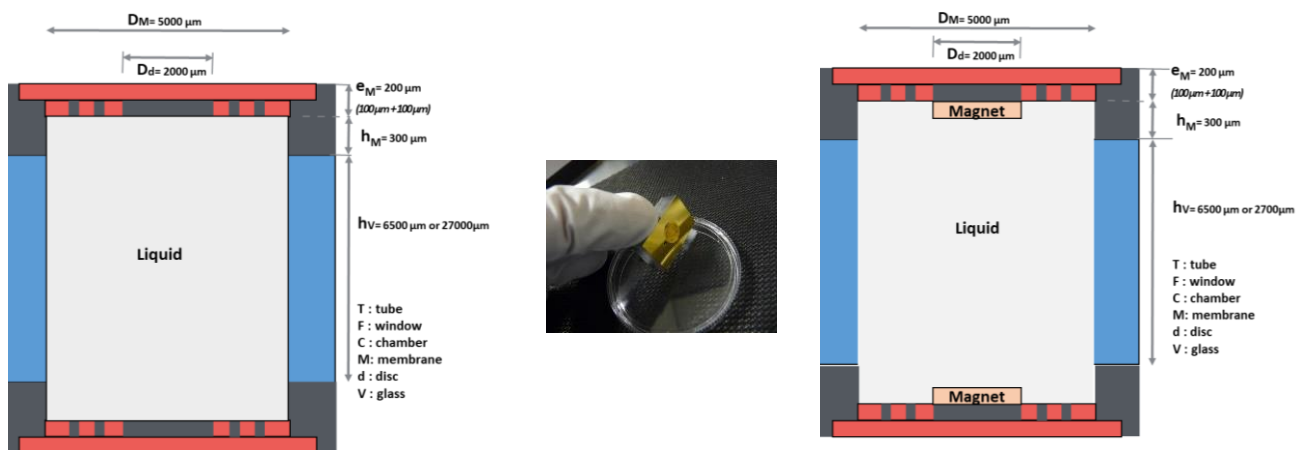


Figure 5-8 : Scheme and photo of the membranes assembled and connected via an incompressible liquid. On the left, the version without magnet for operation in motor mode. On the right, the version with magnets for operation in cooling mode. In the middle, a picture of the assembly.

– With a “solid piston” (*cf.* Figure 5-9): the diameter of the rod (“solid piston”) used in our machines was determined to be well outside the fluid boundary layer.

- For the engine mode, the piston is a borofloat 33 glass rod, with 2mm diameter, therefore, to avoid friction, much smaller than the 5mm diameter chamber in which it moves. The height of the rod corresponds to the height ( $h_V$ ) of the intermediate chamber plus the height of the backward DRIE to suspend the membranes ( $2h_M$ ).

- For cooling mode: the solid piston is a plastic rod made by additive manufacturing (3D printing). One or two magnets can be added on either side of this rod so the final height corresponds to that of the intermediate chamber ( $h_V$ ) plus the height of the backward DRIE to suspend the membranes ( $2h_M$ ).

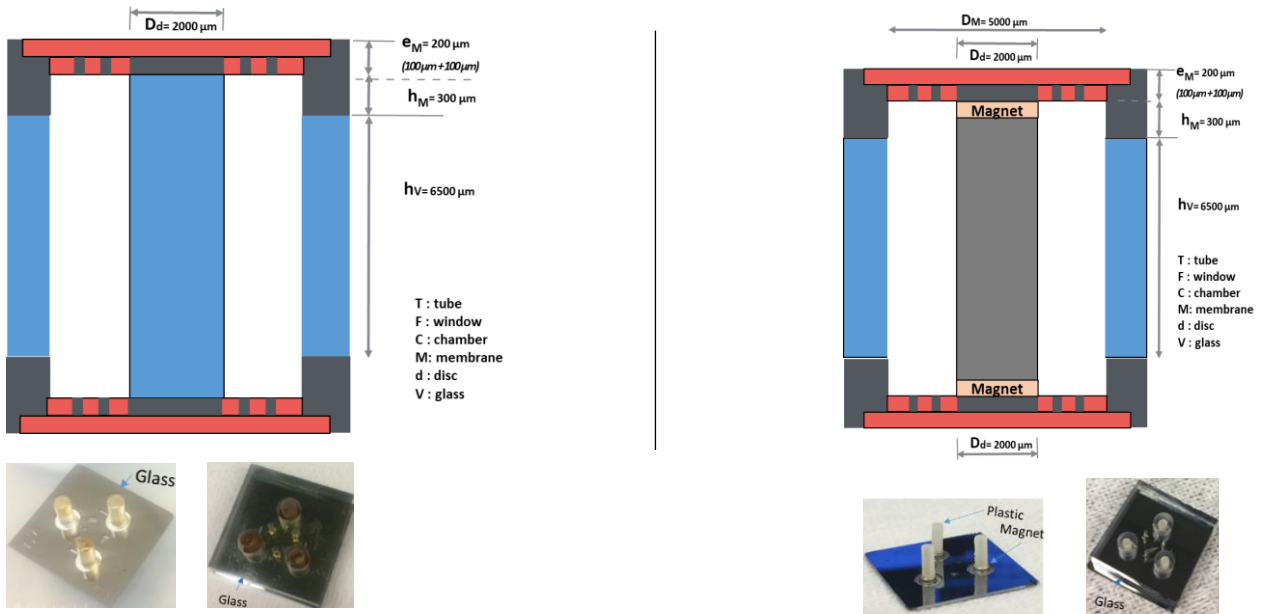


Figure 5-9 : Scheme and photo of the membranes assembled and connected via a rod. On the left, the version with a glass rod for operation in motor mode. On the right, the version with magnet and a plastic rod for operation in cooling mode.

The major difficulty encountered in making these solid rod lies in the centering process of the rods, which is complex because of the flexibility of the membranes on which they must be fixed. For instance, the fully assembled system for the motor mode is on the Figure 5-10. Note that different chambers' heights were tested (glass thickness of either 6.5 or 2.7 mm, *i.e.* total middle chamber height of either 7.1 mm or 3.3 mm).

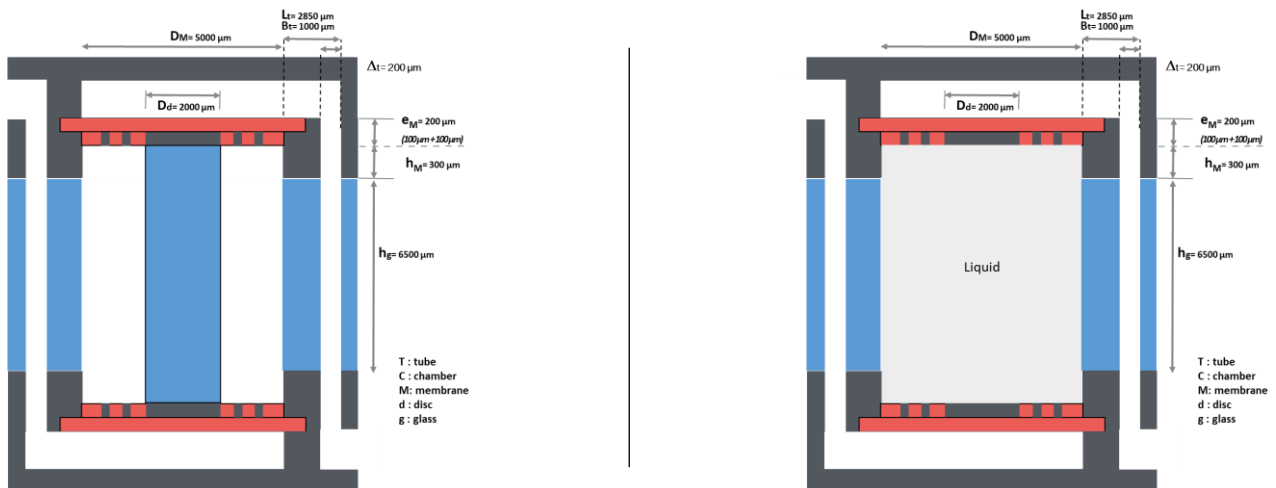


Figure 5-10 : Scheme and photo of the full engine (for motor mode) with cold & hot chambers and with membranes connected via a rod (on the left) and via an incompressible liquid (on the right).

The different version of assembly were dynamically characterized with the same procedure than the one presented on the section 4.7.1 (using the laser Doppler vibrometer). The obtained results of eigen frequencies for those assemblies are grouped in the Table 5-3. As expected, the eigen frequency is lower for assembled membranes than for single ones. We can note that the assembly of membranes with solid or liquid pistons enable the decreasing of the eigen frequency by a factor from almost two to about ten. The influence of the type of assembly (materials used) is visible, for membranes with spiral, on the Figure 5-11. Even though if plastic is lighter than glass, the addition of magnets enables to keep a low eigen frequency. From an initial frequency of about 2.8 kHz for single membranes, the assembly of the full motor enable to decrease to 0.25 kHz.

Thus, we can conclude that, for the different assembly listed in Table 5-3, all the obtained frequencies are below 1kHz, which can have interesting applications in the field of harvesting vibrational energy for example. These eigen frequencies can be easily tuned by adjusting some geometrical parameters (for instance, adding some weight by changing the DRIE process on the central disk): so, it is important to note that these types of membranes and assemblies can have a larger range of applications than the one restricted to the Stirling motor.

Single membrane (cf. Chapter 4 : )	Eigen frequency
Single membrane with a spiral (thickness Si/RTV : 100 $\mu$ m/100 $\mu$ m; central disk of 2mm)	<b>2794 Hz</b> <b><math>\pm</math>70Hz</b>
Single membrane with a 2mm central disk in its middle (thickness Si/RTV : 100 $\mu$ m/100 $\mu$ m)	<b>856 Hz</b> <b><math>\pm</math>16Hz</b>
Liquid piston (cf. Figure 5-8)	
Incompressible liquid without magnet, membranes with a 2mm central disk in its middle (thickness Si/RTV : 100 $\mu$ m/100 $\mu$ m) Thickness of the middle chamber : 3.3 mm (2.7 mm in glass+ 600 $\mu$ m DRIE in Silicon)	<b>480 Hz</b> <b><math>\pm</math>50Hz</b>
Solid piston (cf. Figure 5-9)	
Borofloat 33 piston, membranes with a spiral (thickness Si/RTV : 100 $\mu$ m/100 $\mu$ m; central disk of 2mm) Thickness of the middle chamber and of the piston:7.1 mm (6.5 mm in glass+ 600 $\mu$ m DRIE in Silicon)	<b>670 Hz</b> <b><math>\pm</math>50Hz</b>
Plastic with 2 magnets, membranes with a spiral (thickness Si/RTV : 100 $\mu$ m/100 $\mu$ m; central disk of 2mm) Thickness of the glass chamber and of the piston (piston alone : 5mm) : 7.1 mm (6.5 mm in glass+ 600 $\mu$ m DRIE in Silicon)	<b>238 Hz</b> <b><math>\pm</math>50Hz</b>
Fully assembled engine (cf. Figure 5-10)	
Liquid piston, membranes with a disc (thickness Si/RTV : 100 $\mu$ m/100 $\mu$ m; central disk of 2mm) Thickness of the middle chamber : 7.1 mm	<b>319 Hz</b> <b><math>\pm</math>50Hz</b>
Liquid piston, membranes with a spiral (Si/RTV : 100 $\mu$ m/100 $\mu$ m and 2mm disc) Thickness of the middle chamber : 7.1 mm	<b>475 Hz</b> <b><math>\pm</math>50Hz</b>
Borofloat 33 piston, membranes with a spiral (thickness Si/RTV : 100 $\mu$ m/100 $\mu$ m; central disk of 2mm) Thickness of the middle chamber : 7.1mm	<b>250 Hz</b> <b><math>\pm</math>50Hz</b>

Table 5-3 : Vibration Eigen frequencies for different types of assembly.

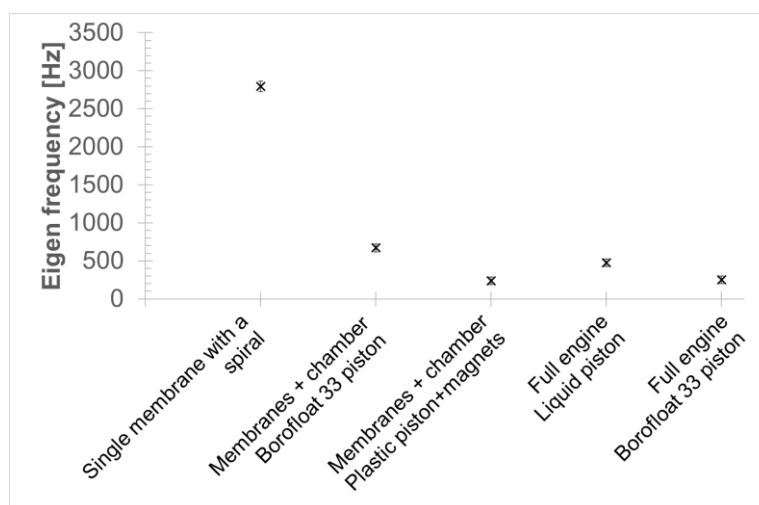


Figure 5-11 : Eigen frequency evolution for different types of assemblies and for spiral membranes (Silicon thickness: 100 $\mu$ m embedded in RTV silicone. Over layer of RTV: 100 $\mu$ m. Central disk of the spiral: 2mm). Middle chamber thickness : 7.1 mm.

After having determined eigen frequencies of the assembled micro-machines, we wanted to proceed to their characterizations. For this purpose, we have developed and mounted two characterization benches, according to the type of micro-machine assembled and to the operating mode that we wanted to test (presented later on). Indeed, a Stirling machine can operate in two modes: motor or cooling one (hence the presence of magnets, necessary to actuate the membranes). For both modes, temperature measurements are mandatory. To measure precisely temperatures, we used platinum resistance thermometer (PT100) which we decided to calibrated to obtain a better accuracy. Details of the sensors calibration and connexion are given in the next section.

### 5.5. Temperature measurements: Platinum resistance thermometer calibration

To measure the temperatures on both sides of the micro-motor, we decided to use platinum resistances (PT100). Since the expected temperature difference in the cooling mode should be very low, we had to be certain of the precision of the temperature sensors. Thus, we proceed a calibration of the PT100 probes to precisely determine the actual temperatures associated with the values of the measured electric resistances. These sensors are small (fine) enough to detect fast temperature variations (*cf.* Table 5-4 ). However, without calibration, the discrepancy between values given for a same temperature could vary, including more uncertainties.

To calibrate the sensors, we used a convective calibration bench, certified by AOIP. Its schematic diagram is shown in Figure 5-12. It consists of a Gemini portable oven (550 LRI), a PT100 precision reference temperature sensor (0.005°C) and a digital multimeter PHP 601. This bench allows the calibration of multiple probes at a time through programmable temperature steps, from ambient temperature up to 550°C. Measurements of digital or analog parameters from sensors to be measured are provided by two Keithley 2100 precision multimeters to increase measurement accuracy. Everything is driven by a Labview control and acquisition program.

Model	Dimension	Class	Heating up	Temperature range	Stability
Pt100 (100Ω at 0°C)	2 x 5.0mm	A	< 0.5°C/mW	-50 to 500	±0.05 %

Table 5-4: characteristics of the Pt100 platinum resistors (manufacturer's data: RS).

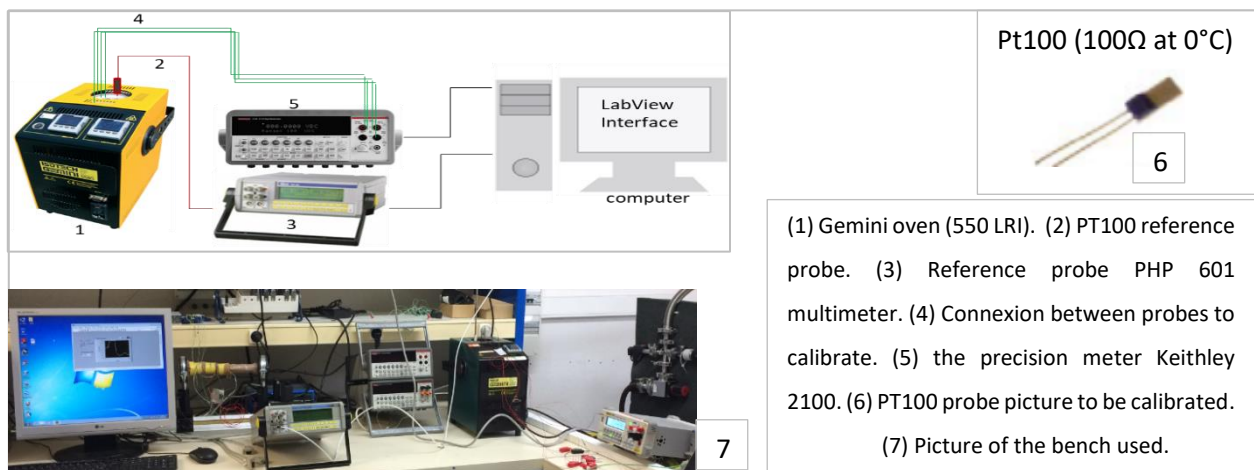


Figure 5-12: PT100 probe calibration bench

In our case, we calibrated four PT100 sensors at the same time. Two sensors were 4-wire connected (*cf.* Figure 5-13), whereas the other two were 2-wire connected. Indeed, even if the 4-wire connexion (KELVIN method) is a little more difficult to do than the 2-wire one, it is more precise. Indeed, since it is expected that a small difference in temperature will be measured during micro-machine cooling operation, the electrical resistance measurement accuracy of the PT100 probes must be improved by eliminating the electrical resistance of the connection wires (or contact). This will make it possible to know the exact value of the electrical resistance of the probe itself (in contact with the micromachine under test) after a variation of temperature after contact. In fact, contact resistors are a major source of error when measuring low-voltage thin-film electrical resistance. Indeed, the contact resistance may exceed the value of the resistance that we want to measure. The technique used to eliminate this source of error is to deliver a constant current of high stability on 2 wires and to associate a voltage measurement on 2 other

wires. This technique is called « 4-wire measurement » and requires that the voltmeter used to measure the potential difference across the resistor must have a high input impedance and a good measurement accuracy. The diagram below shows the 4-wire measurement principle used on our PT100 probes.

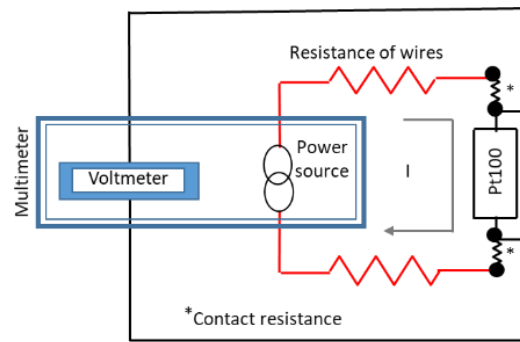


Figure 5-13: 4-wire circuit diagram made on PT100 probes.

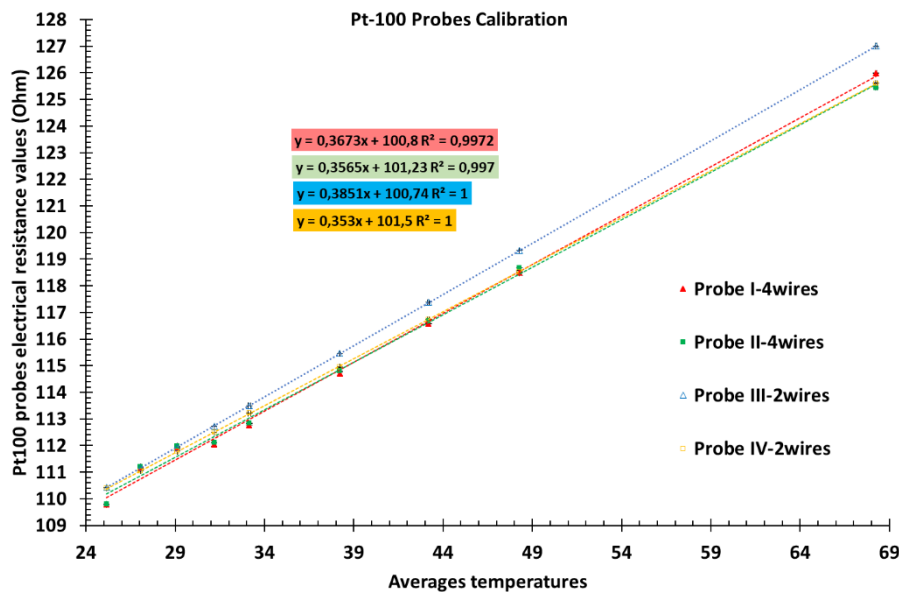


Figure 5-14: the four PT100 probe calibration curves and the associated governing equations.

For the calibration process, the four probes were introduced altogether in the Gemini oven, thus they were calibrated at the same time. We decided to carry out resistance measurements for nine given temperatures (25, 27, 29, 31, 33, 39, 44, 49 and 69°C). Those values were chosen quite low since the expected temperature in the cooling mode was around the ambient one. It is important to note that it took almost a full day to obtain those nine temperatures since the Gemini oven can only heat (no cooling system). Thus, before the resistance is measured, the stabilization period can be quite long (more than 30 minutes as an average). By plotting the resistance curves as a function of temperature, the slopes make it possible to determine the conversion factors between measured resistance and temperature for the exact determination of the temperatures during the characterization of the micro-machine. The result of the PT100 probes calibration is shown in the Figure 5-14 : we can see that, for an identical temperature, there exists a small discrepancy in the measured values of resistance. For platinum probes, the evolution of the resistance versus the temperature is known to be a straight line. The associated equation for the 4 probes are given on the Figure 5-14 and from them, knowing the resistance, the temperature can be accurately determined.

Now that the temperature probes are calibrated, we will present in the next sections the two experimental benches, which were developed during this PhD to test the micro-machine in the motor mode as well as in the cooling mode.

## 5.6. Motor mode

In this section, we will focus on the micro-machines that were assembled specially for the motor mode, *i.e.* either with incompressible liquid, or with a glass solid piston between the membranes (each time, without magnets, *i.e.* left part of the Figure 5-8 and Figure 5-9).

### 5.6.1. Test bench for the motor mode

For the motor mode, the aim was to measure the membrane's displacement when applying a given temperature difference between the hot and the cold parts. The test bench developed for the motor mode is represented on the Figure 5-15 and consists of the following elements:

- **Two supports:** adjustable in z (height), among which one is also adjustable in the lateral direction. The first support will carry the displacement sensor, whereas the second one, with x-y displacements, will carry the micro-machine.
- **Heating and cooling elements on both sides of the micro-machine:** the heating system was composed of three small Peltier modules (1.2W, dimensions 6 x 6 x 3.8 mm<sup>3</sup>) to be placed on the upper surface (through which we can see the membranes). The cooling system was provided by a larger Peltier module (20.9W, dimensions: 25x25x3.8mm<sup>3</sup>), which is placed on the bottom surface of the machine. Indeed, we made efforts to avoid as much as possible heat inputs by natural convection along the vertical faces of the engine (which could have occurred by placing the heating elements underneath). Thus, the three small Peltier modules were used to heat, whereas the larger Peltier module was used to cool. A multi-channel DC power supply was linked to all the Peltier modules. Later on, to increase the temperature gradient between hot and cold plate, we used a hot convective blower (measured temperatures up to 120°C on the surface) instead of the small Peltier modules.
- **Temperature measurements:** on the hot surface (top of the engine), it was ensured with a PT100. But, on the cold face of the engine, since we needed a contact on the whole surface of the engine with the cold wall (Peltier), it was not possible to use a PT100 (which would induce a space between the cold wall and the bottom face of the micro-machine). Thus, we used a K-type thermocouple that was embedded in a highly conductive copper block located between the Peltier module and the micro-machine. A layer of thermal grease between the micro-machine and the copper block underneath ensures a good thermal conductivity. The larger Peltier module (cold wall) was “glued” on the downward face of the copper block by a double-sided copper coated tape. Since in the Peltier module, one face is a heater whereas the other one is a cooler, the heat produced by the Peltier module had to be removed: to do so, the Peltier module was placed on top of a heatsink (caloduc with a ventilator fan), the thermal contact being ensured again by thermal grease. The three small Peltier modules as well as the PT100 probes were also attached to the top of the micromachine with a copper tape. The temperature sensors (PT100 and thermocouple) were plugged into the NI hardware racks that was connected to the PC. The choice of an “external” instrumentation is justified by our choice to avoid intrusive methods: indeed, introducing sensors inside gas chambers would increase the risk of leakage by the wire vias, could modified the fluid flow and would also increase dead volumes.
- **Membrane displacement measurements:** to access the membranes after complete assembly of the micro-machine, three orifices of 1.5 mm diameter located above the center of the three membranes were etched in the silicon plates carrying the outer chambers (*cf.* Figure 5-6). To ensure airtightness, these holes were covered with glass thin plates to make non-intrusive deflection measurements. Those measurements were done either with a laser motion sensor (Panasonic HG-C1030), or with a confocal sensor (STIL CHR 150-L). The laser motion sensor has the advantage to work on all types of surfaces, whereas confocal sensor is more efficient on reflective surfaces (the signal is noisy on the RTV silicone). On the other hand, the confocal sensor is more accurate.
  - The Panasonic laser sensor measures the vertical displacement of the membranes. Both the measurement principle and some characteristics given by the manufacturer are provided in Figure 5-16. The sensor principle is to measure the distance to the object, by using the triangulation principle. The laser diode converts the position of the optical spot on the light-receiving element to a distance. The advantages of this contactless sensor are the long sensing distance, a measurement with a small beam spot and at high-speed. The signal recovery is provided to a LabVIEW program by an analog output connected to the NI interface.
  - The chromatic confocal sensor (STIL: CHR 150-L with CL4 sensor, *cf.* Figure 5-17) used consists of a controller (1), an optical probe shaped like a pen (2) and a fiber optic cable (3). The sensor's optical probe is connected to an acquisition interface (with an analog output) through an optical fiber. This sensor measures the height (z coordinate) of reflecting points located on the optical axis. The optical principle of chromatic confocal imaging (STIL SA patent) is illustrated in the scheme of Figure 5-17. This principle of

chromatic imaging consists of providing a "color coding" along the optical axis from an incident white light pinhole imaged through a chromatic objective into a continuum of monochromatic images along the z-Axis. When an object is present in this "colored" field, a unique wavelength is perfectly focused at its surface and then reflected into the optical system. This backscattered beam passes through a filtering pinhole into a spectrograph, which determines the wavelength that has been perfectly focused on the object, and then accurately determine its position in the measuring field. This confocal chromatic imaging gives access to reliable, accurate and reproducible dimensional measurements with extremely high resolution [246].

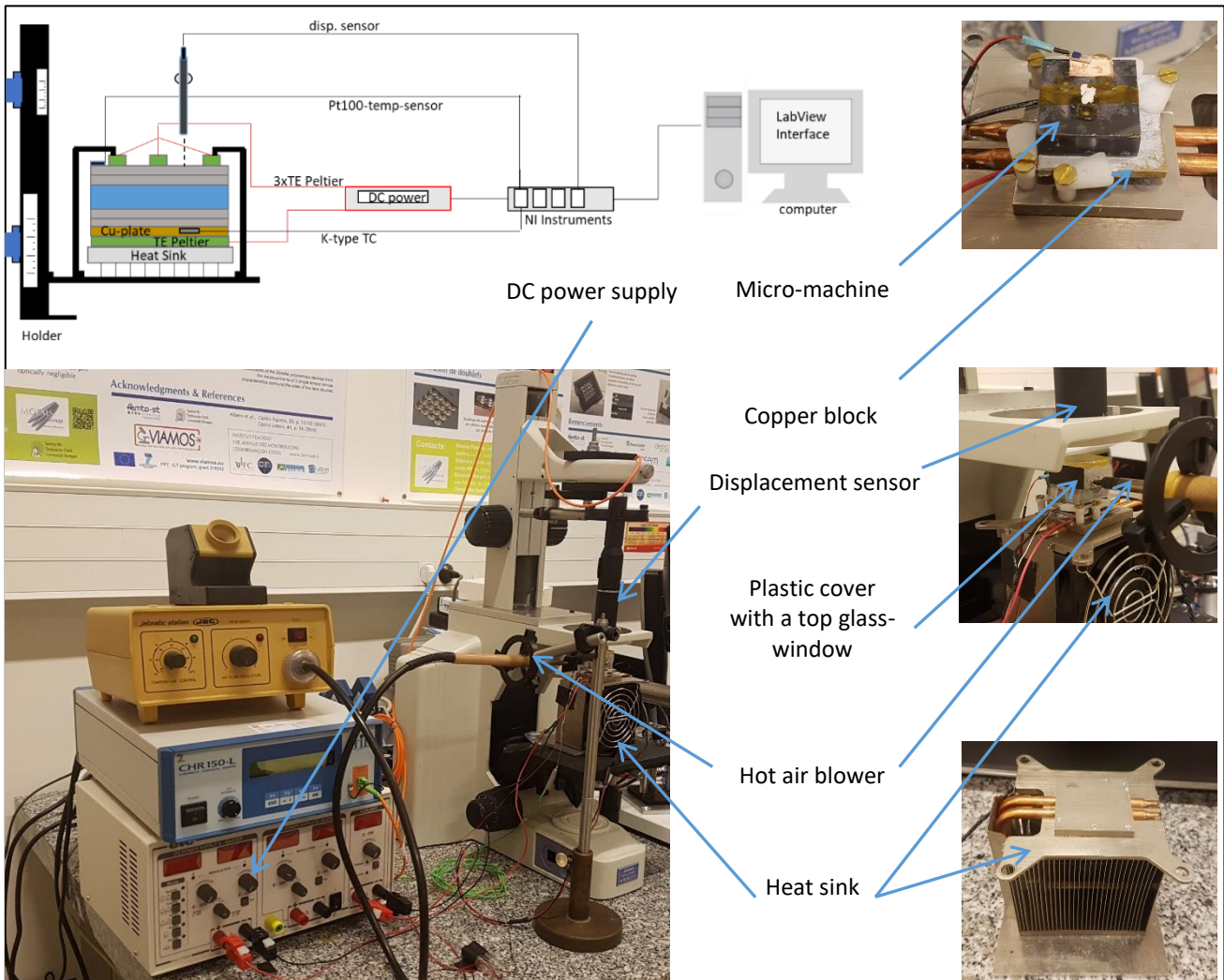


Figure 5-15: On the top: a block diagram of the experimental setup built to test the micro-machine in motor mode. On the bottom and on the right: a picture of the experimental setup with the constitutive elements.

Reference	HG-C1030
Central distance installation and measuring range	30 ± 5mm
repeatability	10 μm
linearity	±0.1% Full scale
Laser spot size	~ 50 μm
Response time	10ms / 5ms / 1.5ms

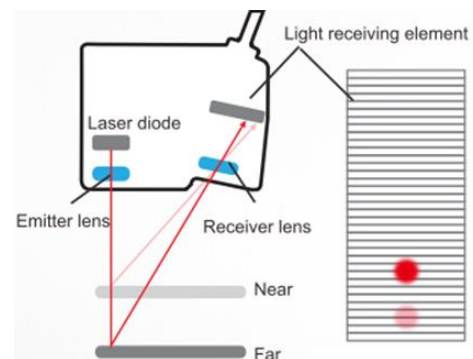


Figure 5-16: Panasonic HG-C1030: on the left, some relevant characteristics and on the right, the triangularisation principle [247].



Reference	STIL CHR 150-L with CL4 sensor
Spot diameter	8 $\mu\text{m}$
Axial resolution	From 0.3 $\mu\text{m}$
Measuring Range	up to 2.5mm
Technology	Chromatic confocal imaging
Measuring rate	Up to 10kHz

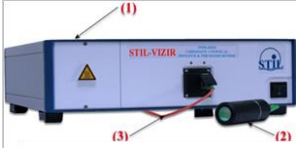
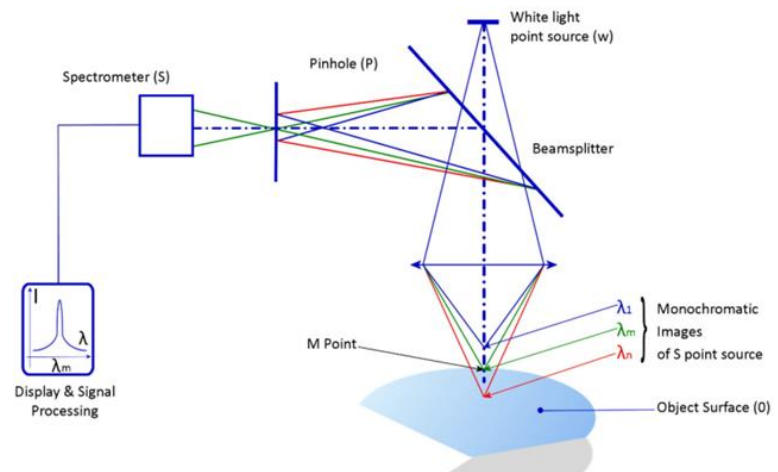



Figure 5-17: Chromatic confocal sensor STIL CHR 150-L : on the left, some relevant characteristics and on the right, the confocal principle [246].

– **Data acquisition:** all data from the sensors (displacement and temperature) were acquired thanks to a national instrument station (NI cDAQ-9178) linked to a computer. The LabVIEW interface on the computer was developed to both control and synchronize the onset of data acquisition of temperature and displacement. This program was developed to run either for the engine or for the cooling mode (control of the frequency of membrane oscillation using permanent magnets and by controlling the imposed electromagnetic field). For the engine mode of the micro-machine, the program allows simultaneous acquisition of the hot (at the top of the micro-machine) and cold (bottom) temperatures (and thus the temperature difference) as well as the displacement and the oscillation frequency of the membrane of the micro-machine.

### 5.6.2. Experimental results for the motor mode

We carried out experiments with various temperature differences: from  $20^\circ\text{C} \pm 1^\circ\text{C}$  for the lowest, to  $110^\circ\text{C} \pm 1^\circ\text{C}$  for the highest. When using Peltier modules as heating system, we did not manage to overcome a temperature's difference of almost  $50^\circ\text{C}$ . For such temperature's differences, no motion in the membranes was detected. Then, we decided to increase the temperature gradient. Instead of the heating Peltier, we used a convective air blower. The temperature difference we manage to reach was about  $70^\circ\text{C} \pm 1^\circ\text{C}$ . Unfortunately, this time again, no motion was detected as it can be seen on the Figure 5-18 for two differences of temperatures ( $43^\circ\text{C}$  and  $70^\circ\text{C}$ ).

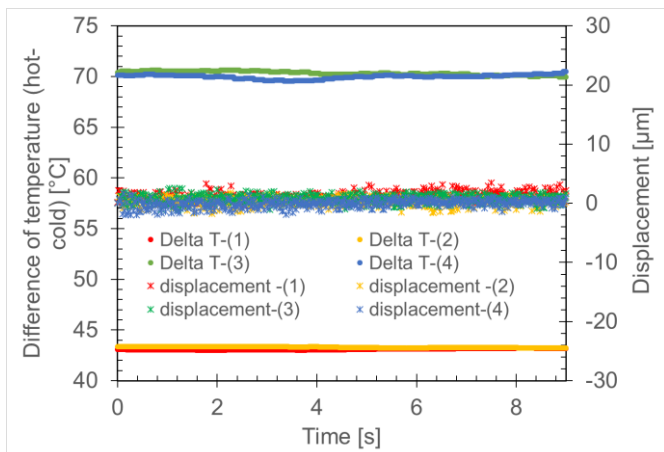


Figure 5-18 : Measured temperature difference (called "Delta T", on the left axis) and associated membranes' displacement (called "displacement", on the right axis) versus time. Two Delta T were tested and for each Delta T, results from two different tests are represented (1 and 2 for Delta T of  $43^\circ\text{C}$ ; 3 and 4 for Delta T of  $70^\circ\text{C}$ ).

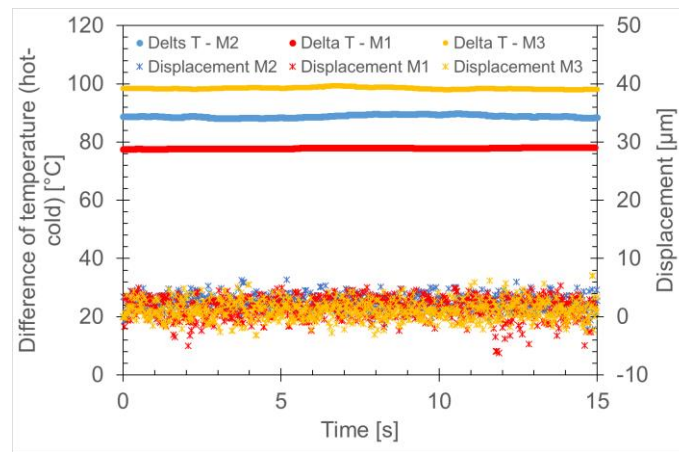


Figure 5-19: Measured temperature difference (called "Delta T", on the left axis) and associated membranes' displacement (called "displacement", on the right axis) versus time. Experiments carried out with the plastic cover with a top glass-window.

Combined with the use of a plastic cover with a top glass-window, on the top of the machine has enabled us to reach temperatures differences up to  $110^{\circ}\text{C} \pm 1^{\circ}\text{C}$ . Nevertheless, even at those large temperature gradients, we unfortunately did not observe any membrane displacement, as it is visible on the Figure 5-19.

Since the micro-machine failed to move in the motor mode, we decided to test the cooling mode by using micro-machines with magnets. Note that an attempt to explain why the machine did not work in motor mode is given in the section 5.7.3.

## 5.7. Cooling Mode

There are two types of micro-machines used to test the cooling operation mode. We assembled a machine with liquid coupling and two magnet and a second one with a solid plastic rod and two magnet (*cf.* the right part of Figure 5-8 and Figure 5-9). To test the micro-machine in cooling mode, actuation of two membranes out of phase by  $120^{\circ}$  is required. The movement of the micro motor membranes is linear (not rotating) therefore the initial idea was to integrate piezoelectric layers on the silicon spiral. However, this choice proved incompatible with the technology of squeegee deposition used for the RTV-silicone material. Therefore, we decided to use an electromagnetic actuator and kept the spiral in silicon to control the movement of the membrane. This linear electromagnetic actuator was made by gluing a small permanent magnet on the face of the central disk that is not in contact with the chambers and to actuate it from outside the machine using an electromagnetic coil.

### 5.7.1. Test bench for the cooling mode

The experimental bench for the cooling mode is given on the Figure 5-20. It is quite similar to the one for the motor mode. Thus, we will only present the new elements (for details and complements, please check the section 5.6.2), which consist of:

- **Two supports** (for the displacement sensor and for the micro-machine)
- **Temperature measurements** using the four PT100 probes that were calibrated (a 2-wires and a 4-wires connected on each face of the machine).
- **Membrane displacement measurements:** with a laser motion sensor (Panasonic HG-C1030), or with a confocal sensor (STIL CHR 150-L).
- **Membranes actuation:** on this test bench, one of the coils is placed above the micro-machine vertically aligned to one of the 3 upper membrane containing a magnet, while the other coil is below, aligned with an opposite membrane containing the second magnet. The micro-machine and the coils are fixed on a mechanical support made of polycarbonate specially designed to avoid parasitic effects related to the presence of electromagnetic fields. A detail of this support is given on the right part of the Figure 5-20. To avoid interaction and to ensure alignment, but also to allow on optical access to measure the membrane displacement, the coils we choose had the same diameter than the RTV silicone overlayer on the membranes (6 mm). Other types of coils were used later on when the first one proved not powerful enough for the full motor. Those coils are presented in the Figure 5-21. The whole was maintained by the adjustable plate of the large adjustable support in height.
- Continuous and alternative power supplies for sensors and coils and current amplifier (coils).
- **Data acquisition:** all the data from the sensors (displacements/temperature) were acquired with the national instrument station (NI cDAG-9178) linked to a computer with a specific LabVIEW program.

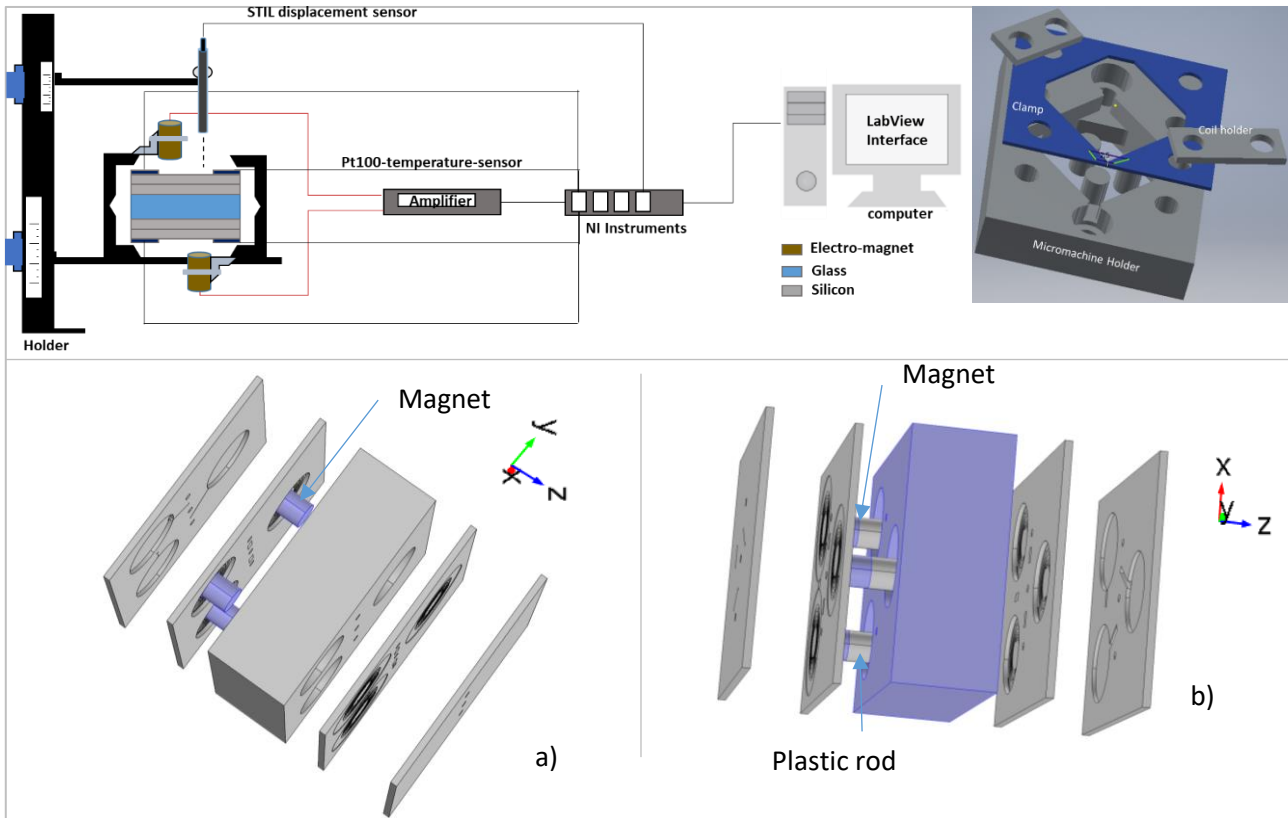


Figure 5-20: On the top : a block diagram of the apparatus used for the for the micro-machine test in cooling mode (left part) and a detail of the support designed for the motor and the coils (ight part). Below : a) Stirling microengine with magnet and liquid. b) Stirling microengine with magnet and plastic rods.



Characteristics & picture of the first type of coil		Characteristics & picture of the second type of coil	
Inductance: $24 \mu\text{h} \pm 10\%$ Q-Factor (@ 125 kHz/ 10 mA): 16 Saturation Current : 1 A Operating Temperature: $20 \text{ }^\circ\text{C}$ up to $+105 \text{ }^\circ\text{C}$		Resistance = 100 ohms $U_{\text{max}} = 12\text{V}$ (Extracted from a power relay)	

Figure 5-21: The characteristics of the coils used for the operation in cooling mode of the micro-machine.

### 5.7.2. Experimental results for the cooling mode

The first engine we decided to test in cooling mode was the one with the liquid. Underneath each membrane, we introduced one small permanent magnet. We have used six identical  $\text{Nd}_2\text{Fe}_{14}\text{B}$  magnets to ensure both homogeneity and symmetry. The first magnets we tested had a magnetic influence range of 1.2cm. Since the membranes are spaced 1 cm apart, this has led to problems of magnetic interaction between magnets (*cf.* schematic view on Figure 5-22). To avoid interaction in both vertical and horizontal directions, we demagnetized four of them in an oven heated above the Curie temperature. On the three magnets on one side of the machine, two were thus demagnetized. To set the membranes in motion, we planned to use two external coils placed above or underneath the machine and on the membranes's location where magnets are active. With the coils presented on the Figure 5-21, we carried out some tests with single membranes and then with the full engine. The first coils could not actuate the membranes with displacements greater than a few microns; therefore, we decided to use more powerful coils, used in Power Relays (*cf.* Figure 5-21, on the right). These coils were very large; therefore, it was not possible to keep the micro-engine with 3 magnets on each side: the coil attracted all magnets (active and demagnetized) at the same time. We decided to assemble another engine: instead of the liquid one, we assembled one with solid plastic rods made by 3D printing, but with a configuration that was not symmetric. Only one magnet was located on each side, and on opposite chambers. Thus, we had two rods composed of plastic + one magnet, and the last rod was only composed of plastic.

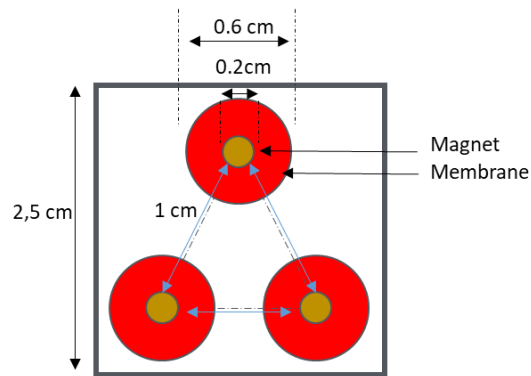


Figure 5-22: Diagram showing the possible locations of the magnets at the level of the membranes (problem of interaction between the magnets).

We performed two experiments: one with only one membrane actuated (to verify the global behavior) and another one with two membranes actuated (one on the top, the other one on the bottom of the micro-machine):

– **The first test: by actuating a single membrane** (to check the response of the other membranes).

The corresponding experimental setup is visible in the Figure 5-23. Only one electromagnet is installed under the membrane N°1, which has a magnet located on the underside of the machine. Membrane N°2 is the one that contains no magnets, and the membrane N°3 is the one with the second magnet, placed on top of the machine. Displacement measurements can be made from the top of the machine. The actuating signal was amplified by a current amplifier. Before being amplified, the voltage was set at 1 Vpp. The amplifier enables to adjust the current at 1.8 A (rms). For four actuating frequencies (1, 2, 5 and 10 Hz), we recorded the displacement of each of the membranes using the confocal sensor. Measurements were made under the same operating conditions (same position of the electromagnet with respect to the membranes, same voltage values delivered to the electromagnet). The results for four frequencies are given on the Figure 5-24.

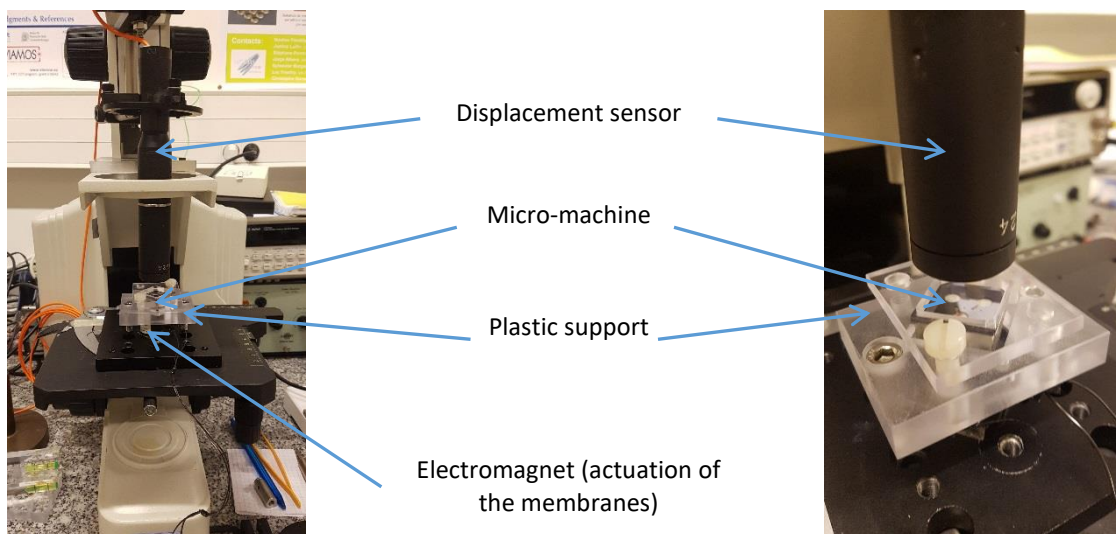


Figure 5-23 : experimental setup for the actuation of one membrane

It can be seen that the movement imposed on membrane 1 (M1) is well transmitted to membranes 2 (M2) and 3 (M3). On the other hand, there is a very strong attenuation of the displacement amplitude on membranes 2 and 3. We have several possible explanations for this. Despite relatively low frequencies, there may be damping related to mechanical resistance and/or pressure drops in the microchannels and/or compression effects (especially at high frequencies). However, with two membranes operated out of three, these problems should be partially reduced. Nevertheless, due to the size of the electromagnets, it will not be possible to measure displacement (no optical access) with two actuated membranes.

It is also noted on this figure that the frequency has a direct effect on the amplitude of displacement of the membranes. The Figure 5-26 shows the evolution of the average amplitude of displacement of the membranes as a function of the frequency imposed on the electromagnet. It can be seen that the displacement amplitude for both membranes 2 and 3 increases with frequency, while the amplitude of the displacement of the membrane 1 seems

to reach a maximum around 5Hz and then decreases. The decrease at low frequencies is probably due to the amplifier cutoff for low frequencies.

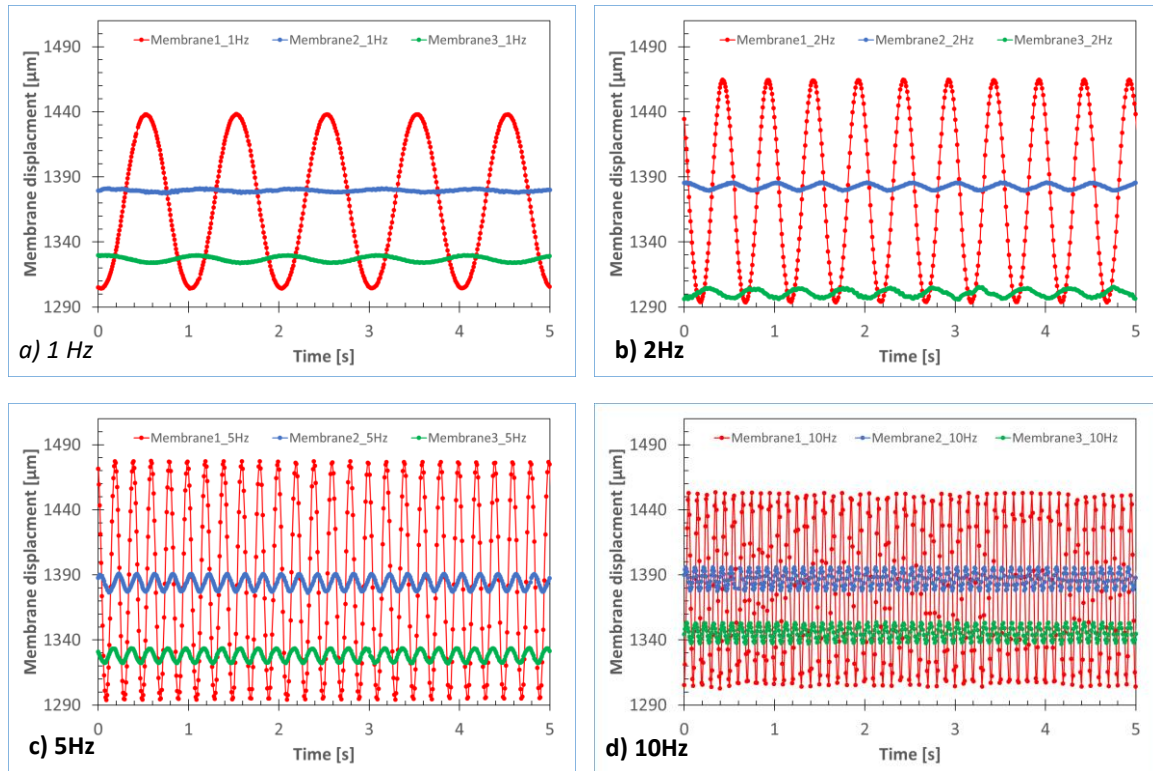


Figure 5-24 : Membranes displacement for one membrane actuated (membrane 1) at different frequencies (1, 2 5 and 10Hz)

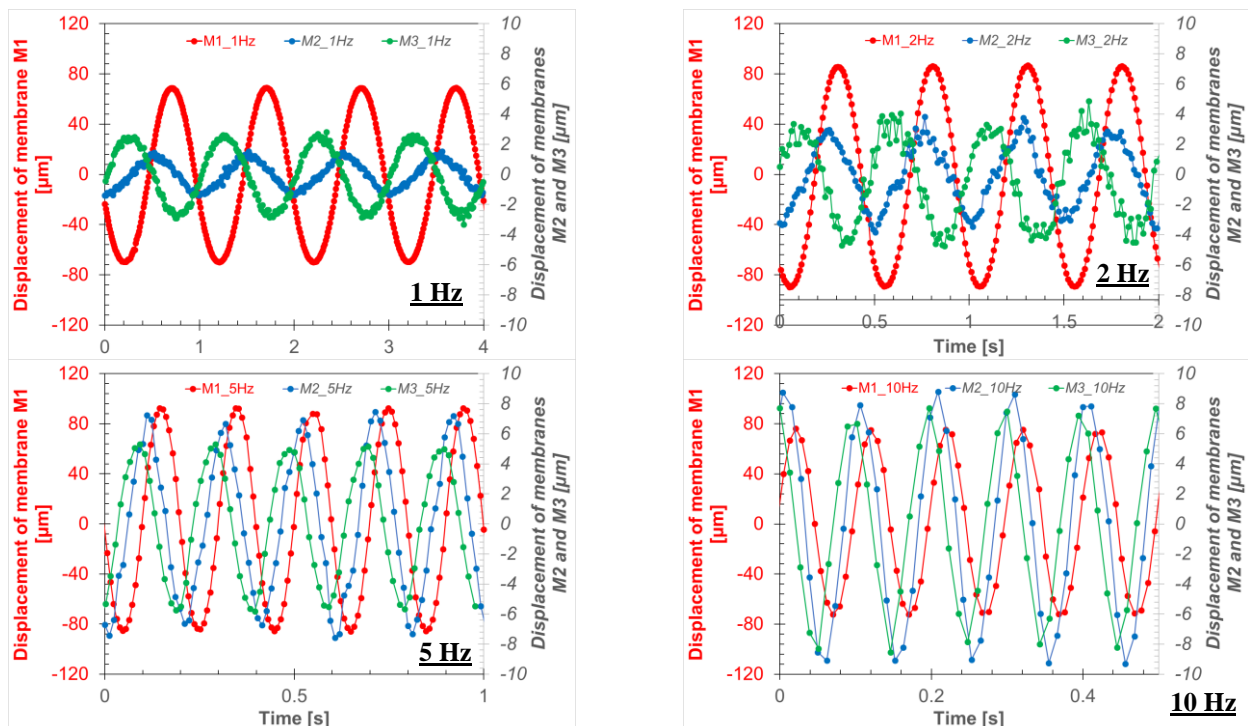


Figure 5-25 : Phase shift occurring between the membranes M1, M2 and M3 when only the membrane M1 is activated. Tests carried out for four frequencies : 1Hz, 2Hz, 5Hz and 10Hz.

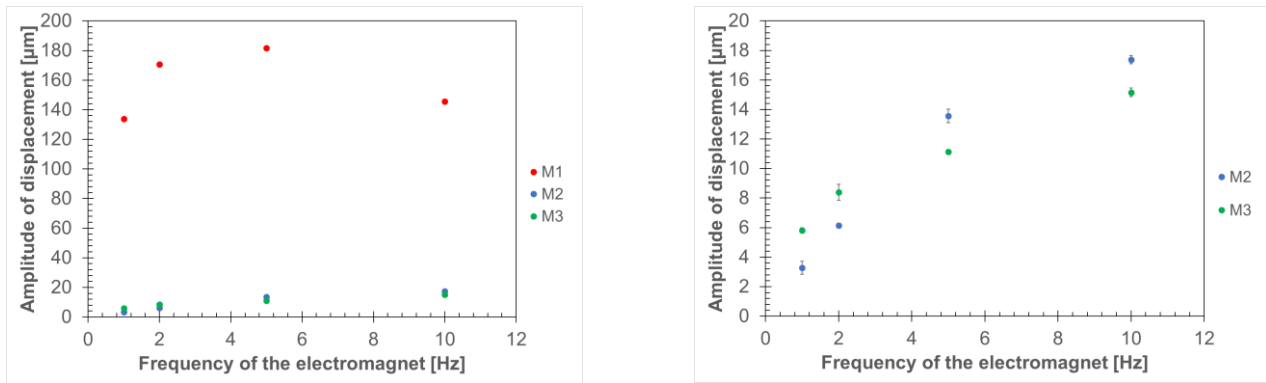


Figure 5-26: Mean amplitude of displacement for membranes M1, M2 and M3 on the top surface, versus frequency of the electromagnet (note that the scale is divided by 10 for displacements on M2 & M3. Only the membrane opposite to M1 is actuated).

When the membrane opposite to M1 is actuated, it is shown on Figure 5-25 that the M2 and M3 membranes are moving with a phase shift. The phase shifts that was observed between the movements of the upper membranes are difficult to explain: for very low frequencies, we expected no phase shift. The lowest frequency that we were able to reach was 0.25 Hz since the amplifier that we use does not amplify DC currents. For this low frequency, although the signals are quite low, is still possible to observe that one of the membranes is out of phase ( $180^\circ$  phase shift with the driving one). Therefore, we imagined that it may be due to the fact that the driving magnet is influencing the magnet located on the top side of the machine (weakly attracting it), thus generating a movement that is not linked to the gas flow inside the machine. For this reason, these experiments have to be verified in further studies.

This first setup that we just presented allowed us to check the correct movement of the membrane when it was actuated by an electromagnet. Then, this setup was completed by adding the second electromagnet above membrane 3, *i.e.* the membrane on the upper side below which the second magnet is placed.

– **The second test: by actuating two membranes** (one on the upper side of the machine, the other one on its bottom side)

The actuation signal was generated via a Labview board, by fixing the phase shift between the two channels at  $2\pi/3$ . Each signal was then amplified on two signal amplifiers, adjusted to the same parameters (current intensity, gain). Each electromagnet was therefore powered by an alternating current of the same characteristics but with a  $2\pi/3$  phase shift. This phase shift was verified on a digital oscilloscope for the different frequencies studied. PT100 sensors were placed on each side of the machine, allowing the measurement of temperatures. The temperature of the room was also recorded in order to know the operating conditions as well as possible and thus try to ensure good reproducibility. A close-up of the experimental setup is given on the right part of the Figure 5-27.

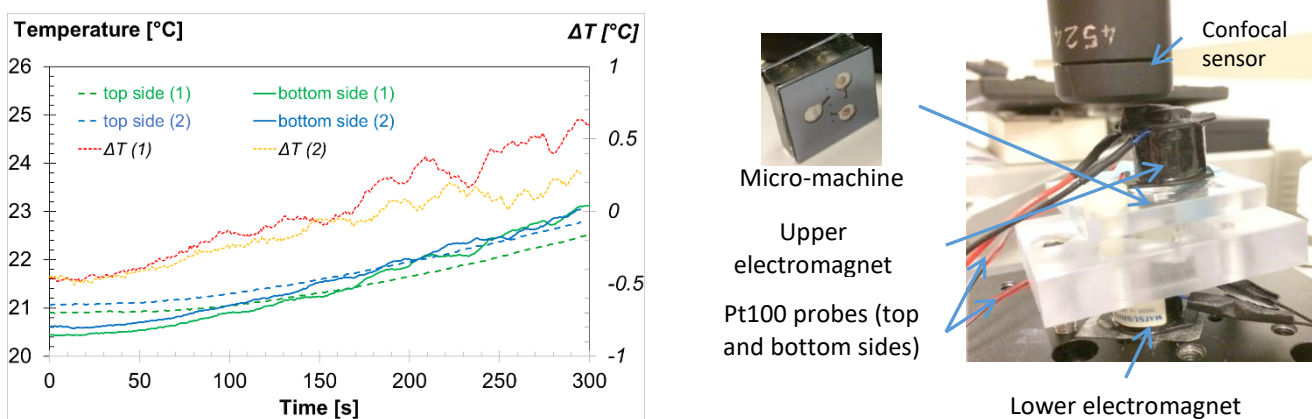


Figure 5-27: On the left : Temperatures measured (left axis) on both sides of the machine in cooling mode versus time and associated temperature's difference  $\Delta T$  (right axis). On the right : a close-up of the exeperiment.

With an actuation signal set at a frequency of 5Hz, and current and tension at respectively 1.8 A (rms) and 1 Vpp, the Figure 5-27 shows (left part) an exemple of temperatures measurements. The temperature rises on both side of the micro-machine, but not in the same way for the top and bottom sides. When calculating the temperature's difference ( $\Delta$ ) between the bottom and the top side, it is found that this  $\Delta T$  also increases versus time (*cf.* Figure 5-27). This may be due to the cooling mode of the Stirling motor, but it could also be due to purely thermal conduction/convection phenomena of the heat generated by the electromagnet itself. These first tests did not make it possible to determine with certainty whether or not a temperature difference was created on either side of the machine. Indeed, to be effective, the electromagnets are placed close (a few millimeters) to the machine faces. However, these electromagnets heat up quickly when a current flow through them. This heating then results in a rise in the temperature measured on the micromachine. Moreover, since the two amplifiers are not identical (not the same models) and the electro magnets come from two different batches, we cannot, at this stage, state that the difference we saw would not rather come from a different heating of the two electromagnets.

An attempt to differentiate between the influence of cooling (Stirling effect) and heating of the coils was made by testing different phase shifts between the two actuated membranes. For a phase shift equal to zero, the micro-machine should not follow the Stirling cycle and no cooling effect should be observed. We therefore carried out consecutive tests with a phase shift of  $0^\circ$  and  $120^\circ$ . The temperatures were measured on both sides of the micro-machine. The evolution of the temperatures as a function of time for the two-phase shifts is given in the left part of Figure 5-28. The trends are quite similar, but with a different slope. Moreover, with a phase shift of  $0^\circ$ , the curves corresponding to the temperatures measured on the upper and lower sides of the machine intersect, which is not the case for the  $120^\circ$  phase shift. We calculated the  $\Delta T$  between the top and the bottom faces:

$$\Delta T = T_{top} - T_{bottom}.$$

Since with a  $0^\circ$  phase shift, no effect related to the Stirling cycle should occur, the corresponding temperature's difference between top and bottom faces was used as a reference.

Then we calculated the difference "Delta T" which is the difference between the temperature difference at a given phase shift ( $\Delta T_{X^\circ}$ ), and that at a phase shift of  $0^\circ$  ( $\Delta T_{0^\circ}$ ):

$$\Delta T = \Delta T_{X^\circ} - \Delta T_{0^\circ}$$

For an actuation frequency of 5Hz, the corresponding curve is given on the right part of the Figure 5-28. On these preliminary results, it seems that a small cooling effect (less than  $1^\circ\text{C}$ ) occurs with a phase shift of  $120^\circ$ .

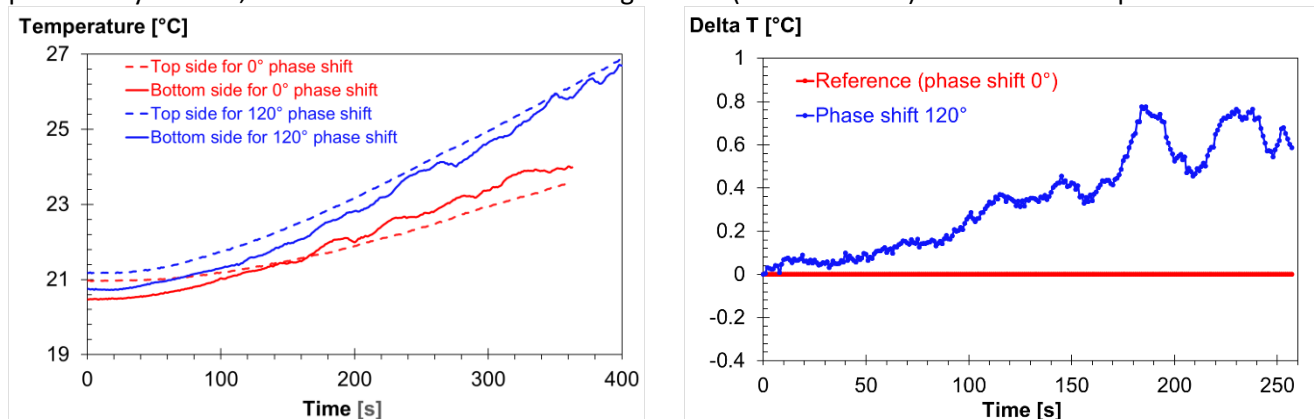


Figure 5-28 : For an actuation frequency of 5Hz, on the left : tempertaure measurements on the top side and on the bottom side of the mico-machine for two phase shift between membranes :  $0^\circ$  and  $120^\circ$ . On the right : Difference between the temperature difference (between top and bottom side of the micromachine at a given phase shift) and the one at a phase shift of  $0^\circ$ .

The result showed above are encouraging since a small cooling effect seems to occur, however, only one frequency was tested. Since the cooling effect is rather small and because the electromagnets are also heating the micro-machine, it is not yet possible to be sure that this effect is really related to the Stirling effect. For this reason, further studies are required. Thus, in order to try answering to this interrogation, we plan to repeat the experiments (to verify the reproductibility of the tests) and to carry out complementary experiments, for a given input power, by modifying:

- The tested actuation frequency
- The phase shift between the membrane
- The orientation of the assembly (vertical or horizontal) in order to modify the effect of natural convection and therefore on the heating of the machine by the driving electromagnets
- The connection of the electrodes: we have swapped the current amplifiers that drive the membranes: we will thus have a direct influence on the Stirling effect.

### 5.7.3. Possible explanations for the problems encountered with the fabricated 3-phases micro-machine and perspectives for a simpler test architecture

The micro-machine was tested in motor and cooling mode. Whereas some encouraging results were obtained in the cooling mode, no results were obtained in the motor mode. We listed some possible explanations to the fact that the micro-machine did not give an operating result in motor mode during the test phases.

- **Some possible explanation of the problem encountered in motor mode:**

- **Possible degradation of the membranes due to the high temperature anodic bonding.** The Stirling liquid coupled micro-machine has been entirely manufactured in a clean room, so we are confident about the techniques used. The critical steps would be the 330°C applied during anodic bonding. As shown in chapter 4, anodic bonding could have damaged our membranes (for the record: test results at 300°C showed that the natural frequency of the membranes changes, as well as tests at 330°C that showed a deterioration of RTV-silicone membranes). Knowing that the anodic bonding was done at 330°C (otherwise welding quality problem were observed), one of the hypotheses is that the membranes are no longer waterproof following this step. The solution to overcome this problem has already been developed: we have demonstrated in the chapter 3 room temperature thermocompression that can replace anodic bonding with comparable performances and without heating. Using this technology, we will guarantee correct wafer assemblies without any damage to the polymer membranes.

- **Uncontrolled filling technique of the liquid.** Presently, there is no way to monitor the filling process of the liquid inside the machine. Therefore, filling with an excess of liquid is always possible. Therefore, the membranes could already be pre-stressed - with an initial deflection - which would limit the possibility to move them. Due to the material used (silicon), it was difficult to ensure that the membranes at rest was actually flat. To avoid this problem, the solution that was adopted was to replace the liquid with a solid rod made of plastic (for less heat conduction) or glass (for more weight since it decreases in the natural frequency of oscillation of the membranes).

- **Thermal gradient between the hot and cold part not sufficient to trigger the micromachine.** We are limited by the geometrical characteristics of our machine and therefore the possible power ranges of the Peltier modules. In order to reach higher temperature gradient values, the heating system would have to be modified: the use of heating resistors, coupled or not with heat exchangers, could be an interesting alternative. In addition, the cooling system would most certainly also have to be modified in order to achieve higher power dissipation and therefore a higher temperature difference between the hot and cold sources.

- **No starter on the machine.** Another reason for not operating in motor mode is that our micromachine has symmetrical geometry: there is no thermal imbalance between the different membranes in the same plane or face. Thus, there is no possibility to send a "pulse" to unbalance/dephase the system and thus initiate the oscillations of the membranes.

A solution to avoid all these difficulties is a change in geometry by further simplifying it. Switching to a 2D machine would simplify the process, facilitate assembly, free from right angles creating singular pressure losses, limit dead volumes, facilitate instrumentation and optical access for measuring membrane oscillations (all in the same plane). This will also make it easier to operate the membranes and to reach higher temperature's differences in motor mode respectively because membranes would be in the same plane and because they would be further apart than in the 3D version (higher thermal resistance). This new version of the test micromachine is currently being finalized and is presented below:



- **New 2D test-machine under construction**

To study the Stirling cycle with a machine that is easier to control and to monitor, we designed the machine represented in Figure 5-29 with its view from above (top scheme) and from the side (bottom scheme). This new micromachine consists of two membranes (30 mm in diameter) resting on chambers connected by a square section channel (0.2mm thick). The stack is sealed by a machined plastic film embedded between two plates. The first plate contains two observation holes (optical access) 5 mm in diameter, located at the level of the membranes. The second plate is the one in which the two chambers (compression and expansion) and the square-section channel connecting them are located. Permanent magnets can be glued to the diaphragms for electromagnetic actuation. This micromachine is currently being manufactured at the FEMTO-ST Institute. Its advantages are:

- A large separation between hot and cold parts of the machine, with a rather long insulating plastic part
- The possibility of actuation by two high power electromagnets placed below the machine while enabling observation from the top
- To avoid diffusion of the produced heat, a small metal part that will be heated or cooled
- Two RTV-silicone membranes to implement an Alpha type machine whose operating conditions are defined and controlled by changing the phase shift between membranes movements
- Integration of temperature and pressure sensors on the metal parts for better monitoring of the Stirling cycle
- This architecture should allow accurate measurement of motion transfer times between the two membranes across the channel and measure its microfluidic characteristics. It will also be possible to detect the limits of actuation frequencies (or cut-off frequencies) not to be exceeded with electromagnetic coils to obtain a good fluid transfert.

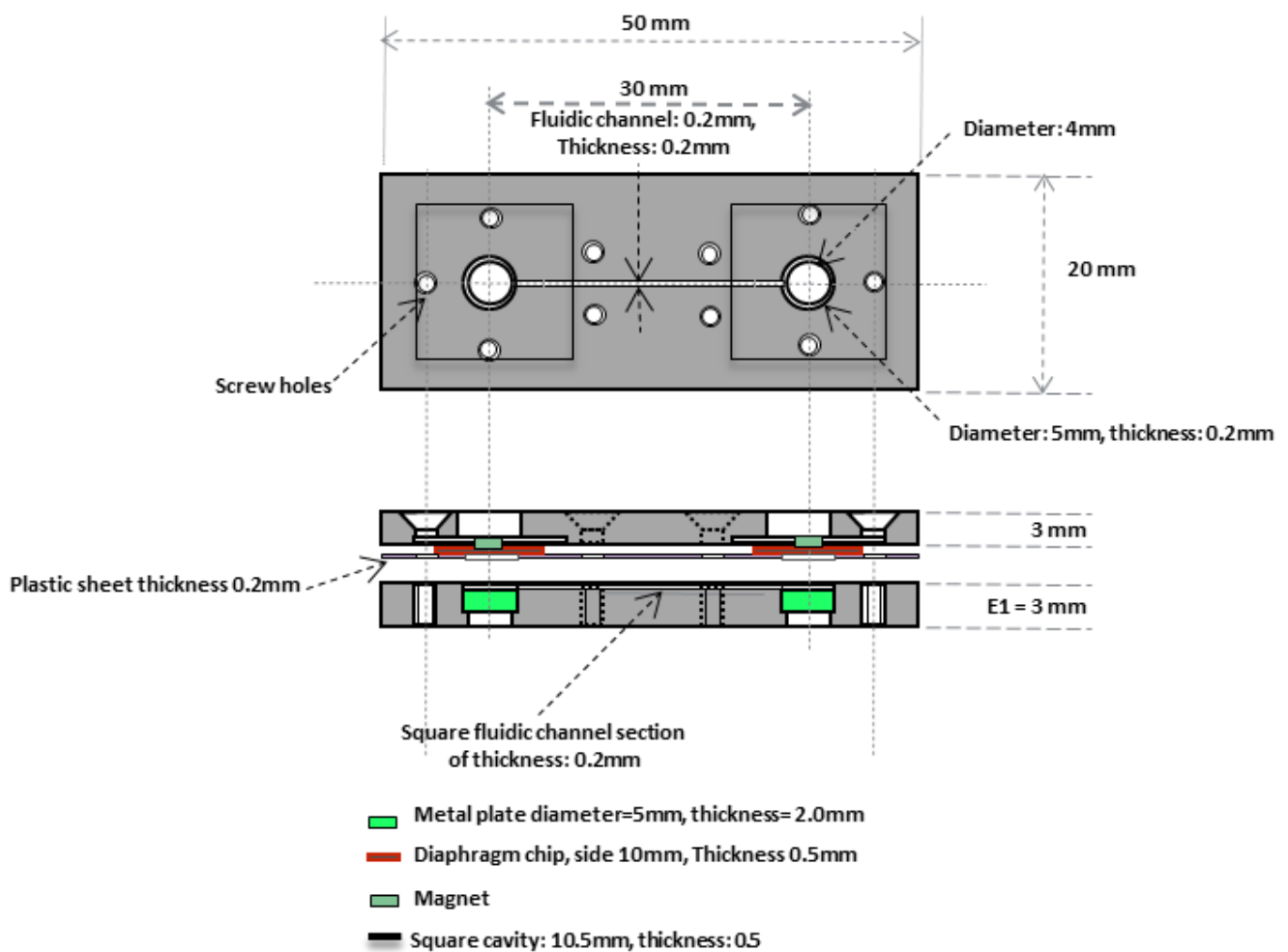


Figure 5-29: New 2D architecture of the micromachine

### 5.7.4. Conclusion

In this chapter, the assembled Stirling micro-machines in motor and cooling mode were characterized and tested. Four different micromachines were assembled with different types of mechanical connections between the membranes (incompressible liquid or solid bonding rods). Some dynamic characterization showed that the eigen frequency of the micro-machine could reach values lower than 300Hz, and that they could be decreased again by adjusting geometric parameters. These types of membranes and assemblies can thus have a large range of applications, such as vibrational harvesting for instance. To test both motor and cooling mode, two specific experimental setups were developed. The micro-machines were then tested and, if no results were obtained in the motor mode, the cooling mode seemed to be promising.

**To conclude on this chapter, we will recall here the main results we obtained:**

1. A test of the **membrane/chamber assembly** has allowed observing the ability to expel air from one chamber to the other one.
2. Tests of the **complete micromachine in the motor mode** were carried out with a temperature difference between the hot and cold part that reached **more than 100 °C but no movement** of the membranes was observed yet.
3. Tests of the **complete micromachine in cooling mode** were carried out. To do so, some machines have been assembled **with magnets** inserted on some of the membranes to be able to actuate them and to observe the cooling effect of the Stirling machine. First results are **encouraging but further experiments are required** to be able to discrete with certainty the effect of the electromagnet of the cooling effect related to the Stirling cycle.
4. **Possible reasons for the observed failure** of motor mode have been listed.
5. **A design of a simpler Alpha-type Stirling micromachine** that will enable testing in more details the fluidic and thermal behavior of the machine is now under construction.

---

## CONCLUSION

The work on Stirling micromachines presented in this manuscript has made it possible to review the challenges involved in miniaturizing these machines and to estimate the performance in terms of mechanical power supplied that can be expected. The work focused on the feasibility of a micromachine architecture that was proposed as part of the ANR MISTIC project [107] and that was the subject of detailed modeling.

First, the design of the micromachine was studied and chosen, based on various physical principles (thermal, fluidics...) and on clean-room possibilities. Then, the main work consisted in developing a complex microfabrication process to produce micromachines using MEMS type technologies in clean rooms.

The key element of these micromachines is the membrane, which plays the same role as the piston with which macroscopic Stirling machines are built. This membrane was developed using a Silicone elastomer "RTV (Room Temperature Vulcanizing)" which has not been used extensively in clean room manufacturing processes and whose mechanical properties have therefore been studied in details. A Young's modulus of this polymer in the order of 1 MPa was measured and its stiffness was calculated and found to be in the range of 0.1 to 0.2 N/mm. The 5 mm diameter membranes that were designed and fabricated have proved to be very robust and to allow deflections of about 1 (spiral) to 2 mm (central disk) at the centre without breaking. Their resonance frequencies range from 850 Hz to 2800 Hz, depending on whether or not they incorporate a silicon spiral structure.

Their ageing characteristics at high temperatures have been estimated and it appears that they can operate at 200°C without observed ageing and up to about 300°C without significant deterioration. Hybrid fluidic membranes, made of pairs of RTV-silicone membranes coupled by an intermediate liquid, allowing mechanical coupling between two opposite chambers of the machine, were also designed and tested. These hybrid fluidic membranes offer sufficient performance for the micromachine under consideration and their resonance frequencies were lower than for the membrane alone, which may be an advantage and can have numerous applications possibilities in the field of harvesting.

As the machine consisted of an assembly of various structured plates, the development of these assembly techniques was a major work challenge. In particular, a complete study of an assembly process at room temperature by gold thermocompression was carried out to prevent future damage to the polymer membranes during assembly (classical anodic bonding requires temperatures above 300°C). This study made it possible to produce very tight assemblies with tensile failure stresses in the order of 20 to 30 MPa, which are among the best reported in the literature. This technique will therefore make it possible to preserve the mechanical qualities of the membranes, but also enable the use of a gas at a pressure higher than 10 bar without causing the assemblies to rupture.

The first tests of operation in motor mode of these machines were carried out but unfortunately proved unsuccessful: despite a temperature difference of about 100 °C between the hot and cold springs, the micromachine did not start. On the other hand, tests carried out with micromachines operating in cooling mode and activated by magnets and electromagnets were encouraging. Indeed, preliminary results showed very slight cooling. However, these results need to be consolidated and supplemented by systematic measurements.

In view of the difficulty encountered in visualising and measuring the membranes motions, the pressures and temperatures of the gases inside this machine, it will also be necessary in the future to produce easily instrumentable subassemblies of this machine, which can be optimised separately. In particular, it will be necessary to incorporate electromechanical actuators to move the membranes. The influence of these electromagnets (heating) will have to be taken care of. The implementation of a system of actuation will enable to check the efficiency of the gas transfers inside the machine and to optimize the pressure drops according to the amplitude and frequency of the internal gas flows. To this end, thanks to the present work, the necessary technological building blocks are now available and should enable these studies to be continued in the future under much more comfortable conditions than at the outset.

## APPENDIX A: TRANSDUCERS

### 1.1. Comparisons of various energy harvesters

Flexoelectric polymers are ideal for energy harvesting in smart textiles, since they can withstand high stresses.

Principles	Alternative Expression	Common Materials	Pros	Constrains
<b>Electromagnetic</b>	Electromechanc electrodynamic DC generator	Neodymium iron boron (NdFeB)	Simple construction on a large scale Low output impedance Higher output current	Low output voltage (<1 V) Downsizing limitations Affected by electromagnetic field
<b>Piezoelectric</b>	Piezoelectricity	Lead zirconate titanate	Simple structure on a small scale High output voltage (>5 V) High coupling coefficient	Low output current Low strain limit Brittle
<b>Electrostatic</b>	Triboelectric capacitive	Conductive capacitor	Very high output voltage (>100 V) Smart material not needed Ease of voltage rectification and frequency tuning	Biased voltage required High impedance needed Low output current
<b>Magnetostrictive</b>	Electrostriction	Metglas	High energy density Long life cycle	Affected by electromagnetic field Downsizing limitation
<b>Flexoelectric</b>	Polymeric	Barium strontium titanate	High-strain limit	High dielectric permittivity Low stress limit
<b>Hybrid</b>	Thermoelectric- electromagnetic	Chromel-alumel- NdFeB	Multi-energy sources	Complexity

Table 5-5: Comparisons of various energy harvesters [15].

### 1.2. Comparison of energy harvester architecture

Table 5-6 : Comparison of energy harvester architecture [15].

Architecture	Simplicity	Low Frequency	Wide Bandwidth	Multi Degree of Freedom	Microscaling	Mesoscaling	HighStrain Ratio
<b>Cantilever</b>	✓	✓ (polymeric material)	✓ (cantilever array)	X	✓	X	X
<b>Linear</b>	✓ (coil-spring magnet)	✓	X	X	X (electrostatics)	✓	✓
<b>Spiral</b>	X	✓ (levitation magnet)	✓	✓ (translation and torsion)	✓	X	X
<b>Rotational</b>	X	✓	✓ (hybrid)	✓ (translation and rotation)	✓	X (vulnerable to heavy ball magnet impact)	✓
<b>Aeroelastics</b>	X	X	X	X	✓	X	✓
<b>Mechanical</b>	✓ (market- ready DC generator)	✓ (gear reduction tuning)	X	X	X	✓	✓ (gear reduction)
<b>Hydraulic</b>	✓ (market- ready DC generator)	✓	X	X	X	✓	✓

Mechanisms	Architecture	Power, mW	Area, mm <sup>2</sup>	Volume, mm <sup>3</sup>	Acceleration, m/s <sup>2</sup>	Vibration Frequency, Hz	Bandwidth, Hz, min-max	
ES	Linear	0.01	...	...	19.62	10	...	...
EM	Linear	0.493	...	1940	29.43	13	...	...
PE	Spiral	0.046	...	203.4	39.24	52	...	...
PE + PV	Linear	0.02	...	...	...	17	...	...
EM	Flutter	0	...	2625	...	...	...	...
EM + PE	Linear + cantilever	0.913	...	...	...	31.2	30	34
FE	Linear	0.404	720	...	5	74	72.75	75.25
PE	Spiral	0.00033	...	8000	...	100	...	...
ES	Linear	0.1	529	...	...	43.5	...	...
PE	Cantilever	0.03	...	300	...	30	...	...
PE	Flutter	0.0114	...	...	...	...	...	...
EM	Linear	6000	...	100 500	9.81	15.5	...	...
EM	Pendulum	0.9702	...	...	4.905	3.5	...	...
EM + PE	Cantilever	3.32	...	4000	2.943	33.5	25.5	62
EM + PE	Linear	0.55	...	48 433	...	3	...	...
PE	Flutter	0.00001	560	...	...	20	...	...
ES	Diaphragm	40	18870.93	...	...	...	...	...
ES	Diaphragm	345.42	700	...	...	40	2	54
ES	Rotation	2.808	...	...	...	2.5	...	...
EM	Rotation	21.6	...	...	...	2.5	...	...
PE	Diaphragm	0.01786	0.2	...	...	2	...	...
PE + MS	Cantilever	...	...	...	0.981	21	...	...
ES	Linear	1.23	...	428 750	29.43	...	2.5	7.5
ES	Rotation	0.128	...	...	...	10	...	...
EM	Linear	304	...	7700	0.73575	6.7	...	...
EM	Linear	410	...	7700	0.981	6.7	...	...
EM	Linear	50 000	...	31 800	7.848	3.33	...	...
EM	Linear	14 550	...	12 500	0.38259	8	...	...
EM	Linear	90 000	...	150 000	19.62	37	...	...
EM	Linear	28 300	...	22 500	29.43	20	...	...
EM	Linear	1180	...	7400	15.696	9	...	...
FE	Diaphragm	...	...	...	...	...	...	...
EM	Cantilever	0.53	...	240	...	322	...	...
EM	Linear	0.4	...	23 500	...	2	...	...
EM	Linear	0.025	...	25 000	...	...	...	...
EM	Diaphragm	0.01	...	1000	0.0001	64	...	...
FE	Diaphragm	0.29	...	8624	...	102	...	...
FE	Diaphragm	0.153	...	8624	...	41	...	...
PE	Rotational	0.043	...	1850	...	2	...	...
EM	Mechanical	4302	...	...	...	2.5	...	...
EM	Mechanical	33 400	...	...	...	1.67	...	...

Table 5-7: Data on VEH R&D based on mechanism and architecture. Abbreviations: EM (electromagnetic); ES (electrostatic); FE (flexoelectric); PE (piezoelectric); MS (magnetostrictive); R&D (research and development); VEH (vibration - based energy harvester). [15]

### 1.3. Piezoelectric transducers: state-of-the-art devices and materials

Piezoelectric MEMS Transducers (PMT) are materials that can convert mechanical energy into electrical energy based on mechanical stress or strain effect that generates an electrical polarization inside them as illustrated in Figure 5-30 a). PMTs are preferable to electromagnetic and electrostatic transducers in the specific application of cantilevers harvesters because of their higher energy density and their CMOS technology compatible manufacturing process [17]. PMTs have two modes of piezoelectric operation: the  $d_{31}$  or  $d_{33}$  mode. In the first mode, the stress or the deformation is perpendicular to the direction of generation of the charges, whereas in the second mode, the stress and the electric field have the same direction. Figure 5-30 b) illustrates the stack of material used in the fabrication of the MEMS piezoelectric micro-cantilevers vibration harvester.

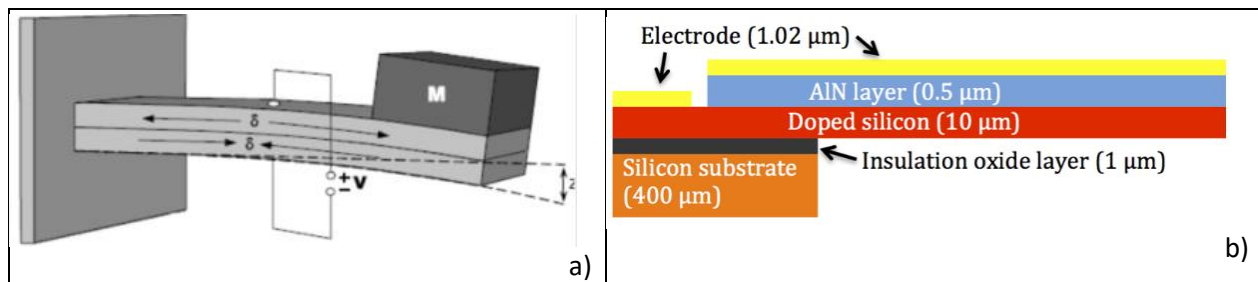


Figure 5-30: a) Stress or strain in a piezoelectric material causes an asymmetric charge distribution in the material, and hence a voltage over a capacitor b) A MEMS-based piezoelectric micro-cantilevers design [248], [7].

Almost any moving or bending structure (e.g. membrane) can be covered with a piezoelectric layer to convert the resulting mechanical stress or strain into electrical charges (*i.e.* a voltage over a capacitor). The piezoelectric transducer quality factor ( $Q = f_0/\Delta f$ ) decreases slightly at higher accelerations due to the air damping, which is a well-known mechanical loss factor [249]. In the literature, thin films of piezoelectric materials were widely proposed for piezoelectric transducers. Commonly used piezoelectric materials such as piezoceramics (lithium niobate  $\text{LiNbO}_3$ , barium titanate  $\text{BaTiO}_3$ , lead titanate  $\text{PbTiO}_3$ , lithium tantalate  $\text{LiTaO}_3$ ) and quartz crystals are relatively large size and incompatible with silicon substrates [7]. Moreover, lead-zirconate-titanate (PZT), which is most extensively used transducer material in the field of energy harvesting, is brittle in nature and need a polishing and/or post-baking step to present a piezoelectric effect. Therefore, these materials are not suitable for vibration micro harvester's fabrication since silicon is the basic materials in MEMS technology. Moreover, as Lead-based piezoelectric materials are toxic in nature, for medical application, researchers are interested in synthesizing Lead-free piezoelectric material such as piezoelectric thin film based on polyvinylidene fluoride polymer (PVDF), layers of polycrystalline zinc oxide (ZnO) and of aluminum nitride (AlN), which are compatible with standard microelectronic processing technologies for MEMS transducer fabrication. PVDF is also commonly used piezoelectric polymer, which is flexible, light weight, biocompatible and inexpensive [250] PZT is fragile as compared to PVDF and has low energy conversion efficiency [251].

To allow larger resulting strains in the piezoelectric material (*i.e.* effectively harvesting energy from vibrations), both material and device architecture should be designed in such way to mechanically amplify the applied stresses, providing larger charge/voltage generation. The efficiency of the conversion of a mechanical strain into an electrical energy is described by the electromechanical coupling coefficient, which is the most significant property of a piezoelectric material. This coefficient depends directly on piezoelectric parameters and elastic modulus, while it is inversely proportional to the dielectric constant of the material.

The PZT piezoceramic has been for a long time the preferred choice for the fabrication of the piezoelectric harvesters since it has the highest electromechanical coupling coefficient among the most used piezoelectric materials for vibration energy harvesting applications. However, it has a low dielectric constant. Moreover, the extreme fragility of the PZT limits the maximum of deformation before rupture and its treatment remains delicate. PZT requires polishing or annealing after deposition of the film. In addition, the PZT is a ferroelectric material, so it cannot withstand temperatures above the Curie temperature which is below 300 °C for PZT thin films.

### 1.3.1. PZT thin films

Despite all the microfabrication stresses associated with the PZT thin film, there are some interesting achievements in the literature. A harvester based on an aluminum cantilever beams with a steel proof mass and PZT layers glued on the top and bottom of the proof mass was proposed by Mitcheson and al in [252]. For  $47 \text{ ms}^{-2}$  vibrations at 150 Hz, this harvester can generate  $32.5 \mu\text{W}$ . The model of transducers developed by Zhou *et al.* in [253], relying on interdigitated electrodes (in order to operate in the more efficient  $d_{33}$  mode), could generate a power density greater than  $2 \mu\text{W} \cdot \text{mm}^{-2} \cdot \text{g}^{-1}$  (for  $100 \mu\text{m} \times 200 \mu\text{m}$  PZT cantilever of 1 kHz of resonance frequency). In [254], Jeon *et al.* reported  $1 \mu\text{W}$  of continuous electrical power delivered to a  $5.2 \text{ M}\Omega$  resistive load at 2.4 V with a PZT cantilever beam of 13.9 kHz of resonance frequency and dimensions of  $170 \mu\text{m} \times 260 \mu\text{m}$ . In [255], a  $1.64 \mu\text{m}$  thick layer of PZT on a cantilever produces a voltage of 898 mV and a power of  $2.16 \mu\text{W}$  at a resonance frequency of 608 Hz under an acceleration of 1 g. In [256], Isarakorn *et al.* mentioned a  $1000 \times 2500 \times 0.5 \mu\text{m}^3$  PZT epitaxially grown thin film on a silicon platform exhibiting a power of  $13 \mu\text{Wmm}^{-2} \cdot \text{g}^{-1}$  at a resonance frequency of 2.3 kHz for an optimal resistive load of 5.6 k $\Omega$ . Shen *et al.* in [257], demonstrated that a micromachined SOI (silicon-on-insulator) -based PZT cantilever structure exhibited an average power of  $0.32 \mu\text{W}$  and power density of  $416 \mu\text{Wcm}^{-3}$  at 0.75g acceleration at its resonant frequency of 183.8 Hz.

A piezoelectric material such as aluminum nitride (AlN), whose manufacturing process is easier and fully compatible with MEMS technology is often chosen instead of a PZT. Indeed, AlN thin films can be deposited using low temperature techniques used for MEMS device's microfabrication [7].

### 1.3.2. AlN thin films

This material has been recently proposed for the vibration harvesting transducers fabrication. AlN material has a lower electromechanical coupling coefficient compared to PZT. However, its lower dielectric constant allows to generate a much higher voltage compared to PZT, and the harvested power can either be equal to, or exceed, the power obtained with PZT. Moreover, AlN thin films are biocompatible and can be grown below  $400^\circ\text{C}$  (by sputtering for instance) on different substrates including dielectrics, semiconductors, metals and flexible substrates like polymers. Molybdenum was often chosen as the AlN electrode material because it promotes a preferential orientation (002) of the AlN film. It has a low resistivity and it can be easily etched by  $\text{H}_2\text{O}_2$ , thus reducing the complexity of device fabrication [7]. The AlN layer can also be etched by an  $\text{H}_3\text{PO}_4$ -based solution for its structuration [7]. A few AlN thin films energy harvesting transducers started to be reported in the literature.

In [258], a  $1.5 \times 0.75 \text{ mm}^2$  AlN ( $1 \mu\text{m}$  layer) cantilever device has been shown to produce an analytical power output of 60 nW for an optimal resistive load at 900 Hz with an acceleration of  $10 \text{ ms}^{-2}$ . Van Schaijk *et al.*, in [259], presented a MEMS-based AlN cantilever providing an output power of  $10 \mu\text{W}$  under an acceleration of about 8g at a resonance frequency around 1 KHz. Based on this work, Elfrink *et al.* also reported on a MEMS AlN-based cantilever beam of  $2.1 \times 7 \times 0.8 \text{ mm}^3$  oscillating at 572 Hz and generating an output power of  $60 \mu\text{W}$  under 2g acceleration [260]. At the nanoscale, other piezoelectric materials such as GaN and ZnO, look particularly promising because of their piezoelectric and mechanical properties discussed in [261], [262], [263].

Unfortunately, scaling the energy harvester transducer sizes proportionally reduces the power that can be extracted from vibrations. Moreover, it increases the transducer resonant frequency at which the harvesting device operates at the maximum efficiency far away from the spectrum of vibration frequency available in the environment, thus contributing to further lower the collected power. Another piezoelectric energy harvester promising application concerns their use on soft substrates such as Kapton or polyethylene terephthalate (PET) compatible with soft electronics, thus allowing to recover much more power because of the bending of the entire electronic system structure [7]. In this context, mechanical and electrical properties of transducers based on AlN thin films on polyimide flexible substrates have already been developed [264].

## 1.4. Electromagnetic transducers

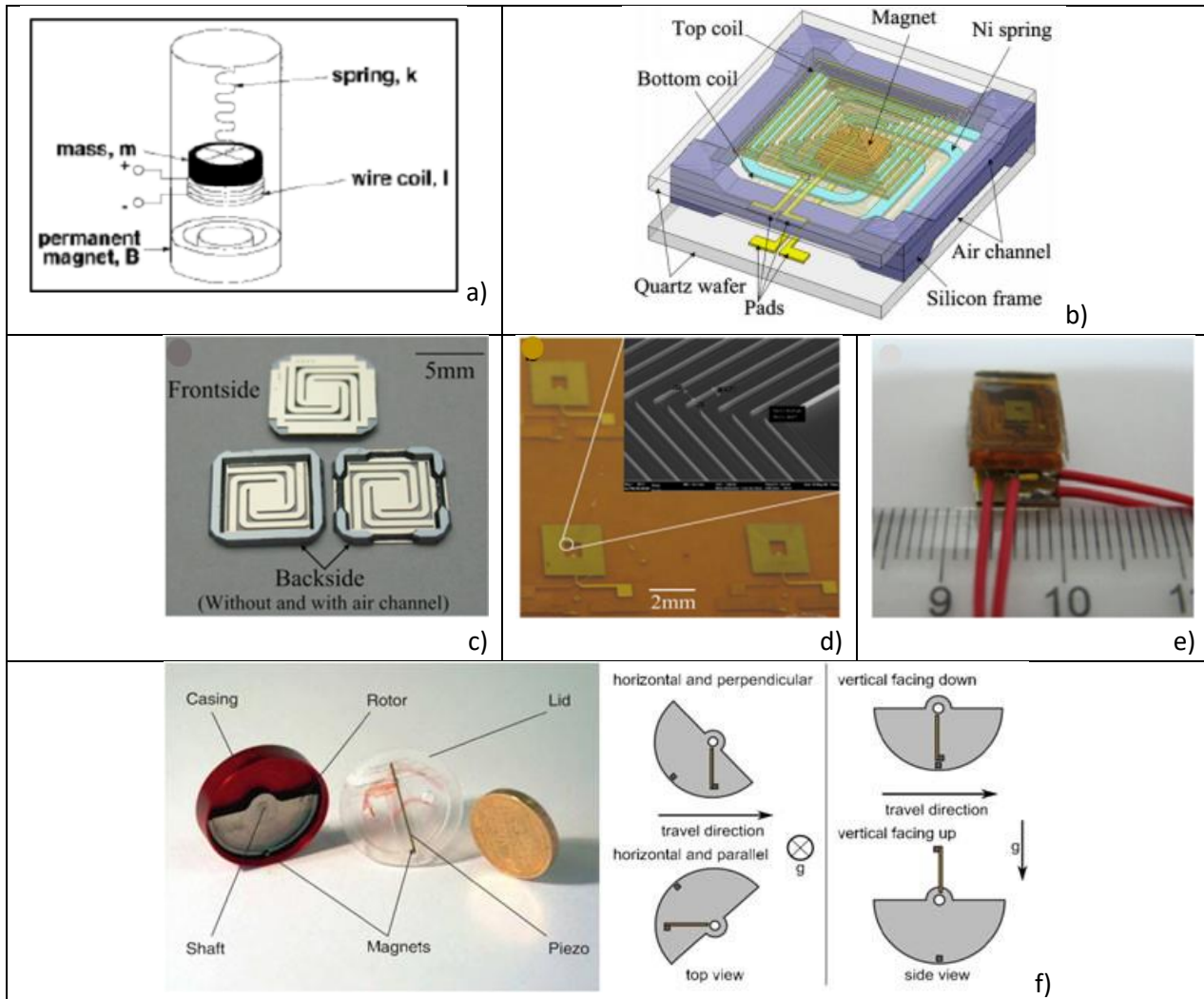


Figure 5-31: a) The coil and the magnetic field move relative to each other, inducing a voltage  $V = -d\phi/dt$  in the coil [7]. b) A Schematic 3D view of the sandwiched vibration-based power generator [265]. Photographs of fabricated Ni spring: c) Cu coils, d) the assembled prototype, e) and f) The orientations of eccentric proof mass energy harvester [15].

Electromagnetic harvesting transducers are based on a time varying magnetic field inducing an electric current into a conductor according to Faraday's law. The time varying magnetic field can be generated by the movements of the electrical conductor (typically a coil) relative to a permanent magnet and vice versa (*cf.* Figure 5-31 a). Electromagnetic energy harvester's miniaturization is still limited by the miniaturization of permanent magnet (PM). Macro sized PMs are still used to provide the required magnetic field because the development of films of PMs is still a challenge. Moreover, Arnold [266] concluded that power density decreases as the dimensions of the device are reduced. Tabeling has shown that, at small scale (on the order of a few hundred micrometers), when using a magnetic field (whether produced locally or from the exterior) the electromagnetic forces generated are lower than those associated with electrostatic forces [108]. Therefore, integration of electromagnetic energy harvesters is still a challenge for research.

**Wang *et al.*** in [265], proposed a micromachined spiral nickel spring with an NdFeB permanent magnet in the middle located between two fixed micromachined spirals copper coil (*cf.* Figure 5-31 b)) integrated with silicon frame. The load voltage generated by the prototype is 162.5 mV at its resonance frequency (280.1Hz) and the input vibration acceleration is  $8 \text{ ms}^{-2}$ . When the load resistance is  $81 \Omega$ , the maximal load power obtained is about  $21.2 \mu\text{W}$  [265].



---

## APPENDIX B: STIRLING MOTOR

### 1.1. Carnot efficiency

Sadi Carnot was interested in the optimization of thermal machines. In 1824, he published a book entitled «*Réflexions sur la puissance motrice du feu et sur les machines propres à développer cette puissance*» in which he thus developed a theoretical thermodynamic cycle whose efficiency is maximum [23]. This cycle is called the Carnot cycle [23]. It is a cycle supposed to function without dissipative phenomenon (i.e a reversible cycle). It is a motor cycle, which is only valid theoretically. It consists of these four successive transformations:

- Isothermal compression reversible at a cold temperature ( $T_c$ ),
- Reversible adiabatic compression,
- Reversible isothermal relaxation at a hot temperature ( $T_h$ ),
- Reversible adiabatic relaxation.

He defines the output of this cycle as the ratio between the useful output work ( $W$ ) and the input thermal energy ( $Q$ ).

$$\eta_c = \frac{-W}{Q_h} \quad (2.1)$$

By introducing the first principle of thermodynamics for a closed system with the heat rejected by the system, and the Clausius-Carnot equation that is derived from the second principle of thermodynamics for a reversible system, he finally obtains the equation :

$$W + Q_c + Q_h = 0 \quad (2.2)$$

$$\frac{Q_c}{T_c} + \frac{Q_h}{T_h} = 0 \quad (2.3)$$

$$\eta_c = 1 - \frac{T_c}{T_h} \quad (2.4)$$

This yield therefore represents the maximum yield that can have a thermal machine operating with a hot temperature  $T_h$  and a cold temperature  $T_c$ . Note that the unit yield ( $\eta_c = 1$ ) is impossible to obtain except in the theoretical case where  $T_c = 0$  K.

In our case study of low temperatures, with  $T_h = 500$  K (230 °C) and  $T_c = 293$  K (20°C), we have a maximum yield of 41.7%. It should be noted that with these temperature levels, under no circumstances will it be possible to exceed this yield.

This yield of Carnot which constitutes the ideal case thus makes it possible to compare the different systems of conversion of thermal energy to a theoretical maximum, and this even when the levels of the temperatures between these machines are different. It therefore serves as a reference for existing thermal machine technologies. Consequently, the efficiency ( $\eta_r$ ) of any thermal machine is the ratio between the yield of the machine in question ( $\eta$ ) and the yield of the Carnot cycle calculated at the same temperatures:

$$\eta_r = \frac{\eta}{\eta_c} \quad (2.5)$$

If we consider the theoretical case of a perfect regenerator (i.e a transfer without loss of heat from the cooling phase to the heating phase), the efficiency of the Stirling machine becomes equal to the yield of Carnot. Therefore, the invention of the regenerator by Robert Stirling has significantly improved the performance of its motor.

## 1.2. Advantages and disadvantages of Stirling motors

### 1.2.1. - Advantages

#### 1.2.1.a. *As motorization motor (direct operation): Rotation work and electricity production*

Since future cars are more likely to be powered by electric motors or fuel cells, Stirling motors (with their high conversion efficiency) could serve as an electrical source for driving these electric motors. Stirling motors work best in machines that require continuous mechanical or electrical energy using a temperature gradient. They are also ideal for exploiting the heat of the sun by using a mirror that concentrates this energy on a surface that can be used as a source of heat for the motor [267].

In the air, since an aircraft motor runs almost all the time at constant power, the Stirling motor is really in its field of predilection. Associated with this, its silence and its low vibratory level, compared to a traditional motor, the Stirling motor can constitute an asset as well for the passengers of the plane. In addition, at altitude, since the outside air drops in temperature, it can be the cold source of the Stirling motor and allow an aircraft to fly faster. However, it would essentially be necessary to develop a Stirling motor which also has a good power / weight ratio to be able to compete in the field of aviation. Indeed, during the years 1940 to 1980, the company Philips studied the applications of the Stirling motor in the Ford Torino car, but this test was not transformed and the project was abandoned [41]. Probably, the reasons, apart from the high cost of the project compared to the standardization of traditional thermal motors at that time, are related to the difficulty of having a motor capable of quickly varying its power and its speed. A prototype 4-cylinder Stirling motor, however, was built in 1976 and developed 170 hp at 4000 rpm (code name was 4-215 D.A). NASA made the same attempt with an American Motors Corporation (AMC) Spirit car in 1979. The name of this motor was P40 [268].

To conclude, we can cite the production by General Motors in 1968 of a hybrid car named STIR-LEC consisting of Stirling motor charging batteries [269]. These provided the energy needed for an electric motor to propel it. At sea, the Kockums company developed during the 1980s its Stirling Air-Independent Propulsion (AIP) motor [270]. It also has been used aboard the French submarine SAGA [271].

#### 1.2.1.b. *As cooler or heat pump (Reverse operation)*

When you apply mechanical energy into a Stirling motor and run it backward, the motor will effectively remove heat from the heat sink (cooled part of the motor) and will expel it towards the part that should be heated (heat source). That turns a Stirling motor into a very efficient cooling device ("cryocooler") [29].

Due to the high efficiency achieved by Stirling macro machines for cooling, Stirling micro chillers are a potentially interesting alternative for small devices cooling. In a micro scale Stirling cooler, heat is released from the hot chamber during the compression phase and absorbed from the cold chamber during the expansion phase. The craze for the miniaturization of Stirling coolers for application in the cooling of electronics for example, have been restrained to scale by the use of traditional components (eg pistons, crank-rod and pressurized chamber) [99], [100]. Efforts to build a micro-scale Stirling cooler prototype, through a series of cryocooler patents ([94], [101]), have solved the problems of friction losses and gas leaks by replacing conventional pistons and the associated links by electrostatic diaphragms.

### 1.2.1.c. As a lost heat harvester

The energy needs of the industry (ENI) continue to increase and represent more than 1/3 of the total energy consumed (TEC) in the industrialized countries. For example, on 2014 in France the ENI was 19.2% (Energy balance of France for 2014), in China 70% [3], in the USA 33% [4]. The problem that must be emphasized is that 20 to 50% of this consumption is dissipated by conduction, convection and radiation from hot equipment or in the form of hot smoke as is the case in the USA [5]. In France, for example, it is estimated that more than 27 TWh of heat whose temperature is between 100 and 200°C is lost each year. In the United Kingdom, it is estimated that 14 TWh / year is recoverable, which represents 4% of its annual energy consumption. Even in an internal combustion motor, it is estimated that 75% of the thermal energy generated during combustion is lost through the motor equipment [6].

This lost thermal energy is in the form of three categories that can be defined as follows [4]:

- The heat is considered at low temperature when below 230 °C.
- average temperature when heat temperatures are between 650 and 230 °C.
- High temperature when temperature heat above 650 °C.

Stirling macro and micro machines can reduce this huge waste of energy. For instance, cogeneration systems are commercialized, consisting of a conventional boiler that provides heat to homes and a Stirling motor coupled to it that recovers heat losses to convert it into electricity [9].

### 1.2.2. Disadvantages

Car motorization experiences with Stirling motors have not always been successful. The problem lies partly in the fact that Stirling motors do not start instantly (it takes time for the all-important heat exchanger to warm up and the flywheel to run up to speed), and they do not work so well in stop-start operation (unlike internal combustion motors). To effectively expel waste heat, they also need large radiators. That are some reasons why their direct use in cars seem to be less suitable than an ordinary internal combustion motor.

In conclusion, because Stirling motor don't internally involve burning fuel, the biggest advantage of Stirling is that they can be much cleaner and environmental friendly and can run from all kinds of different fuels (we could imagine a less volatile, less explosive, less polluting) They are They are much quieter than or internal combustion motors, because they do not have the complex system of opening and closing valves and, Moreover, unlike steam motors and internal combustion motors, which typically burn coal (to boil water) or fuel (to use explosion).

## 1.3. Schmidt model

### 1.3.1. Zero order analysis

Based on experimentally obtained results, the zero-order analysis developed by William Beale during the 1970s [33], makes it possible to determine corrective coefficients for the theoretical formulas. According to Beale, when considering a Stirling machine running in the motor cycle, its mechanical power could be expressed by the following relation:

$$W_m = C_t \cdot P_{cycle} \cdot f \cdot V_{swc} \cdot f(T) \quad (2.6)$$

Around 1980, Walker [Walker (1980)] based on several practical tests on Stirling machines, proposed the following formulation of Beale's initial formula:

$$W_m = 0.15 P_{cycle} \cdot f \cdot V_{swc} \quad (2.7)$$

In general, the Beale formula is used in optimizing the choice of the temperature regime. Its formula has been widely used by Sent (1982), West (1986) and Organ (1992). These scientists validated it by including the effects of the temperature ratio. According to West, Beale's formula should be modified as follows:

$$W_m = 0.25 P_{cycle} \cdot f \cdot V_{swc} \frac{T_h - T_c}{T_h + T_c} \quad (2.8)$$

For Stirling machines operating in a cooling cycle (cryogenic), Walker in 1983 based on the Beale formula, establishes an expression to approximate the cooling capacity of a Stirling machine based on the analysis of experimental results. The formula he proposed is the following:

$$Q_c = 10^{-6} P_{cycle} \cdot f \cdot V_{swc} T_c \quad (2.9)$$

Table5-8.2.

W. Beale	$P= K \cdot Pmc \cdot f \cdot Vsc \cdot f(T)$
Walker	$K \cdot f(T) = 0,15$
West	$K=0,25$ et $f(T)= \frac{T_k - T_h}{T_k + T_h}$

Table 5-9: Theoretical expressions of power and efficiency for zero order analysis

### 1.3.2. First order analysis or Ideal Isothermal Analysis

The first order analysis (or isothermal), proposed by Gustave Schmidt in 1871 [37], makes it possible to estimate the mechanical power of an motor as well as his performance from its geometry. It is often the basis of pre-studies of the Stirling motor. . In Schmidt's model there are assumptions: The movement of the pistons is sinusoidal and their oscillation frequency is constant. The evolution of compression and expansion phases are isothermal. The gas is ideal so the perfect gas state equation is applicable. The regenerator is perfect (infinite heat capacity). The mass of injected gas is constant and its instantaneous pressure is uniform (no leakage) so that the conservation of the mass applies. The thermal equilibrium conditions are then assumed to be established. All these hypotheses lead to thermal efficiency equal to that of Carnot.

The motor is divided into three zones (hot side expansion, cold side compression and the regenerator) and five cells designated by the first letter of their names: c, k, r, h and e respectively designating the compression chamber, the cold exchanger, the regenerator, the hot exchanger and the expansion chamber. There is no mass accumulation inside a chamber. The known data are the volumes of the spaces k, r, and h and the temperatures of k, and h.

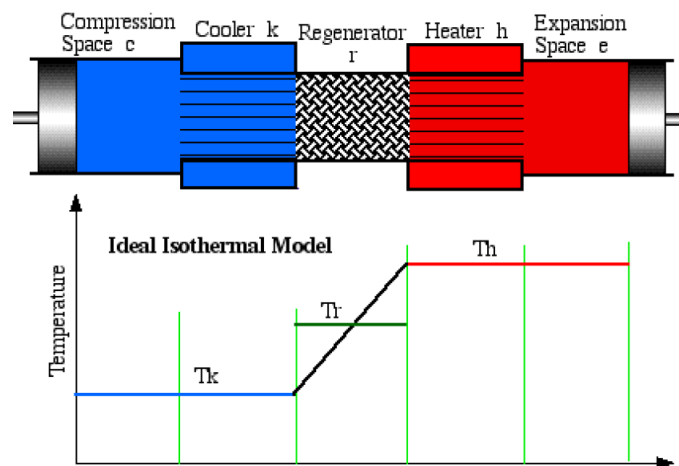


Figure 2.5-32 : Schematic view of the zones and cells of the isothermal model [Urieli, 1984]

Extracted from <https://www.ohio.edu/mechanical/stirling/>

Expression of the pressure variation P of the gas

The total mass of the gas inside the machine is constant in the thermodynamic cycle and implies:

$$m = \sum_{i=1}^5 m_i = m_c + m_k + m_r + m_h + m_e = cste$$

Eq. 5-1

and the gas is perfect so:

$$P V_i = m r T_i \quad \text{then}$$

$$m = \frac{P}{r} \sum_{i=1}^5 \frac{V_i}{T_i} \tag{Eq. 5-2}$$

Since there is no leakage, the pressure P of the gas is constant, so:

$$P = \frac{m r}{\frac{V_c}{T_k} + \frac{V_k}{T_k} + \frac{V_r}{T_r} + \frac{V_h}{T_h} + \frac{V_e}{T_h}} \tag{Eq. 5-3}$$

The expression of the regenerator temperature is determined as follows:

As the regenerator is supposed perfect so:

$$T_r = \frac{P V_r}{m_r r} \tag{2.13}$$

Since dT follows a straight its slope is:  $\frac{(T_h - T_k)}{L_r}$  with  $L_r$ , regenerator length and his ordinate at the origin is  $T_k$  so:

$$T(x) = \frac{(T_h - T_k)}{L_r} x + T_k \tag{2.14}$$

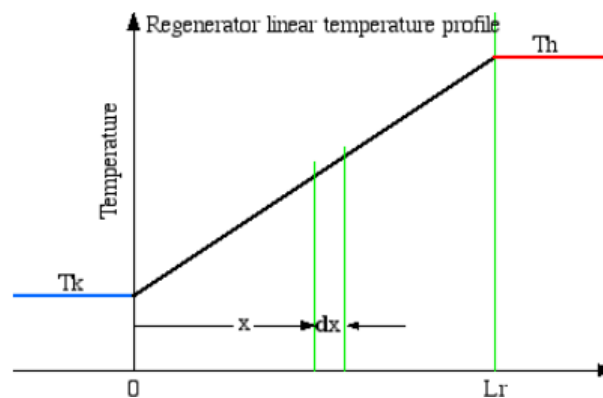


Figure 2.9 : Temperature gradient of the gas along the regenerator

However  $m_r = \int_0^{L_r} \rho(x) A dx$ , with  $\rho$  the density of the gas and A the regenerator depth.

$$m_r = \int_0^{L_r} \frac{P}{r T(x)} A dx \quad (2.15)$$

Then replacing  $T(x)$  by his expression in  $m_r$  :

$$m_r = \frac{P V_r}{r} \frac{\ln\left(\frac{T_h}{T_k}\right)}{(T_h - T_k)} \quad (2.16)$$

By identification, in relation to

$$m_r = \frac{P V_r}{r T_r} \Rightarrow T_r = \frac{(T_h - T_k)}{\ln\left(\frac{T_h}{T_k}\right)} \quad (2.17)$$

Then by replacing the expression of  $T_r$  in that of the pressure, it comes:

$$P = \frac{m r}{\frac{V_c}{T_k} + \frac{V_k}{T_k} + V_r \frac{\ln\left(\frac{T_h}{T_k}\right)}{(T_h - T_k)} + \frac{V_h}{T_h} + \frac{V_e}{T_h}} \quad (2.18)$$

The movements of the motor pistons and displacers being considered sinusoidal, for an Alpha configuration, the variations of volumes are expressed as follows:

$$\begin{cases} V_c = V_{clc} + \frac{V_{swc}}{2} [1 + \cos(\theta)] \\ V_e = V_{cle} + \frac{V_{swe}}{2} [1 + \cos(\theta + \alpha)] \end{cases} \quad (2.19 \text{ a,b})$$

With:

$V_{clc}$  and  $V_{cle}$  respectively the dead spaces of the chambers of compression and expansion;  $V_{swc}$ ,  $V_{swe}$ , are respectively the swept volumes in the compression and expansion chambers;  $\alpha$  is the phase shift between the piston the displacer. This angle represents the phase advance of the expansion space volume variations with respect to the compression space volume variations;

$\theta$  the angle of the cycle.

Replacing the expressions of the volumes in that of the pressure, it comes:

$$P = \frac{m r}{s + \frac{V_{swc} \cos(\theta)}{2 T_k} + \frac{V_{swe} \cos(\theta + \alpha)}{2 T_h}} \quad (2.20)$$

Where

$$s = \frac{V_{clc}}{T_k} + \frac{V_{swc}}{2T_k} + \frac{V_k}{T_k} + V_r \frac{\ln\left(\frac{T_h}{T_k}\right)}{(T_h - T_k)} + \frac{V_h}{T_h} + \frac{V_{cle}}{T_h} + \frac{V_{swe}}{2T_h} \quad (2.21)$$

By developing the expression in  $\cos(\theta + \alpha)$ , it comes the following:

$$P = \frac{m r}{s + \left( \frac{V_{swc}}{2T_k} + \frac{V_{swe}}{2T_h} \cos \alpha \right) \cos \theta - \frac{V_{swe} \sin \alpha}{2T_h} \sin \theta} \quad (2.22)$$

We introduce the two parameters:

$$c = \frac{1}{2} \sqrt{\left( \frac{V_{swe}}{T_h} \right)^2 + 2 \frac{V_{swc}}{T_k} \frac{V_{swe}}{T_h} \cos \alpha + \left( \frac{V_{swc}}{T_k} \right)^2}$$

$$\beta = \arctan \left( \frac{\frac{V_{swe} \sin \alpha}{T_h}}{\frac{V_{swc}}{T_k} + \frac{V_{swe}}{T_h} \cos \alpha} \right) \quad (2.24)$$

Introducing  $c$  and  $\beta$  into the expression of pressure yields a simpler form for the pressure  $P$ :

$$P = \frac{m r}{s(1 + b \cos \phi)} \quad (2.25)$$

Where

$$\phi = (\theta + \beta) \quad (2.26)$$

And  $b = \frac{c}{s}$  (2.27)

The mean pressure on a cycle is written as follows:

$$P_{\text{mean}} = \frac{1}{2\pi} \int_0^{2\pi} P d\phi = \frac{1}{2\pi} \int_0^{2\pi} \frac{m r}{s(1 + b \cos \phi)} d\phi \quad (2.28)$$

Using integration tables, the average pressure is expressed as follows:

$$P_{\text{mean}} = \frac{m r}{s\sqrt{1 - b^2}} \quad (2.29)$$

This equation also makes it possible to calculate the mass of gas in the motor knowing the average pressure. As we have the pressure we can calculate the work.

- Expression of the work  $W$

Knowing that for the compression and expansion volumes:

$$\begin{cases} Q_c = W_c \\ Q_e = W_e \end{cases} \quad (2.30a,b)$$

The work during the cycle becomes:

$$W = W_e + W_c = \int p dV_e - \int p dV_c = \int p \left( \frac{dV_e}{d\theta} + \frac{dV_c}{d\theta} \right) d\theta \quad (2.31)$$

With:

$$\begin{cases} \frac{dV_c}{d\theta} = -\frac{1}{2} V_{swc} \sin \theta \\ \frac{dV_e}{d\theta} = -\frac{1}{2} V_{swe} \sin(\theta + \alpha) \end{cases} \quad (2.32a,b)$$

$$\begin{cases} W_c = \int_0^{2\pi} p \frac{dV_c}{d\theta} d\theta \\ W_e = \int_0^{2\pi} p \frac{dV_e}{d\theta} d\theta \end{cases} \quad (2.33a,b)$$

It comes:

$$\begin{cases} W_c = \int_0^{2\pi} p \left( -\frac{1}{2} V_{swc} \sin \theta \right) d\theta \\ W_e = \int_0^{2\pi} p \left( -\frac{1}{2} V_{swe} \sin(\theta + \alpha) \right) d\theta \end{cases} \quad (2.34a,b)$$

Then replacing the pressure with its value, see Eq. (2.25), we obtain:

$$\begin{cases} W_c = -\frac{1}{2} V_{swc} \int_0^{2\pi} \frac{m r}{s(1 + b \cos(\theta + \beta))} \sin \theta d\theta \\ W_e = -\frac{1}{2} V_{swe} \int_0^{2\pi} \frac{m r}{s(1 + b \cos(\theta + \beta))} \sin(\theta + \alpha) d\theta \end{cases} \quad (2.35a,b)$$

$$\begin{cases} W_c = \pi V_{swc} P_{mean} \sin \beta \frac{(\sqrt{1-b^2} - 1)}{b} \\ W_e = \pi V_{swe} P_{mean} \sin(\beta - \alpha) \frac{(\sqrt{1-b^2} - 1)}{b} \end{cases} \quad (2.36a,b)$$

With the expressions (2.30a,b), (2.31) and (2.36a,b), one can calculate:

- The power of the Stirling cycle:



$$\dot{W} = W f \quad \text{where } f \text{ is the frequency} \quad (2.37)$$

- The efficiency:

$$\eta = \frac{W}{Q_e} \quad (2.38)$$

These integrals are solved using tables. For the beta and gamma configurations these are the expressions of the volumes that change but the principle remains as it is.  $V_k$ ,  $V_r$  and  $V_h$ , volumes are considered as dead spaces.

The performance of the motor depends of the nature of the gas and is directly proportional to the average pressure and the volume swept.

So we can rewrite Schmidt's equation as

$$W = W_c + W_e = P_{\text{mean}} \pi \left( \frac{\sqrt{1-b^2} - 1}{b} \right) [V_{\text{swc}} \sin \beta + V_{\text{swe}} \sin(\beta - \alpha)] = S_c P_{\text{mean}} V_{\text{sw}} \quad (2.39)$$

Where  $S_c$  is the Schmidt number:

$$S_c = \pi \left[ \frac{V_{\text{swc}}}{V_{\text{sw}}} \sin \beta + \frac{V_{\text{swe}}}{V_{\text{sw}}} \sin(\beta - \alpha) \right] \frac{(\sqrt{1-b^2} - 1)}{b} \quad (2.40)$$

The Schmidt number characterizes the efficiency with which one can transform the size of the motor ( $V_{\text{sw}}$ ) and its average pressure ( $P_{\text{mean}}$ ) in exploitable power.  $V_{\text{sw}}$  is the total swept volume (i.e.  $V_{\text{sw}} = V_{\text{swc}} + V_{\text{swe}}$ ).

Based on this analysis, the table 2.X presents the the main equations describing the performances of a Stirling motor.

Parameters	Expressions
Dead space ratio	$\chi = \frac{(V_k + V_r + V_h)}{V_{\text{sw}}}$
Temperature ratio	$\tau = \frac{T_h}{T_c}$
Swept volume ratio	$\kappa = \frac{V_{\text{swe}}}{V_{\text{sw}}}$
Phase shift	$\alpha$
<b>Expressions to be calculated</b>	
Schmidt number	$S_c = \pi \left[ \frac{V_{\text{swc}}}{V_{\text{sw}}} \sin \beta + \frac{V_{\text{swe}}}{V_{\text{sw}}} \sin(\beta - \alpha) \right] \frac{(\sqrt{1-b^2} - 1)}{b}$

	$\beta = \arctan \left( \frac{\frac{V_{swe}}{T_h} \sin \alpha}{\frac{V_{swc}}{T_k} + \frac{V_{swe}}{T_h} \cos \alpha} \right)$
	$c = \frac{1}{2} \sqrt{\left( \frac{V_{swe}}{T_h} \right)^2 + 2 \frac{V_{swc}}{T_k} \frac{V_{swe}}{T_h} \cos \alpha + \left( \frac{V_{swc}}{T_k} \right)^2}$

Parameters	Expressions
	$s = \frac{V_{clc}}{T_k} + \frac{V_{swc}}{2T_k} + \frac{V_k}{T_k} + V_r \frac{\ln \left( \frac{T_h}{T_k} \right)}{(T_h - T_k)} + \frac{V_h}{T_h} + \frac{V_{cle}}{T_h} + \frac{V_{swe}}{2T_h}$
	$b = \frac{c}{s}$

Table 5-10: Parameters and expressions for isothermal analysis

<b>Mean pressure</b>	$P_{\text{mean}} = \frac{m r}{s \sqrt{1 - b^2}}$
<b>Work</b>	$W = S_c P_{\text{mean}} V_{sw}$
<b>Power</b>	$\dot{W} = W f$
<b>Heat</b>	$Q_e = \pi V_{swe} P_{\text{mean}} \sin(\beta - \alpha) \frac{(\sqrt{1 - b^2} - 1)}{b}$
<b>Efficiency</b>	$\eta = \frac{W}{Q_e}$

### 1.3.3. Second order analysis or Ideal Adiabatic Analysis

This analysis allows to determine the effects of the adiabatic operation of the compression and expansion spaces on the motor performance and to examine the detailed behavior of the relevant variables across the cycle (temperature ratio, phase angle, swept volume ratio, ratio of dead space). This model is more realistic for estimating the mechanical power of an motor as well as its performance from its geometry. The known data are the volumes of spaces k, r, and h and the temperatures of k, and h.

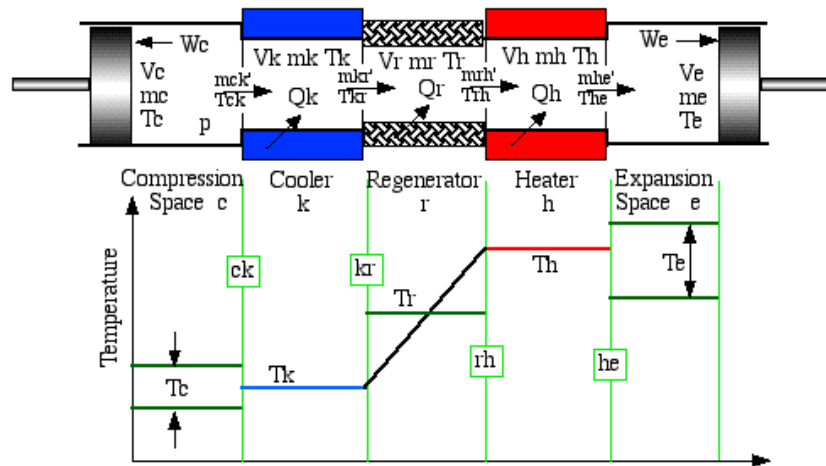


Figure 5-33: Schematic view of the zones and cells of the adiabatic model [28].

Extracted from <https://www.ohio.edu/mechanical/stirling/>

The advantages of this analysis are that the amount of heat transferred to the regenerator is estimated and the method may include heat transfer and friction flow analysis of the heat exchangers. The disadvantage is that this analysis leads to nonlinear differential equations that can only be solved numerically.

The Table 2.4 presents the set of differential equations resulting from the ideal adiabatic analysis of a Stirling motor, [28].

Table 5-11: Parameters and expressions for adiabatic analysis

Parameters	Equations
Pressure	$P = \frac{m r}{\frac{V_c}{T_c} + \frac{V_k}{T_k} + \frac{V_r}{T_r} + \frac{V_h}{T_h} + \frac{V_e}{T_e}} \quad \text{and} \quad \frac{dP}{d\theta} = \frac{-\gamma P \left( \frac{1}{T_{ck}} \frac{dV_c}{d\theta} + \frac{1}{T_{he}} \frac{dV_e}{d\theta} \right)}{\frac{V_c}{T_{ck}} + \gamma \left( \frac{V_k}{T_k} + \frac{V_r}{T_r} + \frac{V_h}{T_h} \right) + \frac{V_e}{T_e}}$
Masses	$m_c = \frac{P V_c}{r T_c}; \quad m_k = \frac{P V_k}{r T_k}; \quad m_r = \frac{P V_r}{r T_r}; \quad m_h = \frac{P V_h}{r T_h} \quad \text{and} \quad m_e = \frac{P V_e}{r T_e}$
Mass accumulations	$m_c = \left( P \frac{dV_c}{d\theta} + \frac{V_c}{\gamma} \frac{dP}{d\theta} \right) / (r T_{ck}); \quad m_e = \left( P \frac{dV_e}{d\theta} + \frac{V_e}{\gamma} \frac{dP}{d\theta} \right) / (r T_{he})$ $\frac{dm_k}{d\theta} = m_k \frac{1}{P} \frac{dP}{d\theta}; \quad \frac{dm_r}{d\theta} = m_r \frac{1}{P} \frac{dP}{d\theta} \quad \text{and} \quad \frac{dm_h}{d\theta} = m_h \frac{1}{P} \frac{dP}{d\theta}$
Mass flows	$mck' = -\frac{dm_c}{d\theta}; \quad mck_r = mck' - \frac{dm_k}{d\theta}; \quad mhe' = \frac{dm_h}{d\theta};$ $mrh' = mhe' + \frac{dm_h}{d\theta}$
Conditional temperatures	<p>if <math>mck' &gt; 0</math> then <math>T_{ck} = T_c</math> else <math>T_{ck} = T_k</math></p> <p>if <math>mhe' &gt; 0</math> then <math>T_{he} = T_h</math> else <math>T_{he} = T_e</math></p>
Temperatures	$\frac{dT_c}{d\theta} = T_c \left( \frac{1}{P} \frac{dP}{d\theta} + \frac{1}{V_c} \frac{dV_c}{d\theta} - \frac{1}{m_c} \frac{dm_c}{d\theta} \right)$ $\frac{dT_e}{d\theta} = T_e \left( \frac{1}{P} \frac{dP}{d\theta} + \frac{1}{V_e} \frac{dV_e}{d\theta} - \frac{1}{m_e} \frac{dm_e}{d\theta} \right)$
Energy	$\frac{dQ_k}{d\theta} = V_k \frac{c_v}{r} \frac{dP}{d\theta} - c_p (T_{ck} mck' - T_{kr} mck_r)$ $\frac{dQ_r}{d\theta} = V_k \frac{c_v}{r} \frac{dP}{d\theta} - c_p (T_{ck} mck' - T_{kr} mck_r)$ $\frac{dQ_h}{d\theta} = V_h \frac{c_v}{r} \frac{dP}{d\theta} - c_p (T_{rh} mck_r - T_{he} mhe')$ $\frac{dW_c}{d\theta} = P \frac{dV_c}{d\theta}$ $\frac{dW_e}{d\theta} = P \frac{dV_e}{d\theta}$ $\frac{dW}{d\theta} = \frac{dW_c}{d\theta} + \frac{dW_e}{d\theta}$

## APPENDIX C: MICROFLUIDICS

### 1.1. For permanent flows

#### 1.1.1. Effect of low Reynolds number in Microsystems

Low Reynolds number determination in micro canals with rectangular cross-sections (*cf.* Figure 5-34 a) where the aspect-ratio ( $w/b$ ) of the cross-section of the canal is arbitrary [108] is challenging but of big interest.

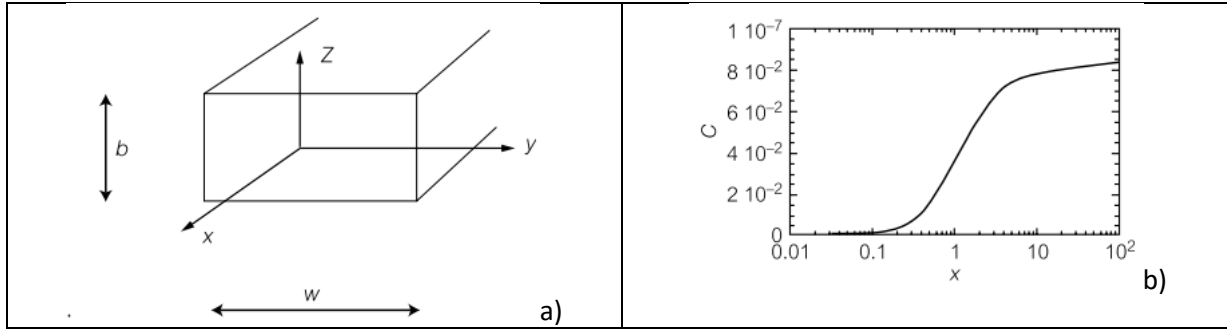


Figure 5-34: a) Schema of the cross section of a rectangular channel. b) The friction factor ( $C$ ) variation, for a channel characterized by a ratio of  $X = w / b$  [108].

For  $b \leq w$ , an estimate of the flux (up to about 10%) is established from the following expression [108]:

$$Q \approx \frac{wb^3 G}{12\mu} \left(1 - \frac{6b^2}{\pi^5 w}\right)$$

The coefficient  $C$  linking the flow  $Q$  to the pressure gradient  $G$  is the friction factor defined by.

$$Q = C \frac{wb^3 G}{\mu}$$

The variations of the friction factor as a function of the aspect ratio  $\chi = w/b$  for a rectangular channel are illustrated in Figure 5-34 b, for  $X$  varying between 1 and 100. The analysis of this curve  $C(\chi)$  shows that once the form factor  $\chi$  is greater than 10, we find the asymptotic value  $1/12$ , which corresponds to the limit of the Poiseuille plane. In a symmetrical way, in the case where  $\chi$  is very small, the evolution of the factor  $C(\chi)$  is as follows [108]:

$$C(\chi) \approx \frac{\chi^2}{12}$$

#### 1.1.2. hydrodynamic resistance notion

To determine what will be the flows in each branch of a given microfluidic circuit, since they are often quite complex, it is useful to revisit the idea of hydrodynamic resistance. The following relation introduces the notion of hydrodynamic resistance  $R$  of a channel [108].

$$\Delta P = R Q_m$$

where  $\Delta P$  and  $Q_m$  are respectively the pressure difference along the canal and the mass flux through the canal. An electronic analogy can be made in which the pressure corresponds to a voltage and the flow corresponds to the intensity of the current. At very low Reynolds numbers, this analogy is robust in the case of a constant, incompressible flux along an invariant channel in the  $x$  direction and depends only on  $y$  and  $z$ , which represent the transverse coordinates of the flux. The pressure drop associated with a flow of fluid in a channel of section  $S$  and length  $L$ , crossed by a flow  $Q_m$ , can be expressed as follows [108]:

$$\Delta P = K v \frac{L}{S} = R Q_m$$

In the case of a plane Poiseuille flux between two plates separated by a distance  $b$  and a width  $w$  (with  $b \ll w$ ),  $K$  which represents a dimensional factor, is expressed as follows:

$$K = \frac{12}{b^2}$$

The hydrodynamic resistance  $R$  for the case of a planar Poiseuille flow, is expressed as follows:

$$R = \frac{12\nu L}{b^2 S}$$

This expression resembles that of electrical resistance with the resistivity here being represented by the factor  $12\nu / b^2$ . The hydrodynamic resistance has the unit  $m^{-1}s^{-1}$ . Analysis of this relationship shows that the hydrodynamic resistance increases considerably as the scale (or length of the channel) decreases. In the most general case where the cross-section of the channel has a ratio of given length,  $R$  is expressed as follows [108] :

$$R = \frac{\nu L}{C(\chi) b^3 w}$$

Hydrodynamic circuits function as electronic circuits. For example, in a hydrodynamic circuit, two resistors  $R_1$  and  $R_2$  placed in series equivalent to a resistor  $R_1 + R_2$ , and two resistors in parallel equivalent to a resistor whose expression is:

$$R = \frac{R_1 R_2}{R_1 + R_2}$$

When it comes to micro-fluidic circuits with several branches of canals, these analogies are extremely useful.

To conclude, note that local equations are not equivalent between electrokinetics and Stokes fluxes in microchannels [108]. Indeed, in the Stokes approximation, the velocity does not come directly from a potential itself, whereas in electrokinetics, the density of the electric current is proportional to the local electric field, which derives from a potential. So, this analogy applies only to global quantities and for a Reynolds number not much larger than 1 and as long as the non-linearities of the Navier-Stokes equation do not cease to be negligible. The channels are assumed to be invariant in the flow direction [108].

### 1.1.3. hydrodynamic capacity notion

When deformable elements (control membranes or mechanical microvalves) are used in a micro-fluidic circuit (cf. Figure 5-35), the notion of hydrodynamic capacity becomes relevant [108]. The hydrodynamic capacitance (unit  $ms^2$ ) notion of an element can be introduced with this formula:

$$Q_m = C \frac{d\Delta P}{dt}$$

Let us consider an nondeformable channel of volume  $V$ , closed, containing a compressible fluid whose density  $\rho(t)$  varies with time. There appears a mass of fluid  $Q_m$  among the density variations of this volume of fluid, which is given by the expression:

$$Q_m = V \frac{d\rho}{dt}$$

Indeed, the variations of density are related to the variations of pressure by the relation [108]]:

$$\Delta P = \kappa^{-1} \frac{\delta\rho}{\rho}$$

In this relation  $\kappa$  represents the compressibility of the fluid. The expression of the hydrodynamic capacity is deduced in this particular case:

$$C = \kappa m_0$$

Where  $m_0$  represents the fluid mass in the element. Let's now consider the case where the canal is deformable by a membrane introduction, but the fluid is incompressible. Figure 5-35 illustrate the system.

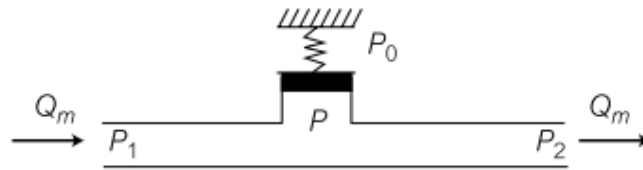


Figure 5-35: Flow system in which a deformable membrane (schematized by a piston / spring system) is located inside a microchannel [108].

The membrane in question is schematized by a piston / spring system. A pressure difference ( $\Delta P = P_1 - P_2$ ) imposed between the inlet ( $P_1$ ) and the output ( $P_2$ ) of the microchannel allows the circulation of the flow inside. In such a system, the flow is related to the pressure drop by the following equation [108]:

$$Q_m = R\Delta P + C \frac{\Delta P}{dt}$$

In this expression R is the hydrodynamic resistance of the channel and C its capacity, which is expressed as follows:

$$C = \frac{2\rho}{k}$$

$k$  in this relation is the constant of the spring which comes from the measurement of the rigidity of the spring or the membrane. It is possible for example by this type of calculation to determine the response time constant of a valve of a microfluidic circuit. The time constant is RC in this example. The Reynolds number is intrinsically small in microsystems. Consequently, these types of flows are governed by Stokes equations with moderate Reynolds numbers of the order of several tens. This is the case for example of micro flux for the extraction of heat from microprocessors. These exchangers must operate at moderately high Reynolds numbers to achieve efficient heat transfer. This is also the case in inkjet printers, in which the speeds are of the order of several meters per second, for jet diameters around  $100 \mu\text{m}$ . The Reynolds number is therefore about 100. However, such a Reynolds number is too high for the use of the Stokes approximation, but is not high enough to produce hydrodynamic instabilities [108].

#### 1.1.4. The bottleneck effects

The plug effect is an effect related to the compressibility of a gas. The plug effect imposes a particular design ratio between chamber and microfluidic channel, especially in the case of gas. For a rigid system, the bottleneck effect occurs in a chamber containing a movable piston connected to a capillary when the piston suddenly sweep the gas (cf. Figure 5-36). Consider the case where the capillary is a microchannel of rectangular cross-section. Thus, the piston being stationary initially, then starts to move abruptly at a predetermined speed  $U$  to move the fluid. The flow is then directed along the  $x$  axis, where  $x = 0$  is the initial position of the piston. In the plane of the piston chamber cross-section, the flow rate of the fluid is assumed to be uniform. The equations governing the problem under these conditions are then expressed as follows:

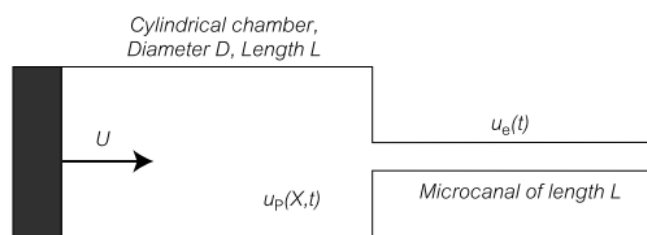


Figure 5-36: Diagram illustrating the geometry of the bottleneck effect [108].

$$\frac{\partial \rho}{\partial t} + \frac{\partial(\rho U_c)}{\partial x} = 0$$

$$\rho \frac{DU_c}{Dt} = -\frac{\partial p}{\partial x} + \mu \frac{\partial^2 U_c}{\partial x^2}$$

where  $\rho$ ,  $\mu$ ,  $U_c$ ,  $t$  and  $p$  are respectively the fluid density, its viscosity, the velocity in the chamber, the time variable and the pressure. Even though the velocities themselves are very small compared to the speed of sound propagation, we have assumed that the fluid is compressible because this character is essential for the effect we are discussing. For liquids, compressibility can be characterized by the following equation [108]:

$$\frac{\partial p}{\partial \rho} = \frac{E}{\rho}$$

where  $E$  represents the Young's modulus. At very low Reynolds numbers, the inertial term in the Navier-Stokes equation can be neglected, leading to the following approximation [108]:

$$p + \frac{\mu}{E} \frac{\partial p}{\partial t} = F(t)$$

where  $F(t)$  being a time-dependent function. For normal fluids such as water, the time constant  $\mu / E$  is of the order of  $10^{-12}$  s. We can therefore neglect it, if we consider the evolution of the phenomena described here, this time constant is extremely fast. Therefore  $p \approx F(t)$ . In other words, the pressure and the density are uniform in the piston chamber. Thus, in the piston chamber, the velocity of the fluid decreases linearly with the coordinate  $x$ . The junction with the microchannel takes place at  $x = L$  and this microchannel or the capillary of length  $l$  has a rectangular cross section of width  $w$  and height  $b$ . The flux conservation at the chamber - microchannel junction is expressed as follows [108].

$$U_c(L, t) = \frac{4wb}{\pi D^2} U_{can}(t)$$

where  $D$  represents the diameter of the chamber. At the level of the microchannel or capillary, if it is a thin channel (where  $w \gg b$  (height)), we have the following relation, if for simplicity, the pressure is assumed to be zero at the output of the microchannel:

$$U_{can}(t) \approx \frac{b^2}{12l\mu} p$$

Or into the form of a differential equation [108]:

$$(1 - \alpha t) \frac{\partial p}{\partial t} + \frac{p}{\tau} = \frac{UE}{L}$$

Here,  $\alpha = \frac{U}{L}$ , and  $\tau$  is a time constant expressed as follow:

$$\tau = \frac{3\pi l \mu D^2 L}{E w b^3}$$

If we assume that  $\alpha t$  is largely inferior to 1, (which is equivalent to saying that the piston is still far from reaching the chamber-channel junction), we obtain the following solution [108]:

$$p(t) = p_{inf}(1 - e^{-t/\tau})$$

Thus, the equilibrium of the flow is reached once the time  $\tau$ , above, has elapsed. Note that in this type of microsystems, it is possible that  $\tau$  becomes higher, since it varies with the inverse of the height of the microchannel



at power 3. By way of example,  $\tau$  is of the order of a few tens of seconds for the water pushed into a microchannel of length 2 cm, 1 micrometer height and width 100  $\mu\text{m}$ . On the other hand, if this same type of microchannel had a height of 100 nm, this characteristic time would have been of the order of a few hours. It is therefore essential to consider this characteristic time during the design of ultraminiaturized microfluidics systems. To overcome this time constant, it is necessary to work with a flow at constant pressure, but not at constant speed or constant flow. To put the fluids in motion in microchannels in this case, the use of pressure sources is preferable to syringes.

A standard Stirling micromachine can be composed of two opposite flat faces, consisting of one side of a flexible membrane in a cold chamber and the other side of another flexible membrane in a hot chamber, with three microchannels for connecting these two chambers as illustrated in Figure 5-37. These three microchannels necessarily consist of a first horizontal microchannel, followed by a second vertical microchannel, then a third horizontal microchannel, the vertical microchannel containing the regenerator. The first horizontal microchannel connects the hot chamber to the regenerator, the latter being connected to the third horizontal microchannel leading into the cold chamber. Horizontal microchannels are necessary because in the case of membranes, there is no gap between the circumference of the membrane and its displacement chamber as is the case with a piston and its sliding chamber. On each side, one of the flat faces of these chambers is in contact with a thermal source (hot or cold) and the other plane being occupied by the membrane which compresses and / or displaces the working gas.

The simplest (and most compact) size and shape of the upper wall of the chamber is obtained when its shape and perimeter correspond to the perimeter of the membrane, since this upper wall (*i.e.* the exchanger) and the membrane share the same workspace. The diameter of the membrane can be chosen between 5 and 10 mm, with a thickness between 50 to 250 microns, to limit its resonance frequency to kHz.

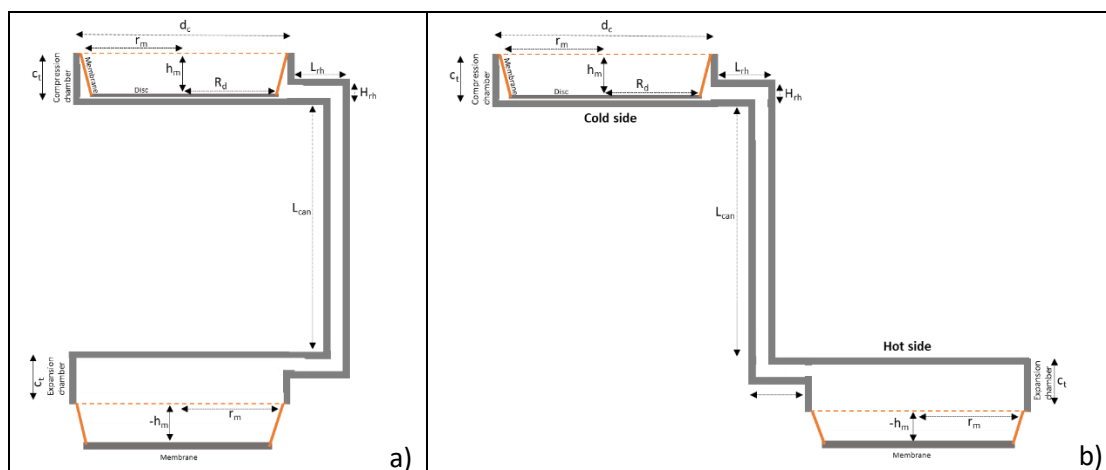


Figure 5-37: Schema of two potential models of 3D Stirling micromachines (alpha configurations) with. a) two aligned chambers. b) two unaligned chambers

The Stirling micromachine system exploits the inertia of suspended membranes to act on the working gas. Thus, the cyclic pressure applied between the membranes causes a phasing of the latter at a well-defined phase angle. In motor mode, the membranes produce a work due to the expansion of the working gas but also compresses and displaces the latter during the thermodynamic cycle.

### 1.1.5. Fluid-structure interaction

A better heat transfer between the alternating flow gas and the walls of the chambers and the regenerator is essential for a better operation of the Stirling machines (operating in alternating mode), because of the primordial influence of thermal exchanges on the thermodynamic efficiency. During alternating compressions and detents of the gas, the boundary layer gas and the center cylinder gas is both heated, or cooled, by the wall. In addition, during compression of the gas, its atomic density near the wall is greater than that in the center and vice versa when the gas is in expansion. Finally, the working fluid in Stirling machines undergoes non-simultaneous variations in pressure and temperature during the cycle. In general, from a theoretical point of view, fins are added at the inner walls to increase the surface exchange between the gas and the wall as illustrated in Figure 5-38. But, physically, the integration of fins in micrometric chambers can cause a problem of flow of the oscillating gas by increasing friction.

From a technologically point of view, microfabrication of these blades can be a complicated operation resulting in the increase of dead spaces that can kill the operation of the miniature machine.

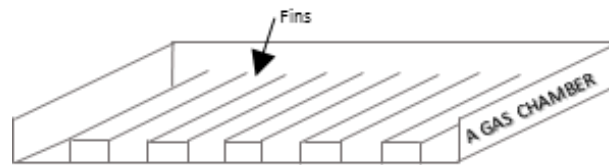


Figure 5-38: Problem of heat exchange between fluid and chamber; grids difficult to integrate

The thermal regenerator is between the hot and cold heat exchangers (*cf.* Figure 5-39). In conventional machines, it often has either a porous matrix or an assembly of small gratings of thin metal fabric, plates or balls, within which the working gas flows alternately.

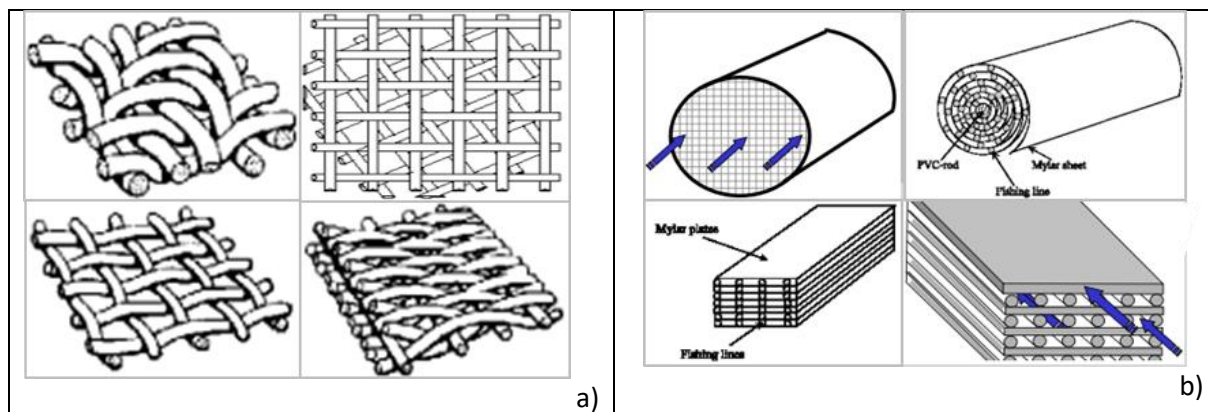


Figure 5-39: a) various structures of grids for regenerator. b) Coiled or plate stacks for regenerator matrix [95].

Theoretically during the thermodynamic cycle of the motor, when the gas returns to the hot chamber, it receives heat from the porous material of the regenerator. On the other hand, when it returns to the cold part, the gas supplies heat to the porous material. According to Reader and Hooper, a Stirling motor without regenerator should absorb up to five times more heat at the hot source to achieve the same performance as if it had a regenerator [13]. Consequently, the amount of cooling will be considerably affected.

The coefficient of pressure loss according to various experimental and numerical studies ([95]- [95]) can be put under the following general expression Table 5-12:

$$C'_f = \frac{a}{Re} + bRe^c \quad Re = \frac{Ud_h}{\nu} \quad Re_\omega = \frac{\omega d_h^2}{\nu}$$

In this equation, the Reynolds number  $Re$  is based on the maximum value of the velocity in the channel. When considering the alternation of the flow, the Reynolds number in alternating flow is defined by  $Re_\omega$  equation [106]:

Flow	Geometry of the channels	$a$	$b$	$c$	Media	Comments
Oscillating	Fabrics	129	2.91	-0.103	Porous	
	Random fibers	192	4.53	-0.067		
	Stacking spheres	$79 \epsilon^{-0.6}$	$1.1 \epsilon^{-0.6}$	0		
	Rectangular sections		$64b'$	0	0	$Re_\omega \leq 277.6$
			$64b' \left( \frac{Re}{277.6} \right)^{1/2}$ $b' = 1.47 - 1.48d + 0.92d^2$	0	0	$Re_\omega > 277.6$
Circular sections		64			Laminar flow	

	Parallel plans	96				
<b>Permanent</b> $Re = \frac{Ud_h}{\nu}$	Circular sections	64	0	0	<i>Non porous</i>	Laminar flow developed
	Flat plates	96	0	0		
	Square sections	57	0	0		

Table 5-13: Relationships concerning the coefficient of pressure drop  $C'_f$  ([106]). The parameter  $d$  is the smallest ratio of the sides of the rectangle.

Kahleras *et al.* have studied experimentally the dynamic operation of a metal regenerator (in isothermal condition and axial temperature gradient) crossed by air in alternating flow [119]. From their dynamic and nonstationary measurements of the pressure, velocity and temperature of the gas at the ends and inside the regenerator channels, they were able to establish a semi-empirical expression of the pressure drop coefficient. This regenerator (porosity rate  $\varepsilon = 35\%$ ), made from a rapid prototyping technique using laser melting of metal powder, consists of a porous matrix made of 316L stainless steel with a total length  $L_{tot} = 80$  mm and an external diameter  $D_{ext} = 9.5$  mm constructed on the basis of linear channels with square sections of hydraulic diameters  $d_h = 0.5$  mm as illustrated in Figure 5-40 a). The Figure 5-40b) shows the different measuring points and

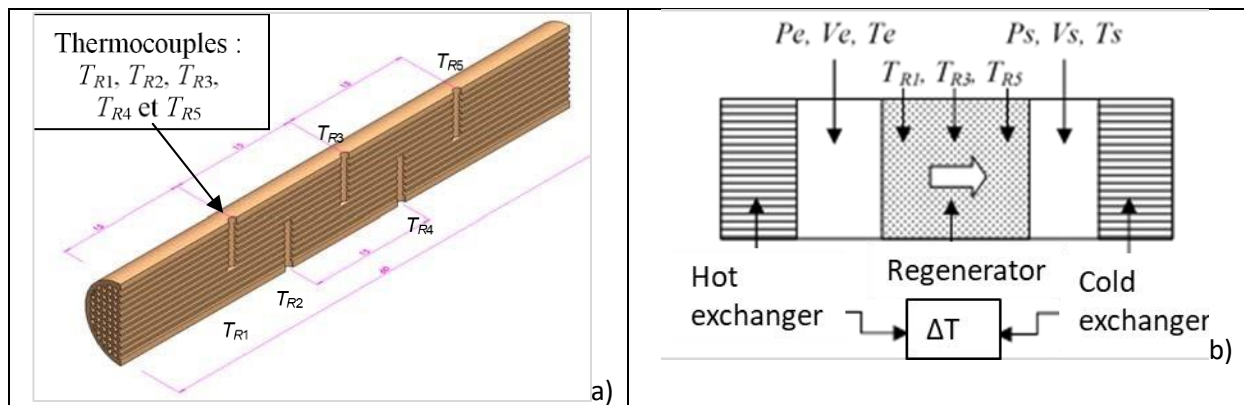


Figure 5-40: Transverse section of a regenerator with implantation of micro thermocouples ( $L_{tot} = 80$  mm,  $D_{ext} = 9.5$  mm). The temperature sensors are micro thermocouples of type K (Chromel-Alumel) of diameter =  $12.7 \mu\text{m}$  (measurement uncertainty  $\leq 0.1$  °C, cut-off frequency  $f_c \approx 30$  Hz in forced convection). b) Measurement diagrams with details of instantaneous quantities measured on the test bench (pressures  $P$ , local velocities  $V$  and temperatures  $T$ ) [106].

## 1.2. Permanent Vs Alternate flows

Kahleras tests of alternate flows were carried out in the frequency band  $0 < f < 15$  Hz, the inertia of the sensors is then negligible ( $f < f_c$ ). The wall gas pressure (Kulite XT190 sensor), the speed (TSI 1201 hot wire probe) and the fluid temperature at the center of the tube are measured at the inlet and outlet of the regenerator. A temperature gradient ( $0 < \Delta T < 90$  °C) is maintained along the regenerator by a "hot" exchanger and a "cold" exchanger placed at each end of the regenerator. From these instantaneous measurements (pressures, temperatures and speeds) at both ends of the regenerator and the gas temperatures at three equidistant points within the regenerator, the dynamic characteristics of the regenerator are determined.

### 1.2.1. Permanent Flow

The regenerator, in constant isothermal flow ( $\Delta T = 0^\circ\text{C}$ ), is subjected to a flow of air at ambient temperature ( $T_{amb} = 24$  °C) and under an absolute feed pressure upstream of the regenerator ( $P_{alim} = 2$  bar). Figure 5-41 d) is the steady state pressure drop curve. It shows a classical behavior of the form:  $\Delta P = K Q_m^2$

### 1.2.2. Alternate flow at $\Delta T = 0^\circ\text{C}$

The alternate isothermal flow is achieved by a pneumatic cylinder whose swept volume allows to cross the entire gas through the regenerator. The absolute supply pressure of the bench is  $P_{alim} = 2$  bar during the tests, and the

atmospheric pressure is  $P_{\text{atm}} = 0.987\text{bar}$ . The effects of fluid compressibility were neglected for a temperature gradient of zero, since the average temperature of the gas recorded during the tests did not vary and  $T_e = T_s = 24.5^\circ\text{C}$ .

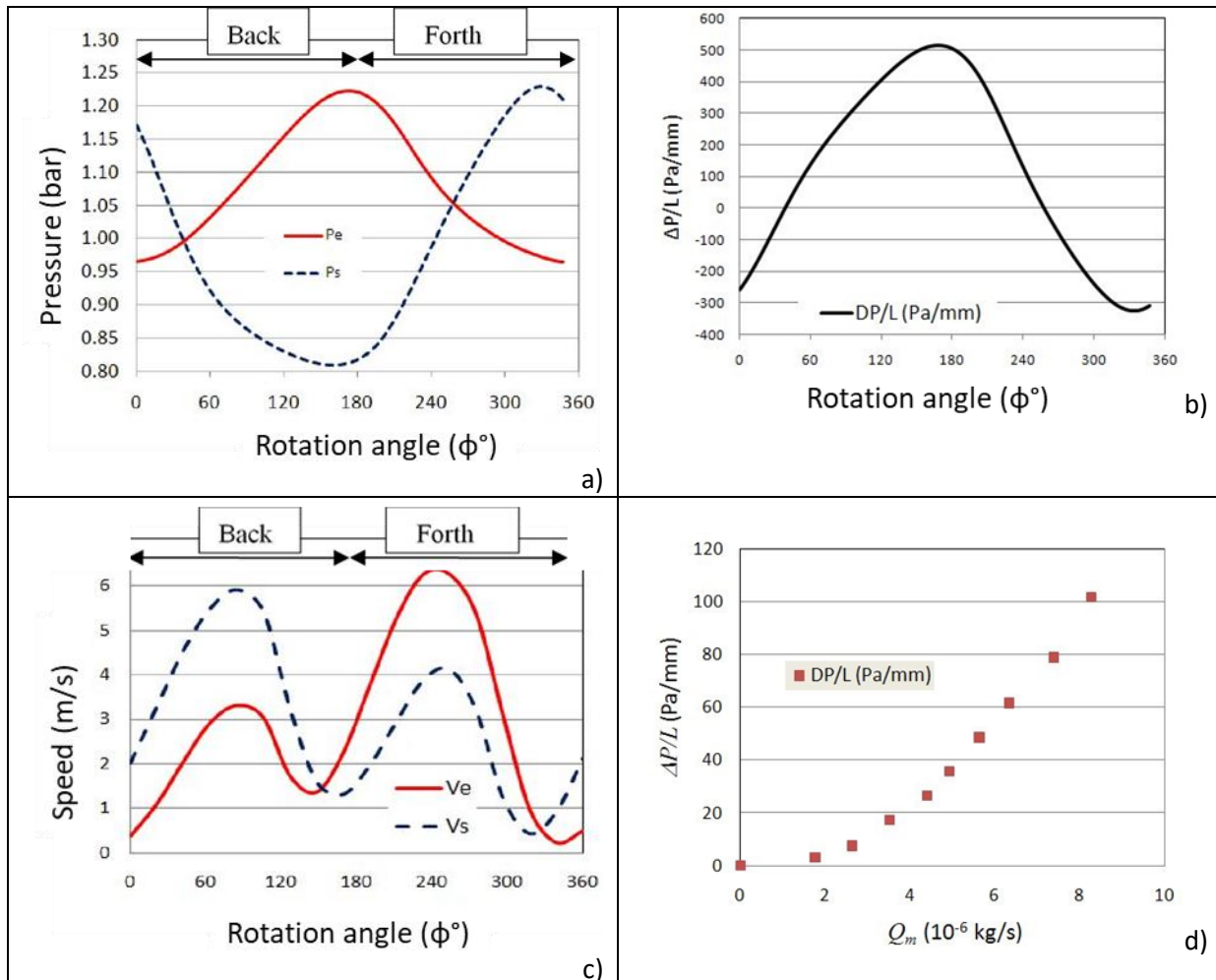


Figure 5-41: At  $f = 6$  Hz,  $\Delta T = 0^\circ\text{C}$ : a) Instantaneous pressures at both ends of the regenerator depending on the angle of rotation. b) Regenerator linear pressure loss. c) Instantaneous speeds at both ends of the regenerator according to the angle of rotation. d) Linear charge loss ( $\Delta P/L$ ) of the regenerator as a function of the mass flow rate  $Q_m$  ( $P_{\text{atm}} = 2$  bar) in steady state conditions [106].

Figure 5-41 a) shows the pressure variations as a function of the rotation angle of the drive motor of the cylinder ( $360^\circ$  corresponding to a round trip, for a rotation frequency of 6 Hz) and in an operating mode in steady state. In the "go" phase ( $0^\circ < \phi < 180^\circ$ ), at the inlet of the regenerator, the pressure  $P_e$  increases, while at the same time, due to the pressure drop, the pressure  $P_s$ , at the outlet, decreases almost symmetrically. In "return" phase ( $180^\circ < \phi < 360^\circ$ ), the phenomenon observed in the "go" phase is reversed. Thus, the linear pressure drop (represented in Figure 5-41 b) shows a maximum value for a rotation angle of  $\phi = 180^\circ$  corresponding to the half-cycle period for which the volume of gas has been swept by the piston. The gas velocities  $V_e$  and  $V_s$  (cf. Figure 5-41 c) also have reversed gaits. At  $\phi = 180^\circ$ , they decrease strongly when  $\Delta P/L$  tends towards its maximum value. The maximum speeds (for  $\phi = 90^\circ$  and  $270^\circ$ ) are  $90^\circ$  out of phase with the maximum linear pressure drop (at  $\phi = 180^\circ$ ).

The pressure drop curves in the case of permanent flow (Figure 5-41 d) and in the oscillating case (Figure 5-41 b) show that these two phenomena are completely different. This is explained by the fact that in alternating flow velocities and pressures vary over time, which is not the case in permanent flow. The analysis of these curves shows that the maximum pressure drop amplitude for  $\phi = 180^\circ$  is 750 Pa/mm (Figure 5-41 b).

### 1.2.3. Alternate flow at $\Delta T = 40^\circ\text{C}$

In alternating flow, when the regenerator is subjected to a temperature gradient ( $\Delta T = 40^\circ\text{C}$ ) at its extremities, the observed effect is an increase in the amplitude of the pressures at its ends (cf. Figure 5-42 a) as well as the linear

pressure drop (Figure 5-42 b). The maximum linear pressure drop increases by 80% due to the increase of the temperature gradient (from 0 to 40 °C) to  $\phi = 180^\circ$  and  $\Delta P/L_{\max} = 1350 \text{ Pa/mm}$ . Velocities  $V_e$  and  $V_s$  also increase (Figure 5-42 c) compared to the isothermal case (Figure 5-41 c). The speed  $V_s$  on the cold side is higher than that  $V_e$  on the warm side, because the viscosity forces have increased with temperature. The analysis of Figure 5-42 d) shows that the temperatures of the gas at the heart of the regenerator have maximum values for  $\phi = 180^\circ$ , corresponding to the point of maximum pressure and minimum speeds. This effect is more marked on the hot side (TR1) than on the cold side (TR5). In this same figure, the temperature increase of 20°C with respect to the inlet temperature for  $\phi = 0^\circ$  ( $TR1_{\max} = 81^\circ\text{C}$ ,  $TR1 = 60^\circ\text{C}$ ) can be linked to the compressibility of the gas.

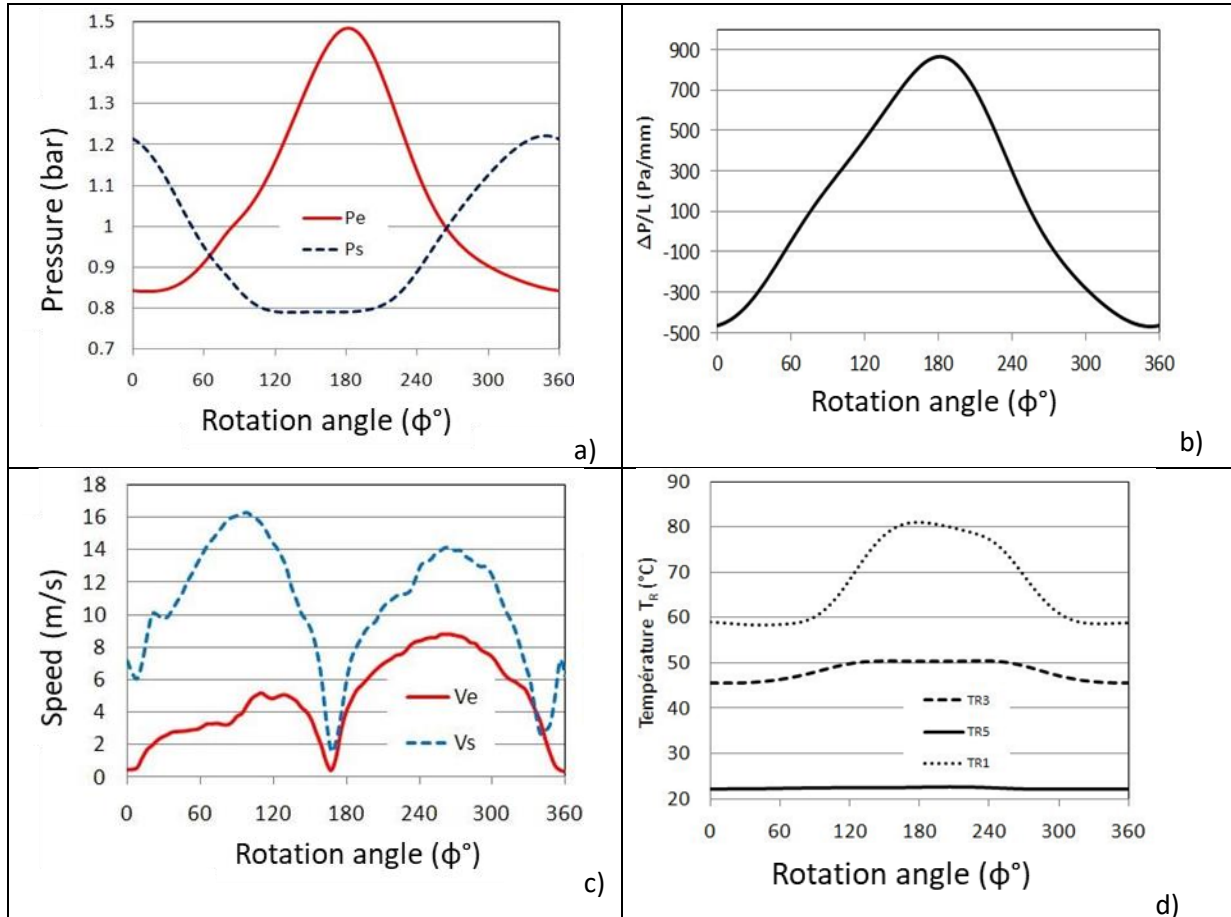


Figure 5-42: At  $f = 6 \text{ Hz}$ ,  $DT = 40^\circ\text{C}$ : a) Instantaneous pressures at both ends of the regenerator according to the angle of rotation. b) Linear charge loss of the regenerator. c) Instantaneous speeds at both ends of the regenerator according to the angle of rotation. d) Instantaneous temperature of the fluid within the regenerator [106].

The central temperature TR3 ( $TR3_{\max} = 50^\circ\text{C}$  for  $\phi = 180^\circ$ ) is less affected by the compressibility of the gas; in addition, at this point of the regenerator, part of the heat has been transferred to the solid matrix. The temperature  $TR5 = 22.4^\circ\text{C}$  is almost constant over a period. This shows the efficiency of the cold exchanger to cool the cold zone of the regenerator. In sum, the regenerator in oscillating flow condition, undergoes changes in internal temperatures over time at each location. Therefore, the temperature of the gas in a regenerator cannot, therefore, be represented by a linear expression as is often the case in the literature.

### 1.3. Oscillating flow pressure drop coefficient

The expression of the pressure drop coefficient is deduced from the expressions in Table 5-14. The Reynolds number in alternating flow  $Re\omega$  will be in the range  $0.1 < Re\omega < 1.53$  for the frequency range  $1 < f < 15 \text{ Hz}$  since the oscillating flow takes place in a porous medium consisting of square section channels, side  $d$  equal to the hydraulic diameter  $dh = 0.5 \text{ mm}$ . In this configuration,  $Re\omega$  will always be lower than the value 277.6 (Table 5-15) and the Reynolds number  $Re$  will be determined on the maximum value of the velocity within a channel of hydraulic diameter  $dh = 0.5 \text{ mm}$  as follow.

$$C'_{f\omega} = \frac{94}{Re}$$

With  $a = 64b'$ ;  $b' = 1.47 - 1.48d + 0.92d^2$ ;  $a = 0.5\text{mm}$ ;  $b = 0$ ;  $c = 0$ .

The maximum velocity of the fluid in the cross-section at the inlet of the regenerator is calculated according to formula [108]:

$$u_{max} = \frac{2\pi V_{pist} N_{pist}}{30 A_{reg}}$$

with  $V_{pist}$  the volume swept by the piston,  $N_{pist}$  the piston speed,  $A_{reg}$  the cross-section of the regenerator. Tanaka *et al.* [120] proposed a correlation for the pressure drop coefficient as a function of maximum Reynolds number for  $10 \leq Re_{\omega} \leq 1000$ :

$$C_f = \frac{175}{Re_{max}} + 1.60$$

The authors concluded that the choice of the hydraulic diameter  $D_h$  as reference length for the calculation of the Reynolds number and the pressure drop coefficient, ensures the validity of the correlation for different forms and materials of regenerators. They also show that the coefficient of pressure loss in oscillating flow is greater than the coefficient of pressure loss in unidirectional continuous flow [11].

The instantaneous displacement of an incompressible fluid for an alternating flow in a regenerator (of woven metal filaments) can be expressed by [106]:

$$x_p = \frac{(x_{max})_p}{2} (1 - \cos(\omega t))$$

where  $(x_{max})_p$  is the maximum displacement of fluid in the regenerator with:

$$(x_{max})_p = \frac{x_{max}}{\varepsilon} = \frac{V_{pist}}{\varepsilon A_{reg}}$$

For the maximum loss of load coefficient, they propose the relationship:

$$C_{fmax} = \frac{1}{A_{D_h}} \left[ \frac{403.2}{Re_{\omega}} + 1789.1 \right]$$

The authors then deduce a correlation of the average pressure loss coefficient in the form:

$$C_{fav} = \frac{1}{A_{D_h}} \left[ \frac{247.3}{Re_{\omega}} + 1003.6 \right]$$

With  $0.001 \leq Re_{\omega} \leq 0.13$ ;  $614.73 \leq A_{D_h} \leq 2827.56$  and  $Pr = 0.71$

According to them, the loss of charge increases with the Reynolds number frequency  $Re_{\omega}$  and the adimensional displacement of the fluid  $A_{D_h}$ . Their study also shows that the coefficient of pressure drop in alternating flow is 4 to 6 times greater than that of the permanent unidirectional flow. Their experimental results have also demonstrated for a Reynolds number frequency  $Re_{\omega} = 0.055$ , the existence of a phase shift of  $24^\circ$  between the pressure drop and the speed and that this phase shift strongly depends on the frequency Reynolds number  $Re_{\omega}$  and slightly the adimensional displacement of the fluid  $A_{D_h}$ . Isshiki *et al.* [272] show that, for a Womersley number  $W_0 = 1.2$ , the ratio between the alternating and continuous flow friction factor is close to 1, then it grows rapidly with the Womersley number, and reaches 4.1 for a Womersley number  $W_0 = 5$ . In addition, the phase difference between the pressure drop and the fluid speed tends to  $72^\circ$  for a Womersley number  $W_0 = 5$ . For low Womersley numbers ( $W_0 < 1$ ), they find that the viscous force is dominant and represents almost the entire total pressure drop. On the other hand, for Womersley numbers greater than 1, the influence of the inertia force is significant and reaches 76% of the total pressure drop for a Womersely number equal to 5.

Otherwise, the ability to accurately predict pressure drop and heat transfer rates in a regenerator is of paramount importance for the optimal design of a Stirling micromotor or a Stirling micro chiller. The most common correlation equation used in designing a regenerator to estimate pressure drop is given by Tong and London [227], who, on the basis of continuous flow through stacked screens, were able to obtain data. All correlation equations obtained on stacked screens are expressed in terms of the Reynolds number in the steady flow case. For instance, Miyabe *et al.* in their study of pressure drop through a stack of woven screens, obtained the following equation of correlation of a steady flow [273]:

$$f_{st} = \frac{\frac{\Delta p_{st}}{n}}{\frac{1}{2}\rho(u_{st})_p^2} = \frac{33.6}{Re_\beta} + 0.337$$

$$Re_\beta = \frac{(u_{st})_p \beta}{\nu}$$

where  $\Delta p_{st}$  represents the steady flow pressure drop,  $n$ , the number of screens packed in the column,  $(u_{st})_p$  is the cross-sectional mean flow velocity in the packed column,  $\beta$  characterize the distance between meshes and  $Re$  is the Reynolds number. Correlation equations based on a steady flow was apparently not suitable to predict correctly the pressure drop in a regenerator since Stirling-cycle machines operates under periodically reversing gas flow conditions. For example, Martini and Rix have found that to obtain a good agreement between the pressure drop simulation and the experimental measurements, the friction coefficient supplied by Tong and London must be arbitrarily adjusted from a constant value of 3 to 5.

---

## **APPENDIX D: MEMS MANUFACTURING TECHNIQUES**

At FEMTO-ST Institute, we have a clean room called "MIMENTO" dedicated to the manufacture of microsystems.

### **1.1. Use of MEMS technologies: environment, materials used and limitations**

Silicon is the most commonly used structuring material because of its well-known properties and well-developed manufacturing tools. The fabrication of a MEMS prototype in a clean room occurs by first patterning a substrate (a silicon wafer for example) by lithography and then depositing or removing material from it. Often, many of these steps are repeated to create 'features' on the substrate. Sometimes it is then necessary to assemble several substrates to produce the final product or for encapsulation to protect a device against the aggression of the environment (to increase its lifetime). The clean room manufacturing assembling techniques used in our work are presented in detail here.

There are two types of micromachining identified, surface and bulk, and they are defined by whether the material is deposited onto the wafer (substrate) surface or three-dimensional features are etched into the bulk of the wafer. Often, many modern MEMS features incorporate both surface and bulk micro-machining into their processing. In fact, surface micro-machining is commonly used for static and thermoelectric systems fabrication whereas bulk micromachining techniques are more applicable for thermomechanical systems. The term "thermo-mechanical" is used here to describe systems that transform thermal energy through mechanical means.

### **1.2. The clean room environment**

Microfabrication is carried out in a "clean room" that is an extremely clean and maintained environment. Before describing what is a clean room, note that a dust seed has a micrometer size and tend to adsorb on surfaces. Therefore, their presence in a microfluidic canal for example, because of their size causes problem. This is one of the reasons that we work in clean rooms. Because of this, the classification The quality of the clean room, in term of cleanliness, is based on the number of dust particles whose size is less than 4  $\mu\text{m}$ , contained in a volume equal to one inch-cube (*i.e.* 2.54  $\text{cm}^3$ ). For the microfabrication of MEMS, we find the clean rooms whose class goes from 1000 to 10000 and for microelectronics (microprocessors fabrication spaces), the quality level is higher and varies from 10 to 1. A clean room is defined as an environment regulated in light (white and yellow in general), in temperature (around 20°C), in hygrometry and permanently crossed by filtered air streams allowing the uninterrupted elimination of dust and gases that inevitably enter the workspace due to human presence and chemical processes. However, to preserve the cleanliness of the room for a class of 1000 to 10000, the users of the room should wear specialized clothing, cover hair and put on gloves and shoe-covers. While these precautions are not necessary for rooms of higher classes (*i.e.* less 'clean').

Note that in clean rooms, equipment cannot structure all materials. In general, only silicon and glass are used as basic materials to be structured.

### **1.4. MEMS scales**

When one makes a device whose geometric dimensions (length, width or thickness) is a fraction of a micron up to the millimeter, one is in the field of microfabrication. However, if it has a nanometer value, the nanomanipulation techniques apply, including the so-called bottom-up approach. We will not tackle this vast subject here, and will limit ourselves only to micrometric scales and the associated fabrication methods. The microfabrication technologies can be divided into two categories: silicon technologies and "soft" technologies, which use materials like elastomers or plastics.

### **1.5. Basic material in clean room**

Basic materials in MEMS technology are divided into two classes according to their stiffness as follows:



### 1.5.1. Hard technologies

Silicon and glass or hard technologies is a very mature technology. Silicon is an available material with very documented properties (crystallographic orientations for example) and whose integration with electronic circuits is easy (*cf.* [108]). Silicon is delivered in the form of wafers (*cf.* [108] b) that constitute without defects almost a monocrystal. Working with silicon is advantageous because it allows taking advantage of existing sophisticated knowledge and equipments. This material has very interesting physicochemical characteristics.

The silicon can be doped to change its electrical conductivity otherwise it is an insulator at room temperature.

Silicon is a good thermal conductor comparable to a metal with low thermal expansion. For example, at 300 K, the coefficient of expansion is  $2.33 \cdot 10^{-6} \text{ (K}^{-1}\text{)}$  which is comparable to that of glass, this coefficient decreases with temperature and becomes negative at the temperature of 100 K.

The native oxide of silicon, which is called silica, adheres well to the substrate, has a very good thermal stability, excellent resistance to certain important reactive elements of etching and is not soluble in water. In other words, silica is very interesting as a mask for dry and wet etching.

There are 3 and 6-inch silicon wafer sizes used in microfabrication and 8 and 12-inch wafers for microelectronics. On the other hand, these wafers have a standard thickness of 500  $\mu\text{m}$ .

There are also wafers SOI (silicon on insulator) which are composed of three layers including two in silicon and one in silicon oxide, which make it easier to achieve several devices including those involving sacrificial layers such as beams for example.

Properties	Values	Units
Rupture strength	7	GPa
Young's modulus	190	GPa
Density	2.33	$\text{g/cm}^3$
Thermal conductivity	2.33	$\text{W/cm.K}$
Electrical resistivity	$2.3 \cdot 10^5$	$\Omega.\text{cm}$
Thermal diffusivity	0.9	$\text{cm}^2/\text{s}$
Specific heat (at constant pressure)	0.7	$\text{J/g.K}$
Fusion temperature	1415	K

Table 5-16: Physical properties of monocrystalline silicon wafers [108].

Silicon is an ordered crystal in the minimum energy state, while glasses are not ordered and not stable systems. However, silicon and glass wafers are fragile material that have not a plastic zone. This signifies that, beyond the elastic deformation zone, is the mechanical rupture zone, corresponding to a limit of 7 GPa (a maximal strain of about 3.5%) [108].

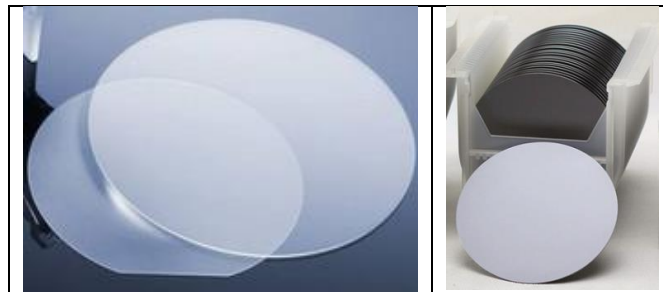


Figure 5-43: a) Standard glass wafer 4 inch thickness 500  $\mu\text{m}$ . b) Standard 4 inch (10cm of diameter) silicon wafer 500  $\mu\text{m}$  thick.

Glass wafers (*cf.* 2.11a) are also used in clean rooms. Taking into account that many microstructures are often created on wafers by ultrasonic drilling or a combination of photolithography and dry or wet etching. Among the most efficient and used glass materials, BOROFLOAT 33 glass wafers (BF33) stand out for their mechanical resistance and stability during these processes. Among the many characteristics of BF33 glass wafers are:

- their adaptation for anodic bonding (silicon + glass), particularly because of their low coefficient of linear thermal expansion close to that of silicon, a good flatness and their stability in the face of sudden temperature rise without breaking or deforming,
- their resistance to acids, alkalis and organic substances, because during chemical etching based on masks, an aggressive mixture of corrosive chemicals are applied in order to create high definition channels with controlled depths,
- exceptionally high UV transmission and light transparency,
- Excellent mechanical strength,
- High chemical durability.

Thermal properties	Values
Coefficient of Linear Thermal Expansion (C.T.E.) $\alpha$ (20 - 300 °C)	$3.25 \times 10^{-6} \text{ K}^{-1} *$
Specific heat capacity $c_p$ (20 - 100 °C)	0.83 kJ/(kg·K)
Thermal conductivity $\lambda$ (90 °C)	1.2 W/(m·K)

Table 5-17: Properties of BOROFLOAT 33 glass wafers. Extracted from <https://www.schott.com/borofloat/english/download/index.html>

Maximum operating temperatures	Values
Maximum Operating Temperature For short-term usage (< 10 h)	500 °C
For long-term usage ( $\geq$ 10 h)	450 °C

Mechanical properties	Values
Density $\rho$ (25 °C)	2.23 g/cm <sup>3</sup>
Young's Modulus E	64 kN/mm <sup>2</sup>
Poisson's Ratio $\mu$	0.2
Bending Strength $\sigma$	25 MPa

Material	Critical forces	
	Mean value $F_c$ [mN]	Stadev.* [mN]
BOROFLOAT® 33	363.8	4.3
Other borosilicate glass	271.2	1.9
Soda-lime flat glass	214.4	4.6

\* According to ISO 7991

### 1.5.2. Soft technologies

Plastics, polymers and elastomers or soft technologies are an evolving area. Note that plastics have the advantage of being, in general, 100 times cheaper than silicon. Moreover, their time of prototyping and cost of manufacturing is lower. Some polymer materials allow the development of a microfluidic circuit in just a few minutes by using an in-situ polymerization [108] and their aspect like surface effects, transparency, diversity of materials are native. While silicon-based technologies, require times typically about one week. They are also very interesting materials for observation because of their transparency, which is also very useful in the field of microfluidics. Elastomers are often used when a very flexible component is needed for example an actuation membrane, a pneumatic system or for thermomechanical systems based on fluid expansion. The term "plastic

MEMS" is also widely used when working with elastomers (like PDMS) or plastic (like PMMA). "Plastic MEMS" occupy a domain between 0.5 and 500  $\mu\text{m}$  in size of microfabrication of devices [108].

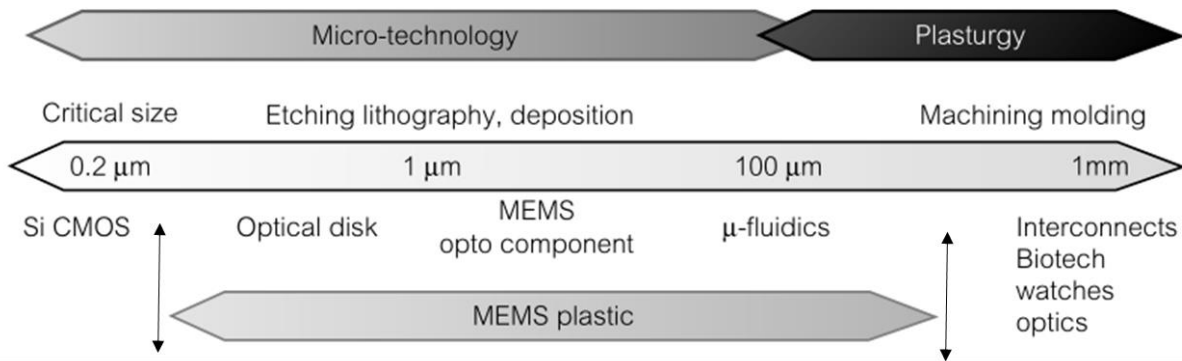


Figure 5-44: Scale and different types of microtechnologies [108].

These particular MEMS are made, depending on the materials, from the direct method (for example by laser ablation) or replication implying the use of a mold to be built first (as is the case with the PDMS). All these techniques result from an intelligent adaptation of techniques well mastered in the field of plastics.

## 1.6. Photolithography method

Lithography technique is the transfer of a master pattern or design feature to the working substrate. There are several types of lithography classified according to the combination of material and energy used to transfer the pattern on the substrate. The choice of the type of lithography to use depends on the resolution or the size of the smallest desired pattern. There are two major types of lithography, electronic lithography using an electron beam as structuring energy and photolithography based on light beam (generally UV between 300 and 400 nm). In our work, we used this last technique, which resolution is between 0.13  $\mu\text{m}$  linewidth to 5  $\mu\text{m}$ .

In conventional photolithography, the working substrate is initially coated with a light sensitive chemical material called photoresist. The photoresist layer is then patterned by exposure to UV light through a pattern mask and reducing or enlarging optics of a dedicated equipment. A mask is a master image of the desired pattern made on a quartz plate by chromium deposit forming the patterns with submicron precision. The photoresist is deposited on the substrate using a spin-coater rotating at a speed between 1000 and 10000 rev / min. Indeed, it is a drop which is deposited in the center of the substrate then the substrate is rotated. The thickness ( $h$ ) of photoresist obtained is uniform to about ten nanometers. Knowing the characteristics of the photoresist ( $c$  and  $\mu$ ) and the characteristic of the spinner one can find the speed of rotation to use to obtain the desired thickness with the following equation [108].

$$h = k \cdot c \left( \frac{\mu}{\omega^2} \right)^{1/3} \quad (2.41)$$

$k$  is a constant characteristic of the spin,  $c$  is the initial concentration of the photoresist in the solution,  $\mu$  is its viscosity and  $\omega$  is the speed of rotation of the spin.

The photosensitive resist has a non-Newtonian flow and its viscosity increases over time due to the evaporation of the solvent it contains. This evaporation occurs during the stretching because the surface-to-volume ratio increases considerably, which promotes evaporation, so the resist concentration increases favoring the initiation of the polymerization process. Thus at the end of this process, the film no longer has a liquid structure but rather that of glass. As the thickness of the resin increases, the accuracy of the pattern decreases as the penetration and homogeneity of the luminous flux during the exposure decreases. Therefore, the thin deposits are preferred, but depend on the selectivity of the etching technique that will follow. After spreading, the resist typically still contains 15% of solvent, which must be evacuated to avoid cracks once the film has completely polymerized. The film is slightly heated (around 100  $^{\circ}\text{C}$  for a few minutes) to evaporate the rest of the solvent before the next step, which

is insolation. During this insolation step, the luminous flux initiates physicochemical reactions involving a modification (weakening or strengthening of the chemical bonds) of the solubility of the resist relative to certain liquid solvents called developers. Depending on the type of resin, this step does not bring about the same effects.

For a so-called positive resist, it will cause a rupture or weakening of the covalent internal bonds by causing a rearrangement of the latter in a soluble form in a specific solution. For a so-called negative resist, there will be on the contrary a formation of covalent bonds between main or secondary chain, making them insoluble in a specific developer. Negative resists adhere better to the substrate and are more chemically resistant, while positive resists have the advantage of having higher photosensitivity contrast. Then a development process allows for the removal of UV exposed areas of the substrate generating the desired pattern on the substrate in the case of positive resist. While in the case of a negative resist, this action will dissolve the parts not exposed to UV. It is obvious that the microfabricated object will not have a geometric precision superior to that of the mask used. Masks are often made using electron beams lithography technique, which will not be described here.

Subsequent surface or bulk micromachining (etching or depositing) then will defines a feature directly on the surface or in the volume of the substrate. Depending on the complexity of the desired feature, this lithography and micromachining process is repeated until the desired structure is fabricated. Feature resolution on the substrate depends on the wavelength of light used during the exposure. Currently, deep UV lamps exist with research oriented towards the use of extreme UV.

Note that technologies based on lithography, etching and deposition techniques can be applied in the range of scales between 0.2 and 500 micrometers. These are called the “hard” technologies, because they use hard materials such as glass or silicon. The combination of these three techniques makes it possible to obtain complex microfluidic devices that are open or closed, containing sputtered or evaporated electrodes allowing electrical access to the exterior.

## 1.7. Thin film Deposition techniques onto silicon and glass

There is a variety of deposition techniques that make it possible to deposit metals, insulators, polymers and even proteins on a substrate. These techniques are classified in two categories:

**Physical vapor deposition (PVD).** In this technique, the substrate is put into contact with a gas containing species, certain species in the gas adsorb on the substrate, forming a layer that constitutes the deposit. There is two types of PVD thin film deposition. There is thermal evaporation and deposition by sputtering.

In the case of thermal evaporation, the solid material to be deposited is placed in a chamber maintained at low pressure of the order of  $10^{-8}$  Torr. Then, the system is heated to high temperature the material is then sublimed and produces a flux of atoms that adsorbs on the surface of the target. But the concern is that if the chamber was not at high pressure the deposit of the desired material will take place simultaneously with other molecules contained in the chamber. In addition, the deposition rates are not very high (a few Å per second), and the method is mainly reserved for metal deposits.

Regarding sputtering, the materials to be deposited is placed on the cathode and the substrate is placed on the anode. The system is then placed in a cold plasma. The cathode is then subjected to a high energy particle flux (of the order of 0.3 to 2 keV) which produces an ejection of material deposited on the substrate due to the electric polarization. Good adhesion between the layer and the substrate is achieved because the energetic ions collect at the target and penetrate one or two of the first molecular layers of the substrate.

**Chemical vapor deposition CVD.** In this case, species in contact with the substrate surface react, forming components that are chemically bonded to the surface. In the case of CVD, after the substrate is brought into contact with a gas containing reactive species. There are two reactions that can occur:

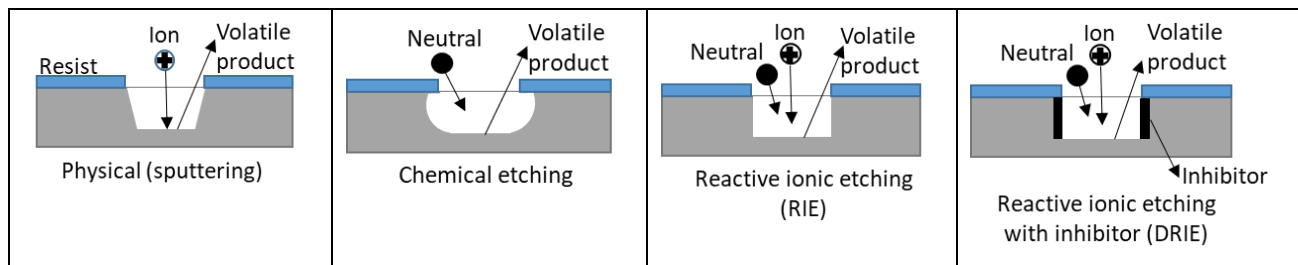
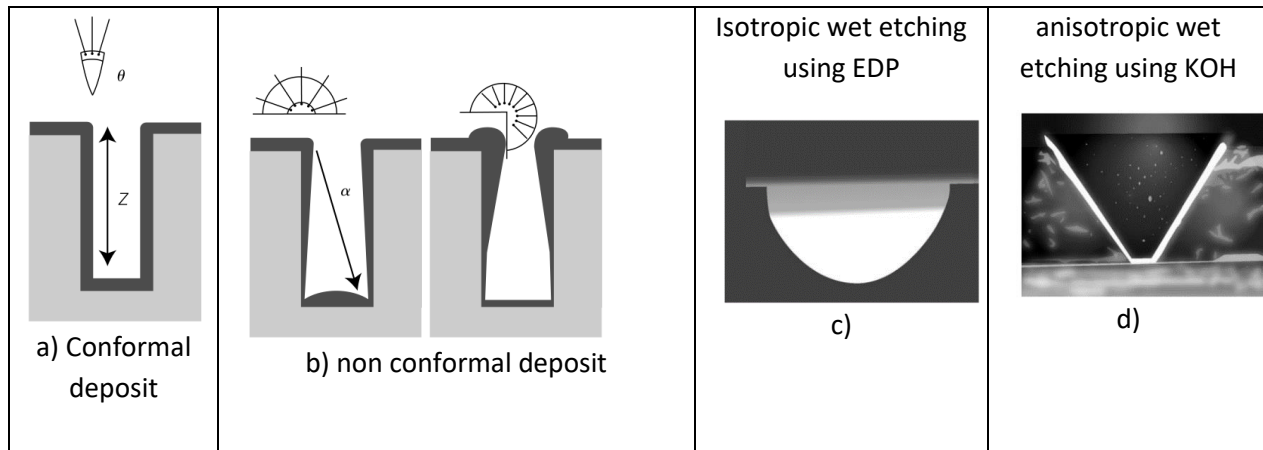
- the reaction occurs in the gas and the products of the reaction are adsorbed on the surface of the substrate resulting in a homogeneous reaction;
- the reaction takes place directly on the surface of the substrate, resulting in a heterogeneous reaction.

Note that most CVD deposition equipment is based on heterogeneous reactions, since the adhesion of the produced film is superior compared to that of the homogeneous case. However, the evaporation of a material on

a substrate containing a pre-existing relief does not necessarily lead to layers of uniform thickness. The deposit may result in a compliant or non-compliant layer (*cf.* [108] a):

- In the case where the deposit is compliant, the deposited film has a constant thickness at all points of the surface substrate.
- Non-compliant deposit: in this case, the deposited film does not have a constant thickness and has rolls and crevices.

And in the case of physical deposit, to obtain a consistent deposit, the incident particles must be sufficiently energetic to diffuse towards the target surface before forming chemical bonds.



e)

Figure 5-45: a) and b) Conformal and non-conformal deposition. c) Isotropic wet etching using EDP and d) anisotropic wet etching using KOH lead to rounded or faceted forms, respectively (From [108]). e) Different types of dry etching for silicon (from left to right): physical, chemical, physico-chemical, and physico-chemical with inhibitor

## 1.8. Etching techniques of silicon and glass

There are two types of etching in the clean room: isotropic and anisotropic

- In the case of an isotropic etching (*cf.* [108] b), the etching takes place in the three directions of the material with the same speed. For example, with this method, one can create spherical cavities in silicon and glass.
- On the contrary, an anisotropic etching (*cf.* [108] b) is an etching, which is carried out preferentially along certain crystalline planes of the material. With this technique, trapezoidal cavities bringing out the planes (111) are produced in silicon. Note that since the glass is not a crystal (*i.e.* amorphous solid) this type of etching is excluded.

To etch materials in a clean room, the two commonly used methods are:

### 1.8.1.a. Wet etching

Wet etching is based on liquid chemicals. However, the combinations of the chemicals differ according to whether it is desired to carry out an isotropic or anisotropic etching and also according to the material to be etched.

**Wet anisotropic silicon etching:** facets (111) are produced using KOH in basic medium. It makes it possible to make cavities of flat surfaces, wells or canals with flat walls, but of trapezoidal section. The etching rate increases with temperature and is not the same for different crystallographic orientations. For example, the etching speed according to the plans (111) is slow of the order of 13 microns / hour while it is fast in the other planes. It can be deduced that a silicon crystal immersed in the chemical solution KOH will spontaneously reveal cut-out shapes according to the planes where the etching rate is the slowest (*i.e.* the dense planes), *i.e.* the planes (111). Moreover, the surface state is atomically smooth formed of terraces. Note, however, that with KOH, hydrogen bubble (H<sub>2</sub>) production will introduce fluctuations in the local concentration of chemical reagents in the solution. This phenomenon leads to inhomogeneities in etch rates leading to rough surface conditions. To avoid this, as the production of H<sub>2</sub> bubbles increases with temperature, the KOH solution must be maintained at moderately high temperatures and stir the solution. In practice, in a well-controlled standard process, the surfaces have a local roughness of around 20 nm [108].

**Isotropic wet etching of silicon and glass:** Hydrofluoric acid (HF) makes it possible to create spherical cavities in the glass, whereas in the case of silicon, it is an EDP solution that is used. For the latter material, the acid product generally used is HNA, which is a mixture of HF, HNO<sub>3</sub> and CH<sub>3</sub>COOH at room temperature. In general, an accuracy of about 10% is obtained on the depth. In practice, the mask is also etched chemically by the solution of the order of a few percent of that of the etching of the substrate material. For example, the silica, which is often used as a mask in the case of the HNA solution, is attacked by the latter, but at a speed 80 times lower than that of silicon. Another problematic phenomenon is that the chemical reagents of the solution not only etch in volume under the exposed parts (*i.e.* intentionally not protected by the mask), but also under the mask. Therefore, one finds oneself at the end of the engraving with larger diameter cavities than what was provided on the mask [108].

### 1.8.1.b. Dry etching of silicon

The dry etching can be categorized in 4 types that are obtained by playing on the nature of the etching plasma containing the ions as illustrated in figure 2.13c). In this type of etching, it is the attack of a substrate by an ionic species contained in a gas phase or plasma. Depending on the type of etching conditions, the shapes obtained may be isotropic or anisotropic. Note that this anisotropy is controlled by the system and not by the crystalline structure of the substrate material to be etched. For example, one can, thanks to that, etching channels with right angles in glass. The 4 types of dry etching are organized as follows:

**Physical etching** or sputtering of the material to be etched: ions are accelerated by an electric field (of the order of 10 to 5 keV) and bombard the unprotected surface of the substrate. This results in an etching effect produced by the physical action of the incident ion flux. This type of etching is anisotropic and not very selective. At low ion beam etching (IBE), the etching rate is in the range of 0.6 to 18  $\mu\text{m}\cdot\text{h}^{-1}$ .

**Chemical etching:** In the case of chemical etching, chemical species subjected to an electric field in a pressurized chamber (about  $10^{-1}$  to 1 Torr), migrate to the surface of the substrate and develop chemical reactions, producing volatiles species. The etching rates are of the order of a few micrometers per minute and a surface roughness of the order of one micrometer. It is an isotropic etching that occurs in this case.

**Physico-chemical etching:** In this type of etching, which is the most common in the field of microfabrication, the two actions (physical and chemical etchings) are combined. It is a reactive ion etching (RIE) in an RF (Radio Frequency) plasma that increases the temperature. It is carried out by removal of material by bombarding the surface of the sample with active ions and by chemical reaction of reactive species in the plasma. The etching rates are of the order of 0.1  $\mu\text{m}\cdot\text{min}^{-1}$ . It is a technique often used to etch not only the silicon, but also its oxide coated with a photoresist mask, this allows to transfer the pattern of the resin mask to the silica to be used in turn as a mask for a wet etching.

**Physico-chemical etching with inhibitor** or DRIE: The difference with simple physicochemical etching is the use of a protective layer along the sides of the etched cavities while the bottom is attacked chemically and physically by the reactive species and plasma ions. This type of engraving makes it possible to produce geometries with a high aspect ratio. We then speak of deep reactive ion etching DRIE or ionic etching with inhibitor and it now requires specific equipment for MEMS that can achieve it. This technique makes it possible to obtain very deep engravings of more than 500  $\mu\text{m}$  with aspect ratios exceeding 100:1. It also makes it possible to perform in-depth complex shapes that are not based on the crystallographic planes of the substrate material. This technique requires the

creation of a cold plasma that makes it possible to produce reactive species from a gas that is not spontaneously reactive with silicon. This is the case for example  $\text{CF}_4$ -based plasma, this compound alone does not attack the silicon, but the  $\text{CF}_3^+$ ,  $\text{CF}_3$  and  $\text{F}$  ions formed in its plasma, are reactive with respect to silicon. This makes it possible to reduce the roughness. With respect to the etching mechanism of the DRIE, the chemical reactions at the surface of the substrate create nonvolatile compounds, which are subject to the action of the ion flux, are ejected out of the exposed surfaces. These ions adsorb to adjacent vertical surfaces and form a polymerized protective film. This subtle process enhances the anisotropic effect of etching. In an RIE process, an inhibitory film is formed with plasmas produced from  $\text{CCl}_4$  and  $\text{CF}_2$ . ( $2\text{Cl}_2$ ) compounds. This phenomenon, coupled with plasma energy sources called Ion Plasma Coupling (ICP), gives rise to very deep etchings that can cross the thickness of the standard 1mm silicon wafer with a fast speed of the order of  $10 \mu\text{m} / \text{min}$ . It is also called a BOSCH process that alternates a silicon etching phase ( $\text{SF}_6$  Sulfur Hexafluoride) and a deposition phase (or passivation) producing a layer very close to Teflon due to the decomposition of  $\text{C}_4\text{F}_8$ . The passivation of the flanks of the etching makes it possible to preserve the anisotropy.

## 1.9. Bonding techniques

Bonding techniques are critical steps in fabrication and assembly of MEMS devices. Bonding techniques can be briefly classified into two major categories—direct bonding and bonding with an intermediate layer.

### 1. Direct Bonding = Anodic bonding, fusion bonding, and activated surface bonding

- Anodic bonding : cleaned extensively, aligned, and brought into pressure contact. High voltage ( kV) and high temperature cause an irreversible bond to form between the substrates. for bonding glass or glass coated substrates with silicon and nitride substrates.

- Fusion bonding : the attractive forces that exist between extremely clean flat surfaces in contact to form a strong bond between them. the alignment and bonding process is usually performed under vacuum with external pressures to help form good contact. followed by a thermal cycling process to strengthen the bond. for bonding silicon wafers.

- Surface activation bonding : the substrates are pre-treated with oxygen plasma, hydration processes or other chemicals to increase the reactivity, and then brought into contact with or without external pressure and high temperature to form an irreversible bond. The effect of surface treatment processes lasts only for a small time interval and the bonding processes including alignment need to be completed within this time window. for bonding PDMS devices to PDMS or glass (commonly used materials in prototyping microfluidic devices)

### 2. Bonding With Intermediate Layer = Adhesive bonding, eutectic bonding, bonding bonding, and thermocompression bonding

- Adhesive bonding : requires a thin adhesive layer on the device, (by spin coating or spray coating when the wafers to be bonded have nonuniform topography). Some typical adhesives used are epoxy, spin-on-glass and UV curable glue.

- Eutectic bonding : uses a thin gold layer as an adhesive to bond silicon wafers. The wafers to be bonded are brought into contact and the temperature is raised (sometime by in situ electrical heating using patterned gold lines) to gold-silicon eutectic point to form an irreversible bond. Localized bonding overcomes the high temperature problem but requires the deposition and patterning of one or more additional bonding layers (gold, silicon). This may not be compatible with some device materials like plastics and polymers or with some fabrication processes.

- Thermocompression bonding : the deposition and patterning of additional layers like bonding or other soft metals and use either heat and/or pressure to form bonds between substrates.

Bonding techniques	Conditions / Procedures	Applications	Limitations
Direct Bonding	Anodic bonding, fusion bonding, and activated surface bonding		
Anodic bonding	Cleaned extensively, aligned, and brought into pressure contact. High voltage (kV) and high temperature cause an irreversible bond to form between the substrates	glass or glass coated substrates with silicon and nitride substrates Glass-Silicon hermetic and irreversible bonding	The bonding temperatures in combination with voltage required may not always be compatible with electronic wafers
Fusion bonding	The attractive forces that exist between extremely clean flat surfaces in contact to form a strong bond between them. The alignment and bonding process is usually performed under vacuum with external pressures to help form good contact. Followed by a thermal cycling process to strengthen the bond.	silicon wafers	
surface activation bonding (SAB) Plasma activated	The substrates are pre-treated with oxygen plasma, hydration processes or other chemicals to increase the reactivity, and then brought into contact with or without external pressure and high temperature to form an irreversible bond.	PDMS devices to PDMS or glass (commonly used materials in prototyping microfluidic devices). Can be used to bond flexible materials like polymers. is a derivative of direct bonding, uses surface activation prior to bonding without the use of any intermediate layer,	The effect of surface treatment processes lasts only for a small time interval and the bonding processes including alignment need to be completed within this time window. But patterning of the bond, i.e. bonding of specific area on the substrate, cannot be done
Bonding With Intermediate Layer	Adhesive bonding, eutectic bonding, bonding bonding, and thermocompression bonding		
Adhesive bonding	Requires a thin adhesive layer on the device, (by spin coating or spray coating when the wafers to be bonded have nonuniform topography). Some typical adhesives used are epoxy, spin-on-glass and UV curable glue.	between Silicon and Pyrex wafers. A low-temperature adhesive bonding, typically polymer adhesives, such as SU-8, are used.	known to be less hermetic and have a small range of temperature stability
Eutectic bonding	Uses a thin gold layer as an adhesive to bond silicon wafers. The wafers to be bonded are brought into contact and the temperature is raised (sometime by in situ electrical heating using patterned gold lines) to gold-silicon eutectic point to form an irreversible bond.	flip-chip, in metal alloy bonding high bond strength and hermeticity, eutectic bonding in [3], which is among the best reported bonding strengths.	Localized bonding overcomes the high temperature problem but requires the deposition and patterning of one or more additional bonding layers (gold, silicon). This may not be compatible with some device materials like plastics and polymers or with some fabrication processes. sensitive to oxides near the surface and hence use of a flux or a reducing atmosphere is necessary. Au/Si à 380°C



Bonding techniques	Conditions / Procedures	Applications	Limitations
Bonding bonding and thermocompression bonding	the deposition and patterning of additional layers like bonding or other soft metals and use either heat and/or pressure to form bonds between substrates. several materials can be bonded, But better for solid (rigid) material.	bonding between two substrates. . (Most of the successful approaches use copper or gold as the bonding material). The results suggest that an increase of the bonding time can compensate a lower bonding temperature,	The softening of the material as temperature increases is used to lower the pressure re-quirement for the formation of a strong bond. oxides occurring naturally on the surface of the material prevent the formation of strong bonds. removing contaminants on the surface by UV radiation require a temperature of about 300 °C. tremendous pressure would be required to achieve thermocompression bonding at room tempera-ture, which would probably damage the bonded parts. no strong bond can be obtained below a bond-ing temperature of 150 °C [18]

Table 5-18: All bonding techniques usually used in clean rooms

---

## BIBLIOGRAPHY

- [1] A. B. Awan et Z. A. Khan, «Recent progress in renewable energy--Remedy of energy crisis in Pakistan,» *Renewable and Sustainable Energy Reviews*, vol. 33, pp. 236-253, 2014.
- [2] M. Tanaka, «Development of desktop machining microfactory,» *Riken Review*, 2001.
- [3] H. Lu, L. Price et Q. Zhang, «Capturing the invisible resource: Analysis of waste heat potential in Chinese industry,» *Applied Energy*, vol. 161, pp. 497-511, 2016.
- [4] W. H. BCS Recovery, «Technology and Opportunities in US Industry,» *Industrial Technologies Program. US Department of Energy*. Dostupné z: <http://www1.eere.energy.gov/manufacturing>, 2008.
- [5] G. FENIES, «Développement et optimisation d'un moteur Stirling pour la valorisation d'énergie thermique,» 2016.
- [6] «MEMS Bi-stableheatharvester». Brevet US9,972,763B2, 2018.
- [7] L. Larcher, S. Roy, D. Mallick, P. Podder, M. De Vittorio, T. Todaro, F. Guido, A. Bertacchini, R. Hinchet, J. Keraudy et others, «Vibrational energy harvesting,» *Beyond-CMOS Nanodevices 1*, pp. 89-134, 2014.
- [8] N. Salamon, «Development of thermal energy harvesting systems,» 2018.
- [9] F. Lanzetta, J. Boucher et P. Nika, «Etude et réalisation d'une pompe à eau Fluidyne,» *Journée SFT: Machines thermiques exotiques*, 2004.
- [10] A. Der Minassians et S. R. Sanders, «Multiphase stirling engines,» *Journal of Solar Energy Engineering*, vol. 131, p. 021013, 2009.
- [11] F. Formosa, A. Badel et J. Lottin, «Equivalent electrical network model approach applied to a double acting low temperature differential Stirling engine,» *Energy Conversion and Management*, vol. 78, pp. 753-764, 2014.
- [12] R. Chutani, F. Formosa, M. Labachelerie, A. Badel et F. Lanzetta, «Microfabrication of hybrid fluid membrane for microengines,» chez *Journal of Physics: Conference Series*, 2015.
- [13] E. Dellali, S. Begot, F. Lanzetta, E. Gavignet, R. Chutani et J.-y. Rauch, «Design, fabrication and CFD modeling of a Stirling engine microregenerator.»
- [14] F. Cottone, H. Vocca et L. Gammaitoni, «Nonlinear energy harvesting,» *Physical Review Letters*, vol. 102, p. 080601, 2009.
- [15] J. Siang, M. H. Lim et M. Salman Leong, «Review of vibration-based energy harvesting technology: Mechanism and architectural approach,» *International Journal of Energy Research*, vol. 42, pp. 1866-1893, 2018.
- [16] S. Roundy, P. K. Wright et J. M. Rabaey, «Energy scavenging for wireless sensor networks,» *Norwell*, pp. 45-47, 2003.
- [17] S. P. Beeby, R. N. Torah, M. J. Tudor, P. Glynn-Jones, T. O'donnell, C. R. Saha et S. Roy, «A micro electromagnetic generator for vibration energy harvesting,» *Journal of Micromechanics and microengineering*, vol. 17, p. 1257, 2007.

- 
- [18] L. Wang et F. G. Yuan, «Vibration energy harvesting by magnetostrictive material,» *Smart Materials and Structures*, vol. 17, p. 045009, 2008.
- [19] Y. Ammar, A. Buhrig, M. Marzencki, B. Charlot, S. Basrour, K. Matou et M. Renaudin, «Wireless sensor network node with asynchronous architecture and vibration harvesting micro power generator,» chez *Proceedings of the 2005 joint conference on Smart objects and ambient intelligence: innovative context-aware services: usages and technologies*, 2005.
- [20] M. Ericka, D. Vasic, F. Costa et G. Poulain, «Predictive energy harvesting from mechanical vibration using a circular piezoelectric membrane,» chez *Ultrasonics Symposium, 2005 IEEE*, 2005.
- [21] P. Murali, M. Marzencki, B. Belgacem, F. Calame et S. Basrour, «Vibration energy harvesting with PZT micro device,» *Procedia Chemistry*, vol. 1, pp. 1191-1194, 2009.
- [22] C. A. Frangopoulos et B. Ramsay, «EDUCOGEN, The European educational tools on cogeneration,» *European Commission. Dec*, vol. 17, 2001.
- [23] S. Carnot, «Réflexions sur la puissance motrice du feu et sur les machines propres à développer cette puissance,» chez *Annales scientifiques de l'École Normale Supérieure*, 1872.
- [24] P. W. Atkins, *The second law*, New York, NY : Scientific American Library, 1984. - 230 p.536.73, 1984.
- [25] R. Stirling, «Improvements for Diminishing the Consumption of Fuel and in Particular an Engine Capable of being Applied to the Moving of Machinery on a Principle Entirely New,» *English Patent 4081*, 1816.
- [26] R. Gheith, «Etude expérimentale et théorique des moteurs Stirling à apport de chaleur externe: application aux machines de types Bêta et Gamma,» 2011.
- [27] A. Lallemand, «Convertisseurs thermomécaniques: Cycles moteurs à gaz: Stirling et Joule,» *Techniques de l'ingénieur. Génie énergétique*, 2007.
- [28] I. Urieli et D. M. Berchowitz, *Stirling cycle engine analysis*, Taylor & Francis, 1984.
- [29] C. Woodford, «(2012) Stirling engines. Retrieved from <https://www.explainthatstuff.com/how-stirling-engines-work.html>. [Accessed (Insert date here)],» 2012.
- [30] D. W. Kirkley, «Determination of the optimum configuration for a Stirling engine,» *Journal of Mechanical Engineering Science*, vol. 4, pp. 204-212, 1962.
- [31] W. Wang, J. Cao, N. Zhang, J. Lin et W.-H. Liao, «Magnetic-spring based energy harvesting from human motions: Design, modeling and experiments,» *Energy Conversion and Management*, vol. 132, pp. 189-197, 2017.
- [32] G. Walker et J. R. Senft, «Free-piston Stirling engines,» chez *Free piston stirling engines*, Springer, 1985, pp. 23-99.
- [33] G. T. Reader et C. Hooper, *Stirling Engines, E. & FN Spon*, London, Appendix A, 1983.
- [34] W. T. Beale, «Free piston Stirling engines-some model tests and simulations,» 1969.
- [35] E. H. Cooke-Yarborough, «A Proposal for a heat powered non-rotating electrical alternator,» *AERE, M-1881*, 1967.
- [36] N. Nakajima, K. Ogawa et I. Fujimasa, «Study on micro engines-miniaturizing Stirling engines for actuators and heatpumps,» chez *Micro Electro Mechanical Systems, 1989, Proceedings, An Investigation of Micro Structures, Sensors, Actuators, Machines and Robots. IEEE*, 1989.

- 
- [37] G. Schmidt, «Theore der Lehmannschn Calorischen Maschine,» *Zeitschrift des Vereines deutscher Ingenieure*, vol. 15, pp. 98-112, 1871.
- [38] N. M. L. G. P. Rochelle, «Modélisation TDF des moteurs isothermes avec pertes : application à l'évaluation d'un moteur Stirling LTD,» *Journal of energy*, 2015.
- [39] M. C. C. H. a. T. F. S. Petrescu, «Application of the Direct Method to irreversible Stirling cycles with finite speed,» *International journal of energy research*, Vols. %1 sur %2589-609, n° %110.1002, p. 26, 2002.
- [40] G. Walker, «Stirling engines,» 1980.
- [41] J. R. Senft, «Theoretical limits on the performance of Stirling engines,» *International journal of energy research*, vol. 22, pp. 991-1000, 1998.
- [42] C. D. West, «Liquid piston Stirling engines,» 1983.
- [43] A. J. Organ, *The regenerator and the Stirling engine*, vol. 624, Mechanical Engineering Publications London, 1997.
- [44] M. Madou, «Etch-Stop Techniques,» *Fundamentals of Microfabrication*, CRC Press, New York, pp. 193-199, 1997.
- [45] G. T. A. Kovacs, N. I. Maluf et K. E. Petersen, «Bulk micromachining of silicon,» *Proceedings of the IEEE*, vol. 86, pp. 1536-1551, 8 1998.
- [46] D. C. Walther et J. Ahn, «Advances and challenges in the development of power-generation systems at small scales,» *Progress in Energy and Combustion Science*, vol. 37, pp. 583-610, 2011.
- [47] S. Whalen, M. Thompson, D. Bahr, C. Richards et R. Richards, «Design, fabrication and testing of the P3 micro heat engine,» *Sensors and Actuators A: Physical*, vol. 104, pp. 290-298, 2003.
- [48] A. Epstein, S. Senturia, O. Al-Midani, G. Anathasuresh, A. Epstein, S. Senturia, O. Al-Midani, G. Anathasuresh, A. Ayon, K. Breuer et others, «Micro-Heat Engines, Gas Turbines, and Rocket Engines-The MIT Microengine Project,» chez *28th Fluid Dynamics Conference*, 1997.
- [49] Q. C. Tang, Y. L. Yang et X. Li, «Bi-stable frequency up-conversion piezoelectric energy harvester driven by non-contact magnetic repulsion,» *Smart Materials and Structures*, vol. 20, p. 125011, 2011.
- [50] Y. Ju et K. Maruta, «Microscale combustion: technology development and fundamental research,» *Progress in Energy and Combustion Science*, vol. 37, pp. 669-715, 2011.
- [51] Felix et J. Weinberg, «The first half million years and todays burning problems,» chez *Energy and Combustion Science (Student Edition One)*, Student Edition One éd., N. A. CHIGIER, Éd., Pergamon, 1979, pp. 17-31.
- [52] Y. Chen, N. Chiotellis, L.-X. Chuo, C. Pfeiffer, Y. Shi, R. G. Dreslinski, A. Grbic, T. Mudge, D. D. Wentzloff, D. Blaauw et others, «Energy-autonomous wireless communication for millimeter-scale Internet-of-Things sensor nodes,» *IEEE Journal on Selected Areas in Communications*, vol. 34, pp. 3962-3977, 2016.
- [53] A. Pisano, «Microelectromechanical systems (MEMS) program,» *DARPA/ETO, BAA*, pp. 97-43, 1997.
- [54] W. Tang, «Micro power generation (MPG),» *DARPA MTP program BAA*, pp. 1-9, 2001.
- [55] K. Maruta, K. Takeda, L. Sitzki, K. Borer, P. D. Ronney, S. Wussow et O. Deutschmann, «Catalytic combustion in microchannel for MEMS power generation,» chez *The third Asia-Pacific conference on combustion*, 2001.

- 
- [56] J. G. B. F. Vican, B. F. Gajdeczko, F. L. Dryer, D. L. Milius, I. A. Aksay et R. A. Yetter, «Development of a microreactor as a thermal source for microelectromechanical systems power generation,» *Proceedings of the Combustion Institute*, vol. 29, pp. 909-916, 2002.
- [57] K. Fu, «Design and experimental results of small-scale rotary engines,» chez *2001 ASME International Mechanical Engineering-Congress and Exposition*, 2001.
- [58] M. G. Allen, «Ceramic micromachining technology,» chez *DARPA Workshop on Combustion-based MEMS Power Generation on the Microscale, for the Microscale*, Washington, DC, 1998.
- [59] A. C. Fernandez-Pello, A. P. Pisano, K. Fu, D. C. Walther, A. Knobloch, F. Martinez, M. Senesky, C. Stoldt, R. Maboudian, S. Sanders et others, «MEMS rotary engine power system,» *IEEJ Transactions on Sensors and Micromachines*, vol. 123, pp. 326-330, 2003.
- [60] A. Mehra, X. Zhang, A. A. Ayón, I. A. Waitz, M. A. Schmidt et C. M. Spadaccini, «A six-wafer combustion system for a silicon micro gas turbine engine,» *Journal of Microelectromechanical systems*, vol. 9, pp. 517-527, 2000.
- [61] K. Annen, D. Stickler et J. Woodroffe, «Linearly-oscillating miniature internal combustion engine (MICE) for portable electric power,» chez *41st Aerospace Sciences Meeting and Exhibit*, 2003.
- [62] R. A. Yetter, V. Yang, M. H. Wu, Y. Wang, D. Milius, I. A. Aksay et F. L. Dryer, «Combustion issues and approaches for chemical microthrusters,» *International Journal of Energetic Materials and Chemical Propulsion*, vol. 6, 2007.
- [63] M.-H. Wu, R. Yetter et V. Yang, «Development and characterization of ceramic micro chemical propulsion and combustion systems,» chez *46th AIAA Aerospace Sciences Meeting and Exhibit*, 2008.
- [64] D. H. Lewis Jr, S. W. Janson, R. B. Cohen et E. K. Antonsson, «Digital micropropulsion,» *Sensors and Actuators A: Physical*, vol. 80, pp. 143-154, 2000.
- [65] V. K. Shrivastava et A. Agrawal, «Thermal Analysis of a Diesel Piston with different material parameter,» 2017.
- [66] C. M. Miesse, R. I. Masel, C. D. Jensen, M. A. Shannon et M. Short, «Submillimeter-scale combustion,» *AIChE Journal*, vol. 50, pp. 3206-3214, 2004.
- [67] S. H. Davy, «Some researches on flame,» *Philosophical Transactions of the Royal Society of London*, 1817.
- [68] L. Sitzki, K. Borer, S. Wussow, E. Maruta et P. Ronney, «Combustion in microscale heat-recirculating burners,» chez *39th Aerospace Sciences Meeting and Exhibit*, 2001.
- [69] J. Ahn, C. Eastwood, L. Sitzki et P. D. Ronney, «Gas-phase and catalytic combustion in heat-recirculating burners,» *Proceedings of the Combustion Institute*, vol. 30, pp. 2463-2472, 2005.
- [70] F. J. Weinberg, D. M. Rowe, G. Min et P. D. Ronney, «On thermoelectric power conversion from heat recirculating combustion systems,» *Proceedings of the Combustion Institute*, vol. 29, pp. 941-947, 2002.
- [71] P. D. Ronney, «Analysis of non-adiabatic heat-recirculating combustors,» *Combustion and Flame*, vol. 135, pp. 421-439, 2003.
- [72] C. Zhang, K. Najafi, L. P. Bernal et P. D. Washabaugh, «An integrated combustor-thermoelectric micro power generator,» chez *Transducers' 01 Eurosensors XV*, Springer, 2001, pp. 34-37.
- [73] P. D. Ronney, «Analysis of non-adiabatic heat-recirculating combustors,» *Combustion and Flame*, vol. 135, pp. 421-439, 2003.

- 
- [74] K. Yoshida, K. Kobayashi, T. Nakajima, D. Satoh, S. Tanaka et M. Esashi, «Micro thermoelectric generator using catalytic combustor,» *power mems*, 2002.
- [75] D. C. Kyritsis, I. Guerrero-Arias, S. Roychoudhury et A. Gomez, «Mesoscale power generation by a catalytic combustor using electrosprayed liquid hydrocarbons,» *Proceedings of the Combustion Institute*, vol. 29, pp. 965-972, 2002.
- [76] A. Gomez, J. J. Berry, S. Roychoudhury, B. Coriton et J. Huth, «From jet fuel to electric power using a mesoscale, efficient Stirling cycle,» *Proceedings of the Combustion Institute*, vol. 31, pp. 3251-3259, 2007.
- [77] W. Yang, U. Bonne et others, «MEMS free piston knock engine,» chez *Book of abstracts for poster presentation, Twenty-Eight International Symposium on Combustion, The Combustion Institute, Edinburgh, UK*, 2000.
- [78] W. Dahm, J. Mijit, R. Mayor, G. Qiao, A. Benajmin, Y. Gu, Y. Lei, M. Papke et S. Wu, «Micro internal combustion swing engine (MICSE) for portable power generation systems,» chez *40th AIAA Aerospace Sciences Meeting & Exhibit*, 2002.
- [79] D. H. Lee, D. E. Park, J. B. Yoon, E. Yoon et S. A. Kwon, «MEMS reciprocating device powered by micro combustion,» *Proceedings of the Combustion Institute*, vol. 29, 2002.
- [80] L. G. Fréchette, S. A. Jacobson, K. S. Breuer, F. F. Ehrich, R. Ghodssi, R. Khanna, C. W. Wong, X. Zhang, M. A. Schmidt et A. H. Epstein, «High-speed microfabricated silicon turbomachinery and fluid film bearings,» *Journal of Microelectromechanical Systems*, vol. 14, pp. 141-152, 2005.
- [81] J. Peirs, T. Waumans, T. Verstraeten, K. Liu, D. Reynaerts and R. Van den Braembussche, "Measurement of compressor and turbine maps for an ultra-miniature gas turbine," 2008.
- [82] «Advances in the Development of a Micro-Gas Turbine Engine at Onera. ASME.,» 2013.
- [83] N. Chigier et T. Gemci, «A review of micro propulsion technology,» chez *41st Aerospace Sciences Meeting and Exhibit*, 2003.
- [84] S. V. Karnik, M. K. Hatalis et M. V. Kothare, «Palladium based micro-membrane for water gas shift reaction and hydrogen gas separation,» chez *Microreaction Technology*, Springer, 2001, pp. 295-302.
- [85] C. Xu, J. Hall, C. Richards, D. Bahr et R. Richards, «Design of a micro heat engine,» chez *ASME MEMS*, 2000.
- [86] J.-H. Cho, C. S. Lin, C. D. Richards, R. F. Richards, J. Ahn et P. D. Ronney, «Demonstration of an external combustion micro-heat engine,» *Proceedings of the combustion institute*, vol. 32, pp. 3099-3105, 2009.
- [87] G. A. Landis, *MEMS closed chamber heat engine and electric generator*, Google Patents, 2005.
- [88] M. Thompson, S. Whalen et C. Richards, «Design, Fabrication, and Testing of a Micro Heat Engine (p3),» *NanoTech 2002 - "At the Edge of Revolution"*, 2002.
- [89] T. Huesgen, J. Ruhhammer, G. Biancuzzi et P. Woias, «Detailed study of a micro heat engine for thermal energy harvesting,» *Journal of Micromechanics and Microengineering*, vol. 20, p. 104004, 2010.
- [90] A. Arnaud, J. Boughaleb, S. Monfray, F. Boeuf, O. Cugat et T. Skotnicki, «Thermo-mechanical efficiency of the bimetallic strip heat engine at the macro-scale and micro-scale,» *Journal of Micromechanics and Microengineering*, vol. 25, p. 104003, 2015.
- [91] M. Moran, S. Stelter et M. Stelter, «Micro-Scale Regenerative Heat Exchanger,» chez *CANEUS 2004 Conference on Micro-Nano-Technologies*, 2004.

- 
- [92] M. Ibrahim, «A Microfabricated Involute-Foil Regenerator for Stirling Engines,» *5th International Energy Conversion Engineering Conference and Exhibit (IECEC) 25 - 27 June 2007, St. Louis, Missouri, 2007.*
- [93] S. Vanapalli, H. J. M. Brake, H. V. Jansen, J. F. Burger, H. J. Holland, T. T. Veenstra et M. C. Elwenspoek, «Pressure drop of laminar gas flows in a microchannel containing various pillar matrices,» *Journal of micromechanics and microengineering*, vol. 17, p. 1381, 2007.
- [94] M. E. Moran, *Micro-Scalable Thermal Control Device*, Google Patents, 2002.
- [95] E. DELLALI, «Etude theorique et experimentale des ecoulements oscillants alternes d'un gaz au sein de micro et milli-régénérateurs de moteur Stirling,» 2018.
- [96] R. B. Peterson, «Size limits for regenerative heat engines,» *Microscale Thermophysical Engineering*, vol. 2, pp. 121-131, 1998.
- [97] F. Formosa, «Global design and optimization of a membrane micro Stirling generator.,» chez *Proc. 10th International Workshop on Micro and Nanotechnology for Power Generation and Energy Conversion Applications, Power MEMS 2010*, Leuven, 2010.
- [98] T. W. Steiner et G. D. S. Archibald, «A high pressure and high frequency diaphragm engine: Comparison of measured results with thermoacoustic predictions,» *Applied Energy*, vol. 114, pp. 709-716, 2014.
- [99] G. W. Swift, «Thermoacoustic engines,» *The Journal of the Acoustical Society of America*, vol. 84, pp. 1145-1180, 1988.
- [100] N. B. Stetson, *Miniature Integral Stirling Cryocooler*, Google Patents, 1991.
- [101] L. Bowman, D. M. Berchowitz et I. Urieli, *Microminiature Stirling cycle cryocoolers and engines*, Google Patents, 1995.
- [102] D. E. Patterson, K. D. Jamison, M. Durrett, A. Kashani et D. Gedeon, «CVD diamond based miniature stirling cooler,» chez *International cryocooler conference Google Scholar*, 2007.
- [103] D. Guo, J. Gao, A. J. H. McGaughey, G. K. Fedder, M. Moran et S.-C. Yao, «Design and evaluation of a MEMS-based Stirling microcooler,» *Journal of Heat Transfer*, vol. 135, p. 111003, 2013.
- [104] D. Guo, «Design, Analysis, Modeling and Testing of a Micro-scale Refrigeration System,» 2014.
- [105] A. H. Epstein, S. D. Senturia, G. Anathasuresh, A. Ayon, K. Breuer, K. S. Chen, F. Ehrich, G. Gauba, R. Ghodssi, C. Groshenry, S. Jacobson, J. Lang, C. C. Mehra, J. M. Miranda, S. Nagle, D. Orr, E. Piekos, M. Schmidt, G. Shirley, S. Spearing, C. Tan, Y. S. Tzeng et I. Waitz, «Power MEMS and microengines,» chez *Solid State Sensors and Actuators, 1997. TRANSDUCERS '97 Chicago., 1997 International Conference on*, 1997.
- [106] Hachey, «Reducing heat exchanger pressure losses in a microscale Free Piston Stirling Engine,» *Proceedings of POWERMEMS*, 2015.
- [107] F. Formosa et L. G. Fréchette, «Multi-physics modelling approach for oscillatory microengines: application for a microStirling generator design,» chez *Journal of Physics: Conference Series*, 2015.
- [108] P. Tabeling, *Introduction to microfluidics*, Oxford University Press on Demand, 2005.
- [109] C. T. Pan, Z. H. Liu, Y. C. Chen et C. F. Liu, «Design and fabrication of flexible piezo-microgenerator by depositing ZnO thin films on PET substrates,» *Sensors and Actuators A: Physical*, vol. 159, pp. 96-104, 2010.

- 
- [110] M. Liu, J. Sun, Y. Sun, C. Bock et Q. Chen, «Thickness-dependent mechanical properties of polydimethylsiloxane membranes,» *Journal of Micromechanics and Microengineering*, vol. 19, p. 035028, 2009.
- [111] H. Pfriem, «Periodic heat transfer at small pressure fluctuations,» 1943.
- [112] Saint-Gobain, Introduction a la thermique du batiment Introduction à la thermique du bâtiment, Les essentiels de l'habitat, 2012.
- [113] F. P. Incropera, D. P. Dewitt, T. L. Bergman et A. S. Lavine, Fundamentals of Heat and Mass Transfer, sixth edition éd., John Wiley & sons, 2007.
- [114] S. M. Sze, Semiconductor sensors, J. Wiley, 1994.
- [115] Howell, Thermal Radiation Heat Transfer. Boca Raton: CRC Press., 2015.
- [116] S. W. Churchill et H. H. S. Chu, «Correlating equations for laminar and turbulent free convection from a vertical plate,» *International Journal of Heat and Mass Transfer*, vol. 18, pp. 1323-1329, 1975.
- [117] S. A. Lloyd et F. J. Weinberg, «Limits to energy release and utilisation from chemical fuels,» *Nature*, vol. 257, p. 367, 1975.
- [118] J. R. Lloyd et W. R. Moran, Natural Convection Adjacent to Horizontal Surface of Various Planforms,, D. J. Heat Transfer 96, Éd., J. Heat Transfer, 1974.
- [119] F. Lanzetta et Kahleras et P. N. I. K. A. Guillaume LAYES, «Caractérisation expérimentale d'un régénérateur en fonctionnement dynamique,» 2016.
- [120] M. Tanaka, I. Yamashita et F. Chisaka, «Flow and heat transfer characteristics of the Stirling engine regenerator in an oscillating flow,» *JSME international journal. Ser. 2, Fluids engineering, heat transfer, power, combustion, thermophysical properties*, vol. 33, pp. 283-289, 1990.
- [121] C. Shin, «Tortuosity correction of Kozeny's hydraulic diameter of a porous medium,» *Physics of Fluids*, vol. 29, p. 023104, 2017.
- [122] M. Knudsen, «M. Knudsen, Ann. Phys. 28, 75 (1909).,» *Ann. Phys.*, vol. 28, p. 75, 1909.
- [123] S. G. Kandlikar, S. Garimella, D. Li, S. Colin et M. R. King, Heat Transfer and Fluid Flow in Minichannels and Microchannels- Chapter 2 - Single-phase gas flow in microchannels, h. 4/50004-9, Éd., Elsevier Science Ltd, pages = "9 - 86", 2006.
- [124] W. J. Koehler, S. V. Patankar et W. E. Ibele, «Numerical prediction of turbulent oscillating flow in a circular pipe,» chez *Proceedings of the 25th Intersociety Energy Conversion Engineering Conference*, 1990.
- [125] T. S. Zhao et P. Cheng, «Oscillatory pressure drops through a woven-screen packed column subjected to a cyclic flow,» *Cryogenics*, vol. 36, pp. 333-341, 1996.
- [126] E. G. Richardson et E. Tyler, «The transverse velocity gradient near the mouths of pipes in which an alternating or continuous flow of air is established,» *Proceedings of the Physical Society*, vol. 42, p. 1, 1929.
- [127] P. LAMBOSSY, «Oscillations forcées d'un liquide incompressible et visqueux dans un tube rigide et horizontal, calcul de la force frottement,» *Helv. Phys. Acta*, vol. 25, pp. 371-386, 1952.
- [128] T. W. Simon et J. R. Seume, «A survey of oscillating flow in stirling engine heat exchangers,» 1988.
- [129] N. C. Markatos, «Convective Heat Transfer , L.C.Burmeister, John Wiley ,New York, 1983 , ix+790 pp,» vol. 28, pp. 2393-2394, 1 1985.
-



- 
- [130] K. C. Leong et L. W. Jin, «Characteristics of oscillating flow through a channel filled with open-cell metal foam,» *International Journal of Heat and fluid flow*, vol. 27, pp. 144-153, 2006.
- [131] D. Gedeon, «Mean-parameter modeling of oscillating flow,» *Journal of Heat Transfer*, vol. 108, pp. 513-518, 1986.
- [132] L. Sun, T. Simon, S. Mantell, M. Ibrahim, D. Gedeon et R. Tew, «Thermo-fluid Experiments Supporting Microfabricated Regenerator Development for a Stirling Space Power Engine,» chez *7th International Energy Conversion Engineering Conference*, 2009.
- [133] M. T. Pamuk et M. Özdemir, «Friction factor, permeability and inertial coefficient of oscillating flow through porous media of packed balls,» *Experimental thermal and fluid science*, vol. 38, pp. 134-139, 2012.
- [134] Y. Ju, Y. Jiang et Y. Zhou, «Experimental study of the oscillating flow characteristics for a regenerator in a pulse tube cryocooler,» *Cryogenics*, vol. 38, pp. 649-656, 1998.
- [135] X. L. Wang, M. G. Zhao, J. H. Cai, J. T. Liang et W. Dai, «Experimental flow characteristics study of a high frequency pulse tube regenerator,» chez *Cryocoolers 13*, Springer, 2005, pp. 439-444.
- [136] J. R. Womersley, «XXIV. Oscillatory motion of a viscous liquid in a thin-walled elastic tube—I: The linear approximation for long waves,» *The London, Edinburgh, and Dublin Philosophical Magazine and Journal of Science*, vol. 46, pp. 199-221, 1955.
- [137] C. Loudon et A. Tordesillas, «The Use of the Dimensionless Womersley Number to Characterize the Unsteady Nature of Internal Flow,» *Journal of Theoretical Biology*, vol. 191, pp. 63-78, 1998.
- [138] U. H. Kurzweg, E. R. Lindgren et B. Lothrop, «Onset of turbulence in oscillating flow at low Womersley number,» *Physics of Fluids A: Fluid Dynamics*, vol. 1, pp. 1972-1975, 1989.
- [139] F. Loth, M. A. Yardimci et N. Alperin, «Hydrodynamic modeling of cerebrospinal fluid motion within the spinal cavity,» *Journal of biomechanical engineering*, vol. 123, pp. 71-79, 2001.
- [140] H. B. Atabek et C. C. Chang, «Oscillatory flow near the entry of a circular tube,» *Zeitschrift für angewandte Mathematik und Physik ZAMP*, vol. 12, pp. 185-201, 1961.
- [141] C. Walther, H.-D. Kühl, T. Pfeiffer et S. Schulz, «Influence of developing flow on the heat transfer in laminar oscillating pipe flow,» *Forschung im Ingenieurwesen*, vol. 64, pp. 55-63, 1998.
- [142] P. Bouvier, «Transferts thermiques en écoulement oscillant dans une conduite cylindrique: Application au moteur Stirling,» 2000.
- [143] T. Zhao et P. Cheng, «A numerical solution of laminar forced convection in a heated pipe subjected to a reciprocating flow,» *International Journal of Heat and Mass Transfer*, vol. 38, pp. 3011-3022, 1995.
- [144] B. Morgan, «Mecanique des fluides,» *Résumé de Cours, Ecole Normale Supérieure de Cachan*, 2009.
- [145] A. A. Kornhauser, «Gas-wall heat transfer during compression and expansion,» 1989.
- [146] B. E. Rapp, «Chapter 9 - Fluids,» chez *Microfluidics: Modeling, Mechanics and Mathematics*, B. E. Rapp, Éd., Oxford, Elsevier, 2017, pp. 243-263.
- [147] T. W. Simon et J. R. Seume, «A survey of oscillating flow in stirling engine heat exchangers,» 1988.
- [148] R. C. Tew et S. M. Geng, «Overview of NASA supported Stirling thermodynamic loss research,» 1992.
- [149] M. Hino, M. Sawamoto et S. Takasu, «Experiments on transition to turbulence in an oscillatory pipe flow,» *Journal of Fluid Mechanics*, vol. 75, pp. 193-207, 1976.

- 
- [150] P. Blondeaux et G. Vittori, «Wall imperfections as a triggering mechanism for Stokes-layer transition,» *Journal of Fluid Mechanics*, vol. 264, pp. 107-135, 1994.
- [151] S. Moreau, «Conception d'un dispositif expérimental et étude de l'écoulement oscillant en résonateur acoustique fort niveau pour la caractérisation de phénomènes non-linéaires: transition à la turbulence et écoulements redressés,» 2007.
- [152] G. Vittori et R. Verzicco, «Direct simulation of transition in an oscillatory boundary layer,» *Journal of Fluid Mechanics*, vol. 371, pp. 207-232, 1998.
- [153] M. Ohmi, M. Iguchi et I. Urahata, «Flow patterns and frictional losses in an oscillating pipe flow,» *Bulletin of JSME*, vol. 25, pp. 536-543, 1982.
- [154] M. Hino, M. Kashiwayanagi, A. Nakayama et T. Hara, «Experiments on the turbulence statistics and the structure of a reciprocating oscillatory flow,» *Journal of Fluid Mechanics*, vol. 131, pp. 363-400, 1983.
- [155] L. H. Juárez et E. Ramos, «Direct numerical simulation of transition to turbulence in an oscillatory channel flow,» *Comptes Rendus Mécanique*, vol. 331, pp. 55-60, 2003.
- [156] P. Bouvier, P. Stouffs et J.-P. Bardon, «Experimental study of heat transfer in oscillating flow,» *International Journal of Heat and Mass Transfer*, vol. 48, pp. 2473-2482, 2005.
- [157] S. I. Sergeev, «Fluid oscillations in pipes at moderate Reynolds numbers,» *Fluid Dynamics*, vol. 1, pp. 121-122, 01 1966.
- [158] J. R. S. Park et M. H. I. Baird, «Transition phenomena in an oscillating manometer,» *The Canadian Journal of Chemical Engineering*, vol. 48, pp. 491-495, 1970.
- [159] P. P. Grassmann et M. Tuma, «Applications of the electrolytic method—II. Mass transfer within a tube for steady, oscillating and pulsating flows,» *International Journal of Heat and Mass Transfer*, vol. 22, pp. 799-804, 1979.
- [160] Delwaulle, Pertes de charges linéaires et singulières dans les conduites fluidiques, 2012.
- [161] NIKA, «Aspects dynamiques et thermiques de l'écoulement oscillant dans la matrice poreuse d'un régénérateur de machine Stirling,» *Congrès Français de Thermique, Elsevier*, 2004.
- [162] W. R. Smith, «One-dimensional models for heat and mass transfer in pulse-tube refrigerators,» *Cryogenics*, vol. 41, pp. 573-582, 2001.
- [163] D. Pfund, D. Rector, A. Shekarriz, A. Popescu et J. Welty, «Pressure drop measurements in a microchannel,» *AIChE Journal*, vol. 46, pp. 1496-1507, 2000.
- [164] G. T. A. Kovacs et others, «Micromachined transducers sourcebook,» 1998.
- [165] C. K. Kang, S. M. Lee, I. D. Jung, P. G. Jung, S. J. Hwang et J. S. Ko, «The fabrication of patternable silicon nanotips using deep reactive ion etching,» *Journal of Micromechanics and Microengineering*, vol. 18, p. 075007, 2008.
- [166] S. Angers, «L'usinage ultrasonore, un autre procédé de microfabrication,» *Institut Pierre Vernier*, [http://endirect.univ-fcomte.fr/index.php?id=numeroipv\\_243\\_13\\_1&art=2638](http://endirect.univ-fcomte.fr/index.php?id=numeroipv_243_13_1&art=2638), 2011.
- [167] B. O. Y. Jean-Jacques, «Usinage abrasif par ultrasons,» *FEMTO-ST*, 2018.

- 
- [168] T. Tekin, H.-D. Ngo, O. Wittler, B. Bouhlal et K.-D. Lang, «Packaging of mems/moems and nanodevices: Reliability, testing, and characterization aspects,» chez *Reliability, Packaging, Testing, and Characterization of MEMS/MOEMS and Nanodevices X*, 2011.
- [169] M. Esashi, «Wafer level packaging of MEMS,» *Journal of Micromechanics and Microengineering*, vol. 18, p. 073001, 2008.
- [170] S. J. Bleiker, V. Dubois, S. Schröder, G. Stemme et F. Niklaus, «Adhesive wafer bonding with ultra-thin intermediate polymer layers,» *Sensors and Actuators A: Physical*, vol. 260, pp. 16-23, 2017.
- [171] S. Li, C. B. Freidhoff, R. M. Young et R. Ghodssi, «Fabrication of micronozzles using low-temperature wafer-level bonding with SU-8,» *Journal of Micromechanics and Microengineering*, vol. 13, p. 732, 2003.
- [172] F. Niklaus, G. Stemme, J.-Q. Lu et R. J. Gutmann, «Adhesive wafer bonding,» *Journal of applied physics*, vol. 99, p. 2, 2006.
- [173] K. Okumura, E. Higurashi, T. Suga et K. Hagiwara, «Influence of air exposure time on bonding strength in Au-Au surface activated wafer bonding,» chez *Electronics Packaging and iMAPS All Asia Conference (ICEP-IACC), 2015 International Conference on*, 2015.
- [174] T. Matsumae, M. Nakano, Y. Matsumoto et T. Suga, «Room temperature bonding of polymer to glass wafers using surface activated bonding (SAB) method,» *ECS Transactions*, vol. 50, pp. 297-302, 2013.
- [175] S. Charlot, P. Pons, M. Dilhan, I. Vallet et S. Brida, «Hermetic cavities using gold wafer level thermocompression bonding,» chez *Multidisciplinary Digital Publishing Institute Proceedings*, 2017.
- [176] T. Suni, «Direct wafer bonding for MEMS and microelectronics,» 2006.
- [177] M. Argoud, «Mécanismes de collage et de transfert de films monocristallins dans des structures à couches de polymères,» 2012.
- [178] R. Cuthrell et D. Tipping, «The bonding characteristics of gold in ultrahigh vacuum,» *IEEE Transactions on parts, hybrids, and packaging*, vol. 10, pp. 4-10, 1974.
- [179] R. F. Tylecote, *The solid phase welding of metals*, Arnold, 1968.
- [180] G. G. Zhang, X. F. Ang, Z. Chen, C. C. Wong et J. Wei, «Critical temperatures in thermocompression gold stud bonding,» *Journal of Applied Physics*, vol. 102, p. 063519, 2007.
- [181] Y. Kurashima, A. Maeda et H. Takagi, «Room temperature wafer scale bonding of electroplated Au patterns processed by surface planarization,» chez *Electronics Packaging (ICEP), 2014 International Conference on*, 2014.
- [182] J. Jellison, «Effect of surface contamination on the thermocompression bondability of gold,» *IEEE Transactions on Parts, Hybrids, and Packaging*, vol. 11, pp. 206-211, 1975.
- [183] B. K. Kurman et S. G. Mita, «Gold-Gold (Au-Au) thermocompression (TC) bonding of very large arrays,» chez *Electronic Components and Technology Conference, 1992. Proceedings., 42nd*, 1992.
- [184] C. H. Tsau, S. M. Spearing et M. A. Schmidt, «Fabrication of wafer-level thermocompression bonds,» *Journal of Microelectromechanical systems*, vol. 11, pp. 641-647, 2002.
- [185] M. M. V. Taklo, P. Storås, K. Schjøberg-Henriksen, H. K. Hasting et H. Jakobsen, «Strong, high-yield and low-temperature thermocompression silicon wafer-level bonding with gold,» *Journal of Micromechanics and Microengineering*, vol. 14, p. 884, 2004.

- 
- [186] E. Jing, B. Xiong et Y. Wang, «Low-temperature Au/a-Si wafer bonding,» *Journal of Micromechanics and Microengineering*, vol. 21, p. 015013, 2010.
- [187] G.-S. Park, Y.-K. Kim, K.-K. Paek, J.-S. Kim, J.-H. Lee et B.-K. Ju, «Low-temperature silicon wafer-scale thermocompression bonding using electroplated gold layers in hermetic packaging,» *Electrochemical and Solid-State Letters*, vol. 8, pp. G330–G332, 2005.
- [188] Ö. Vallin, K. Jonsson et U. Lindberg, «Adhesion quantification methods for wafer bonding,» *Materials Science and Engineering: R: Reports*, vol. 50, pp. 109-165, 2005.
- [189] E. Higurashi, D. Chino, T. Suga et R. Sawada, «Au–Au surface-activated bonding and its application to optical microsensors with 3-D structure,» *IEEE Journal of Selected Topics in Quantum Electronics*, vol. 15, pp. 1500-1505, 2009.
- [190] S. Satyanarayana, R. N. Karnik et A. Majumdar, «Stamp-and-stick room-temperature bonding technique for microdevices,» *Journal of Microelectromechanical Systems*, vol. 14, pp. 392-399, 2005.
- [191] M. M. V. Taklo, D. N. Wright, A.-S. Vardøy, A. Attard, Z. Hajdarevic, S. Bulacher, M. Saliba, J. Wijgaerts, J. Borg et D. O. Vella, «Thermomechanical reliability of gold stud bump bonding for large volume MEMS devices,» chez *2015 IEEE 65th Electronic Components and Technology Conference (ECTC)*, 2015.
- [192] M. Liu, J. Sun et Q. Chen, «Influences of heating temperature on mechanical properties of polydimethylsiloxane,» *Sensors and Actuators A: Physical*, vol. 151, pp. 42-45, 2009.
- [193] G. Zhou, Q. Li, Z. Y. Li et Q. Li, «A miniature thermoacoustic stirling engine,» *Energy Conversion and Management*, vol. 49, pp. 1785-1792, 2008.
- [194] D. C. Roberts, H. Li, J. L. Steyn, O. Yaglioglu, S. M. Spearing, M. A. Schmidt et N. W. Hagood, «A piezoelectric microvalve for compact high-frequency, high-differential pressure hydraulic micropumping systems,» *Journal of Microelectromechanical Systems*, vol. 12, pp. 81-92, 2 2003.
- [195] H. D. Schneider et U. Wallrabe, «Mechanical properties of silicones for MEMS,» *Proc. Int. Conf. New Actuator 2006*, vol. 18, p. 124, 2006.
- [196] M. Zdeblick, *Integrated, microminiature electric to fluidic valve and pressure/flow regulator*, Google Patents, 1990.
- [197] M. A. Unger, H.-P. Chou, T. Thorsen, A. Scherer et S. R. Quake, «Monolithic microfabricated valves and pumps by multilayer soft lithography,» *Science*, vol. 288, pp. 113-116, 2000.
- [198] D. C. Duffy, O. J. A. Schueller, S. T. Brittain et G. M. Whitesides, «Rapid prototyping of microfluidic switches in poly (dimethyl siloxane) and their actuation by electro-osmotic flow,» *Journal of Micromechanics and Microengineering*, vol. 9, p. 211, 1999.
- [199] H.-P. Chou, M. A. Unger et S. R. Quake, «A microfabricated rotary pump,» *Biomedical Microdevices*, vol. 3, pp. 323-330, 2001.
- [200] K. Lim, S. Kim et J. H. Hahn, «Roller-type squeezing pump with picoliter handling capability,» *Sensors and Actuators B: Chemical*, vol. 92, pp. 208-214, 2003.
- [201] A. Groisman, M. Enzelberger et S. R. Quake, «Microfluidic memory and control devices,» *Science*, vol. 300, pp. 955-958, 2003.
- [202] J. M. H. Lee, S. C. L. Yuen, W. J. Li et P. H. W. Leong, «Development of an AA size energy transducer with micro resonators,» chez *Circuits and Systems, 2003. ISCAS'03. Proceedings of the 2003 International Symposium on*, 2003.
-

- 
- [203] H. Kudo, T. Sawada, E. Kazawa, H. Yoshida, Y. Iwasaki et K. Mitsubayashi, «A flexible and wearable glucose sensor based on functional polymers with Soft-MEMS techniques,» *Biosensors and Bioelectronics*, vol. 22, pp. 558-562, 2006.
- [204] J.-S. Heo, J.-H. Chung et J.-J. Lee, «Tactile sensor arrays using fiber Bragg grating sensors,» *Sensors and Actuators A: Physical*, vol. 126, pp. 312-327, 2006.
- [205] «Dow Corning 2005 Product information sheet of Sylgard 184».
- [206] S. R. Quake et A. Scherer, «From micro-to nanofabrication with soft materials,» *Science*, vol. 290, pp. 1536-1540, 2000.
- [207] B. Michel, A. Bernard, A. Bietsch, E. Delamarche, M. Geissler, D. Juncker, H. Kind, J.-P. Renault, H. Rothuizen, H. Schmid et others, «Printing meets lithography: Soft approaches to high-resolution patterning,» *IBM Journal of Research and Development*, vol. 45, pp. 697-719, 2001.
- [208] J.-H. Kim, K.-H. Na, C. J. Kang et Y.-S. Kim, «A disposable thermopneumatic-actuated micropump stacked with PDMS layers and ITO-coated glass,» *Sensors and Actuators A: Physical*, vol. 120, pp. 365-369, 2005.
- [209] Colas, «Silicones: Preparation, Properties and Performance,» *Dow Corning, Life Sciences*, 1990.
- [210] Plueddemann, «Silane Coupling Agents,» *Plenum Press, New York*, 1982.
- [211] Stark, «Comprehensive Organometallic Chemistry. The Synthesis, Reactions, and Structures of Organometallic Compounds,» *Organometallics*, vol. 3, pp. 1135-1136, 1984.
- [212] W. Noll, *Chemistry and Technology of Silicones*, 1st Edition, Academic Press, 1968.
- [213] S. Ripã et others, «Mechanical properties of a silicone for high temperature applications,» 2009.
- [214] D. Tranchida et S. Piccarolo, «Local mechanical properties by atomic force microscopy nanoindentations,» chez *Applied Scanning Probe Methods XI*, Springer, 2009, pp. 165-198.
- [215] G. Bracco et B. Holst, *Surface science techniques*, Springer Science & Business Media, 2013.
- [216] O. Tabata, K. Kawahata, S. Sugiyama et I. Igarashi, «Mechanical property measurements of thin films using load-deflection of composite rectangular membranes,» *Sensors and actuators*, vol. 20, pp. 135-141, 1989.
- [217] H. Guckel, T. Randazzo et D. W. Burns, «A simple technique for the determination of mechanical strain in thin films with applications to polysilicon,» *Journal of Applied Physics*, vol. 57, pp. 1671-1675, 1985.
- [218] M. G. Allen, M. Mehregany, R. T. Howe et S. D. Senturia, «Microfabricated structures for the insitu measurement of residual stress, young's modulus, and ultimate strain of thin films,» *Applied Physics Letters*, vol. 51, pp. 241-243, 1987.
- [219] D. Maier-Schneider, J. Maibach et E. Obermeier, «A new analytical solution for the load-deflection of square membranes,» *Journal of microelectromechanical systems*, vol. 4, pp. 238-241, 1995.
- [220] D. Yalcin, «<https://www.admet.com/effect-specimen-geometry-tensile-testing-results/>,» July 26th, 2017.
- [221] F. Schneider, T. Fellner, J. Wilde et U. Wallrabe, «Mechanical properties of silicones for MEMS,» *Journal of Micromechanics and Microengineering*, vol. 18, p. 065008, 2008.
- [222] A. Boudet, *Voyage au cœur de la matiere plastique*, CNRS Editions, 2003, CNRS Editions, 2003.
- [223] E. O. Hall, «The deformation and ageing of mild steel: III discussion of results,» *Proceedings of the Physical Society. Section B*, vol. 64, p. 747, 1951.
-

- 
- [224] J. D. Anderson, G. Schubert, R. A. Jacobson, E. L. Lau, W. B. Moore et J. L. Palguta, «Discovery of mass anomalies on Ganymede,» *Science*, vol. 305, pp. 989-991, 2004.
- [225] PERMATEX Group : <https://www.permatex.com/products/gasketing/gasket-makers/permatex-high-temp-red-rtv-silicone-gasket/>.
- [226] S. P. Desai, D. M. Freeman et J. Voldman, «Plastic masters—rigid templates for soft lithography,» *Lab on a Chip*, vol. 9, pp. 1631-1637, 2009.
- [227] L. Tong, M. Mehregany et L. G. Matus, «Mechanical properties of 3C silicon carbide,» *Applied physics letters*, vol. 60, pp. 2992-2994, 1992.
- [228] A. L. Thangawng, R. S. Ruoff, M. A. Swartz et M. R. Glucksberg, «An ultra-thin PDMS membrane as a bio/micro--nano interface: fabrication and characterization,» *Biomedical microdevices*, vol. 9, pp. 587-595, 2007.
- [229] S. P. Timoshenko et S. Woinowsky-Krieger, *Theory of plates and shells*, McGraw-hill, 1959.
- [230] D. Armani, C. Liu et N. Aluru, «Re-configurable fluid circuits by PDMS elastomer micromachining,» chez *Micro Electro Mechanical Systems, 1999. MEMS'99. Twelfth IEEE International Conference on*, 1999.
- [231] W. Yang, «Liquid piston chip engine,» chez *Proceedings of the DARPA/MTO MEMS/MPG/NMASP Principal Investigators' Meeting, Bloomington, CO*, 2002.
- [232] P. Specifications, «Parylene Conformal Coatings Specifications and Properties,» *Specialty Coating Systems, Inc., Indianapolis*, 1994.
- [233] S. Timoshenko, *Strength of materials Part 2*, D. Van Nostrand Co., Inc, 1941.
- [234] W. K. Schomburg, «Introduction,» chez *Introduction to Microsystem Design*, Springer, 2015, pp. 1-2.
- [235] K. E. Petersen, «Silicon as a mechanical material,» *Proceedings of the IEEE*, vol. 70, pp. 420-457, 5 1982.
- [236] E. CuChe, «Simultaneous amplitude-contrast and quantitative phase-contrast microscopy by numerical reconstruction of Fresnel off-axis holograms,» *Applied Optics*, 1999.
- [237] A. JALLOULI, «Modeling and characterization of nonlinear phenomena in circular capacitive micromachined ultrasonic transducers with geometrical imperfections,» 2018.
- [238] Hariharan, *Basics of Interferometry*, 2nd Edition, Academic Press, 2006.
- [239] KARPATI, *Mechanica Properties of Sea I. Behavior of Si icone Sea Mechanical Properties of Sealants Behavior of Silicone Sealants as a Function of Temperature*, Journal of paint technology USA, 1972.
- [240] A. Diallo et al «Study of dynamic response of silicone elastomer microfabricated hybrid membranes versus temperatures and aging time,» chez *Proceedings of the PowerMEMS 2017 : Conference Series*, 2017.
- [241] G. E. Amrane Sofiane et L. François, «Experimental and theoretical study of microthermocouple used as cooling device,» *High Temperatures - High Pressures*, vol. 43, 1, pp. 13 - 37, 2014.
- [242] L. F. G. E. Dellali Emna et R. Jean-Yves, «Pressure drop analysis of oscillating flows through a miniature porous regenerator under isothermal and nonisothermal conditions,» *Experimental Thermal and Fluid Science*, vol. 103, pp. 394 - 405, 2019.
- [243] G. Eric et L. François, «Dynamic operation of a micro-thermocouple sensor as a vacuum gauge,» *Vacuum*, vol. 100, pp. 18 - 21, 2014.

- 
- [244] L. François et G. Eric, «Temperature Measurements : Thermoelectricity and Microthermocouples,» *Thermal Measurements and Inverse Techniques* edited by Helcio R.B. Orlande, Olivier Fudym, Denis Maillet, Renato M. Cotta, CRC Press, Heat Transfer, 3, pp. 95 - 142, 2011.
- [245] G. E. Bouaanani Youness et L. François, «Performance of a thermocouple subjected to a variable current,» *International Journal of Thermal Sciences*, vol. 134, pp. 440 - 452, 2018.
- [246] «<http://catalog.stil-sensors.com/?lang=FR> (visited on 17/07/2019)».
- [247] «<https://www.panasonic-electric-works.com/fr/capteur-analogique-hg-c.htm> (visited on 17/07/2019)».
- [248] Y. Jia et A. A. Seshia, «Five topologies of cantilever-based MEMS piezoelectric vibration energy harvesters: a numerical and experimental comparison,» *Microsystem Technologies*, vol. 22, pp. 2841-2852, 01 12 2016.
- [249] R. Dayal, S. Dwari et L. Parsa, «Maximum energy harvesting from vibration-based electromagnetic microgenerator using active damping,» *Electronics letters*, vol. 46, pp. 371-373, 2010.
- [250] S. Nain, J. S. Rathore et N. N. Sharma, «Comparison of Piezo-material based Energy Transduction Systems for Artificial Nanoswimmer,» *IOP Conference Series: Materials Science and Engineering*, vol. 346, p. 012079, 2018.
- [251] Chang, «Direct-Write Piezoelectric Polymeric Nanogenerator with High Energy Conversion Efficiency,» *Nano Letters*, 2010.
- [252] P. Mitcheson et E. Yeatman, «Energy harvesting for pervasive computing,» *PerAda Mag*, pp. 1-3, 2008.
- [253] W. Zhou, W.-H. Liao et W. J. Li, «Analysis and design of a self-powered piezoelectric microaccelerometer,» chez *Smart Structures and Materials 2005: Smart Electronics, MEMS, BioMEMS, and Nanotechnology*, 2005.
- [254] Y. B. Jeon, R. Sood, J.-H. Jeong et S.-G. Kim, «MEMS power generator with transverse mode thin film PZT,» *Sensors and Actuators A: Physical*, vol. 122, pp. 16-22, 2005.
- [255] H.-B. Fang, J.-Q. Liu, Z.-Y. Xu, L. Dong, L. Wang, D. Chen, B.-C. Cai et Y. Liu, «Fabrication and performance of MEMS-based piezoelectric power generator for vibration energy harvesting,» *Microelectronics Journal*, vol. 37, pp. 1280-1284, 2006.
- [256] D. Isarakorn, D. Briand, P. Janphuang, A. Sambri, S. Gariglio, J. M. Triscone, F. Guy, J. W. Reiner, C. H. Ahn et N. F. De Rooij, «The realization and performance of vibration energy harvesting MEMS devices based on an epitaxial piezoelectric thin film,» *Smart Materials and Structures*, vol. 20, p. 025015, 2011.
- [257] D. Shen, J.-H. Park, J. H. Noh, S.-Y. Choe, S.-H. Kim, H. C. Wickle III et D.-J. Kim, «Micromachined PZT cantilever based on SOI structure for low frequency vibration energy harvesting,» *Sensors and actuators A: physical*, vol. 154, pp. 103-108, 2009.
- [258] M. Marzencki, S. Basrour, B. Charlot, A. Grasso, M. Colin et L. Valbin, «Design and fabrication of piezoelectric micro power generators for autonomous microsystems,» chez *Proc. of DTIP'05*, 2005.
- [259] R. Van Schaijk, R. Elfrink, T. M. Kamel et M. Goedbloed, «Piezoelectric AlN energy harvesters for wireless autonomous transducer solutions,» chez *Sensors, 2008 IEEE*, 2008.
- [260] R. Elfrink, T. M. Kamel, M. Goedbloed, S. Matova, D. Hohlfeld, Y. Van Andel et R. Van Schaijk, «Vibration energy harvesting with aluminum nitride-based piezoelectric devices,» *Journal of Micromechanics and Microengineering*, vol. 19, p. 094005, 2009.

- 
- [261] R. Hinchet, J. Ferreira, J. Keraudy, G. Ardila, E. Pauliac-Vaujour, M. Mouis et L. Montès, «Scaling rules of piezoelectric nanowires in view of sensor and energy harvester integration,» chez *Electron Devices Meeting (IEDM), 2012 IEEE International*, 2012.
- [262] M. Minary-Jolandan, R. A. Bernal, I. Kuljanishvili, V. Parpoil et H. D. Espinosa, «Individual GaN nanowires exhibit strong piezoelectricity in 3D,» *Nano letters*, vol. 12, pp. 970-976, 2012.
- [263] X. Xu, A. Potié, R. Songmuang, J. W. Lee, B. Bercu, T. Baron, B. Salem et L. Montès, «An improved AFM cross-sectional method for piezoelectric nanostructures properties investigation: application to GaN nanowires,» *Nanotechnology*, vol. 22, p. 105704, 2011.
- [264] S. Petroni, C. La Tegola, G. Caretto, A. Campa, A. Passaseo, M. De Vittorio et R. Cingolani, «Aluminum Nitride piezo-MEMS on polyimide flexible substrates,» *Microelectronic Engineering*, vol. 88, pp. 2372-2375, 2011.
- [265] P. Wang, H. Liu, X. Dai, Z. Yang, Z. Wang et X. Zhao, «Design, simulation, fabrication and characterization of a micro electromagnetic vibration energy harvester with sandwiched structure and air channel,» *Microelectronics Journal*, vol. 43, pp. 154-159, 2012.
- [266] D. P. Arnold, «Review of microscale magnetic power generation,» *IEEE Transactions on Magnetics*, vol. 43, pp. 3940-3951, 2007.
- [267] B. Kongtragool et S. Wongwises, «A review of solar-powered Stirling engines and low temperature differential Stirling engines,» *Renewable and Sustainable Energy Reviews*, vol. 7, pp. 131-154, 2003.
- [268] A. M. C. Spirit, «AMC Spirit,» *AMC*, vol. 56, 2017.
- [269] K. Rajashekara, «History of electric vehicles in General Motors,» *IEEE transactions on industry applications*, vol. 30, pp. 897-904, 1994.
- [270] B. Ross, «Status of the emerging technology of Stirling machines,» *IEEE Aerospace and Electronic Systems Magazine*, vol. 10, pp. 34-39, 6 1995.
- [271] H. Nilsson, «Submarine Power Systems Using the V4-275R Stirling Engine,» *Proceedings of the Institution of Mechanical Engineers, Part A: Power and Process Engineering*, vol. 202, pp. 257-267, 1988.
- [272] S. Isshiki, Y. Takasaki, I. Ushiyama et N. Isshiki, «An experimental study on flow resistance of regenerator wire meshes in oscillatory flow [in Stirling engines],» chez *Energy Conversion Engineering Conference, 1997. IECEC-97., Proceedings of the 32nd Intersociety*, 1997.
- [273] H. Miyabe, K. Hamaguchi et K. Takahashi, «An approach to the design of Stirling engine regenerator matrix using packs of wire gauzes,» chez *Proc., Intersoc. Energy Convers. Eng. Conf.:(United States)*, 1982.
- [274] F. P. Incropera, D. P. Dewitt, T. L. Bergman et A. S. Lavine, *Fundamentals of Heat and Mass Transfer*, sixth edition éd., John Wiley & sons, 2007.
- [275] M. Argoud, «Mécanismes de collage et de transfert de films monocristallins dans des structures à couches de polymères,» 2012.
- [276] H. Zhou, H. Q. Li, V. Sharma et M. A. Schmidt, «A single-stage micromachined vacuum pump achieving 164 torr absolute pressure,» chez *2011 IEEE 24th International Conference on Micro Electro Mechanical Systems*, 2011.
- [277] M.-H. Zhao, Z.-L. Wang et S. X. Mao, «Piezoelectric characterization of individual zinc oxide nanobelt probed by piezoresponse force microscope,» *Nano Letters*, vol. 4, pp. 587-590, 2004.



- 
- [278] J. D. Zahn, A. A. Deshmukh, A. P. Papavasiliou, A. P. Pisano et D. Liepmann, «An integrated microfluidic device for the continuous sampling and analysis of biological fluids,» chez *Proceedings of the 2001 ASME - IMECE, Nov.11-16, 2001, New York, N.Y., 2001.*
- [279] B. Yang, C. Lee, W. L. Kee et S.-P. Lim, «Hybrid energy harvester based on piezoelectric and electromagnetic mechanisms,» *Journal of Micro/Nanolithography, MEMS, and MOEMS*, vol. 9, p. 023002, 2010.
- [280] D. Yalcin, «How do different specimen geometries affect tensile test results».
- [281] C. B. Williams et R. B. Yates, «Analysis of a micro-electric generator for microsystems,» *sensors and actuators A: Physical*, vol. 52, pp. 8-11, 1996.
- [282] L. W. Weiss, J. H. Cho, K. E. McNeil, C. D. Richards, D. F. Bahr et R. F. Richards, «Characterization of a dynamic micro heat engine with integrated thermal switch,» *Journal of Micromechanics and Microengineering*, vol. 16, p. S262, 2006.
- [283] A. S. Weddell, M. Magno, G. V. Merrett, D. Brunelli, B. M. Al-Hashimi et L. Benini, «A survey of multi-source energy harvesting systems,» chez *2013 Design, Automation Test in Europe Conference Exhibition (DATE)*, 2013.
- [284] C. M. Waters, M. R. Glucksberg, E. P. Lautenschlager, C.-W. Lee, R. M. Van Matre, R. J. Warp, U. Savla, K. E. Healy, B. Moran, D. G. Castner et others, «A system to impose prescribed homogenous strains on cultured cells,» *Journal of applied physiology*, vol. 91, pp. 1600-1610, 2001.
- [285] B. Warneke, M. Last, B. Liebowitz et K. S. J. Pister, «Smart Dust: communicating with a cubic-millimeter computer,» *Computer*, vol. 34, pp. 44-51, 1 2001.
- [286] Y. Wang, B. Liu, Q. Li, S. Cartmell, S. Ferrara, Z. D. Deng et J. Xiao, «Lithium and lithium ion batteries for applications in microelectronic devices: A review,» *Journal of Power Sources*, vol. 286, pp. 330-345, 2015.
- [287] P.-H. Wang, X.-H. Dai, D.-M. Fang et X.-L. Zhao, «Design, fabrication and performance of a new vibration-based electromagnetic micro power generator,» *Microelectronics Journal*, vol. 38, pp. 1175-1180, 2007.
- [288] P. Wang, X. Dai, X. Zhao et G. Ding, «A micro electromagnetic vibration energy harvester with sandwiched structure and air channel for high energy conversion efficiency,» *Proceedings PowerMEMS 2009*, pp. 296-299, 2009.
- [289] D.-A. Wang et K.-H. Chang, «Electromagnetic energy harvesting from flow induced vibration,» *Microelectronics Journal*, vol. 41, pp. 356-364, 2010.
- [290] D.-A. Wang et K.-H. Chang, «Electromagnetic energy harvesting from flow induced vibration,» *Microelectronics Journal*, vol. 41, pp. 356-364, 2010.
- [291] N. Vichaidit, N. Aksornpromrat et S. Kijswang, «Design and construction of free-piston type Stirling engine,» *Final year project report, Department of Mechanical Engineering, Siam University*, 2009.
- [292] K. T. Turner, R. Mlcak, D. C. Roberts et S. M. Spearing, «Bonding of bulk piezoelectric material to silicon using a gold-tin eutectic bond,» *MRS Online Proceedings Library Archive*, vol. 687, 2001.
- [293] «Millimeter-Scale, MEMS Gas Turbine Engines,» 2003.
- [294] G. J. Tortora et S. R. Grabowski, *Introduction to the human body*, Harper & Row, 1988.
- [295] T. Toriyama, S. Sugiyama et K. Hashimoto, «Design of a resonant micro reciprocating engine for power generation,» chez *TRANSDUCERS, Solid-State Sensors, Actuators and Microsystems, 12th International Conference on, 2003*, 2003.

- 
- [296] R. Torah, P. Glynne-Jones, M. Tudor, T. O'donnell, S. Roy et S. Beeby, «Self-powered autonomous wireless sensor node using vibration energy harvesting,» *Measurement science and technology*, vol. 19, p. 125202, 2008.
- [297] N. Tiwari et A. K. Singh, «Exhaust Waste Heat Recovery System».
- [298] A. P. Taylor et L. F. Velásquez-García, «3-D printed miniaturized diaphragm vacuum pump,» chez *2017 IEEE 30th International Conference on Micro Electro Mechanical Systems (MEMS)*, 2017.
- [299] Y. Suzuki, «Energy harvesting from vibration using polymer electret,» chez *Micro-NanoMechatronics and Human Science, 2008. MHS 2008. International Symposium on*, 2008.
- [300] R. Srinivasan, I. Hsing, P. E. Berger, K. F. Jensen, S. L. Firebaugh, M. A. Schmidt, M. P. Harold, J. J. Lerou et J. F. Ryley, «Micromachined reactors for catalytic partial oxidation reactions,» *AIChE Journal*, vol. 43, pp. 3059-3069, 11 1997.
- [301] H. Snyman, T. M. Harms et J. M. Strauss, «Design analysis methods for Stirling engines,» *J. Energy South. Afr.*, vol. 19, pp. 4-19, 2008.
- [302] R. Shoureshi, «Analysis and design of Stirling engines for waste-heat recovery,» 1981.
- [303] T. Shimatsu et M. Uomoto, «Atomic diffusion bonding of wafers with thin nanocrystalline metal films,» *Journal of Vacuum Science & Technology B, Nanotechnology and Microelectronics: Materials, Processing, Measurement, and Phenomena*, vol. 28, pp. 706-714, 2010.
- [304] C. Shearwood et R. B. Yates, «Development of an electromagnetic microgenerator,» *Electronics Letters*, vol. 33, pp. 1883-1884, 1997.
- [305] F. K. Shaikh et S. Zeadally, «Energy harvesting in wireless sensor networks: A comprehensive review,» *Renewable and Sustainable Energy Reviews*, vol. 55, pp. 1041-1054, 2016.
- [306] C. Scott A. Whalen et R. F. Richards, «Low Frequency Operation of the P3 Micro Heat Engine,» chez *ASME 2002 International Mechanical Engineering Congress and Exposition*, 2002.
- [307] SCHOTT Compagny: «[www.schott.com](http://www.schott.com)».
- [308] L. Schlapbach, «Hydrogen as a fuel and its storage for mobility and transport,» *MRS bulletin*, vol. 27, pp. 675-679, 2002.
- [309] I. Sari, T. Balkan et H. Kulah, «An electromagnetic micro power generator for wideband environmental vibrations,» *Sensors and Actuators A: Physical*, vol. 145, pp. 405-413, 2008.
- [310] I. Sari, T. Balkan et H. Kulah, «A wideband electromagnetic micro power generator for wireless microsystems,» chez *Solid-State Sensors, Actuators and Microsystems Conference, 2007. TRANSDUCERS 2007. International*, 2007.
- [311] C. R. Saha, T. O'donnell, N. Wang et P. McCloskey, «Electromagnetic generator for harvesting energy from human motion,» *Sensors and Actuators A: Physical*, vol. 147, pp. 248-253, 2008.
- [312] D. R. Sadoway et A. M. Mayes, «Portable Power: Advanced Rechargeable Lithium Batteries,» *MRS Bulletin*, vol. 27, p. 590-596, 2002.
- [313] S. Roundy, D. Steingart, L. Frechette, P. Wright et J. Rabaey, «Power sources for wireless sensor networks,» chez *European workshop on wireless sensor networks*, 2004.
- [314] ROCHOW, Silicon and silicones, Springer-Verlag, 1987.

- 
- [315] Rinaldi, «Loi physique de comportement des polymères amorphes et intégration dans un code éléments finis,» 2006.
- [316] C. Richards, D. Bahr, C.-G. Xu et R. Richards, «The P<sup>3</sup> Micro Power Generation System,» *ASME-PUBLICATIONS-HTD*, vol. 369, pp. 425-436, 2001.
- [317] D. R. Reyes, D. Iossifidis, P.-A. Auroux et A. Manz, «Micro total analysis systems. 1. Introduction, theory, and technology,» *Analytical chemistry*, vol. 74, pp. 2623-2636, 2002.
- [318] E. B. Qvale et J. L. Smith, «A mathematical model for steady operation of Stirling-type engines,» *Journal of Engineering for Power*, vol. 90, pp. 45-50, 1968.
- [319] J. Peirs, D. Reynaerts, F. Verplaetsen, F. Norman et S. Lefever, «Development of a micro gas turbine for electric power generation,» chez *MME 2003, The 14th MicroMechanics Europe Workshop*, 2003.
- [320] J. Peirs, D. Reynaerts et F. Verplaetsen, «A microturbine for electric power generation,» *Sensors and Actuators A: Physical*, vol. 113, pp. 86-93, 2004.
- [321] OWEN, Chemtech, 1981.
- [322] A. J. Organ, The regenerator and the Stirling engine, Mechanical Engineering Publications London, 1997.
- [323] h.-m.-a. neodyme-303.htm, «Small thin neodymium (NdFeB or Neo, Ø3 x 1,5mm) Tiny Magnets strong N52 craft disc Spider Magnetics Ltd».
- [324] S. Nakano, K. Hashimoto, T. Toriyama et S. Sugiyama, «C5-3 Design of a Reciprocating Engine for Micro Power Generator,» chez *PROCEEDINGS OF THE SENSOR SYMPOSIUM ON SENSORS MICROMACHINES AND APPLIED SYSTEMS*, 2002.
- [325] O. H. M. I. Munekazu et M. IGUCHI, «Critical Reynolds Number in an Oscillating Pipe Flow,» 1982.
- [326] S. E. Moon, S. Q. Lee, S.-k. Lee, Y.-G. Lee, Y. S. Yang, K.-H. Park et J. Kim, «Sustainable Vibration Energy Harvesting Based on Zr-Doped PMN-PT Piezoelectric Single Crystal Cantilevers,» *ETRI journal*, vol. 31, pp. 688-694, 2009.
- [327] M. McCarthy, C. M. Waits, M. I. Beyaz et R. Ghodssi, «A rotary microactuator supported on encapsulated microball bearings using an electro-pneumatic thrust balance,» *Journal of Micromechanics and Microengineering*, vol. 19, p. 094007, 2009.
- [328] W. R. Martini, «Thermodynamic design of Stirling engines by computer,» *Martini Engineering*, 1980.
- [329] H. K. Ma, B. R. Hou, H. Y. Wu, C. Y. Lin, J. J. Gao et M. C. Kou, «Development and application of a diaphragm micro-pump with piezoelectric device,» *Microsystem Technologies*, vol. 14, pp. 1001-1007, 2008.
- [330] H. Löwe, W. Ehrfeld et V. Hessel, Micromixing technology, American Institute of Chemical Engineers, 2000.
- [331] J. C. Lötters, W. Olthuis, P. H. Veltink et P. Bergveld, «The mechanical properties of the rubber elastic polymer polydimethylsiloxane for sensor applications,» *Journal of Micromechanics and Microengineering*, vol. 7, p. 145, 1997.
- [332] A. L. London, J. W. Mitchell et W. A. Sutherland, «Heat-transfer and flow-friction characteristics of crossed-rod matrices,» *Journal of Heat Transfer*, vol. 82, pp. 199-213, 1960.
- [333] J.-Q. Liu, H.-B. Fang, Z.-Y. Xu, X.-H. Mao, X.-C. Shen, D. Chen, H. Liao et B.-C. Cai, «A MEMS-based piezoelectric power generator array for vibration energy harvesting,» *Microelectronics Journal*, vol. 39, pp. 802-806, 5 2008.

- 
- [334] K. Lee, I. P. Krepchin et W. M. Toscano, «Thermodynamic description of an adiabatic second order analysis for Stirling engines,» chez *Proc., Intersoc. Energy Convers. Eng. Conf.:(United States)*, 1981.
- [335] S. Kwankaomeng, B. Silpsakoolsook et P. Savangvong, «Investigation on Stability and Performance of a Free-piston Stirling Engine,» *Energy Procedia*, vol. 52, pp. 598-609, 2014.
- [336] S. Kulkarni, S. Roy, T. O'Donnell, S. Beeby et J. Tudor, «Vibration based electromagnetic micropower generator on silicon,» *Journal of Applied Physics*, vol. 99, p. 08P511, 2006.
- [337] E. Koukharenko, S. P. Beeby, M. J. Tudor, N. M. White, T. O'Donnell, C. Saha, S. Kulkarni et S. Roy, «Microelectromechanical systems vibration powered electromagnetic generator for wireless sensor applications,» *Microsystem technologies*, vol. 12, pp. 1071-1077, 2006.
- [338] T. J. Kazmierski et S. Beeby, *Energy harvesting systems*, Springer, 2014.
- [339] S. Kaviani, M. Bahrami, A. M. Esfahani et B. Parsi, «A modeling and vibration analysis of a piezoelectric micro-pump diaphragm,» *Comptes Rendus Mécanique*, vol. 342, pp. 692-699, 2014.
- [340] G. E. M. Karniadakis, A. Beskok et M. Gad-el-Hak, «Micro flows: fundamentals and simulation,» *Applied Mechanics Reviews*, vol. 55, p. B76, 2002.
- [341] J. Kao, X. Wang, J. Warren, J. Xu et D. Attinger, «A bubble-powered micro-rotor: conception, manufacturing, assembly and characterization,» *Journal of Micromechanics and Microengineering*, vol. 17, p. 2454, 2007.
- [342] J. Kao, X. Wang, J. Warren, J. Xu et D. Attinger, «A bubble-powered micro-rotor: conception, manufacturing, assembly and characterization,» *Journal of Micromechanics and Microengineering*, vol. 17, p. 2454, 2007.
- [343] Y. Jiang, T. Fujita, M. Uehara, K. Kanda, T. Toyonaga, K. Nakade, K. Higuchi et K. Maenaka, «Fabrication and evaluation of NdFeB Microstructures for electromagnetic energy harvesting devices,» *Proc. PowerMEMS 2009 (Washington DC, USA)*, pp. 582-5, 2009.
- [344] S. A. Jacobson et A. H. Epstein, «An informal survey of power MEMS,» chez *The international symposium on micro-mechanical engineering*, 2003.
- [345] G. Hetsroni, A. Mosyak et Z. Segal, «Two-phase flow in microchannels,» *ASME-PUBLICATIONS-HTD*, vol. 369, pp. 87-94, Hetsroni2001.
- [346] M. Herz, D. Horsch, G. Wachutka, T. C. Lueth et M. Richter, «Design of ideal circular bending actuators for high performance micropumps,» *Sensors and Actuators A: Physical*, vol. 163, pp. 231-239, 2010.
- [347] HARDMAN, *Radiopaque Polymers to Safety, Volume 14, Encyclopedia of Polymer Science and Encyclopedia of Polymers, 2nd Edition*, Wiley-Interscience, 1989.
- [348] A. Harb, «Energy harvesting: State-of-the-art,» *Renewable Energy*, vol. 36, pp. 2641-2654, 2011.
- [349] K. Hamaguchi, S. Takahashi et H. Miyabe, «Pressure drop of regenerator matrix,» *Trans. JSME B*, vol. 48, pp. 2207-2216, 1982.
- [350] J. D. Hall, N. E. Apperson, B. T. Crozier, C. Xu, R. F. Richards, D. F. Bahr et C. D. Richards, «A facility for characterizing the dynamic mechanical behavior of thin membranes for microelectromechanical systems,» *Review of Scientific Instruments*, vol. 73, pp. 2067-2072, 2002.
- [351] L. G. Fréchette, C. Lee, S. Arslan et Y.-C. Liu, «Design of a microfabricated Rankine cycle steam turbine for power generation,» chez *ASME 2003 International Mechanical Engineering Congress and Exposition*, 2003.

- 
- [352] F. Formosa et J.-J. Chaillout, «Free Piston Stirling engine design using similitude theory,» *Power MEMS*, pp. 562-565, 2009.
- [353] F. Formosa, A. Badel et H. Favreliere, «Development of low frequencies insulating thick diaphragms for power MEMS applications,» *Sensors and Actuators A: Physical*, vol. 189, pp. pp 370-379, 2012.
- [354] A. R. M. Faisal, C. Hong et G.-S. Chung, «Multi-frequency electromagnetic energy harvester using a magnetic spring cantilever,» *Sensors and Actuators A: Physical*, vol. 182, pp. 106-113, 2012.
- [355] T. Finkelstein et A. J. Organ, *Air engines : the history, science, and reality of the perfect engine*, 1 éd., ASME Press, 2009.
- [356] M. Ferrari, M. Bau, M. Guizzetti et V. Ferrari, «A single-magnet nonlinear piezoelectric converter for enhanced energy harvesting from random vibrations,» *Sensors and Actuators A: Physical*, vol. 172, pp. 287-292, 2011.
- [357] G. Féliès, F. Formosa, J. Ramousse et A. Badel, «Double acting Stirling engine: Modeling, experiments and optimization,» *Applied energy*, vol. 159, pp. 350-361, 2015.
- [358] F. W. G. Fearon, *High performance polymers*, edit. R. Seymour and G. Kirsbaum, Elsevier, 1986.
- [359] M. El-Hami, P. Glynne-Jones, N. M. White, M. Hill, S. Beeby, E. James, A. D. Brown et J. N. Ross, «Design and fabrication of a new vibration-based electromechanical power generator,» *Sensors and Actuators A: Physical*, vol. 92, pp. 335-342, 2001.
- [360] M. El-Hami, P. Glynne-Jones, E. P. James, S. P. Beeby, N. M. White, A. D. Brown et M. Hill, «A new approach towards the design of a vibration-based microelectromechanical generator,» 2000.
- [361] G. R. Dochat, «Stirling space power demonstrator engine test/analytical comparison,» *Acta Astronautica*, vol. 15, pp. 341-346, 1987.
- [362] L. Condra, J. Svitak et A. Pense, «The high temperature deformation properties of gold and thermocompression bonding,» *IEEE Transactions on Parts, Hybrids, and Packaging*, vol. 11, pp. 290-296, 1975.
- [363] S. K. Chou, W. M. Yang, K. J. Chua, J. Li et K. L. Zhang, «Development of micro power generators--a review,» *Applied Energy*, vol. 88, pp. 1-16, 2011.
- [364] J. H. Cho, L. W. Weiss, C. D. Richards, D. F. Bahr et R. F. Richards, «Power production by a dynamic micro heat engine with an integrated thermal switch,» *Journal of Micromechanics and Microengineering*, vol. 17, p. S217, 2007.
- [365] J. Chen, D. Chen, T. Yuan et X. Chen, «A multi-frequency sandwich type electromagnetic vibration energy harvester,» *Applied Physics Letters*, vol. 100, p. 213509, 2012.
- [366] V. R. Challa, M. G. Prasad, Y. Shi et F. T. Fisher, «A vibration energy harvesting device with bidirectional resonance frequency tunability,» *Smart Materials and Structures*, vol. 17, p. 015035, 2008.
- [367] V. R. Challa, M. G. Prasad et F. T. Fisher, «A coupled piezoelectric--electromagnetic energy harvesting technique for achieving increased power output through damping matching,» *Smart materials and Structures*, vol. 18, p. 095029, 2009.
- [368] S. Chalasani et J. M. Conrad, «A survey of energy harvesting sources for embedded systems,» chez *IEEE SoutheastCon 2008*, 2008.
- [369] J. F. Burger, «Cryogenic microcooling,» *PhD [E hesis, University ofTwente*, 2001.

- 
- [370] A. Boudet, «Les polymeres Leurs structures et leurs proprietes».
- [371] T. K. Bose, P. Benard et A. Hourri, «HYDROGEN ENERGY FOR A CLEANER ENVIRONMENT,» *International Journal of Energy for a Clean Environment*, vol. 6, 2005.
- [372] L. Borel et D. Favrat, *Thermodynamique et énergétique*, vol. 1, PPUR presses polytechniques, 2005.
- [373] S. P. Beeby, M. J. Tudor et N. M. White, «Energy harvesting vibration sources for microsystems applications,» *Measurement science and technology*, vol. 17, p. R175, 2006.
- [374] W. T. Beale, «Free piston Stirling engines-some model tests and simulations,» 1969.
- [375] H. K. Bardaweel, M. J. Anderson, R. F. Richards et C. D. Richards, «Optimization of the dynamic and thermal performance of a resonant micro heat engine,» *Journal of Micromechanics and Microengineering*, vol. 18, p. 104014, 2008.
- [376] L. R. Arana, S. B. Schaevitz, A. J. Franz, K. F. Jensen et M. A. Schmidt, «A microfabricated suspended-tube chemical reactor for fuel processing,» chez *Micro Electro Mechanical Systems, 2002. The Fifteenth IEEE International Conference on*, 2002.
- [377] X. F. Ang, G. G. Zhang, J. Wei, Z. Chen et C. C. Wong, «Temperature and pressure dependence in thermocompression gold stud bonding,» *Thin Solid Films*, vol. 504, pp. 379-383, 2006.
- [378] B. Ando, S. Baglio, C. Trigona, N. Dumas, L. Latorre et P. Nouet, «Nonlinear mechanism in MEMS devices for energy harvesting applications,» *Journal of Micromechanics and Microengineering*, vol. 20, p. 125020, 2010.
- [379] B. Ando, S. Baglio, C. Trigona, N. Dumas, L. Latorre et P. Nouet, «Nonlinear mechanism in MEMS devices for energy harvesting applications,» *Journal of Micromechanics and Microengineering*, vol. 20, p. 125020, 2010.
- [380] S. K. Andersen, H. Carlsen et P. G. Thomsen, «Numerical study on optimal Stirling engine regenerator matrix designs taking into account the effects of matrix temperature oscillations,» *Energy Conversion and Management*, vol. 47, pp. 894-908, 2006.
- [381] W. Al-Ashtari, M. Hunstig, T. Hemsell et W. Sestro, «Frequency tuning of piezoelectric energy harvesters by magnetic force,» *Smart Materials and Structures*, vol. 21, p. 035019, 2012.
- [382] R. Akhavan, R. D. Kamm et A. H. Shapiro, «An investigation of transition to turbulence in bounded oscillatory Stokes flows Part 1. Experiments,» *Journal of Fluid Mechanics*, vol. 225, pp. 395-422, 1991.
- [383] M. Abbas, N. Said et B. Boumeddane, «Optimisation d'un moteur Stirling de type gamma,» *Revue des Energies Renouvelables*, vol. 13, pp. 1-12, 2010.
- [384] EV Group GmbH (AT) : [https://www.evgroup.com/products/bonding/permanent-bonding-systems/evg501/bonder Manuel](https://www.evgroup.com/products/bonding/permanent-bonding-systems/evg501/bonder%20Manuel).
- [385] SFT: Amelioration de l'efficacite energetique des machines Thermoacoustiques, SFT 2010, Paris.